ISSN 0044-4537

Том 83, Номер 9 Сентябрь 2009

ЖУРНАЛ ФИЗИЧЕСКОЙ ХИМИИ

http://www.naukaran.ru
http://www.maik.ru

"НАУКА"

Российская академия наук

ЖУРНАЛ ФИЗИЧЕСКОЙ ХИМИИ

том 83 № 9 2009 Сентябрь

Основан в 1930 г.
Выходит 12 раз в год
ISSN: 0044-4537

Журнал издается под руководством
Отделения химии и наук о материалах РАН

Адрес редакции: 119049 Москва, Мароновский пер., 26
тел. 8-499-238-21-88
E-mail: belenkina@maik.ru

Москва
Издательство "Наука"

СОДЕРЖАНИЕ

Том 83, номер 9, 2009

9th International Conference on Fundamental and Applied Aspects of Physical Chemistry: Physical Chemistry 2008

(Belgrade, September 24–26, 2008)

Chemical Thermodynamics and Thermochemistry

Chemical Kinetics and Catalysis

Structure of Matter and Quantum Chemistry

Physical Chemistry of Surface Phenomena

Physical Chemistry of Separation Processes. Chromatography

Colloid Chemistry and Elecrochemistry

Photochemistry and Magnetochemistry

Biophysical Chemistry

Other Problems of Physical Chemistry

Сдано в набор 18.03.2009 г. Подписано к печати 30.06.2009 г. Формат бумаги 60 × 88 1/8
Цифровая печать Усл. печ. л. 25.0 Усл. кр.-отт. 6.1 тыс. Уч.-изд. л. 25.1 Бум. л. 12.5
Тираж 240 экз. Зак. 543

Учредители: Российская академия наук

Издатель: Академиздатцентр "Наука", 117997 Москва, Профсоюзная ул., 90
Оригинал-макет подготовлен МАИК "Наука/Интерпериодика"
Отпечатано в ППП «Типография "Наука"», 121099 Москва, Шубинский пер., 6

ЖУРНАЛ ФИЗИЧЕСКОЙ ХИМИИ, 2009, том 83, № 9, с. 1605

9th INTERNATIONAL CONFERENCE ON FUNDAMENTAL AND APPLIED ASPECTS OF PHYSICAL CHEMISTRY: PHYSICAL CHEMISTRY 2008 (BELGRADE, SEPTEMBER 24–26, 2008)

В сентябре 2008 г. в Белграде состоялась очередная Международная конференция по фундаментальным и прикладным аспектам физической химии, организованная Обществом физикохимиков Сербии при участии Института катализа Болгарской академии наук, Сибирского отделения Российской академии наук, факультета физической химии Белградского университета, Белградского института химии, технологии и металлургии, а также Белградского института общей и физической химии. Председателем оргкомитета конференции был проф. Слободан Анич (S. Anić), а программный комитет возглавляла Анкица Антич-Йованович (A. Antić-Jovanović).

На конференции был представлен широкий спектр докладов по различным направлениям физической химии и физико-химическим аспектам смежных наук. Доклады, посвященные проблемам химической кинетики и катализа, представляли работы по экспериментальному изучению кинетики конкретных химических реакций, по кинетике адсорбции, кинетике реакций во внешних полях, текстуре и свойствам поверхности различных катализаторов, в том числе поверхности носителей для нанесенных катализаторов, по использованию нанотехнологий при приготовлении катализаторов и по ряду других направлений. На отдельной секции были представлены работы по изучению электрохимических реакций в растворах и электрохимического поведения поверхности катализаторов.

К этим работам тесно примыкают работы по нелинейной динамике химических реакций, анализу временных последовательностей в спектрах колебательных реакций, изучению влияния коротковолнового и микроволнового излучения, катализаторов и температуры на кинетику колебательных реакций.

Работы по спектроскопии и молекулярной структуре были связаны как непосредственно с интерпретацией спектроскопических данных на основе представлений о структуре соединений и межмолекулярных взаимодействиях, так и с теоретической разработкой методов анализа таких данных.

Большое число работ было представлено по биофизической химии, фотохимии и радиационной химии. В частности, можно упомянуть работы по изучению активности и ингибирования ферментов, по анализу самосборки амилоидных структур, моделированию биомембран, по использованию различных физико-химических методов при анализе фото- и биохимических реакций и активности различных катализаторов в таких реакциях. На отдельных секционных заседаниях были заслушаны доклады по адсорбции и поверхностным явлениям, по физической химии полимеров, радиохимии и защите окружающей среды, по физико-химическим аспектам наук о материалах и комплексных соединениях.

В данном номере "Журнала физической химии" представлена лишь небольшая часть сообщений, заслушанных на конференции. Краткое изложение всей совокупности материалов конференции дано в "Physical Chemistry. Proceedings of the 9th International Conference on Fundamental and Applied Aspects of Physical Chemistry", September 24–26, 2008, Vol. 1, 2. Belgrade, Serbia.

Председатель международного оргкомитета Конференции Слободан Анич

Председатель программного комитета Анкица Антич-Йованович

Вице-председатель локального оргкомитета Желько Чупич

Заместитель главного редактора "Журнала физической химии" Н.Ф. Степанов

ЖУРНАЛ ФИЗИЧЕСКОЙ ХИМИИ, 2009, том 83, № 9, с. 1606–1611

CHEMICAL THERMODYNAMICS AND THERMOCHEMISTRY

УДК 536.7

ENTHALPY OF FORMATION OF ACYCLIC SATURATED KETONES

© 2009 S. Marković, A. Despotović, D. Jovanović, I. Đurović

Faculty of Science, University of Kragujevac, Serbia

E-mail: mark@kg.ac.yu

Abstract – The dependences of $\Delta_f H$ on the size of molecule, position of carbonyl group, and branching of molecule are investigated at the PM5 level of theory. The major part of $\Delta_f H$ is determined with the size of molecule, whereas fine structure of $\Delta_f H$ is determined with the branching of molecule and position of carbonyl group.

INTRODUCTION

Enthalpy of formation ($\Delta_f H$) is an important physico-chemical property of substances, from which one can calculate enthalpies of reactions before performing experiments. Like many other properties, enthalpy of formation is dependent on molecular structure. This is illustrated with Fig. 1, where a plot of $\Delta_f H$ versus the number of carbon atoms n of 2-ketones is presented. The dependence of $\Delta_f H$ on the size of molecule is obviously linear, where only the value for 2-octanone deviates from linearity (the correlation coeffitient for this straight line where 2-octanone is excluded from consideration is equal to –0.99997).

It is well-known that boiling points of ketones are influenced by the position of carbonyl group within a molecule. One can suppose that enthalpy of formation of ketones also depends on the position of carbonyl group, and perhaps on some other structural details. To examine the dependence of enthalpy of formation of ketones on molecular structure it is necessary to calculate the values for those ketones for which the experimental enthalpies are not available.

In the past decade, accurate prediction of the enthalpies of formation of gas-phase molecules has been achieved via high level quantum chemistry methods. For more information on the applications of quantum chemical calculations to thermochemical quantities a reader is referred to the review [1]. and the references given therein. As for ketones, the G2 ab initio approach was applied to calculate enthalpies of formation of cyclopropenone, cyclopropanone, and acetone [2]. Similar methodologies have not been employed in calculation of $\Delta_f H$ values of larger ketones.

To examine the dependence of $\Delta_f H$ of ketones on molecular structure, molecules of interest are much larger than those that can be studied by means of G2 and G3 theories. Thus, computational methods that are less CPU demanding are necessary. Bond and group additivity approaches based on an empirical experimental data set have been widely used in estimating enthalpies of formation. A combined HF/6-31* – empirical scheme for calculating enthalpies of formation of carbonyl compounds was developed [3]. In addition, molecular mechanics MM3 and MM4 calculations of the enthalpies of formation for about 50 open chain, ring, and fused ring carbonyl compounds were performed [4]. The MM4 calculated enthalpies of formation showed improvement over those of MM3.

In some cases, the disagreement between the experimental and calculated values (using either the bond and group equivalent scheme or molecular mechanics methods) was observed [3, 4]. It was concluded that the experimental enthalpies of formation of some carbonyl compounds (e.g. cycloheptanone and norbornanones) were seriously in error.

There is an ever growing demand for semiempirical methods, especially for investigations of larger molecular systems, where *ab initio* and density functional theory are not suitable. In the Parametric Method 5 (PM5) a new parameter set, called PM5, has been added [5]. Parameters are available for all non-radioactive main-group elements, Zn, Cd, and Hg. It is supposed that the average accuracy for enthalpies of formation over all parameterized elements is improved

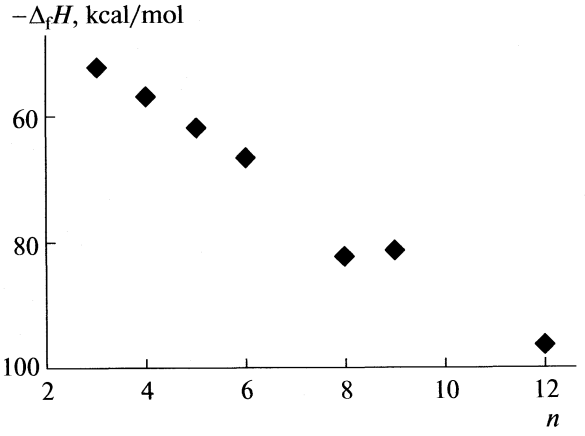

Fig. 1. Experimental enthalpy of formation of 2-ketones versus number of carbon atoms.

by approximately a factor of four, compared to the AM1 and PM3 parameterizations [5].

PM5 was successfully applied in the investigations of the Schiff base of gossypol with 3,6-dioxadecylamine [6]. Monensial A allyl ester and its complexes [7]. Oligomycin A complex structures with some divalent metal cations [8]., calculation of molecular hyperpolarizability of fluorenyl molecular system [9], etc. On the other hand, the presumed PM5 superior performance against AM1 and PM3 was not observed for the stilbene structures [10].

The main goal of this work is to investigate the dependence of the enthalpy of formation of ketones on molecular structure (i.e. the size of molecule n, position of carbonyl group c, and branching of molecule b) by means of PM5.

COMPUTATIONAL PROCEDURES

The calculation of the enthalpies of formation of ketones is complicated with the fact that a ketone molecule can adopt more than one conformation, where each conformation has its own enthalpy. Therefore, to determine the enthalpy of formation of a ketone, it is necessary to construct all its conformations, calculate the enthalpy of formation of each single conformer, and finally, calculate $\Delta_f H$ of the ketone using the formula [11]:

$$\Delta_f H = \sum_i N_i (\Delta_f H)_i, \qquad (1)$$

where $(\Delta_f H)_i$ and N_i represent the enthalpy of formation and mole fraction of the ith conformer, and N_i is given by the formula:

$$N_i + \sum_{j \neq i} N_i / \exp \frac{(\Delta_f H)_j - (\Delta_f H)_i}{RT} = 1. \qquad (2)$$

Program package Spartan'02 provides facilities for carrying out conformational search at the semiempirical levels of theory [12]. Thus, Spartan'02 is used to construct a series of low-energy conformers for each ketone molecule under investigation, at the PM3 level of theory. The geometries of all molecular structures correspond to the energy minima in a vacuum. Only conformers within 10 kcal mol^{-1} of the global minimum are kept. Maximum number of conformers is set to 100. This implies that, in those cases where a ketone molecule can adopt less than 100 conformations, all conformers are taken into account; and, in those cases where a ketone molecule can adopt more than 100 conformations, the program attempts to select the most diverse set of 100 conformers, representing the entire population.

The so obtained structures are used as input geometries for the program package CAChe 6.01 13, which enables calculation of the enthalpies of formation employing PM5 Hamiltonian. In this way a series of the PM5 enthalpy values is formed for each ketone.

The enthalpies of formation for all investigated ketones are computed using Eqs (1) and (2), at the PM5 levels of theory.

Note that CAChe 6.01 does not provide facilities for performing conformational search at quantum mechanical level. In this way, the programs Spartan and CAChe are combined to obtain PM5 enthalpies of formation using the PM3 geometries of the ketones conformers.

RESULTS AND DISCUSSION

Following the above described procedure, the $\Delta_f H$ values for 30 saturated acyclic ketones are calculated employing PM5 Hamiltonian. This set embraces all ketones for which the experimental gas phase values for $\Delta_f H$ are available in literature [14, 15]. In Fig. 2 the calculated conformers of some ketones are presented. Our calculations show that acetone has C_{2v} symmetry, where the methyl hydrogen eclipses the carbonyl oxygen. Our findings are in agreement with the results of microwave spectroscopy [16, 17] and the electron diffraction method [18] concerning the structure of acetone. Spartan creates a set consisting of 3 conformers for 2-butanone: two gauche and one eclipsed conformations (structures 1–3 in Fig. 2). PM5 calculation favors eclipsed conformation. Experimental methods, like microwave spectroscopy [19], electron diffraction [20], and Raman spectroscopy confirm that the eclipsed form is the most stable conformation of 2-butanone. Structures 4–11 in Fig. 2 represent the conformations of 2-pentanone. Similarly to 2-butanone, PM5 predicts that the eclipsed form (structure 4) is the most stable conformation of 2-pentanone. As for 2,4-dimethyl-3-pentanone, a gas-phase electron diffraction study revealed three conformers of this compound with symmetries C_1, C_2, and C_s, with the first being the most stable [21]. Our investigation also reveals one conformer with C_2 symmetry (structure 12 in Fig. 2), one conformer with C_s symmetry (structure 16), and six conformers with C_1 symmetry (structures 13–15, and 17–19). PM5 favors conformers 12 and 13 (with C_2 and C_1 symmetries) having almost identical $\Delta_f H$ values. Conformers 17–19 can be neglected, since their mole fractions are lower than 1%. Thus, there are two major conformations with C_1 symmetry: 13 and 14. The mole fractions of the conformers with C_1, C_2, and C_s symmetries amount to 63, 30, and 7%, respectively. The PM5 calculated mole fractions agree well with the quantum mechanical [21]. and molecular mechanical calculations [3, 4], but not as well with the experimental results [21].

Table 1 collects the experimental and PM5 values for $\Delta_f H$ of investigated ketones. The average relative error is equal to 2.5%, whereas the correlation coefficient amounts to 0.990.

It is noticeable that the experimental $\Delta_f H$ for 2-octanone significantly deviates from linearity (Fig. 1). It is very difficult to account for any physico-chemical

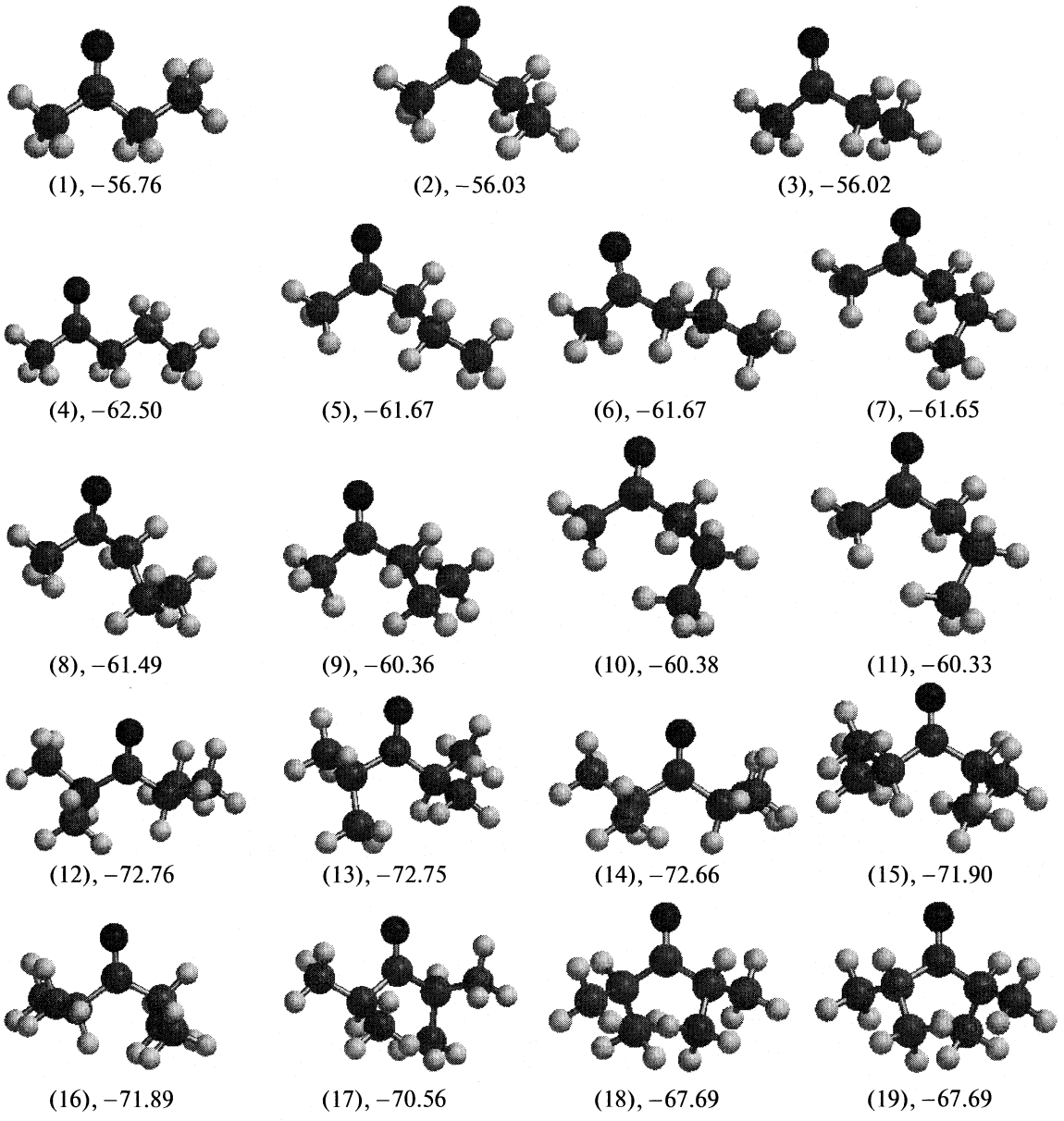

Fig. 2. Conformers and their PM5 $\Delta_f H$ values in kcal/mol for 2-butanone (structures 1–3), 2-pentanone (4–11), and 2,4-dimethyl-3-pentanone (12–19).

reason for such occurrence. It is reasonable to decide that the experimental $\Delta_f H$ for 2-octanone is in error. It will be shown later that the major part of the enthalpy of formation of ketones is determined by the size of molecule. In agreement with this, the experimental values of octanones are mutually very similar (Table 1). Thus, one can conclude that a systematic error was included while determining the experimental $\Delta_f H$ values of all unbranched octanones. It is worth noting that octanones were not included either in the set of carbonyl compounds used to evaluate the increments [3], or for optimizing the enthalpy of formation parameters [4]. If only unbranched ketones are considered, and octanones are excluded from consideration, the average relative error and correlation coefficient for the PM5 approximation amount to 1.0% and 0.9990, respectively. It should be pointed out that several of these molecules can adopt more than 100 conformations, and their PM5 enthalpies are calculated on the basis of representative sets consisting of 100 conformers, created by Spartan'02.

As for branched ketones, the average relative error and correlation coefficient amount to 2.8% and 0.996, respectively. The relative errors of branched ketones are generally higher than those of unbranched ketones. Note than none of the branched ketones can addopt more than 100 conformations, implying that all possible conformers for each ketone are taken into

Table 1. Experimental (Exp) and PM5 enthalpies of formation ($-\Delta_f H$, kcal/mol, RE denotes relative error)

Ketone	Exp	PM5	RE
2-Propanone	52.23	51.56	1.3
2-Butanone	57.02	56.49	0.9
2-Pentanone	61.91	62.01	0.2
3-Pentanone	60.60	61.79	2.0
2-Hexanone	66.87	67.47	0.9
3-Hexanone	66.50	67.28	1.2
4-Heptanone	71.30	72.87	2.2
2-Octanone	82.47	78.20	5.2
3-Octanone	80.93	78.12	3.5
4-Octanone	83.49	78.09	6.5
2-Nonanone	81.45	81.79	0.4
5-Nonanone	82.44	82.94	0.6
6-Undecanone	92.59	92.01	0.6
2-Dodecanone	96.62	98.85	1.3
3-Methyl-2-butanone	62.76	62.15	1.0
3,3-Dimethyl-2-butanone	69.47	67.49	2.8
3-Methyl-2-pentanone	67.90	67.43	0.7
4-Methyl-2-pentanone	69.60	68.10	2.2
2-Methyl-3-pentanone	68.40	67.29	1.6
3,3-Dimethyl-2-pentanone	72.60	72.03	0.8
4,4-Dimethyl-2-pentanone	76.60	73.62	3.9
2,2-Dimethyl-3-pentanone	75.00	72.65	3.1
2,4-Dimethyl-3-pentanone	74.40	72.57	2.5
3,3,4-Trimethyl-2-pentanone	78.50	76.23	2.9
2,2,4-Trimethyl-3-pentanone	80.86	77.76	3.8
3,3,4,4-Tetramethyl-2-pentanone	83.10	79.11	4.8
2,2,4,4-Tetramethyl-3-pentanone	82.65	77.58	6.1
2,6-Dimethyl-4-heptanone	85.49	84.49	1.2
2,2,5,5-Tetramethyl-3-hexanone	94.14	88.70	5.8
2,2,6,6-Tetramethyl-4-heptanone	100.70	95.30	5.4

Note. 2-nonanone, 2-dodecanone, 2-, 3- and 4-octanone not investigated in Refs [3, 4].

account. This fact indicates that construction of representative sets cannot be a reason for deviation of PM5 values from experimental values.

It can be concluded that PM5 reproduces $\Delta_f H$ of saturated ketones with reasonably high accuracy, and successfully predicts the structure of the most stable conformation. In the further investigation PM5 is used to predict $\Delta_f H$ of numerous unbranched and branched ketones.

Dependence of $\Delta_f H$ on Molecular Structure of Ketones

The dependences of $\Delta_f H$ on the size of molecule n (number of carbon atoms), position of carbonyl group c, and branching of molecule b (number of methyl substituents) are considered. When the dependence of $\Delta_f H$ on a certain structural feature is examined, the other two are kept constant. It is expected that the influence of all structural features can be better expressed in this manner, because a smaller influence of some structural property is protected from possible screening by a much larger influence of another structural property.

$\Delta_f H$ values are calculated for all unbranched ketones up to $n = 11$ (Tables 1 and 2). In agreement with the experimental results (Fig. 1), $\Delta_f H$ of ketones decreases with the increasing size of molecule by approximately 5 kcal/mol per methylene group. The dependence of $\Delta_f H$ on n is linear. The correlation coefficients for the homologous series of 2-, 3-, and 4-ketones are equal to −0.9993, −0.995, and −0.995, respectively.

The dependence of $\Delta_f H$ on c is examined in the series of unbranched isomers where $n = 7–11$. For example, when this dependence is investigated for $n = 8$, then the $\Delta_f H$ values of 2-, 3-, and 4-octanones are mutually compared. Tables 1 and 2 show that the influence of the position of carbonyl group is smaller than that of the size of molecule. For lower values of n (i.e. $n \leq 8$) the $\Delta_f H$ values in a series of isomers differ by no more than 0.2 kcal/mol. For $n \geq 9$ the differences among the $\Delta_f H$ values of the members of isomeric ketones become more pronounced, but do not exceed

Table 2. $\Delta_f H$ values in kcal/mol of investigated ketones whose experimental values are not available in literature, calculated using PM5

Ketone	$-\Delta_f H$	Ketone	$-\Delta_f H$	Ketone	$-\Delta_f H$
2-Heptanone	72.85	4-Decanone	85.18	3-Methyl-2-hexanone	72.75
3-Heptanone	72.79	5-Decanone	85.70	4-Methyl-2-hexanone	72.73
3-Nonanone	81.13	2-Undecanone	91.49	5-Methyl-2-hexanone	73.08
4-Nonanone	81.54	3-Undecanone	89.83	2-Methyl-3-hexanone	72.81
2-Decanone	87.38	4-Undecanone	90.78	4-Methyl-3-hexanone	72.69
3-Decanone	84.49	5-Undecanone	90.80	5-Methyl-3-hexanone	73.21
				3,4-Dimethyl-2-pentanone	72.69

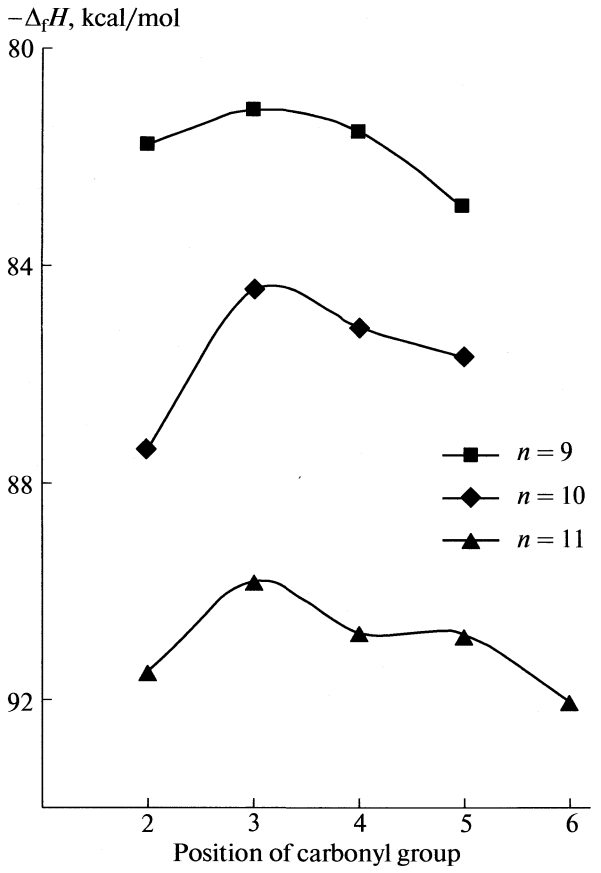

Fig. 3. Dependence of the enthalpy of formation on the position of carbonyl group for the unbranched nonanones ($n = 9$), decanones ($n = 10$), and undecanones ($n = 11$).

2 kcal/mol. Fig. 3 illustrates the influence of c upon $\Delta_f H$ of higher isomeric ketones.

In each examined series of isomeric ketones the $\Delta_f H$ value of 3-ketone is higher than that of 2-ketone (Tables 1 and 2, Fig. 3). As the carbonyl group is further shifted towards the middle of a molecule, enthalpy of formation decreases. In case of decanones, where n is even number, 2-decanone exhibits the lowest $\Delta_f H$ value. In case of nonanones and undecanones, where n is odd number, the lowest $\Delta_f H$ values are associated with 5-nonanone and 6-undecanone, respectively. This occurence can be a consequence of a possibility that $((n + 1)/2))$-ketones (where n is odd number) adopt conformations with C_{2v} symmetry. It is worth pointing out that there are experimental results for 4-heptanone, 2-nonanone, 5-nonanone (5-nonanone is more stable), 6-undecanone, and 2-dodecanone. Our findings are apparently in perfect accord with the experimental results on $\Delta_f H$ of acyclic saturated ketones. An interesting feature of Fig. 3 is that the $\Delta_f H$ values of 4- and 5-undecanones are mutually very similar. We suppose that larger ketones will also exhibit this behavior, implying that, in cases where carbonyl group is sufficiently separated from the end and middle of the molecule, enthalpy of formation becomes indipendent of c.

To investigate the dependence of $\Delta_f H$ on b, all unbranched and branched heptanones ($b = 0$–2) are examined. The results of this investigation are presented in Tables 1 and 2. One or two α methyl groups, relative to carbonyl group, contribute to the enthalpy of formation elevation. This is probably a consequence of steric hindrance caused with the vicinity of carbonyl and methyl groups. When methyl groups are not in α positions the $\Delta_f H$ values are in most cases lowered in comparison to those where $b = 0$.

The difference between the lowest and highest $\Delta_f H$ value (for 4,4-dimethyl-2-pentanone and 3,3-dimethyl-2-pentanone, respectively) amounts approximately 1.6 kcal/mol. It is noticeable that this value is lower than the differences between the $\Delta_f H$ values of 2-octanone and 3,3,4-trimethyl-2-pentanone of 2 kcal/mol (Table 1); and, 2-nonanone and 3,3,4,4-tetramethyl-2-pentanone of 2.7 kcal/mol. It can be supposed, on the basis of these facts, that the influence of the branching of molecule is stronger in case of larger molecules, where there is larger number of distinguished isomers, and b can take larger values.

ACKNOWLEDGMENTS

This work is supported by the Ministry of Science and Environment of Serbia, project № 142025.

REFERENCES

1. W. M. F. Fabian, Monatsh. Chem. **139**, 309 (2008).
2. D. W. Rogers, F. J. McLafferty and A. V. Podosenin, J. Org. Chem. **63**, 7319 (1998).
3. L. R. Schmitz, I. Motoc, C. Bender, J. K. Labanowski and N. L. Allinger, J. Phys. Org. Chem. **5**, 225 (1992).
4. C. H. Langley, J. Lii, N.L. Allinger, J. Comput. Chem. **22**, 1476 (2001).
5. J. J. P. Stewart, MOPAC 2002, Fujitsu L. td, Tokyo, Japan (2002).
6. P. Przybylski, W. Lewandowska, B. Brzezinski and F. Bartl, J. Mol. Struct. **797**, 92 (2006).
7. A. Huczyjski, D. Michalak, P. Przybylski, B. Brzezinski and F. Bartl, J. Mol. Struct. **828**, 130 (2007).
8. P. Przybylski, B. Brzezinski and F. Bartl, J. Mol. Struct. **830**, 58 (2007).
9. K. M. Nalin de Silva, J. Mol. Struct. (Theochem) **725**, 243 (2005).
10. R. Vendrame, V. R. Coluci and D. S. Galvão, J. Mol. Struct. (Theochem) **686**, 103 (2004).

11. W. J. Hehre, A. J. Shusterman and J. E. Nelson, The Molecular Modeling Workbook for Organic Chemistry, Wavefunction Inc., Irvine, 1998.
12. Spartan'02, Wavefunction, Inc., Irvine, CA.
13. CaChe 6.01, Fujitsu Limited, Tokyo, Japan.
14. J. D. Cox and G. Pilcher, Thermochemistry of Organic and Organometallic Compounds, Academic Press, London, New York 1970.
15. J. D. Pedley, R.D. Naylor and S.P. Kirby, Thermochemical Data of Organic Compounds, 2nd ed. Chapman and Hall, London, 1986.
16. J. D. Swalen, C. C. Costain, J. Chem. Phys. **31**, 1562 (1959).
17. T. Iyma, M. Kimura, Bull. Chem. Soc. Jpn. **42**, 2159 (1969).
18. C. Kato, S. Konaka, T. Iijima, M. Kimura, Bull. Chem. Soc. Jpn. **42**, 2148 (1969).
19. L. Pierce, C.K. Chang, M. Hayashi, R. Nelson, J. Mol. Spectrosc. **5**, 449 (1969).
20. M. Abe, K. Kuchitsu, T. Shimanouchi, J. Mol. Struct. **4**, 245 (1969).
21. H. Takeuchi, T. Sakurai, K. Takeshita, K. Fukushi, S. Konaka, J. Phys. Chem. **94**, 1793 (1990).

ЖУРНАЛ ФИЗИЧЕСКОЙ ХИМИИ, 2009, том 83, № 9, с. 1612–1617

CHEMICAL KINETICS AND CATALYSIS

УДК 541.128

CHARACTERISATION OF DOUBLE OXIDE SYSTEM Cu–Cr–O SUPPORTED ON γ-Al_2O_3

© 2009 Z. Cherkezova-Zheleva*, H. Kolev*, J. Krstić**, D. Dimitrov***, K. Ivanov***, D. Loncarević**, D. Jovanović**, I. Mitov*

*Institute of Catalysis, Bulgarian Academy of Sciences, Acad. G. Bonchev St., Block 11, 1113 Sofia, Bulgaria

**ICh TM-Center of Catalysis, Njegoševa 12, 11000 Belgrade, Serbia

***Agricultural University, 4000 Plovdiv, Bulgaria

E-mail: zzhel@ic.bas.bg

Abstract – Series of alumina supported chromium–copper catalysts were prepared by co-impregnation method. The samples were characterized by X-ray diffraction, X-ray photoelectron spectroscopy and UV-visible diffuse reflectance spectroscopy. Dispersion and porosity was also obtained. The experimental and catalytic test results have drawn a conclusion that an interaction between copper and chromium ions takes place. This interaction is responsible for the enhanced catalytic activity of studied catalysts in reaction of total oxidation of industrial formaldehyde production exhaust gas, which contains CO, dimethyl ether and methanol as main components.

INTRODUCTION

The industrial formaldehyde production all over the world produce huge amount of dusts and exhaust gases. Therefore their complete oxidation is of high importance for environmental protection. In catalytic studies, much attention is paid to systems containing two different oxide phases deposited on the support in order to obtain enhanced catalytic activity and lower catalyst deactivation – phase stability, absence of agglomeration, etc. [1–3]. Interaction between two oxide phases may lead to changes in the surface structure and modification of their catalytic properties in comparison to the systems containing such oxides separately. The type of interaction between supported oxides and the structure of the material formed depend on the chemical and crystallochemical properties of each component.

Thus, we considered it interesting to follow the changes in the surface structure of the system containing CuO and Cr_2O_3 supported on γ-Al_2O_3 and make an attempt to correlate the appearing surface species with catalytic activity.

EXPERIMENTAL

Sample Preparation

Series of copper–chromium oxide catalysts were prepared by co-impregnation method [4, 5]. The samples were obtained by mixing of support γ-Al_2O_3 with an aqueous solution of chromium anhydride and copper nitrate. The amount of solution taken was sufficient for incipient wetness to be observed. The samples were calcinated at different temperatures: sample 1 – 300°C, sample 2 – 500°C; sample 3 – 700°C; sample 4 – 800°C; sample 5 – 500°C (triple impregnated).

Sample Characterization

The phase composition, structure and dispersity of the samples was determined by N_2 physisorption, X-ray diffraction (XRD), X-ray photoelectron spectroscopy (XPS) and Diffuse reflectance UV- visible (UV-VIS) measurements.

A Sorptomatic 1990 (Thermo Finningen) was used to determined nitrogen physisorption isotherms at 77K. Appropriate software – WinADP 5.1 was used to determinate textural parameters: specific surface area (S_{BET}), micropore volume (V_{mic}) and mesopore volume (V_{mes}).

XRD patterns were obtained on TUR M62 apparatus, HZG-4 goniometer with Bregg-Brentano geometry, CoK_α radiation and Fe filter. JCPDF data base was used for the phase identification [6].

XPS was carried out using ESCALAB MkII (VG Scientific) electron spectrometer at a base pressure in the analysis chamber of 5×10^{-10} mbar (during the measurement 1×10^{-8} mbar), using MgK_α X-ray source (excitation energy $h\nu = 1253.6$ eV) (AlK_α X-ray source (excitation energy $h\nu = 1486.6$ eV)). The pass energy of the semispherical analyzer was 20 eV (because of its small signal for Cu2*p* and Cr2*p* 50 eV pass energy was used), 6 mm slit widths (entrance/exit). The instrumental resolution measured at the full width at a half maximum (FWHM) of the Ag3$d_{5/2}$, photoelectron peak is 1 eV. The energy scale is corrected to the C1*s* peak maximum at 285 eV for electrostatic

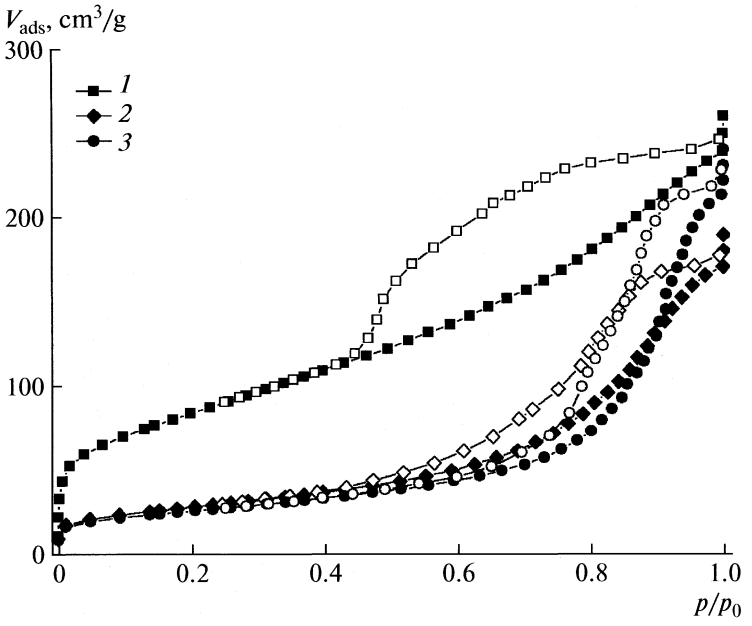

Fig. 1. Adsorption isotherms of (*1*) γ-Al_2O_3, (*2*) sample 2 and (*3*) sample 3 (empty symbols correspond to desorption data and solid to adsorption data).

charging. The fitting of the recorded XPS spectra was performed, using a symmetrical Gaussian–Lorentzian curve fitting after Shirley-type [7] subtraction of the background.

Diffuse reflectance UV-VIS spectra were recorded using a Nicolet Evolution 500 spectrometer with a diffuse reflectance accessory using white reference standard. Reflectance (*R*) data were converted to pseudo-absorbance $f(R)$ using the Kubelka – Munk equation. Samples were ground, heated overnight at 110°C, and then scanned from 200 to 850 nm.

Catalytic activity tests

The catalytic behavior of samples was studied in the pilot plant, which includes the following equipment: (i) flow-line equipment with isothermal reactor, allowing precise control of methanol oxidation parameters, including the amount of by-products fabrication, and (ii) flow-line equipment with an adiabatic reactor for additional deep oxidation of the outlet gases, which includes CO, dimethyl ether (DME) and methanol. An industrial iron – molybdenum catalyst, produced by Neochim S.A. [4] was used in the first reactor. Alumina supported $CuO–Cr_2O_3$ catalyst with 10% active component was used in the second reactor. The pilot plant reaction conditions were kept to be the same as those in the industrial reactor. The temperature in the first reactor was retained in the range 300–320°C, which ensured the same methanol, CO and DME concentrations in the pilot plant outlet gas as those in the industrial reactor. The reactant and product gases were analyzed for methanol and DME by an on-line gas chromatograph, equipped with flame-ionization detector and Porapak Q column. Second gas chromatograph, equipped with a thermal conductivity detector MS–13X and Porapak Q columns was used for CO, CO_2, O_2 and N_2 determination.

RESULTS AND DISCUSSION

Nitrogen adsorption–desorption isotherms of support and two chosen samples (assigned sample 2 and sample 3) are given on Fig. 1. Even all three isotherms can be classified as same type (according to IUPAC nomenclature isotherm type IV) there are obvious differences between intensity of hysteresis loop for starting support and samples prepared by co-impregnation method. Clearly, applied procedure caused some changes of textural parameters. Samples 2 and 3 additionally show considerable differences in total N_2 adsorbed volume, which points out the influence of temperature of calcinations on textural characteristic of obtained samples.

Textural properties of the support (γ-Al_2O_3) and samples 2 and 3

Sample	S_{BET}, m^2/g	V_{mic}, cm^3/g	V_{mes}, cm^3/g
γ-Al_2O_3	305.7	0.119	0.370
Sample 2	102.2	0.038	0.282
Sample 3	92.8	0.035	0.346

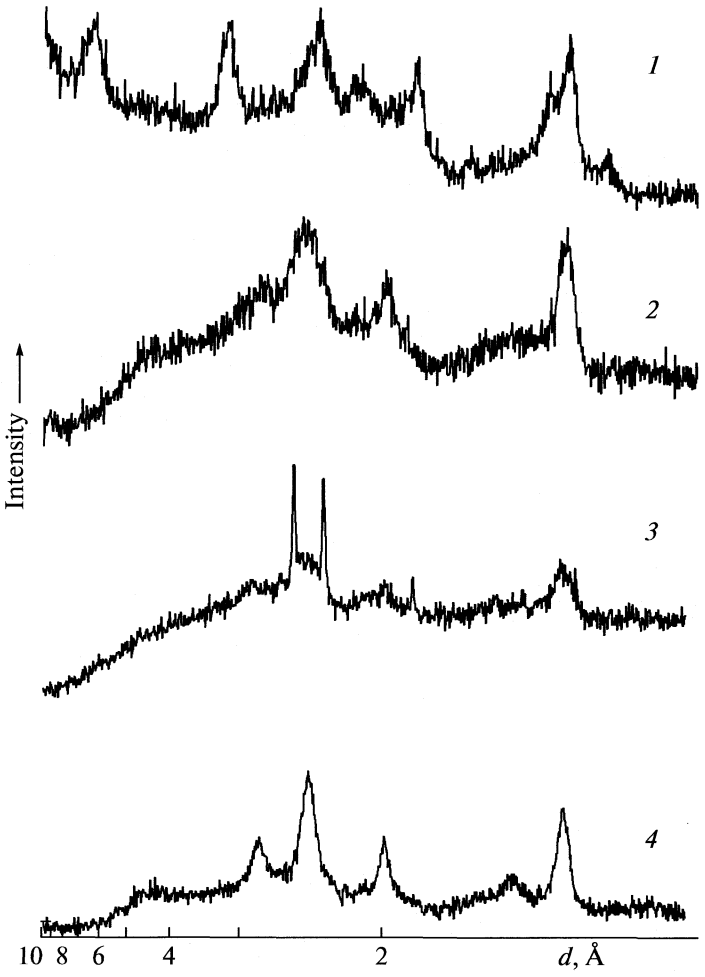

Fig. 2. Powder XRD patterns of studied samples: (*1*) – support, (*2*) – sample 1, (*3*) – sample 4 and (*4*) – sample 5.

Results of corresponding calculated values S_{BET}, V_{mic} and V_{mes} are present in table. Decrease of specific surface area for any of two chosen samples is adequate to decrease of V_{mic} (1/3 of starting micropore volume for the support), showing that decrease of S_{BET} value indubitable originates from partial blocking of micropores system initially presented in support. Further, change of mesopore volume indicates that deposition of added copper–chromium species is presented in this pore segment, which causes change of pores shape, perceived through change of hysteresis shape. Higher temperature of calcinations opened system of mesopores (but not system of micropores) contributing in difference of total adsorbed volume of N_2 for samples 2 and 3.

The XRD patterns of studied samples showed the presence of broadened and low intensity diffraction lines. The pattern of the support is exposed on Fig. 2(*1*). It was registered aluminum hydroxide phase – α-AlOOH [6] beside of main crystalline phase – γ-Al_2O_3 [6]. The registered spectra of some more representative samples are shown on Fig. 2 (*2–4*). It can be seen that diffractograms of double oxide Cu–Cr–O supported on γ-Al_2O_3 samples (Fig. 2 (*2–4*)) include mainly characteristic pattern of the support, as well as broadened lines of low intensity, belonging to highly dispersed phases. The reasons of this are the small crystallite size, as well as low crystallinity degree of supported phases, which complicated the exact phase analysis. The aluminum hydroxide phase was not registered in the XRD patterns after thermal treatment. The obtained supported phases are Cu and Cr single oxide phases in sample 2 – CuO/CuO_2 and CrO_3/Cr_2O_3 (Fig. 2 (*2*)) [6]. The crystallinity of supported phases slowly increased, some agglomeration occurs and mixed Cu-Cr oxide phases (as $CuCr_2O_4$, $Cu_2Cr_2O_4$ and $CuCrO_4$) are obtained with an increase of thermal treatment temperature (Fig. 2 (*3*, *4*)). There are no evidences of supported Cu-Cr oxides and alumina support interaction.

We have also characterized the samples by XPS. The obtained spectra showed that the intensity of the satellite of the Cu2*p* peek increases from samples 1 to

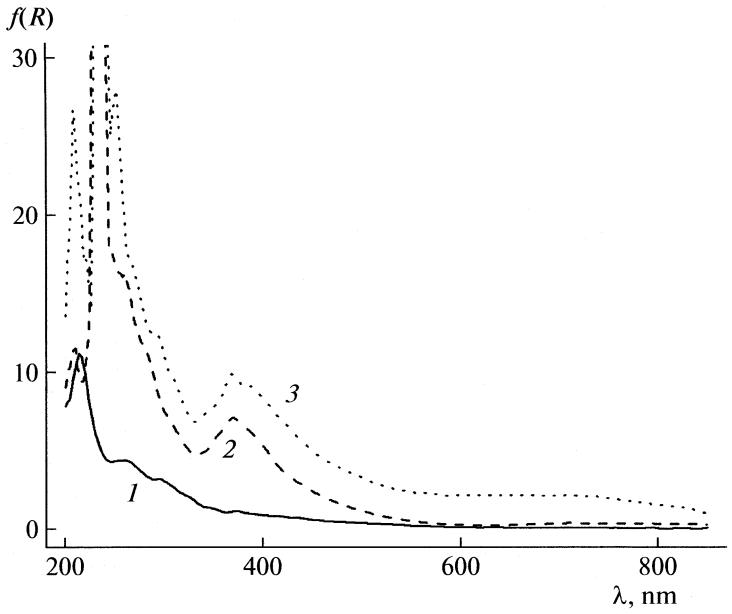

Fig. 3. Diffuse reflectance spectra of some studied samples (*1*) γ-Al_2O_3, (*2*) sample 2 and (*3*) sample 3.

5. This means that oxidation state of copper changes from Cu^+ to mixture of Cu^+ and Cu^{2+}. The established $Cu^+/(Cu^+ + Cu^{2+})$ ratio is as follow: for sample 1 – 1, sample 2 – 0.85, sample 3 – 0.67, sample 4 – 0.25 and sample 5 – 0.47 (triple impregnated). These values are in very good agreement with XRD analysis. They clearly show the increasing of mixed Cu–Cr oxides formation with an increase of treatment temperature, besides the presence of single oxide phases at low calcination temperature. The peek form and FWHM of Cr2*p* show that the chromium exists in two oxidation states (Cr^{3+} and Cr^{6+}). The intensity of the Cr^{6+} peek decreases from samples 1 to 5, i.e., with the temperature increase. Thus, the oxidation of chromium ions takes place.

The diffuse reflectance spectra of studied samples are recorded in the 200–850 nm range (Fig. 3). Two intense bands are observed at 270 and 370 nm. These bands are generally assigned to $O^{2-} \longrightarrow Cr^{6+}$ charge transfer transitions for chromate species. Broad peaks centered at 460 and 600 nm, similar to those of solid Cr_2O_3 are not observed [8].

Figure 4 presents the temperature dependence of CO, DME and methanol conversion in total oxidation on the optimal catalyst – studied sample 2 (calcinated at 500°C) in the temperature interval of 180–320°C. The obtained results clearly show that the catalyst activity is very different depending on the type of outlet gas compounds. Notwithstanding the low concentration of methanol in outlet gas, its remarkable oxidation begins at temperatures, significantly lower than 180°C and its conversion is 100% at about 190°C for all studied catalysts. But their activity in respect to the oxidation of CO and DME is considerably different. CO oxidation at the mentioned conditions is significantly higher than this of DME oxidation. The oxidation of both compounds was not complete even at 300°C. Comparing catalytic features of the samples, it can be concluded, that increasing of thermal treatment temperature slightly decreases conversion degree for the studied reagents. Probably it's due to the surface area decreasing, pore blocking and partial agglomeration of active phases.

Cu2*p* and Cr2*p* X-ray photoelectron spectra obtained for sample 2 (calcinated at 500°C) are shown in Fig. 5. The numbers *1*, *2*, *3* and *4*, nearby the Cu2*p* and Cr2*p* lines represents the spectra measured for fresh sample at the surface, used sample at the surface, the bulk of the fresh sample and the bulk of the used sample, respectively. The Cu2*p* spectra show increasing of

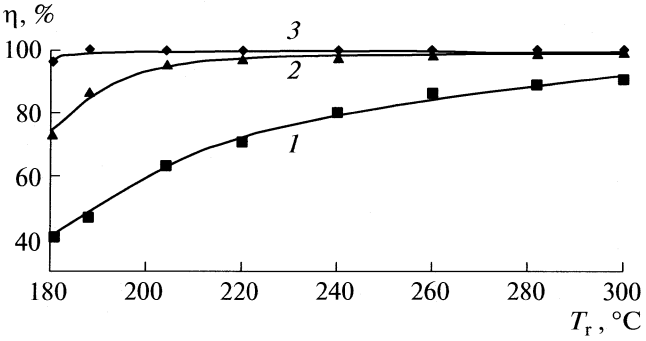

Fig. 4. Temperature dependence of total conversion of (*1*) CO, (*2*) DME and (*3*) methanol on catalyst 2; η is conversion degree, T_r is inlet temperature of the adiabatic reactor.

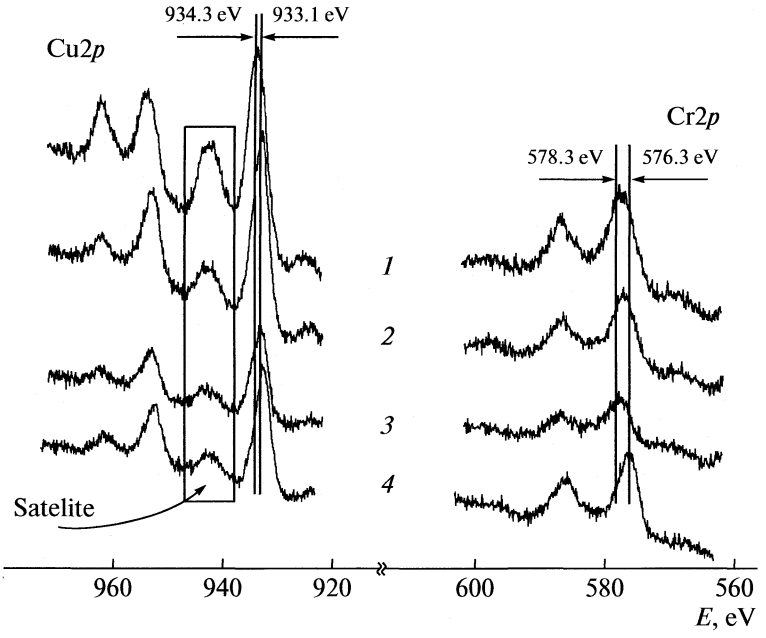

Fig. 5. XPS spectra of Cu2*p* and Cr2*p* for investigated samples: (*1*) fresh bulk, (*2*) used bulk, (*3*) fresh surface and (*4*) used surface; *E* is the binding energy.

Cu^{2+} part of the spectra going from surface to the bulk of the fresh sample. From the line shape of the Cu2*p* spectrum and the shake up satellite structure, one can conclude that the bulk consists of Cu^{2+} only. Going to used sample, we observe the similar behavior of the dispersion of the Cu^{+} and Cu^{2+}. But, the amount of Cu^{2+} is less present in comparison with the bulk of the fresh sample. Therefore, we conclude that catalytic reaction changes the oxidation state of the elements. Looking at the Cr2*p* spectra, we obtained the similar change of ion oxidation state. The bulk of the fresh and the used samples, as well as the fresh sample surface contain mixture of Cr^{3+} and Cr^{6+}, whereas the spectrum of the used sample surface is typical for the presence of Cr^{3+} only. Therefore, one can conclude the coexistence of various copper and chromium species CuO/CuO_2 and CrO_3/Cr_2O_3 or $CuCr_2O_4/Cu_2Cr_2O_4$ on the surface. According to Wojciechowska and coauthors [1] the presence of Cu^{2+} facilitates the redox processes. On the other hand, the presence of Cr_2O_3 stabilizes at the surface the Cr^{3+} ions. Since the redox potential of the copper ions system is much higher than that of chromium ions system, there is a tendency for a transfer of electrons to form Cr^{6+} and Cu^{+} ions, playing the role of active sites in catalytic reaction.

The catalytic tests of studied samples in pilot plant reveal that the optimal preparation temperature seems to be 500°C. This catalyst shows the best CO, DME and methanol oxidation activity. Summarizing the results presented on Fig. 4 we can conclude that the presence of an interaction between copper and chromium ions and formation of Cu^{+} and Cr^{6+} centers forms active components of the mixed Cu–Cr oxide supported catalysts. The intimate contact of such phases and possibility of charge transfer in course of catalytic reaction, as well as highest dispersion of supported phases are probably responsible for highest catalytic activity of sample 2. The presence of number of compounds (CuO, CrO_3, Cr_2O_3, $CuCrO_2$ and $CuCr_2O_4$) in all studied samples leads to a synergistic effect and enhanced CO, DME and methanol conversion than the sum of conversions on each oxide supported on the carrier separately [4, 5].

CONCLUSIONS

Complex copper-chromium oxide catalysts supported on γ-Al_2O_3 have been prepared by co-impregnation method. The characterization methods have shown a high-dispersed and low crystalline supported copper-chromium oxide phases. The obtained data show an interaction between copper and chromium ions and formation of Cu^{+} and Cr^{6+} centers. With an increase of the treatment temperature the crystallinity of the supported phases increases and mixed Cu–Cr oxide phases (as $CuCr_2O_4$, $CuCrO_2$ and $CuCrO_4$) are obtained. This result is supported by the obtained change of oxidation state of ions. All this explains the observed catalytic activity of samples in reaction of deep oxidation of CO, dimethyl ether and methanol, which is an outlet gas mixture of industrial process – methanol to formaldehyde selective oxidation.

ACKNOWLEDGMENTS

The authors are grateful to the Bulgarian National Science Fund at the Ministry of Education and Science (Project VU X-305/2007) and to the Serbian Ministry of Science for the financial support through the Project 166001B.

REFERENCES

1. M. Wojciechowska, J. Haber, S. Łomnicki, J. Stoch, Journal of Molecular Catalysis A: Chemical, **141**, 155 (1999).
2. G. Xanthopoulou, G. Vekinis, Applied Catalysis Section B: Environmental, 37 (2001).
3. J. Thomas, K. Zamaraev Eds., Perspectives in Catalysis, Blackwell Scientific Publications, 1992.
4. K. Ivanov, BG patent No 60779 B1 (1993).
5. D. Dimitrov, PhD Thesis, 2008, Sofia.
6. Powder Diffraction Files, Joint Committee on Powder Diffraction Standards, Philadelphia PA, USA, 1997.
7. Shirley D.A., Phys. Rev. B **5**, 4709 (1972).
8. Sihem Khaddar-Zine, Abdelhamid Ghorbel, Claude Naccache, Journal of Molecular Catalysis A: Chemical **150**, 223 (1999).

ЖУРНАЛ ФИЗИЧЕСКОЙ ХИМИИ, 2009, том 83, № 9, с. 1618–1622

CHEMICAL KINETICS AND CATALYSIS

УДК 541.128

OXIDATION OF FORMIC ACID ON PLATINUM SURFACES DECORATED WITH COBALT(III) MACROCYCLIC COMPLEXES

© 2009 S. Stevanović*, K. Babic-Samardžija**, S. P. Sovilj***, A. Tripković* and V. M. Jovanović*

*ICTM, Department of Electrochemistry, University of Belgrade, Njegoševa 12, P.O. Box 815, 11000 Belgrade, Serbia

**Baker Hughes Incorporated, 12645 West Airport Blvd., Sugar Land, TX 77478, USA

***Faculty of Chemistry, University of Belgrade, P.O. Box 158, 11001 Belgrade, Serbia

E-mail: vlad@tmf.bg.ac.rs

Abstract – Platinum electrode decorated with three different mixed-ligand cobalt(III) complexes of the general formula [Co(Rdtc)cyclam]$(ClO_4)_2$ [cyclam = 1,4,8,11-tetraazacyclotetradecane, $Rdtc^-$ = morpholine- (Morphdtc), piperidine- (Pipdtc), and 4-methylpiperidine- (4-Mepipdtc) dithiocarbamates, respectively] was used to study oxidation of formic acid in acidic solution. The complexes were adsorbed on differently prepared Pt surfaces, at open circuit potential. The preliminary results show increased catalytic activity of Pt for formic acid oxidation with complex ion adsorbed on the polycrystalline surfaces. The increase in catalytic activity depends on the structure of the complex applied and follows the order of metal-coordinated bidentate ligand as Morphdtc > Pipdtc > 4-Mepipdtc. Based on IR and NMR data, the main characteristics of the Rdtc ligands do not vary dramatically, but high symmetry of the corresponding complexes decreases in the same order. Accordingly, the complexes are distinctively more mobile, causing chemical interactions to occur on the surface with appreciable speed and enhanced selectivity. The effect of the complexes on catalytic activity presumably depends on structural changes on Pt surfaces caused by their adsorption.

INTRODUCTION

In effort to improve activity of platinum for the reactions in fuel cells, several kind of catalysts have been proposed including bi- or ternary carbon supported one [1, 2], platinum-based alloys [3], platinum dispersed on new type of carbon supports [4, 5] and recently investigated platinum mixed with organic cobalt complexes [6–9]. Enhanced activity of Pt for methanol oxidation reaction (MOR) is increased for more than several 10-fold times when proper mass ratio of Pt:Co was applied [6, 7]. According to the authors, the coexistence of Pt-based sites and sites derived from metal complex is crucial for this improved activity, which also depends on the structure of metal complex precursor. Okada and coworkers studied the complexes with MN_3, MN_4 and MN_2O_2 moiety as catalytically active sites [8, 9]. The higher catalytic activity is attributable to more retained metal coordinated structure on the catalyst. The ligand nature affects the electronic state of a central metal ion in the complex [9]. Consequently, the stronger activity for MOR exhibits the complex with the larger interaction energy with OH^- [8]. According to the authors, the higher binding energy stabilizes the OH^- species on the surface that enhances oxidation of CO on the metal surface composing the catalyst to act bifunctionally.

In this sense cobalt(III) mixed-ligand complexes with cyclam (MN_4 chromophore) and bidentate ligands [10–14] could be attractive from electrochemical point because structural and electronic factors may simultaneously affect the potential of reaction on the surfaces. For example, cyclic voltammetric data for mixed-ligand cobalt(III)oxalato cyclam complex show a large electrochemical stability of the compound as well as its catalytic effect on electrochemical CO_2 reduction [12]. The electrochemical examination of cobalt(III) complexes with cyclam and dithiocarbamato ligands in aqueous solutions show the influence of the bidentate heterocyclic S,S'-ligands on the electrochemical behavior of the complexes [13]. The relationship between structural parameters and electrochemical properties, as electrocatalytic oxygen reduction and inhibition of iron corrosion, was established [14].

The aim of this work is to examine effect of mixed-ligand cobalt(III) complexes with tetraazamacrocyclic ligand and heterocyclic dithiocarbamates of the general formula [Co(cyclam)Rdtc]$(ClO_4)_2$ on formic acid oxidation at Pt polycrystalline electrode.

EXPERIMENTAL

Three heterocyclic cobalt(III) complexes of the general formula [Co(cyclam)Rdtc]$(ClO_4)_2$, [cyclam = = 1,4,8,11-tetraazacyclotetradecane, $Rdtc^-$ = morpholine- (Morphdtc), piperidine- (Pipdtc), and 4-methylpiperidine- (4-Mepipdtc) dithiocarbamates, respectively] were used to modify the surfaces of Pt polycrystalline electrode

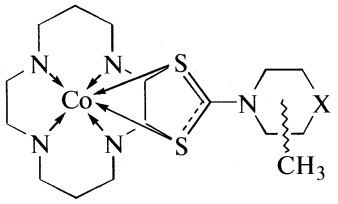

X = O (Morphdtc),
$=CH_2$, (Pipdtc),
$=CH_2$, *para*-CH_3 (4-Mepipdtc)

Pt electrode was prepared by mechanical treatment with diamond past followed by electrochemical potential cycling in 0.5 M H_2SO_4 between – 0.2 V and 1.2 V vs. SCE (Saturated Calomel Electrode). SCE was used in all experiments as reference electrode. In order to study the structural effect, Pt electrode was prepared by potential in the range between – 0.2 V and 0.2 or 0.6 V vs. SCE. Adsorption of each of the examined complexes was performed by immersion of Pt electrode in 10^{-3} to 10^{-5} M solution during 60 s and by immersion in 10^{-3} M during 30, 60 and 90 s at the open circuit potential.

All of the experiments were conducted at room temperature in three-electrode compartment electrochemical cell with a Pt wire as the counter electrode and bridged SCE as the reference electrode. The electrocatalytic activity of Pt modified with adsorbed Co complex was studied in 0.5 M H_2SO_4 + 0.5 M HCOOH solution. Formic acid was added in the solution while holding the electrode potential at – 0.2 V.

Selected IR spectral data (cm^{-1}) of the Co(Rdtc)cyclam$(ClO_4)_2$ complexes

Rdtc	ν(C----N)	ν(C----S)
Morphdtc	1466_s	1012_s
Pipdtc	1465_s	1008_s
4-Mepipdtc	1446_{vs}	962_s

Abbreviations: vs, very strong; s, strong.

The potential was cycled between – 0.2 V and 0.9 V with a sweep rate of 50 and 1 mV s^{-1}.

RESULTS AND DISCUSSION

Surface applied [Co(cyclam)Rdtc]$(ClO_4)_2$ complexes contain a macrocyclic ligand cyclam and bidentate dithiocarbamates with oxygen (heteroatom) or methyl group as substituent in the piperidine ring, as is shown in table.

Cyclic voltammetry (CV) of Pt electrode decorated with Co(III) complex in 0.5 M H_2SO_4 shows that coverage of the Pt surface depends on the complex structure i.e. nature of dithiocarbamato ligand. The adsorbed complex decreases charge in hydrogen adsorption/desorption region (Fig. 1) in order of Rdtc ligand: Morphdtc > Pipdtc > 4-Mepipdtc

The activity of Pt surfaces with adsorbed complex for the reaction of formic acid oxidation becomes

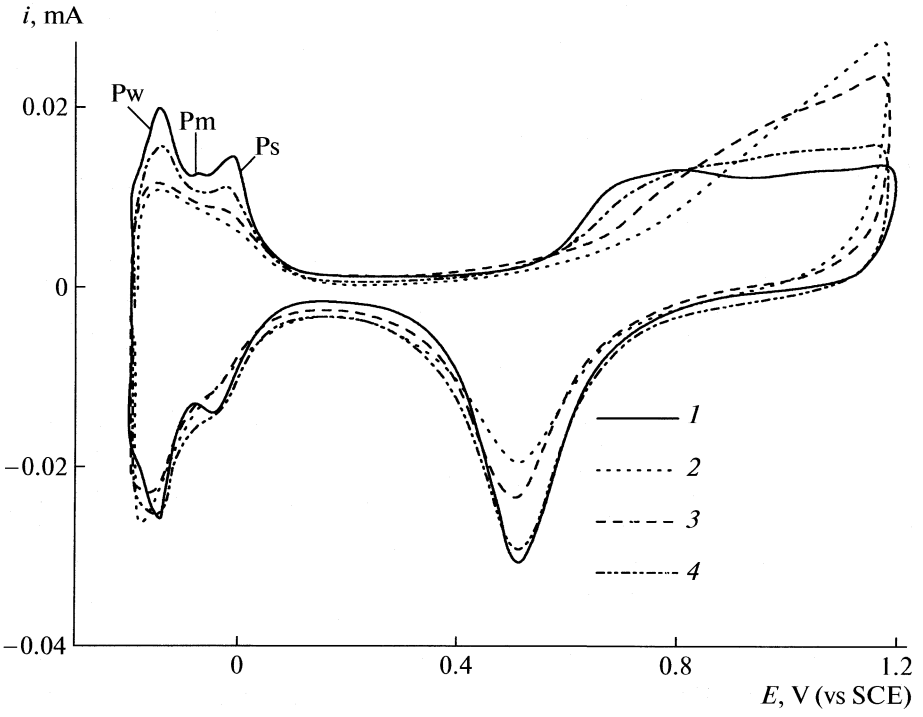

Fig. 1. Cyclic voltammograms of (*1*) Pt and (*2–4*) Pt/[Co(Rdtc)cyclam]$(ClO_4)_2$ in 0.5 M H_2SO_4 (sweep rate 50 mV/s, complex adsorbed from 10^{-4} M solution); R = (*2*) Morphdtc, (*3*) Pipdtc, (*4*) 4 = Mepipdtc.

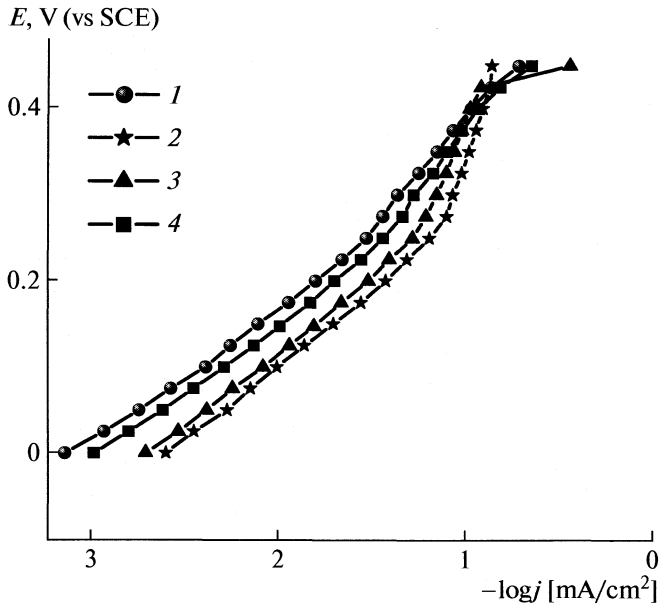

Fig. 2. Tafel plots for the oxidation of 0.5 M HCOOH in 0.5 M H_2SO_4 on Pt and Pt decorated with [Co(Rdtc)cyclam]$(ClO_4)_2$ complexes (sweep rate 1 mV/s, complex adsorbed from 10^{-4} M solution); *1–4* see Fig. 1.

higher than untreated one. The degree of activity improvement depends also in the same order established (Fig. 2). As cited from previous investigations [8], strong dependence of the activity of mixed catalysts is based on Pt structure of organic complexes for oxidation of methanol.

Influence of the complex concentration leads to the multiple raise in activity with the adsorption from the concentrated solutions. However increase with time of adsorption (30, 60 or 90 s) from the same solution resulted in moderate activity increase. Higher adsorption of the complex at 10^{-3} M during 60 or 90 s, results in negligible difference in activity of Pt electrode. These results correspond to earlier findings from which Pt:Co(complex) ratio influences the activity of the catalyst composed of Pt mixed with Co compound [6].

The effect of the complexes on catalytic activity is certainly related to structural changes of Pt surface due to adsorption of complex ion. In favor to this assumption speaks the fact that the enhanced activity is related to the morphology of Pt surface (Fig. 3). Electrochemical oxidation of formic acid at platinum electrode follows the dual path mechanism [15] involving a reactive intermediate (main path – dehydrogenation) and adsorbed CO as a poisoning species (parallel path – dehydratation), well known as the structural sensitive reaction [16–19]. This structural sensitivity is based on the influence of surface structure on poisoning capabilities.

The most active plane Pt (111) shows negligible poisoning over the entire potential region where the reaction occurs. Introduction of monoatomic steps in a flat (111) structure, leads to formation of stepped or high index single crystals, decreases its activity by increasing of CO_{ads} coverage mostly on the step sites. Consequently, the surfaces with the highest step densities, i.e. with the smallest terrace length, have the lowest activity [20, 21]. Structural properties of Pt supposed to reflect in hydrogen adsorption/desorption region on CVs of Pt in basic electrolyte. Thus, for polycrystalline Pt (Fig. 1), cathodic peak in this region for weakly bonded hydrogen (Pw) features (110) crystal face, middle peak for medium bonded hydrogen (Pm) features (111) face and anodic peak for strongly bonded hydrogen (Ps) features (100) crystal plane [22]. Recently, it has been shown that structural properties of Pt monocrystalline electrodes significantly depend on the preparation procedure [23]. Whether or not the procedure involves potential cycling, especially the positive potential limits have a great impact on the surface morphology and activity. Our results, presented in Fig. 3 show that activity of polycrystalline Pt for the oxidation of formic acid significantly depends on the limits applied during potential cycling in preparation procedure. Voltammetric profile obtained by cycling the potential up to 0.2 V revels characteristics of (111) plane (Fig. 3a). Increasing the potential to more anodic values, 0.6 V and 1.2 V (Figs. 3b and 3c) results in appearance of the peaks in hydrogen region for weakly and strongly bonded hydrogen, respectively. The activity of Pt is decreased probably due to introduction of step sites with low reactivity of CO induced by its significantly higher adsorption energy compared to CO on the terrace [24].

IRAS (Infra Red Adsorption Spectroscopy) demonstrates active sites for the oxidation of CO adsorption layer on Pt of either (110) or (100) orientation [25]. Adsorption of complex ion at Pt surface treated by cycling the potential between – 0.2 and 1.2 V, Fig. 1 and Fig. 3c, mostly decreases peak highs for strongly and weakly bonded hydrogen that features (110) and (100) facets. The largest influence exhibits [Co(Morphdtc)cyclam]$^{2+}$ complex in which presence the activity of the electrode for formic acid oxidation increases in highest degree. Analyzing Fig. 3 revels that the less the peaks for strongly bonded hydrogen are build up (Figs. 3b and 3a) the coverage of the Pt surface with adsorbed complex ion is lower as well as an increase of activity due to Co complex ion. Therefore, it can be assumed that the influence of the [Co(Rdtc)cyclam]$^{2+}$ complexes on the Pt activity for formic acid oxidation is due to its adsorption on step sites on the surface that prevents adsorption of CO and decrease the poisoning capabilities of the electrode surface. However, this assumption does not exclude other possible influences of the complex as discussed by Okada and coworkers[8].

As already stated, the increase in activity depends on nature of heterocyclic S,S'-ligand. This may well be enlighten with correlation of spectroscopic IR and NMR results of the [Co(Rdtc)cyclam]$(ClO_4)_2$ com-

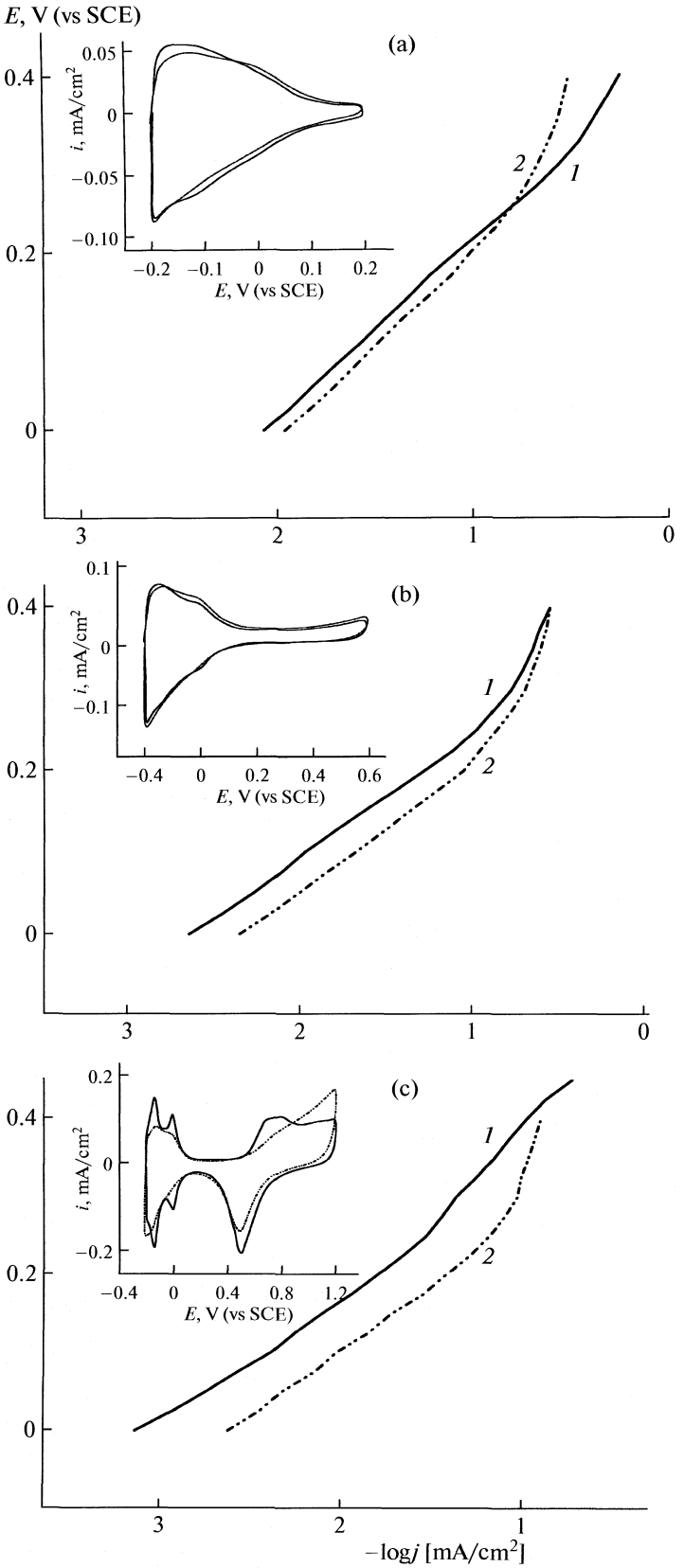

Fig. 3. Tafel plots for the oxidation of 0.5 M HCOOH in 0.5 M H_2SO_4 on differently prepared polycrystalline Pt surfaces (*1*) without and (*2*) with adsorbed [Co(Morphdtc)cyclam]$(ClO_4)_2$ (sweep rate 1 mV/s, complex adsorbed from 10^{-4} M solution). Inserts: CVs of Pt and Pt/[Co(Morphdtc)cyclam]$(ClO_4)_2$ in 0.5 M H_2SO_4 (sweep rate 50 mV/s, complex adsorbed from 10^{-4} M solution) cycled in different potential regions; change from −0.2 V to 0.2 V (a), 0.6 V (b) and 1.2 V (c).

plexes [5, 6]. Shift in frequencies of partially delocalized >C---N bond in IR spectra of the ligating $>NCS_2$ group (table) is due to positive inductive effect of methyl group in 4-Mepipdtc where ν(C---N) bond is located to lower energies. Heteroatom, on the other side in Morphdtc, influences the delocalized bond because of the ability to release electrons, which gives higher electron density on the $>NCS_2$ group and shifts the ν(C---N) bond to higher energies. Activity of the examined Pt electrodes decorated with Co complexes could be controlled by electrostatic as well as hydrophobic interaction between the surface and the complex ion [26]. The main characteristics of binding of the Rdtc ligands as shown in table, do not vary dramatically from complex to complex, but an important difference being that relatively high complex symmetry decrease in order with Morphdtc > Pipdtc > 4-Mepipdtc, taking in account IR and NMR data. Accordingly to this order, the complexes are distinctively more mobile, causing chemical interactions occur on the surface with appreciable speed and enhanced selectivity. This approach opens up further intriguing prospects for future studies.

CONCLUSSION

Pt with adsorbed $[Co(Rdtc)cyclam]^{2+}$ complex ion exhibits enhanced catalytic activity for formic acid oxidation in comparison with pure polycrystalline Pt. The increase in activity depends on the structure of the complex applied and nature of Rdtc ligand in the order of Morphdtc > Pipdtc > 4-Mepipdtc.

Based on the correlation parameters between spectroscopy data and results obtained from oxidation of formic acid at the Pt surfaces exposed to Co complexes it can be proposed that the effect of the complexes on catalytic activity is reliable on structural changes of Pt stepped site surfaces due to efficient adsorption of complex ion.

ACKNOWLEDGMENTS

This work was supported by Ministry of Science of R. Serbia (project no. 142056).

REFERENCES

1. Z. Jusys, T. J. Schmidt, L. Dubau, K. Lasch, L. Jörissen, J. Garche and R.J. Behm, J. Power Sources **105**, 297 (2002).
2. J. W. Guo, T. S. Zhao, J. Prabhuram, R. Chen and C. W. Wong, J. Power Sources **156**, 345 (2006).
3. S. Lj. Gojković, A. V. Tripković, R. M. Stevanović and K. V. Krstajić, Langmuir **23**, 12760 (2007).
4. C. Arbizzani, S. Beninati, E. Manferrari, F. Soavi and M. Mastragostino, J. Power Sources **161**, 826 (2006).
5. G. Wu and B.-Q. Xu, J. Power Sources **174**, 48 (2007).
6. T. Okada, Y. Suzuki, T. Hirose and T. Ozawa, Electrochim. Acta **49**, 385 (2004).
7. T. Okada, Y. Suzuki, T. Hirose, T. Toda and T. Ozawa, Chem. Commun. 2492 (2001).
8. M. Saito, H. Shiroishi, C. Ono, S. Tsuzuki, T. Okada and Y. Uchimoto, J. Molec. Catalysis A: Chem. **248**, 99 (2006).
9. T. Okada, N. Arimura, C. Ono and M. Yuasa, Electrochim. Acta **51**, 1130 (2005).
10. S. P. Sovilj, G. Vucković, K. Babić, T. J. Sabo, S. Macura and N. Juranić, J. Coord. Chem. **41**, 19 (1997).
11. S. P. Sovilj and K. Babić-Samardžija, Synth. React. Inorg. Met.-org. Chem. **29**, 1655 (1999).
12. S. P. Sovilj, G. Vučković, K. Babić, N. Matsumoto, M. Avramov-Ivić and V.M. Jovanović, J. Coord. Chem. **31**, 167 (1994).
13. V. M. Jovanović, K. Babić-Samardžija and S. P. Sovilj, Electroanalysis, **13**, 1129 (2001).
14. K. Babić-Samardžija, V. M. Jovanovi and S. P. Sovilj, J. Serb. Chem. Soc. **73**, 761 (2008).
15. A. Capon and R. Parsons, J. Electroanal. Chem., **45**, 205 (1973).
16. R. Adžić, A.V. Tripković and W. O'Grady, Nature **296**, 137 (1982).
17. R. R. Adžić, in: Advances in Electrochemistry and Electrochemical Engineering; H. Gerischer, C. W. Tobias (Eds), Willey, New York, 1984, p. 159
18. J. Clavilier, R. Parsons, R. Duard, C. Lamy and J. M. Leger, J. Electroanal. Chem. **124**, 32 (1981).
19. C. Lamy, J.M. Leger, J. Clavilier and R. Parsons, J. Electroanal. Chem. **150**, 71 (1983).
20. N. M. Marković, A. V. Tripković, N. S. Marinković and R. R. Adžić, in: M. P. Soriaga (Ed.), Electrochemical Surface Science, American Chemical Society, Washington, DC, 1988, p. 473
21. A. Tripković, K. Popović and R. Adžić, J. Chim. Phys. **88**, 1635 (1991).
22. F.G. Will, J. Electrochem. Soc. **48**,157 (1973).
23. D. S. Strmćnik, D. V. Tripković, D. van der Vliet, K. C. Chang, V. Komanicky, H. You, G. Karapetrov, J. P. Greeley, V. R. Stamenković and N. M. Marković, J. Am. Chem. Soc. **130**, 15332 (2008).
24. J. T. Yates Jr., J. Vac. Sci. Technol. A **13**, 1359 (1995).
25. N. P. Lebedeva, A. Rode4s, J. M. Feliu, M. T. Koper and R. A. Santen, J. Phys. Chem. B **106**, 9863 (2002).
26. N. C. Gianneschi, M.S. Masar III and C. A. Mirkin, Acc. Chem. Res. **38**, 825 (2005).

ЖУРНАЛ ФИЗИЧЕСКОЙ ХИМИИ, 2009, том 83, № 9, с. 1623–1627

CHEMICAL KINETICS AND CATALYSIS

УДК 541.124

IODINE(+1) REDUCTION BY HYDROGEN PEROXIDE

© 2009 G. Schmitz

Faculté des Sciences Appliqueés, Université Libre de Bruxelles, Belgium

E-mail: gschmitz@ulb.ac.be

Abstract – The iodine(+1) reduction by hydrogen peroxide is catalyzed by different buffers and its rate is a complicated function of the acidity and of the iodide concentration. The seemingly inconsistent published experimental results are reanalyzed and a new kinetic model is proposed. A key step is the catalysis by the buffers of the formation of the intermediate compound IOOH. This model reconciles the previous works.

INTRODUCTION

Although the reduction of iodine(+1) by hydrogen peroxide has been studied during more than eighty years, there is no consensus in the literature about its kinetics. The first investigations [1–3] dealt with the catalytic decomposition of hydrogen peroxide by iodine. The following mechanism was postulated in neutral or dilute acidic solutions:

$$I_2 + H_2O \rightleftharpoons IOH + I^- + H^+, \quad (1)$$

$$I_2 + I^- \rightleftharpoons I_3^-, \quad (2)$$

$$IOH \rightleftharpoons IO^- + H^+, \quad (3)$$

$$IO^- + H_2O_2 \longrightarrow I^- + H_2O + O_2, \quad (4)$$

$$I^- + H_2O_2 \longrightarrow IO^- + H_2O. \quad (5)$$

In more acidic solutions, the mechanism includes also reactions

$$IOH + H_2O_2 \longrightarrow I^- + H^+ + H_2O + O_2, \quad (6)$$

$$I^- + H^+ + H_2O_2 \longrightarrow IOH + H_2O. \quad (7)$$

The sum of reactions (4) and (5) or (6) and (7) gives the decomposition

$$2H_2O_2 \longrightarrow 2H_2O + O_2. \quad (8)$$

The reduction of iodine(+1) by hydrogen peroxide is also important as a part of the Bray–Liebhafsky oscillating reaction, that is the decomposition (8) catalyzed by iodate and iodine in acidic solutions [4–9]. This decomposition is the result of the global reactions

$$2IO_3^- + 2H^+ + 5H_2O_2 \longrightarrow I_2 + 5O_2 + 6H_2O, \quad (9)$$

$$I_2 + 5H_2O_2 \longrightarrow 2IO_3^- + 2H^+ + 4H_2O. \quad (10)$$

In reaction (9), hydrogen peroxide acts as a reducing agent but its direct reaction with iodate is much too slow to explain the observed rates. The mechanism is complicated and the reducing action of hydrogen peroxide is mainly the result of reaction (6). Liebhafsky [3, 10] and Furrow [11] have tried to isolate this reaction and to measure its rate constant but their values differ by a factor ten.

A third group of investigations deals with the importance of the iodine(+1) reduction by hydrogen peroxide in analyzing the iodine behavior after a nuclear reactor accident. ^{131}I is one of the most toxic fission products that would be released in the atmosphere and the behavior of iodine has been the subject of extensive studies for the nuclear industry [12–16]. An important part of these studies were devoted to the iodine reactions in solution controlling the distribution of iodine between volatile compounds (I_2 and organic compounds) and non-volatile compounds (mainly I^- and IO_3^-). Hydrogen peroxide being one of the products of the water radiolysis, the reactions of iodine(+1) with hydrogen peroxide producing iodide or iodate are important processes that would influence the release of ^{131}I in the atmosphere. The present state of our knowledge about the reduction of iodine(+1) by hydrogen peroxide is mainly the result of the works of Liebhafsky [2, 3], of Shiraishi et al. [12, 13] and of Ball and Hnatiw [16, 17].

Liebhafsky (1932) has studied the catalytic decomposition (8) in an acetate buffers between pH 4 and 6 and in a phosphate buffers between pH 6 and 8 [2]. He has concluded that, under his experimental conditions, the rate of iodide oxidation (5) is nearly equal to the rate of the iodine(+1) reduction (4). From the observed rates of hydrogen peroxide decomposition and the well-known rate constant k_5 [18], he has calculated $k_4 = 6 \times 10^9$ mol^{-1} dm^3 s^{-1}. The obtained values were independent on the acidity, the nature of the buffer and the iodide concentration. In another work [3] he has measured the rate of oxygen production by reaction (4) far from the steady state and has obtained $k_4 = 3.3 \times 10^9$ mol^{-1} dm^3 s^{-1} in satisfactory agreement with the above value. Both works suggest that the rate is proportional to $[IO^-]$ and is independent on the acidity, the phosphate concentration and the iodide concentration. It is this simplicity that led Liebhafsky to think that (4) was the rate determining step but further measurements have shown that it was an illusion.

Shiraishi et al. (1991) have discovered that phosphate buffers catalyze the iodine(+1) reduction by hydrogen peroxide while citrate buffers do not [12]. For

this reason they have performed a new kinetic study in a citrate buffer between pH 5.5 and 7 [13] and found a new term in the rate law, proportional to $[I^-]$. To explain this term, they have added reactions

$$IOH + I^- \rightleftharpoons I_2OH^-, \quad (11)$$

$$I_2OH^- + H_2O_2 \longrightarrow 2I^- + H^+ + H_2O + O_2 \quad (12)$$

to the mechanism proposed by Liehhafsky. Their value $k_4 = 7 \times 10^7$ mol^{-1} dm^3 s^{-1} is much lower than Liebhafsky value.

Ball and Hnatiw (2001) [16] have observed deviations from the rate law of Shiraishi et al. and have decided to perform a more complete kinetic study as a function of acid, hydrogen peroxide, iodide and buffer concentration in three different buffers [17]. On the basis of this very important experimental work they have proposed the mechanism including (11) and reactions:

$$I_2OH^- + H_2O_2 \rightleftharpoons I^- + IOOH + H_2O, \quad (13)$$

$$IOOH + OH^- \longrightarrow I^- + H_2O + O_2, \quad (14)$$

$$IOOH + B^- \longrightarrow I^- + BH + O_2, \quad (15)$$

where B^- denotes the anion of the buffer. This mechanism explains their experimental results but we will see that it is inconsistent with the former works. We can reject proposed mechanisms but we cannot ignore experimental results without a good reason. Thus, we have analyzed the published rate measurements, found that they are compatible and that a modification of the Ball and Hnatiw mechanism can explain them all.

ANALYSIS OF THE EXPERIMENTAL RESULTS

The observed evolutions of the iodine concentration discussed in this work are the result of two reactions, the reduction of iodine(+1) by hydrogen peroxide and the oxidation of iodide to iodine by reaction (5). Denoting by $[I_2]_t$ the total iodine(+1) concentration, $[I_2]_t = [I_2] + [I_3^-] + [IO^-] + [IOH] + [I_2OH^-]$, and by $k_{obs}\,[I_2]_t$ the global rate of iodine(+1) reduction, the expression of the observed rates is (16) where $r_5 = k_5[I^-][H_2O_2]$:

$$-d[I_2]_t/dt = k_{obs}[I_2]_t - r_5. \quad (16)$$

During the reduction of iodine(+1), $k_{obs}[I_2]_t$ decreases and r_5 increases until $k_{obs}[I_2]_t = r_5$. Then, the system has reached the steady state of the catalytic decomposition studied by Liebhafsky.

The different authors have presented their experimental results differently and in order to compare them it is necessary to choose a common presentation. For this reason, we define the following new function Z (mol^2 dm^{-6} s^{-1}). Its values can be calculated using the information published by the different authors and we will see that its variations with the experimental conditions gives a convenient representation of the effects discussed in this work:

$$Z = \frac{[I^-][H^+]^2}{[H_2O_2]}\frac{[I_2]_t}{[I_2]}k_{obs} \times 10^{14}.$$

Under the conditions of all the works discussed here the reactions (1)–(3) are quasi at equilibrium and the concentrations $[IO^-]$ and $[I_2OH^-]$ can be neglected in the iodine mass balance. This gives the following relations:

$$[IOH][I^-][H^+] = K_1[I_2], \quad [I_3^-] = K_2[I_2][I^-],$$

$$[IO^-][H^+] = K_3[IOH],$$

$$[I_2]_t = [I_2]\,(1 + K_2[I^-] + K_1/[I^-][H^+]).$$

The mechanism proposed by Liebhafsky assumes that $k_{obs}\,[I_2]_t = k_4[IO^-][H_2O^2]$ where $[IO^-] = K_1K_3[I_2]/[I^-][H^+]^2$. If so, these expressions introduced in the definition of Z would give $Z = k_4K_1K_3 \times 10^{14}$. However, the experimental values of Z are not constant. The effects of the buffers, the acidity and the iodide concentration on the Z values show the kinetic complications revealed by further works.

Kinetics in citrate buffers

Shiraishi et al. as well as Ball and Hnatiw have concluded that citrate buffers do not catalyze significantly the iodine(+1) reduction by hydrogen peroxide. On the other hand, Shiraishi et al. have observed a marked effect of the iodide ions, not observed by Ball and Hnatiw. The values given in their figures allow the calculation of Z and lead to

$$Z = 0.2 + 1.8 \times 10^8[H^+][I^-]. \quad (17)$$

A careful analysis of the results of Ball and Hnatiw reveals why they have not observed this effect: in the rate expression (16) $d[I_2]_t/dt$ is proportional to $[I_2]_t$ only if r_5 can be neglected. Shiraishi et al. have analyzed their results using the complete expression (16) but Ball and Hnatiw have calculated k_{obs} assuming a simple first order rate law. This approximation was correct for nearly all their measurements but not for their study of the $[I^-]$ effect in citrate buffers. At high iodide concentrations the r_5 term is important and their k_{obs} values are too low. They did not publish the details of their measurements but the available information suggests that their values corrected for the r_5 term would be similar to Shiraishi et al. values.

Kinetics in phosphate buffers

Ball and Hnatiw have measured k_{obs} between pH 6.2 and 7.7 with phosphate total concentrations equal to 0.02 or 0.05 mol dm^{-3} and iodide concentrations equal to 5×10^{-4} or 1×10^{-3} mol dm^{-3}. Figure 1 shows the increase of their reaction rates with $[H^+][B^-]$. Iodide has a much smaller effect than the buffer. Figure 1 shows also the Z values calculated from the Liebhafsky measurements between pH 5.8 and 7.2 in 0.2 mol dm^{-3} phosphate buffer with $[I^-]$ between 0.001 and 0.1 mol dm^{-3}. The scatter is important but these values are in qualita-

tive agreement with Ball values. They are higher because the phosphate buffer concentration is higher and they seem independent on $[I^-]$. Liebhafsky measurements suggest that Z reaches a limiting value at high buffers concentrations. For comparison, Figure 1 shows also the Z value calculated from the measurements by Shiraishi et al. for the reaction not catalyzed without effect of iodide ($Z = 0.2$ mol^2 dm^{-6} s^{-1}). The experimental results of these different works are in good agreement and the kinetic model must explain them all.

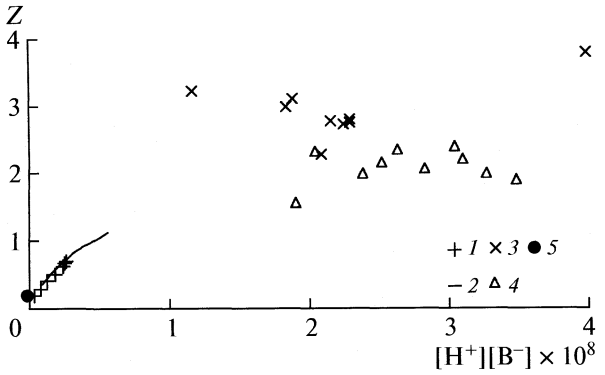

Fig. 1. Comparison of the Z values obtained by different authors. Values calculated from Ball and Hnatiw measurements in phosphate buffers (*1*) 0.02 M and (*2*) 0.05 M [17] and from Liebhafsky measurements in phosphate buffers (*3*) 0.20 M [2] or (*4*) [3]; (*5*) value for the non-catalyzed reaction [13].

Kinetics in barbital buffers

Most of the Ball and Hnatiw results were obtained in barbital buffers. The authors have explained the observed effects of the buffer and of the iodide concentrations by the mechanism (13)–(15) giving the rate law

$$k_{obs}[I_2]_t = k_{13}[I_2OH^-][H_2O_2] \times \times \frac{k_{14}[OH^-] + k_{15}[B^-]}{k_{-13}[I^-] + k_{14}[OH^-] + k_{15}[B^-]}.$$

With the quasi-equilibrium (11) and $K_w = [H^+][OH^-] = 10^{-14}$, the corresponding expression of Z is

$$Z = \frac{k_{13}K_1K_{11} \times 10^{14}[I^-][H^+](k_{14}K_w + k_{15}[B^-][H^+])}{k_{-13}[I^-][H^+] + k_{14}K_w + k_{15}[B^-][H^+]}. \quad (18)$$

This expression can be fitted to the author's experimental values but is inconsistent with the other works. In citrate buffers the catalytic term $k_{15}[B^-][H^+]$ can be neglected, the rate constants obtained by Ball and Hnatiw give $k_{14}K_w/k_{-13} = 2 \times 10^{-12}$ mol^2 dm^{-6} and the expression of Z reduces to

$$Z = K_{13}K_1K_{11}k_{14}[I^-][H^+]/([I^-][H^+] + 2 \times 10^{-12}).$$

The range of $[I^-][H^+]$ values is 5×10^{-11} to 6×10^{-10} for the Ball and Hnatiw experiments and 5×10^{-11} to 8×10^{-9} for the Shiraishi et al. experiments. In both cases $[I^-][H^+]$ is larger than 2×10^{-12} and Z should be independent on $[I^-][H^+]$. This is in contradiction with Shiraishi et al. results and also with Ball and Hnatiw k_{obs} values if they are corrected for the effect of reaction (5) as indicated above. The expression (18) is also inconsistent with the results of Liebhafsky in phosphate and acetate buffers. The experimental Z values at high acetate or phosphate concentrations shown in Fig. 1 are independent on $[I^-]$. However, the expression (18) predicts the opposite: when the term $k_{15}[B^-][H^+]$ becomes so large that Z becomes independent on the buffer concentration, Z should become proportional to $[I^-][H^+]$. Liebhafsky has mentioned in a footnote ([2], p. 1798) results obtained at a lower phosphate concentration showing "a positive trend with increasing $[I^-]$". Unfortunately he has discarded these results but this footnote confirms that the effect of $[I^-]$ on Z decreases when the buffer concentration increases. In summary, Ball and Hnatiw mechanism is inconsistent with Shiraishi et al. measurements, with Ball and Hnatiw k_{obs} values in citrate buffers corrected for the effect of reaction (5) and with Liebhafsky measurements.

PROPOSED MECHANISM

The above contradictions can be resolved considering the following mechanism where reactions (3) and (11) are quasi at equilibrium.

$$IOH \rightleftharpoons IO^- + H^+, \quad (3)$$

$$IOH + I^- \rightleftharpoons I_2OH^-, \quad (11)$$

$$IO^- + H_2O_2 \rightleftharpoons IOOH + OH^-, \quad (19)$$

$$IOH + B^- + H_2O_2 \rightleftharpoons IOOH + BH + OH^-, \quad (20)$$

$$I_2OH^- + H_2O_2 \rightleftharpoons IOOH + I^- + H_2O, \quad (13)$$

$$IOOH + OH^- \rightleftharpoons I^- + H_2O + O_2, \quad (14)$$

$$IOH + H_2O_2 \rightleftharpoons IOOH + H_2O. \quad (21)$$

This mechanism is similar to the one proposed by Ball and Hnatiw but the catalysis of the IOOH decomposition (15) is replaced with the catalysis of its formation (20). The non-catalyzed reaction (21) can be neglected under the experimental conditions of the studies discussed here but is probably important in non-buffered acidic solutions. The reactions (19), (20) and (13) are kinetically equivalent to the catalysis of (21) by OH^-, B^- and I^- respectively. This mechanism gives the rate law:

$$k_{obs}[I_2]_t = k_{14}[H_2O_2] \times \times \frac{k_{19}[O^-] + k_{20}[IOH][B^-] + k_{13}[I_2OH^-]}{k_{14} + k_{-19} + k_{-20}[BH] + k_{-13}[I^-][H^+]/K_w}.$$

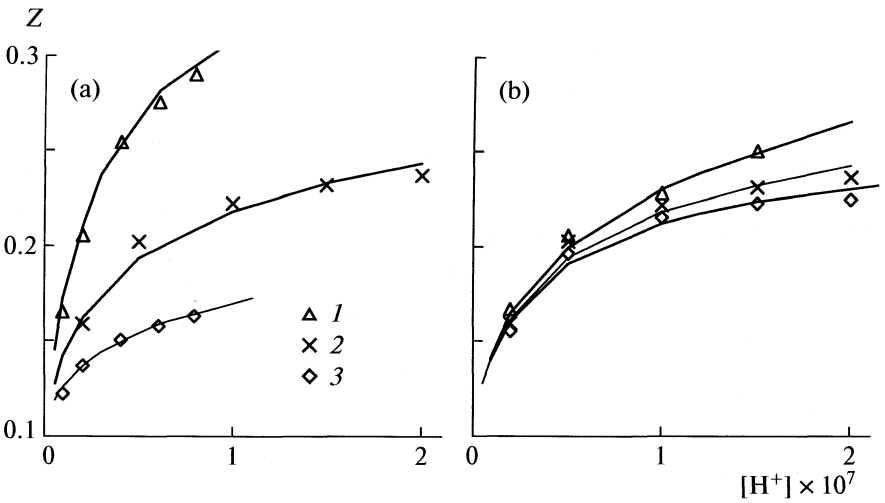

Fig. 2. Comparison of the calculated Z values (lines) with experimental values in barbital buffers [17]; (a) $[I^-] = 5 \times 10^{-4}$, [Barbital] = (*1*) 1×10^{-2}, (*2*) 5×10^{-3} and (*3*) 2.5×10^{-3} M; (b) [Barbital] = 5×10^{-3} M, $[I^-]$: (*1*) 1×10^{-3} M, (*2*) 5×10^{-4} and (*3*) 2.5×10^{-4} M.

The rate constants are related by the condition of internal consistency of reaction mechanisms [19]. As (11) + (13) = (21) we must have $K_{11}K_{13} = K_{21}$ or $K_{11}k_{13}/k_{-13} = K_{21}$. Similar relations for reactions (19) and (20) give

$$K_{21} = K_{11}\frac{k_{13}}{k_{-13}} = \frac{K_3}{K_w}\frac{k_{19}}{k_{-19}} = \frac{K_B}{K_w}\frac{k_{20}}{k_{-20}}, \qquad (22)$$

where $K_B = [H^+][B^-]/[HB]$. These relations introduced in the rate law lead to

$$Z = 10^{14}k_{14}K_{21}K_1K_w \times$$

$$\times \frac{k_{19}K_3 + k_{13}K_{11}[I^-][H^+] + k_{20}[B^-][H^+]}{k_{14}K_{21}K_w + k_{19}K_3 + k_{13}K_{11}[I^-][H^+] + k_{20}[B^-][H^+]}. \qquad (23)$$

Let us show firstly that this expression is in qualitative agreement with the experimental results if $k_{14}K_{21}K_w$ is much larger than $k_{19}K_3 + k_{13}K_{11}[I^-][H^+]$ giving the approximate expression

$$Z \sim k_{14}K_{21}K_1 \times$$

$$\times \frac{k_{19}K_3 + k_{13}K_1[I^-][H^+] + k_{20}[B^-][H^+]}{k_{14}K_{21}K_w + k_{20}[B^-][H^+]}. \qquad (24)$$

In citrate buffers the catalytic term $k_{20}[B^-][H^+]$ can be neglected and this expression reduces to $Z = K_1(k_{19}K_3 + k_{13}K_{11}[I^-][H^+])/K_w$ in accordance with equation (17) obtained by Shiraishi et al. The expression (24) explains also the maximum value of Z observed by Liebhafsky in concentrated buffers. When $k_{20}[B^-][H^+]$ is very large Z approaches $k_{14}K_{21}K_1$ and $[I^-]$ has no effect. When $k_{20}[B^-][H^+]$ is smaller, the term $k_{13}K_{11}[I^-][H^+]$ explains the small effect of $[I^-]$ observed. Thus, the simplified equation (24) explains qualitatively all the observations. To show that the agreement is also quantitative, we have estimated the rate constants using the complete equation (23). For numerical reasons, this was performed in two steps. A first analysis of all the different works shows that $k_{14}K_{21}K_1$ must be about 4 s^{-1}. Then, keeping this value, the adjustment of the other rate constants to Shiraishi et al. results gives $k_{19}K_3K_1 = 2 \times 10^{-15}$, $k_{13}K_{11}K_1 = 2.3 \times 10^{-6}$ and k_{20} very small, as expected in citrate buffers. The adjustment to Ball and Hnatiw results in barbital buffers gives $k_{19}K_3K_1 = 1.1 \times 10^{-15}$, $k_{13}K_{11}K_1 = 2.8 \times 10^{-6}$, in fair agreement with Shiraishi et al. values, and $k_{20}K_1 = 9 \times 10^{-6}$. These values depend somewhat on the chosen K_B value and we have used $pK_B = 7.5$ for 0.2 mol dm^{-3} ionic strength. Figure 2 shows the agreement between the experimental and calculated values.

The rate constants of the steps (13), (14) and (19) can be estimated as follow. The equilibrium constants $K_1^0 = 5.3 \times 10^{-13}$, $K_3^0 = 2.3 \times 10^{-11}$ and $K_{11}^0 = 320$ are well known at zero ionic strength [20]. The values of $[H^+]$ given by Shiraishi and by Ball are actually those of 10^{-pH} or a_{H^+} and a correction for the ionic strength must be applied only to the monovalent negative ions. With a value 0.8 for their activity coefficients, $k_{13}K_{11}K_1 = 2.8 \times 10^{-6}$ gives $k_{13} = 1.3 \times 10^4$ mol dm^{-3} s^{-1} and $k_{19}K_3K_1 = 1.1 \times 10^{-15}$ gives $k_{19} = 5.8 \times 10^7$ mol dm^{-3} s^{-1}. The rate constants in the backward directions could be calculated using the relations (22) if the equilibrium constant K_{21} was known. It is not but some indirect estimation can be obtained. From $k_{14}K_{21}K_1 = 4$ s^{-1} we calculate $k_{14}K_{21} = 6 \times 10^{12}$ and note that k_{14} cannot be larger than about 5×10^9, the value for a diffusion controlled reaction. As a consequence, K_{21} must be larger than 10^3. On the other hand, a too large value of K_{21}

would imply an unobserved large value of [IOOH] and the value of K_{21} is probably between 10^3 and 10^4.

CONCLUSIONS

Liebhafsky had used two different experimental methods in different acetate and phosphate buffers and had obtained about the same value of Z. This let him to conclude logically that reaction (4) was the rate determining step. Actually, he had observed a special kind of homogeneous catalysis, a catalytic reaction whose rate can be independent on the nature and on the concentration of the catalyst. The proposed mechanism explains Liebhafsky results: when the action of the buffer is very effective, reaction (20) is quasi at equilibrium and the rate determining step is (14). We have shown that in this case Z is close to $k_{14}K_{21}K_1$, independent on $[B^-]$ and also on K_B. The work of Liebhafsky is instructive for another reason: it shows that we can never discard experimental results just because they seem abnormal. Liebhafsky had observed that at low phosphate concentrations the values of Z were lower but had discarded these results because they seemed abnormal. Actually, they were the most informative results revealing the complication of the kinetics of the iodine(+1) reduction by hydrogen peroxide. It is only sixty years later that Shiraishi et al. have discovered the catalytic effect of the buffers and the complicated effect of the iodide concentration. Recently, Ball and Hnatiw have measured more precisely these effects but their mechanism does not explain all the former observations. The mechanism we propose explains all the well established experimental facts but we do not pretend that this is the end of the story.

REFERENCES

1. E.Z. Abel, Z. physik. Chem., **96**, 1 (1920); idem **136**, 16 (1928).
2. H.A. Liebhafsky, J. Amer. Chem. Soc., **54**, 1792 (1932).
3. H.A. Liebhafsky, J. Amer. Chem. Soc., **54**, 3499 (1932).
4. G. Schmitz, J. chim. phys. **84**, 957 (1987).
5. Lj. Kolar-Anić and G. Schmitz, J. Chem. Soc., Faraday Trans. **88**, 2343 (1992).
6. Lj. Kolar-Anić, Ž. Cupić, S. Anić and G. Schmitz. J. Chem. Soc., Faraday Trans. **93**, 2147 (1997).
7. G. Schmitz, Phys. Chem. Chem. Phys. **1**, 4605 (1999).
8. G. Schmitz, Phys. Chem. Chem. Phys. **3**, 4741 (2001).
9. G. Schmitz, Lj. Kolar-Anić, S. Anić, T. Grozdić and V.J. Vukojević, Phys. Chem. A **110**, 10361 (2006).
10. I. Matsuzaki, R. Simic and H.A. Liebhafsky, Bull. Chem. Soc. Japan **45**, 3367 (1972).
11. S. Furrow, J. Phys. Chem. **91**, 2129 (1987).
12. K. Ishigure, H. Shiraishi, H. Okuda and N. Fujita, Radiat. Phys. Chem. **28**, 601 (1986).
13. H.Shiraishi, H. Okuda, Y. Morinaga and K. Ishigure in *Proc. 3rd CSNI Workshop Iodine Chem. Reactor Safety*, 1991, JAERI-M-92-012, Japan, 1992, p.152.
14. J. C. Wren and J. M. Ball, Radiat. Phys. Chem. **60**, 577 (2001).
15. B. Clément, L. Cantrel, G. Ducros, F. Funke, L. Herranz, A. Rydl, G. Weber and C. Wren, *State of the Art Report on Iodine Chemistry*, Nuclear Energy Agency, NEA/CNSI/R(2007)1.
16. J.M. Ball, J.B. Hnatiw and H.E. Sims in *Proc. 4th CSNI Workshop Iodine Chem. Reactor Safety*, 1996, Edited by S.Guntay. Switzerland, 1997, p. 169.
17. J.M. Ball and J.B. Hnatiw, Can. J. Chem. **79**, 304 (2001).
18. H.A. Liebhafsky and A. Mohammad, J. Amer. Chem. Soc. **55**, 3977 (1933).
19. G. Schmitz, J. Chem. Phys. **112**, 10714 (2000).
20. G. Schmitz, Int. J. Chem. Kinet. **36**, 480 (2004).

ЖУРНАЛ ФИЗИЧЕСКОЙ ХИМИИ, 2009, том 83, № 9, с. 1628–1632

CHEMICAL KINETICS AND CATALYSIS

УДК 541.128

THEORETICAL AND EXPERIMENTAL STUDIES OF THE ALL GAS-PHASE IODINE LASER

© 2009 M. Endo*, T. Nakamura*, T. Masuda** and Taro Uchiyama**

*Department of Physics, School of Science, Tokai University, 1117 Kitakaname, Hiratsuka 259–1292, Japan

**Department of System Design Engineering, Faculty of Science and Engineering, Keio University, 3–14–1 Hiyoshi, Kohokuku, Yokohama 223–8522, Japan

E-mail: endo@tokai.ac.jp

Abstract – All gas-phase iodine laser (AGIL) powered by the decomposition of nitrogen trichloride (NCl_3) is studied. This reaction scheme uses commonly available reagents and reaction paths are milder than the previously studied azide-based AGIL. Theoretical studies revealed the necessary operational conditions for achieving positive gain. An apparatus is made based on the results of the theoretical works. Positive gain at iodine $I(^2P_{1/2})$–$I(^2P_{3/2})$ transition is observed for the first time.

INTRODUCTION

The chemical oxygen-iodine laser (COIL) is a continuous-wave, near-infrared chemical laser. It offers excellent properties for applications that require high-power laser output from a mobile platform. The best-known example of a COIL system may be the "Airborne Laser" ballistic missile defense weapon system[1], which uses a multi-megawatt laser with good beam quality. For very-high-power applications, chemical lasers are still advantageous over solid-state and fiber lasers, in terms of its scalability and beam quality. Therefore, intensive studies are being conducted not only in the U. S., but also in other countries, including Japan. A typical COIL depends on the energy transfer from singlet oxygen $O_2(^1\Delta)$ to the iodine atom, which is the lasing species. The $O_2(^1\Delta)$ is typically generated by the following chemical reaction:

$$H_2O_2 + 2KOH + Cl_2 \longrightarrow 2H_2O + 2KCl + O_2(^1\Delta). \quad (1)$$

This reaction illustrates an inherent drawback for the mobile laser systems: the reactant, basic hydrogen peroxide (BHP) aqueous solution is bulky to carry and it decomposes over time, which limits both long-term storage of BHP and applications in remote places.

Because iodine is an ideal for the lasing species, scientists have sought an alternative donor that is compatible with singlet oxygen but does not depend on wet chemistry. In 2000, Henshaw et al. succeeded in operating an all-gas-phase iodine laser (AGIL)[2]. The energy donor of AGIL is an excited NCl molecule in the singlet state. Generating $NCl(^1\Delta)$ is achieved by the following chain of gas-phase reactions:

$$F + DCl \longrightarrow DF + Cl, \quad (2)$$

$$Cl + HN_3 \longrightarrow HCl + N_3, \quad (3)$$

$$Cl + N_3 \longrightarrow NCl(^1\Delta) + N_2. \quad (4)$$

While this reaction avoids BHP, it still requires highly toxic and explosive hydrogen azide, highly corrosive fluorine, and expensive DCl. In search of a more friendly reaction, Exton et al. demonstrated that decomposition of nitrogen trichloride (NCl_3) produces $NCl(^1\Delta)$ with high yield by the following reactions,

$$NCl_3 + H \longrightarrow NCl_2 + HCl, \quad (5)$$

$$NCl_2 + H \longrightarrow NCl(^1\Delta) + HCl, \quad (6)$$

and this could be used as an energy source of the AGIL[3]. To distinguish this concept from the previously demonstrated AGIL, the former is often called "azide- AGIL", and the later is called "amine-AGIL". Since then, studies have conducted in line of this scheme, and in 1993, energy transfer from the chemically generated NCl_3 to the iodine atom is demonstrated[4]. In 2005, breaching-out of the absorption loss at the $I(^2P_{1/2})$–$I(^2P_{3/2})$ transition is reported by Bauer et al.[5]. Nevertheless, positive gain at this transition has not been reported yet to date.

THEORETICAL

We have started the study of amine-AGIL with the numerical simulations. Based on the successful CFD/chemistry hybrid simulation[6], we modeled the chemical reaction of amine-AGIL by a one-dimensional multiple leaky-streamtube model. Figure 1 illustrates the description of the model. The flow field is divided into n stream tubes of primary flow layers, and second, third, fourth flow layers those contain different species. The main-flow direction is defined as x and the perpendicular axis is defined as y. The flows of adjacent layers are not mixed until the predefined injector position is reached. Downstream of the each injector, diffusive mixing of adjacent layers is assumed. A rooftop optical resonator is placed where the interac-

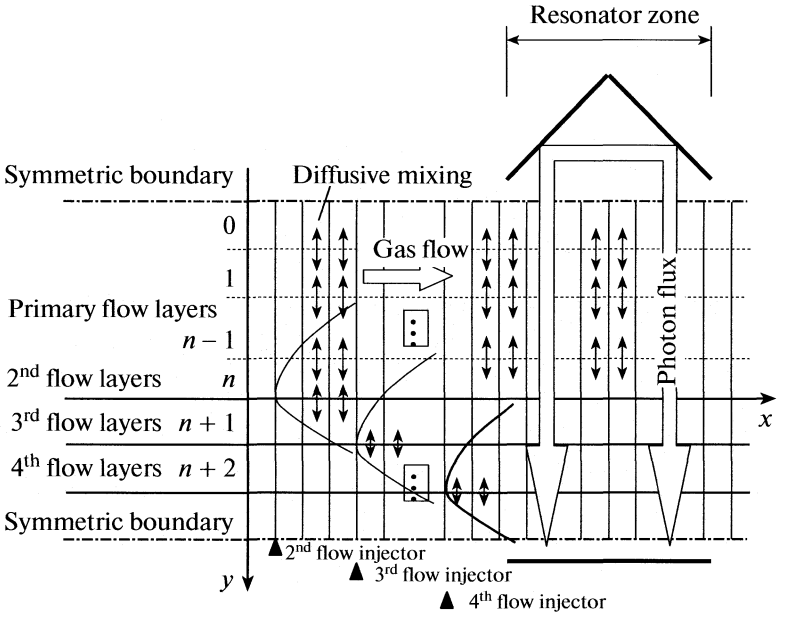

Fig. 1. Schematic drawing of the one-dimensional, multiple leaky-stream-tube kinetics model.

tion of iodine atoms and photon flux is calculated. Since top and bottom boundaries are assumed to be symmetric, layer 0 represents the center of the duct, while the boundary of $(n + 2)$th layer represents the top and bottom walls of the flow duct if a wall injection scheme is assumed.

The partial differential equation governing the flow field is as follows:

$$\frac{\partial M^i(x, y, t)}{\partial t} = \sum_g C_g^2[T(x, y, t)] M^j(x, y, t) M^k(x, y, t) + \sum_h C_h^3[T(x, y, t)] M^0(x, y, t) M^p(x, y, t) M^q(x, y, t) - \frac{\partial}{\partial x}\{M^i(x, y, t) H(x) v(x)\}/H(x) - D_a \frac{\partial^2 M^i(x, y, t)}{\partial y^2} - \delta \frac{\partial n_p(x, t)}{\partial t}. \quad (7)$$

Here, $M^i(x, y, t)$ is the number density of the ith species [1/cm^3], $C_g^2[T]$ is the rate constant of the gth reaction of 2nd order [cm^3/s], $C_h^3[T]$ is the rate constant of the hth reaction of 3rd order [cm^6/s], T is the gas temperature [K], $H(x)$ is the height of the duct [cm], $v(x)$ is the gas velocity at position x [cm/s], D_a is the artificial diffusion constant, and n_p is the photon density [1/cm^3]. $\delta = -1$ if i represents the upper state of the iodine atom, $\delta = 1$ if i represents the ground state of the iodine atom, and $\delta = 0$ for the other cases.

The differential equation is discretized by the upwind finite difference method. The upstream boundary condition is given by the set of equations,

$$M^i(0, t) = M_0^i. \quad (8)$$

The difference equation is explicitly integrated in the time domain with first-order accuracy. The rate equation set used in this work is not shown here, but readers would find the complete description of the model in [7]. The numbered reaction constants hereafter is in consistent with those appears in [7].

Soon after the initial calculations, we realized there are two key factors of the amine-AGIL reaction system that strongly affects the small signal gain. The primary one is the self annihilation reactions of NCl($^1\Delta$). Unlike the $O_2(^1\Delta)$, the reaction constants of self annihilation reactions

$$NCl(^1\Delta) + NCl(^1\Delta) \xrightarrow{k_{26}, k_{27}, k_{28}} \text{products} \quad (9)$$

are on the order of 10^{-12} cm^3/s. Since the reaction occurs at the rate of [NCl($^1\Delta$)]^2, local high concentration of NCl($^1\Delta$) should be avoided. The second important factor is the Cl atom accumulation. Cl atom is inherently generated as a by-product of amine-AGIL reaction system, for example, by

$$NCl(^1\Delta) + NCl(^1\Delta) \xrightarrow{k_{28}} N_2 + 2Cl, \quad (10)$$

where k_{28} is 7.02×10^{-12} cm^3/s. Since it is a strong quencher of the I* as

$$I^* + Cl \xrightarrow{k_{40}} I + Cl, \quad (11)$$

where k_{40} is 1.5×10^{-11} cm^3/s, the accumulation of Cl atom affects the laser performance considerably. We found that changing the order of injectors is effective for both avoiding local high concentration of NCl($^1\Delta$)

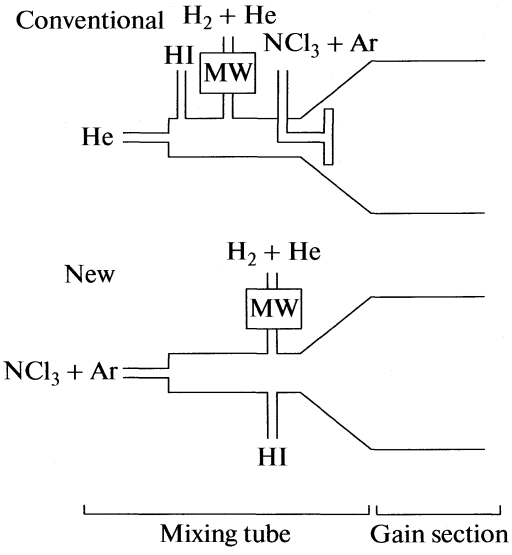

Fig. 2. Comparison of the injector arrangements. Conventional: Ref. [5], New: this work, MW: microwave.

and rapid gain build-up before accumulation of Cl atom. Figure 2 shows the comparison of the injector arrangements. The "Conventional" arrangement was that of the first amine-AGIL setup[5]. We changed the order so that the NCl_3 is contained in the main flow, and HI is injected at the same position as H atoms.

Figure 3 shows the $NCl(^1\Delta)$ concentration contours in the flow field with the conventional arrangement and the new arrangement. It is seen that $NCl(^1\Delta)$ is generated locally and in a high density when conventional arrangement is used. On the other hand, the concentration of $NCl(^1\Delta)$ is more uniformly distributed when the new arrangement is used. Figure 4 shows the concentrations of Cl atom and population inversion, namely, $\Delta N = [I^*]-(1/2)[I]$, with the conventional arrangement and the new arrangement.

Population inversion is directly connected to the small signal gain g_0 of the laser medium as

$$g_0 = \sigma \Delta N, \quad (12)$$

where σ is the stimulated emission cross section, and therefore the most important parameter of any laser. The factor 1/2 applied to the ground state [I] comes from the quantum state degeneracy of the iodine atom. It is seen that the inversion evolution of the new arrangement is much faster than that of the conventional case, and its peak is reached before Cl atom accumulation. Therefore, I* suffers less deactivation by Cl atom. As a result, a higher peak population inversion (and gain) by a factor of two is seen in this figure.

Also, flow rates of the species, operating pressure, and the position of the optical axis are the parameters to be optimized. Numerical model was useful to find an optimum set from the vast parameter space. After a numerous runs of various boundary conditions, we found a recommended operational condition of the amine-AGIL as table.

EXPERIMENTAL

Figure 5 shows the schematic drawing of the experimental setup. Amine-AGIL is composed of a simple mixing tube and a flow duct equipped with transparent windows. The mixing tube is made of a 25.4 mm Pyrex glass tube. Three injectors are devised as branches, namely, a 12.7 mm NCl_3 injector carried by Ar, a 12.7 mm H atom injector passing through a microwave resonator, and a 6.35mm HI tube. H atom branch is made of silica glass for better thermal durability. Microwave is generated with a commercial magnetron (Panasonic) of 600 W output originally designed for microwave oven. A microwave resonator having a pair of holes is connected to the magnetron through a waveguide and the H_2 tube is passing through it. H_2 is carried by He to help easier production of discharge plasma. Pressure of the mixing section is measured by a capacitance manometer (MKS Baratron). In the typical operational conditions, the pressure is 1000 Pa.

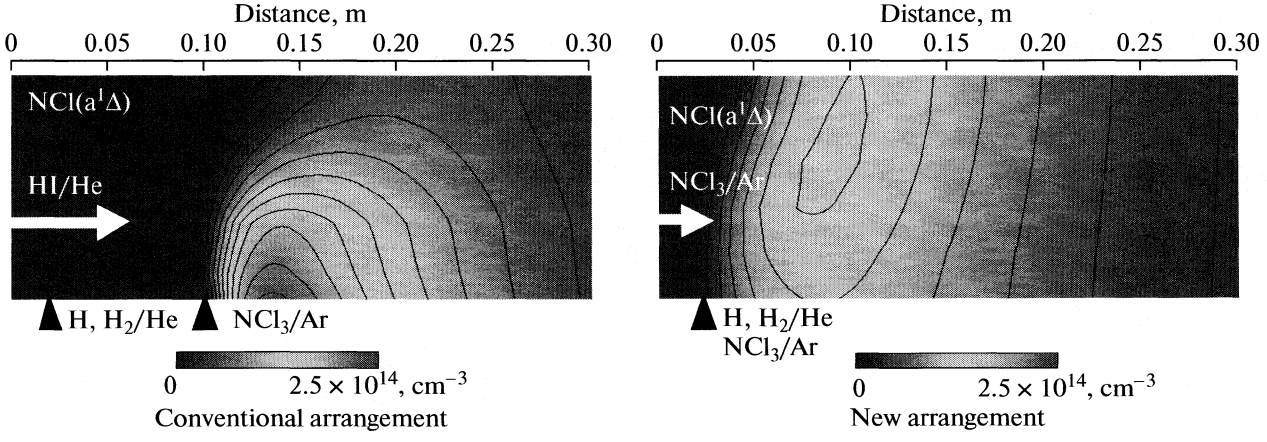

Fig. 3. Comparison of two injector arrangements: $NCl(^1\Delta)$ density contour.

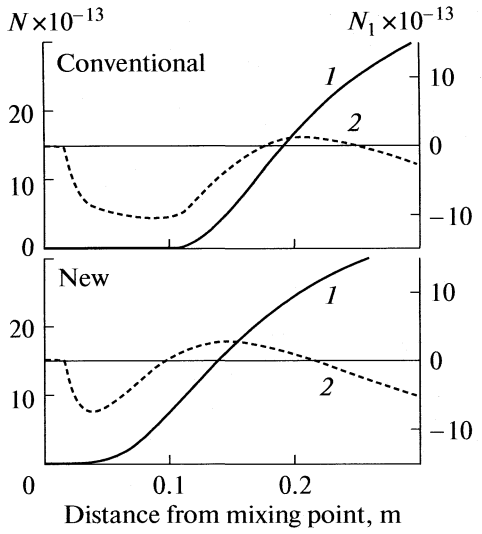

Fig. 4. Comparison of two injector arrangements: (*1*) Cl_2 atom density (N) and (*2*) population inversion density (N_1), cm^{-3}.

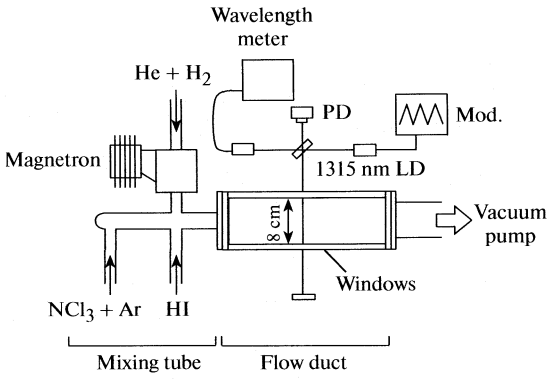

Fig. 5. Experimental setup.

The upstream end of the flow duct is 50 mm wide, 10 mm high, and it is directly connected to the mixing section. The duct can be set to diverging at an angle of 4 degrees or straight. Straight condition gave better result since we operated the laser at the subsonic flow conditions. Duct width at the intermediate section is 80 mm (enlarged from 50 mm to gain the optical path). A vacuum pump of 1.000 l/s capacity is driving the flowing gas, however, the capacity is greatly reduced by the variable restrictor devised at the inlet. The pressure at the center of the flow duct is monitored by a capacitance manometer (MKS Baratron) and the pressure is controlled to match the condition tabulated in table.

Small signal gain is measured by a distributed feedback laser diode (NTT Electronics NLK1B5EAAA) operated at 1.315 μm, and its wavelength is modulated at 1.200 Hz near the 3–4 hyperfine level of the iodine transition, $I(^2P_{1/2})$–$I(^2P_{3/2})$. The absolute wavelength is assured by a wavelength meter (Advantest TQ8325).

RESULTS AND DISCUSSION

Figure 6 shows the results. The traces show the intensity of the beam passed through the laser media, as a function of the LD frequency. Due to the vibration coming from the vacuum system and very small (on the order of 0.1%) round trip gain/loss, the signal to noise ratio of the traces were not good. Nevertheless, we could see the clear difference between two traces.

As we use the microwave generator originally mounted on the commercial microwave oven, it works only the half cycle of the alternate current. The blue line (dip) shows the absorption of the 3–4 hyperfine level of the $I(^2P_{1/2})$–$I(^2P_{3/2})$ transition when the microwave is off. Iodine atom is present probably by the following reaction,

$$HI + Cl \longrightarrow I + HCl, \qquad (13)$$

but not pumped. When the microwave is "on" cycle, the trace turns to negative to positive and that is the proof of the following energy transition,

$$NCl(^1\Delta) + I \longrightarrow NCl + I^*. \qquad (14)$$

The round-trip small signal gain is not yet enough to achieve lasing and lower than what we expected from the theoretical works. The reason is presumably that the performance of the hydrogen discharge chamber is limited by the poor coupling of the microwave power to the flowing gas. In addition, During the process of NCl_3 synthesis [5], notable amount of Cl_2 is also trapped in the reservoir, and that is admixed to the supplied NCl_3. Since Cl_2 molecule is a strong quencher of $NCl(^1\Delta)$ as

$$NCl(^1\Delta) + Cl_2 \xrightarrow{k_{18}} NCl + Cl_2, \qquad (15)$$

where k_{18} is 2.9×10^{-11} cm^3/s, it should cause a serious influence to the laser performance. Simulation result predicted that a 20% Cl_2 admixture in the NCl_3 supplied is sufficient to extinguish the positive gain observed when Cl_2 was absent. We have not quantified the purity of the NCl_3 we have synthesized yet, however, an applicable contamination is suspected since the color of the trapped yellow liquid differed day-by-day

Recommended flow conditions of the amine-AGIL

Species	Mole fraction, %	P, Pa
HI	0.13	0.86
NCl_3	0.32	2.15
H_2	1.61	10.76
H	1.61	10.76
He (NCl_3 carrier)	48.17	322.74
He (H_2 carrier)	24.08	161.37
He (HI carrier)	24.08	161.37
Total	100	670

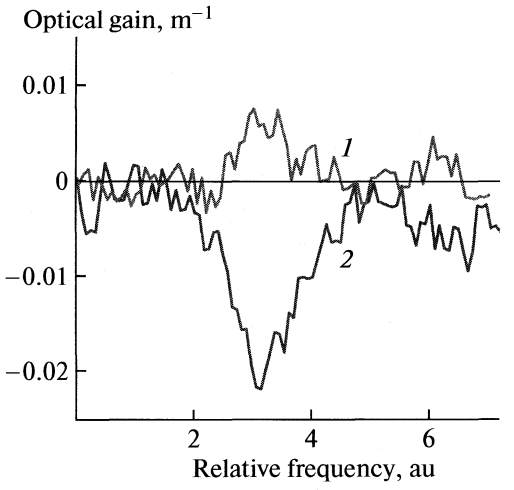

Fig. 6. Result of the gain measurement experiment; (*1*) and (*2*) with and without microwave discharge respectively.

in accordance with the change of synthesis conditions, indicating the existence of Cl_2 molecule. Reduction of the residual Cl_2 in the NCl_3 supplied is one of the keys to achieve higher gain.

SUMMARY

An amine-based all gas-phase iodine laser (AGIL) was studied theoretically and experimentally. The numerical simulation code was developed to find the optimum operational conditions of the amine-AGIL. It was found that the arrangement of the injectors was the key for both avoiding a local high-concentration of $NCl(^1\Delta)$ atoms, and rapid gain build-up before excited iodine atoms were quenched by Cl atoms. Based on the knowledge obtained by the theoretical works, we fabricated an experimental setup and conducted gain measurement experiments. As a result, a positive gain at iodine $I(^2P_{1/2})$–$I(^2P_{3/2})$ transition was observed for the first time. Currently, the absolute gain magnitude is limited by the low hydrogen concentration due to the insufficient H_2 atom decomposition, and/or by the admixed Cl_2 molecule in the supplied NCl_3.

ACKNOWLEDGMENTS

We are very grateful to Dr. Steven J. Davis of Physical Sciences Inc. for his useful advices. We are also grateful to Kawasaki Heavy Industries Ltd, for the lease of their vacuum system and measurement devices. This work is partly supported by the Society of Iodine Science.

REFERENCES

1. S. Lamberson, H. Schall and P. Shattuck, Proc. SPIE **6346**, 63461M, (8pp), 2007.
2. T. L. Henshaw, G. C. Manke II, T. J. Madden, M. R. Berman1 and G. D. Hager, Chem. Phys. Lett. **325**, 537, (2000).
3. D. B. Exton, J. V. Gilbert, and R. D. Coombe, J. Phys. Chem. **91**, 2692 (1991).
4. R. W. Schwenz, J. V. Gilbert and R. D. Coombe, Chem. Phys. Lett. **207**, 526 (1993).
5. A. J. R. Bauer, S. Lee, D. Vu, K. L. Galbaly, W. J. Kessler, and S. J. Davis, "Studies of an Advanced Iodine Laser Concept," in **AIAA2005–5040**, *AIAA 36th Plasmadynamics and Lasers Conference, Toronto, Ontario, Canada*, 2005.
6. M. Endo, T. Masuda, and T. Uchiyama, AIAA Journal **45**, 90 (2007).
7. T. Masuda, M. Endo and T. Uchiyama, J. Phys. D: Appl. Phys. **41** 055101 (8pp), 2008.

ЖУРНАЛ ФИЗИЧЕСКОЙ ХИМИИ, 2009, том 83, № 9, с. 1633–1636

CHEMICAL KINETICS AND CATALYSIS

УДК 541.124

INFLUENCE OF DIFFERENT DEGRADATION MEDIUM ON RELEASE OF ASCORBIC ACID FROM Poly (D,L-LACTIDE-CO-GLYCOLIDE)NANO AND MICROSPHERES

© 2009 M. Stevanović*, D. Uskoković*

*Institute of Technical Sciences of the Serbian Academy of Sciences and Arts, Belgrade; Serbia

E-mail:Magdalena@int.sanu.ac.rs; magdalena.stevanovic@gmail.com

Abstract – The major goals of the present study were to examine the effects of the type of release medium on the resulting drug release kinetics and to get further insight into the underlying drug release mechanisms. Spherical micro and nanoparticles were prepared by a physicochemical solvent/non-solvent method with polyvinyl pyrrolidone as a surfactant and characterized with ultraviolet spectroscopy and scanning electron microscopy before and upon exposure to various release media.

INTRODUCTION

Controlled drug delivery occurs when a polymer, whether natural or synthetic, is judiciously combined with a drug or other active agent in such a way that the active agent is released from the material in a predesigned manner. The release of the active agent may be constant over a long period, it may be cyclic over a long period, or it may be triggered by the environment or other external events. In any case, the purpose behind controlling the drug delivery is to achieve more effective therapies while eliminating the potential for both under- and overdosing [1–5]. Polymers have been used in the pharmaceutical and biomedical fields as delivery vehicles, (such as, microspheres and nanoparticles) and as scaffold materials as a consequence of their biodegradability and relative biocompatibility [6]. Biodegradable nano/microparticles of poly(D,L-lactide-co-glycolide) (PLGA) and PLGA-based polymers are widely explored as carriers for controlled delivery of therapeutics such as proteins, peptides, vaccines, genes, antigens, growth factors, vitamins, etc [7–10].

Vitamins are crucial for normal physiologic functioning of the organism, and vitamin deficiencies are relatively often associated with modern life style including inappropriate dietary habits, increased vitamin requirements or different diseases. Ascorbic acid (vitamin C) is known to be very unstable and easily destroyed by temperature, pH, oxygen, etc. [11–14]. In order to overcome some of these shortcomings of ascorbic acid, the microencapsulation technique may be suitable for ascorbic acid. System for the controlled delivery PLGA/vitamin can bring to the more balanced and efficient concentration of the vitamin throughout the extended period of time.

Polymer degradation plays a key role in medicament release from sustained release polyester systems, therefore in order to elucidate the mechanism governing release, it appears essential to analyze the in vitro degradation behavior of these devices [14–18]. Release from PLGA microspheres occurs via diffusion, polymer erosion or a combination thereof [17, 19]. PLGA erosion occurs via hydrolysis of the ester bonds in the polymer backbone. It is widely established that PLGA degradation starts with water uptake, and that hydrolysis leads to the production of acidic oligomers [17].

The selection of an appropriate release medium for in vitro tests simulating in vivo conditions can be very important for getting rapid feedback on the release characteristics of a specific batch.

The aim of the present study was to examine the effects of the type of degradation medium on the resulting drug release kinetics and to get further insight into the underlying drug release mechanisms.

EXPERIMENTAL

Materials

In the experiment we used poly(DL-lactide-co-glycolide) (PLGA) which was obtained from Durect, Lactel and had a lactide-to-glycolide ratio of 50:50. Molecular weight of the polymer was 40000–50000 g/mol. Molecular weight of ascorbic acid is 176.13 g/mol (Microvit™, Adisseo). Polyvinyl pyrrolidone (povidone, PVP) was obtained from Merck Chemicals Ltd (k-25, Merck, Germany). All other chemicals and solvents were of reagent grade.

Methods

Poly(DL-lactide-co-glycolide) micro and nanoparticles without and with encapsulated ascorbic acid were prepared using a physicochemical solvent/non-solvent method as we reported in our previously work [9, 10]. Ascorbic acid was encapsulated into the poly-

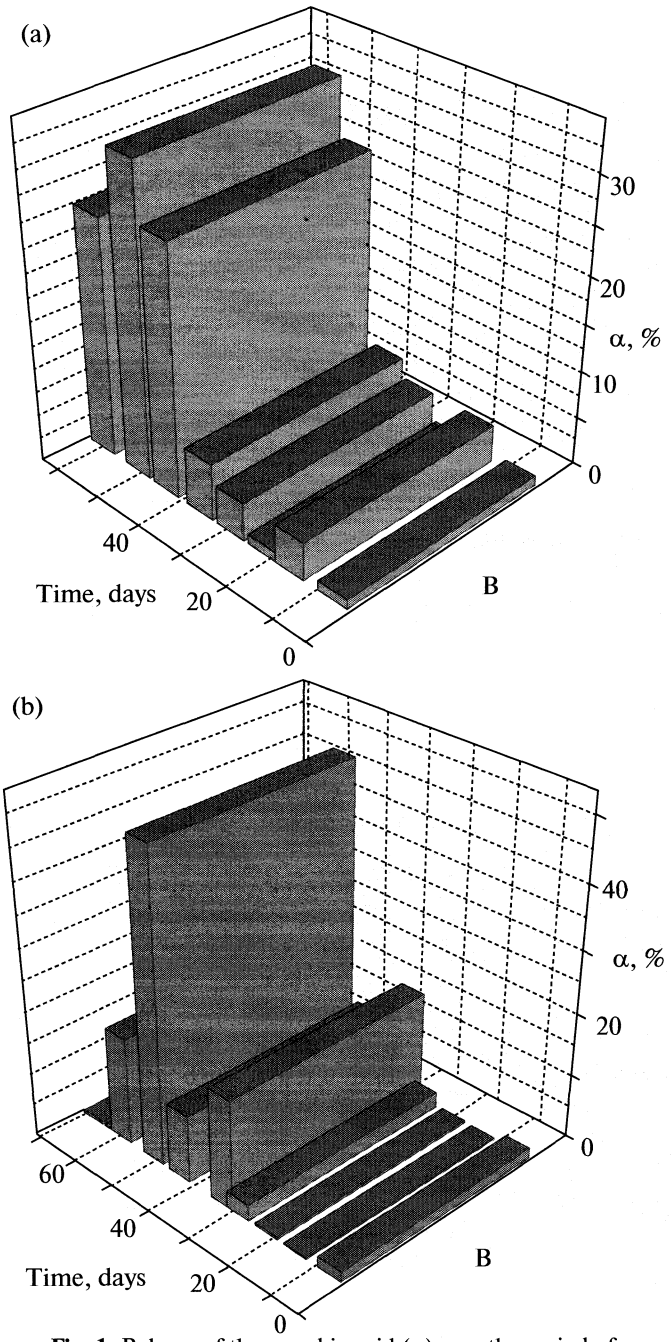

Fig. 1. Release of the ascorbic acid (α) over the period of time of the degradation in case of (a) physiological solution and (b) phosphate buffered saline as a degradation medium (relative review) from PLGA/ascorbic acid 85/15% nanoparticles.

mer matrix by means of homogenization of aqueous and organic phases. Polyvinyl pyrrolidone (povidone, PVP) was used as a stabilizer of the particles. Ascorbic acid-loaded PLGA nanoparticles were separated from the suspension by centrifugation, decantation followed by drying.

The degradation of the PLGA/ascorbic acid nanoparticles and release rate of the ascorbic acid were studied for more than fifty days in a physiological solution (0.9% sodium chloride in water) or in phosphate buffered saline (PBS, one tablet dissolved in 200 ml of deionized water yields 0.137 M sodium chloride, 0.01 M phosphate buffer and 0.0027 M potassium chloride) with sodium azide (0.1M solution natriumazid NaN_3) as a degradation medium. In the PBS was added 110 μl sodium azide because sodium azide acts as a bacteriostatic.

The UV measurements were performed on Perkin-Elmer Lambda 35 UV-VIS Spectrophotometer in the frequency interval of 200–400 nm. The pH of the physiological solution or PBS has been measured using pH indicator strips obtained from Merck (KGaA, Germany) at various time periods to follow the acidity of the degrading medium with time. The morphology of PLGA/ascorbic acid 85/15% nanoparticles has been examined, after two, 24 and 39 days of the degradation in physiological solution and after 17 and 28 days of the degradation in phosphate buffered saline, by scanning electron microscope JEOL JSM-649OLV.

RESULTS AND DISCUSSION

The degradation of the PLGA and release of the ascorbic acid have been tracked based on the intensity of the absorbance maximum which is in the correlation with the concentration of the PLGA and ascorbic acid within the solution. PLGA degrades via backbone hydrolysis (bulk erosion) and the final degradation products are the monomers, lactic acid and glycolic acid. PLGA completely degrades within period of 8 weeks in physiological solution (Fig. 1a) as a degradation medium as well as in phosphate buffered saline (Fig. 1b), fully releasing all the encapsulated ascorbic acid.

Morphological changes of degraded PLGA/ascorbic acid 85/15% nanoparticles including particle size, shape and surface were monitored throughout the 39 days incubation in physiological solution and during the 28 days in PBS. At a beginning of the degradation, PLGA nanoparticles displayed a relatively smooth and nonporous surface. From the Figs. 2 and 3 we can see that during the degradation the particles were first agglomerated, then forming the film. The particles are in a very close contact during the degradation process which brings to higher agglomeration of the particles and creation of the porous film. By the end of the experiment the particles have fully degraded and there were no more traces of them in the solution.

Polymer degradation and drug release kinetics of ascorbic acid from PLGA microspheres were investigated under, initial, neutral pH conditions in different degradation medium. The pH of the solution began to decrease after two days of immersion. From the Fig. 4 it can be noted that during the time of the degradation pH of the solution decreases as a result of the accumulation of PLGA degradation products and ascorbic

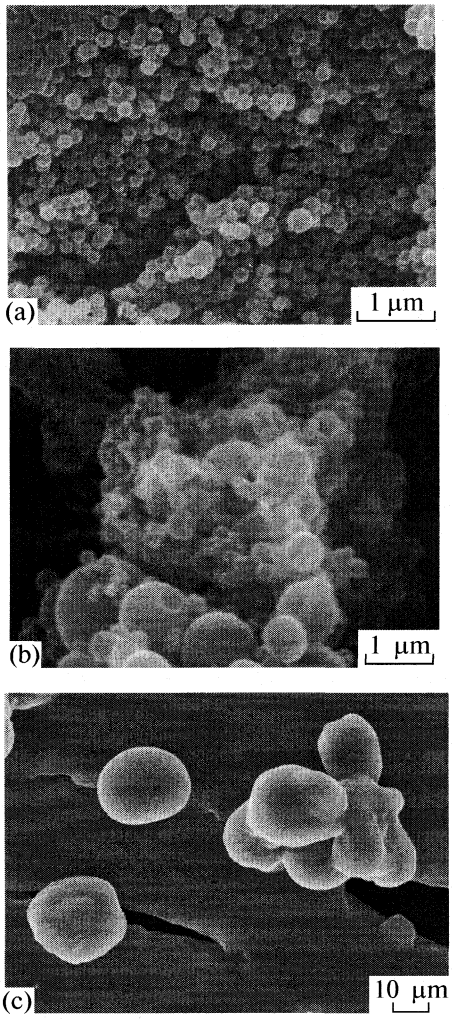

Fig. 2. SEM images of PLGA/ascorbic acid 85/15% nanospheres after (a) two,(b) 24 and (c) 39 days of the degradation in physiological solution.

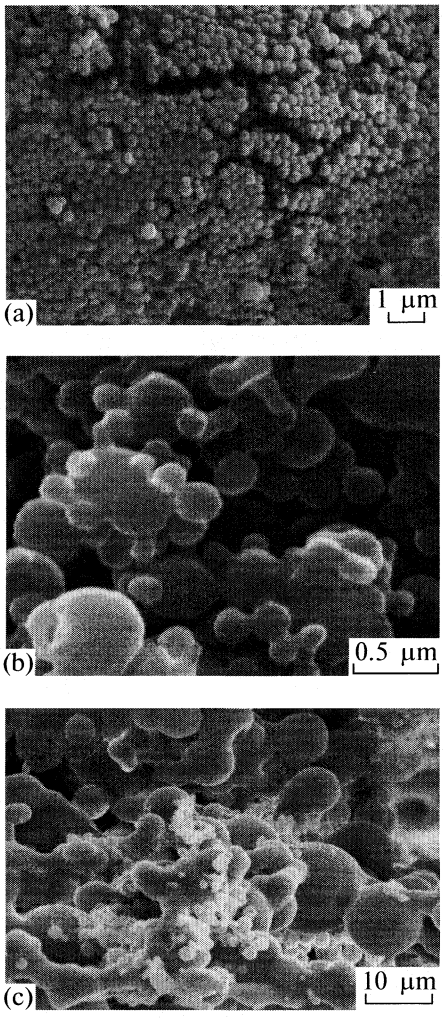

Fig. 3. SEM images of PLGA/ascorbic acid 85/15% nanospheres (a) before and after (b) 17 and 28 (c) 28 days of the degradation in phosphate buffered saline.

acid. It could be expected that the faster degradation of the lower molar mass fraction, present in copolymer, increase the local acidity, thereby, accelerating the hydrolysis of higher molar mass species. In other words, when acid accumulation creates a local pH drop, catalytic degradation of the polymer itself occurs. pH of the physiological solution had dropped from pH 7.0 to 2.6, as well as pH of the PBS with sodium azide, in the case of the PLGA/ascorbic acid 85/15% nanoparticles.

CONCLUSION

The release dynamics of the ascorbic acid from the polymer matrix is different when PLGA particles degrade in PBS and when they degrade in physiological solution, as a degradation medium. The ascorbic acid is released slower from the PLGA particles at the beginning, when PBS is used. This is explained with the

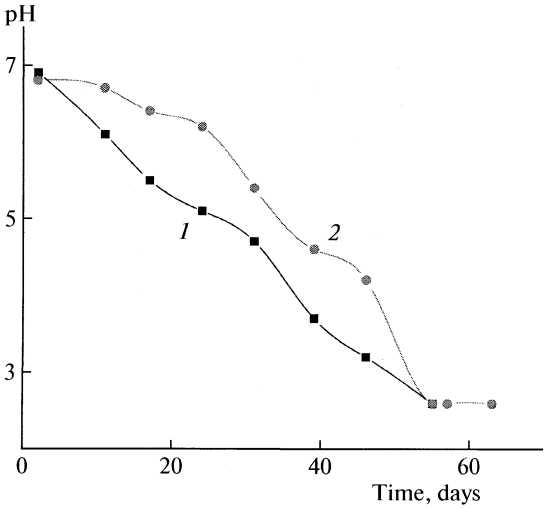

Fig. 4. Changes in the pH of the degradation medium with immersion time for the PLGA/accorbic acid 85/15% nanoparticles in the case of (*1*) physiological solution and (*2*) phosphate buffered saline.

slower change of pH solution as well as with the presence of sodium azide.

ACKNOWLEDGMENTS

Authors would like to thank Miloš Bokorov for his help in SEM analysis. The Ministry of Science and Technological Development of Republic of Serbia supports this work through the project No. 142006.

REFERENCES

1. L. Brannon-Peppas, J. O. Blanchette, Advanced Drug Delivery Reviews **56**, 1649 (2004).
2. R. K. Kulkarni, E. G. Moore, A. F. Hegyeli, F. Leonard, Journal of Biomedical Material Research **5**, 169 (1971).
3. J. H. Park, S. Lee, J. H. Kim, K. Park, K. Kim, I. C. Kwon, Progress in Polymer Science **33** (1), 113 (2008).
4. B. Sumer, J. Gao, Nanomedicine **3** (2), 137 (2008).
5. A. V. Kabanov, H. E. Gendelman, Progress in Polymer Science **32** (8–9), 1054 (2007).
6. S. S. Feng. L. Mu, K. Yin Win, G. Huang, Current Medicinal Chemistry **11**, 413 (2004).
7. M. Stevanović, N. Ignjatović, B. Jordović, D. Uskoković, Journal of Materials Science: Materials in Medicine **18**, 1339 (2007).
8. M. Stevanović, A. Radulović, B. Jordović, D. Uskoković, Journal of Biomedical Nanotechnology **4**(3), 349 (2008).
9. M. Stevanović, B. Jordović, D. Uskoković, Journal of Biomedicine and Biotechnology, 2007, article id 84965
10. M. Stevanović, J. Savić, B. Jordović, D. Uskoković, Colloids and Surfaces B: Biointerfaces **59**, 215 (2007).
11. V. Ratnam, D. D. Ankola, V. Bhardwaj, D. K. Sahana, M. N. V. Ravi Kumar, Journal of Controlled Release **113**, 189 (2006).
12. Q. Chen, M. G. Espey, M. C. Krishna, J. B. Mitchell, C. P. Corpe, G. R. Buettner, E. Shacter, M. Levine, The Proceedings of the National Academy of Sciences U S A **102**, 38, 1360 (2005).
13. J. H. Park, S. O. Choi, R. Kamath, Y. K. Yoon, M. Allen, M. Prausnitz, Biomedical Microdevices **9** (2), 223 (2007).
14. M. Stevanović, D. Uskoković, Current Nanoscience, 2009, in press.
15. M. Therin, P. Christel, S. Li, H. Garreau, M. Vert, Biomaterials **13** (9), 594 (1992).
16. M. Vert, J. Mauduit, S. Li, Biomaterials **15** (15), 1209 (1994).
17. R. A. Miller, J. M. Brady, D. E. Cutright, Journal of Biomedical Materials Research **11**, 5, 711–719 (1977).
18. N. Faisant. J. Siepmann, J. P. Benoit, European Journal of Pharmaceutical Sciences **15**, 355 (2002).
19. R. Baker, Introduction. In: R. Baker, Editor, Controlled Release of Biologically Active Agents, Vol., A. Wiley-Interscience Publication, 1987, 1–18.

ЖУРНАЛ ФИЗИЧЕСКОЙ ХИМИИ, 2009, том 83, № 9, с. 1637–1643

CHEMICAL KINETICS AND CATALYSIS

УДК 541.128

THE STATE OF NICKEL IN THE SILVER MODIFIED NiMg/SiO_2 VEGETABLE OIL HYDROGENATION CATALYSTS

© 2009 M. Gabrovska*, D. Nikolova*, J. Krstić**, M. Stanković**, P. Stefanov***, R. Edreva-Kardjieva*, D. Jovanović**

*Institute of Catalysis, Bulgarian Academy of Sciences, Sofia, Bulgaria

**Institute of Chemistry, Technology and Metallurgy, Department of Catalysis and Chemical Engineering, Belgrade, Serbia

*** Institute of General and Inorganic Chemistry, Bulgarian Academy of Sciences, Sofia, Bulgaria

E-mail: margo@ic.bas.bg

Abstract – Two series of silver modified Ni–Mg materials were synthesized by precipitation-deposition on SiO_2 support derived from two silica sources: diatomite activated at 800°C (*Series a*; Mg/Ni = 0.1 and SiO_2/Ni = 1.07) and synthetic water glass (*Series b*; Mg/Ni = 0.1 and SiO_2/Ni = 1.15). The modification with silver was made at three molar Ag/Ni ratios, namely 0.0025, 0.025 and 0.1. The effects of the source of the silica support and the silver presence and content on the nickel state in the silver modified reduced-passivated NiMg/SiO_2 precursors of the vegetable oil hydrogenation catalyst were established by X-ray diffraction and X-ray photoelectron spectroscopy techniques. The passivation procedure was applied in order to protect the metallic nickel particles from further oxidation. The crystallization of the formed nickel hydrosilicate phases depends on the source of the silica support, more expressed in the diatomite supported samples. It was shown that the silver modification of the NiMg/SiO_2 precursors enhances the reduction of the nickel hydrosilicates accompanied by formation of relatively smaller metallic nickel particles, more pronounced in the water glass supported precursors. The increase of the silver content in the water glass deposited samples is responsible for the metallic nickel dispersion increase. The higher content of the Ni^0 particles on the surface of the diatomite deposited samples is in accordance with the higher stability of the larger metallic nickel crystallites to oxidation during the passivation step. On contrary, higher dispersed Ni^0 particles on the surface of the water glass supported samples are more susceptible to the oxidation.

INTRODUCTION

The catalytic hydrogenation of vegetable oils continues being one of the most versatile ways to modify the physical properties, oxidative and thermal stability, the melting characteristics of the fat and its color. The process is widely used in the elaboration of margarines, shortenings and products of bakery [1]. The carbon double bonds are partially or fully saturated during the hydrogenation. Concomitantly, the isomerization of naturally occurring *cis* fatty acids (CFA) to *trans* fatty acids (TFA) takes place [2]. The selectivity of the process represents a considerable challenge, aiming to enhance the hydrogenation activity and simultaneously to suppress the isomerization [3].

The composition and properties of final product depend on various operating factors, including catalyst type and concentration, agitation, hydrogen pressure and temperature. Although it has been experienced with several metals, including the noble metals, the most widely used commercial catalyst remains the metallic nickel supported on a SiO_2 carrier [2] because of its lower cost.

It has been published that Ni–Mg catalysts, supported on SiO_2 derived from two siliceous sources, either diatomite or water glass, demonstrate both high soybean oil hydrogenation activity and high quantity of detrimental TFA production [4]. According to our data, the addition of Ag to the Ni-Mg/diatomite catalyst suppresses the TFA formation in the hydrogenated products [5].

The aim of this work was to estimate the effect of the source of the silica support (diatomite or water glass) as well as the silver presence and content on the nickel state in the silver modified reduced-passivated NiMg/SiO_2 catalyst precursors for vegetable oil hydrogenation. The passivation procedure was applied in order to protect the metallic nickel particles from further oxidation. The unreduced samples are studied for the sake of comparison.

EXPERIMENTAL

Sample preparation

The diatomite, designated as D, was obtained from Baroševac – field B ("Kolubara" coal basin, Lazarevac, Serbia). The crude diatomite was mechanically, chemically (HCl) and thermally (800°C) treated in order to obtain pure and activated support [6]. The water glass material, designated as W, is a synthetic commercial product with module (molar ratio)

Table 1. The chemical composition of the precursors, at. %

№	Sample	Ni	Mg	Ag	Si
	Series a				
1	Ni/D	46.10	4.61	–	49.29
2	0.1AgNi/D	46.03	4.58	0.11	49.27
3	1.0AgNi/D	45.56	4.54	1.13	48.77
4	4.0AgNi/D	44.06	4.40	4.41	47.13
	Series b				
1'	Ni/WG	44.45	4.45	–	51.10
2'	0.1AgNi/WG	44.40	4.43	0.11	51.10
3'	1.0AgNi/WG	43.95	4.38	1.10	50.57
4'	4.0AgNi/WG	42.56	4.26	4.26	48.92

SiO_2/Na_2O = 3.0 (GALENIKA - Magmasil A. D., Zemun (Belgrade, Serbia).

Two series of silver modified Ni–Mg materials were synthesized by precipitation-deposition of the corresponding metal nitrates with 10% w/w Na_2CO_3 aqueous solution under vigorous stirring at temperature of 90°C and constant value of pH 10.0 ± 0.1 on SiO_2 support derived from two silica sources: activated diatomite (*Series a*; Mg/Ni = 0.1 and SiO_2/Ni = 1.07) and synthetic water glass (*Series b*; Mg/Ni = 0.1 and SiO_2/Ni = 1.15). After ageing of the obtained slurry, the corresponding source of silica support as 2.0 wt % diatomite aqueous suspension or as 2.0 wt % water glass aqueous solution was added to the reaction mixture to form the final catalyst precursor. The resulting materials were aged again under constant stirring and than filtered and thoroughly washed with hot distilled water until absence of NO_3^- and Na^+ ions have been obtained. The precursors were dried for 24 h in an oven at 105°C and ground to a powder. The modification with silver was made at three molar Ag/Ni ratios, namely 0.0025, 0.025 and 0.1. The unmodified reference Ni–Mg samples were prepared by the same procedure on both siliceous sources and denoted as Ni/D or Ni/WG.

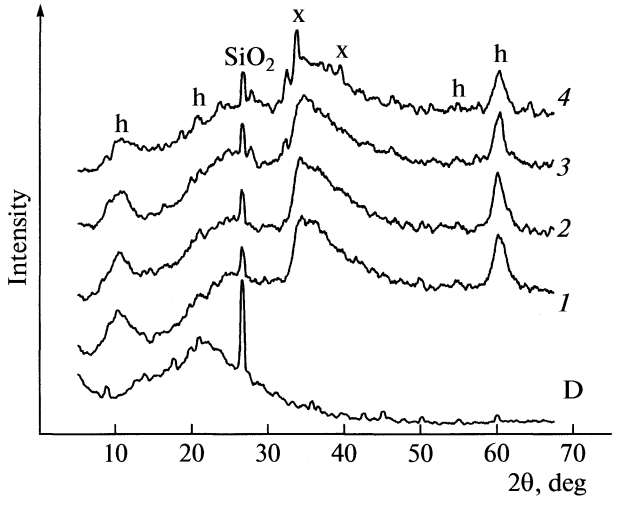

Fig. 1. XRD patterns of the unreduced precursors 1–4 (see Table 1) from *Series a*; (h) nickel hydrosilicate and (x) α-Ag_2CO_3.

The samples were referred as *x*AgNi/Z, where *x* is the atomic % of Ag (Table 1) and Z is the source of the support – D or WG.

The reduction (activation) of the precursors was performed in a laboratory set-up by a "dry reduction" method with a gas mixture of H_2/N_2 (1/1 v/v) at the flow rate of 5 $dm^3\ h^{-1}$. The reduction temperature was raised up to 430°C at the heating rate of 1.5 K min^{-1} and held constant for 5 h. After cooling down to room temperature, the reduced precursors were passivated with a mixture of 350 ppm of O_2 in nitrogen for 2 h. For the sake of simplicity these samples were denoted with the prefix **r**, for example, r-Ni/D.

Sample characterization

The chemical compositions of the precursors were determined by atomic absorption spectroscopy (Varian AA 775 spectrophotometer). The silica content was determined by a classical silicate analysis and a chemical procedure applicable in the analysis of sediment rocks.

The X-ray diffraction studies were accomplished on a Bruker D8 Advance powder diffractometer employing CuK_α radiation, operated at U = 40 kV and I = = 40 mA.

The X-ray photoelectron spectroscopy measurements were performed in a VG ESCALAB II electron spectrometer using AlK_α radiation with energy of 1486.6 eV. The binding energies (E) were determined with an accuracy of ±0.1 eV utilizing the C1*s* line at 285.0 eV (from an adventitious) as a reference. The composition and chemical state of the precursors were investigated on the basis of the areas and binding energies of Ni2$p_{3/2}$, Ag3*d*, Mg1*s*, O1*s*, and Si2*p* photoelectron peaks (after linear subtraction of the background) and Scofield's photoionization cross-sections. The peak fitting software was Phimat program.

RESULTS AND DISCUSSION

The results from the silicate and chemical analysis of the synthesized precursors are summarized in the Table 1. The obtained data demonstrate hat the samples posses a chemical composition very close to the theoretical values.

X-ray diffraction (XRD)

Unreduced precursors. The diffractogram of the diatomite source (Fig. 1, curve D) shows reflections characteristic of amorphous silica (silica halo peak centered at $2\theta \approx 21°$) and well-crystallized quartz phase ($2\theta \approx 26°$; JCPDS 46-1045). The dried water glass represents badly crystallized solid (Fig. 2, curve WG).

The precipitation–deposition of Ni and Mg on the surface of both siliceous sources results in obtaining of the unmodified reference samples Ni/D and Ni/WG. Their XRD patterns are significantly different from the spectra corresponding to diatomite and water glass (Figs. 1 and 2). The signals are weak and broad, denoting poorly crystallized, well-dispersed nickel compounds [7]. It has been established that two types of hydrosilicates seem to coexist in Ni/D and Ni/WG precursors: nickel silicate hydroxide phase ($2\theta \approx 10$, 20, 24, 34, 37 and 60°; JCPDS file 22-0754) and antigorite phase ($2\theta \approx 12$, 14, 15, 17, 19, 25, 35, 37, 41 and 54°; JCPDS 21-0963). Similar XRD patterns for Ni/diatomite catalysts, prepared by deposition-precipitation have been reported by Echeverria and Andres [7].

The XRD pattern of the Ni/D sample (Fig. 1, curve *1*) manifests more and better formed reflections of the nickel hydrosilicate phases in comparison with its analogue Ni/WG from *Series b*. The peak of the well crystallized quartz phase is preserve in the spectrum of Ni/D sample however with low intensity. The registered high background below $2\theta = 10°$ on the diffractogram of Ni/WG precursor indicates advanced amorphisation of the observed phases than in Ni/D one. It may be suggest that the use of the water glass as a source of the silica support provokes higher dispersion of the nickel hydrosilicate phases.

The observed phenomenon proves that during the synthesis of the precursors, an interaction occurs between the nickel salt and the silica from the support resulting in formation of nickel hydrosilicate layers, which covered the external surface of the silica particles. The poorly crystallized nickel hydrosilicate compounds with imperfect nickel antigorite and/or nickel montmorillonite-like structure are always formed during the co-precipitation of nickel nitrate and alkali silicate solutions at temperature under 100°C [8]. The XRD patterns of nickel hydrosilicates are not clearly defined due to its turbostratic structure [8–10].

The modification of the Ni/D and Ni/WG samples with silver alters their XRD patterns in different degree. The main reflections of the nickel hydrosilicate phases are detected on the diffractograms of modified samples from *Series a* (Fig. 1, curves *2–4*). Two additional lines at $2\theta \approx 33$ and 39°, characteristics of α-Ag_2CO_3 phase (JCPDS file 31-1237) is registered only for the sample with the highest silver content (4.0AgNi/D). Contrariwise, the XRD patterns of the nickel hydrosilicate phases are not visible on the diffractograms of the modified samples from *Series b* (Fig. 2, curves *2'–4'*).

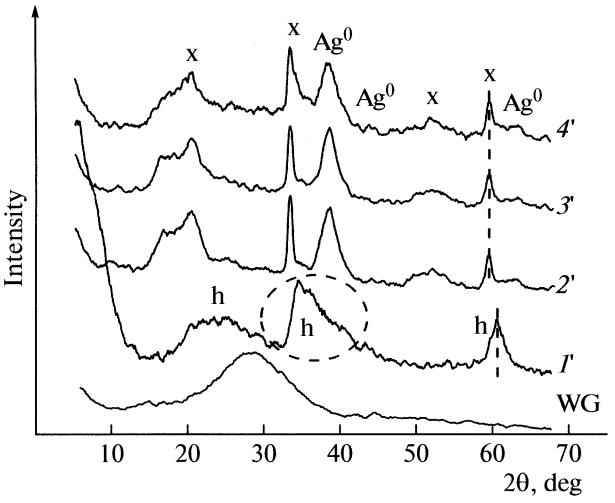

Fig. 2. XRD patterns of the unreduced precursors *1'–4'* (see Table 1) from *Series b*; (h) nickel hydrosilicate and (x) α-Ag_2CO_3.

Moreover, the reflections of α-Ag_2CO_3 phase are more as number ($2\theta \approx 19$, 33, 51 and 61°) and much more intensive in all Ag-containing precursors from *Series b*. Supplementary, these precursors display extra diffraction lines at $2\theta \approx 38$, 44 and 64°, typical of the cubic metallic silver phase (JCPDS file 4-0783). Its presence indicates that the Ag^+ ions are weakly bounded to the silica from the water glass source in comparison to the diatomite. As a result, part of Ag^+ ions seems to be already reduced to the metallic state during the preparation of the precursors.

It can be summarized that the silver presence in the unreduced precursors from *Series a* causes partial amorphisation of the nickel hydrosilicates, whereas these phases are probably fully amorphizated or "hidden" by the silver entities in the samples from *Series b*.

Reduced-passivated precursors. The reduction-passivation procedure of the samples from both series causes appearance of the diffraction lines at $2\theta \approx 44$, 52, 76 and 93° (Figs. 3, 4). These reflections are characteristics of the metallic nickel phase (JCPDS file 4-0850), better formed in the samples from *Series a*. Some reflections of nickel hydrosilicate phases are also observed in the samples from both series, suggesting incomplete reduction of the Ni^{2+} entities.

It may be seen that the presence of silver diminishes the intensity of the nickel hydrosilicate phases indicating facilitated reduction of the Ni^{2+} ions, more expressed with the increase of the silver loading in the samples.

This deduction was confirmed by our former study based on the TPR experiments performed on the samples under study [11]. It was found that the silver addition enhances the reducibility of the bulk Ni^{2+} entities

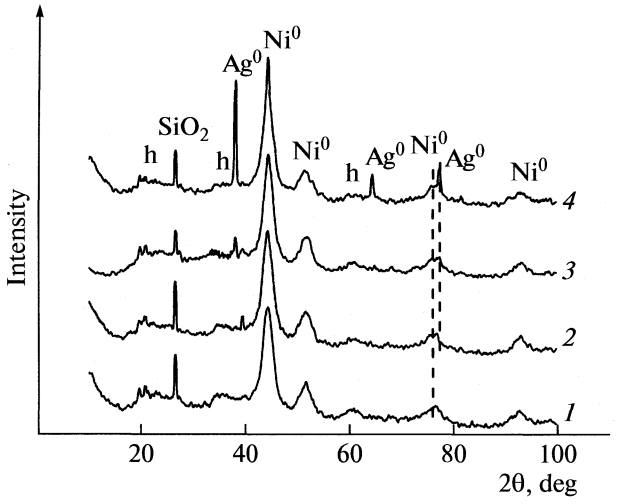

Fig. 3. XRD patterns of the reduced-passivated precursors 1–4 (Table 1) from *Series a*; (h) nickel hydrosilicate.

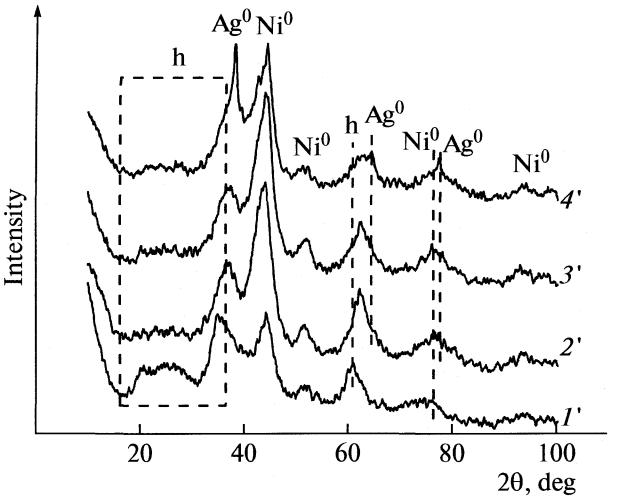

Fig. 4. XRD patterns of the reduced-passivated precursors 1'–4' (see Table 1) from *Series b*; (h) nickel hydrosilicate.

depending on the source of both carriers and the silver concentration. Moreover, the reduction temperatures decrease with the increase of Ag content. The results indicate that the use of the water glass as a silica source ensures reduction of the Ni^{2+} species in all modified samples at temperatures lower than in their analogues prepared on diatomite. The results obtained are in agreement with the scarce studies published in the literature on the reducibility of supported NiAg oxides. Ertl and Knözinger [12] reported that the presence of silver decreased the reduction temperature of nickel supported on SiO_2. The role of Ag in promoting the Ni^{2+} reduction is likely associated with the fact that Ag_2O can easily be reduced to metal state at temperature lower than NiO. Taking into consideration that silver and nickel do not form a solid solution at any composition under equilibrium conditions [13] it is assumed that metallic Ag might plays an essential role in provoking the activation of H_2 and the removal of oxygen atom from the Ni-containing phases via weakening vicinal Ni–O bonds.

The appearance of the nickel hydrosilicate phase after reduction of the samples from *Series b* (Fig. 4) supports our assumption that the silver phases "hidden" the nickel hydrosilicates in the unreduced samples (see Fig. 2). A plausible explanation is that the interaction of Ni^{2+} ions is presumably different with diatomite and water glass, during the precipitation-deposition of the Ni^{2+} ions onto the supports, which can cause differences in nucleation and growth of the nickel species.

The well-formed signals of the metallic silver phase at $2\theta \approx 38$, 64 and 77° appear only in the samples with the highest silver content (r-4.0AgNi/D and r-4.0AgNi/WG), better organized in the precursor from *Series a*. The XRD study shows no influence of silver on the bulk structure of nickel, thus the metallic nickel and metallic silver present as separate phases. The reflections of NiO, AgO and Ag_2O phases are not detected as results of the passivation of the reduced samples.

It is necessary to mention that the most intensive peak of the Ni^0 phase ($2\theta \approx 44.5°$) overlaps the second in intensity diffraction line of the Ag^0 phase ($2\theta \approx 44.3°$). On this reason, the mean Ni^0 crystallite size is estimated from the reflection at $2\theta \approx 52°$. The results show that the values of the metallic nickel particles of the precursors from *Series a* are located in the nanosize region, namely: 7.0 nm (r-Ni/D), 6 nm (r-0.1AgNi/D), 5.4 nm (r-1.0AgNi/D) and 4.5 nm (r-4.0AgNi/D), respectively. This trend demonstrates the increase of the Ni^0 phase dispersion with the increase of the silver content in the diatomite supported samples [5].

The reflection at $2\theta \approx 52°$ on the XRD patterns of the samples from *Series b* is very broad and therefore, the determination of the mean Ni^0 particle size is practically nonsense. The broadening indicates the presence of smaller particles of the Ni^0 than in the precursors from *Series a*. The metallic nickel appears as more dispersed in the modified precursors from *Series b* in comparison with this one from *Series a*.

It can be summarized that the usage of diatomite as silica source provokes better crystallization of the Ni^0 and Ag^0 phases after the reduction-passivation procedure than the water glass one. The presence of silver and its amount increase the reducibility of the Ni^{2+} entities in the samples from both series. Moreover, the silver modification affects the degree of the Ni^0 phase crystallization and leads to the formation of relatively smaller Ni^0 particles. With addition of the silver modifier, the dispersion extent of the metallic Ni increase. This effect is more pronounced in the reduced-passivated precursors from *Series b*.

Table 2. XPS data of the unreduced (I) and reduced-passivated (II) precursors from both series

Sample	Surface concentrations, at. %				E, eV (Ni2$p_{3/2}$)			Nickel oxidation state contribution, % (II)	
	Ni		Ag		I	II			
	I	II	I	II	Ni^{2+}	Ni^0	Ni^{2+}	Ni^0	Ni^{2+}
Series a									
Ni/D	11.1	4.2	–	–	855.3	853.5	856.6	5.6	94.4
0.1AgNi/D	13.6	3.1	0.2	–	856.0	852.2	854.8	6.5	93.5
1.0AgNi/D	12.2	3.5	0.3	0.3	855.8	851.9	855.2	11.0	89.0
4.0AgNi/D	10.3	4.3	0.8	0.8	855.6	853.5	856.7	13.9	86.1
Series b									
Ni/WG	15.0	17.7	–	–	856.1	853.6	856.6	3.6	96.4
0.1AgNi/WG	17.8	16.4	–	–	855.7	852.5	855.0	6.1	93.9
1.0AgNi/WG	21.0	19.2	0.4	0.6	855.7	852.8	856.0	4.5	95.5
4.0AgNi/WG	15.0	15.8	1.2	1.4	855.6	852.3	854.9	6.3	93.7

X-ray photoelectron spectroscopy (XPS)

Unreduced precursors. The binding energy (E) values of the main Ni2$p_{3/2}$ peak in unreduced precursors are presented in Table 2. As expected, nickel is presented in Ni^{2+} oxidation state on the surface of the samples from both series. The differences in the E values of the unmodified Ni/D (855.3 eV) and Ni/WG (856.1 eV) samples may be attributed to the different Ni^{2+} state in the nickel hydrosilicates on the surface of the samples [7, 14].

The silver modification of the samples from *Series a* leads to the shifting of Ni2$p_{3/2}$ peak towards higher E values (Table 2), more clearly expressed in the sample with the lowest silver content (0.1AgNi/D). The shifting may be assigned to the stronger interaction between the nickel and the diatomite surface.

However, the silver presence in the samples from *Series b* does not arouse the shifting of the Ni2$p_{3/2}$ peak, on the analogy of *Series a*. It may be observed that the increase of the silver amount provokes the shifting of Ni2$p_{3/2}$ peak towards lower binding energies, which suggested weakening of the interaction between the nickel and the water glass surface. The data obtained corroborate the facilitated reduction of the Ni^{2+} ions, more expressed with the increase of the silver loading in the samples.

The E values of Ag3$d_{5/2}$ peak of the modified samples from *Series a* are situated in the range of 367.4–367.3 eV; the corresponding ones from *Series b* – in the range of 368.1–367.7 eV. These energies can not be attributed to the definite Ag–O species or Ag^0, because of the narrow E interval of the different Ag entities, namely 368.3–367.9 eV for Ag^0, 367.8–367.5 eV for Ag_2CO_3, 368.1–367.3 eV for AgO and 368.4–367.7 eV for Ag_2O respectively [15]. However, the higher E values of Ag3$d_{5/2}$ peak in *Series b* confirm the presence of the metallic silver as it has been registered by XRD (Fig. 2)

It may be seen from Table 2 that a small amount of silver raises the nickel surface concentration in 0.1AgNi/D sample from *Series a*. The increase of the silver concentration leads to the lessening of Ni content in the order: 0.1AgNi/D > 1.0AgNi/D > 4.0AgNi/D. It is interesting that the nickel surface concentration on the water glass supported samples is higher (15.0–21.0 at. %), comparing with their analogues deposited on diatomite (10.3–13.6 at. %). The detected surface concentrations of nickel on the samples from *Series b* indicate a higher dispersion of Ni entities [16].

Reduced-passivated precursors. The reduction-passivation procedure provokes a strong impoverishment of the nickel on the surface of the samples from *Series a* (Table 2). The nickel content decrease may be associated with the diminished dispersion [17]. The surface nickel concentration remains practically unchanged on the surface of the samples from *Series b*. Obviously the use of the water glass as a silica source preserves the higher dispersion of the Ni entities on the sample surface. The silver is not registered on the samples with lowest Ag content from both series (0.1AgNi/D and 0.1AgNi/WG).

The general view of the Ni2p level reveals the asymmetry of the main Ni2$p_{3/2}$ peak towards lowers E (Fig. 5 and Table 2). The peak-fitting of the composite Ni2p level evidences the presence of the two types of the nickel oxidation states, Ni^0 and Ni^{2+}.

The values of the E in the range of 853.5–851.9 eV for *Series a* and 853.6–852.3 eV for *Series b* characterize the Ni^0. The presence of metallic nickel after

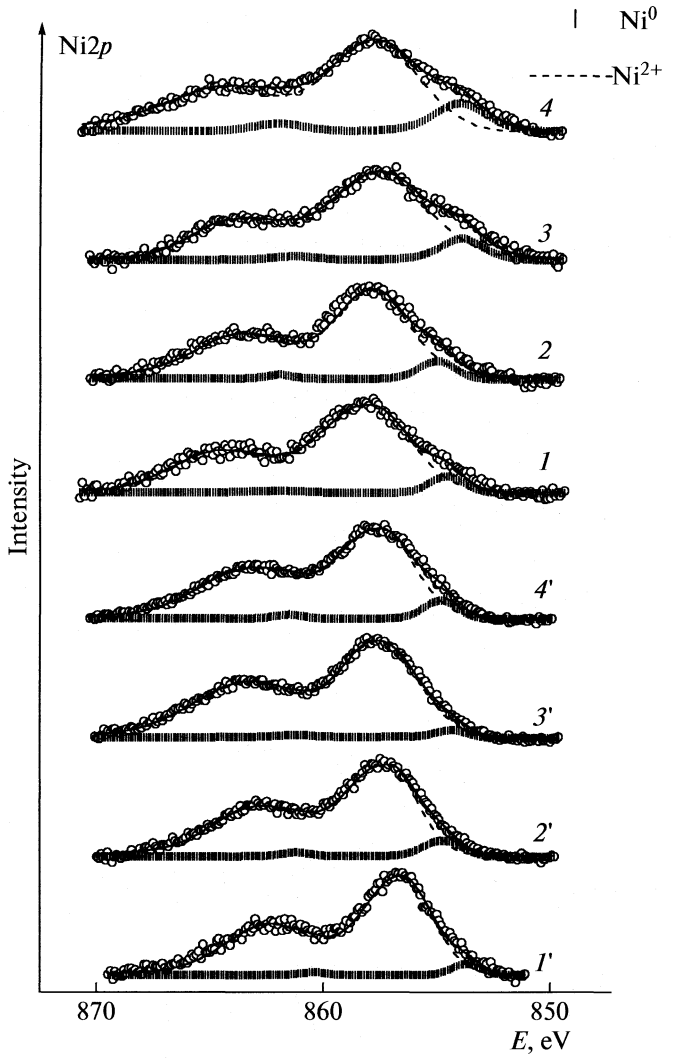

Fig. 5. Peak-fitting of the Ni2*p* photoelectron spectra of the reduced-passivated precursors *1*–*4* and *1'*–*4'* (see Table 1); *E* is the binding energy.

passivation is supported by X-ray diffraction data (Figs. 3, 4).

The *E* values in the range of 856.7–854.8 eV for *Series a* and 856.6–854.9 eV for *Series b*, respectively, characterize Ni^{2+} state in Ni–O species originated both from the unreduced nickel phylosilicate phase and dispersed two-dimensional "NiO"-like phase on the metallic nickel particles.

The Ni^0 oxidation state contribution on the samples from *Series a* increases with the silver presence and content. However, this effect is not clearly pronounced in the samples from *Series b* (Table 2). The higher content of the Ni^0 particles on the surface of the diatomite deposited samples is in accordance with the higher stability of the larger metallic nickel crystallites to oxidation during the passivation step (XRD data). On contrary, the higher dispersed Ni^0 particles on the surface of the water glass supported samples are more susceptible to oxidation.

CONCLUSIONS

It may be concluded that:

The crystallization of the nickel hydrosilicate phases depends on the source of the silica support, more expressed in the diatomite supported samples.

The modification with silver enhances the reduction of the nickel hydrosilicates in both series.

The higher content of the Ni^0 particles on the surface of the diatomite deposited samples is in accordance with the higher stability of the larger metallic nickel crystallites to oxidation during the passivation step. On the contrary, the higher dispersed Ni^0 particles on the surface of the water glass supported samples are more susceptible to oxidation.

The increase of the silver content increase the dispersion of the metallic nickel more pronounced in the water glass deposited samples. It is assumed that metallic Ag provokes the activation of H_2 and the removal of oxygen atom from the Ni-containing phases via weakening vicinal Ni–O bonds.

ACKNOWLEDGMENTS

The authors gratefully acknowledge the partial financial support of the Ministry of Education and Science of Bulgaria (Project X-1411) and the Serbian Ministry of Science (Project-166001B and thank Assist. Prof. MSc. Genoveva Atanasova for XPS spectra recording (Institute of General and Inorganic Chemistry of Bulgarian Academy of Sciences).

REFERENCES

1. M. Fernández, G. Tonetto, G. Crapiste, D. Damiani, J. Food Engineering **82**, 199 (2007).
2. J. Weldsink, M. Bouma, N. Schöön, A. Beenackers, Catal. Rev. Sci. Eng. **39**, 253 (1997).
3. K. Belkacemi, A. Boulmerka, J. Arul, S. Hamoudi, Topics in Catalysis **37**, 113 (2006).
4. M. Gabrovska, J. Krstić, R. Edreva-Kardjieva, M. Stanković, D. Jovanović, Appl. Catal. A: General **299**, 73 (2006).
5. M. Stanković, M. Gabrovska, J. Krstić, P. Tzvetkov, M. Shopska, Ts. Tsacheva, P. Banković, R. Edreva-Kardjieva, D. Jovanović, J. Mol. Catal. A: Chemical **297**, 54 (2009).
6. D. Jovanovic, R. Radovic, L. Mares, M. Stankovic, Br. Markovic, Catal. Today **43**, 21 (1998).
7. S. Echeverria and V. Andres, Appl. Catal. **66**, 73 (1990).
8. J. van Eijk van Voorthuijsen, P. Franzen, Rec. Trav. Chim. **70**, 793 (1951).
9. K. Ghuge, A. Bhat, G. Babu, Appl. Catal. A: Gen. **103**, 183 (1993).
10. P. Burattin, M. Che, C. Louis, J. Phys. Chem. **B 101**, 7060 (1997).

11. M. Gabrovska, I. Shtereva, J. Krstić, M. Stanković, R. Edreva-Kardjieva, D. M. Jovanović, 9th International Conference on Fundamental and Applied Aspects of Physical Chemistry, PHYSICAL CHEMISTRY 2008, September 24–26, 2008, Belgrade, Serbia, Vol. 1, p. 178.

12. G. Ertl, H. Knözinger, J. Weitkemp (Eds.), Handbook of Heterogeneous Catalysis, VCH, Weinheim, vol. 2, p. 439 (1997).

13. Binary Alloy Phase Diagrams, 2nd ed., edited by T. B. Massalski, H. Okamoto, P. Subramanian, and Kacprzak (ASM International, Metals Park, OH, 1990).

14. M. Rodrigo, L. Daza and S. Mendioroz, Appl. Catal. A: Chemical **88**, 101 (1992).

15. http://srdata.nist.gov/XPS/

16. K. Hadjiivanov, M. Mihaylov, D. Klissurski, P. Stefanov, N. Abadjieva, E. Vasileva, L. Minchev, J. Catal. **185**, 314 (1999).

17. M. Mihaylov, K. Hadjiivanov, D. Klissurski, L. Petrov, Ch. Bonev, G. Kadinov (Eds.), Heterogeneous Catalysis, Proceedings of the 9th International Symposium, Varna, Bulgaria, 2000, p. 429.

ЖУРНАЛ ФИЗИЧЕСКОЙ ХИМИИ, 2009, том 83, № 9, с. 1644–1648

CHEMICAL KINETICS AND CATALYSIS

УДК 541.128

ACTIVITY OF POLYMER SUPPORTED COBALT CATALYST IN THE BRAY-LIEBHAFSKY OSCILLATOR

© 2009 S. Anić*, J. Maksimović*, D. Lončarević**, N. Pejić***, Ž. D. Čupić**

*Faculty of Physical Chemistry, University of Belgrade, Studentski trg 12–16, P.O. Box 137, YU–11001 Belgrade, Serbia

**ICh TM, Center of Catalysis and Chemical Engineering, Njegoševa 12, 11000 Belgrade, Serbia

***Faculty of Pharmacy, Vojvode Stepe 450, University of Belgrade, 11000 Belgrade, Serbia

E-mail: boban@ffh.bg.ac.yu

Abstract – The infuence of poly-4-vinylpyridine-co-divinylbenzene-Co^{2+} catalyst on the Bray–Liebhafsky (BL) oscillator used as the matrix for establishing catalyst's activity was analyzed. The addition of the catalyst do not change the dynamics of the reaction in the BL matrix, but the periods of the oscillatory evolution as well as the preoscillatory period (τ_1) and the duration from the beginning of the reaction to the end of the oscillatory state (τ_{end}). All experimental results are simulated satisfactory.

INTRODUCTION

The oscillatory processes have been successfully applied for the analytical purposes [1–17]. Some of them were used for the characterization of catalysts [18–23]. Namely, the properties of the catalyst based on polymer functionalized by iron [18–21] and enzyme peroxidaze [21,23] was tested by the Bray–Liebhafsky oscillator as the matrix.

The subject of this paper is the polymer supported cobalt catalyst examined by a perturbation of the BL matrix.

The Bray–Liebhafsky oscillatory reaction is the decomposition of hydrogen peroxide into the water and oxygen in the presence of iodate and hydrogen ions [24, 25]:

$$2H_2O_2 \xrightarrow[k_D]{H^+, IO_3^-} 2H_2O + O_2. \qquad (D)$$

In this reaction numerous intermediates as I^-, I_2, HOI, HOOI etc., exist [24–28]. The reaction (D) is the result of the oxidation (O) of iodine to iodate

$$I_2 + 5H_2O_2 \xrightarrow{k_0} 2IO_3^- + 2H^+ + 4H_2O, \qquad (O)$$

and the reduction (R) of iodate to iodine

$$2IO_3^- + 2H^+ + 5H_2O_2 \xrightarrow{k_R} I_2 + 5O_2 + 6H_2O. \qquad (R)$$

The decomposition of hydrogen peroxide (D) in the BL matrix can be described by equation

$$\tau_{end} = -\frac{1}{k_D}\ln[H_2O_2]_{end} + \frac{1}{k_D}\ln[H_2O_2]_0, \qquad (1)$$

where $[H_2O_2]_0$ is initial concentration and $[H_2O_2]_{end}$ the concentration at the end of oscillogram [29]. In the particular system consisting of hydrogen peroxide, potassium iodate and sulfuric acid, the rate constant k_D is a function of potassium iodate and sulfuric acid

$$k_D = k[KIO_3]_0[H_2SO_4]_0^q. \qquad (2)$$

Influence of sulfuric acide on the reaction (D) is complex, between first and second order ($1 < q < 2$) depending on the range of values of $[H_2SO_4]_0$.

It was also found that there is the relations between the rate constants of the reactions (D), (R), and (O), and the periods τ_1 and τ_{end}, and also the total number of oscillations (n) [23, 30, 31]. Therefore, the mentioned periods can be used in kinetics analysis instead the rate constants.

EXPERIMENTAL

Catalyst was prepared by wetness impregnation of cobalt(II)-nitrate on the macroreticular copolymer of poly-4-vinylpyridine with divinylbenzene. The cobalt content on polymer was 5.72 wt % [32].

All experiments were conducted in the closed well-stirred reactor. Volume of the reaction mixture was 52 ml. The reaction between 25 ml of sulphuric acid, 25 ml of potassium iodate and 2 ml of hydrogen peroxide was examinated in the reaction vessel (METHROM EA 876–20) protected from light. The I^- ion sensitive electrode (Metrohm 6.0502.160) as the working electrodes, and reference Ag/AgCl electrode (Metrohm 6.0726.100) were used. In the reference Ag/AgCl electrode, the inner electrolyte was a 3 mol l^{-1} KCl and the outer electrolyte was a saturated solution of K_2SO_4. The potential changes of I^- electrodes during the experiment were followed and written down using data collector (EH4 pH meter-"Measuring instruments Miljkovic Budimir and others" O.D.) connected with PC computer. Thermometer and condenser were immersed into the reaction vassel.

During the experiments, the temperature of reaction vessel was regulated by a thermostat (Julabo ED, Germany) with precision ±0.1 K. The reaction mixture was stirred by a magnetic stirrer (IKA-COMBIMAG RET) at 900 rpm.

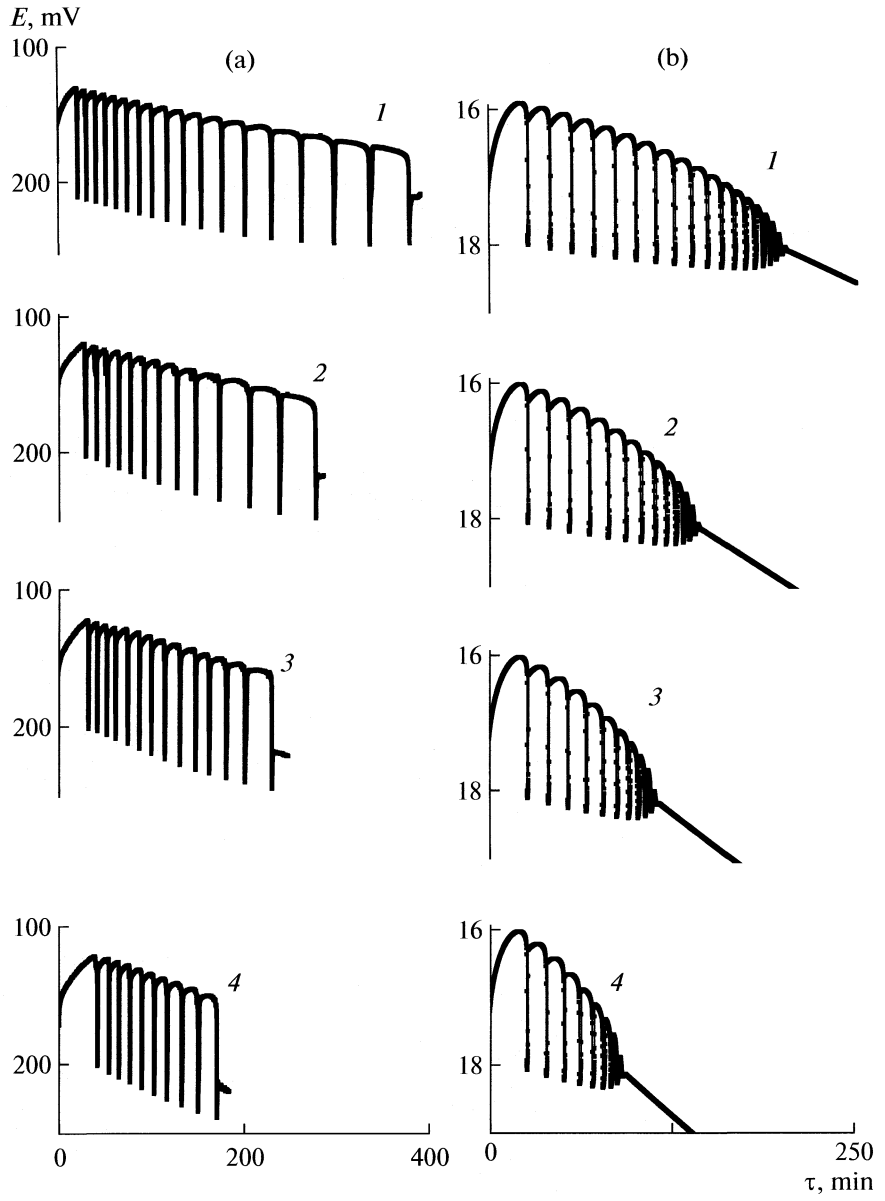

Fig. 1. The experimental (a) and calculated (b) oscillograms of the matrix and perturbed matrix by cobalt catalyst; (*1*) BL, (*2*), (*3*) and (*4*) BL + 0.03, 0.05 and 0.07 g catalyst respectively.

All substances were produced by Merck (Darmstadt, Germany). The solutions were prepared by p.a. chemicals and with deionization water with specific resistance 18 MΩ/cm.

In all experiments, next parameters were kept constant: $[KIO_3]_0 = 7.2 \times 10^{-2}$ mol/dm^3, $[H_2SO_4]_0 = 4.8 \times \times 10^{-2}$ mol/dm^3, $[H_2O_2]_0 = 4.6 \times 10^{-2}$ mol/dm^3, stirrer speed equal 900 rpm and $T = 62°C$.

The measurements were done in two independent series: in homogenous BL matrix, and in the heterogeneous mixture of BL matrix and the catalyst. The substances were added in the reaction vessel by the following order: catalyst, KIO_3, H_2SO_4 and finally H_2O_2 was added when the temperature and the potential were standardized. For the beginning of the reaction, the moment when of hydrogen peroxide was added to the vessel, was taken.

RESULTS AND DISCUSSION

The iodide oscillograms of the BL matrix and the matrix with various amounts of polymer supported cobalt catalyst are presented in Fig. 1. Oscillograms of the same type are obtained, indicating that the dynamics of the observed processes is not changed. Moreover, the number of oscillations (n) and the duration of the oscillograms (τ_{end}) decrease, whereas the preoscillato-

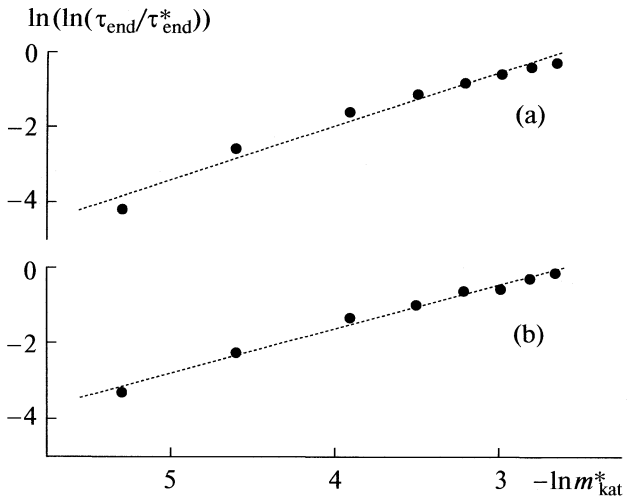

Fig. 2. Experimental (a) and calculated (b) dependence of [ln (τ_{end}/τ^*_{end})] on m^*_{kat}.

ry period (τ_1) increases, when amount of catalyst increases (Fig. 1).

In the presence of the catalyst in the matrix we must involve new rate constant for the overall process (D). Similar as in the [33] we can suppose that the catalyst influences on k_D by the relation

$$k^* = k_D(\exp(x(m^*_{kat})^y)), \quad (3)$$

where m^*_{kat} is dimensionless mass of the catalyst normalized with respect to mass units, x and y are empirical kinetic parameters. Since the dynamics of the BL reaction does not change in the presence of catalyst, the equation (1) can be applied on perturbed BL system. In this case according to equations (1) and (3) we obtained following relation:

$$\ln[\ln(\tau_{end}/\tau^*_{end})] = \ln x + y\ln m^*_{kat}, \quad (4)$$

where τ^*_{end} is length of oscillograms of perturbed BL system. The validity of equation (4) is illustrated in Fig. 2. From linear dependence of $\ln(\ln(\tau_{end}/\tau^*_{end}))$ on $\ln(m^*_{kat})$, we evaluate the parameters x and y, which amounts, $x = 21.1$ and $y = 1.2$.

NUMERICAL SIMULATIONS

The numerical simulations of the Bray–Liebhafsky reaction were carried out using the MATLAB program package and under the conditions used in the experi-

Rate constants and activation energies (in kJ/mol) used in numerical simulations of the Bray–Liebhafsky reaction and its perturbation [34–38]

Rate	Rate constant at 62°C	E_a
$k^0_1[I^-][IO_3^-][H^+]^2 = k_1[I^-]$	$k^0_1 = 3.40 \times 10^5\ M^{-3}\ min^{-1}$	30.4
$k^0_{-1}[HIO][HIO_2] = k_{-1}[HIO][HIO_2]$	$k^0_{-1} = 8.81\times 10^7\ M^{-1}\ min^{-1}$	50.0
$k^0_2[HIO_2][I^-][H^+] = k_2[HIO_2][I^-]$	$k^0_2 = 5.59 \times 10^{11}\ M^{-2}\ min^{-1}$	51.5
$k^0_3[I_2O] = k_3[I_2O]$	$k^0_3 = 7.7 \times 10^3\ min^{-1}$	75.8
$k^0_{-3}[HIO]^2 = k_{-3}[HIO]^2$	$k^0_{-3} = 3.43 \times 10^8\ M^{-1}\ min^{-1}$	40.0
$k^0_4[HIO][I^-] = k_4[HIO][I^-]$	$k^0_4 = 3.07 \times 10^{11}\ M^{-1}\ min^{-1}$	10.5
$k^0_{-4}[I_2]/[H^+] = k_{-4}[I_2]$	$k^0_{-4} = 5.22\ M min^{-1}$	69.0
$(k'_5 + k''_5[H^+])[HIO][H_2O_2] = k_5[HIO][H_2O_2]$	$k'_5 = 12.91 \times 10^3\ M^{-1}\ min^{-1}$	34.0
	$k''_5 = 32.3 \times 10^3\ M^{-2}\ min^{-1}$	34.0
$k^0_6[I_2O][H_2O_2] = k_6[I_2O][H_2O_2]$	$k^0_6 = 5.24 \times 10^5\ M^{-1}\ min^{-1}$	22.0
$(k'_8 + k''_8[H^+])[IO_3^-][H_2O_2] = k_8[H_2O_2]$	$k'_8 = 12.17 \times 10^{-4}\ M^{-1}\ min^{-1}$	115.0
	$k''_8 = 4.84 \times 10^{-2}\ M^{-2}\ min^{-1}$	98.0
$k^0_9[Co^{2+}][H_2O_2][H^+] = k_9[Co^{2+}][H_2O_2]$	$k^0_9 = 1.37 \times 10^2\ M^{-2}\ min^{-1}$	124.0
$k^0_{10}[HO^\bullet][H_2O_2] = k_{10}[HO^\bullet][H_2O_2]$	$k^0_{10} = 6.5 \times 10^{10}\ M^{-1}\ min^{-1}$	1.33
$k^0_{11}[Co^{3+}]HO_2^\bullet] = k_9[Co^{3+}][HO_2^\bullet]$	$k^0_{11} = 4.51 \times 10^2\ M^{-1}\ min^{-1}$	1.3

Note: k_i is the rate constant of reaction R*i*.

ments. In our simulations, a set of reactions (R1)–(R6), (R8), suggested in [34–37]

$$IO_3^- + I^- + 2H^+ \rightleftharpoons HIO + HIO_2, \quad (R1)$$

$$HIO_2 + I^- + H^+ \longrightarrow I_2O + H_2O, \quad (R2)$$

$$I_2O + H_2O \rightleftharpoons 2HIO, \quad (R3)$$

$$HIO + I^- + H^+ \rightleftharpoons I_2 + H_2O, \quad (R4)$$

$$HIO + H_2O_2 \longrightarrow I^- + H^+ + O_2 + H_2O, \quad (R5)$$

$$I_2O + H_2O_2 \longrightarrow HIO + HIO_2, \quad (R6)$$

$$HIO_2 + H_2O_2 \longrightarrow IO_3^- + H^+ + H_2O, \quad (R7)$$

$$IO_3^- + H^+ + H_2O_2 \longrightarrow HIO_2 + O_2H_2O \quad (R8)$$

must be complete by three new reactions for the interaction of the BL matrix with polymer supported cobalt catalyst:

$$Co^{2+} + H_2O_2 + H^+ \longrightarrow Co^{3+} + HO^\bullet + H_2O, \quad (R9)$$

$$HO^\bullet + H_2O_2 \longrightarrow HO_2^\bullet + H_2O, \quad (R10)$$

$$Co^{3+} + HO_2^\bullet \longrightarrow Co^{2+} + H^+ + O_2. \quad (R11)$$

Almost all rate constants (table) were taken from earlier numerical simulations [30, 35]. The rate constant for reaction (R3) was changed slightly to obtain better agreement with the experimental results. The rate constant for reaction (R10) was found in the literature [38], while the rate constants for reactions (R9) and (R11) were obtained in this work.

Figure 1b shows the simulation results of the Bray–Liebhafsky reaction without and with various amounts of polymer supported cobalt catalyst. In view of imperfect model, we have not obtained same value for the duration of the oscillograms, but there is a good trend (fig. 2b). We have received a good agreement of the parameters x and y ($x = 40.44$, $y = 1.4$) with experimental ones ($x = 21.1$ and $y = 1.2$)

CONCLUSION

Presence of the catalyst under applied conditions did not change the dynamics of the BL reaction. By the formal kinetic analysis we did evaluate the activity of the tested catalyst. All experimental results were simulated using a reaction model with eleven steps.

ACKNOWLEDGMENTS

The authors would like to thank mr Nebojša Begović from the Institute of General and Physical Chemistry in Belgrade for help in finding the rate constants for new reactions. The present investigations are partially supported by the Ministry of Science and Environmental Protection of the Republic of Serbia, Project no. 142025 and 142019.

REFERENCES

1. R. Jiménez-Prieto, M. Silva, D. Pérez-Bendito, Talanta **44**, 1463 (1997) and references therein.
2. Y. Ke, M. Wanhong, C. Ruxiu, L. Yhixin, G. Nanqin, Anal. Chim. Acta **413**, 115 (2000).
3. R. Jiménez-Prieto, M. Silva, D. Pérez-Bendito, Analyst **122**, 287 (1997) and references therein.
4. N. Gan, R. Cai, Y. Lin, Anal. Chim. Acta **466**, 257 (2002) and references therein.
5. J. Wang, S. T. Yang, R. X. Cai, Z. X. Lin, Z. H. Liu, Talanta **65**, 799 (2005) and references therein.
6. V. Vukojević, N. Pejić, D. Stanisavljev, S. Anić, Lj. Kolar-Anić, Analyst **124**, 147 (1999).
7. N. Pejić, S. Blagojević, S. Anić, V. Vukojević, Lj. Kolar-Anić, Anal. Bioanal. Chem. **381**, 775 (2005) and references therein.
8. N. Pejić, Lj. Kolar-Anić, S. Anić, D. Stanisavljev, J. Pharm. Biomed. Anal. **41**, 610 (2006).
9. N. Pejić, S. Blagojević, S. Anić, V. Vukojević, M. Mijatović, J. Ćirić, Z. Marković, S. Marković, Lj. Kolar-Anić, Anal. Chim. Acta **582**, 367 (2007).
10. N. Pejić, S. Blagojević, S. Anić, Lj. Kolar-Anić, Anal. Bioanal. Chem. **389**, 2009 (2007).
11. N. Pejić, S. Blagojević, J. Vukelić, Lj. Kolar-Anić, S. Anić, Bull. Chem. Soc. Jpn. **80**, 1942 (2007).
12. J. Gao, G. Zhao, Z. Zhang, J. Zhao, W. Yang, Microchim. Acta **157**, 35 (2007) and references therein.
13. R. Jimenez-Prieto, M. Silva, D. Perez-Bendito, Analyst **23** 1R–8R (1998).
14. J. Gao, H. Chen, H. Dai, D. Lv, J. Ren, L. Wang, W. Yang, Anal. Chim. Acta **571**, 150 (2006) and references therein.
15. G. Hu, P. Chen, W. Wang, L. Hu, J. Song, L. Qiu, J. Song, Electrochim. Acta 52, 7996 (2007) and references therein.
16. J. Gao, J. Ren, W. Yang, X. Liu, H. Zang, Q. Li, H. Deng, J. Electoanal. Chem. **520**, 157 (2002) and references therein.
17. P. E. Strizhak, O. Z. Didenko, T. S. Ivashchenko, Anal. Chim. Acta **428**, 15 (2001) and references therein.
18. Л.Н. Тихонова, А.С. Коваленко и И.Ф. Лабунская, Журн. неорг. химии **33**, 649 (1988).
19. Ž. Čupić, S. Anić, A. Terlecki-Baričević, Lj. Kolar-Anić, React. Kinet. Catal. Lett. **54**, 43 (1995).
20. A. Terlecki-Baricevic, Ž. Čupić, S. Anić, Lj. Kolar-Anić, S. Mitrovski, S. Ivanović, J. Serb. Chem. Soc. **60**, 969 (1995).
21. N. Pejić, Ž. Čupić, S. Anić, V. Vukojević, Lj. Kolar-Anić, Sci. Sintering **33**, 107 (2001).
22. M. Milošević, N. Pejić, Ž. Čupić, S. Anić, Lj. Kolar-Anić, Mater. Sci. Forum. **494**, 369 (2005).
23. Lj. Kolar-Anić, S. Anic, Ž. Čupić, Characterization of the Catalysts by Means of an Oscillatory Reaction // "Finely Dispersed Particles: Micro-, Nano-, and Atto-Engineering", Eds. A. Spasic and Jyh-Ping Hsu, CRC (earlier: Marcel Dekker), Inc., New York 2005, pp. 191–216 and references therein.

24. W. C. Bray, J. Am. Chem. Soc. **43**, 1262 (1921).
25. W. C. Bray, H.A. Liebhafsky, J. Am. Chem. Soc. **53**, 38 (1931).
26. I. Matsuzaki, J. H. Woodson, H. A. Liebhafsky, Bull. Chem. Soc. Jpn. 43 (1970) 3317. and references therein
27. M. G. Peard, C. F. Cullis, Trans. Faraday Soc. **47**, 616 (1951).
28. H. Degn, Acta Chem. Scand. **21**, 1057 (1961).
29. S. Anić, Lj. Kolar-Anić, J. Chem. Faraday Trans. I. **84**, 3413 (1988).
30. S. Anić, Lj. Kolar-Anic, E. Koros, React. Kinet. Catal. Lett. **61**, 111 (1997).
31. S. R. Anić, J. Serb. Chem. Soc. **62**, 65 (1997)
32. D. Lončarevic, Ž. Čupić, Mater. Sci. Forum **494**, 363 (2005).
33. M. Kragović, S. Anić, in Physical Chemistry 2008, A. Antić-Jovanović(ed.), SPCS, Belgrade, 2008, 238–240.
34. Lj. Kolar-Anić, G. Schmitz, J. Chem. Soc. Faraday Trans., **88**, 2343 (1992).
35. Lj. Kolar-Anić, D. Mišljenović, S. Anić, G. Nicolis, React. Kinet. Catal. Lett. **54**, 35 (1995).
36. Lj. Kolar-Anić, Ž. Čupić, S. Anić, G. Schmitz, J. Chem. Soc. Faraday Trans. **93**, 2147 (1997).
37. G. Schmitz, Lj. Kolar-Anić, Russian J. Phys. Chem. **81**, 1380 (2007).
38. R. Atkinson, D. L. Baulch, R. A. Cox, J. N. Crowley, R. F. Hampson, R. G. Hynes, M. E. Jenkin, M. J. Rossi, J. Troe, Atmos. Chem. Phys. **4**, 1461 (2004).

ЖУРНАЛ ФИЗИЧЕСКОЙ ХИМИИ, 2009, том 83, № 9, с. 1649–1653

CHEMICAL KINETICS AND CATALYSIS

УДК 541.124

INFLUENCE OF MICROWAVE IRRADIATION ON ENZYME KINETICS

© 2009 V. M. Pavelkić*, D. R. Stanisavljev**, K. R. Gopčević***, M. V. Beljanski***

*Institute Kirilo Savic Belgrade, Serbia
E-mail: vpavelkic@gmail.com
**Faculty of Physical Chemistry, Belgrade, Serbia
E-mail: dragisa@ffh.bg.ac.yu
***School of Medicine, University of Belgrade, Belgrade, Serbia
E-mail: kristinakgopcevic@yahoo.com
****Institute of General and Physical Chemistry, Belgrade, Serbia
E-mail: mbel@matf.bg.ac.yu

Abstract – The *in vitro* effect of 2.45 GHz microwave irradiation on porcine pepsin activity under controlled temperature and absorbed microwave power *via* kinetic parameters was evaluated. Kinetic study with respect of time of irradiation demonstrated the existence of an inactivation effect of microwaves at pH 2 on pepsin molecule. Bovine serum albumin (BSA) – bromphenol blue (BPB) complex was used as substrate for the assay of pepsin by kinetic method. Depending on absorbed microwave dose, the degree of caused inactivation varies from 39.11 to 45.91% for 5 and 20 min of pepsin MW irradiation, respectively. The V_{maxapp} and K_{mapp} were calculated for low (5 min of MW irradiation) and higher specific absorbed dose (20 min of MW irradiation), as well as for untreated enzyme, from double reciprocal Lineweaver – Burk plot. The effect of microwaves on substrate (BSA–BPB complex) was also investigated. For reaction performed with MW irradiated substrate for 5 min the reaction rate was decreased for 15.15%, while for 20 min of substrate irradiation reaction rate was decreased for 25.52% compared to the control reaction.

INTRODUCTION

After several decades of research on interaction of microwaves with biological matter, heating arising from the absorption of microwaves by the ubiquitous water has been recognized as their main effect. On the other hand, numerous observations indicate that in addition to heating, microwave radiation might also induce non-thermal effects [1]. Although microwave-assisted reactions are widely applied in various domains of organic chemistry, biological molecules, living organisms, their use in the area of enzyme chemistry has been limited, due to the high temperatures associated with the microwave heating [2, 3]. The thermal effects caused by microwave radiation are related to the fast increase of temperature due to the efficient absorption of MW energy by the irradiated medium and specific thermal effects due to the nonstandard evolution of heat in the reaction media [3]. Knowledge about molecular mechanisms involved in non-thermal effects that could involve energy transfer from the electromagnetic field to the vibration modes of macromolecules altering their conformation is still obscure [3, 4]. Microwaves cause different biological effects depending on applied field strength, frequencies and duration of exposure that are attributed to the either thermal of non-thermal microwave effects. Microwave irradiation can alter the rate of enzyme-catalysed reactions, although the role of any non-thermal factors in such processes is controversial [5–9]. The exact mechanism of effects of MW on proteins have not been specified yet, the present data purposed that the MW either caused ions to accelerate and collide with other molecules or caused dipoles to rotate and line up rapidly with alternating electric field, resulting in protein conformation change [5, 10–12].

The information about kinetic properties of the enzyme under MW irradiation is essential for understanding of MW effects on enzyme catalysis. Despite of increasing use of microwaves in every-day life effects of MW irradiation on enzymatic activity remained largely unknown.

We investigate the effects of 2.45 GHz microwave irradiation on pepsin under controlled conditions. The effort was made to keep constant both parameters, temperature and absorbed power, providing well defined experimental conditions. There are currently numerous models available for mechanism-based inactivation systems, but no methodology that yields quantitative predictions for enzyme inactivation caused by absorbed MW radiation. Porcine pepsin A, the best understood of aspartic protease family, was used as a model enzyme. Its structure as well as enzyme specificity, catalytic mechanism and inhibition have been well-documented [13–17], giving a good

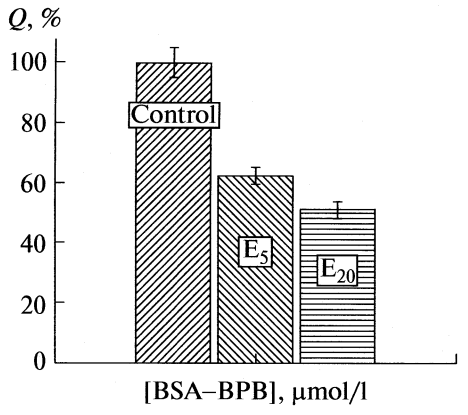

Fig. 1. The remaining activity (*a*) Control (without microwave irradiation); E_5 – reaction with irradiated enzyme solution for 5 min; E_{20} – reaction with irradiated enzyme solution for 20 minutes. Each point represents the mean of three determinations.

opportunity to investigate functional properties of proteins in the MW field. Based on experimental results, kinetic parameters of the MW-modified pepsin were estimated.

MATERIALS AND METHODS

Chemicals. Porcine pepsin A (EC 3.4.23.1), bovine serum albumin (BSA), bromphenol blue sodium salt (BPB) as well as PAGE-reagents were purchased from Sigma-Aldrich. All chemicals were used without further purification. Double distilled, deionised water was used for all solutions.

Microwave irradiation was performed in a single mode focused CEM reactor (Model Discover, CEM Co., Matthew, NC) working at 2.45 GHz. Temperature in the system was measured by fibber optic temperature sensor preventing interaction with MW and influence on temperature reading. External cooling reaction mixture provided the constant temperature and irradiation power. The absorbed MW power, $P_{abs} = mC_p(dT/dt)_i$, was calculated by the calorimetric method measuring temperature increase during the initial heating period. The initial heating period was characterized with the linear increase of temperature $(dT/dt)_i$, during which dissipation of heat by the external thermostat was small (after certain time, of about 3 min, system achieved stationary state where heat removed by the thermostat and heat evolved by microwaves are equilibrated). The heat capacity C_p of the solution was approximated with the capacity of water. All experiments were done under the similar conditions by keeping constant irradiation power, temperature and mixture volume (6 ml).

From seven independent experiments absorbed power was calculated to be 2.8 ± 0.3 W (the emitted power by the instrument was 30 W). The stated error represents 95 % confidence limit of the mean. With the applied experimental design, the temperature of 37°C was maintained within 1°C in all experiments as well as the specific absorbed rate (SAR) of 0.47 ± 0.05 W/g.

Substrate characterisation. The composition of albumin–bromphenol Blue (BSA–BPB) complex was determined by the equilibrium:

$$m\text{BSA} + n\text{BPB} \Leftrightarrow \text{BSA}_m - \text{BPB}_n,$$

where, $m = n = 1$, i.e. BSA and BPB react in one-to-one molar ratio. There are two absorption peaks: 445 nm characteristic for free dye and 605 nm characteristic for BSA–BPB complex [18]. Pepsin acting on this complex appears to break BSA–BPB complex and regenerate the free BPB (the characteristic absorption maximum of free dye at 445 nm increase, while maximum at 605 nm decrease implying degradation of BSA–BPB complex). The change in absorbance during enzymatic reaction was followed at 605 nm.

Enzyme assay. Porcine pepsin assays were carried out with BSA–BPB complex as a substrate. All of the assays were performed at pH 2 by following the initial velocity of the enzymatic reaction with irradiated enzyme (0.03 mM pepsin) in a constant MW field and temperature of 37°C. The K_m and V_{max} were determined for enzyme reaction performed in various experimental conditions, using a linear regression on Lineweaver–Burk double reciprocal plots. In order to investigate the effects of MW on pepsin molecule, the reaction was followed with irradiated enzyme. After reaching working temperature of 37°C enzyme aliquots of 0.150 ml were taken in different time of 5, 10, 20 and 30 min and used for an enzyme assay. Substrate concentrations range from 10 to 100 μM and absorbance change was followed at 605 nm. The appropriate control reactions were carried out at 37°C in water bath with conventional heating.

Spectroscopic measurements were performed with Cintra 10 spectrophotometer in the quartz cell with the optical path of 10 mm. The data were analyzed by the software package Origin 6.1.

Polyacrylamide gel electrophoresis (PAGE). SDS-PAGE was performed with 10% polyacrylamide gel under reducing (with mercaptoethanol and boiling) conditions according to the Laemmli procedure [19]. All of the samples were diluted with sample buffer in ratio 1:1 (v/v) and applied on gel in volume of 10 μl. The gels were stained with Coomassie Brilliant Blue G-250 (CBB) and silver stained [20] (data not shown) and destained by conventional procedures. The gels were scanned and processed using Corel Draw 11.0 software package.

RESULTS AND DISCUSSION

The influence of MW irradiation on porcine pepsin activity was investigated at specific absorbing rate of 0.45 W/g applied to enzyme during different exposure time from 5 to 30 min. The effects of chosen experimental conditions i.e. absorbed dose of MW on *in vitro*

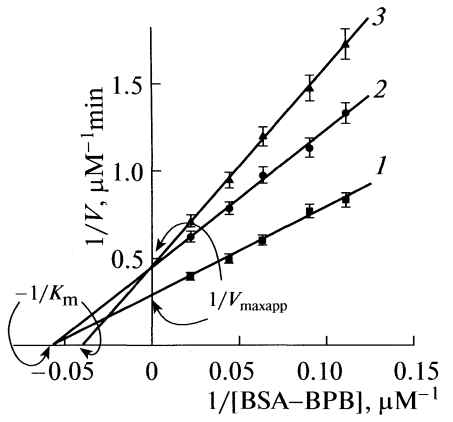

Fig. 2. Lineweaver–Burk plot of pepsin inhibition caused by induced MW radiation. Comparison between two different irradiation times; (*1*) control reaction under conventional heating in water bath at 37°C; (*2*) and (*3*) reaction with irradiated enzyme solution for 5 and 20 min respectively.

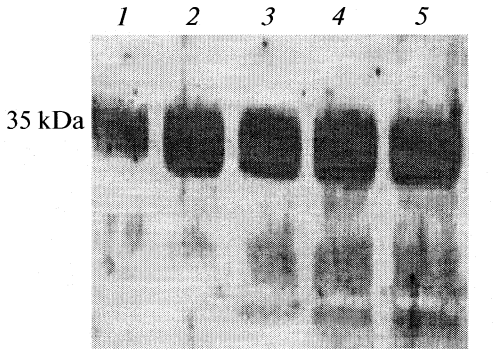

Fig. 3. SDS PAGE reducing electrophoregrams; (1) control; (2), (3), (4) and (5) correspond to 5, 10, 20 and 30 min of exposure time of MW irradiation.

pepsin activity are presented in Fig. 1. Values are expressed as a percent of decreased activity related to the control, which considered as 100%. The decrease of pepsin activity caused by absorbed MW radiation varies from 39.11 to 45.91% for 5 and 20 min of pepsin MW irradiation respectively (Fig. 1).

The initial velocity (V_0) of the reactions were calculated and plotted versus BSA–BPB concentrations, generating saturation plots for each monitored reaction. The plots follow Michaelis–Menten kinetics (data not shown) with MW induced decrease of the reaction rates in all cases.

A double reciprocal plot of velocity vs. substrate concentration at increasing exposure time (5 and 20 min were chosen as representatives) resulted in a linear plots intersecting at different points at 1/[S] axis. It is noticeable that for the irradiation times of 5 and 20 min the apparent velocity of enzyme reaction, i.e. the value of V_{maxapp} is not significantly changed although changes relatively to control is observable (Fig. 2). Compared to the control reaction, V_{max} of both irradiated samples was decreased. The apparent Michaelis–Menten constants for 5 min irradiated sample and control experiment are almost identical while the value for 20 min irradiation is noticeably different. At low specific absorbed dose (5 min of MW irradiation) $K_{mapp} = 17.39 \pm \pm 0.87$ μM, while at higher specific absorbed dose (20 min of MW irradiation) $K_{mapp} = 24.94 \pm 1.25$ μM (Fig. 2).

Since temperature in all experiments is maintained constant (within 1°C) it seems that observed changes in kinetic parameters of irradiated enzyme are result of specificity of microwave heating. Obtained intercepts defining V_{maxapp} and K_{mapp} show that microwave does not induce enzyme inhibition through usual mechanisms [21].

To evaluate possible changes in pepsin molecule caused by absorbed MW energy, SDS-PAGE under reducing conditions was performed. SDS-PAGE (under reducing conditions) electrophoregrams of non-irradiated and MW irradiated pepsin are presented in Fig. 3. Compared to the control band (position *1*), bands that correspond to irradiated pepsin specimens are more diffuse and wider preserving high intensity of pepsin band. Electrophoretic mobility is increased and proportional to time of MW irradiation. In addition, the presences of smaller fragments at higher irradiation times were observed.

As the quanta of MW energy are too small for peptide bond breaking and because of constant temperature in all experiments, it seems that appearance of fragments is the result of increased enzyme auto-digestion in MW field. In microwave field, auto digestion is more pronounced due to the induced changes of enzyme. Considering the microscopic view on the mechanism of microwave heating [22], the significant number of hydrogen bonds of surrounding solvent are breaking and reforming resulting in efficient transformation of electromagnetic energy to heat. In view of the fact that MW changed structure of hydrogen-bond-network may change reaction dynamics [23, 24] it is reasonable to assume that fraction of proteins may not be in their optimal conformation under MW heating. Because of somewhat relaxed protein structure, peptide bonds could be more exposed to the intact pepsin autocatalysis and manifested through the appearance of fragments in electrophoresis experiments (Fig. 3). The possibility of auto-digestion was tested by virtual auto digestion of pepsin, using Peptide-Cutter [25] at different pH values. Possible hydrolysis of 90

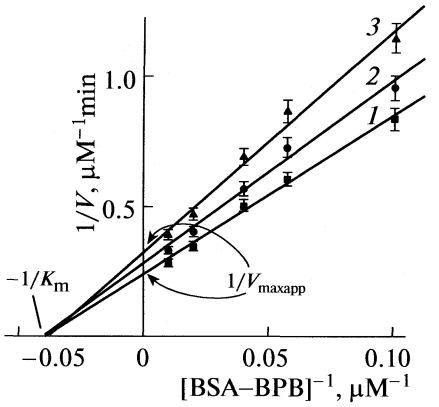

Fig. 4. Lineweaver–Burk plot of pepsin inhibition caused by MW treated substrate; (*1*) control reaction under conventional heating in water bath at 37°C; (*2*) and (*3*) reaction with irradiated BSA–BPB solution for 5 and 20 min respectively.

and 128 peptide bonds at pH 2.0 and pH 1.3 were obtained respectively supporting our assumption.

As it is shown in Figs. 1 and 2, microwaves modify the kinetic parameters of the irradiated enzyme. We also investigated the effect of microwaves on BSA–BPB substrate. For that purpose substrate was irradiated for 5 and 20 minutes (at constant temperature and absorbed MW power) and the reaction was conducted with untreated enzyme. When reactions were performed with MW irradiated substrate the reactions rates were decreased from 15.15 to 25.52% for 5 and 20 min. of substrate irradiation compared to the control reaction.

It is noticeable that microwaves can change the enzyme reaction by modifying the properties of substrate too.

To evaluate kinetic parameters of induced effects by microwave irradiated substrate (relatively to the control experiments) (Fig. 4), Lineweaver – Burk linearization of Michaelis equation was used. The Michaelis–Menten constant (K_m) and maximum reaction rate (V_{max}) for control experiments as well as apparent values for K_{mapp} and V_{maxapp} for microwave irradiated enzyme and substrate are collected in table.

Kinetic parameters evaluated from double reciprocal Lineweaver–Burk plots

Sample	V_{maxapp}, μM min^{-1}	K_{mapp}, μM
Control	3.52 ± 0.18	17.39 ± 0.87
E_5	2.20 ± 0.11	17.39 ± 0.87
E_{20}	2.20 ± 0.11	24.94 ± 1.25
S_5	3.03 ± 0.15	18.03 ± 0.90
S_{20}	2.56 ± 0.13	18.24 ± 0.91

Note. The V_{maxapp} and K_{mapp} were determined by their respective regression equations; E_5 and E_{20} – MW irradiated enzyme solution for 5 and 20 min respectively; S_5 and S_{20} – MW irradiated substrate solution for 5 and 20 min respectively.

CONCLUSION

The MW irradiation causes a decrease of enzymatic activity as a function of the absorbed MW irradiation dose. Since all experiments were performed under well-controlled conditions, keeping constant absorbed MW energy (SAR = 0.47 ± 0.05 W/g), as well as temperature of 37 ± 1°C, observed changes in kinetic parameters of enzyme reaction is not a thermal effect and can be ascribed to specificity of microwave heating. Although MW quanta have no energy to break peptide bonds, mechanism of MW heating assumes excessive breaking and reforming hydrogen bonds of surrounding solvent. Accordingly, changes of the solvent dynamics can induce relaxing of the protein structure with decreased enzyme activity. It is experimentally indicated by somewhat increased auto digestion of pepsin in presence of MW. Based on experimental data, our analysis suggests existence of at least two forms of enzyme with different kinetic parameters in presence of microwaves. Beside of the ability to change the kinetic parameters of pepsin, microwaves can influence the properties of substrate as well.

Obtained results show that enzyme kinetics in presence of microwaves can be a complex process resulting from induced changes on both enzyme and substrate. Although it imply considerable influence of microwaves on living organisms, observed effects are obtained at relatively high absorbed microwave energy which is fortunately far above environmental microwave pollution.

ACKNOWLEDGMENTS

This study was supported by Ministry of Science of Republic of Serbia, Project No. 142025.

REFERENCES

1. R. Weissenborn, K. Diederichs, W. Welte, G. Maret, T. Gisler, Acta Cryst. **61**, 163 (2005).
2. B. Rejasse, S. Lamare, M. D. Legoy, T. Besson, J. Enz. Inh. Med. Chem. **22**, 519 (2007).
3. C. O. Kappe, Curr. Opin. Chem. Biol. **6**, 314 (2002).
4. A. Loupy, Microwaves in Organic Synthesis, Wiley-VCH, Weinheim, (2002).
5. I. Roy, M. N. Gupta. Current Science, **85**, 1685 (2003).
6. S. Rai, U. P. Singh, G. D. Mishra, S. P. Samarketu, Electro Magnetobiol. **13**, 253 (1994).
7. M. Porcelli, G. Cacciapuoti, S. Fusco, R. Massa, G. d'Ambrosio, C. Bertoldo, M. De Rosa, V. Zappia, FEBS Letters. **402**, 102 (1997).
8. D. I. De Pomerai, B. Smith, A. Dawe, K. North, T. Smith, D. B. Archer, I. R. Duce, D. Jones, E. P. M. Candido, FEBS Letters. **543**, 93 (2003).

9. H. Hinrikus, M. Bachmann, R. Tomson, J. Lass, The Environmentalist. **25**, 187 (2005).
10. S. Banik, S. Bandyopadhyay, S. Ganguly, Bioresource Technology. **87**, 155 (2003).
11. S. S. Lin, C. H. Wu, M. C. Sun, C. M. Sun, Y. P. Ho, J. Am. Soc. Mass Spectrum. **16**, 581 (2005).
12. H. Bohr, J. Bohr, J. Physical Review Part E. **61**, 4310 (2000).
13. T. L. Blundell, J. Jenkin, B. T. Sewell, L. H. Pearl, J. B. Cooper, I. J. Tickle, B. Veerapandian, S. P. Wood, J. Mol. Biol. **211**, 919 (1990).
14. V. B. Pedersen, B. Foltmann, FEBS Lett. **35**, 250 (1973).
15. P. Sepulveda, J. Marciniszyn, D. Lui, J. Tang, J. Biol. Chem. **250**, 5082 (1975).
16. R. Sielecki, A. A. Fedorov, A. Boodhoo, N. S. Andreeva, M. N, J. Mol. Biol. **214**, 143 (1990).
17. J. B. Cooper, G. Khan, G. Taylor, I. J. Tickle, T. L. Blundell, J. Mol. Biol. **214**, 199 (1990).
18. T. L. Blundell, J. Jenkin, B. T. Sewell, L. H. Pearl, J. B. Cooper, I. J. Tickle, B. Veerapandian, S. P. Wood, J. Mol. Biol. **211**, 919 (1990).
19. V. B. Pedersen, B. Foltmann, FEBS Lett. **35**, 250 (1973).
20. P. Sepulveda, J. Marciniszyn, D. Lui, J. Tang, J. Biol. Chem. **250**, 5082 (1975).
21. M. Dixon, Webb E. C., Enzymes, 3th ed. London: Longmans; 1979. P 339–398.
22. D. R. Stanisavljev, Djordjevic, V. D. Likar-Smiljanic, Chem Phys Let. **412**, 420 (2005).
23. D. R. Stanisavljev, Djordjevic, V. D. Likar-Smiljanic, Chem Phys Let. **423**, 59 (2006).
24. D. Halliday, R. Resnick, J. Walker, Fundamentals of physics, Fifth edition, Wiley, (1997).
25. http://us.expasy.org / cgi-bin / peptidecutter/

ЖУРНАЛ ФИЗИЧЕСКОЙ ХИМИИ, 2009, том 83, № 9, с. 1654–1660

CHEMICAL KINETICS AND CATALYSIS

УДК 543.422.25:541.124

KINETIC ANALYSIS OF EXPERIMENTAL INTENSITY CURVES OBTAINED DURING ZEOLITE A SYNTHESIS USING *IN SITU* ^{27}Al NMR SPECTROSCOPY

© 2009 Z. Miladinović*, J. Zakrzewska*, V. Dondur**

*Institute of General and Physical Chemistry, Studentski trg, Belgrade, Serbia

**Faculty of Physical Chemistry, University of Belgrade, Serbia

E-mail address: zmiladinovic@iofh.bg.ac.rs

Abstract – Intensity curves obtained by in situ ^{27}Al NMR spectroscopy during zeolite A synthesis have been used as a method for comparative kinetic investigation of zeolite crystallization. Based on inflection point analysis of intensity curves, the times of t_{sed} for process of sedimentation, t_{start} for initiation and t_{finish} for completion of process in liquid phase connected to crystallization were evaluated. Obtained values for t_{start} and t_{finish} indicated that the rate of processes in liquid phase, connected with gel dissolution and growth of zeolite crystal, decreases with the increase of SiO_2/Al_2O_3 molar ratio for the same Na_2O concentration. On the other hand, increase of Na_2O concentration for any of specified SiO_2/Al_2O_3 molar ratio increases the rate of the same processes.

INTRODUCTION

Zeolites are synthesized under highly alkaline hydrothermal conditions from silicate, aluminosilicate, or mixed oxide solutions containing different cationic or other organic structure-directing species. During the hydrothermal reaction, in the presence of "mineralising" agent (most commonly alkaline metal hydroxide) the crystalline zeolite product containing Si–O–Al linkages is created [1]. Under such conditions, a variety of silicate and/or other anions have been observed to be present in solution and have been studied with respect to their roles in zeolite crystallization [2].

According to early investigation of Barer [3, 4], mechanism of crystallization and observed acceleration in formation of solid phase was explained by association of prior formed secondary building units, rather then growing by involving single TO_4^- units from solution phase. In the investigation of Breck and Flaning [5, 6], crystal growth was assumed to proceed by an OH^- catalysed polymerisation and depolymerisation process, involving predominantly the solid phase but with some contribution from solution phase. The studies performed by Zhdanov [7] and Kerr [8, 9] provided a more solution-oriented perspective. Their experiments proved that synthesis of zeolite proceeded via dissolution of gel by sodium hydroxide followed by deposition of zeolite crystals from gel-derived species into solution phase. The combination of these soluble species with nuclei or zeolite crystals to yield the zeolitic product is the rate-determing step.

Kinetic investigations play significant role in understanding the mechanism of zeolite formation. Different kinetic studies of zeolite crystallization performed using mostly diffraction techniques [10], particularly their *in situ* applications, could provide sufficient number of experimental data points necessary for further kinetic analysis [11]. Crystallization curves obtained from such experiments are therefore used for evaluation of kinetic parameters. Typically, model based on Avrami–Erofe'ev equation [12–15] is exploited for this purpose, consequently providing rate constant k and Avrami coefficient n. *In situ* techniques also provide some additional information concerning crystallization mechanism. Crystallization curves obtained during in situ EDXRD investigations by Walton et al [11] show that the choice of silica source can have a great influence not only on the induction time for crystallization and the rate of crystallization, but also the course of the zeolite formation. Moreover, with a given silica source, there appears to be a point at which the zeolite A formation is halted momentarily before its growth proceeds further.

NMR studies, mostly *ex situ* investigations of quenched samples, have been frequently used in the study of zeolite formation because it is possible to gain detailed information about speciation in both solid and liquid phase as well as the degree of crystallization [2, 16–18]. First *in situ* investigation of the evolution of order during the conversion of amorphous intermediate gels to crystalline zeolites followed by solid-state ^{27}Al and ^{29}Si MAS NMR was performed by Shi et al. [19]. It was observed that during the growth of zeolite A, the NMR lines narrowed indicating that NMR can be used to probe the onset of long range ordering within a growing zeolitic structure. In our previous paper, Sharp–Hancock method was used for determination of kinetic parameters using experimental intensity curves obtained from in situ ^{27}Al NMR spectra, corresponding to the changes of aluminum in solution

Table 1. Molar composition used for zeolite A synthesis

Sample	SiO_2/Al_2O_3 (x)	Na_2O/Al_2O_3 (y)	H_2O/Al_2O_3 (z)	y/x	z/y
S-1	1.7	2.64	84.30	1.55	32
S-2	1.7	3.18	63.44	1.87	20
S-3	1.82	3.80	71.54	2.09	19
S-4	2.0	3.09	98.78	1.55	32
S-5	2.0	5.03	160.62	2.52	32
S-6	2.0	4.08	81.48	2.04	20
S-7	2.5	5.10	162.94	2.04	32
S-8	2.5	6.54	208.85	2.62	32
S-9	2.5	6.54	130.53	2.62	20

phase [20]. Here, the inflection point analysis of intensity curves is used in order to examine influence of chemical batch composition on the crystallization kinetics.

EXPERIMENTAL

All synthesis of zeolite A presented in this paper was performed under hydrothermal conditions at constant atmospheric pressure and temperature of 82°C. Polyethylene cylindrical bottle, with an inner volume of 1000 ml was used as a reaction vessel. The molar compositions of synthesis: Al_2O_3: x SiO_2: y Na_2O: z H_2O, with molar ratios y/x and z/y are given in Table 1. Total reaction volume was ranged between 700 and 800 ml according to calculated values for particular batch composition. For each molar ratio $SiO_2/Al_2O_3 = 1.7$, 2.0 and 2.5, molar ratios of Na_2O/SiO_2 ranged from 1.5 to 2.5, while H_2O/Na_2O ratio takes values of 20 and 32.

Sodium aluminate solutions were prepared by dissolving appropriate amounts of commercial anhydrous Al_2O_3 (Mira Lanza, Italy) and sodium hydroxide beads (analytical grade) in distilled water under stirring and heating during dissolving. Aluminate solutions were filtered to remove impurities formed during the dissolving process and stored at room temperature in polypropylene bottles. The silica source was a commercial water glass solution (Galenika, Serbia) with molar composition of 6.18 M SiO_2 and 2.81 M Na_2O, density 1.438g/cm^3 with molar ratio $SiO_2/Na_2O = 2.2$.

Prior to mixing aluminate and silicate component, an appropriate amount of water was added into the reaction vessel, and thermostated in a water bath at 82°C. Both silicate and aluminate solutions were thermostated at 82°C for about 10–15 min before mixing, and then poured simultaneously for about 1–2 min into reaction vessel with vigorous stirring. The formed hydrogel was stirred for another 2 min and 3 ml was transferred into the NMR tube which was previously heated to ~82°C. The remaining amount of reaction suspension was not stirred during crystallization, in order to simulate the static condition of the NMR experiment.

For the purpose of chemical analysis of liquid phase, 25 ml of zeolite suspension was taken in appropriate time intervals depending on synthesis condition. Separation of liquid and solid phase was performed by vacuum filtration. The concentration of alumina species was determined using standard complexometric titration with 0.1M EDTA.

The ^{27}Al NMR spectra of *in situ* crystallization were recorded on Bruker MSL 400 NMR spectrometer at 104.262 MHz. Single pulse mode was used with 2 μs pulse width (which is less then $\pi/12$ to accomplish the quantitative experimental condition according to Engelhardt [21]) and 128 scans of 4K data points with a repetition rate of 0.3 s. The number of collected spectra was between 30 and 60 per synthesis. The interval between spectra in particular synthesis was 180 or 300 s depending on experimental conditions. Chemical shifts were determined relative to $AlCl_3$ solution as an external standard. The NMR spectrometer probe was previously thermostated approximately 30 min to 1 hour before the onset of experiment, at the reaction temperature, 82 ± 0.5°C. All experiments were performed in 10 mm glass NMR tubes [20].

All intensity curves obtained from ^{27}Al NMR spectra are presented as plot of normalized intensities of line at 79 ppm : $(I_t - I_{min})/(I_{max} - I_{min})$, where I_{max} and I_{min} denote intensities at the beginning and the end of synthesis respectively, while I_t represent intensity of NMR line at any particular time of synthesis.

RESULTS AND DISCUSSION

In situ ^{27}Al NMR spectroscopy was used as a method to monitor changes in solution and solid phase simultaneously during zeolite A synthesis. NMR spectra acquired in particular times during synthesis are presented in Fig 1. Two NMR lines can be clearly distinguish in these spectra: narrow one at 79 ppm, corresponding to the tetrahedral AlO_4^- ions presented in liquid phase, and broad one at 59 ppm, associated with

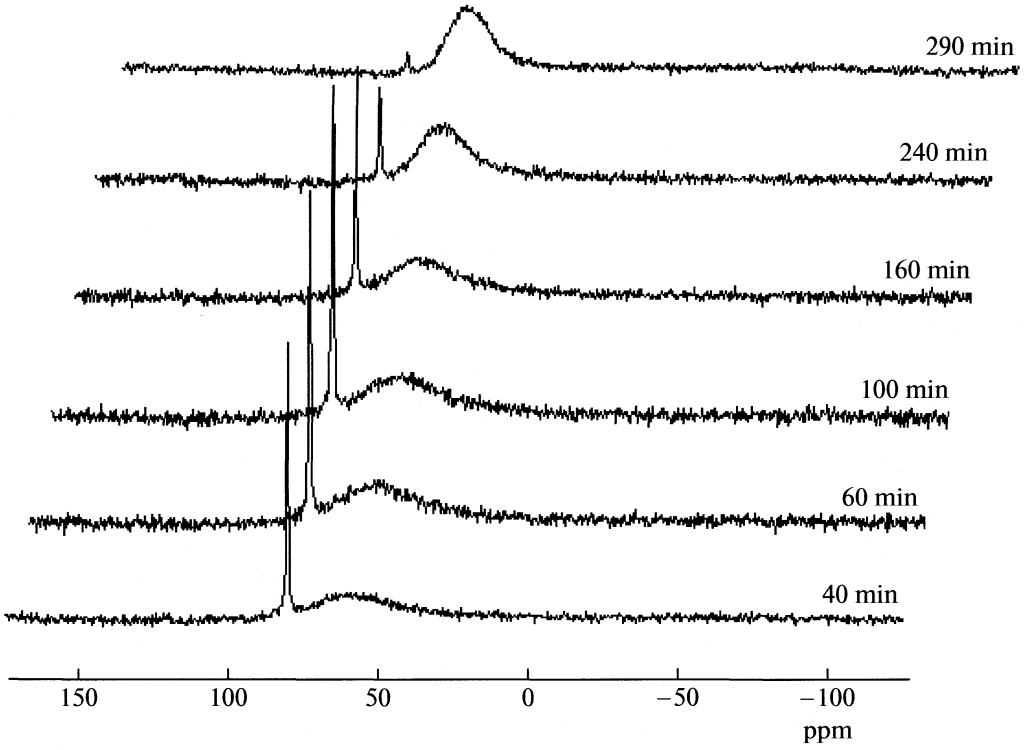

Fig. 1. ^{27}Al NMR spectra obtained for different time intervals during a synthesis of zeolite A.

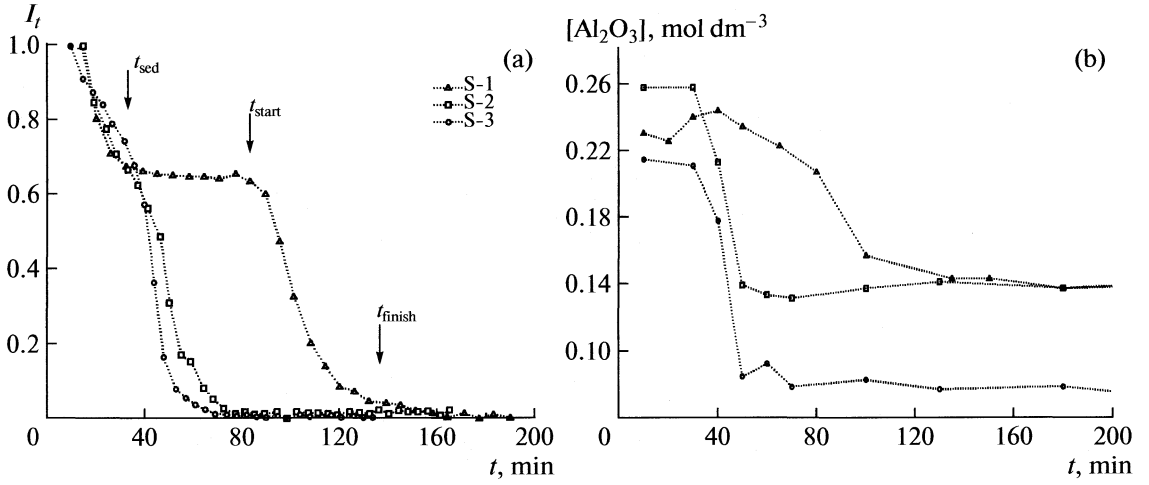

Fig. 2. Changes of (a) normalized intensity I_t of ^{27}Al NMR line at 79 ppm and (b) normalized concentration of Al_2O_3 during reaction time of zeolite synthesis for molar ratio $SiO_2/Al_2O_3 = 1.7$ and for different absolute concentrations of Na_2O presented in Table 1. Arrows indicate time periods denoted as t_{sed}, t_{start} and t_{finsh} given in Table 2 related to S-1 synthesis

$Al(OSi)_4^-$ aluminosilicate building units from solid/gel phase [22–24]. During the crystallization, simultaneous changes in intensity and shape of both NMR lines could be observed. As intensity of narrow line at 79 ppm slowly decreases, the intensity of broad line at 59 ppm increases with simultaneous decrease of width at half-height, as the tetrahedral $Al(OSi)_4$ form began to dominate [20].

Obtained ^{27}Al NMR spectra could be used in several ways in order to represent crystallization processes occurring during synthesis [19, 25]. One of the approaches for following changes of alumina species present in liquid phase assumes analysis of intensity of narrow line at 79 ppm, as it was demonstrated in our previous paper [20]. In Figs. 2, 3, and 4, typical pattern of decaying trend of narrow line intensity is presented.

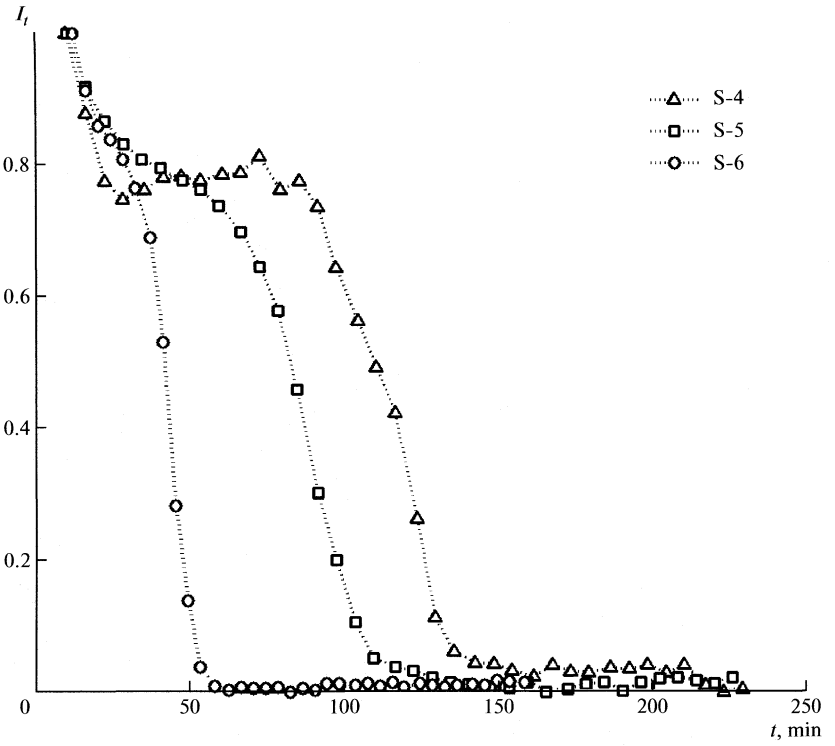

Fig. 3. Changes of normalized intensity of ^{27}Al NMR line at 79 ppm during reaction time of zeolite synthesis for molar ratio SiO_2/Al_2O_3 =2.0 and for different absolute concentration of Na_2O presented in Table 1.

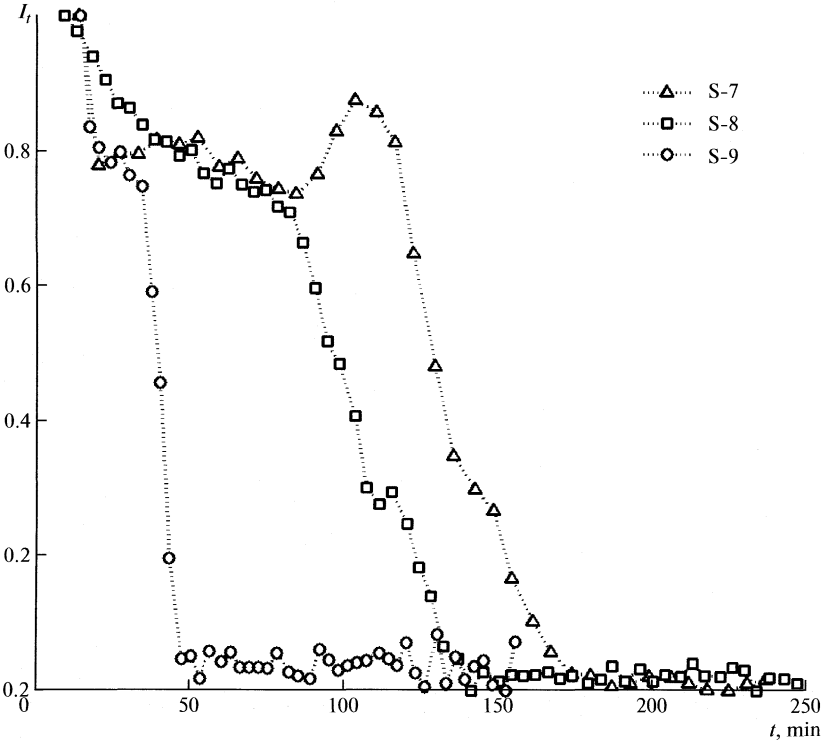

Fig. 4. Changes of normalized intensity of ^{27}Al NMR line at 79 ppm during reaction time of zeolite synthesis for molar ratio SiO_2/Al_2O_3 =2.5 and for different absolute concentration of Na_2O presented in Table 1.

Table 2. Different values of times of sedimentation, start and finishing obtained from normalized intensity curves during zeolite synthesis for different absolute Na_2O concentration and molar batch composition

Sample	t_{sed}, min	t_{start}, min	t_{finish}, min	Na_2O, mol/dm^3
S-1	25	88	117	1.685
S-2	19	45	62	2.671
S-3	16	38	51	2.858
S-4	28	88	145	1.681
S-5	24	70	107	1.711
S-6	17	36	52	2.683
S-7	22	110	150	1.700
S-8	31	85	134	1.713
S-9	19	34	46	2.702

On the other hand, broad line at 59 ppm shows complex variation in its shape during synthesis, primarily connected with the changes in solid/gel phase which can not be interpreted in a straightforward manner. Relative constant area of broad line observed in these spectra results from simultaneous increase of its intensity and reduction in width at half-height as the crystallization proceeds, which is attributed to formation of crystalline zeolite A product (Fig. 1) [19].

All curves presented in Figs. 2 to 4 show similar shapes with three clearly distinctive steps, corresponding to the processes occurring during synthesis in an *in situ* NMR experimental condition. Intensity of the line at 79 ppm decreases during crystallization for several reasons. Rapid drop of normalized intensity during first 15–30 min is associated with the process of sedimentation of aluminum-silicate gel in NMR tube [20]. The induction period is represented as relatively flat part on intensity curve, followed by crystallization process manifested as a fast drop in intensity of NMR signal, indicating rapid depletion of free alumina in solution phase and their incorporation into the solid crystalline phase [20].

Concentration dependence of the rate of crystal growth [26, 27] is initial assumption for using normalized intensity curves of the line at 79 ppm for further detailed analysis of kinetics aspects of zeolite crystallization. The rate of linear crystal growth and rate of gel dissolution depends on concentration of aluminum and aluminosilicate species in solution phase. Besides, the rate constants for both of these processes are connected with diffusion coefficients, which in some extent contribute to the overall rate of crystallization [26, 27].

The changes of alumina concentration obtained from chemical analysis of solution phase are presented in Fig 2b. Both intensity and concentration curves in Fig. 2 show similarity in their shapes and declining rates, indicating that the intensity curves obtained from the in situ ^{27}Al NMR spectra represent appropriately processes which are connected with changes in alumina concentration during synthesis. Moreover, NMR intensity curves provide more precise data and give a new insight into processes which occur during synthesis.

The simplest approach, demonstrated in this paper, for analyzing intensity curves, could be achieved by comparing times of beginning and ending of intensity decay which could be associated with crystallization period (inflection point analysis). Inflection points, evaluated from presented S-shaped intensity curves denoted as t_{sed}, t_{start} and t_{finish} for sedimentation, beginning and ending of intensity decay respectively, are given in Table 2, and are used for kinetic analysis of processes occurred during zeolite crystallization. All data presented in Table 2 are placed in increasing ordered of absolute Na_2O batch concentration and grouped with equal molar ratios of SiO_2/Al_2O_3. It can be seen from Table 2 that with increasing Na_2O concentration, values of t_{start} and t_{finish} decrease for any particular value of SiO_2/Al_2O_3. Furthermore, for given Na_2O concentration, general increasing trend of t_{start} and t_{finish} is consistent with increasing molar ratio SiO_2/Al_2O_3 in order $1.7 > 2.0 > 2.5$ (for example synthesis S-1, S-4, and S-7 regarding t_{finish}). Overall above trends indicate obvious connection between initial batch composition and rates of processes responsible for crystal growth.

Changes in observed rate of sedimentation depend on sample volume in NMR tube used for particular synthesis, coefficient of diffusion, viscosity of solution phase, middle radius of gel particles [28], but no significant dependency on batch composition was observed (Table 2).

Induction period can be determined as difference of t_{start} and t_{sed} (Table 2). Dependency of induction period on absolute concentration of Na_2O and SiO_2/Al_2O_3 molar ratio is similar to that of crystallization period, indicating that rate of nucleus formation is also controlled by batch composition. Further analysis of induction and/or nucleation period, based on *in situ* NMR investigation was shown to be inappropriate as it was demonstrated by Shi et al. [19]. Besides, due to static condition during NMR experiment, it is impossible to distinguish clearly the times of sedimentation and induction processes.

Base assumption presented here is that quantity of alumina species present in solution phase, represented by changes of intensity of narrow line at 79 ppm at any moment of synthesis, is contribution of two opposite processes: gel dissolving which is responsible for the increase of alumina concentration, and depletion of aluminosilicate species due to constant deposition at the surface of growing zeolite crystal. Apparently, the rates of both of these processes depend on the reaction conditions such as temperature and concentration of OH^- ions present in solution phase [29]. Mechanism and kinetics of gel dissolution and their dependency on temperature and NaOH concentration was in de-

tailed investigated by Antonić at al [30–32]. Based on their findings, the process of dissolution of amorphous aluminosilicate precursors in NaOH solutions can be explained by the action of OH- ions from the liquid phase on the solid/liquid interface which causes breaking of the surface Si–O–Si and Si–O–Al bonds of the precursor and formation of soluble aluminate and silicate species.

The rate of formation of the soluble silicate and aluminate species is assumed to be proportional to the number of OH^- ions that act to the unit surface area of the precursor. Hence, the rate at which the soluble silicate and aluminate species leave the solid/liquid interface increases with increasing concentration of NaOH, and is directly proportional to the surface area exposed to the action of OH^- ions. Investigations of McNicol et al. [33, 34] indicate that the solutions in equilibrium with aluminosilicate gels used in zeolite synthesis contain different silicate species and only one monomeric aluminate ion. Especially, these investigations show that the solution contains no aluminosilicate species. Therefore, the process of the dissolution of the amorphous aluminosilicate is strictly connected to hydrolysis of all Si–O–Al bonds, and the formation of these bonds in the final product must occur during the crystallization process [35]. Our results presented in Table 2 could be explained by above mechanism which includes gel dissolution and consequent crystal growth. Increase of Na_2O concentrations from about 1.7 to 2.7 mol dm^{-3} results in reduction of both t_{start} and t_{finish} for any particular SiO_2/Al_2O_3 molar ratio.

"Excess" of aluminium in the liquid phase increases both the rate of crystallization and the rate of the crystal growth of zeolite A. On the other hand, the increase of the silicon concentration in the liquid phase causes a decrease in both crystallization and crystal growth rates of zeolite A [36]. This is in accordance with results obtained for t_{start} and t_{finish}, which are increasing with increase of SiO_2/Al_2O_3 molar ratio for the same Na_2O concentration. For example for Na_2O = 1.7 mol dm^{-3}, t_{finish} drops from 150 min for SiO_2/Al_2O_3 = 2.5 to 117 min for SiO_2/Al_2O_3 = 1.7.

For some synthesis (Fig 3 and 4, samples: S-4, S-7 and S-8), pauses or sudden increases in ^{27}Al NMR line intensity at 79 ppm during crystallization time are observed. This, so called "stop effect" [11, 20], has been interpreted by autocatalytic mechanism [37, 38] and space distribution of nuclei through amorphous gel [39]. However, by comparison results presented in Table 2 and shapes of obtained normalized intensity curves, it could be concluded that "stop effect" appears in synthesis with batches rich in silica components (SiO_2/Al_2O_3 = 2.5 for S-7, S-8 and SiO_2/Al_2O_3 = 2.0 for S-4) and with lower absolute concentration of Na_2O (~1.7 mol dm^{-3}). Besides, evaluated times (t_{start}–t_{sed}) associated with induction and nucleation period are significantly higher (ranged from 54 to 88 min) for these synthesis compared to the data obtained for the others (see Table 2), indicating lower rates of induction and nucleation process. It is well known that larger silicate oligomers are favored by high Si concentration and low alkalinity [40–42]. It is reasonable to expect that large polymer silicate chains and low OH^- concentration causes decrease in rate of nuclei formation [43, 44], therefore explanation for "stop effect" should include both the rate of nuclei formation and space distribution of nuclei.

Increase of ^{27}Al NMR line intensity at the beginning of crystallization curve (during induction period) observed for synthesis S-7 could be explained by inhomogeneity of prepared aluminosilicate gel rich in silica component (SiO_2/Al_2O_3 = 2.5). Moreover, findings of Ogura et al. [45] indicate that zeolite crystallization may not occur solely by conversion of amorphous aluminosilica gel intermediates, but may involve the incorporation of other siliceous solution-phase species from the reaction mixture along with possible depletion of Al species from the gel back into solution [2]. Such depletion of alumina could be responsible for unusual findings in synthesis S-7.

ACKNOWLEDGMENTS

This work has been partially supported by the Ministry of Science of the Republic of Serbia (Contract No. 142055, 20120).

REFERENCES

1. C. S. Cundy, P. A. Cox, Micropor. Mesopor. Mater. **82** (1–2), 1 (2005).
2. J. D. Eppinga and B. F. Chmelka, Curr. Opin. Colloid Interface Sci. **11** (2–3), 81 (2006).
3. R. M. Barrer, J. W. Baynham, F. W. Bultitude, W. M. Meier, J. Chem. Soc. 195 (1959).
4. R. M. Barrer, Chem. Brit. 380 (1966).
5. E. M. Flanigen, D. W. Breck, *137th Meeting of the ACS, Division of Inorganic Chemistry* (Cleveland, Ohio 1960), 33-M.
6. D. W. Breck, J. Chem. Ed. **41** (12), 678 (1964).
7. S. P. Zhdanov, in: E. M. Flanigen, L. B. Sand (Eds.), *Molecular Sieve Zeolites-I*, ACS Adv. Chem. Ser., **101**, 20 (1971).
8. G. T. Kerr, J. Phys. Chem. **70** (4), 1047 (1966).
9. G. T. Kerr, Zeolites **9** (5), 451 (1989).
10. R. J. Francis, D. O'Hare, J. Chem. Soc., Dalton Trans. **19**, 3133 (1998).
11. R. I. Walton, F. Millange, D. O'Hare, A. T. Davies, G. Sankar and R.A. Catlow, J. Phys. Chem. B **105** (1), 83 (2001).
12. M. J. Avrami, J. Chem. Phys. **7** (12), 1103 (1939).
13. M. J. Avrami, J. Chem. Phys. **8** (2), 212 (1940).
14. M. J. Avrami, J. Chem. Phys., **9** (2), 177 (1941).
15. B. V. Erofe'ev, C. R. Dokl. Acad. Sci. URSS, **52**, 511 (1946).
16. J. Klinowski, Anal. Chim. Acta **283** (3), 929 (1993).

17. G. Engelhardt, B. Fahlke, M. Mägi and E. Lippmaa, Zeolites **3** (4), 292 (1983).
18. G. Engelhardt, B. Fahlke, M. Mägi and E. Lippmaa, Zeolites **5** (1), 49 (1985).
19. J. Shi, M.W. Anderson and S.W. Carr, Chem. Mater. **8** (2), 369 (1996).
20. Z. Miladinović, J. Zakrzewska, B. Kovačević, G. Bačić, Mater. Chem. Phys., **104** (2–3), 384 (2007).
21. G. Engelhardt, D. Michel, *in High Resolution Solid-State NMR of Silicates and Zeolites*, (John Wiley & Sons Ltd., New York, 1987), p. 144.
22. R. J. Francis, S. O'Brien, A. M. Fogg, P. S. Halasyamani, D. O'Hare, T. Loiseau, G. Ferey, J .Am. Chem. Soc., **121** (5), 1002 (1999).
23. A. K. Cheetham, C. F. Mellot, Chem. Mater. **9** (11), 2269 (1997).
24. R. Grizzetti, G. Artioli, Micropor. Mesopor. Mater. **54** (1–2), 105 (2002).
25. P. Bodart, J. B. Nagy, Z. Gabelica, E. G. Derouane, J. Chim. Phys. Chim. Biol. **83** (11), 777 (1986).
26. S. Bosnar, B. Subotić, Micropor. Mesopor. Mater., **28** (3), 483 (1999).
27. S. Bosnar, B. Subotić, Crot. Chem. Acta, **75** (3), 663 (2002).
28. M. Mason, W. Weaver, Phys. Rev. **23** (3), 412 (1924).
29. S. P. Zhdanov, N. N. Samulevich, in: L.V.C. Rees (Ed.), *Proceedings of the Fifth International Conference on Zeolites*, (Heyden, London, 1980), 75.
30. T. Antonić, A. Čižmek, C. Kosanović, B. Subotić, J. Chem. Soc. Faraday Trans., **89** (11), 1817 (1993).
31. T. Antonić, A. Čižmek, B. Subotić, J. Chem. Soc. Faraday Trans., **90** (13), 1973 (1994).
32. T. Antonić, A. Čižmek, B. Subotić, J. Chem. Soc. Faraday Trans. **90** (24), 3725 (1994).
33. B. D. McNicol. G. T. Pott, K. R. Loos, and N. Mulder, Adv. Chem. Ser. **121**, 152 (1973).
34. B. D. McNicol, G. T. Pott, K. R. Loos, J. Phys. Chem. **76** (23), 3388 (1972).
35. H. Kacirek, H. Lechert, J. Phys. Chem. **80** (12), 1291 (1976).
36. S. Bosnar, J. Bronić, I. Krznarić B. Subotić, Croat. Chem. Acta **78** (1), 1 (2005).
37. B. Subotic, ACS Symp. Ser. **398**, 110 (1989).
38. S. Gonthier, L. Gora, I. Guray, R. W. Thompson, Zeolites **13** (), 414 (1993).
39. B. Subotic, T. Antonic, S. Bosnar, J. Bronic, M. Skreblin, Stud. Surf. Sci. Catal. **125**, 157 (1999).
40. T. W. Swaddle, Coordination Chem. Rev. **219–221**, 665 (2001).
41. T. W. Swaddle, J. Salerno, P. A. Tregloan, Chem. Soc. Rev. **23** (5), 319 (1994).
42. S. D. Kinrade, T. W. Swaddle, Inorg. Chem. **27** (23), 4253 (1988).
43. H. Lechert and H. Kacirek, Zeolites **13** (3),192 (1993).
44. J. L. Bass, G. L. Turner, J. Phys. Chem. B **101** (50), 10638 (1997).
45. H. Takahashi and T. Okubo, Chem. Mater. **15** (13), 2661 (2003).

ЖУРНАЛ ФИЗИЧЕСКОЙ ХИМИИ, 2009, том 83, № 9, с. 1661–1665

CHEMICAL KINETICS AND CATALYSIS

УДК 541.128

STRUCTURAL AND TEXTURAL PROPERTIES OF Al,Fe-PILLARED CLAY CATALYSTS

© 2009 P. Banković*, A. Milutinović-Nikolić*, A. Rosić* N. Jović-Jovičić*, D. Jovanović*

*University of Belgrade – Institute of Chemistry, Technology and Metallurgy, Department of Catalysis and Chemical Engineering, Njegoševa 12, 11000 Belgrade, Serbia

E-mail: predragb@nanosys. ihtm. bg. ac. rs

**University of Belgrade – Faculty of Mining and Geology, Đušina 7, 11000 Belgrade, Serbia

Abstract – Metal oxide pillared interlayered clays (PILCs) represent a new class of materials that have found a wide range of potential applications including catalytic oxidative degradation of organic pollutants in water. Al,Fe-pillared smectite clays with different Fe content were synthesized for possible catalytic application. Starting clay and the obtained PILCs were characterized. Phase composition, textural and morphological properties of the starting clay and synthesized PILCs were determined using X-ray diffraction, physisorption of nitrogen and scanning electron microscopy. Chemical composition of the PILCs was determined using EDX. It was found that the synthesized PILCs have similar phasal composition, textural and morphological properties differing only in Fe content in accordance with the amount of Fe introduced to clay during the pillaring process.

INTRODUCTION

Layered silicates (phyllosilicates) are the most significant naturally occurring one dimensional nanomaterials that have crystal lattice consisting of two-dimensional layers where central octahedral sheet of alumina $[AlO_3(OH)_3]^{6-}$ is fused to two external silica $(SiO_4)^{4-}$ tetrahedrons so that the oxygen ions are shared between sheets [1, 2].

These layers organize themselves to form stacks with a regular Van der Walls gap in between them called interlayer or gallery. Isomorphic substitution within the layers generates negative charges that are counterbalanced by alkali or alkaline earth cations (exchangeable cations) situated in the interlayer. As the forces that hold the stacks together are relatively weak, the intercalation of small molecules between the layers is easy. Among phyllosilicates smectites are particularly easy to modify in various manners due to their swelling properties and ion exchangeability [1, 2].

Pillaring is one of the methods of smectite modification used for the obtention of materials that have found a wide range of potential applications in catalytic, adsorption and separation processes [3]. Common procedure for pillared clay (PILC) preparation is: swelling of smectite in water; exchanging interlayer cations by partially hydrated polymeric or oligomeric metal cation complexes in the interlamellar region of starting clay; drying and calcining of wet cake formed of expanded clay in order to transform the metal polyoxocations into metal oxide pillars [4].

As catalysts, PILCs play important role in environmental protection in the processes of wastewater treatment. Industrial wastewaters of different origins may contain phenols, polyphenols and BTEX (benzene, toluene, ethylbenzene and *o*-, *m*- and *p*-xylene) compounds, which are toxic and may inhibit biological treatment, and therefore require a pretreatment [5]. Dye containing effluents also represent environmental, as well as aesthetic problems since they have light-absorbing effect in recipients (rivers, lakes, etc.), thus interfering with aquatic biological processes [6]. Although some dyes do not show significant toxicity themselves their degradation products are often carcinogenic and mutagenic [7].

Pillared clay catalysts have shown to be a promising solution for the elimination of organic water pollutants when employed in the catalytic wet peroxide oxidation (CWPO) process. This method has been proven as extremely effective under mild conditions for the degradation of these pollutants partially or completely transforming them to CO_2. Moreover, hydrogen peroxide is a desirable environment friendly oxidizing agent since it is nontoxic and does not form harmful by-products [8].

The efficiency of CWPO is highly influenced by the properties of applied PILC catalyst. PILC properties are affected by various synthesis parameters such as solid-liquid ratio, clay origin, particle size, type of oligomeric metal cation or mixture of cations, intercalation conditions, temperature and duration of calcining etc. Certain physical-chemical properties of catalysts, including texture, directly determine their catalytic efficiency. Therefore, the first step that follows the synthesis of a catalyst is its characterization.

Table 1. Selected textural properties of investigated samples

Sample	S_{BET}, m^2/g	$V_{0.98}$, cm^3/g	V_{mic}, cm^3/g	D_{max}, nm	D_{med}, nm
Raw clay	96	0.111	0.045	3.8	3.9
Na-exchanged	99	0.094	0.041	3.9	3.9
AlFe10 PILC	167	0.219	0.082	3.8	9.2
AlFe15 PILC	171	0.227	0.089	3.8	9.5

Notes: S_{BET} is specific surface area; $V_{0.98}$ is total pore volume, V_{mic} is micropore volume, D_{max} is the pore diameter where the maximum of derivative cumulative volume curves is reached; D_{med} is median value of pore diameter.

In the present work two catalysts based on smectite clay from Bogovina (Serbia) were synthesized by pillaring with Al^{3+} together with Fe^{3+} as catalytically active component. The conditions of synthesis such as clay size and origin, type of pillaring cations, cation/clay ratio, drying and calcining conditions etc., were maintained constant and the obtained PILCs differed only in Fe^{3+} content. The samples were characterized and their properties were compared. Phase composition, textural and morphological properties of the starting clay and synthesized PILCs were determined using X-ray diffraction, physisorption of nitrogen and scanning electron microscopy. Chemical composition of the PILCs was determined using EDX.

EXPERIMENTAL

The starting material was a characterized domestic clay from Bogovina [9, 10]. The ≤2 μm fraction of this clay with cation exchange capacity (estimated by ammonium acetate method) of 765 mmol kg^{-1} was used in further experiments and denoted as raw clay. The raw clay was submitted to the Na-exchange procedure by repeated stirring with 1M NaCl followed by filtering. Thus obtained filtration cake was rinsed with distilled water in order to remove NaCl and other exchangeable cations excess from the sample. The rinsing was repeated until the filtrate was Cl^- free (confirmed by $AgNO_3$ precipitation test). The Na-exchanged clay was dried at 110°C.

The process of pillaring was carried out according to a common procedure comprising the following steps: grinding, sieving, Na exchange, pillaring, drying and calcination [11]. Pillaring solutions were adjusted to have the atomic ratio $Fe^{3+}/(Al^{3+} + Fe^{3+})$ of either 10 or 15% and $OH^-/(Al^{3+} + Fe^{3+}) = 2.0$. The procedure included continuous stirring at 60°C for 3 h and at room temperature overnight. In the next step the appropriate amount of the pillaring solutions, required for the ratio – mmol $(Al^{3+} + Fe^{3+})$/g clay – to be 10, was dropwise added into Na-exchanged bentonite suspension in water. After being rigorously stirred at 80°C for 3 h the final suspension was stirred at room temperature overnight, and filtered through a Buchner funnel. The obtained cake was rinsed with hot distilled water until the filtrate was NO_3^- free (tested by UV-VIS spectrophotometry), and finally air-dried overnight at 110°C. It was then calcined at 300°C for 2 h and referred to as AlFel0 PILC and AlFel5 PILC, respectively, for the materials made from solutions having $Fe^{3+}/(Al^{3+} + Fe^{3+})$ ratios of 10 and 15%.

The X-ray diffraction (XRD) patterns for powders of raw and pillared clays were obtained using a Philips PW 1710 X-ray powder diffractometer with a Cu anode ($\lambda = 0.154178$ nm).

Nitrogen adsorption–desorption isotherms were determined on Sorptomatic 1990 Thermo Finningen at –196°C. Samples were outgassed at 160°C, during 20 h. Various models and appropriate software-WinADP were used to analyze obtained isotherms. Specific surface area of the samples, S_{BET}, was calculated according to Brunauer, Emmett, Teller method [12, 13]. Total pore volume was calculated according to Gurvitch method for $p/p_0 = 0.98$ [12, 13]. Pore size distribution for mesopores was calculated according to Barrett, Joyner, Halenda method from the desorption branch of isotherm [14]. Micropores were analyzed using Dubinin–Radushkevich method [9, 15]. SEM microphotographs were obtained using SEM JSM-646 OLV JEOL. The PILCs were analyzed by EDX method using INCA X-sight Oxford Instruments.

RESULTS AND DISCUSSION

According to X-ray diffraction patterns (Fig. 1) the following phases were identified in the investigated samples: smectite, quartz, feldspar and a small amount of amorphous phase [16, 17]. Apart from smectite, other phases remained unaffected. The Na-exchange process lowered d_{001} smectite basal spacing from 1.53 nm ($2\theta = 5.78°$) for raw clay to 1.28 nm ($2\theta = 6.92°$), but the clay retained its swelling properties. The pillaring process increased and fixed the basal spacing of smectite. This resulted in the shift of the (001) smectite peak to $2\theta = 5.40°$ ($d_{001} = 1.64$ nm) for AlFel0 PILC and $2\theta = 5.66°$ ($d_{001} = 1.56$ nm) for AlFel5 PILC. According to the obtained XRD results the pillaring process was proven as successful. Fe as catalytically active specie is expected to be incorporated within Al pillars in the obtained PILCs.

Nitrogen adsorption–desorption isotherms were obtained for all investigated samples. Acquired results in these experiments are presented in the form of diagram (Fig. 2). Due to similarity between the curves obtained for raw and Na-exchanged clay, and between the curves obtained for both PILCs, in order to avoid overlapping only those related to raw clay and AlFe 10 PILC were shown as the representative ones. Relevant data for all samples obtained using WinADP software are presented in Table 1.

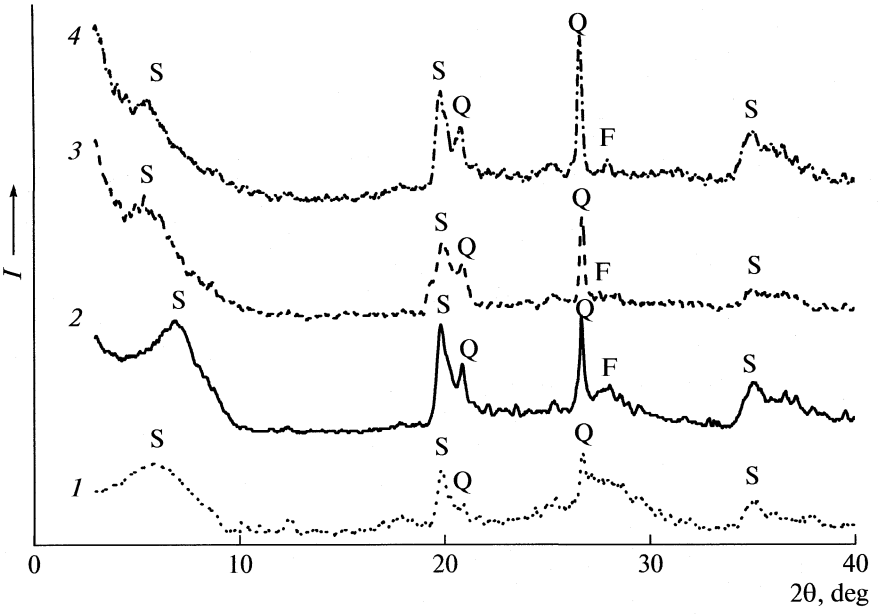

Fig. 1. X-ray diffraction patterns off (*1*) raw clay, (*2*) Na-exchanged clay, (*3*) AlFe10 PILC and (*4*) AlFe15 PILC, where S – smectite, Q – quartz and F – feldspar.

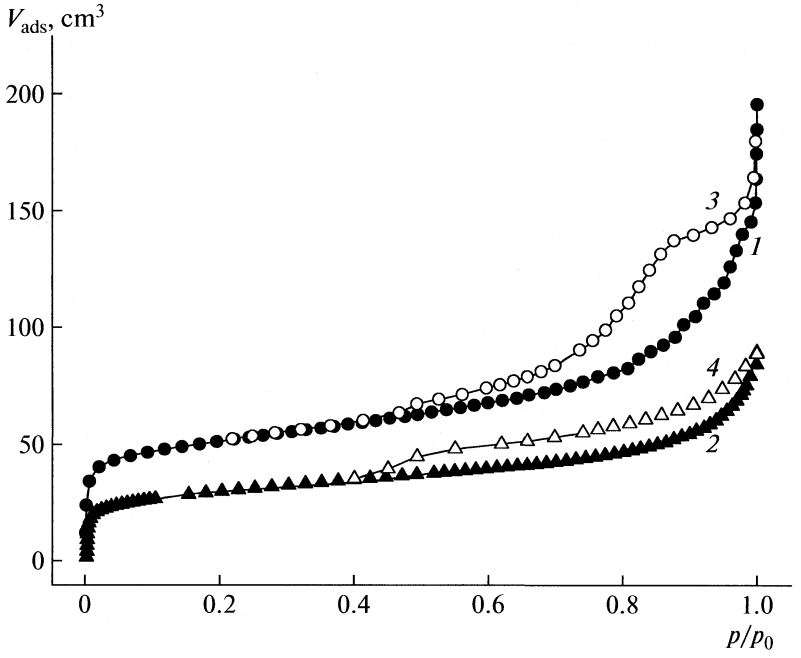

Fig. 2. Nitrogen adsorption (*1*, *2*) – desorption (*3*, *4*) isotherms; (*1*, *3*) – AlFe10PILC, (*2*, *4*) – raw clay.

The curves correspond to the type II isotherms according to IUPAC classification [13]. All the isotherms have reversible part at low relative pressures and hysteresis loops at higher relative pressures corresponding to the H3 type of hysteresis loop. This type of hysteresis loop is characteristic for aggregated and agglomerated plate particles forming slit shape pores [9, 13]. It can be observed that the pillaring process lead to significant increase in the amount of adsorbed nitrogen in the micropore region indicating higher mi-

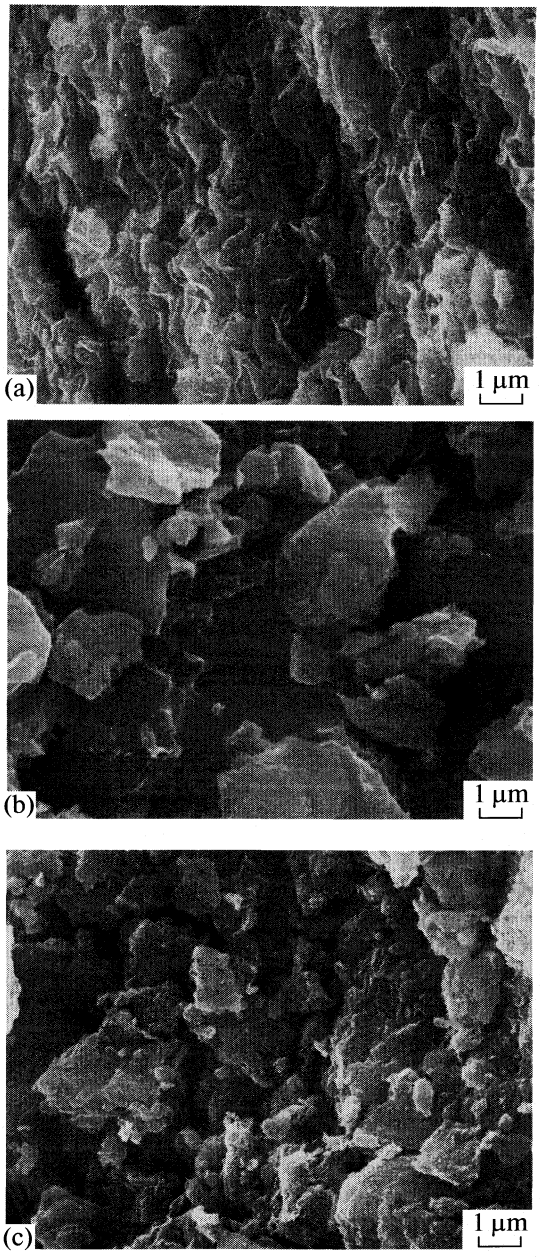

Fig. 3. SEM microphotographs of (a) raw clay,(b) Na-exchanged clay, (a) AlFe10 PILC.

Table 2. Chemical composition based on EDX results (at. %)

Element	Raw clay	AlFe10 PILC	AlFe15 PILC
O	60.37	58.63	57.15
Si	23.11	24.41	18.33
Al	8.89	7.27	8.97
Fe	2.55	7.53	13.37
Ti	0.15	0.15	0.17
Mg	2.08	0.97	0.98
K	1.12	0.43	0.45
Na	1.11	0.61	0.59
Ca	0.62	–	–

croporosity. The enlargement of the hysteresis loop due to pillaring implies nonuniformity in shape and size of pores [18].

Table 1 shows expected increase in the specific surface area, total pore volume and volume of micropores for pillared samples comparing to the non-pillared one. From D_{max} and D_{med} values can be concluded that the pillaring process lead to the shift of mesoporefractions toward grater mesopore diameters.

In Fig. 3 are given selected SEM microphotographs of raw Na-exchanged and AlFel0 pillared clay samples taken under the same magnification (×10000). The microphotograph of AlFel5 PILC is omitted due to similarity with the microphotograph of the other PILC sample.

According to the presented microphotographs it can be concluded that the degree of agglomeration decreases in the following order: raw clay > Na-exchanged clay > AlFe PILC. The layered structure typical for phyllosilicates is retained in all samples. EDX analysis was applied in order to give closer information on the chemical composition of the starting clay and synthesized PILCs. The weight percentage of detected elements is given in Table 2. An increase in the Fe content can be observed after pillaring. Comparing results for the two PILCs it can be concluded that greater amount of Fe was incorporated in the structure of AlFe 15 PILC, as expected.

CONCLUSION

Two Fe pillared clays with different Fe contents were synthesized from domestic clay. Their phase composition and textural properties were investigated. The pillaring process increased and fixed the basal spacing of the clay proving incorporation of pillars into the clay structure. The increase in the specific surface area from approximately 100 m^2/g for starting and Na-exchanged clay to around 170 m^2/g for both pillared clays was registered. The textural analysis confirmed that pillaring process enabled permanent microporosity and large surface area – the important properties for future catalytic application of these materials. EDX analysis confirmed higher degree of Fe incorporation in the PILC obtained using pillaring solution richer in Fe. Similarity in the textural properties of the two synthesized PILCs indicates that possible difference in their catalytic performance should be ascribed to the difference in the Fe content.

ACKNOWLEDGMENTS

This work was supported by the Ministry of Science and Technological Development of the Republic of Serbia (Projects ON 166001B and ON 142019B).

REFERENCES

1. Ray, S. S., Okamoto, M., Prog. Polym. Sci. **28**, 1539 (2003).
2. Alexandre, M., Dubois, P., Mater. Sci. Eng. **28**, 1 (2000).
3. Chae, H. J., Nam, I.-S., Ham, S. W., Hong, S. B., Catal. Today **68**, 31 (2001).
4. Carriazo, J. G., Guelou, E., Barrault, J., Tatibouet, J. M., Moreno, S., Appl. Clay Sci. **22**, 303 (2003).
5. Caudo, S., Centia, G., Genovese, C., Perathoner, S., Appl. Catal. B **70**, 437 (2007).
6. Xu, X. R., Li, H. B., Wang, W. H., Gu, J. D., Chemosphere **59**, 893 (2005).
7. Danish Environmental Protection Agency, 2007, accessed on December 19, 2008, http://www2.mst.dk/common/Udgivramme/Frame.asp?http://www2.mst.dk/udgiv/publications/1999/87-7909-548-8/html/kap05_eng.htm
8. Gil, A., Gandia, L. M., Vicente, M. A., Cat. Rev. – Sci. Eng. **42**, 145 (2000).
9. Vuković, Z., Milutinović-Nikolić, A., Krstić, J., Abu-Rabi, A., Novaković, T., Jovanović, D., Mater. Sci. Forum **494**, 339 (2005) .
10. Vuković, Z., Milutinović-Nikolić, A., Rožić, L., Rosić, A., Nedić, Z., Jovanović D., Clays Clay Miner. **6**, 697 (2006).
11. Kaloidas, V., Koufopanos, C. A., Gangas, N. H., Papayannakos, N. G., Microporous Mater. **5**, 97 (1995).
12. Gregg, S. H., Sing, K. S., *Adsorption, Surface Area and Porosity,* New York, NY, USA: Academic Press, 1967.
13. Rouquerol, F., Rouquerol, J., Sing, K., *Adsorption by Powders and Porous Solids*, London, UK: Academic Press, 1999.
14. Webb, P. A., Orr, C, *Analytical Methods in Fine Particle Technology,* Norcross, GA, USA: Micrometrics Instrument Corporation, 1997.
15. Dubinin, M. M., *Progress in Surface and Membrane Science*, New York, NY, USA: Academic Press, 1975.
16. International Center for Diffraction Data, Joint Committee on Powder Diffraction Standards (JCPDS), Swarthmore, PA, USA, 1990.
17. Banković, P., Milutinović-Nikolić, A., Mojović, Z., Rosić, A., Čupić, Ž., Lončarević, D., Jovanović, D., Chin. J. Catal. **30**, 14 (2009) .
18. Sing, K., Everett, D., Haul, R., Moscou, L., Perolti, R., Rouquerol, J., Siemieniewska, T., Pure Appl. Chem. **57**, 603 (1985).

ЖУРНАЛ ФИЗИЧЕСКОЙ ХИМИИ, 2009, том 83, № 9, с. 1666–1671

CHEMICAL KINETICS AND CATALYSIS

УДК 541.128

DYNAMIC STATES OF THE BRAY–LIEBHAFSKY REACTION WHEN SULFURIC ACID IS THE CONTROL PARAMETER

© 2009 N. Pejić*, J. Maksimović**, D. Ribič** and Lj. Kolar-Anić**

*Faculty of Pharmacy, University of Belgrade, Serbia

E-mail: bimesel@eunet.yu

**Faculty of Physical Chemistry, University of Belgrade, Serbia

Abstract – Dynamic behavior of hydrogen peroxide decomposition catalyzed by iodate and hydrogen ions (the Bray–Liebhafsky reaction), in a continuous stirred tank reactor is investigated. The experimental results are obtained at one operational point in concentration phase space by varying mixed inflow concentrations of the sulfuric acid. The experimental evidences for the onset and termination of oscillatory behavior *via* the saddle node infinite period bifurcation as well as some kind of the Andronov–Hopf bifurcation are presented. In addition, the possibility of excitability of a stable steady state by thiamine was observed.

INTRODUCTION

The investigation of non-linear chemical systems with their self-organization and temporal dynamic structures have become very important, since the obtained results are of general relevance for other complex dynamics systems in various fields (life science, physics, mathematics, economy, and others) [1–3]. In these reaction systems carried out in a continuously fed well stirred tank reactor (CSTR), the stable non-equilibrium stationary states, simple periodic oscillations, period doubling, quasi-periodicity and chaotic dynamics may be found, by adjustment of the control parameters such as the specific flow rate, temperature and mixed inflow concentrations of the feed species [1, 2].

The Bray–Liebhafsky (BL) homogeneous oscillating chemical reaction [4, 5] is a good example for studying mentioned phenomena. It involves the catalytic decomposition of hydrogen peroxide in the presence of hydrogen and iodate:

$$2H_2O_2 \xrightarrow{H^+, IO_3^-} O_2 + 2H_2O, \qquad (D)$$

The apparently simple BL reaction, is a net result of two main kinetic pathways: the reduction of iodate to iodine

$$5H_2O_2 + 2IO_3^- \longrightarrow I_2 + 6H_2O + 5O_2 \qquad (R)$$

and its subsequent oxidation back to iodate,

$$5H_2O_2 + I_2 \longrightarrow 2IO_3^- + 4H_2O + 2H^+. \qquad (O)$$

The (R) and (O) pathways consist of numerous elementary steps during which iodine-containing intermediates such as I, I_2, HIO and HIO_2 are being formed and decomposed. The elementary steps are intertwined and form a complex self-regulating network of molecular interactions [6–13].

The dynamics of BL reaction has been studied comprehensively in batch reactors [4–7, 9, 10, 13–20], whereas there are only few studies in CSTR [21–23]. In the last case, the stable non-equilibrium stationary states, simple periodic oscillations, complex oscillations, bursts and deterministic chaos are discovered [21–23].

These examinations have numerous intentions, from theoretical investigations and modeling [3, 24–26] of the considered system or related ones, to its application in analytical purposes with the aim to measure concentrations below current detection limits [27–30] or to depict kinetic characterizations of catalysts [31]. Therefore, the dynamic states under various combinations of control parameters and their sensitivity on the perturbations must be examined what is also the case in this paper. The investigations presented here are devoted to the dynamic behavior of the BL reaction realized in the CSTR, when the control parameter is the sulfuric acid. Moreover, we have analyzed two distinct stable steady states of the BL system by applying pulsed perturbations with defined amounts of thiamine.

EXPERIMENTAL

Only analytically graded reagents without further purification were used for preparing the solutions. Potassium iodate, sulfuric acid and hydrogen peroxide were obtained from Merck (Darmstadt, Germany), and thiamine from Fluka, BioChemika (Buchs, Switzerland). For the solutions of KIO_3, H_2SO_4, H_2O_2 and thiamine (VB1) deionized water (ρ = 18 MΩ cm, Milli-Q, Millipore, Bedford, MA, USA) was used. Standard stock solutions of thiamine was prepared at the concentration 1.0×10^{-1} M by dissolving 0.8432 g of the pure substances in the 25 ml volumetric flask with water.

The experiments were conduced in the CSTR. A schematic diagram of the instrumental setup is shown

in [29]. In all experiments, the feed substances, aqueous solutions of H_2SO_4, KIO_3 and H_2O_2, were kept in reservoirs at room temperature and were introduced into reaction vessel separately and without being previously thermostated.

The experiments were performed in a 50 ml glass reaction vessel (Metrohm model 876–20) shielded from light and surrounded by thermostating jacket. The volume of the reaction mixture was kept constant at $V = 22.2 \pm 0.2$ ml by removing the surplus volume of the reaction mixture through the U-shaped glass tube, ending at the free surface over the reaction mixture. The solution was stirred magnetically (magnetic stirrer, IKA–COMBIMAG RCH, Staufen, Germany) with a Teflon coated stir bar (polygon shaped 2 cm × 0.8 cm).

The flows of the reactants through the reaction vessel were driven by peristaltic pumps (Ole Dich Instrumentmakers, Hvidovre, Denmark). Viton tubes (Deutch & Neuman, Berlin, Germany) were used to transport the aqueous solutions of potassium iodate and sulfuric acid, whereas tygon tubes (Ismatec, Glattbrugg–Zurich, Switzerland) were used for hydrogen peroxide. These tubes were connected to teflon tubes (Varian, Darmstadt, Germany), and the reagents were introduced to the reaction vessel through them. The temperature of the reaction mixture was controlled within 0.1 K using a water bath (Series U8, MLW, Freital, Germany).

Temporal evolution of the system was recorded by means of a Pt electrode (Model 6.0301.100, Metrohm, Herisau, Switzerland) and double junction Ag/AgCl electrode (Model 6.0726.100, Metrohm, Herisau, Switzerland) as a reference. In the reference Ag/AgCl electrode, the inner electrolyte was a 3 mol l^{-1} KCl and the outer electrolyte was a saturated solution of K_2SO_4. The potential output was fed via a PC-Multilab EH4 16-bit ADC converter into a PC-AT compatible computer.

For investigated operation point, the BL reaction was run at elevated temperatures. Working at these temperatures causes evaporation of the electrolytes from the reference electrode. This causes a change of the measured potential value. Therefore, fresh electrolytes were added every morning in both the inner and the outer electrolytes compartment.

Perturbations resulting in the instantaneous increase in the thiamine concentration were performed manually by addition of thiamine. A 50 μl shot is estimated to last about 0.5 s.

The thermostated (56.0 ± 0.1°C) and protected from light, reaction vessel was filled up by the three separate inflows of the reactants, 5.90×10^{-2} mol l^{-1} KIO_3, 6.47×10^{-2} mol l^{-1} H_2SO_4 and 1.50×10^{-1} mol l^{-1} H_2O_2, at the maximal flow rate (12 ml min^{-1}). Under these conditions, within 3.5 min, about twice the volume of the reaction mixture becomes charged. Then, the inflows were stopped, the stirrer was turned on 900 rpm, and the excess of the reaction mixture was sucked out through the U-shaped glass tube, in order to achieve the actual reaction mixture volume 22.2 ± 0.2 ml. Hence, the reaction commenced under the bath conditions. After two bath oscillations (after about 20 min) the inflows were turned on at the required specific flow rate (j_0) 2.95×10^{-2} min^{-1} and the mixed inflow concentration of sulfuric acid was varied inside interval, 4.22×10^{-2} mol $l^{-1} \le [H_2SO_4] \le 9.00 \times 10^{-2}$ mol l^{-1}. Under the investigated conditions, it is sufficient to wait for three residence times ($t_r = 1/j_0 \sim 33.9$ min) to obtain any stable dynamic structures for the examined mixed inflow concentration of sulfuric acid.

RESULTS AND DISCUSSION

Under conditions that are given in Experimental procedure different dynamic states are observed when mixed inflow concentration of sulfuric acid varied from 4.22×10^{-2} to 9.00×10^{-2} mol l^{-1}. Some time series, showing dynamic structures observed under the above conditions are presented in Fig. 1a. The dynamic behavior of the BL reaction in a CSTR as a function of the concentration of sulfuric acid as the control parameter (Fig. 1a), i.e. bifurcation analysis, is presented by related bifurcation diagram (Fig. 1b). Moreover, the characterization of the bifurcation points in parameter phase spaces is performed.

Obtained bifurcation diagram (Fig. 1b), showing the envelope of the simple periodic oscillations (for mixed inflow concentration of sulfuric acid in the range 5.63×10^{-2} mol $l^{-1} \le [H_2SO_4] \le 7.46 \times 10^{-2}$ mol l^{-1} (zone II)) as well as two distinct stable stationary states characterized by higher and lower potential values of the stable non-equilibrium stationary states (for the respective intervals of mixed inflow concentration of sulfuric acid: $4.22 \times 10^{-2} - 5.50 \times 10^{-2}$ mol l^{-1} (zone I) and $8.02 \times 10^{-2} - 9.00 \times 10^{-2}$ mol l^{-1} (zone IV)) are presented in Fig 1b. Also, for mixed flow concentration of sulfuric acid in the range $7.61 \times 10^{-2} - 7.88 \times 10^{-2}$ mol l^{-1} (zone III) a region of mixed mode oscillations is entered. The lower bifurcation point (B_1) is in the region $5.50 \times 10^{-2} < [H_2SO_4] < 5.63 \times 10^{-2}$ mol l^{-1}, and the higher one (B_2) denoting the transition between the nonstable and stable non-equilibrium stationary state obtained for higher values of sulfuric acid concentrations, is in the region $7.88 \times 10^{-2} < [H_2SO_4] < 8.02 \times 10^{-2}$ mol l^{-1}.

Transition from the stable nonequilibrium stationary state (characterized by low potential values (zone I, Fig. 1b), into oscillatory (zone II) goes through a saddle node infinite period (SNIPER) bifurcation what is based on the following certainties. When the bifurcation point B_1 is approached from the oscillatory side, the period of simple periodic oscillation increases, whereas their amplitudes remain constant. The bifurcation occurs at the mixed flow concentration of sulfuric acid having the value between 5.50×10^{-2} and 5.63×10^{-2} mol l^{-1}, the very same value as the one ob-

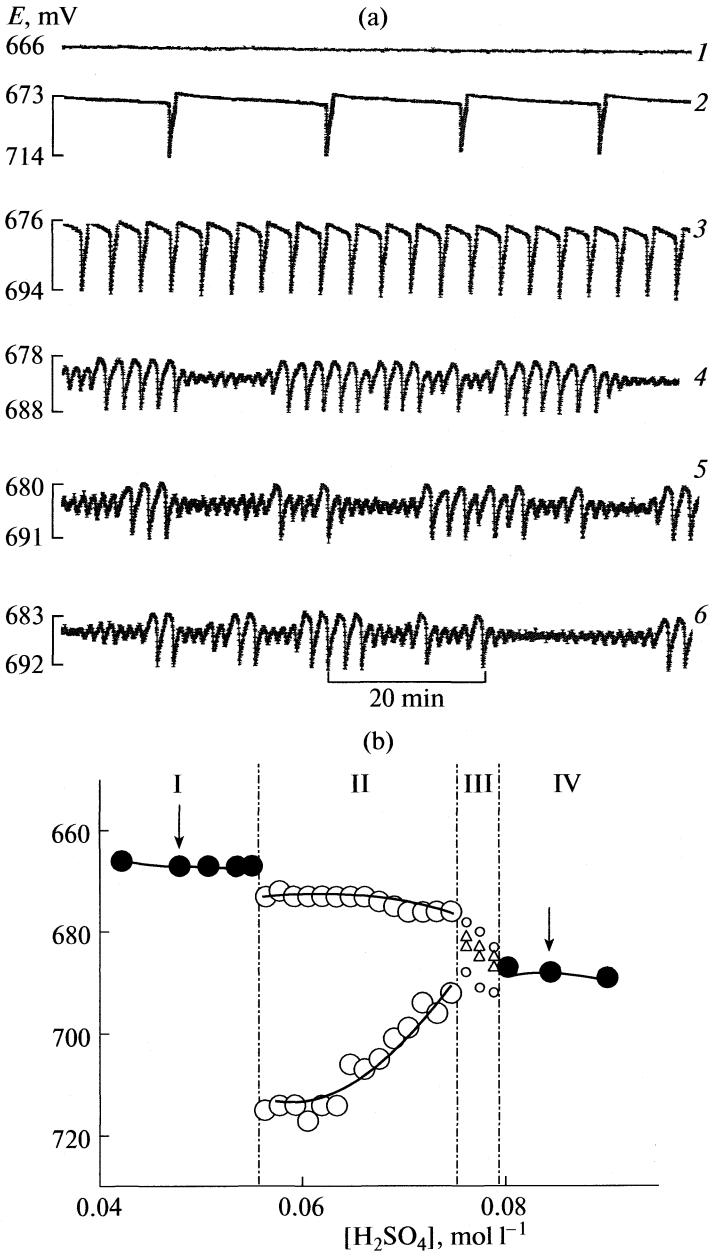

Fig. 1. (a) Time series obtained under the given experimental conditions and mixed inflow concentrations of sulfuric acid (in mol l^{-1}): (*1*) 0.042, (*2*) 0.0591, (*3*) 0.0704, (*4*) 0.0761, (*5*) 0.0774 and (*6*) 0.0788. (b) Bifurcation diagrams show transition from the stable stationary state (solid circles) to the large-amplitude oscillations (open circles) and small amplitude oscillation (triangle) denoting minimal and maximal potential in as oscillation: dash doted lines show the boundary between different dynamic structures: stable stationary states (I and IV), oscillatory states (II) and aperiodic mixed mode oscillations (III). The perturbed stable non-equilibrium stationary states are indicated by arrows.

tained with the increased sulfuric acid concentration; i.e., hysteresis was not observed. By these quantitative observations, it can be concluded that the transitions from the stable steady states to periodic orbits, and vice versa, proceed via SNIPER bifurcation [32–35]. Moreover, by perturbing the stable steady state in zone I with any analyte, the excitability is found.

In Fig. 2 we can see such results when perturbing agent was thiamin. This figure illustrates the sensitivity of the matrix system when it is in the stable stationary state obtained for $[H_2SO_4] = 4.79 \times 10^{-2}$ mol l^{-1}, after perturbations with different amounts of thiamin. Before perturbation, the system is in a stable stationary state and the corresponding potential denoted as E_s is constant. An injection of thiamin in an concentration interval, from 0.01 to 0.15 μmol does not lead to detectable changes in potential whereas the injected amount of thiamin in an interval from 0.3 to 3.0 μmol

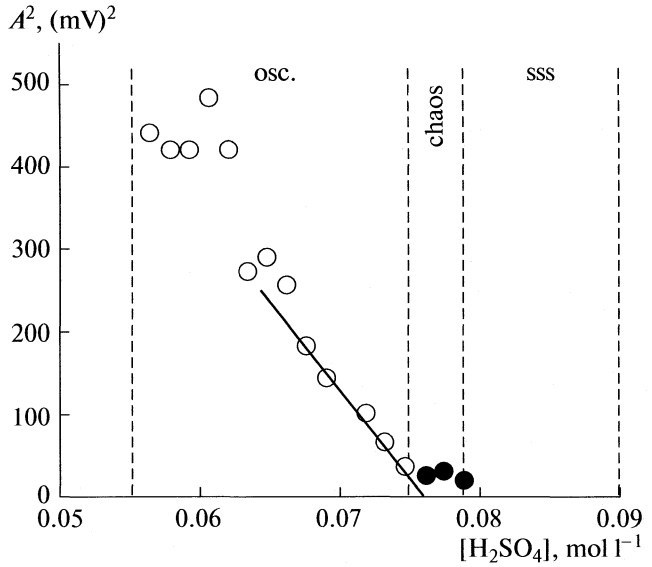

Fig. 2. Plot of the square of the oscillation amplitudes as a function of mixed inflow concentration of sulfuric acid. Amplitudes of regular oscillations and large-amplitude chaotic oscillations are denotes as open and solid circles, respectively.

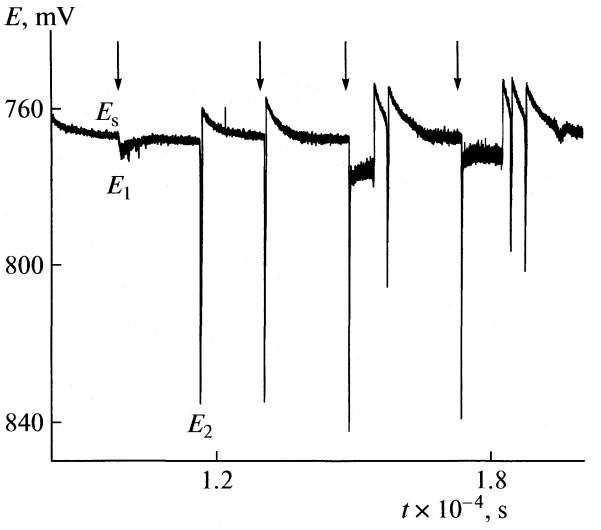

Fig. 3. Perturbations of a stable stationary state found at a mixed inflow concentration of sulfuric acid, [H_2SO_4] = $= 4.79 \times 10^{-2}$ mol l^{-1}. The intensity of perturbations are (from left to righ): [thiamine] = 0.3, 0.45, 1.0 and 3.0 μmol. Arrows indicate the moments at which stable stationary were perturbed.

causes excitation of a new oscillation. For example, the injection of 0.3 μmol of thiamin causes both the abrupt small rise of the potential to the value E_1, and after some time the abrupt large rise of the potential to the value E_2; in fact, we shall have excite a new oscillation. When the applied amount of thiamin is in the interval from 0.45 mol to 3.0 μmol a new oscillation excites immediately. Therefore, in vicinity of the lower bifurcation point B_1, the emergence of excitable state was discovered. The obtained result is additional evidence of SNIPER bifurcation occurring in our system [33].

Transition from the oscillatory state (zone II) to the stable nonequilibrium stationary state (characterized by higher potential values (zone IV), Fig. 1b) goes through an aperiodic dynamic (zone III). Particularly, between 7.61×10^{-2} and 7.88×10^{-2} mol l^{-1} (Fig. 1b), zone III), chaotic dynamics with different complexity is revealed. First, trains of burst-like large-amplitude oscillations emerge chaotically from an irregular procession of small-amplitude oscillations. This aperiodic dynamics, shown in Fig.1 (*4–6*) is terminated for [H_2SO_4] = 8.02×10^{-2} mol l^{-1} where a stable stationary state branch characterized by high potential values is reached (Fig. 1b, zone IV). Comparing these results with the ones obtained when [H_2SO_4] decreased, the hysteresis is not observed. Last dynamic states with regular sustained oscillations before the bifurcation point B_2 are analyzed by linear extrapolation of a plot of the square of the amplitude of the oscillations (Fig. 3). The critical value is [H_2SO_4]$_c$ = 7.56×10^{-2} mol l^{-1}. In addition, the period of oscillation in vicinity of this point [H_2SO_4]$_c$ = 7.56×10^{-2} mol l^{-1} depends linearly on the bifurcation parameter displacement, Δ = $= [H_2SO_4] - [H_2SO_4]_c$. Thus, we assumed that the underlying dynamic structure consists of a stationary state loosing stability through probably Andronov–Hopf bifurcation [2], but the obtained intersection cannot be ascribed easily to this bifurcation point since two kinds of oscillations emerge from it [31]. Namely, between small amplitude oscillations, observed close to the bifurcation point and stable nonequilibrium stationary state, relatively narrow chaotic window occurs.

The sensitivity of the matrix system being in the stable non-equilibrium stationary state obtained for [H_2SO_4] = 8.44×10^{-2} mol l^{-1}, after perturbations by thiamine is illustrated in Fig. 4. It shows typical dynamic profiles for the matrix system obtained before and after its perturbation by thiamine. In this case, the responses of matrix system are significantly different with respect to the previous case. Before perturbation, as in previous case, the system is in a stable stationary state and the corresponding potential denoted as E_s is constant. An injection of thiamine causes an abrupt change in potential. The potential value denoted as E_p is the maximal value of the potential that is being reached. After perturbation system relaxes to some stable stationary state that is slightly different from initial stable stationary state (Fig. 4), which happens in the system when it is very close to the bifurcation point [2]. From this point of view, we can divide the recorded a measured signal (potentiometric trace, Fig. 4) into two parts: the initial maximal potential difference and an autonomous relaxation back to the some stable stationary state. For all examined perturbation strenght, the relaxation potential–time curves are qualita-

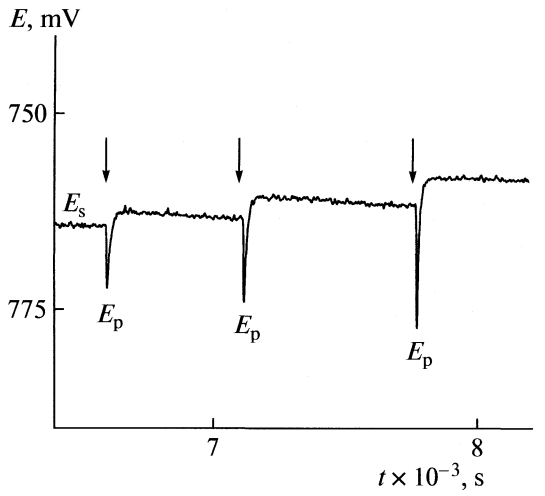

Fig. 4. Perturbations of a stable stationary state found at a mixed inflow concentration of sulfucic acid, $[H_2SO_4] = 8.44 \times 10^{-2}$ mol l^{-1}. The intensities of perturbations are (from left to right): [thiamine] = 0.08, 0.15 and 0.75 μmol. Arrows indicate the moments at which stable stationary states were perturbed.

tively similar (Fig. 4). However, it was found that the maximal potential difference, $\Delta E_m = E_p - E_s$, is linearly proportional to the perturbation strength over the range of 0.01–1.0 μmol [36].

Both analyzed stable nonequilibrium stationary states that are connected with oscillatory region are sensitive to thiamine, but in different manners. However, obviously perturbations performed under the conditions where excitability is observed, are not appropriate for quantitative determination of thiamin since in that case the maximal potential displacement, $\Delta E_m = E_p - E_s$ does not depend on the analyte concentration, but depend on the characteristics of the system, more precisely the value of the amplitude is determined by the form of slow manifold in the examined point. In addition, the above described examination of sensitivity different dynamic states, as expected, gives further information about the type of the bifurcation in BL dynamic system.

CONCLUSION

Dynamic behavior of the BL reaction was investigated in the CSTR. When the mixed inflow concentration of sulfuric acid was varied, different types of dynamic regions including stable non-equilibrium stationary states, simple periodic oscillations and chaotic mixed-mode oscillation were noticed. The experimental evidence for the onset and termination of oscillatory behavior *via* the saddle node infinite period (SNIPER) bifurcation as well as some kind of Andronov–Hopf bifurcation are presented.

Finally, we showed that both examined stable steady states in vicinity of their transitions to unstable ones are sensitive to the concentration of thiamine. Particularly, in vicinity of the higher bifurcation point, a maximal potential shift, ΔE_m depends linearly on the concentrations of the considerate analyte, what can be basis for a development of kinetic method for quantitative determination of thiamine. Finally, by perturbation of the system with thiamin we obtained excitability of a stable nonequilibrium stationary state that is in vicinity of lower bifurcation point. These conditions are not appropriate for quantitative determination of thiamin by employing the maximal potential displacement, ΔE_m.

ACKNOWLEDGMENTS

The present investigations were partially supported by the Ministry of Sciences of the Republic of Serbia, under Project 142025.

REFERENCES

1. R. J. Field and M. Burger (eds.) *Oscillations and Traveling Waves in Chemical System* (Wiley, New York, 1985).
2. P. Gray and S. Scott, *Chemical Oscillations and Instabilities: Nonlinear Chemical Kinetics* (Oxford University Press, Oxford, 1990).
3. G. Schmitz and Lj. Kolar-Anic, Russ. J. Phys. Chem. **81**, 1380 (2007).
4. W. C. Bray, J. Am. Chem. Soc. 43, 1262 (1921).
5. W. C. Bray and H. A. Liebhafsky, J. Am. Chem. Soc. **53**, 38 (1931).
6. I. Matsuzaki, J. Woodson and H. Liebhafsky, Bull. Chem. Soc. Jpn. **43**, 3317 (1970).
7. K. R. Sharma and R. M. Noyes, J. Am. Chem. Soc. **98**, 4345 (1976).
8. D. Edelson and R. M. Noyes, J. Phys. Chem. **83**, 212 (1979).
9. S. Anić and Lj. Kolar-Anić, Ber. Bunsen-Ges. Phys. Chem. **90**, 1084 (1986).
10. S. Anić and Lj. Kolar-Anić, J. Chem. Faraday Trans. **84**, 3413 (1988).
11. L. Treindl and R. M. Noyes, J. Phys. Chem. **97**, 11354 (1993).
12. Lj. Kolar-Anić, Ž. Čupić, S. Anić and G. Schmitz, J. Chem. Faraday Trans. **93**, 2147 (1997).
13. P. Ševčík and Lj. Adamčíková, Chem. Phys. Lett. **267**, 307 (1997).
14. S. Anić, D. Mitić and Lj. Kolar-Anić, J. Ser. Chem. Soc. **50**, 53 (1985).
15. G. Schmitz, J. Chim.Phys. **84**, 957 (1987).
16. S. Anić, D. Stanisavljev, G. Kranjski Belovljev and Lj. Kolar-Anić, Ber. Bunsen-Ges. Phys. Chem. **93**, 488 (1989).
17. S. Anić, D. Stanisavljev, Ž. Čupić, M. Radenković, V. Vukojević and Lj. Kolar-Anić, Sci. Sintering **30**, 49 (1998).
18. D. Stanisavljev, N. Begović and V. Vukojević, J. Phys. Chem. A **102**, 6887 (1998).

19. D. Stanisavljev, A. Đorđević and V. Likar-Smiljanić, Chem. Phys. Chem. **5**, 140 (2004).

20. J. Ćirić, S. Anić, Ž. Čupić and Lj. Kolar-Anić, Sci. Sintering **32**, 187 (2000).

21. V. Vukojević, S. Anić and Lj. Kolar-Anić, J. Phys. Chem. **104**, 10731 (2000).

22. Lj. Kolar-Anić, V. Vukojević, N. Pejić, T. Grozdićand S. Anić, in *Experimental Chaos* Ed. by S. Boccaletti, B. J. Gluckman, J. Kurths, L. Pecora, R. Meucci, Q. Yordanov (American Institute of Physics, AIP Conference Proceedings; Volume 742: Melville, New York, 2004), pp. 3–8.

23. N. Pejić and J. Maksimović, Bray-Liebhafsky Reaction. Dynamic States When Sulfuric Acid Is the Control Parameter, in *Physical Chemistry 2008*, Ed. by A. Antić–Jovanović (Society of Physical Chemists of Serbia, Belgrade, 2008), pp. 235–237.

24. Lj. Kolar-Anić, T. Grozdić, V. Vukojević, G. Schmitz and S. Anić, in Selforganization in Nonequilibrium Systems, Ed. by S. Anić, Ž. Čupić and Lj. Kolar-Anić (Society of Physical Chemists of Serbia, Belgrade, 2004), pp. 115–118.

25. G. Schmitz, Lj. Kolar-Anić, T. Grozdić and V. Vukojević, J. Phys. Chem. **110**, 10361 (2006).

26. A. Ivanović, Ž. Čupić, M. Janković, Lj. Kolar-Anić and S. Anić, Phys. Chem. Chem. Phys. **10**, 5848 (2008).

27. V. Vukojević, N. Pejić, D. Stanisavljev, S. Anić and Lj. Kolar-Anić, Analyst **124**, 147 (1999).

28. N. Pejić, S. Blagojević, S. Anić, V. Vukojević, M. Mijatović, J. Ćirić, Z. Marković, S. Marković and Lj. Kolar-Anić, Anal. Chim. Acta **582**, 367 (2007).

29. N. Pejić, S. Blagojević, J. Vukelić, Lj. Kolar-Anić and S. Anić, Bull. Chem. Soc. Jpn. **80**, 1942 (2007).

30. N. Pejić, S. Blagojević, S. Anić and Lj. Kolar-Anić, Anal. Bioanal. Chem. **389**, 2009 (2007).

31. M. Milošević, N. Pejić, Ž. Čupić, S. Anić and Lj. Kolar-Anić, Materials Science Forum **494**, 369 (2005).

32. J. Maselko, J. Chem. Phys. **67**, 17 (1982).

33. Z. Noszticzius, Stirling P. and M. Wittman, J. Chem. Phys. **89**, 4914 (1985).

34. V. Gáspár and P. Galambosi, J. Phys. Chem. **90**, 2222 (1986).

35. S.K. Scott, Chemical Chaos (Clarendon Press, Oxford U.K., 1991)

36. J. Maksimović, N. Pejić, D. Ribič and Lj. Kolar-Anić, Pulse Perturbation Technique for Determination of Thiamin in Pharmaceuticals Using an Oscillatory Reaction System, in *Physical Chemistry 2008*, Ed. by A. Antić–Jovanovic (Society of Physical Chemists of Serbia, Belgrade, Belgrade 2008) pp. 235–237.

ЖУРНАЛ ФИЗИЧЕСКОЙ ХИМИИ, 2009, том 83, № 9, с. 1672–1677

CHEMICAL KINETICS AND CATALYSIS

УДК 541.124

TEMPERATURE INFLUENCE ON THE MALONIC ACID DECOMPOSITION IN THE BELOUSOV–ZHABOTINSKY REACTION

© 2009 S. M. Blagojević*, S. R. Anić**, Ž. D. Čupić***, N. D. Pejić* and Lj. Z. Kolar-Anić**

*Faculty of Pharmacy, University of Belgrade, Serbia

E-mail: slavica.blagojevic@pharmacy.bg.ac.rs;

**Faculty of Physical Chemistry, University of Belgrade, Serbia

***ICh TM, University of Belgrade – Department of Catalysis and Chemical Engineering, Serbia

Abstract – The kinetic investigations of the malonic acid decomposition ($8.00 \times 10^{-3} \le [CH_2(COOH)_2]_0 \le 4.30 \times 10^{-2}$ mol dm^{-3}) in the Belousov–Zhabotinsky (BZ) system in the presence of bromate, bromide, sulfuric acid and cerium sulfate, were performed in the isothermal closed well stirred reactor at different temperatures ($25.0 \le T \le 45.0$°C). The formal kinetics of the overall BZ reaction, and particularly kinetics in characteristic periods of BZ reaction, based on the analyses of the bromide oscillograms, was accomplished. The evolution as well as the rate constants and the apparent activation energies of the reactions, which exist in the preoscillatory and oscillatory periods, are also successfully calculated by numerical simulations. Simulations are based on the model including the Br_2O species.

INTRODUCTION

The Belousov–Zhabotinsky (BZ) reaction exhibits various dynamic regimes depending on experimental conditions [1]. Here we are focused on the kinetics of malonic acid decomposition and the influence of the temperature and initial malonic acid concentration on the overall process in the presence of bromate, bromide and cerium ions in the well stirred closed reactor.

The influence of initial malonic acid concentration on the overall BZ reaction was subject of investigation from its discovery [1–6]. The kinetics of the BZ reaction under the closed isothermal reactor condition can be analyzed by two manners. In first of them the time evolutions of the concentration of the related species [6] were examined classically, whereas in the second one the evaluation of characteristic times of the reaction were considered as in our previous publications [7–12]. In both cases, the kinetics of the BZ reaction was accepted as the first order reaction with respect to the malonic acid concentration. Instead of such rate constant, the period or related frequency of the considered oscillation or oscillations in selected sequence of oscillogram is used [13]. Later was found that the characteristic period τ_{end}, where τ_{end} is the time interval between the beginning of the reaction and the end of the last incomplete oscillation [7–10] is an appropriate parameter for the kinetic analysis of the BZ reaction [11, 12]. Namely, τ_{end} is useful for analysis of any oscillatory reaction when the order of reaction with respect to reactant can be proposed [9–12]. To be exact, in our case where the first order reaction with respect to malonic acid is found, the following relation [11, 12] is valid:

$$\tau_{end} = \frac{1}{k_{end}} \ln \frac{[MA]_0}{[MA]_{end}}, \quad \text{or} \quad \tau_{end} = -\frac{1}{k_{end}} \ln [MA]_{end} + \frac{1}{k_{end}} \ln [MA]_0. \tag{1}$$

Here, $[MA]_0$ and $[MA]_{end}$ denote the concentrations of malonic acid in t = 0 and t = τ_{end}, respectively; k_{end} is the rate constant of the net overall BZ reaction, being malonic acid removal. We could assume that $[MA]_{end}$, the malonic acid concentration at τ_{end} is practically constant, and independent of the initial malonic acid concentration. From the experiments in which only concentrations $[MA]_0$ were varied, we easily obtained the rate constant k_{end} [11, 12]. The influence of the other species on the overall BZ reaction is included in the complex rate constant k_{end}.

Otherwise, the temperature dependence of BZ reaction is relatively less investigated [6, 13,14]. From the early beginning, when frequency of the oscillations [13], preoscillatory period [14] and kinetics of accumulation of the bromomalonic acid in the preoscillatory period were analyzed [6], it was noted that apparent activation energies depend on the examined characteristic periods of the considered reaction. Thus, in the first paper [13], plotting the logarithm of the reciprocal value of the period of the second or third oscillations (or the frequencies of the oscillations ω) obtained at different temperatures versus T^{-1}, the overall

activation energy E_ω of 67.5 kJ mol^{-1} was obtained. Activation energies calculated from the frequencies (E_ω) are higher than those obtained from rate constants of bromomalonic acid accumulation. Analyzing the temperature dependence of the rate constant of the bromomalonic acid accumulation in the monotonous preoscillatory period by Arrhenius relation [6], activation energy value between 48.7 and 56.9 kJ mol^{-1} was obtained. The apparent activation energy determined for the overall process is significantly dependent on the composition of the BZ system [4]. For different initial concentrations of organic substrate no general tendency has been found for activation energies of overall BZ reaction [4].

EXPERIMENTAL

The isothermal BZ oscillatory reaction was generated in an isothermal closed reactor with a reaction volume of 5.1×10^{-2} dm^3 equipped with a magnetic stirrer (the stirring rate was 700 rpm). The experiments were repeated at different temperatures ($25.0 \le T \le 45$°C). The temporal evolution of the BZ oscillator was monitored by potentiometric method, where a bromide ion–sensitive electrode versus double junction Ag/AgCl as the reference was used. The reaction solution was used without further purification with nitrogen because its presence do not influence the evolution of BZ systems in our investigation [12, 15]. The experiments were carried out with various initial malonic acid concentrations ($8.00 \times 10^{-3} \le [MA]_0 \le 4.30 \times 10^{-2}$ mol dm^{-3}). The concentrations of other species were kept constant (in dm mol^{-3}): $[H_2SO_4]_0 = 1.00$; $[KBrO_3]_0 = 6.20 \times 10^{-2}$; $[KBr]_0 = 1.50 \times 10^{-5}$; $[Ce_2(SO_4)_3]_0 = 2.50 \times 10^{-3}$.

RESULTS AND DISCUSSION

Experimental Results

By means of the potentiometric measurements of the evolution of BZ reaction systems by bromide ion–sensitive electrode carried out in the isothermal closed reactor, well developed oscillograms of the same type with one preoscillatory period and one oscillatory period characterized by the large-amplitude relaxation oscillations and characteristic last incomplete oscillation, appropriate for the kinetic analysis of the reaction system [7–10], are obtained (Fig. 1). The oscillograms depend on both, the initial malonic acid concentrations and the temperature. For any initial malonic acid concentration, when the temperature increases, the preoscillatory period τ_1 and period τ_{end} decrease (Fig. 2a, b), whereas the number of oscillations (n) is approximately constant. (Fig. 2c). The same type of the potentiometric traces is an indication that the kinetics of the BZ reaction under the considered conditions is unchanged. The obtained results obey the equation (1) very well for all initial malonic acid concentrations less than, or equal to 3.20×10^{-2} mol dm^{-3}

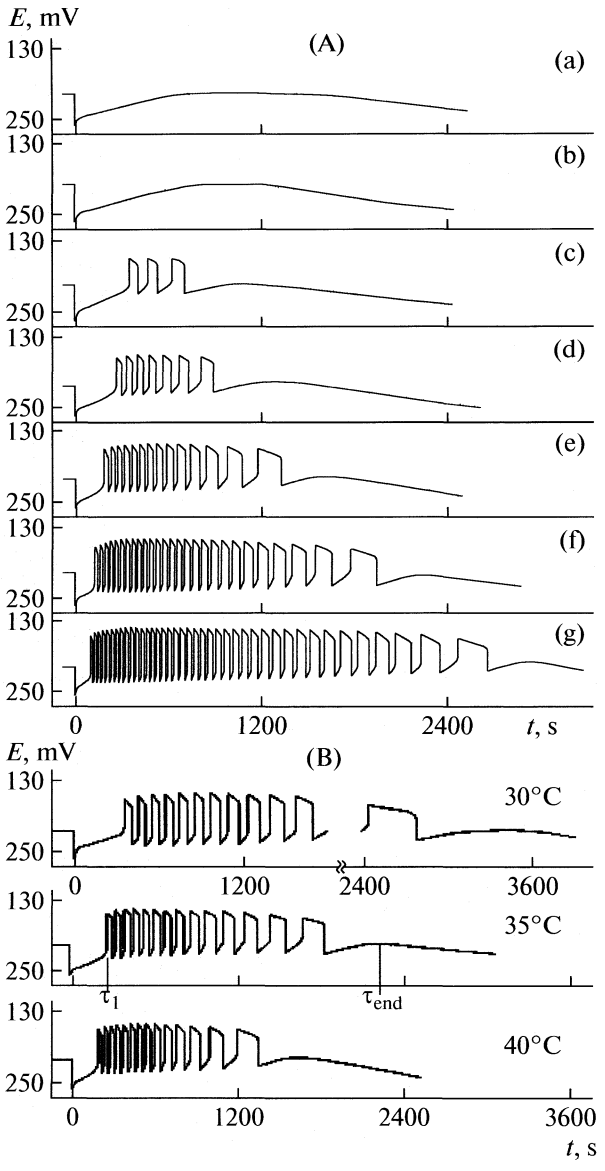

Fig. 1. Potentiometric traces of the bromide ion-sensitive electrode; (A) the experimental results at $T = 4$°C in order of increasing $[MA]_0$ (in mol dm^{-3}): (a) 8.00×10^{-3}, (b) 9.00×10^{-3}, (c) 1.20×10^{-2}, (d) 1.60×10^{-2}, (e) 2.20×10^{-2}, (f) 3.20×10^{-2}, (g) 4.30×10^{-2}; (B): the experimental results at different temperatures for $[MA]_0 = 2.20 \times 10^{-2}$ mol dm^{-3}.

(ln $(3.20 \times 10^{-2}) = -3.44$) as shown in Fig. 3a. Thus, it follows that the malonic acid decomposition can by analyzed as a pseudo-first order reaction with respect to malonic acid in the concentration domain of 1.20×10^{-2} to 3.20×10^{-2} mol dm^{-3}. The rate constant was calculated from the slope of obtained linear dependences between τ_{end} and $\ln[MA]_0$ (Eq. (1), Table 1). Also, we can assume that domination of reaction pathways is not changed in the considered temperature region and that concentration of malonic acid in characteristic times (τ_{end}, τ_1) does not vary signif-

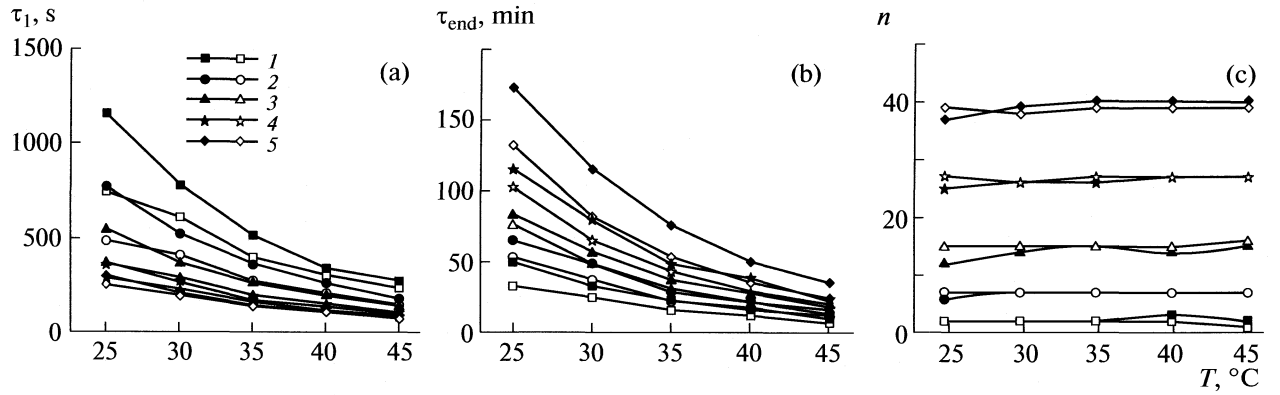

Fig. 2. Values (a) τ_1, (b) τ_{end}, and (c) n, *versus* temperature T at the different initial concentrations of malonic acid $[MA]_0$; (*1*) 1.2×10^{-2}, (*2*) 1.6×10^{-2}, (*3*) 2.2×10^{-2}, (*4*) 3.2×10^{-2}, (*5*) 4.3×10^{-2} mol dm^{-3} (the full symbols denote the experimentally obtained results whereas the empty symbols correspond to the numerically simulated values).

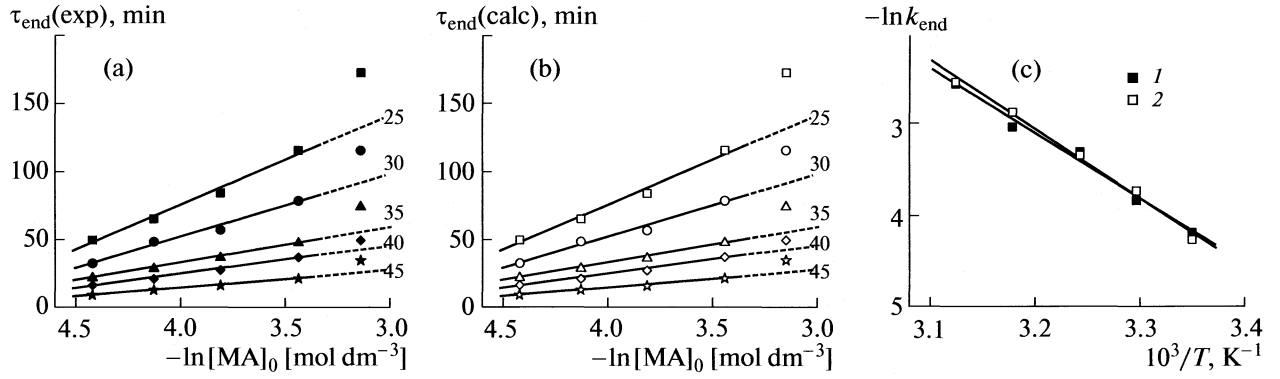

Fig. 3. The time elapsed from the beginning of the reaction until the end of an oscillatory evolution obtained (a) experimentally and (b) numerically as a function of $\ln[MA]_0$, for the different temperatures (in °C).; (c) the Arrhenius dependence between $\ln k_{end}$ and T^{-1} for (*1*) experimental and (*2*) numerically obtained rate constants k_{end}.

icantly with the temperature. Namely, in our cases the calculations show that mentioned concentrations shift to 3% from the mean values.

The temperature dependence of k_{end} was analyzed by Arrhenius law (Fig. 3c). The apparent activation energy of the overall process is found to be $E_{end} = 63.1$ kJ mol^{-1} which is in accordance with the corresponding values obtained in literature [3, 4, 13, 14].

Then, for the equiconcetrational systems at different temperatures, the inverse proportionality between

Table 1. Experimental (I) and calculated (II) values of the pseudo-first order rate constants ($k_{end} \times 10^2$, min^{-1}) at different temperatures

T, °C	I	II
25	1.50	1.39
30	2.14	2.38
35	3.65	3.48
40	4.72	5.59
45	7.60	7.73

Table 2. The apparent activation energies E_1 and E^*_{end} (experimetntal (I) and calculated (II)) for different initial concentrations of malonic acid $[MA]_0$

$[MA]_0 \times 10^2$, mol dm^{-3}	E_1, kJ mol^{-1}		E^*_{end}, kJ mol^{-1}	
	I	II	I	II
1.20	58.3	47.1	63.7	63.1
1.60	56.5	49.2	63.8	63.1
2.20	53.0	50.1	61.5	64.5
3.20	51.6	50.1	63.8	65.6
4.30	48.9	48.9	63.4	66.7

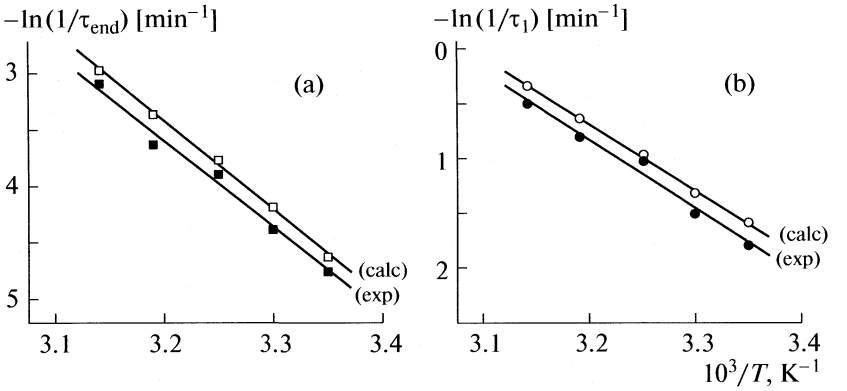

Fig. 4. The dependences (a) $\ln(1/\tau_{end})$ and (b) $\ln(1/\tau_1)$ on $1/T$ for the equiconcentration BZ systems at $[MA]_0 = 3.20 \times 10^{-2}$ mol dm^{-3}.

τ_{end} and rate constant k, follows from the equation (1), since $\ln(c_0/c_{end})$ is now constant:

$$\tau_{end} \propto 1/k. \quad (2)$$

Similar consideration can be applied on preoscillatory period τ_1 where we can assume that corresponding values $\ln(c_0/c_1)$ are independent of temperature for equiconcentration systems. In that case, instead the Arrhenius relation $\ln k = f(T^{-1})$, the relation $\ln(\tau_{end}^{-1}) = f(T^{-1})$ and $\ln(\tau_1) = f(T^{-1})$ can be used for determination of corresponding activation energies E_{end}^* and E_1 (Figs. 4a, 4b).

We can conclude that both methods for the determination of apparent activation energies of overall process, E_{end} and E_{end}^*, based on the temperature dependence of k_{end} (63.1 kJ mol^{-1}, Fig. 3c) and τ_{end} (63.2 ± 1.7 kJ mol^{-1}, Fig. 4a; Table 2) are in the excellent agreement. Their values do not depend significantly on the initial malonic acid concentration while the activation energies E_1 decreases when the malonic acid concentration increases. Our results are in the good agreement with different values between apparent activation energies of the reaction in the preoscillatory and oscillatory periods (Table 2) that was re-

Table 3. Reactions and their rate constants at 30°C and $[H_2O] = 55$ mol dm^{-3} and activation energies used in the numerical simulation

	Reaction	Rate constant	References	E_a, kJ mol^{-1}
R1	$Br^- + HOBr + H^+ \longrightarrow Br_2 + H_2O$	2.55×10^9 mol^{-2} dm^6 s^{-1}	[20]	15.0 [21, 22]
R-1	$Br_2 + H_2O \longrightarrow Br^- + HOBr + H^+$	3.18 s^{-1}	[20]	69.0 [21, 22]
R2	$HBrO_2 + Br^- + H^+ \longrightarrow Br_2O + H_2O$	5.93×10^6 mol^{-2} dm^6 s^{-1}	[12]	25.4
R3	$Br_2O + H_2O \longrightarrow 2HOBr$	3.21×10^3 s^{-1}	[12]	69.9
R-3	$2HOBr \longrightarrow Br_2O + H_2O$	3.22×10^8 mol^{-1} dm^3 s^{-1}	[12]	70.2
R4	$Br^- + BrO_3^- + 2H^+ \longrightarrow HOBr + HBrO_2$	2.86 mol^{-3} dm^9 s^{-1}	[5, 20]	54.0 [21, 22]
R5	$2HBrO_2 \longrightarrow BrO_3^- + HOBr + H^+$	3.49×10^3 mol^{-1} dm^3 s^{-1}	[5, 20]	22.4 [21]
R6	$BrO_3^- + HBrO_2 + H^+ \longrightarrow 2BrO_2^\bullet + H_2O$	44.70 mol^{-2} dm^6 s^{-1}	[5]	44.9
R-6	$2BrO_2^\bullet + H_2O \longrightarrow BrO_3^- + HBrO_2 + H^+$	6.70×10^7 mol^{-1} dm^3 s^{-1}	[20]	69.9
R7	$Ce^{3+} + BrO_2^\bullet + H^+ \longrightarrow Ce^{4+} + HBrO_2$	3.20×10^4 mol^{-2} dm^6 s^{-1}	[5]	69.9
R-7	$Ce^{4+} + HBrO_2 \longrightarrow Ce^{3+} + BrO_2^\bullet + H^+$	1.12×10^4 mol^{-1} dm^3 s^{-1}	[5]	70.0
R8	$MA + Br_2 \longrightarrow BrMA + Br^- + H^+$	4.24 mol^{-1} dm^3 s^{-1}	[20, 21]	64.6
R9	$MA + Ce^{4+} \longrightarrow Ce^{3+} + P_1 + H^+$	0.36 mol^{-1} dm^3 s^{-1}	[5]	67.0 [21]
R10	$BrMA + Ce^{4+} \longrightarrow Ce^{3+} + Br^- + P_2$	47.17 mol^{-1} dm^3 s^{-1}	[5]	67.0 [21]
R11	$Br_2O + MA \longrightarrow BrMA + HOBr$	4.23×10^{-2} mol^{-1} dm^3 s^{-1}	[12]	37.7
R12	Br_2 (sol) $\longrightarrow Br_2$ (g)	1.10×10^{-2} s^{-1}	[18]	72.9

Notes: MA = malonic acid, BrMA = bromomalonic acid, P_1 and P_2 are products of reactions. For reactions R7, R8 and R12 data from references modified in this work to fit experimental data; more details see in ref [12]. For some reactions the activation energies taken from literature, the others activation energies are optimized during a numerical simulation of the BZ reaction.

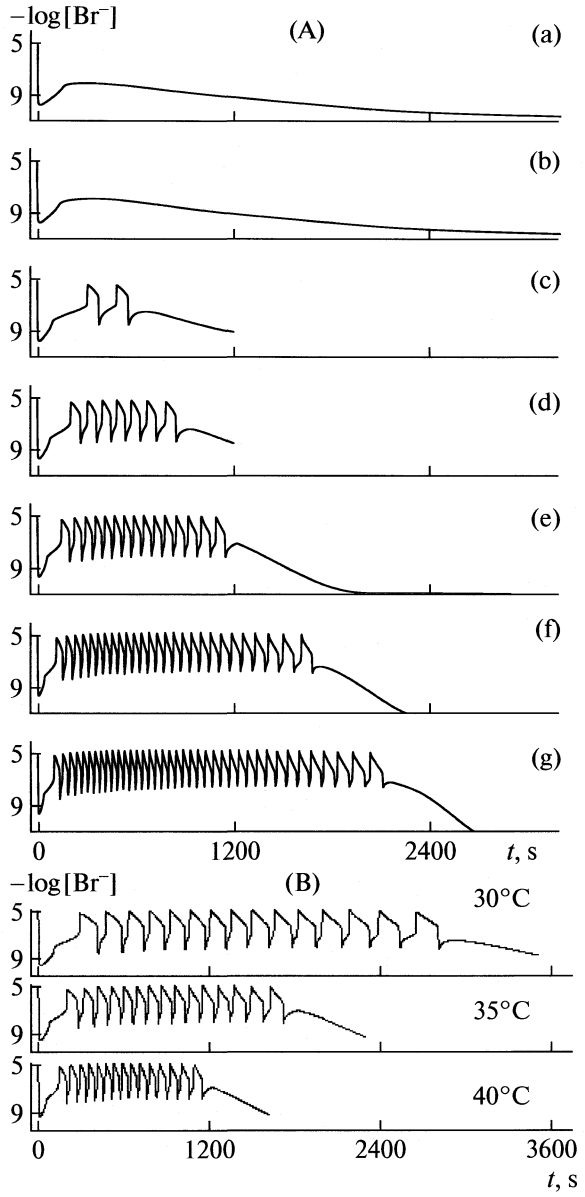

Fig. 5. Time dependence of log[Br⁻] obtained by the numerical simulation (A) the simulated results at $T = 40°C$ in order of increasing initial concentration of malonic acid (see Fig. 1); (B) the simulated results at different temperatures for $[MA]_0 = 2.20 \times 10^{-2}$ mol dm^{-3}, $[HOBr]_0 = 1.50 \times 10^{-8}$ mol dm^{-3}, whereas the initial concentrations of other intermediates are zero in numerical simulations.

ported by Burger and Koros [6] and the other authors [3, 4, 13, 14].

Numerical Simulations

We have tried to reproduce the experimental observed time series in the closed reactor by model presented in our previous paper [12]. The reaction scheme shown in Table 3, is based on the previously proposed GF model, referred to as model B [16], and further accomplished with four new reactions ((R2), (R3), (R-3) and (R11)) including the Br_2O species [17] and reaction (R12) due to evaporation of bromine [18]. Namely, Br_2O species [17] and related reactions are introduced in the model in analogy to I_2O that exists in the model for Bray–Liebhafsky oscillatory reaction [19]. Such introduction of Br_2O species as new intermediate is appropriate one for the fine regulation of the HOBr concentration in the reaction system, since we assume that Br_2O react with malonic acid resulting in bromomalonic acid and HOBr (R11). Preliminary calculations have indicated that reaction system (R1)–(R11) produce oscillations under the experimental conditions but the calculated preoscillatory periods are smaller than the experimental values. Therefore, the reduction of the bromine concentration caused by bromine evaporation from the system (R12) [18] should influence the reaction between bromine and malonic acid (R8), and consequently the prolongation of the preoscillatory period. The simulations based on the model given in Table 3 are carried out under the conditions used in the experiments (Fig. 1). Most rate constants and some activation energies were taken from earlier numerical simulations [5, 12, 16, 18, 20, 21] while others are modified here as indicated in Table 3.

Although all experiments are performed in 1.00 mol dm^{-3} H_2SO_4, in all simulations we use $[H^+]_0 = 1.29$ mol dm^{-3} according to Robertson and Dunford [23]. Most important oscillatory features (characteristic times (τ_1) and (τ_{end}), period of oscillations and number of oscillations (n), are well simulated (Figs. 2 and 5). The rate constants k_{end}, calculated by equation (1) where τ_{end} was determined from numerically simulated oscillograms, are given in Table 1. The apparent activation energy of the overall BZ process obtained by rate constants (Fig. 3c) k_{end} is 67.1 kJ mol^{-1}. It is in good agreement with the one obtained by experiments 63.1 kJ mol^{-1} (Fig. 3c).

Moreover, the numerical values of apparent activation energies performed from relation (2) for different initial concentrations of malonic acid, obtained from numerically simulated oscillograms, are given in Table 2. Their average value (64.6 ± 2.1 kJ mol^{-1}) is close to the one obtained experimentally (63.2 ± 1.7 kJ mol^{-1}). The numerical value of apparent activation energy calculated by means of τ_1 (49.1 ± 2.0 kJ mol^{-1}) is in agreement with experimental ones which change from 58.3 to 48.9 kJ mol^{-1} for the domain malonic acid concentration between 1.20×10^{-2} and 4.30×10^{-2} mol dm^{-3}.

CONCLUSION

The systematic kinetic investigations of the malonic acid decomposition in the Belousov–Zhabotinsky reaction were presented. With aim to evaluate the apparent activation energies for different periods of BZ reaction generated under observed conditions, several methods for examinations of the formal kinetics were

applied. By analyzing the obtained apparent activation energies, the validity of the earlier proposed methods as well as here involved ones are confirmed.

All results are also calculated by numerical simulations based on the proposed variant of the model of the Belousov–Zhabotinsky reaction with Br_2O as intermediate species and using the methods applied in formal kinetics. The obtained values are in a good agreement with the ones evaluated from direct experimental investigations and with the ones found in the literature.

ACKNOWLEDGMENTS

We thank our colleague, prof. Zoltan Noszticzius, from Budapest University for his important and fruitful suggestions during the preparations of the article. This work was partially supported by the Ministry for Science and Environmental protection of the Republic of Serbia (Grants no. 142025 and 142019).

REFERENCES

1. R., Field, M., Burger, *Oscllations and Traveling Waves in Chemical System, "Mir" Moscow*, **78**, 116 (1988).
2. R., Field, E., Körös, R., Noyes, J. Am. Chem. Soc., **94**, 8649 (1972).
3. M., Blandamer, D., Roberts, J. Chem. Soc. Farad. Trans. I, **73**, 1056 (1977).
4. G., Nagy, E., Körös, N., Oftedal, K., Tjelflaat, P., Ruoff, Chem. Phys. Letters, **250**, 255 (1996).
5. B., Johnson, S., Scott, B., Thompson, Chaos, **7**, 350 (1997).
6. M., Burger, E., Körös, J. Phys. Chem., **84**, 496 (1980).
7. S., Anić, Lj., Kolar-Anić, Ber. Bunsenges. Phys. Chem., **90**, 539 (1986).
8. S. Anić, Ljiljana Kolar-Anić, J. Chem. Soc. Faraday Trans. I, **84**, 3413 (1988).
9. S. Anić, D. Stanisavljev, G. Krnajski Belovljev, Lj. Kolar-Anić, Ber. Bunsenges. Phys. Chem., **93**, 488 (1989).
10. S., Anić, Lj., Kolar-Anić, E., Körös, React. Kinet. Catal. Letters, **61**, 111 (1997).
11. S., Blagojević, N., Pejic, S., Anić, Lj., Kolar-Anić, J. Serb. Chem. Soc., **65**, 709 (2000).
12. S., Blagojević, S., Anić, Ž., Čupić, N., Pejić, Lj., Kolar-Anić, Phys. Chem. Chem. Phys., **10**(44), 6658 (2008).
13. E., Körös, Nature, **251**, 703 (1974).
14. M., Blandamer, S., Morris, J. Chem. Soc. Farad. Trans. I, **71**, 2319 (1975).
15. O., Steinbock, C., Hamik, B. Steinbock, J. Phys. Chem. A, **104**, 6411 (2000).
16. L., Györgyi, R., Field, J. Phys. Chem., **95**, 6594 (1991).
17. K., Pelle, M., Wittmann, K., Lovrics, Z., Noszticzius, M., Turco Liveri, R., Lombardo, Phys. Chem. A, **108**, 5377 (2004).
18. Z., Noszticzius, P., Stirliling, M., Wittman, J. Phys. Chem., **89**, 4914 (1985).
19. G., Schmitz, J. Chim. Phys., **84**, 957 (1987).
20. E., Kalishin, M., Goncharenko, V., Khavrus', P., Strizhak, Kinetics and Catalysis, **43**, 23 (2002).
21. P., Strizak, Детерминований хаос в хімії, Академперіодика, Кїев, 2002.
22. G., Kshirsagar, R., Field, J. Phys. Chem., **92**, 7074 (1988).
23. E., Robertson, H., Dunford, J. Am. Chem. Soc., **86**, 5080 (1964).

ЖУРНАЛ ФИЗИЧЕСКОЙ ХИМИИ, 2009, том 83, № 9, с. 1678–1686

STRUCTURE OF MATTER AND QUANTUM CHEMISTRY

УДК 541.124

RATE CONSTANTS OF ATOMIC HYDROGEN FORMATION IN $H_3O^+(H_2O)_n$ + e ⟶ H + $(H_2O)_n$ GAS-PHASE PROCESSES

© 2009 N. F. Stepanov and Yu. V. Novakovskaya

Chemistry Department, Moscow State University, 119991 Russia

E-mail: nifest@classic.chem.msu.su; jvnovakovskaya@gmail.com

Abstract – Using the Maxwellian electron velocity distribution and the Breit-Wigner approximation of the reaction cross section, the kinetic parameters of the hydrogen atom formation upon the electron capture by positively charged hydronium–water clusters are estimated. Calculations of the cross sections and rate constants are based on the data of quantum chemical studies of $H_3O^+(H_2O)_n$ and $H_3O(H_2O)_n$ clusters, particularly on the detailed analysis of the spacing of high-lying states of the radicals and the character of the unpaired electron density distribution, as well as on the general trend in the electron affinity change of the cations depending on the number of water molecules. The lifetimes of the radicals before the dissociation are taken from the classical nonempirical molecular dynamics runs. The results are compared to available experimental data.

INTRODUCTION

Hydronium ion is involved in numerous gas- and liquid-phase processes. Its neutralization plays an important role in electrochemical and bioelectrochemical reactions, as well as in the chemistry of atmosphere, where the composition of clouds depends on the kind of particles predominantly formed upon the H_3O^+ recombination with electrons.

Dissociative recombination of the particles in gas phase may follow any of the four thermodynamically possible channels leading to the appearance of stable neutral species (in parentheses, the energy liberated upon the formation of products in the ground electronic states is given):

$$H_3O^+ + e \longrightarrow H + H_2O\ (6.4\ eV), \quad (1a)$$

$$H_3O^+ + e \longrightarrow H_2 + HO\ (5.8\ eV), \quad (1b)$$

$$H_3O^+ + e \longrightarrow 2H + HO\ (1.3\ eV), \quad (1c)$$

$$H_3O^+ + e \longrightarrow H_2 + H + O\ (1.55\ eV). \quad (1d)$$

We are chiefly interested in the first channel, which seems to represent the primary reaction leading to the appearance of atomic hydrogen. Below, we validate this idea in more detail considering the states of both individual and hydrated hydronium ions, but now it is sufficient to say that the simultaneous formation of two hydrogen atoms seems to be unlikely. More probable is either the step-wise formation of two hydrogen atoms or the formation of a hydrogen molecule (when the breakage of two O–H bonds is counterbalanced by the formation of an H–H bond). Note that in experiments, when the product yield is analyzed according to the supposed set of summary reactions, the simultaneous and step-by-step formation of two hydrogen atoms cannot be distinguished.

According to the measurements at the ASTRID and CRYRING heavy-ion storage rings, the most probable are the first and third reaction channels [1–4]. If N_a, N_b, N_c, and N_d denote the probabilities of the corresponding channels, then $N_a = 0.33 \pm 0.08$ [1, 3], 0.25 ± 0.01 [4], or 0.18 ± 0.05 [2], $N_b = 0.18 \pm 0.07$ [1, 3], 0.14 ± 0.01 [4], or 0.115 ± 0.05 [2], $N_c = 0.48 \pm 0.08$ [1, 3], 0.60 ± 0.02 [4], or 0.67 ± 0.06 [2], and $N_d = 0.01 \pm \pm 0.04$ [1, 3], 0.013 ± 0.005 [4], or 0.04 ± 0.06 [2]. Thus, the fractional contribution to the hydrogen atom formation is $f(H) = N_a + 2N_c + N_d = 1.30 \pm 0.14$ [1], 1.46 ± 0.03 [4], or 1.56 ± 0.12 [2], while the fractional OH-radical contribution is $f(OH) = N_b + N_c = = 0.66 \pm 0.11$ [1], 0.74 ± 0.02 [4], or 0.78 ± 0.06 [2].

The estimates, which were obtained with the flowing afterglow technique combined with the laser induced fluorescence and vacuum ultraviolet absorption spectroscopy [5], differed, namely, $f(H) = 0.80–1.16$ and $f(OH) = 0.65$. The closeness of $f(OH)$ values found in different experiments and the noticeable discrepancy in $f(H)$ values may mean that the relative probabilities of (1b) and (1c) channels, i.e., the probability of the recombination of hydrogen atoms to molecules, may vary depending on particular experimental conditions. However, the probability of (1a) channel seems to be invariant and close to 25%.

It is dissociative recombination of individual hydronium cation and its hydration complexes that we are going to consider in detail:

$$H_3O(H_2O)_n^+ + e \longrightarrow H + (H_2O)_{n+1}. \quad (2)$$

There are essentially two model mechanisms of the hydronium–electron recombination in literature, namely the direct and indirect ones (see e.g. [6]). In the former one, an electron is captured by the ion to produce a radical in an autoionizing excited state, in which the potential energy surface has a repulsive cross section. If the relative motion momentum of the corresponding molecular fragments (or, an atom and a

molecular fragment) is sufficiently large, and they begin to move apart before the autoionization takes place, the radical dissociates and the electron remains captured by one of the fragments.

In the indirect mechanism, the electron capture by a molecular ion is assumed to result in the rotational excitation of the radical formed. As a result, a radical with the electronic configuration of a highly excited Rydberg state appears, in which the ionic core nearly coincides with the electronic configuration of the original ion. Such a radical is unstable and can decay by losing an electron. The lifetime of such radical was estimated as 10^{-11} s [7]. In order the recombination process to take place, the radical stabilization is needed, which may be provided [6] by the excitation of vibrational rather than rotational motion and the existence of additional pre-dissociation channel. The latter is possible when there is an excited state of non-Rydberg kind near the formed Rydberg state, and the potential energy surfaces of the states cross within the so-to-say Frank–Condon region of the process. In this case, the radical can pass to the non-Rydberg state and dissociate. Actually, it is this latter state that plays the main role in the direct mechanism.

Very similar expressions were derived for the rate constant of the direct process in [6] and [8]. For example, in [6], the reaction cross section was estimated as the flow ratio of the products-to-incident electrons, the electron energy was assumed not to exceed 1 eV, being sufficient for the vibrational excitation of the radical, and the lifetime of the resonance state was assumed large compared to the dissociation time. An expression given in [8] differed mainly in the probability estimate of the molecule survival (against autoionization). In both cases, the effective temperature dependence of the rate constant was of $k_r \propto T^{-0.5}$ kind.

In estimating the rate constant of indirect recombination in [6], a Breit–Wigner formula for the reaction cross section and a Maxwellian distribution for incident electrons were used, and the resulting expression provided the following temperature dependence of the rate constant: when the energy difference between a certain vibrationally excited state of the original molecular ion and the Rydberg state of the radical is much less than $k_B T$, the rate constant may decrease with an increase in the electron temperature more rapidly than $\propto T^{-0.5}$, up to $\propto T^{-1.5}$, while the dependence on the ion temperature remains of $\propto T^{-0.5}$ kind. Thus, two model mechanisms, which are based on certain assumptions about the spectrum of eigenstates of the ion and radical in the vicinity of the equilibrium geometry of the ion, predict very different temperature dependences of the electron capture rate. In order to chose among them, one needs experimental information about the process rates.

According to the direct measurements of the mass-identified ion currents and the electron-density decays in the reaction chamber in the microwave afterglow/mass-spectrometer apparatus [9], the summary process rate is very high, which may be due to a high formation probability of the excited states of Rydberg type with lifetimes up to 10^{-5} s. This hypothesis is partly supported by the fact that the effective rate constants (estimated at the same temperature) increase with an increase in the number of water molecules in $H_3O^+(H_2O)_n$ clusters:

n	0	1	2	3	4	5	6
T_{ion}, K	540	415	415	300	205	205	205
$k_r, 10^6$, cm^3/s	1.0 ± 0.2	2.2 ± 0.4	4.0 ± 0.6	4.9 ± 0.8	6.0 ± 1.2	7.5 ± 1.5	≤10

The matter is that the number of nuclear degrees of freedom and, hence, the density of vibrational and rotational states of the radicals increase with an increase in n.

The temperature dependences of rate constants differ for the individual hydronium and its aqua complexes. According to early work [10], the rate constant of hydronium recombination with electrons directly measured in $H_2 + N_2 + O_2 + C_2H_2$ flames in a plasma temperature range of 2020 to 2520 K depends on the temperature as follows:

$$k_r = (0.076 \pm 0.020) T^{-1.6 \pm 0.3}, \quad (3)$$

being ca. 3.97×10^{-7} cm^3/s at 2000 K.

The later indirect estimates [2, 11] obtained from the measured cross sections of the process at a constant ion temperature of 400 K and at the assumptions about the Maxwellian electron velocity distribution and the applicability of the collision theory differed from the above ones. By the data of [11], the character of the temperature dependence of the rate constant varies with the electron temperature as $k_r \propto T^{-0.5}$ at $20 < T_e < 300$ K, $k_r \propto T^{-1.0}$ at $300 < T_e < 3000$ K, and $k_r \propto T^{-1.2}$ at $3000 < T_e < 50000$ K. Near 2000 K, the constant was estimated as $\sim 2 \times 10^{-7}$ cm^3/s. Similar calculations based on independent measurements [2] predicted quite close trends: $k_r \propto T^{-0.83}$ below 1000 K and $k_r \propto T^{-1.1}$ in a range from 1000 to 30000 K. Recent estimations of the same kind [4] provided a $k_r \propto T^{-1.15}$ temperature dependence of the rate constant and its value of $(4.3 \pm 0.6) \times 10^{-7}$ cm^3/s at 300 K.

Assuming that processes (1a)–(1d) proceed in parallel, the author of [12] estimated the rate constants of individual channels as

$$k_r(i) = N_i k_r, \quad (4)$$

where $i = a, b, c$ refers to particular channels. Based on the averaged data of [5] and [13] and taking into ac-

count the degeneracy of channels, the values were 3.6×10^{-7}, 3.0×10^{-7}, and 3.0×10^{-7} cm^3/s respectively at 300 K.

Thus, according to the most of works, the recombination rate constant of individual hydronium with electrons changes with temperature as $k_r \propto T^{-0.5}$ (if it does) only at very low temperature, while the typical dependence looks like $k_r \propto T^{-\alpha}$, where α varies chiefly from 1.1 to 1.6. Such trend cannot be explained by the aforementioned direct mechanism, while the indirect one formally agrees with it.

At the same time, hydronium – water clusters demonstrate quite different behavior. For example, according to the radio-frequency afterglow experiments [14], the effective rate constant of $H_3O^+(H_2O)_n$ recombination with electrons decreases with temperature as $k_r \propto T^{-0.5}$, and even a general approximation of the rate constants (cm^3/s) was constructed for the clusters with $n = 0 - 5$:

$$k_r^{(n)} = (0.5 + 2n)\sqrt{\frac{300}{T}} \times 10^{-6}. \quad (5)$$

Furthermore, in the earlier works [9] and [15], in which microwave afterglow technique was also used, the recombination rate constants (cm^3/s) of $H_3O^+(H_2O)_n$ clusters ($n = 1 - 3$) were found to be almost independent of temperature:

$$k_r^{(1)} = (2.5 \pm 0.5)(300/T)^{0.08} \times 10^{-6}, \quad (6a)$$

$$k_r^{(2)} = (3.0 \pm 0.6)(300/T)^{0.08} \times 10^{-6}, \quad (6b)$$

$$k_r^{(3)} = (3.6 \pm 0.7)(300/T)^{0.00} \times 10^{-6}. \quad (6c)$$

Thus, even if the latter data are not very accurate, and the temperature dependence does exist, though was not determined (for some drawbacks or insensitivity of the experimental technique), the general scope of results [9, 14, 15] shows that it cannot be so substantial, as in the case of individual hydronium. Does it mean that on going from H_3O^+ ion to its aqua complexes, the mechanism of the process changes, e.g., from indirect to direct one? What may cause such a change?

It is worth noting here that the indirect mechanism concept is based on the idea that the potential energy surface of the state of the neutral particle formed upon the electron capture by the ion lies slightly below the potential surface of the cation. Besides that, there is a cross section (or avoided cross section) of the surfaces of this and some other repulsive electronic state. This is the necessary condition of the dissociation. In the direct mechanism, the particle is assumed to directly appear in a repulsive state with the energy higher than that of the ion at its equilibrium configuration.

In our opinion, the existence of the repulsive electronic state of a neutral system in the corresponding energy range and its direct involvement in the process are not the necessary conditions. Furthermore, the neutral particle formed upon the electron attachment to the ion should not necessarily be in a high-lying electronic state. It may appear in highly excited vibrational state in the ground or one of the low-lying electronic states. Speaking about different electronic states, we imply here that, in $\sum_k c_k(t)\Phi_k(\mathbf{r}|\mathbf{R})\chi_k(\mathbf{R})\exp(-iE_kt)$ expansions describing the actual states (where $\Phi_k(\mathbf{r}|\mathbf{R})$ and $\chi_k(\mathbf{R})$ are electronic and nuclear functions of particular adiabatic states), the $|c_k(t)|^2$ weight of a certain $\Phi_k\chi_k$ state dominates.

MODEL

According to our earlier quantum chemical calculations [16], in an energy range from the ground state of $H_3O(H_2O)_n$ radical to its adiabatic ionization potential, there is a large number of excited electronic states of the radical, and all of them are of Rydberg type, which means that the electron density distribution of the cluster in the states is close to a superposition of the nearly undistorted density distribution of $H_3O^+(H_2O)_n$ cation and the density of the highest occupied molecular orbital (HOMO) that is very diffuse in all the states and correlates in the angular dependence with the electronic states of a hydrogen atom in its respective states.

Therefore, upon the electron attachment to hydronium cation and its aqua complexes, one may expect the formation of radicals in either ground or excited states, and the hydrogen atom, which appears as a result of the subsequent dissociation, should be in the corresponding state. Then, a formal kinetic scheme of the process in gas phase may be as follows:

$$H_3O^+(H_2O)_n + e \underset{k_0}{\rightleftharpoons} H_3O(H_2O)_n(0) \xrightarrow{k_{H(0)}} H(0) + (H_2O)_{n+1}, \quad (7a)$$

$$H_3O^+(H_2O)_n + e \underset{k_1}{\rightleftharpoons} H_3O(H_2O)_n(1) \xrightarrow{k_{H(1)}} H(1) + (H_2O)_{n+1}, \ldots, \quad (7b)$$

$$H_3O^+(H_2O)_n + e \underset{k_m}{\rightleftharpoons} H_3O(H_2O)_n(m) \xrightarrow{k_{H(m)}} H(m) + (H_2O)_{n+1}, \quad (7c)$$

where numbers in parentheses after chemical formulas denote the electronic state numbers (0 means the ground state and $i = 1, \ldots, m$, the ith excited state).

Now, let us recall that, according to [16], only the ground states of $H_3O(H_2O)_n$ radicals are metastable with respect to the hydrogen atom detachment. In all the excited electronic states, the detachment requires energy supply because it is excited states of a hydrogen atom (lying above the ground state of the atom by no

less than 10.2 eV) that form. Consequently, the above scheme can be simplified:

$$H_3O^+(H_2O)_n + e \xrightleftharpoons{k_0} \xrightleftharpoons{k_0} H_3O(H_2O)_n(0) \xrightarrow{k_H} H + (H_2O)_{n+1}, \quad (8a)$$

$$H_3O^+(H_2O)_n + e \xrightleftharpoons{k_1} H_3O(H_2O)_n(1), \ldots, \quad (8b)$$

$$H_3O^+(H_2O)_n + e \xrightleftharpoons{k_m} H_3O(H_2O)_n(m). \quad (8c)$$

This scheme reflects an important feature: hydrogen atoms and water molecules may appear as a result of the hydronium ion – electron recombination only if the weight of the ground electronic state in the function describing the intermediate radical is sufficiently large.

The scheme given by Eqs. (8a) – (8c) does not comprise all possible channels. Depending on the particular vibrational excitation of the intermediate radical, several channels may be open. In the case of a hydronium radical, a water molecule can further dissociate onto H and OH particles, or hydrogen atoms can recombine to produce a molecule. Moreover, the radical can directly decompose onto H_2 and OH at the sufficiently high excitation of not only stretching, but also bending vibrations. However, provided that such stages are added to the above scheme, they do not change it principally. In this way, only the number of processes, which are parallel to the one of primary interest (process (1a)), will be increased. Hence, the rate constant of this process will become still much lower compared to the summary rate of the ion–electron recombination.

Due to the similarity of the electronic configurations of an individual hydronium radical and its aqua complexes, the supplements to the scheme should be chiefly the same for the complexes. The sole difference is that the primary product of the radical decomposition is a water cluster. A noticeable part of its excess nuclear energy will probably transform into the kinetic energy of molecular fragments moving apart. Furthermore, the summary excess energy itself will be much smaller, because the energy gap between the ground states of $H_3O^+(H_2O)_n$ cations and $H_3O(H_2O)_n$ radicals rapidly narrows with an increase in n (from 5.25 eV at $n = 0$ to 2.9 eV at $n = 6$, see below). As a result, the excess energy of the radical will be insufficient, for example, for the formation of hydrogen molecules, and the probability of the subsequent dissociation of water molecules will be much lower than in the case of individual hydronium. Hence, the fractional contribution of channels (8a) to the summary reaction rate will be larger.

RATE CONSTANT CALCULATION

The above scheme actually implies the indirect recombination mechanism when a relatively short-living radical appears in the system. To find the rate constants of hydrogen atom formation upon the electron capture by individual and hydrated hydronium cations in gas phase, we used the following basic assumptions. The rate constant is calculated as the rate of reactive binary collisions when the relative velocities of the particles are essentially the electron velocities, which obey the Maxwellian distribution. The reaction cross section is estimated in the Breit – Wigner approximation, which was proposed originally for the capture of slow neutrons by nuclei [17] and generalized later for diverse processes including the electron capture by charged and neutral particles [18, 19]. This is valid since the lifetimes of intermediate $H_3O(H_2O)_n$ radicals are very short, about several tens or hundred femtoseconds [16].

If we assume the Maxwellian electron velocity distribution, the recombination rate may be estimated as

$$k_r = \int \frac{8\pi m\epsilon}{(2\pi m k_B T)^{3/2}} \sigma(E, \epsilon) \exp(-\epsilon/k_B T) d\epsilon, \quad (9)$$

where m and ϵ are the mass and energy of the incident electrons, k_B is the Boltzmann constant, T is the absolute temperature, and $\sigma(E, \epsilon)$ is the reaction cross-section depending on the total energy of the system and the incident electron energy.

Taking into account the reversible character of the formation of the intermediate state upon the electron capture by a hydronium radical, the cross section of the process may be given by the following formula:

$$\sigma = \frac{\lambda^2}{\pi} \frac{2l+1}{2} \frac{\omega_i \omega_d}{\Delta\nu^2 + (\omega_i + \omega_d)^2}, \quad (10)$$

where ω_i and ω_d are the partial half-width parameters of the intermediate-state autoionization and dissociation respectively; λ is de Broglie wavelength of the electrons; l is the effective angular quantum number of the state formed; and $\Delta\nu$ is the probable difference between the total energy of the cation + electron system and the energy of a stationary state of the radical, or, in other words, the average spacing of the levels of the radical.

In the case of hydronium radical and its aquacomplexes, the ω_d value may be estimated as $(4\pi\tau)^{-1}$ where τ is the lifetime of the radical before dissociation, which was found in the aforementioned molecular dynamics studies. The $\Delta\nu$ value may tentatively be estimated as mean spacing of the vibrational states in a "spectrum" obtained by simply superimposing the spectra of vibrational states corresponding to adiabatic electronic states at an assumption that they are similar to that in the ground state. The values rapidly decrease from ca. 100 cm^{-1} in H_3O to 10–20 cm^{-1} in $H_3O(H_2O)_n$.

As to l values, they are actually equal to the angular momentum of the unpaired electron. Taking into account the peculiarities of the electron density distribution in the radicals, we determined the angular character of HOMO using the following procedure. At first,

the center of the HOMO density distribution was found. Then, the density was integrated within spheres of varying radius in order to estimate the sphere within which about 45% density is contained (this value corresponds to the maximum of the radial distribution function of an 1*s*-like orbital). Then, on the selected sphere, the HOMO density was approximated by a linear combination of spherical functions up to $l = 10$. The l value of the function providing the largest contribution to the expansion was assumed to characterize the angular character of the attached electron and taken in the subsequent calculations according to Eq. (10).

Finally, to estimate the ω_i value, a time-dependent perturbation theory was used. Denoting the initial state of the ion + electron system as Ψ_{in} and the resulting state of the radical as Ψ_f, in the first order of the perturbation theory, the probability of the transformation per unit time is determined by

$$\omega_i = |c|^2/\tau, \qquad (11)$$

where τ is the duration of the interaction, while c is the coefficient

$$c = -\frac{i}{\hbar}\int_0^\tau \langle \Psi_f|\hat{H}'|\Psi_{in}\rangle dt. \qquad (12)$$

Assume the initial and final states be the stationary states of the corresponding systems:

$$\Psi_{in} = |\psi_{in}\rangle \exp\left(-\frac{iE_{in}t}{\hbar}\right) \text{ and}$$
$$\Psi_f = |\psi_f\rangle \exp\left(-\frac{iE_f t}{\hbar}\right) \qquad (13)$$

whose energies negligibly differ (their difference divided by $\hbar$ is essentially the above $\Delta\nu$ value), which corresponds to the narrow-resonance situation and enables us to expand the exponent. Accordingly, the interaction time was estimated from the uncertainty relation. Finally, the $\hat{H}'$ perturbation was assumed to be the time-independent interaction between the electron and the residual molecular ion. Then, we come to

$$\omega_i = \frac{\pi}{\hbar^2 \Delta\nu}\left|\langle \psi_f|\hat{H}'|\psi_{in}\rangle\right|^2. \qquad (14)$$

Now, the problem is how to estimate the $\langle \psi_f|\hat{H}'|\psi_{in}\rangle$ integral in the latter equation. It involves two tasks, namely, the description of the interaction operator and the approximation of the initial and final state functions. To solve the former task, we turned to the earlier estimated energies of the $H_3O^+(H_2O)_n + e \longrightarrow H + (H_2O)_n$ processes and derived a general approximation that represents an electron–molecular ion interaction energy depending on the number of water molecules in the cluster.

ENERGETICS OF $H_3O^+(H_2O)_n + e \longrightarrow H_3O(H_2O)_n$ PROCESSES

Adiabatic electron affinity (A_a) of a hydronium cation, which equals the difference of the electronic energies of the original cation and the resulting radical taken at their optimum configurations, as well as the vertical affinity (A_v), which equals the energy difference between the cation and radical taken at the same minimum-energy configuration of the cation, rapidly decrease with an increase in the number of water molecules around hydronium:

n	0	1	2	3	4	5	6	19
A_v, eV	5.15	3.86	3.22	2.77	2.50	2.25	2.05	1.88; 2.07
A_a, eV	5.25	4.06	3.43	3.08	3.05	2.97	2.90	2.10

At $n = 19$ two A_v values correspond to the internal and surface location of H_3O fragment in the cation respectively. Insofar as the former cluster spontaneously dissociates upon the addition of an electron, there is no corresponding A_a value.

The adiabatic value differs from the vertical one by the relaxation energy of the nuclear subsystem of the radical. As was found in [16], configurations of the minimum-energy structures of the neutral and positively charged hydronium aqua complexes are generally very similar, and the main contribution (depending on the number of water molecules) to the A_a value comes from the interaction energy between the captured electron and the $H_3O^+(H_2O)_n$ ionic molecular core.

As was found when integrating the electron density distributions over certain spatial regions, the change in the electron density distribution upon the formation of a neutral aqua complex in place of the cation nearly coincides with the HOMO density distribution in the neutral system. In the HOMO expansion, atomic functions of several closely arranged superficial molecules (which have OH groups uninvolved in hydrogen bonds and directed into the common spatial region) dominate. The center of the aforementioned sphere, which contains about 45% of the HOMO density, was found to be equidistant from the protons of these OH groups, and the radius of the sphere changes depending on the number of water molecules in the following way:

n	0	1	2	3	4	5	6
r, Å	2.00	2.90	3.17	3.70	3.55	3.45	3.38

At $r \sim 2.0$–4.0 Å the HOMO density distribution on these spheres is nearly spherically symmetric: in its expansion, $P_0^0(\cos\theta)$ polynomial dominates. This means that the interaction energy between the electron and the residual ion should change upon appearance of each next molecular layer in reverse proportion to the summary thickness of the layers, or the diameter of

$H_3O^+(H_2O)_n$ cluster. The diameter ($2R$) may be estimated knowing the relation between the volume of the whole system ($V = \frac{4}{3}\pi R^3$) and the volumes of the particles constituting the system (we assume that the effective volumes of a water molecule and a hydronium ion are the same and equal to $v = \frac{4}{3}\pi r_w^3$): $V = (n+1)v$. Then, when the electron is localized in a certain superficial region of the cluster (within a certain region on the surface of an effective sphere of R radius embracing the cluster), we have

$$A \propto \frac{1}{R} = \frac{1}{r_w(n+1)^{1/3}}. \quad (15)$$

Besides the interaction with water molecules, the localized electronic charge interacts with H_3O^+ fragment, the effective charge of which, by different estimates (Mulliken and Löwdin population analysis), lies in a range from 0.60 to 0.87 a.u. Let us, in a first approximation, restrict the model to the Coulombic component of the interaction. It is inversely proportional to the distance between the centers of the distributed positive and negative charges. In (meta)stable radical configurations, as was already said, the negative charge is always localized on the cluster surface, while the H_3O fragment is located either in the middle part of the cluster or on its surface, but at the maximum distance from the HOMO density region. Therefore, the distance between the charges is simply a linear size of the cluster or its half. Consequently, the second component of the interaction energy between the HOMO electron and the residual molecular system is also proportional to $(n+1)^{-1/3}$.

Approximating the above adiabatic electron affinities of $H_3O^+(H_2O)_n$ clusters by $a + b(n+1)^{-1/3}$ dependence we come to equation (at a confidence level of 97%):

$$A_a = 0.27 + 4.81(n+1)^{-1/3}. \quad (16)$$

The vertical values change with an increase in n at nearly the same slope and tend to the limiting zero value. For this reason, they are not considered here.

The $b = 4.81$ eV coefficient may be treated as the potential source (of a spherical shape), with which the incident electron interacts. Hence, setting the frame origin to the center of the HOMO localization region, the probability of the electron capturing is determined by operator

$$\hat{H}' = -\frac{br_w}{|\mathbf{R}-\mathbf{r}|} = -\frac{B}{|\mathbf{R}-\mathbf{r}|} \quad (17)$$

that acts outside the sphere of R radius, where $\mathbf{r}$ is the radius-vector of electron, and $\mathbf{R}$ is the radius-vector of the spatial center of the cluster; and the effective radius of a water molecule is set to $r_w = 1.5$ Å.

INITIAL AND FINAL STATES

Operator (17) is independent of the nuclear coordinates but the potential source position, which is close to the center of mass. Moreover, equilibrium configurations of the positively charged and neutral hydronium–water clusters differ insubstantially. For this reason, we may neglect the contribution from the overlap of the nuclear functions of the initial and final systems. Then, we may treat functions ψ_f and ψ_{in} as the electronic functions of the original and final states and expand them in a finite set of $(N+1)$-electron functions (assuming that the number of electrons in the initial cation equals N), including both $\{\Phi^i_{N+1}\}$ bound states and $\{\hat{A}\Phi^j_N\phi_k^{free}\}$ unbound states, where Φ_M is the function of M-electron system ($M = N$ or $N+1$), ϕ_k^{free} is the function of a free electron (in a state with $\mathbf{k}$ wave vector), and $\hat{A}$ is the antisymmetrizer that involves only permutations of the "added" electron with all the electrons of the N-electron (cationic) system:

$$\psi_{in} = \sum_{j,k}^{L,M} C_{jk}\hat{A}\Phi^j_N\phi_k^{free}, \quad (18)$$

$$\psi_f = \sum_j^P c_j\Phi^j_{N+1}. \quad (19)$$

However, we consider only the formation of a hydronium radical in the ground electronic state upon the electron capture by a hydronium cation, which is also in its ground state. Furthermore, as was found in our quantum chemical studies of hydronium–water cations and radicals, comprising up to 19 water molecules, the electronic wavefunction of neutral clusters is well approximated by an antisymmetrized product of the wavefunction of $H_3O^+(H_2O)_n$ ion and a relatively diffuse function describing the unpaired electron. At the same time, each state of $H_3O^+(H_2O)_n$ cation is well approximated by single Slater determinant. Then, insofar as the operator defined by Eq. (17) depends on the unpaired electron coordinates, the corresponding interaction integral $\langle\psi_f|\hat{H}'|\psi_{in}\rangle$ is reduced to a one-electron integral of the following kind:

$$\frac{1}{N+1}\langle\phi_i^{bound}| - \frac{B}{|\mathbf{R}-\mathbf{r}|}|\phi_k^{free}\rangle, \quad (20)$$

where ϕ_i^{bound} is HOMO of the radical.

Now, let us recall that the HOMO electron density distribution of the radicals in their ground electronic states was found to be well approximated by an $1s$-like function:

$$\phi_i^{bound} = \left(\frac{\alpha^3}{\pi}\right)^{1/2}\exp(-\alpha r), \quad (21)$$

where α is an effective parameter estimated from the maximum of the radial distribution of the HOMO electron density.

The wavefunction of a free electron moving in a Ze/r potential field can be represented by an expansion in Legendre polynomials:

$$\phi_k^{\text{free}} = \frac{1}{kr}\sum_{l=0}^{\infty}(2l+1)i^l e^{i\sigma_l}F_l(\gamma;kr)P_l(\cos\theta). \quad (22)$$

Here,

$$\gamma = \frac{mZe^2}{\hbar^2 k}, \quad \sigma_l = \arg\Gamma(l+1+i\gamma),$$

$\Gamma(l+1+i)$ is Gamma function, and $F_l(\gamma; kr)$ is the regular Coulombic function.

In terms of the model proposed, γ may be approximated by $Bm/k\hbar^2$, where k is the length of the electron wave vector, m is the electron mass, and B is the parameter of the interaction potential (17). For example, at $B = 0.5011$ a.u. (which corresponds to the A_a approximation (16)) and an incident electron energy of 0.1 and 1 eV (i.e., at $k = 0.0862$ and 0.2725 a.u.), γ parameter equals 5.813 and 1.839, respectively.

Insofar as the hydronium–water clusters by no means resemble a spherical potential source, and, when attracted to the positively charged H_3O domain, an incident electron cannot become steadily localized, integral in Eq. (20) should be taken over a narrowed θ range with the upper boundary varied from π/2 to 3π/5 depending on the peculiarities of the nuclear configuration of the cluster.

Now, we have expressions for all the variables involved in Eq. (10) for the reaction cross section and can estimate the rate constant according to Eq. (9).

NUMERICAL RESULTS

The first point that should be discussed is the reaction cross sections and their changes with an increase in the incident electron energy and in the number of water molecules in the cluster. Among other factors, these characteristics depend on the level spacing, which reflects the effect of the nuclear states of the system, which was not taken into account up to now. Above, we assumed that the contribution from nuclear functions may be neglected, which is true only when the vibrational states of the initial and final systems are the same, e.g., ground. However, in this case, the Δν value should be quite large, because there is a large energy gap between the corresponding levels. On the other hand, very small Δν values correspond to such pairs of the initial and final nuclear states which noticeably differ and, as such, overlap insubstantially, but the number of such pairs is very large. As a result, both situations should nearly equally contribute to the summary reaction cross section.

For this reason, we compared the calculated partial cross sections of the most symmetric systems, namely, H_3O, $H_3O(H_2O)_3$, and $H_3O(H_2O)_6$, at various values of Δν parameter. Here, we took into account that the density of states rapidly increases with an increase in the number of water molecules, being the smallest in the case of an individual hydronium and the largest for its hexaaqua complex.

The Δν values considered fall in a range from 10^{-5} to 250 cm^{-1}. As an illustration, some of the partial cross sections are shown in figure. Note that the character of their dependence on the incident electron energy is not monotonic. As can be expected, it always has the same resonance-like bell shape. It is natural for the process determined by the formation of intermediate vibrationally excited states. Furthermore, the position of the bell maximum, its height and width monotonically change depending on Δν: the larger the spacing, the smaller and the wider the bell and the larger its shift to the higher E values. Then, in order to estimate the cross section at an electron temperature of 2000 K (about 0.18 eV), which is often used in experiments, we considered those partial sections, which provided the largest contribution to the summary section. These were those estimated at Δν values of 5 to 100 cm^{-1} depending on the cluster composition. Then, using the determined lifetimes of the radicals before the hydrogen atom detachment (τ = 7, 10, 15, 20, 35, 60, and 100 fs at $n = 0$–6 respectively), we came to the following estimates of the summary cross sections of the hydrogen atom formation upon the electron capture by $H_3O^+(H_2O)_n$ clusters with $n = 0$–6:

n	0	1	2	3	4	5	6
$\sigma \times 10^{15}$, cm^2	3.23	2.82	2.34	1.84	1.68	1.55	1.32

It is interesting that the values nearly monotonically decrease with an increase in n. Probably, this is determined by the balance of the following factors: (i) an increase in the state density of intermediate hydronium–water radicals, (ii) an increase in the lifetime of the radicals, (iii) the one-step dissociation of clusters at $n \le 2$ and the gradual dissociation of the larger clusters proceeding via successive migration of protons, and (iv) a nonmonotonic change in the size of the spatial region where the HOMO density of the radicals is chiefly localized. The radius of the corresponding effective sphere R_{eff} increases from 2.0 to 3.7 Å on going from individual hydronium to its triaqua complex and then decreases to 3.38 Å in the presence of six water molecules. The latter factor seems to be prevailing. Of course, the spherical approximation of the HOMO density distribution is not accurate in the case of asymmetric clusters comprising $n = 1$, 2, 4, or 5 molecules, but the general trend seems to be reproduced correctly.

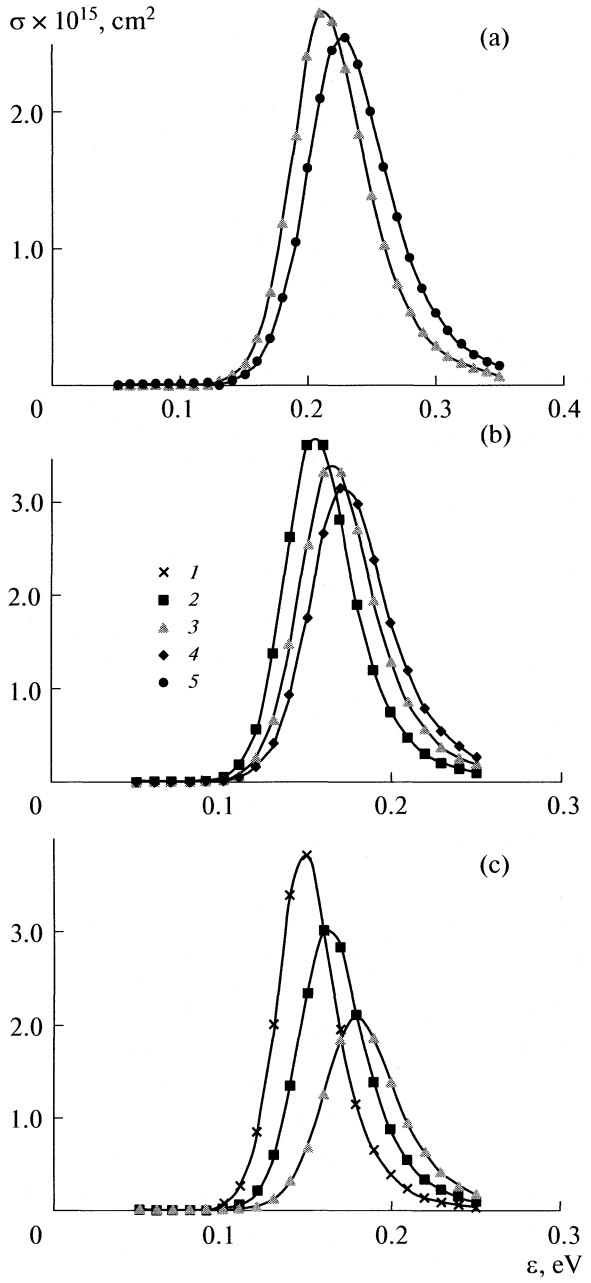

Calculated cross sections of the hydrogen atom formation upon the incident electron capture by (a) H_3O^+, (b) $H_3O^+(H_2O)_3$, and (c) $H_3O^+(H_2O)_6$ cations depending on the electron energy and the supposed state spacing of the intermediate radicals (cm^{-1}): (*1*) 10, (*2*) 25, (*3*) 50, (*4*) 75 and (*5*) 100.

Now, the final point of the work was the estimation of reaction rate constants. They were also obtained at a mean temperature of 2000 K and are as follows:

n	0	1	2	3	4	5	6
$k_r \times 10^8$, cm^3/s	7.82	7.44	7.01	6.65	6.52	6.44	6.31

They are one to two orders of magnitude lower than the values obtained from direct and indirect measurements, when the rate constant is judged from the decrease in the electron density and ion currents in the reaction chamber, and by an order of magnitude smaller than the values calculated according to Eq. (4). Of course, our estimates are by no means absolutely correct, but we can already state that the hydrogen formation rate upon the electron capture by hydrated hydronium is of the same order as in the case of individual hydronium. Moreover, the temperature dependence of the constants should also be of nearly the same character in all the systems.

Concerning the fact that the theoretical values are generally lower than the experimental estimates, we can say the following. As was mentioned above, there is a large number of excited electronic states of hydronium and hydronium–water radicals, and none of them can directly dissociate onto hydrogen atom and water cluster. This channel is energetically "closed" in those states. The HOMO density localization region in those states is larger than in the ground state, but, at least for the lower part of the state spectrum, the difference is not decisive, and the cross sections corresponding to the formation of radicals in these states should be of nearly the same order as of those in the ground state. Then, the summary electron-capture cross-section should be, at least, an order of magnitude larger than the partial cross section corresponding to the hydrogen atom formation channel.

Thus, we believe that, though the above values should further be checked in more accurate calculations, the values may already be taken as preliminary estimates of the rate constants. It is worth noting that these values change monotonically. They gradually decrease with an increase in the number of water molecules around hydronium. Judging from the structure and electron density distribution in $H_3O(H_2O)_{19}$ clusters, it may be expected that the further increase in the number of water molecules should result in a progressive decrease in the hydrogen formation cross section, which agrees with the known rate constant of the same process in liquid water (about 3.65×10^{-11} cm^3/s).

CONCLUSIONS

To estimate the rate constant of hydrogen atom formation upon the electron capture by an individual hydronium cation or a hydronium–water cluster in gas phase, we constructed a model based on five main assumptions, namely, (i) the Maxwellian electron velocity distribution; (ii) the Breit–Wigner approximation of the reaction cross section; (iii) the possibility of restricting to the first order of the time-dependent perturbation theory in estimating the autoionization half-width parameter; (iv) the validity of the interaction potential approximation by the first term in the corresponding multipolar expansion; and (v) the spherical approximation of the HOMO density distribution.

The former assumption is typically used by experimentalists in interpreting the results and is quite

founded under particular experimental conditions. The Breit–Wigner formula adequately approximates the partial reaction cross-section in situations when it is vibrational rather than rotational excitation of the intermediate radical that leads to the appearance of products. We only considered a set of possible level spacings and roughly summed up the partial sections, which were obtained at different $\Delta\nu$ values in order to take into account the actual contribution of diverse states of the systems to the summary process.

The next three assumptions (the latter two being interrelated) are less accurately founded at the moment. The validity of the first-order perturbation theory estimates may be checked by analyzing the corrections introduced in the second order. The interaction potential strongly depends on the constructed approximation of the HOMO density distribution. In the case of symmetric systems, namely, individual hydronium radical and its clusters with three or six water molecules (all with nearly C_{3v} symmetry), the spherical approximation is good. However, in asymmetric structures, involving one, two, four, or five molecules, the HOMO distribution is ellipsoidal rather than spherical, which should affect the final result, though not in a decisive manner. These aspects are the subject of further investigation. However, already now we can state that the proposed simple model provides estimates that give one a key of how the reaction cross section and rate constant change depending on the number of water molecules in the system.

ACKNOWLEDGMENTS

The work was financially supported by the Russian Foundation for Basic Research (project no. 08–03–01042).

REFERENCES

1. L. Vejby-Christensen, L. H. Andersen, Heber, et al., Astrophys. J. **483**, 531 (1997).
2. A. Neau, A. Al Khalili, S. Rosén, et al., J. Chem. Phys. **113**, 1762 (2000).
3. L.H. Andersen, O. Heber, D. Kella, et al., Phys. Rev. Lett. **77**, 4891 (1996).
4. M. J. Jensen, R. C. Bilodeau, C. P. Safvan, et al., Astrophys. J. **543**, 764 (2000).
5. N. G. Adams, C. R. Herd, M. Geoghegan, et al., J. Chem. Phys. **94**, 4852 (1991).
6. J.N. Bardsley, J. Phys. B (Proc. Roy. Soc.) Ser. 1. **1**, 365 (1968).
7. R. C. Stabler, Phys. Rev. **131**, 1578 (1963).
8. D. R. Bates, Phys. Rev. **78**, 492 (1950).
9. M. T. Leu, M. A. Biondi, R. Johnsen, Phys. Rev. A. **7**, 292 (1973).
10. R. Kelly, P. J. Padley, Trams. Far. Soc. **66**, 1127 (1970).
11. R. A. Heppner, F. L. Walls, W. T. Armstrong, G. H. Dunn, Phys. Rev. A. **13**, 1000 (1976).
12. D. R. Bates, J. Phys. B: At. Mol. Opt. Phys. **25**, 3067 (1992).
13. P. M. Mul, J. Wm. McGowan, P. Defrance, J. B. A. Mitchell, J. Phys. B: At. Mol. Phys. **16**, 3099 (1983).
14. R. Johnsen, J. Chem. Phys. **98**, 5390 (1992).
15. C.-M. Huang, M. Whitaker, M. A. Biondi, R. Johnsen, Phys. Rev. A. **18**, 64 (1978).
16. S. K. Chulkov, Yu. V. Novakovskaya, N. F. Stepanov, Russ. J. Phys. Chem. **83** (2009).
17. G. Breit, E. Wigner, Phys. Rev. **49**, 519 (1936).
18. H. A. Bethe, G. Placzek, Phys. Rev. **51**, 450 (1937).
19. P. L. Kapur, R. Peierls, Proc. Roy. Soc. London A. **166**, 277 (1938).

ЖУРНАЛ ФИЗИЧЕСКОЙ ХИМИИ, 2009, том 83, № 9, с. 1687–1690

STRUCTURE OF MATTER AND QUANTUM CHEMISTRY

УДК 539.192

OPTICAL PROPERTIES OF CdSe AND CdSe/ZnS QUANTUM DOTS DISPERSED IN SOLVENTS OF DIFFERENT POLARITY

© 2009 N. D. Abazović, J. Ž. Kuljanin-Jakovljević and M. I. Čomor

Vinča Institute of Nuclear Sciences, 11001 Belgrade, PO Box 522, Serbia

e-mail: mirjanac@vinca.rs

Abstract – Original organic capping TOPO/TOP groups of CdSe and CdSe/ZnS quantum dots (QDs), from mother solution were replaced with 2-mercaptoethanol, which was chosen as model compound, in order to achieve water solubility. Obtained water dispersions of CdSe and CdSe/ZnS QDs were characterized by UV/VIS absorption and luminescence techniques. Luminescence measurements revealed that bare cores are very sensitive to surface capping, transfer into water diminished emission intensity. Core/shell, CdSe/ZnS, QDs are much more resistant to changes of the capping and solvent, and significant part of emission intensity was preserved in water.

INTRODUCTION

One of the major goals in cell biology is realizing complex interactions between biomolecules. In these studies, organic dyes are commonly used for fluorescent labeling of biomolecules what enables following of reaction pathways and mechanism [1]. However, this approach has significant limitations, as organic fluorophores undergo fast photobleaching and have narrow excitation spectra. Furthermore, they often exhibit broad emission spectra with red tailing and therefore are limited in applications involving long-term imaging and multicolor detection.

In the past decade semiconductor quantum dots (QDs) have emerged as principal candidates in replacing organic fluorophores in biological labeling. Major advantage of QDs is possibility of tuning emission spectral range, especially position of max intensity, by changing their size, due to quantization effect – optical and electronic properties are critically influenced by carrier confinement (electron/hole). A broad absorption (excitation) spectrum permits excitation of mixed QDs populations at a single wavelength [1, 2].

Up to now, II–VI group semiconductors have exhibited the most suitable characteristics for biolabeling applications. Beside this, it has been shown that overcoating QDs with higher band gap inorganic materials improves the photoluminescence quantum yields by passivating surface nonradiative recombination sites.

The organic ligand bound to the surface of colloidal QDs plays an important role in determining their electronic and optical properties. A mixture of trioctylphosphine and trioctylphosphine oxide (TOP/TOPO) is the prototypical ligand system for most II–VI semiconductor systems, such as CdSe. These ligands provide colloidal stability in common organic solvents such as hexane and chloroform. However, main request for usage of QDs for biological labeling is to enable their solubility in water. There are three major ways to achieve this objective: a) by exchanging surface ligand with thiol-derived silane – performing surface silanization, b) by coating the surface with amphiphilic polymers or c) by exchanging the hydrophobic surfactant (TOP/TOPO) with bifunctional molecules [3, 4]. Most often, mercaptocarboxylic acids have been used for this purpose. Mercaptocarboxylic acids have mercapto (–SH) group at one side, which can be easily anchored to surface metal ion, and carboxylic (–COOH) group at the other end which enables water solubility of QDs.

Because the final size of QD and its shell is important parameter which determinates possible application, in process of transfer of QDs in aqueous media great concern should be given to both: initial size of synthesized QDs and size/length of chosen bifunctional molecule.

In this article, we report a study of the optical properties of CdSe and CdSe/ZnS QDs, that has been synthesized in noncoordinating organic solvent (TOP/TOPO) at high temperature, dispersed in nonpolar solvent and water. Water solubility have been achieved by substitution of surface attached TOPO by 2-mecraptoethanol (Scheme) which has been chosen as model compound due to its short hydrocarbon chain. We show that capping of QDs with 2-mecraptoethanol readily produces stable water dispersions.

EXPERIMENTAL

All reagents were commercial products of highest purity available (p.a.).

Synthesis of CdSe QDs. Highly crystalline CdSe QDs were synthesized by method previously described by Peng and Peng 5]. Briefly, CdO, TOPO and HPA were loaded in 25 ml flask. The mixture was heated to

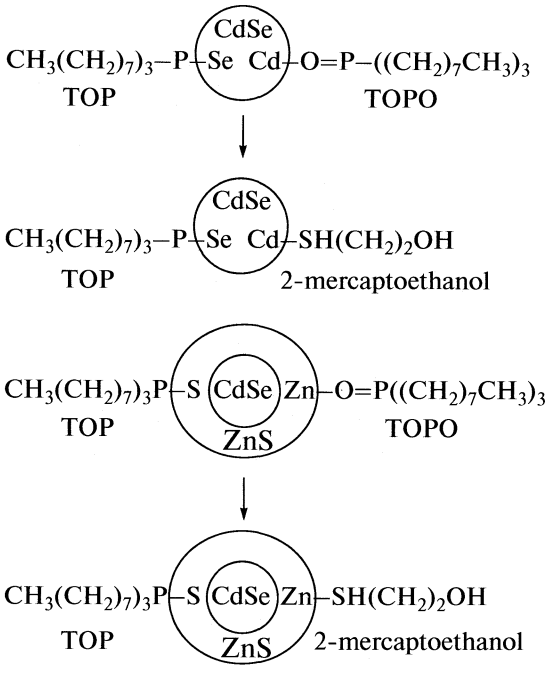

Scheme. Exchange of hydrophobic surfactant on surface of CdSe and CdSe/ZnS QDs.

300–320°C under Ar flow. Selenium stock solution was injected in the mixture at 270°C and left nanocrystals to grow for 4 minutes.

Synthesis of CdSe/ZnS core/shell QDs. Roughly, 0.1 μmol of CdSe QDs dispersed in hexane was transferred into reaction flask with dry TOPO and solvent was pumped out. Then, temperature of the solution was raised to 160°C, and precursors of Zn and S dissolved in TOP were added dropwise over a period of 5 minutes. Concentrations of the precursors were adjusted to be enough for 3 monolayers of ZnS in the schell. The overcoated particles were stored in their mother solution during the night to ensure that the surface of the dots remained passivated with TOPO [6].

Extraction of QDs in water. Equal volumes of CdSe or CdSe/ZnS QDS dispersed in hexane and 0.01 M aqueous solution of 2-mercaptoethanol (pH 8–9) were mixed. Two separated layers were formed, hexane (colored) layer was on the top. After slight shaking, QDs were transferred in aqueous (bottom) layer, and it was used as is for optical measurements.

Optical characterization. Measurements of the absorption spectra were carried out on an Evolution 600 UV–Vis spectrophotometer (Thermo Scientific). The photoluminescence spectra were recorded on Perkin-Elmer LS–45 spectrofluorimeter. Quantum yields of emission were calculated using Tris[2,2'-bipyridyl] Ruthenium(II)chloride as standard.

RESULTS AND DISCUSSION

The absorption spectra of CdSe and CdSe/ZnS QDs are presented in Fig. 1A and B. The positions of the absorption threshold give us band gap energy of CdSe colloidal particles; CdSe bare cores have $E_g \sim$ 2.2 eV and CdSe/ZnS core/shell particles have $E_g \sim$ 2.1 eV (bulk $E_g = 1.79$ eV). Also, overcoating of CdSe QDs with shell of ZnS led to changes in shape and position of peak in absorption spectrum (Figure, a). First exciton absorption peak moved from 543 to 553 nm and its FWHM increased. We used empirical formula proposed by Yu et al. [7], that describes connection between diameter of the CdSe particles and wavelength of the their first absorption peak to calculate diameter of the bare and capped CdSe:

$$D = (1.6122 \times 10^{-9})\lambda^4 - (2.6575 \times 10^{-6})\lambda^3 + \\ + (1.6242 \times 10^{-3})\lambda^2 - (0.4277)\lambda + 41.57. \quad (1)$$

Here D (nm) is the size of the CdSe cores and λ (nm) is the wavelength of the first absorption peak of the corresponding sample. Calculated diameters of bare and capped CdSe QDs were about 2.9 and 3.1 nm, respectively. Since ZnS is transparent in visible part of the spectrum, change of diameter indicated that CdSe QDs sizes seem to be increased and their size distribution is wider in comparison to bare CdSe QDs. Applied temperature for overcoating of CdSe cores with ZnS is too low for Oswald ripening of CdSe QDs. Observed change of diameter can be explained by partial leakage of the excitons from CdSe into the ZnS matrix. This effect is more pronounced in smaller CdSe QDs where the leakage of the exciton into the ZnS shell has a more dramatic effect on the confinement energies of the charge carriers [6]. The difference between diameters of CdSe in bare and core/shell nanoparticles is about 2 Å, that correspond to homogenous shell of 1 Å through which exciton freely leak, just 30% of ZnS monolayer (the definition of a monolayer is a shell of ZnS that measures 3.1 Å along the major axis of the dots). Exchange of capping agent of bare CdSe QDs and their extraction in water didn't affect shape of absorption spectrum (Figure, a and b). Absorption spectrum of CdSe/ZnS QDs lost its original shape and dispersion became turbid (Figure, a and b), but colloidal solution retain stability.

Changes in emission spectra (Figure, c and d) are more prominent. Emission intensity of core/shell QDs increased 10 times ($QY = 4.2\%$) compared to bare CdSe and emission peak moved from 564 to 582 nm. Exchange of capping agent and extraction in water didn't affect shape of emission spectrum just its intensity. Unfortunately, extraction of bare CdSe QDs in water led to disappearance of characteristic emission peak, Figure c (in chloroform $QY \approx 0.42\%$). CdSe/ZnS QDs extracted in water retain a measurable part of their original emission ($QY = 2.55\%$). Reduc-

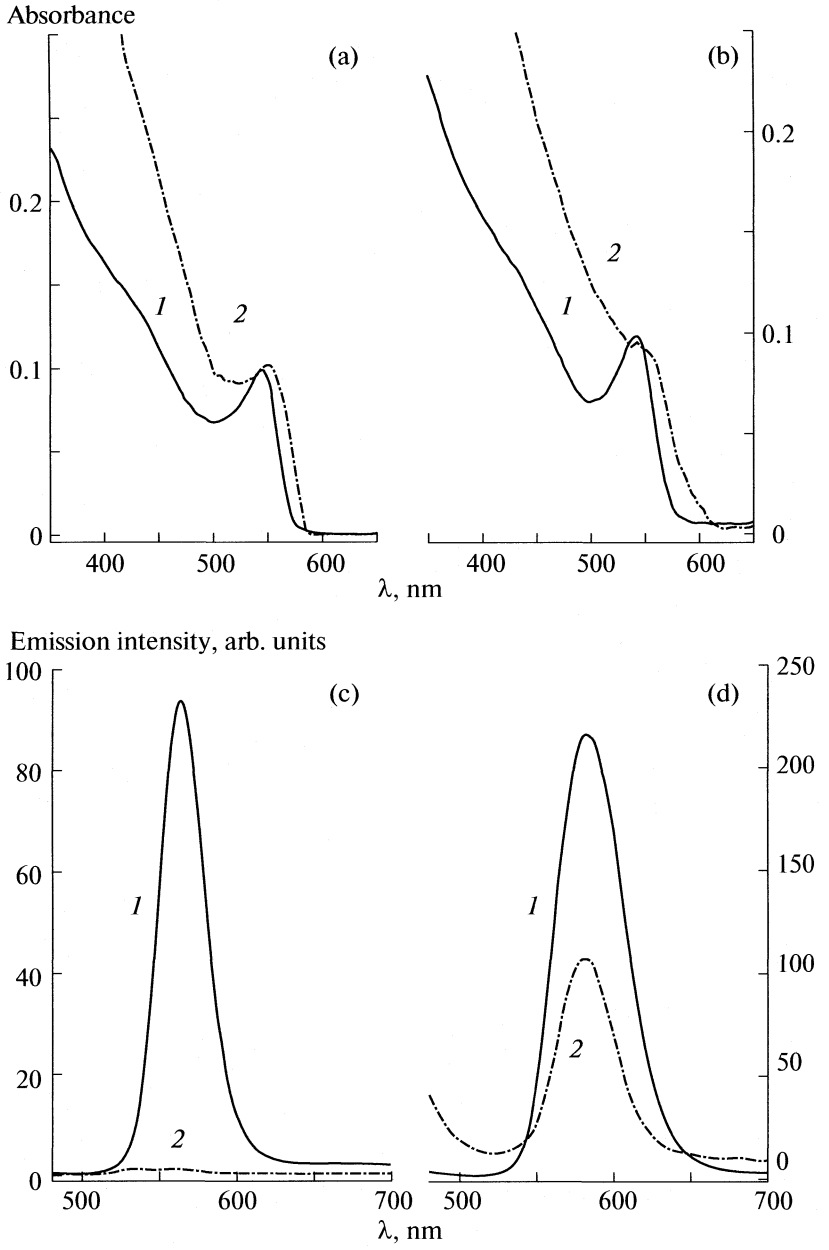

Absorption spectrum of (*1*) CdSe and (*2*) CdSe/ZnS QDs dispersed in (a) chloroform and (b) water; emission spectrum (λ_{exp} = = 450 nm) of (c) CdSe and (d) CdSe/ZnS QDs dispersed in (*1*) chloroform and (*2*) water.

tion of emission *QY* of CdSe and CdSe/ZnS QDs upon capping their surface with 2-mercaptoethanol could be explained through mechanism of formation of disulfide bonds. As Kloepfer et al. [8] have proposed in their study of MAA capped CdSe QDs, surface bonded mercapto-compound can scavenge photocreated hole, which subsequently leads to cleavage of Cd – S bond and formation of mercapto-ion. So-formed ion reacts with neighboring mercapto-molecule and between them disulfide bond is formed. Through this process, surface of CdSe QDs stays exposed to water molecules. As a result of this process emission of CdSe is highly reduced or completely quenched, as it was the case with CdSe QDs capped with 2-mercaptoethanol. The same mechanism stays for CdSe/ZnS QDs, except that emission was basically preserved since the electron transfer process was hindered due to the presence of ZnS shell. Obviously the ZnS shell is inhomogeneous and there were uncovered parts on the surface of CdSe trough which mercapto-compound can scavenge photocreated holes.

Once the QDs are dispersed in the water they can be used to detect different analytes as sensors, as a passive fluorescent labels (through conjugation with se-

lective receptor molecules, antibodies) and design of simple multiplexed immunoassays, for FRET (fluorescence resonance energy transfer) and for labeling biological cells. Obtained results showed that 2-mercaptoethanol is suitable for transfer of core/shell QDs in water. Its functional groups allow excellent capping of the QD surface (SH group and ZnS) from one side, and polarity (OH) of its other side gives good water solubility.

CONCLUSION

The proposed synthetic method resulted in formation of CdSe QDs cores with diameters in the range from 3–4 nm. Addition of shell of ZnS over CdSe core affected optical properties of CdSe cores. CdSe/ZnS QDs have 10 times increased QY of emission in comparison to bare CdSe QDs. Extraction of QDs in water by exchange of capping TOP/TOPO ligand by 2-mercaptoethanol molecules, led to decrease of QY of emission of both bare CdSe and CdSe/ZnS QDs. Core/shell QDs dispersed in water sustained QY of emission large enough to be used for different bio-applications.

ACKNOWLEDGMENTS

This work was supported by the FP6 - NANOMYC (LSHB-CT-2007, contract number 036812) and by Ministry of Science and Technological Development of the Republic of Serbia (Project number 142066).

REFERENCES

1. I. L. Medintz, H. Tetsuo Uyeda, E. R. Goldman and H. Mattoussi, Nature Materials **4**, 435 (2005).
2. H. Mattoussi, J. M. Mauro, E. R. Goldman, G. P. Anderson, V. C. Sundar, F. V. Mikulec and M. G. Bawendi, J. Am. Chem. Soc. **122**, 12142 (2000).
3. R. E. Bailey, A. M. Smith and S. Nie, Physica E **25**, 1 (2004).
4. A.P. Alivisatos, W. Gu and C. Larabell, Annu. Rev. Biomed. Eng. **7**, 55 (2005).
5. Z.A. Peng and X. Peng, J. Am. Chem. Soc. **123**, 183 (2001).
6. B. O. Dabbousi, J. Rodriguez – Viejo, F. V. Mikulec, J. R. Heine, H. Mattoussi, R. Ober, K. F. Jensen and M. G. Bawendi, J. Phys. Chem. B **101**, 9463 (1997).
7. W. W. Yu, L. Qu, W. Guo and X. Peng, Chem. Mater. **15**, 2854 (2003).
8. J. A. Kloepfer, S. E. Bradforth and J. L. Nadeau, J. Phys. Chem. B **109**, 9996 (2005).

ЖУРНАЛ ФИЗИЧЕСКОЙ ХИМИИ, 2009, том 83, № 9, с. 1691–1695

STRUCTURE OF MATTER AND QUANTUM CHEMISTRY

УДК 541.65

ISOTOPE EFFECTS ON BAND INTENSITIES IN THE $B^2\Sigma^+$–$X^2\Sigma^+$ SYSTEM OF GaO ISOTOPOMERS

© 2009 M. Kuzmanović*, V. Bojović*, J. Savović** and A. Antić-Jovanović*

*Faculty of Physical Chemistry, University of Belgrade, P.O.box 47, 11158 Belgrade 118, Serbia

**The Vinča Institute, Laboratory of Physical Chemistry, P. O. Box 522, 11001, Belgrade, Serbia

E-mail: ankica@ffh.bg.ac.yu

Abstract – Relative intensities of eight vibronic bands, belonging to the $\Delta\upsilon = -2$ sequence of the $B^2\Sigma^+ - X^2\Sigma^+$ electronic transition of four GaO isotopomers have been measured and interpreted in terms of possible isotope effects on the parameters governing the band intensity. Obtained results showed very small isotope effect on the Franck–Condon factors and r-centroids and revealed that the observed intensity ratios of the corresponding isotope bands are controlled mainly by the isotope abundance of ^{69}Ga and ^{71}Ga in natural gallium.

INTRODUCTION

Bands of the $B^2\Sigma^+$–$X^2\Sigma^+$ electronic transition lie in the region of 300 – 420 nm, and they are the only GaO bands that have been observed and analyzed so far in a number of reports. A good overview of the essential papers up to 1978 on GaO can be found in the compilation of Huber and Herzberg [1]. After this publication, Yadav et al. [2] reinvestigated B–X system including bands of five sequences, $\Delta\upsilon = 0, \pm1$ and ±2. Their analysis confirmed the vibrational assignments given by previous authors and explained the formation of head of heads in the $\Delta\upsilon = +1$ and + 2 sequences. In 1994–1995, investigating the isotope displacements of the B–X bands using enriched oxygen-18, Bojovic et al. [3] and A. Antić–Jovanović et al. [4] have recorded relatively weak bands of the $\Delta\upsilon = +3, +4$ and +5 sequences of four GaO isotopomers, $^{69}Ga^{16}O$, $^{71}Ga^{16}O$, $^{69}Ga^{18}O$ and $^{71}Ga^{18}O$. In all performed experiments, the bands have been studied via conventional emission spectroscopic technique using high temperature sources (mainly arc discharge), which allowed vibrational analysis of the bands and determination of vibrational constants for both the X and the B states of all recorded isotopic molecules. The rotational analysis of the bands [2, 5–7] has proven to be rather difficult due to severe overlapping of bands and the presence of double heads attributed to isotopic molecules, ^{69}GaO and ^{71}GaO. Difficulties could be overcome using high resolved spectrum, which is not yet obtained. The only available information concerning the intensity of the B–X bands so far is that obtained by visual estimation of the band head intensities on a scale of 10 [2, 5, 8].

This work deals with the first intensity measurement of the B–X bands and the first study of isotope effects on band intensity. The paper contains the results of analysis of relative band-head intensity ratios of the B–X isotopic bands of two pairs of GaO isotopomners, $I(^{69}Ga^{16}O)/I(^{71}Ga^{16}O)$ and $I(^{69}Ga^{18}O)/I(^{71}Ga^{18}O)$ using both the experimental and theoretical data. In our work we have restricted attention on the bands of $\Delta\upsilon = -2$ sequence (407–413 nm) due to well resolved isotopic heads (for about 3–4 cm^{-1}) and the absence of mutual overlapping of the sequence bands in consequence of formation of head of heads that appears in $\Delta\upsilon = +2$ sequence. It is our hope that obtained results can be useful aid for both experimentalists and theoreticals in future research of GaO electronic spectrum because of its importance for technological reasons as well as for fundamental science [9–11].

EXPERIMENTAL

Intensity measurements were performed on the bands produced in discharge of low-pressure arc in the atmosphere of both the oxygen-16 and oxygen-18 (enriched to 90%). Details of experimental apparatus and working conditions are described in earlier papers [3, 4].

Since the natural gallium is a mixture of two isotopes, ^{69}Ga and ^{71}Ga, with a relative abundance of 60.1 and 39.9% respectively [12], in both cases the bands of two corresponding isotopomers, $^{69}Ga^{16}O$ and $^{71}Ga^{16}O$, as well as $^{69}Ga^{18}O$ and $^{71}Ga^{18}O$, were recorded. From a densitometer tracing of the recorded spectrum the peak height at the position of R-heads (R_1 and R_2 heads , appearing in the structure of the $^2\Sigma$–$^2\Sigma$ transition, are not resolved under dispersion used) above the corresponding background for each isotope species was measured and taken as the observed intensity. This "raw" intensity was not corrected for the non-uniformity in the spectral response since measured bands lie in narrow region of about 6 nm. Uncertainty of the measurements was determined to be not more than 10%.

Table 1. Molecular constants for the X and B states of GaO isotopomers used as input in Morse computation

Molecule	μ, amu	State	ω_e, cm^{-1}	$\omega_e x_e$, cm^{-1}	μ, amu	Ref.
$^{69}Ga^{16}O$	12.98225	$X^2\Sigma^+$	766.84	6.21	12.98225	[2]
		$B^2\Sigma^+$	761.54	3.13	»	»
$^{71}Ga^{16}O$	13.05154	$X^2\Sigma^+$	764.82	6.18	13.05154	»
		$B^2\Sigma^+$	759.48	3.11	»	»
$^{69}Ga^{18}O$	14.27215	$X^2\Sigma^+$	731.37	5.65	14.27215	[4]
		$B^2\Sigma^+$	726.31	2.85	»	»
$^{71}Ga^{18}O$	14.35593	$X^2\Sigma^+$	729.25	5.62	14.35593	*
		$B^2\Sigma^+$	724.15	2.83	»	»

* Calculated in this work.

APPROACH

The governing expression for the analysis of the measured intensities of the vibrational bands in emission electronic spectra is [13]:

$$I_{\upsilon'\upsilon''} = DN_{\upsilon'}\nu^4_{\upsilon'\upsilon''}q_{\upsilon'\upsilon''}R^2_e(r), \quad (1)$$

where D is a constant, $I_{\upsilon'\upsilon''}$ is the measured signal produced by the $\upsilon' \longrightarrow \upsilon''$ transition, $N_{\upsilon'}$ is the relative number density in the upper vibrational level υ', $\nu_{\upsilon'\upsilon''}$ is the transition wavenumber, approximated often by the band head position, $q_{\upsilon'\upsilon''}$ is the square of the vibrational overlap integral, $[\langle\psi_{\upsilon'}|\psi_{\upsilon''}\rangle]^2$, named Franck–Condon factor (FCF), and $R_e(r)$ is the electronic transition moment function (ETMF)

Therefore, the isotope effects on band intensities may be due: (i) to differences in relative population of the υ' level; (ii) to the obvious effect of the change in frequency, which is usually very small; (iii) to the effect on $q_{\upsilon'\upsilon''}$, and (iv) to isotope effect on the electronic transition moment (ETM). The last parameter is the most difficult to predict. Any isotope effect on the ETM must be reflected either by an isotope effect on the r-centroid, $r_{\upsilon'\upsilon''}$ (average internuclear separation for a given transition), or on the parameters A, B, C ...in expression:

$$R_e(r) = A + Br + Cr^2 + ..., \quad (2)$$

which describes, in r-centroid approximation [14, 15], the dependence of ETM on internuclear distance.

In order to see to what extent isotopic substitution affects the parameters governing the band intensity in the case of B–X bands, we computed FCFs and r-centroids for the bands of all isotopic molecules involving υ' and υ'' levels up to 10. Since only bands with $\upsilon' \leq 7$ and $\upsilon'' \leq 9$ were recorded, the Morse potential functions and Morse wavefunctions $\psi_{\upsilon'}$ and $\psi_{\upsilon''}$ were taken in computation as fairly satisfactory approximation to realistic wavefunctions. The computation was performed by using modified Felenbok's FCF computer program [16]. The limits of integration were from 1.5 to 2.2 Å with intervals of 0.003 Å. The spectroscopic constants needed for calculation were taken from Ref. [2] for GaO with oxygen-16, and from Refs. [4] and [7] for those with oxygen-18. Vibrational constants for $^{71}Ga^{18}O$, given in Ref. [4], were slightly modified in this work after re-calculation using three bands more. They are collected in Table 1. Reduced masses of four isotopic gallium oxides were calculated from atomic masses of the ^{69}Ga and ^{71}Ga atoms and atomic masses of the ^{16}O and ^{18}O atoms. Equilibrium distances r'_e = = 1.725 Å and r''_e = 1.778 Å were used from Refs. [2] and [7] for both isotopic pairs of molecules.

RESULTS AND DISCUSSION

We recorded eight bands of the $\Delta\upsilon = -2$ sequence in the spectrum of each isotopomers, of which the bands (5,7), (6,8) and (7,9) were detected for the first time. Figure 1 represents the microphotometer tracing of the $^{69}Ga^{18}O$ and $^{71}Ga^{18}O$ bands. They are shifted to lower wavelength side for about 60–40 cm^{-1} (moving from 0,2 to 7,9 band) in comparison with the corresponding bands of $^{69}Ga^{16}O$ and $^{71}Ga^{16}O$ isotopomers , but their features are the same.

The higher members of the sequence lie towards the lower wavelength side of the first band (0, 2), while all bands are red degraded. Because of this and the rapidly decrease of band intensity from the head to tail, the heads of each band are free from overlapping with the neighbouring higher member of sequence. Isotope heads are clearly distinct and separated by about 3–4 cm^{-1} allowing measurement of the head heights with relatively high certainty.

Observed relative band-head intensity ratios of corresponding isotopic bands are listed in Table 2 and 3 (fourth column). Results are analyzed using FCFs and r-centroids evaluated for all isotopic bands arising in transitions between υ' and υ'' levels up to 10. Obtained values in the form of υ',υ'' scheme are given in Table 4. FCFs, which are lower then 10^{-3}, are not included in this scheme.

Due to somewhat different molecular constants, used in present computation, obtained FCFs for

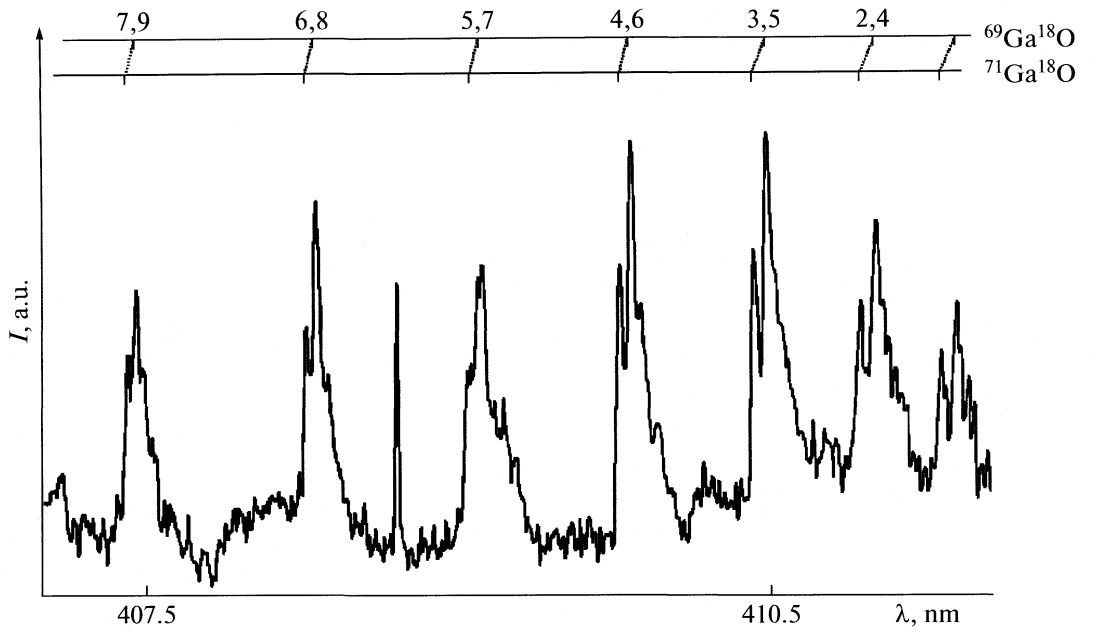

The $^{69}Ga^{18}O$ and $^{71}Ga^{18}O$ B–X bands of the $\Delta\upsilon = -2$ sequence.

Table 2. Wavenumbers in cm^{-1}, observed relative bandhead intensity ratios, isotope ratios of the FCFs (q) and r-centroids (r) in Å for the $\Delta\upsilon = -2$ sequence bands of $^{69}Ga^{16}O$ and $^{71}Ga^{16}O$

υ', υ"	$\nu_{\upsilon'\upsilon"}(1)$	$\nu_{\upsilon'\upsilon"}(2)$	$I(1)/I(2)$	$q(1)/q(2)$	$r(1)$	$r(2)$
0.2	24208.2	24212.1	1.49	0.993	1.9270	1.9264
1.3	235.8	239.7	1.49	0.993	1.9387	1.9380
2.4	263.3	267.1	1.50	0.994	1.9513	1.9510
3.5	298.4	302.1	1.52	0.994	1.9651	1.9643
4.6	339.1	342.7	1.51	0.993	1.9802	1.9793
5.7	384.0	387.2	1.50	0.993	1.9969	1.9959
6.8	437.1	339.7	1.50	0.992	2.0158	2.0146
7.9	492.0	494.5	1.48	0.992	2.0378	2.0364

Notes. Numbers in parentheses 1 and 2 denote $^{69}Ga^{16}O$ and $^{71}Ga^{16}O$, respectively. Wavenumbers for first four bands were used from [2]. Bands (5,7), (6,8) and (7,9) were recorded and measured in this work.

Table 3. Wavenumbers in cm^{-1}, observed relative band-head intensity ratios, isotope ratios of the FCFs (q) and r-centroids (r) in Å for the $\Delta\upsilon = -2$ sequence bands of $^{69}Ga^{18}O$ and $^{71}Ga^{18}O$

υ', υ"	$\nu_{\upsilon'\upsilon"}(3)$	$\nu_{\upsilon'\upsilon"}(4)$	$I(3)/I(4)$	$q(3)/q(4)$	$r(3)$	$r(4)$
0.2	24274.5	24278.4	1.48	0.993	1.9155	1.9149
1.3	297.6	300.8	1.49	0.994	1.9257	1.9250
2.4	325.5	328.9	1.50	0.994	1.9366	1.9359
3.5	355.9	359.6	1.52	0.994	1.9484	1.9476
4.6	392.3	395.5	1.51	0.994	1.9611	1.9603
5.7	432.1	435.0	1.50	0.993	1.9748	1.9739
6.8	479.0	481.5	1.50	0.993	1.9899	1.9889
7.9	528.0	530.0	1.48	0.992	2.0066	2.0054

Notes. Numbers in parentheses 3 and 4 denote $^{69}Ga^{18}O$ and $^{71}Ga^{18}O$, respectively. Wavenumbers for first four bands were used from [4]. Bands (5,7), (6,8) and (7,9) were recorded and measured in this work.

Table 4. FCFs for the $B-X$ bands of GaO isotopomers

υ'\υ"	0	1	2	3	4	5	6	7	8	9	10
0	6.805-1	2.874-1	3.160-2								
	6.798-1	2.879-1	3.181-2								
	6.666-1	2.965-1	3.607-2								
	6.658-1	2.971-1	3.632-2								
1	2.387-1	2.802-1	4.088-1	7.117-2							
	2.391-1	2.790-1	4.091-1	7.164-2	1.010-3						
	2.468-1	2.566-1	4.133-1	8.142-2	1.805-3						
	2.472-1	2.553-1	4.136-1	8.195-2	1.848-3						
2	6.314-2	2.679-1	1.049-1	4.540-1	1.085-1	1.137-3					
	6.335-2	2.681-1	1.039-1	4.538-1	1.092-1	1.181-3					
	6.726-2	2.715-1	8.464-2	4.489-1	1.247-1	2.543-3					
	6.751-2	2.716-1	8.366-2	4.487-1	1.255-1	2.617-3					
3	1.418-2	1.165-1	2.269-1	3.364-2	4.676-1	1.392-1		1.153-3			
	1.424-2	1.168-1	2.270-1	3.300-2	4.670-1	1.401-1		1.154-3			
	1.545-2	1.230-1	2.242-1	2.051-2	4.518-1	1.614-1	2.537-3	1.007-3			
	1.553-2	1.234-1	2.239-1	1.997-2	4.511-1	1.624-1	2.630-3	1.004-3			
4	2.869-3	3.605-2	1.456-1	1.718-1	8.197-3	4.716-1	1.614-1		2.223-3		
	2.883-3	3.619-2	1.459-1	1.715-1	7.862-3	4.707-1	1.625-1		2.228-3		
	3.183-3	3.916-2	1.520-1	1.644-1	1.999-3	4.454-1	1.900-1	1.742-3	2.092-3		
	3.202-3	3.934-2	1.523-1	1.640-1	1.823-3	4.442-1	1.912-1	1.835-3	2.092-3		
5		9.245-3	5.805-2	1.542-1	1.226-1		4.762-1	1.742-1		3.634-3	
		9.287-3	5.825-2	1.545-1	1.222-1		4.750-1	1.755-1		3.653-3	
		1.026-2	6.279-2	1.589-1	1.128-1		4.405-1	2.096-1		3.704-3	
		1.031-2	6.303-2	1.591-1	1.122-1		4.389-1	2.110-1		3.713-3	
6		2.080-3	1.806-2	7.580-2	1.499-1	8.432-2		4.859-1	1.766-1	1.830-3	5.139-3
		2.090-3	1.814-2	7.604-2	1.501-1	8.392-2		4.844-1	1.781-1	1.727-3	5.174-3
		2.348-3	2.003-2	8.161-2	1.521-1	7.379-2	2.843-3	4.417-1	2.196-1		5.736-3
		2.362-3	2.014-2	8.189-2	1.522-1	7.326-2	3.069-3	4.399-1	2.212-1		5.767-3
7			4.754-3	2.776-2	8.789-2	1.391-1	5.630-2		5.018-1	1.681-1	6.887-3
			4.775-3	2.787-2	8.814-2	1.392-1	5.594-2		5.002-1	1.698-1	6.876-3
			5.378-3	3.077-2	9.412-2	1.386-1	4.637-2	4.668-3	4.507-1	2.193-1	1.412-3
			5.409-3	3.092-2	9.440-2	1.385-1	4.591-2	4.961-3	4.487-1	2.211-1	1.400-3
8			1.101-3	8.351-3	3.700-2	9.458-2	1.262-1	3.643-2		5.230-1	1.486-1
			1.106-3	8.387-3	3.714-2	9.483-2	1.261-1	3.613-2		5.214-1	1.504-1
			1.268-3	9.468-3	4.098-2	1.007-1	1.231-1	2.786-2	4.504-3	4.673-1	2.079-1
			1.275-3	9.520-3	4.116-2	1.010-1	1.230-1	2.748-2	4.697-3	4.651-1	2.099-1
9				2.170-3	1.249-2	4.493-2	9.689-2	1.136-1	2.252-2		5.470-1
				2.179-3	1.254-2	4.508-2	9.712-2	1.135-1	2.229-2		5.454-1
				2.508-3	1.419-2	4.970-2	1.026-1	1.083-1	1.570-2	2.774-3	4.900-1
				2.522-3	1.426-2	4.991-2	1.028-1	1.081-1	1.542-2	3.010-3	4.877-1
10					3.585-3	1.674-2	5.113-2	9.596-2	1.029-1	1.284-2	2.575-3
					3.599-3	1.692-2	5.120-2	9.606-2	1.037-1	1.290-2	2.593-3
					4.162-3	1.908-2	5.651-2	1.010-1	9.554-2	7.915-3	
					4.184-3	1.916-2	5.671-2	1.023-1	9.571-2	7.922-3	

Notes. Rows 1–4 for each transition represent the FCFs for $^{69}Ga^{16}O$, $^{71}Ga^{16}O$, $^{69}Ga^{18}O$ and $^{71}Ga^{18}O$, respectively. The negative entry in each listing indicates the decimal exponent.

$^{69}Ga^{16}O$ bands differ slightly from those reported earlier [4]. FCFs for the bands of other three isotopomers are given in this work for the first time.

The values of FCFs (Table 4) predict an increasing of band intensity in $\Delta\upsilon = -2$ sequence up to 6,8 band and gradually decreasing after this band. This pattern of FCFs is in good agreement with band intensity distribution in experimental spectrum, providing good test for reality of computed FCFs.

The isotope ratios of FCFs B–X bands of $\Delta\upsilon = -2$ sequence together with r-centroids for recorded transitions are given in Tables 2 and 3 (fifth, sixth and seventh columns).

Data listed in Tables 2 and 3 (as well as in Table 4) clearly show very small isotope effect on FCFs of corresponding isotope bands and almost the same (very close to unity) ratio $q(^{69}Ga^{16}O)/q(^{71}Ga^{16}O)$, and $q(^{69}Ga^{18}O)/q(^{71}Ga^{18}O)$ for all bands. Isotope effect on r-centroids is negligible. Due to this fact, and due to impossibility to determine any possible isotope effect on the parameters A, B,... in Eq. (2) from the intensity measurements, the assumption of equal transition probabilities was thus reasonable for the analysis of intensity data listed in forth column of Table 2 and 3. As seen, observed band-head intensity ratios for all isotopic bands are almost the same and amount approximately 1.5.

Returning to Eq. (1), it was possible to discuss observed intensity ratios by using the evaluated FCFs and quoted transition wavenumbers in Table 2 and 3. In spite of noticeable isotope effect on bandhead positions, the ratio of fourth power of wavenumbers of isotopic bands, resulting in the same $\upsilon' \longrightarrow \upsilon''$ transition, was found to be 0.9994 for all measured bands. Both, these data, and the fact that natural $^{69}Ga/^{71}Ga$ ratio is 1.507 [12], indicated that the observed intensity ratios of isotopic bands are governed mainly by the number density of isotopic species in υ' levels. Agreement between observed and predicted ratios is within experimental error.

CONCLUSION

Experimental and theoretical studies of isotope effects on band intensity of GaO B–X bands of $\Delta\upsilon = -2$ sequence have been performed. Results showed very small isotope effect on FCFs and r-centroids and indicated that observed bandhead intensity ratios can be related to isotope abundance of ^{69}Ga and ^{71}Ga in natural gallium.

ACKNOWLEDGMENTS

This work was supported by the Ministry of Science of the Republic of Serbia, Project No. 142065.

REFERENCES

1. K. P. Huber and G. Herzberg, "*Constants of diatomic molecules*", Van Nostrand, New York (1979).
2. B.R. Yadav, S.B. Rai and D.K. Rai., Canad. J. Phys. **57**, 496 (1979).
3. V. Bojović, D. S. Pesić and A. Antić-Jovanović, J. Serb. Chem. Soc. **58**, 109 (1993).
4. A. Antić-Jovanovć, V. Bojović and D. S. Pesić, Spectrosc. Lett. **27**, 247 (1994).
5. V. Raziunas, S. Katz and G. J. Macur, J. Chem. Phys. **39**, 1161 (1963).
6. V. Raziunas, G. J. Macur and S. Katz, J. Chem. Phys. **42**, 2634 (1965).
7. M. Pophristić, D. S. Pesić, A. Antić-Jovanović and V. Bojović, Spectrosc. Lett. **29**, 61 (1996).
8. K. L. Guernsey, Phys. Rev. **46**, 114 (1934).
9. L. B. Knight Jr., T. J. Kirk, J. Herlong, J. G. Kaup and E. R. Davidson, J. Chem. Phys. **107**, 7011 (1997).
10. S. Sharma and M. K. Sunkara, J. Am. Chem. Soc. **124**, 12288 (2002).
11. R.Z. Ma and Y. Bando, Chem. Phys. Lett. **367**, 219 (2003).
12. M. Vaygues Pelaes, J. M. Costa Fernandez and A.Sauz-Medel, AAS, **17**, 950 (2002).
13. G. Herzberg, "*Spectra of Diatomic Molecules*", 2nd ed. Van Nostrand, Princeton (1951).
14. P. A. Fraser, Can. J. Phys. **32**, 515 (1954).
15. R.W. Nicholls and W.R. Jarmain, Proc. Phys. Soc. **69**, 253 (1956).
16. P. Felenbok, C.R. Acad. Sc. **256**, 2334 (1963).

ЖУРНАЛ ФИЗИЧЕСКОЙ ХИМИИ, 2009, том 83, № 9, с. 1696–1701

STRUCTURE OF MATTER AND QUANTUM CHEMISTRY

УДК 539.192

ATTENUATED TOTAL REFLECTANCE–FOURIER TRANSFORM INFRARED MICROSPECTROSCOPY OF COPPER(II) COMPLEXES WITH REDUCED DEXTRAN DERIVATIVES

© 2009 G. S. Nikolić*, M. Cakić *, Ž. Mitić**, B. Ilić*** and P. Premović***

*Faculty of Technology, Leskovac, Serbia

E-mail: goranchem_yu@yahoo.com, zak_chem2001@yahoo.com

**Faculty of Medicine, Department of Pharmacy, Belgrade, Serbia

***Laboratory for Geochemistry, Cosmochemistry and Astrochemistry, University of Niš, Lescovac, Serbia

Abstract – Dextran is a water–soluble, extracellular neutral polysaccharide with a linear flexible chain of α–(1 → 6)–linked α–D–glucopyranose units, in a single compounds. In alkali solutions Cu(II) ion forms complexes with reduced low–molar dextran (RLMD). The metal content and the solution composition depended on pH. The complexing process begins in weak alkali solution (pH > 7), and involves OH groups in C-2 and C-3 dextran monomer units. Synthesized copper(II) complexes with RLMD, of average molar mass M_w = 5000 g/mol were investigated by Attenuated total reflectance–Fourier transform infrared (ATR–FT-IR) spectroscopy and FTIR imaging microscopy. ATR–FTIR microspectroscopic data of synthesized complexes are rare in literature. The changes in intensity and width of the IR bands in region 1500–1000 cm^{-1} were related to changes in conformation and short–range interactions of the ligand dextran. FTIR microscopy images shows more and less ordered structures of the Cu(II)–RLMD complexes. ATR–FTIR microspectroscopic data shows homogeneity of the Cu(II)–RLMD samples and green color of the samples confirm existence of Cu(II) ions.

INTRODUCTION

Dextran is a polysaccharide consisting of α-D-glucopyranose units coupled into long branched chains, mainly through the α-(1 → 6) and partly through the α-(1 → 3)-glycosidic linkages (Fig. 1). This unique linkage pattern gives dextran with distinctive physical properties. Due to these properties, dextran has been extensively used as a drug carrier system, including for antidiabetics, antibiotics, anticancer drugs, peptides and enzymes [1, 2]. Dextran is derivatized easily to control its solubility or provide reactive groups. Con-

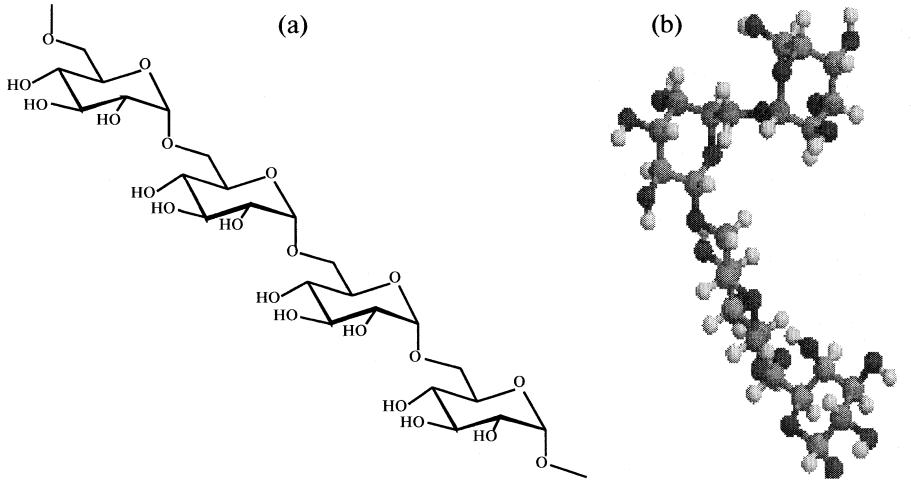

Fig. 1. Molecular structure of a dextran: (a) 2D model, (b) 3D model stick and ball.

sequently, dextran and its derivatives have numerous potential food, pharmaceutical, and industrial applications [3, 4].

The aim of this work is to use attenuated total reflectance – Fourier transform infared (ATR–FTIR) spectroscopy, and FTIR imaging microscopy as the main tools to verify the conformation and structure of this type of ligand around the copper(II) ions.

Many types of polysaccharides such as chitin [5], chitosan [6], heparin [7], alginate [8], inulin [9], dextran [10] and pullulan [11, 12] have been derivatized for biomedical applications. The numerous investigations have indicated that the polysaccharide dextran and its derivatives have the extraordinary power to forming the water–soluble complexes with various biometals [13, 14]. It has been established that the degree of Cu(II) ion binding within the complex depends primarily on the pH of the solution, as well as on the participation both of the OH groups and the H_2O molecules in the first coordination sphere of Cu(II) ion. Reduced low–molar dextran (RLMD), was chosen as a material for complexing, and the subsequent interactions with Cu(II) ions were investigated in this study. Copper(II) complexes were prepared from sodium salts, and investigated in the solid state. ATR–FTIR microspectroscopic data of synthesized complexes are rare in literature. The emergence of modern structural chemical methods such as ATR–FTIR spectroscopy and FTIR microscopy made it possible to assign the binding OH or other groups, and also to characterize the metal ion coordination of polysaccharides, monitoring the ligand conformation or/and configuration changes forced by the complexation processes [15–18]. The major goal of this work is to use of ATR–FTIR microspectroscopy and FTIR imaging as the main tools to verify the conformation and structure of this type of ligand around the copper(II) ions.

EXPERIMENTAL

Copper(II) ion complex synthesis with RLMD have been described in detail by Mitić et al. [16]. FTIR microspectroscopy system, ATR–FTIR spectrometer Bruker Tensor–27 in conjunction with a FTIR Bruker Hyperion–1000/2000 microscopy attachment equipped with a 15× objective and a 250 μm liquid nitrogen cooled, narrow-band mercury–cadmium–telluride (MCT) detector (ATR objective GMBH, Germany) with the range of the IR spectrum from 4000 to 400 cm^{-1} was used in this work. The spectra were measured with 4 cm^{-1} resolution and 320 scans co-addition. The measurements were conducted in the reflection mode. In the region from 4000–400 cm^{-1} all spectra were Interactive polynomials baseline–corrected and area-normalized. A Kubelka–Munk arithmetic method was applied to enhance the resolution in this spectral region. Deconvoluted spectra were smoothed by the 40-point Fourier filter method.

Characteristic bands in ATR–FTIR spectra of polysaccharide dextran and synthesized Cu(II)–RLMD complexes

$\bar{\nu}$, cm^{-1}	Assignation	Comment
3600–3400	ν(O–H)	CH–OH glucopyranose units, H–O–H
~2950	ν(C–H)	C–H
~1640	δ(HOH)	H–O–H
1450–1345	δ(C–H)	C–H
~1420	δ(O–H)	O–H
1150–1010	ν_{as}(C–O), ν_{as}(C–C)	glucopyranose units
1000–700	γ(C–H)	configuration

Thus, various tests can be performed by the Bruker Hyperion microscope, such as transmission, reflection, polarized, and ATR–FTIR measurements, the linear scan and mapping techniques in terms of software, and optic video technology for true video analysis. In addition, spatial-resolution FTIR spectra and functional group imaging can also be acquired and analyzed. For measuring IR spectra by FTIR microscopy accurately, several primary parameters in the operation need to be selected and set first, which include aperture sizes, number of scans, resolution, velocity of motional mirror, and sampling background.

RESULTS AND DISCUSSION

Recently, FTIR spectroscopy was coupled with a microscope and a computer system, capable of microanalysis of minute samples by using a dedicated MCT detector. The resultant FTIR vibrational microspectroscopy can provide molecular information of samples with a high spatial resolution at microscopic level. Samples with microscopic size can be nondestructively analyzed by both vibrational microspectroscopies, particularly in the application of biomedical sciences [19–22]. Thus, the use of vibrational microspectroscopy has extensively become a great potential over other spectroscopic techniques for noninvasive investigation of chemical components of ultrastructual samples (carbohydrates, lipids, proteins, nucleotides) [23, 24]. More recently, FTIR and/or Raman microspectroscopic imaging systems have also been developed for applying to biosciences [25, 26]. ATR–FTIR spectra may be simultaneously collected at a time in a stepwise manner from different areas of a sample. We had to restrict ourselves to a few examples of wide potentialities of the method of FTIR spectroscopy in investigating the relationships between the structure and the properties of extracellular polysaccharide dextran and its complexes with Cu(II) ion. The FTIR spectra of the RLMD and synthesized Cu(II) ion complexes contains following characteristic bands are given in table. The absorbance ATR–FTIR spectra of Cu(II)–RLMD complexes which were

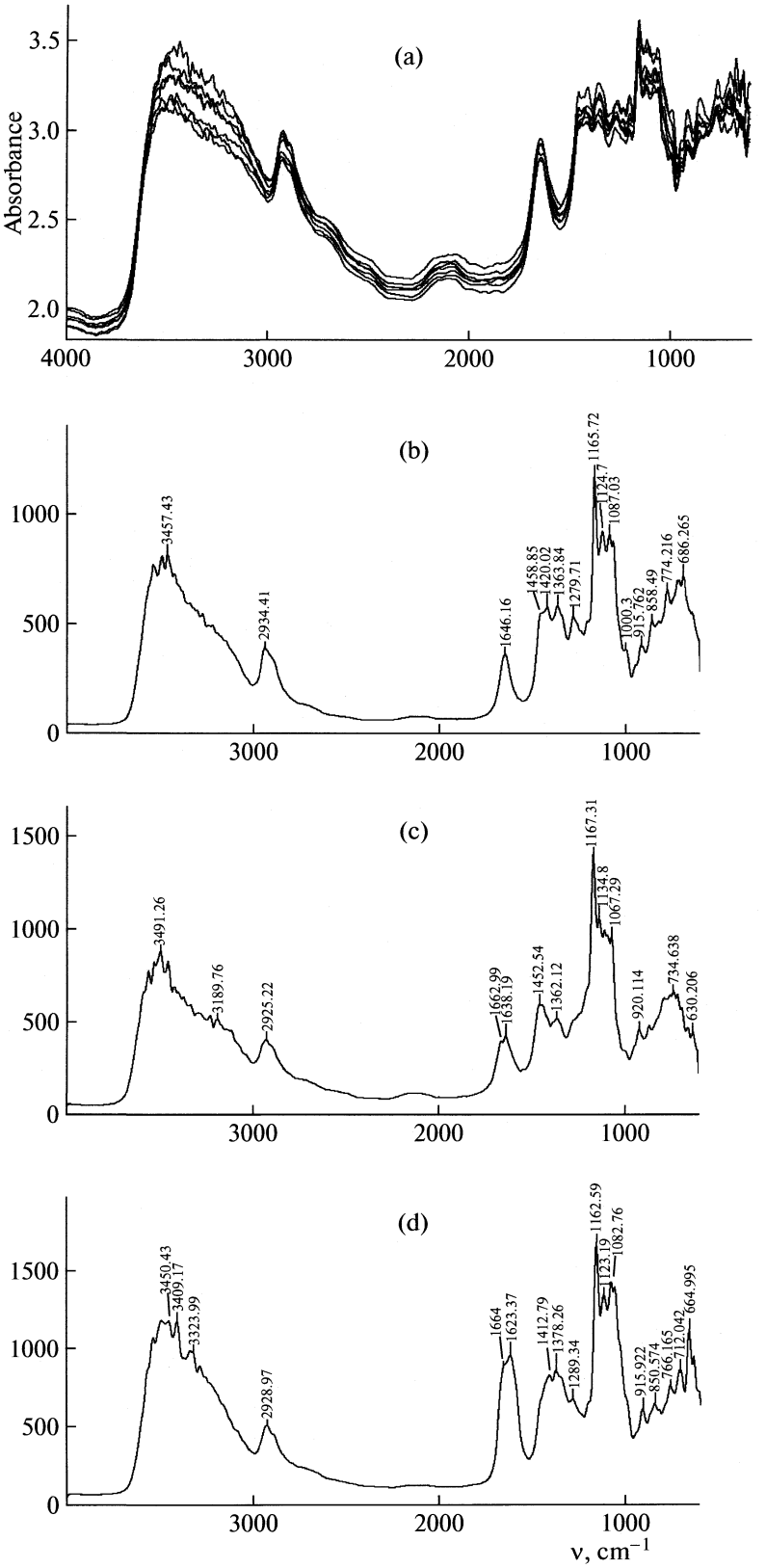

Fig. 2. Typical ATR–FTIR spectra of Cu(II)–RLMD complexes synthesized at boiling point and pH (a) 7.5, (b) 8.0, (c) 10.0, and (d) 12.0.

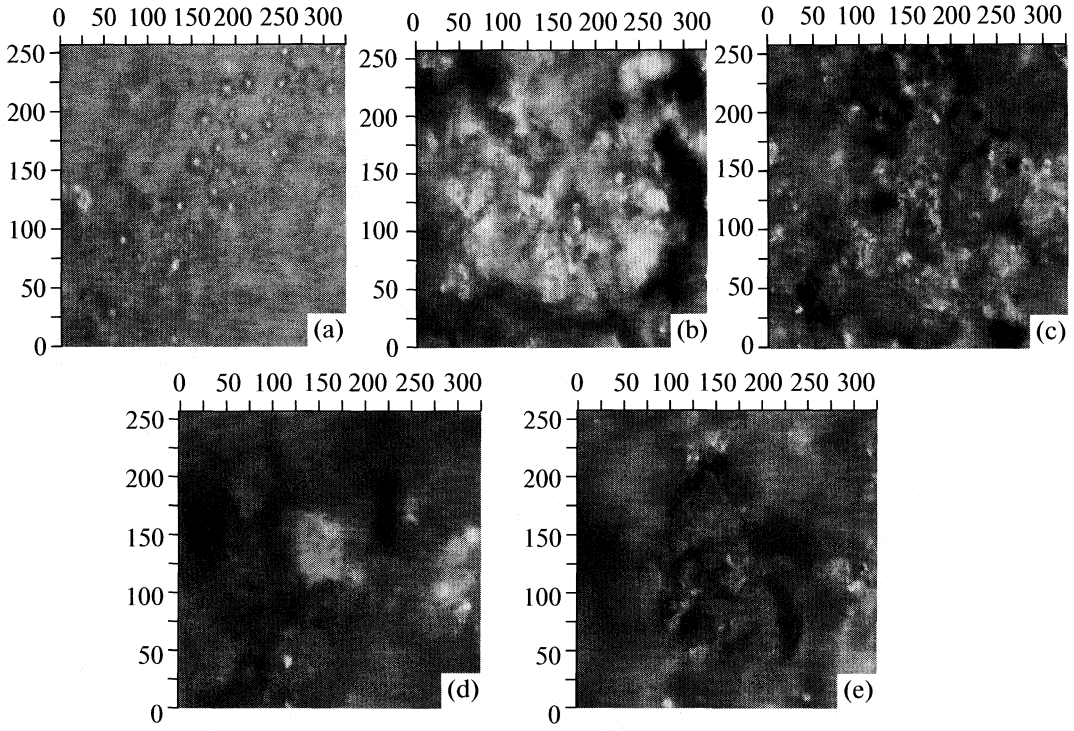

Fig. 3. FTIR microscopy images (250 μm × 300 μm) of (a) RLMD, M_w = 5000 g mol^{-1} and Cu(II)–RLMD complexes synthesized at boiling point and pH (b) 7.5, (c) 8.0, (d) 10.0 and (e) 12.0.

synthesized at pH 7.5, 8.0, 10.0, and 12.0 are shown in Fig. 2.

Spectroscopic ATR–FTIR study in a particular region of O–H (3400 and 1420 cm^{-1}) and C–H (2900, 1460, and 1350 cm^{-1}) vibrations indicates different binding between the central metal ion and ligand, depending on pH and copper(II) ion contents [15, 16].

The difference of the number, frequencies, intensity and shape of the bands (3600–3100 cm^{-1}) implies that in the complexes there is displacement of H_2O molecules by the hydroxyl groups. Cu(II)–RLMD complexes are formed by the displacement of H_2O molecules from the first coordination sphere of copper(II) ion by the OH groups. Copper(II) ion with RLMD unit (Glc) forms three different types of complex (pH 7–8: $Cu(II)(Glc)_2(H_2O)_2$, pH 8–10: $Cu(II)(Glc)_2(H_2O)(OH)$; pH 10–12: $Cu(II)(Glc)_2(OH)_2$) [15–17].

These results agree with a structural studies of the investigated complexes have been based on other spectroscopic techniques [27–32]. The changes in number, frequencies, intensity, and width of the IR bands in the particular region of ν(O–H) vibrations (3400 cm^{-1}), δ(C–H) vibrations (1500–1300 cm^{-1}) and ν(C–O) vibrations (1200–1000 cm^{-1}) were related to changes in the conformation and short-range interactions of the polysaccharide dextran. Very important changes can be observed in the range 1500–1300 cm^{-1} by detailed empirical analysis. Otherwise, the IR range is specific of bending vibrations of CH–OH groups. Namely, exchange position and intensity of complex bands can be registered in this range, where C–H and O–H bending vibrations from the CH–OH groups take part. An approximate effect exists in the stretching of the IR range of C–H vibrations (3000–2800 cm^{-1}). The appearance of bands at about 1460 cm^{-1} and 1370 cm^{-1} from δ(C–H) vibrations and the band at about 1420 cm^{-1} from δ(O–H) vibrations are characteristic for one of more possible positions of the CH–OH group, rotating around the C2–C3 and C3–C4 bond of the glucopyranose unit. The Cu(II) ions in solution have a possible influence on the rotation of CH–OH groups in the complexes.

RLMD and its complexes with the Cu(II) ion have one crystallographic type of the water molecule (1640 cm^{-1}) [15–17]. The band at 1079 cm^{-1} in the spectra of RLMD is attributed to the antisymmetric stretching vibration of C6–O–C1 glycosidic bridge with participation of the deformational vibrations of the C4–C5 bond. The band at 1079 cm^{-1} in the spectra of Cu(II) complex with RLMD is more pronounced than in the spectra of RLMD.

It is known that [33–35] the glucopyranose units exist in six different conformations (*1C*, *C1*, *1B*, *B1*, *3B*, and *B3*). The similarities of the γ(C–H) range indicate that there is no difference in the conformation of the glucopyranose unit in the RLMD and Cu(II)–RLMD complex molecules and they probably exhibit *C1* chair conformation (916 and 850 cm^{-1}).

The absorbance of a band corresponding to a specific chemical component may be plotted as a map. ATR–FTIR spectra were presented in Fig. 2 from different areas of Cu(II)–RLMD complex (Fig. 3) and show high homogeneity of the sample.

A new imaging capability has been established not only to image heterogeneous regions of the samples and simultaneously provide spectroscopic and spatial information, but also to show visually the concentrations of components and to highlight their effect from the three dimensional plot. The application of microscopic FTIR imaging system to the ligand RLMD and Cu(II)–RLMD complexes, were synthesized at pH 7.5–12, is shown in Fig. 3.

FTIR microscopy images of ligand RLMD, as well as images of the synthesized Cu(II)–RLMD complexes differ which also indicates that the complexation process and the creation of coordination compounds took place. FTIR microscopy images confirmed that the changes in the intensity of the analyzed bands are strongly associated with the alterations in the macromolecular order. These bands in the spectra of the complexes can be responsible for more and less ordered structures, respectively (Fig. 2). The changes in color contour may show the content and distribution of copper, and polysaccharides in Cu(II)–RLMD samples (Fig. 3). ATR–FTIR microspectroscopic data shows homogeneity and green color of the Cu(II)–RLMD samples confirm existence of Cu(II) ions (results from other spectroscopic techniques [13–17]).

CONCLUSIONS

Spectroscopic IR study in a particular region of O–H (3400 and 1420 cm^{-1}) and C–H (2900, 1460, and 1350 cm^{-1}) vibrations indicates different binding between the central metal ion and ligand, depending on pH and metal contents. The changes of the intensity on some bands were registered in RLMD complexes (in the ranges of a stretching vibration at about 2930 cm^{-1} and a bending vibration at about 1400 cm^{-1}). The IR band δ(HOH) at the frequency of 1640 cm^{-1} indicated the existence of water molecules in a complex structure. A part of IR spectra, in the range on 1000–700 cm^{-1} of Cu(II) ion complexes with RLMD, indicates no influence of complexing process on the conformation change of *C1* glucopyranose units. ATR–FTIR microspectroscopic data shows homogeneity and green color of the Cu(II)–RLMD samples confirm existence of Cu(II) ions.

REFERENCES

1. Cortesi, E. Esposito, M. Osti, G. Squarzoni, E. Menegatti, S. Davis, C. Nastruzzi, Eur. J. Ph. Bioph. **47**, 153 (1999).
2. K. Ichinose, N. Tomiyama, M. Nakashima, Y. Ohya, M. Ichikawa, T. Ouchi, T. Kanematsu, Anticancer Drugs **11**, 33 (2000).
3. A. Virnik, K. Homyakov, Uspekhi Khimii **44**(7), 1280 (1975).
4. A. N. de Belder, Dextran, Pharmacia AB, Uppsala, Sweden 1985.
5. S. Tanodekaew, M. Prasitsilp, S. Swasdison, B. Thavornyutikarn, T. Pothsree, R. Pateepasen, Biomaterials **25**, 1453 (2004).
6. J. Li, J. Pan, L. Zhang, X. Guo, Y. Yu, J. Biomed. Mater. Res. **67**A, 938 (2003).
7. D. K. Kweon, S. B. Song, Y. Y. Park, Biomaterials **24**, 1595 (2003).
8. A. Perets, Y. Baruch, F. Weisbuch, G. Shoshany, G. Neufeld, S. Cohen, J. Biomed. Mater. Res. **65**A, 489 (2003).
9. G. Nikolić, M. Cakić, Colloid J. **69**(4), 464 (2007).
10. E. London, J. Pharm. Sci. **93**(7), 1838 (2004).
11. Lj. Ilić, S. Ristić. M. Cakić. G. Nikolić, S. Stanković, *Polynuclear Complex Fe(III) with Pullulan Oligomers, Process of Its Obtaining, and Pharmaceutical Preparations on the Basis of the Complex*, PCT WO 02/46241 A2 June 2002, IP Cl. C 08 B 37/00.
12. G. Nikolić, M. Cakić, Lj. Ilić, S. Ristić, Ž. Cakić, Die Pharmazie **57**(3), 155 (2002).
13. G. Nikolić, M. Cakić, Ž. Mitić, R. Nikolić, Lj. Ilić, Chem. Industry **59**(1–2), 9 (2005).
14. Z. Mitić, M. Cakić, G. Nikolić, R. Nikolić, Lj. Ilić, Chem. Industry **61**(5), 257 (2007).
15. G. S. Nikolić, M. Cakić, Ž. Mitić, Lj. Ilić, Russ. J. Coord. Chem. **34**(5), 322 (2008).
16. Ž. Mitić, G. S. Nikolić, M. Cakić, R. Nikolić, Lj. Ilić, Russ. J. Phys. Chem. **81**(9), 1433 (2007).
17. M. Cakić, Ž. Mitić, G.S. Nikolić, Lj. Ilić, G. M. Nikolić, Spectroscopy **22**(2–3), 177 (2008).
18. Ž. Mitić, G. Nikolić, M. Cakić, R. Nikolić, Lj. Ilić, *in Proceeding of the XII European Conference on the Spectroscopy of Biological Molecules (ECSBM'07)* (Paris France, 2007), p. 319.
19. M. Kačurakova, R.H. Wilson, Carbohydr. Polym., **44**, 291 (2001).
20. S.-Y. Lin, M.-J. Li, W.-T. Cheng, Spectroscopy, **21**, 1 (2007).
21. H.-C. Chiu, T. Hsiue, W.-Y. Chen, Polymer, **45**, 1627 (2004).
22. G.S. Nikolić, M. Cakić, Ž. Mitić, B. Ilić, P. Premović, *in Proceeding of the 9th International Conference on Fundamental and Applied Aspects of Physical Chemistry* (Belgrade Serbia, 2008), p. 117.
23. Z. Mousia, I.A. Farhat, M. Pearson, M.A. Chesters, J.R. Mitchell, Biopolymers (Biospectroscopy), **62**, 208 (2001).
24. W. Yu, L. Xiong, J. Appl. Polym. Sci., **96**, 1003 (2005).
25. N. Gierlinger, M. Schwanninger, Spectroscopy, **21**, 69 (2007).
26. D. Chenery, H. Bowring, Spectrosc. Europe, **15**(4), 8 (2003).
27. Ž. Mitic, G.S. Nikolić, M. Cakić, P. Premović, Lj. Ilić, J. Mol. Struct. In press.

28. Ž. Mitić, M. Cakić, R. Nikolić, Lj. Ilić, G.S. Nikolić, World. Polym., 7(5), 225 (2004).

29. G.M. Nikolić, Lj. Ilić, M. Cakić, G.S. Nikolić, R.S. Nikolić, Ž. Mitić, *in Proceeding of the 7th International Conference on Fundamental and Applied Aspects of Physical Chemistry* (Belgrade Serbia, 2004), p. 775.

30. G. Nikolić, M. Cakić, Ž. Mitić, Lj. Ilić, *in Proceeding of the 8th International Conference on Fundamental and Applied Aspects of Physical Chemistry* (Belgrade Serbia, 2006), p. 719.

31. M. Cakić, G. Nikolić, Ž. Mitić, Lj. Ilić, *in Proceeding of the 4th International Conference of the Chemical Societies of the South–Eastern European Countries,* (Belgrade Serbia, 2004), p. 72.

32. G. Nikolić, M. Cakić, Ž. Mitić, Lj. Ilić, *in Proceeding of the 8th International Conference on Fundamental and Applied Aspects of Physical Chemistry* (Belgrade Serbia, 2006), p. 722.

33. R.G. Zhbankov, *Infrared Spectra and Structure of Carbohydrates*, Nauka i Tekhnika, Minsk, 1972.

34. V.P. Panov, R.G. Zhbankov, *Conformations of Sugars, Nauka i Tekhnika*, Minsk, 1976.

35. V.P. Panov, R.G. Zhbankov, *Intra- and Intermolecular Interactions in Carbohydrates*, Nauka i Tekhnika, Minsk, 1988.

ЖУРНАЛ ФИЗИЧЕСКОЙ ХИМИИ, 2009, том 83, № 9, с. 1702–1706

STRUCTURE OF MATTER AND QUANTUM CHEMISTRY

УДК 539.192

LARGE DEVIATION SPECTRA OF CHAOTIC TIME SERIES FROM BRAY–LIEBHAFSKY REACTION

© 2009 A. Z. Ivanović*, Ž. D. Čupić*, Lj. Z. Kolar-Anić**, M. M. Janković*** and S. R. Anić**

*ICHTM – University of Belgrade, Department of Catalysis and Chemical Engineering, Serbia

**Faculty of Physical Chemistry, University of Belgrade, Serbia

***Institute for Nuclear Science, Belgrade, Serbia

E-mail: ana.ivanovic@nanosys.ihtm.bg.ac.rs

Abstract – We applied multifractal analysis on time series obtained by deterministic simulation of the Bray–Liebhafsky oscillatory reaction. Large deviation spectrum was used to represent multifractal properties of the attractor. We obtained spectrums with two peaks, one in region of low and the other in region of high values of Hölder exponent. Their intensity depends on flow rate. The method developed on the results from numerical simulations is tested on the experimental record from the same reaction system and multifractality of the time series is confirmed.

INTRODUCTION

The Bray–Liebhafsky (BL) reaction is the decomposition of hydrogen peroxide into the water and oxygen in the presence of iodate and hydrogen ions:

$$2H_2O_2 \xrightarrow{H^+, IO_3^-} O_2 + 2H_2O. \qquad (D)$$

This apparently simple reaction is a highly nonlinear process that comprises a complex homogeneous catalytic oscillatory evolution involving numerous iodine intermediates [1, 2].

Oscillatory dynamics of the BL reaction is best described by the model consisted of eight reactions

$$IO_3^- + I^- + 2H^+ \rightleftharpoons HIO + HIO_2, \qquad (R1),(R\text{-}1)$$

$$HIO_2 + I^- + H^+ \longrightarrow I_2O + H_2O, \qquad (R2)$$

$$I_2O + H_2O \rightleftharpoons 2HIO, \qquad (R3),(R\text{-}3)$$

$$HIO + I^- + H^+ \rightleftharpoons I_2 + H_2O, \qquad (R4),(R\text{-}4)$$

$$HIO + H_2O_2 \longrightarrow I^- + H^+ + O_2 + H_2O, \qquad (R5)$$

$$I_2O + H_2O_2 \longrightarrow HIO + HIO_2, \qquad (R6)$$

$$HIO_2 + H_2O_2 \longrightarrow IO_3^- + H^+ + H_2O, \qquad (R7)$$

$$IO_3^- + H^+ + H_2O_2 \longrightarrow HIO_2 + O_2 + H_2O. \qquad (R8)$$

Three of them are reversible. Nevertheless, for numerical simulations of the system behavior in the continuous stirred tank reactor (CSTR) the reactions due to flow of hydrogen peroxide through the system and outflow of all species from the reaction vessel must be added. The resulting model for the BL reaction in the CSTR and rate constants are given in [3]. Different variants of the model are additionally elaborated in [4, 5].

With increasing flow rate j_0, in numerical simulations based on this model, various simple, complex and chaotic oscillations were observed [6]. For complex oscillation description, many different methods were applied on BL reaction such as firing numbers, power spectra and Poincaré section [6]. The appearance of deterministic chaos in the experimental and simulated BL reaction was also confirmed and proven by the determination of positive values of the maximal Lyapunov exponents for the sequences of flow rate values as the control parameter [3]. Although typical for chaos quantification, fractal properties of the BL reaction were not tested ever before.

An object (function, set of phase space points or simply data) is usually referred to as fractal if its graph displays such characteristics as (local) selfsimilarity, irregularity, fine structure, and fractional dimension [7]. Dissipative dynamical systems that exhibit chaotic behavior, often has strange attractor in phase space [8]. Strange attractors are typically characterized by fractal dimension D [9]. which is smaller than the number of degrees of freedom F ($D < F$). Moreover, different parts of an attractor may be characterized by different value of the fractal dimension. In such situation, a single value of some fractal dimension is not sufficient to characterize the attractor adequately. For example, two quite different attractors might have the same correlation dimension, but they still could differ widely in their "appearance". One can visualize this multifractal object as a collection of overlapping fractal objects, each with its own fractal dimension [10].

Multifractal techniques and notions are increasingly widely recognized as the most appropriate and straightforward framework to analyze scale dependency of the data, but also their extreme variability over a wide range of scales [11]. However, fractal dimension is measure of global scaling property but multifractality depends on local scaling properties of the object, and therefore, obviously, there is a need for some other

quantity to qualify the system. Hence, the basic numerical expression used in the multifractal analysis is so-called Hölder exponent, α [12]. The Hölder exponent of a data is a local characteristic value calculated at each point in time series. It reflects the decay rate of the amplitude of the function fluctuation μ, in the neighborhood of the point j as the size ε of the neighborhood shrinks to zero:

$$\mu_j(\varepsilon) \propto \varepsilon^{\alpha_j}. \quad (1)$$

A highly irregular point (or singularity) in a data is characterized by a lower value of Hölder exponent and a smoother portion of a data will have a higher value of Hölder exponent. A time series may have different Hölder exponents at different points due to a variation in the local degree of irregularity (or singularity).

The number of intervals $N(\alpha)$ where the time series has Hölder exponents between α and $\alpha + d\alpha$ scale as [13].

$$N(\alpha) \sim \varepsilon^{-f(\alpha)}, \quad (2)$$

where $f(\alpha)$ can be considered as the generalized fractal dimension of the set of boxes with singularities α. The multifractal spectrum is graph, where abscissa represents the Hölder exponent in the signal and the ordinate is the generalized fractal dimension $f(\alpha)$ which measures the extent by which a given singularity is encountered. Multifractal spectrum can be evaluated directly from equations given above (1) and (2) (and actually it is calculated this way in Large deviation spectrum calculations) but it is hard task. More usual and easier procedure for multifracatal spectrum analysis is indirect one, based on generalization of the measure of signal variation to so called partition sum:

$$Z(q, \varepsilon) = \sum_{i=1}^{N(\varepsilon)} \mu_i^q, \quad (3)$$

where q is a real parameter that indicates the order of the moment of the measure. The parameter q can be considered as a powerful microscope, able to enhance the smallest differences of two very similar maps [14]. Furthermore, q represents a selective parameter: high values of q enhance boxes with relatively high values for $\mu_j(\varepsilon)$; while low values of q favor boxes with relatively low values of $\mu_j(\varepsilon)$. Partition sum Z scales as

$$Z(q, \varepsilon) \sim \varepsilon^{\tau(q)}, \quad (4)$$

where $\tau(q)$ is the correlation exponent of the q-th order moment defined as [15].

$$\tau(q) = (q-1)D_q \quad (5)$$

and D_q is generalized dimensions that can be calculated from [16]

$$D_q = \lim_{\varepsilon \to 0}\left(\frac{1}{q-1}\frac{\log Z(q, \varepsilon)}{\log(\varepsilon)}\right). \quad (6)$$

The generalized dimension D_q is a monotonic decreasing function for all real values of q within the domain $[-\infty, +\infty]$.

The connection between the power exponents $f(\alpha)$, which can be considered as the generalized fractal dimension of the set of boxes with singularities α, and $\tau(q)$ is made via the Legendre transformation [13, 15]:

$$f_L(\alpha(q)) = q\alpha(q) - \tau(q) \quad (7)$$

and

$$\alpha(q) = d\tau(q)/dq. \quad (8)$$

Therefore, the multifractal spectrum $f(\alpha)$ is usually obtained from evaluation of generalized dimension D_q and subsequent Legendre transformation of $\tau(q)$ using equations (7) and (8). The $f_L(\alpha)$ is a concave downward function with a maximum at $q = 0$ and it describes properties of multifractal. Single humped function $f(\alpha)$ obtained for multifractal spectrum is very useful and easily discussed in terms of capacity, information and correlation dimension. Therefore it is widely applied [17–19]. However, its shape is mainly consequence of the applied Legendre transform. Actual distribution of the points with various Hölder exponents could be obtained through the Large deviation spectrum.

The large deviation spectrum $f_G(\alpha)$ which is based on the Cramér theory of large deviations [15, 20] is, in accordance with equations (1) and (2), defined as:

$$f_G(\alpha) = \lim_{\varepsilon \to 0} \lim_{n \to \infty} \frac{\ln N_\varepsilon^n(\alpha)}{-\ln \delta_n}. \quad (9)$$

The function $f_G(\alpha)$ reflects the exponentially decreasing rate of $N_\varepsilon^n(\alpha)$ which is the number of intervals having a Hölder exponent, α_i^n, close to a Hölder exponent α up to a precision δ when the resolution n (the number of intervals in the α space) approaches ∞. The $f_G(\alpha)$ yields the large deviations from the "most frequent" singularity exponent and thus displays information about the occurrence of rare events such as bursts (small α).

For detailed comparison of various chaotic states, multifractal analysis is used here, rather than local fractal dimension evaluation, since it may yield additional insight into the complex nature of the chaotic dynamical state [10]. The large deviation spectrum yields information about the statistical behavior of the probability of finding a point with a given Hölder exponent in the signal under changes of resolution [17].

METHODS

Deterministic simulations were performed using the MATLAB program package using the ode15s solver. For the numerical calculation of the large deviation spectrum, the FRACLAB toolbox has been used [21].

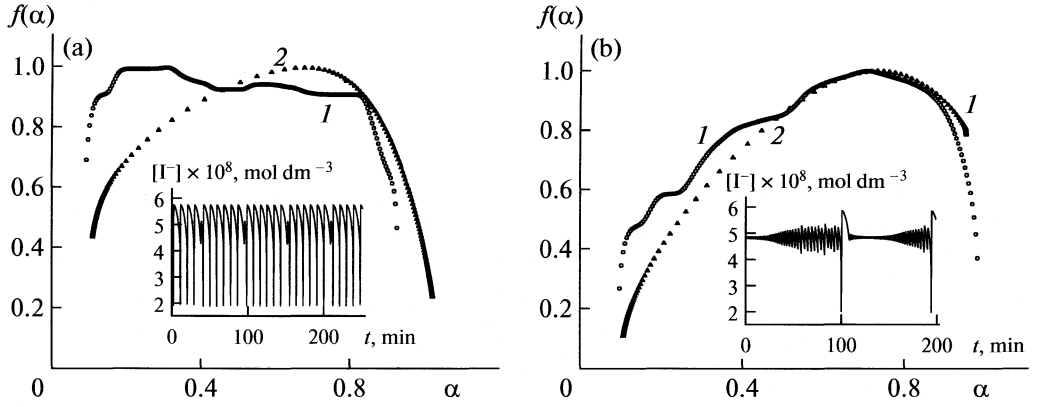

Fig. 1. (*1*) Large deviation and (*2*) Legendre spectrum for the time series from the simulations in the function of the flow rate as a control parameter: (a) 4.82592×10^{-3}, (b) 5.0812×10^{-3} min^{-1}; α is Hölder exponent.

The Bray–Liebhafsky oscillatory reaction, was conducted in CSTR. The procedure is described in more detail earlier [3]. The initial experimental conditions were: $[KIO_3]_0 = 5.9 \times 10^{-2}$ mol dm^{-3}, $[H_2SO_4]_0 = 5.5 \times 10^{-2}$ mol dm^{-3}, $[H_2O_2]_0 = 2.0 \times 10^{-1}$ mol dm^{-3}, $T = 48.6°C$. The specific flow rate was 5.03×10^{-3} min^{-1}. Temporal evolution of the BL system was monitored potentiometrically by Pt (Metrohm–6.0301.100) electrode versus a double junction Ag/AgCl (Metrohm-6.0726.100) electrode as the reference.

RESULTS AND DISCUSSION

Generally, multifractal analysis is the method for examination of time series with highly irregular oscillation periods and their amplitudes. The BL reaction in chaotic regime also have the irregular time series, but with two types of oscillations with significantly different periods and amplitudes. Moreover, the amplitudes of large oscillations are almost same whereas the amplitudes of small oscillations are different between themselves.

The model of the BL reaction system in chaotic regime appears to be very sensitive to changes of the control parameter (similar to the experimental one) and complex dynamic states appear in a very narrow region of flow rates, j_0. In much wider oscillatory region, for low values of j_0 only large amplitude relaxation oscillations are observed. Between complex dynamic states and bifurcation to steady state at high j_0, there is a region of j_0 values where only small-amplitude oscillations are found. The mixed-mode oscillations consist of these two kind of simple sustained oscillations (large-amplitude relaxation and small-amplitude, nearly sinusoidal ones) involved one into the other. The mixed-mode dynamic states appear in the form evolving with flow rate from X^1 to 1^Y, (which denote the number of large and small amplitude oscillations in one sequence, respectively). Among them, windows of more complex dynamic states such as the mixture of regular mixed-mode oscillations, period doubling and deterministic chaos are found.

The insets at the Fig. 1 illustrate two kinds of complex oscillations with dominating X^1 (Fig. 1a) and 1^Y (Fig. 1b) forms of dynamics. We applied both, the Legendre spectrum and the large deviation spectrum on these chaotic time series and results are shown in Fig. 1. Well defined multifractal type spectra were obtained in both cases. By application of large deviation spectrum on these chaotic time series obtained at different flow rates we have found one kind of bimodal distribution which depends on fraction of large and small amplitude oscillations. Legendre spectrum which is more usual in multifractal analysis shows here skewed form with maximum near to the second peak of the large deviation spectrum. Lower Hölder exponents wing of the large deviation spectrum is not covered with Legendre spectrum, indicating significant information lost, which is more pronounced for lower values of the flow rate, where the dynamic state is typically of the X^1 form. Therefore, we decided to use the large deviation spectrum in the multifractal analysis of time series from numerical simulations of the BL reaction.

At lower flow rates ($j_0 = 4.82592 \times 10^{-3}$ min^{-1}) large deviation spectrum gives higher contribution of lower Hölder exponents that correspond to situation when fraction of large amplitude oscillations is higher. The situation is opposite at higher flow rates ($j_0 = 5.0812 \times \times 10^{-3}$ min^{-1}). The large deviation spectrum is analyzed for several values of the flow rate as the control parameter in simulation, keeping all other parameters constant. The intensities of the two peaks, corresponding to the low and high Hölder exponent values, are presented in Fig. 2, in function of the flow rate.

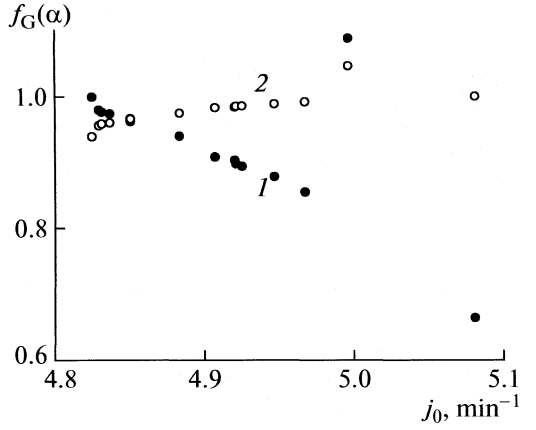

Fig. 2. Intensity of two peaks ((*1*) lower α, (*2*) higher α in the large deviation spectrum in a function of the flow rate.

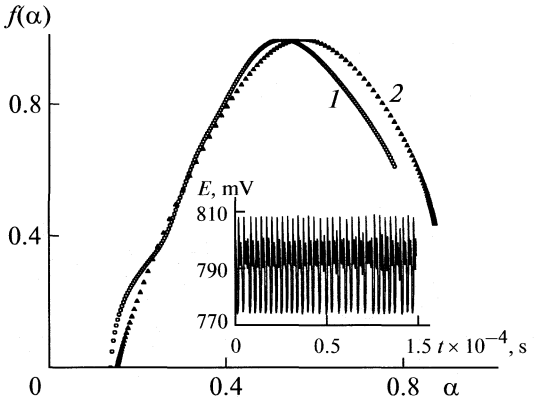

Fig. 3. (*1*) Large deviation and (*2*) Legendre spectrum for the selected experimental time series: the initial experimental conditions were: $[KIO_3]_0 = 5.9 \times 10^{-2}$ mol dm^{-3}, $[H_2SO_4]_0 = 5.5 \times 10^{-2}$ mol dm^{-3}, $[H_2O_2]_0 = 0.2$ mol dm^{-3}, $T = 48.6$°C, flow rate 5.03×10^{-3} min^{-1}.

From Fig. 2 we can see that contribution of lower exponent peak decreases, while higher one increases, with increasing flow rate. It is similar to the pattern followed by the fractions of large and small oscillations, respectively. It can be concluded that, from the statistical point of view, given by large deviation spectrum analysis, the level of singularity in the analyzed numerical time series, continuously decreases with increasing flow rate. Since the large oscillation fraction also decreases in the same direction, it can be connected with measured irregularities in time series. Roughly speaking, in our case, large oscillations correspond to the large fluctuations and therefore to the large concentration of the measure μ and therefore to large q values and small Hölder exponent values.

Since the applicability of the large deviation spectrum is approved in the numerical simulations of the BL reaction, the same method is also used here to test the data obtained from the experimental record of the Pt electrode potentiometric measurements in BL reaction under CSTR conditions. Results for both Legendre spectrum and the large deviation spectrum of the sample experimental time series are presented in Fig. 3.

The same type of spectra is obtained for the experimental record, as previously for the numerical simulations. Relatively good agreement between two spectra is typical for the form of the X^1 dynamical state. The shape of the spectra indicates multifractal nature of the time series and of corresponding attractor in phase space. The maximum of both spectra almost coincide in this case, and it takes Hölder exponent value significantly lower then one, demonstrating highly irregular, chaotic behavior of the BL reaction in CSTR.

CONCLUSION

Time series were obtained by numerical integration of the ordinary differential equations for the Bray–Liebhafsky oscillatory reaction model in the CSTR reactor under the conditions of the deterministic chaos and mixed mode periodic oscillations. The applicability of the multifractal analysis in comparison of various chaotic states was demonstrated. For the low flow rate value, smaller Hölder exponents dominate, indicating appearance of signal fractality, while for the increased flow rate values higher Hölder exponents are more pronounced. Established multifractal analysis method is also successfully applied on the experimentally recorded time series from the BL reaction in CSTR and multifractal nature of the record is confirmed.

ACKNOWLEDGMENTS

The authors thank the partial support of the Fund for Science and Technologies and Development of Serbia (Projects 142019 and 142025).

REFERENCES

1. W. C. Bray, J. Am. Chem. Soc. **43** (6), 1262 (1921).
2. W. C. Bray and H. A. Liebhafsky, J. Am. Chem. Soc. **53** (1), 38 (1931).
3. A. Z. Ivanović, Ž. D. Čupić, M. M. Janković, Lj. Z. Kolar-Anić and S. R. Anić, Phys. Chem. Chem. Phys. **10** (38), 5848 (2008).
4. Lj. Kolar-Anić, N. Vukelić, D. Mišljenović and S. Anić, J. Serb. Chem. Soc. **60** (11), 1005 (1995).
5. Lj. Kolar-Anić, Ž. Čupić, S. Anić and G. Schmitz, J. Chem. Soc., Faraday Trans. **93** (12), 2147 (1997).
6. G. Schmitz, Lj. Kolar-Anić, S. Anić, T. Grozdić, V. Vukojević, J. Phys. Chem. A **110** (34), 10361 (2006).
7. K. Falconer, *Fractal Geometry: Mathematical Foundations and Applications* (Wiley, New York, 1990).
8. D. Rulle and F. Takens, Commun. Math. Phys. **20** (3), 167 (1971).

9. B.B. Mandelbrot, *Fractals-form, Chance and Dimension* (Freeman, San Francisko, 1977)
10. R. C. Hilborn, *Chaos and Nonlinear Dynamics,* 2nd edition (Oxford University Press, Oxford, 2000).
11. D. Schertzer and S. Lovejoy, *EGS Richardson AGU Chapman NVAG3 Conference: Nonlinear Variability in Geophysics: Scaling and Multifractal Processes. Nonlinear Processes in Geophysics, European Geophysical Society*, European Geophysical Society **1**, 77 (1994).
12. L. J. Véhel and R. Vojak, Adv. Appl. Mat. **20** (1), 1 (1998).
13. A. Chhabra and R. Jensen, Phys. Rev. Lett. **62** (12), 1327 (1989).
14. J. M. Diego. E. Martinez-Gonzales, J. L. Sanz, S. Mollerach and V. J. Mart., Mon. Not. R. Astron. Soc. **306** (2), 427 (1999).
15. T. Halsey, M. Jensen, L. Kadanoff, I. Procaccia, and B. Shraiman, Phys. Rev. A **33** (2), 1141 (1986).
16. H. Hentschel, and I. Procaccia, Physica D **8** (3), 435 (1983).
17. M. Meyer and O. Stiedl, Eur. J. Appl. Physiol. **90** (3–4), 305 (2003).
18. S. Peng-Jian and S. Jin-Sheng, Chin. Phys. Soc. **16** (2), 365 (2007).
19. L. Telesca, M. Balasco, G. Colangelo, V. Lapenna and M. Macchiato, Phys. Chem. Earth **29** (4–9), 295 (2004).
20. R. Holley, E. Waymire. Ann. Appl. Prob. **2** (4), 819 (1992).
21. http://apis.saclay.inria.fr/FracLab/download.html

ЖУРНАЛ ФИЗИЧЕСКОЙ ХИМИИ, 2009, том 83, № 9, с. 1707–1712

STRUCTURE OF MATTER AND QUANTUM CHEMISTRY

УДК 539.192

MODIFICATION OF ELECTRONIC PROPERTIES OF Pt(111) SURFACE BY MEANS OF ALLOYED AND ADSORBED METALS: DFT STUDY

© 2009 I. A. Pašti, S. V. Mentus

Faculty of Physical Chemistry, Belgrade University, Studentski trg 12–16, P.O.BOX137, 11001 Belgrade, Serbia, E-mail: igor@ffh.bg.ac.rs

Abstract – Following recent tendencies to predict the electrochemical behaviour of metal surfaces by calculation methods, electronic properties of Pt(111) surface modified by either alloying with, or adsorption of, the Sn and Bi atoms, were studied by DFT calculations. It was shown that work function of the surface shows different type of coverage dependence in the cases of alloying and adsorption. In addition, it was demonstrated how position of *d*-band center of surface Pt atoms is tuned in both of these cases, and the results were commented in terms of catalytic activities of these surfaces toward hydrogen evolution reaction.

INTRODUCTION

Metals belonging to platinum-group are widely used as catalysts and electrocatalysts in number of chemical and electrochemical reactions. Some of these reactions are used in many of important technological processes. In addition, both platinum and platinum based catalysts are commonly used in fuel cell technologies. However, low content of these metals in Earth shell and its high price on the market is the major cumbersome for introducing these catalysts in even greater number of technological processes. Great effort of researchers was invested in the attempts ether to find less expensive catalysts having platinum-like catalytic activity, or to modify platinum and noble metal surfaces in order to obtain higher activity.

Platinum–tin and platinum–bismuth systems were reported to be promising catalysts and electrocatalysts [1–5]. Commonly reported forms of Pt–Sn systems are regular bulk alloys [1], PtSn surface alloys [2] and underpotential deposited Sn on Pt surfaces (Sn_{upd}) [3]. All these systems show particular catalytic activity, different from the one of pure platinum. PtSn bulk alloys were investigated as possible catalysts for electrochemical oxidation of methanol with application in fuel cells [4]. Surface alloys of Pt and Sn were examined in terms of gas phase adsorption of small molecules [2]. Sn_{upd} on Pt(111) was investigated as possible catalysts for electrochemical oxidation of CO, and certain improvement with respect to clean Pt(111) was observed, but not as prominent as in case of PtSn bimetallic alloys [5].

Mixed catalysts consisted of platinum and bismuth have been attracting attention of electrochemists for a long time. Two commonly reported forms of these catalysts are regular bulk alloys, PtBi and $PtBi_2$, and irreversibly adsorbed bismuth (Bi_{ir}–Pt) [6]. High tolerance of PtBi bulk alloys toward poisoning by CO adsorption was demonstrated experimentally [7]. It was reported that the coverage of Pt(111) surface by adsorbed Bi atoms may not exceed 0.33 [8]. This was attributed to the size of Bi atoms and repulsion forces. Compared to pure platinum surface, adsorption of Bi on Pt(111) significantly reduces surface activity toward hydrogen evolution reaction (HER) [9]. It is worthy of mention that pure Bi is extremely poor electrocatalysts for HER.

On the other hand, Greely et al. [10], by means of computational high-throughput screening, have found that Pt_3Bi/Pt(111) and Pt_2Bi/Pt(111) surface alloys should show enhanced activity toward HER. This was shown by electrochemical synthesis and investigation of catalytic activity of PtBi surface alloy with nominal composition $Pt_{1.00}Bi_{0.95}$. Interesting question is why these two types of systems, for example Bi_{ir}–Pt(111) and Pt_xBi_{1-x}/Pt(111), show such a drastic difference in catalytic activity.

In the recent years, lot of attention was paid to computational approach in search for new catalysts. This way of search for new materials follows the principle that catalyst should to bind reactants strong enough to enable the reaction, but the products should not be bonded to strong to poison the surface. That means, the energetics of adsorption of different species on catalysts surfaces plays a crucial role. Since adsorption (chemisorption) presents the reaction between adsorbate and substrate, it is expected that electronic structure of reacting species can be correlated to the energy of adsorption.

Many attempts were done in this direction [11–15]. According to the paper of Hammer and Nørskov [11], the most important parameter for such a purpose is the mean energy of the *d*-band of the atoms of the solid catalyst, usually denoted as ε_d. In a number of studies published later, correlation of ε_d with adsorption energy was confirmed. As expected, if one may tune electronic structure of the surface atoms, position of the ε_d may also been affected, leading to the change in surface reactivity. Modification of electronic struc-

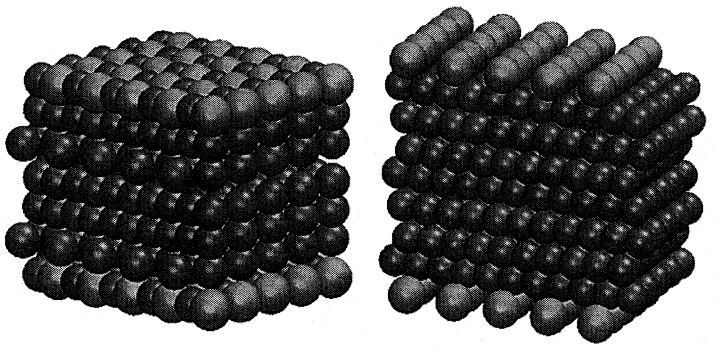

Fig. 1. The model of Pt slabs with alloyed (left) and adsorbed (right) guest (Sn, Bi) metal in surface layers.

ture by incorporation of solute metals in parent metal lattice, measured through ε_d, is mainly attributed to two distinct factors: strain effect [12] and ligand effect [13, 14]. Along with ε_d, one of the most important parameters concerned with surface states is the work function [15]. In many studies, work function was correlated to structural and chemical conditions on the surface, resulting in its very important role in surface characterization.

Although one might say that catalytic activity of the surface depends on its electronic properties, we still cannot a priori know how electronic properties of the bimetallic surface are tuned relative to the parent metal [13]. On the other hand, combining experimental and theoretical results one can obtain deep insight in the surface processes and reactivity. The scope of this work is to study and compare modifications of electronic properties of Pt(111) surface with adsorption and alloying of the surface with tin and bismuth, as there is a lack of such type of analysis in the literature. Comparison is based on the first-principle calculations. Obtained results are compared with the other both calculated and experimentally obtained data if available in the literature.

COMPUTATIONAL DETAILS

DFT calculations were performed using PWscf code which is part of Quantum ESPRESSO package for ab initio calculations [16]. The Perdew–Burke–Ernzerhof (PBE) functional within general gradient approximation (GGA) was used [17]. For platinum, ultrasoft pseudopotential was generated with 10 valence electrons in $5d^9 6s^1 6p^0$ configuration. Configurations of Sn and Bi we used were $4d^{10}5s^2 5p^2$ and $6s^2 6p^3 5d^{10}5f^0$, with 14 and 15 valent electrons, respectively. As a smearing scheme Marzari–Vanderbilt smearing [18] was used with broadening of 0.05 Ry. Kinetic energy cut off was 20 Ry and for Brillouin-zone integration Monkhorst–Pack set of 9 special k-points was used [19]. We used (2 × 2) unit cell for Pt_3Sn and Pt_3Bi surface alloys, and metals adsorbed on Pt at coverage equal to $\theta = 0.25$. In all other considered cases $(\sqrt{3} \times \sqrt{3})R{-}30°$ unit cell was used. Pt(111) surface and Pt_xM_{1-x}/Pt(111) surface alloys were constructed using supercell with a thin slab (Fig.1) separated from its periodic images by a layer of vacuum. In all cases 20 angstroms vacuum layer separated the surfaces, which was proven to lead to convergence of total energy and work function values. Surface alloys, as well as adatoms, were set on both sides of the slab in order to prevent electronic coupling of slabs. For (111) surfaces a hexagonal cells with an interlayer spacing of $a_0/\sqrt{3}$ and an ABCABC stacking was used, where a_0 is the platinum equilibrium lattice parameter. As a platinum equilibrium lattice parameter we used 4.01 angstroms which was obtained by structural optimization of platinum bulk. In all calculations truncated bulk geometries of the surfaces were used.

For work function calculations we employed two different methods. The first one is based on definition of work function and it uses following equation:

$$W = V(+\infty) - E_F, \quad (1)$$

where $V(+\infty)$ is electrostatic potential in the middle of vacuum region, and E_F denotes Fermi energy of the slab. We also applied method based on macroscopic average [20] by which work function is calculated as:

$$W = \Delta V + V_{bulk} - E_{F,bulk}, \quad (2)$$

where ΔV, V_{bulk} and $E_{F,bulk}$ are potential step across the surface, mean electrostatic potential in the bulk and Fermi energy of the bulk metal, respectively. The last two quantities are obtained in separate calculations on clean platinum bulk. The d-band density of states was determined by projection of the plane waves onto spherical harmonic orbitals. Centers of d-bands were calculated with infinite cutoff radius.

RESULTS AND DISCUSSION

Work Function

The results of work function calculations are listed in Table 1. The results of two different methods of cal-

culation agree mutually very well, namely the differences between values obtained by means of Eq. (1) and Eq. (2) are less than 0.05 eV. Furthermore, the data agree well with the corresponding experimental values for Pt(111), Pt_3Sn/Pt(111), Pt_2Sn/Pt(111) and Sn monolayer on Pt(111) are 5.8, 5.4, 5.2 and 4.2 eV, respectively [2].

For surface alloy we would like to emphasize that we confirmed linear relationship between work function and mole fraction of Sn (Fig. 2), found previously experimentally by Paffet et al. [2]. In this sense, one may expect the linear relationship between W and mole ratio (x) in Pt_xBi_{1-x}/Pt(111) surface alloys. This is an interesting behavior, particularly in the light of data that work function of regular bulk alloys show deviation from the additivity line, as shown theoretically by Gelatt and Ehrenreich [21], and demonstrated experimentally by Ishii and co-workers [22]. Observed rule may have significant practical significance, allowing predicting of work function of these particular systems, interesting not only in catalysis and electrocatalysis but also in electronics and related fields.

In Fig. 2 the dependence of work function of Pt(111) surface with adsorbed metal atoms on adsorbate concentration, is presented too. In this case work function displays a remarkable negative deviation from the line of additivity. Most probably this can be understood in terms of direction of dipoles generated on the surface. In the case of surface alloys, dipoles created due to charge transfer from Sn and Bi atoms toward Pt surface atoms are parallel with the surface, while certain charge redistribution between the first and the second surface layers causes decrease of the work function. In case of adsorbed metal atoms, generated dipoles are perpendicular to the surface.

The Electronic Structure

In this section we consider the position of the *d*-band center of studied surfaces. First of all, in view of Fig. 1, it is important to point out that all the Pt atoms in the studied surface Pt_xM_{1-x} alloy layers are equivalent due to the symmetry. In the case of metal adsorption, one can not expect that electronic structure of all of the surface Pt atoms is uniformly modified. For instance, preferential adsorption site for Sn and Bi adsorption may be expected to be fcc hollow site. For such a case, adsorbed atoms touch three Pt surface atoms. Consequently, *d*-bands of closely placed Pt atoms are expected to shift toward lower energies (to be stabilized). However, one cannot know a priori how the electronic structure of other surface atoms is going to be modified.

In the case of the studied surface alloys, one can see that the *d*-band is stabilized as the amount of the solute in the surface layer is increased (Table 2). Stabilization of the *d*-band indicates that Pt–M bonds are stronger than Pt–Pt bond, and that the effective coordination number of the surface Pt atoms is enlarged. Stabilization is soundy with the theory of Ruban et al. [12] explaining it in terms of lateral strain. Namely, larger atom (Bi) causes greater stabilization of the platinum d-band, than the smaller (Sn) one. Analysis of projected density of states (PDOS) reveals that Pt–M interaction is achieved through *sp–d* hybridization. This is presented in Fig. 3a for the case of Pt_2Sn/Pt(111) surface alloy. As it can be seen, *d*-orbitals of Sn remain completely filled (like in isolated atom) and do not participate in the bonding. The same holds for Bi, having in mind that position of the appropriate bands is different due to different position of the atom in the Periodic Table of Elements. In addition, stabilization of *d*-band is in good agreement with reduced adsorption energies of H_2, O_2 and CO species on PtSn surface

Table 1. Work functions values (eV) for (I) alloyed and (II) adsorbed Sn and Bi monoatomic layers on Pt(111) surface, calculated by means of Eq. (1) and Eq. (2) (the later are given in parentheses, X is mole fraction of M (coverage))

X	Sn		Bi	
	I	II	I	II
0*	5.83 (5.88)	5.83*	5.83*	5.83*
0.25	5.49 (5.48)	4.60	5.57 (5.61)	4.63
0.33	5.30 (5.32)	4.54	5.54 (5.59)	4.56
1	4.13 (4.12)	4.13**	4.26 (4.27)	4.26**

* Clean Pt(111) surface.
** Monolayer, the same system is obtained by increasing amount of solute in the surface layer and the adatoms on the surface layer.

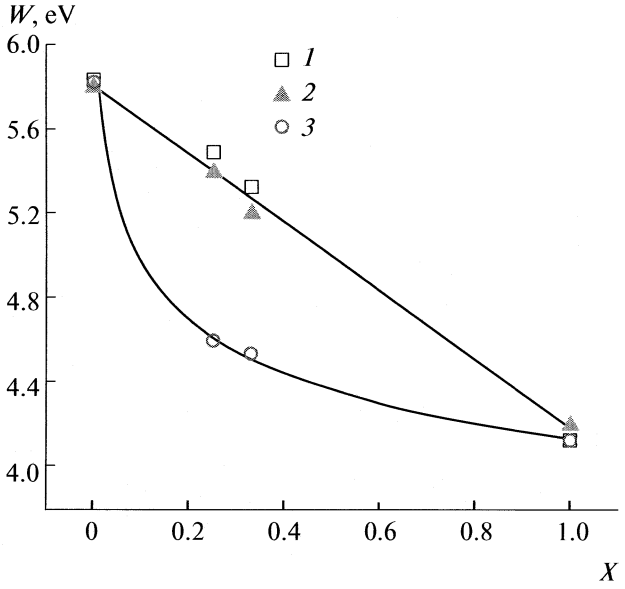

Fig. 2. (*1*) Calculated work functions (W) for Pt_xSn_{1-x} surface alloys and Sn adsorbed on Pt(111) surface; X is mole fraction of Sn in the surface layer (coverage); (*2*) experimentally obtained data for PtSn surface alloys [2]; (*3*) Sn adsorbed on Pt(111) (calculated).

Table 2. Positions of the *d*-band centers (eV) of the surface platinum atoms with respect to Fermi energy

θ	Sn	Bi	Sn	Bi
	surface alloy		adsorbed metal	
0.25	−2.174	−2.268	(−2.398) −2.061	(−2.478) −2.058
0.33	−2.290	−2.302	(−2.415)	(−2.490)

Note. For adsorbed metals, *d*-band centers of bonding Pt atoms are given in parentheses, while the second value corresponds to the position of ε_d of "free" Pt atom. For the case of clean Pt(111) surface $\varepsilon_d = -2.084$ eV

alloys [2]. According to the position of ε_d, one might expect that the adsorption energies of these species decrease if decreases the content of Sn, as already shown experimentally [2]. Furthermore, higher electrocatalytic activity for HER was both predicted and proved by Greely et al. [10] for the case of PtBi surface alloys, which corresponds to the downshift of the ε_d of Pt atoms in PtBi surface alloys, found here.

In the case of the adsorption, situation is slightly more complicated. For preferred fcc hollow sites and the coverage $\theta = 0.25$, three "bonding" Pt atoms interact with one adsorbed atom and with one "free" Pt atom. As expected, all bonding Pt atoms are mutually equivalent, and their *d*-bands are stabilized by adsorption. The data in the Table 2 show that this type of stabilization is more pronounced than the stabilization induced by alloying. In addition, stabilization of *d*-band of platinum is proportional to the adsorption energy: Bi atom has slightly higher adsorption energy than Sn atom which is in direct relationship with stabilization of the band. It is worthy of mention that *d*-band of the "free" surface Pt atom is being destabilized, as ε_d is shifted to the higher values. One might explain this by increased coordination number of bonding Pt atoms which results in destabilization of Pt–Pt bond in the surface. As a result, free Pt atoms are not bonded to neighboring Pt atoms as strong as in clean Pt(111) surface. This is supported by observation that up-shift of the free Pt atom *d*-band is proportional to the adsorption energy of adatoms. When the surface coverage is increased to $\theta = 0.33$ there are three "bonding" Pt atoms and no "free" Pt atoms. That means, due to the symmetry, all Pt atoms in the surface layer become equivalent. In this case we observed more pronounced stabilization of the *d*-band of bonding Pt atoms than in the cases of both lower coverage by adsorbate and alloy formation.

PDOS for bonding Pt atoms and adsorbed Sn atoms are given in Fig. 3b. Both *s* and *p* states of Sn atom participate in bonding, while *d* states of Sn remain highly localized, just like to the case of PtSn surface alloys. It is interesting to note that in the case of surface alloys *s* and *p* states of Sn equally contribute to occupied and unoccupied states. On the other hand, in the case of the adsorption of Sn, *s* states almost completely contribute to the occupied states, while *p* states predominantly contribute to the unoccupied states.

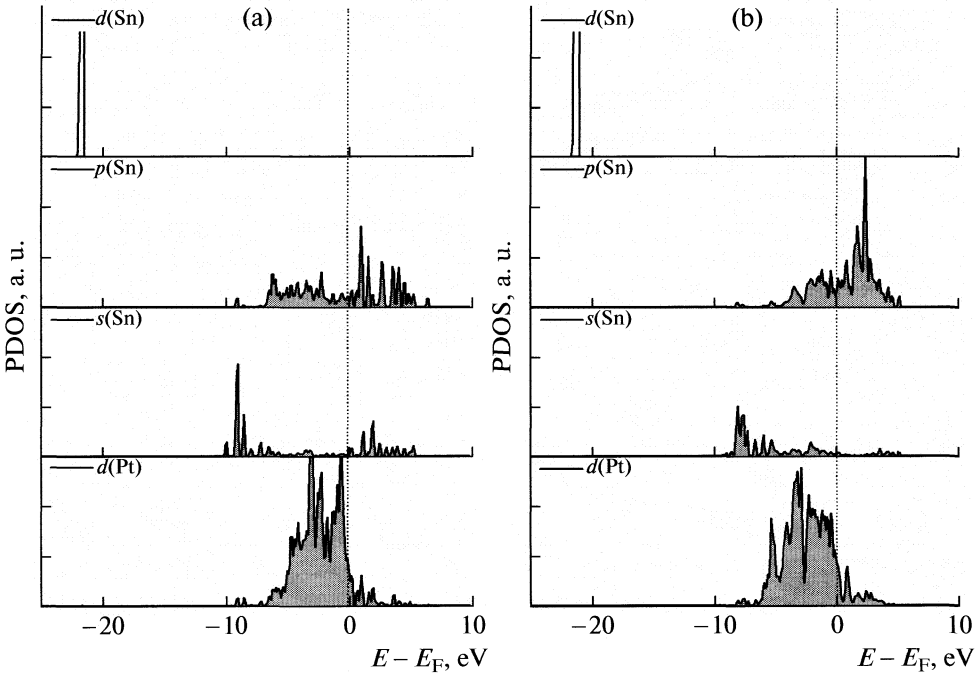

Fig. 3. Projected densities of states (a) of Sn and Pt atoms in the $Pt_2Sn/Pt(111)$ surface alloy layer and (b) of Sn adsorbed onto Pt(111) surface and *d* states of binding Pt atoms.

At this point we would like to comment the electrocatalytic activities of Bi_{ir}–Pt(111) and Pt_xBi_{1-x}/Pt(111) surfaces for HER. In the two mentioned cases, very different activities were observed experimentally: the former surface shows remarkably reduced activity [9], while the later one has improved activity [10] in comparison to pure Pt(111) surface. However, with respect to ε_d values only given in Table 2, similar catalytic activities of both surfaces should be expected, both being higher in comparison to clean Pt(111) surface. This indicates that, in order to explain mentioned differences toward HER, geometrical effects due to size and position of large Bi atoms on (in case of the adsorption) and in the surface layer (in case of the alloying of the surface) should to be taken into consideration. More important, one has to conclude that the geometric effects have the leading role in determination of catalytic activity in these two cases. At this point, it seems to be clear why Gomez and co-workers [9] were able to explain reduced activity of Bi_{ir}–Pt(111) relying only on the geometrical effects and using purely statistical models which do not involve electronic structure of the surface.

We demonstrated for $\theta(Bi) = 0.25$ that electronic structure of surface Pt atoms is tuned in two different ways, depending whether Bi atom is bonded to them or not. In addition, although the position of ε_d is shifted to the more negative values, for "free" Pt atoms it remains very close to the ε_d position of Pt atoms in pure Pt(111) surface. Accordingly, it seems that modification of electronic structure of Pt(111) with adsorption of Bi is not long-ranged, but rather localized to adsorption site. This is opposite to the observation of the Herrero and co-workers [23], who emphasized the work of Feibelman and Hamann [24] that modification of electronic properties of the surface upon adsorption is (generally) long-ranged. Their conclusion was based on analysis of both S adsorption onto Rh(001) surface and local density of states at E_F (LDOS(E_F)). One should be rather careful with the application of these results, because Hammer and Nørskov [11] clearly showed that LDOS(E_F) is not able to represent entire d-band, and, in addition, that states lying below E_F are also involved in bonding and participate in determination of reactivity of the surface. Localization of electronic effects to adsorption site is important due to the fact that Gomez et al. [9] found that one Bi atom blocks approximately 20 platinum surface sites for hydrogen adsorption, which is clearly not expected from presented results. This indicates that certain attention to experimentally observed surface diffusion of Bi adatoms should be paid. In order to elucidate how diffusion of Bi adatom may affect the adsorption of hydrogen, one can imagine large Bi atom moving over the surface, tearing adsorbed H of the surface, such affecting (effectively) more adsorption sites than one can expect on the basis of its size and ability to modify electronic structure of substrate atoms.

CONCLUSION

In the presented paper, the modification of electronic structure of Pt (111) surface by either alloying with, or adsorption of, Sn and Bi atoms, was studied by DFT calculations. In the case of Pt_xM_{1-x}/Pt(111) surface alloys (M = Sn, Bi), linear decrease of the work function with increasing amount of the solute in the surface layer was evidenced. In the case of adsorption, the dependence of the work function on coverage shows decrease accompanied by pronounced negative deviation from additivity, for increased coverage by both Sn and Bi. The later behaviour was attributed to the orientation of generated surface dipoles.

Particularities of the cases of alloying and adsorption were studied also by considering the position of the *d*-band centers. In the case of surface alloys, all surface Pt atoms were considered to be equivalent, and their *d*-band center was found to shift toward higher binding energies, what agrees with the model proposed by Ruban et al. [12]. When Sn and Bi atoms were adsorbed on Pt(111) surface, the modification of electronic structure of the surface Pt atoms was found to be coverage dependent: *d*-bands of bonding Pt atoms are being stabilized, while *d*-band of free Pt atoms are being destabilized. On the basis of calculations performed in this study, and the experimental data published elsewhere [10], catalytic activity of Bi_{ir}-Pt(111) and Pt_xBi_{1-x}/Pt(111) surfaces toward HER was considered. It was concluded that electronic properties only may not explain the experimentally evidenced differences in catalytic activities, but geometrical effects should be considered too.

ACKNOWLEDGMENTS

This work was carried out within the project No. 142047, supported by the Serbian Ministry of Science.

REFERENCES

1. A. N. Haner, P. N. Ross, U. Bardi, Catal. Lett. **8**, 1 (1991).
2. M. T. Paffett, S. C. Gebhard, R. G. Windham, B. E. Koel, J. Phys. Chem. **94**, 6831 (1990).
3. M. C. Santos, L. O. S. Bulhões, Electrochim. Acta **48**, 2607 (2003).
4. Z. Karpinski, J. K. A. Clarke, J. Chem. Soc. Trans. Faraday 2 **71**, 893 (1975).
5. H. A. Gasteiger, N. M. Marković, P. N. Ross, Langmuir **12**, 1414 (1996).
6. N. M. Markovic, P. N. Ross, Surf. Sci. Rep. **45**, 121 (2002).
7. E. Casado-Rivera, Z. Gal, A. C. D. Angelo, C. Lind, F. J. DiSalvo, H. D. Abruňa, Chem. Phys. Chem. **4**, 193 (2003).
8. U. W. Hamm, D. Kramer, R. S. Zhai, D. M. Kolb, Electrochim. Acta **43**, 2969 (1998).

9. R. Gomez, J. M. Feliu and A. Aldaz, Electrochim. Acta **42**, 1675 (1993).
10. J. Greeley, T.F. Jaramillo, J. Bonde, I. Chorkendorff, J. K. Nørskov, Nat. Mater. **5**, 909 (2006).
11. B. Hammer, J.K. Nørskov, Surf. Sci. **343**, 211 (1995).
12. A. Ruban, B. Hammer, P. Stolze, H. L. Skriver, J. K. Nørskov, J. Mol. Catal. A: Chemical **115**, 421 (1997).
13. J. R. Kitchin, J. K. Nørskov, M. A. Barteau and J. G. Chen, J. Chem. Phys., **120**, 10240 (2004).
14. J. R. Kitchin, J. K. Nørskov, M. A. Barteau and J. G. Chen, Phys. Rev. Lett. **93**, 156801 (2004).
15. N. D. Lang, W. Kohn, Phys. Rev. B **28**, 1215 (1971).
16. S. Baroni, A. Dal Corso, S. de Gironcoli, P. Giannozzi, C. Cavazzoni, G. Ballabio, S. Scandolo, G. Chiarotti, P. Focher, A. Pasquarello, Quantum-ESPRESSO, http://www.pwscf.org.
17. J. P. Perdev, K. Burke, M. Ernzerhof, Phys. Rev. Lett. **77**, 3865 (1996).
18. N. Marzari, D. Vanderbilt, A. de Vita, M.C. Payne, Phys. Rev. Lett. **82**, 3296 (1999).
19. H. J. Monkhorst, J. D. Pack, Phys. Rev. B **13**, 5188 (1976).
20. C. J. Fall, N. Binggeli, A. Baldereschi, J. Phys.: Condens. Matter. **11**, 2689 (1999).
21. C. D. Gelatt Jr., H. Ehrenreich, Phys. Rev. B **10**, 398 (1974).
22. R. Ishii, K. Matsumura, A. Sakai, T. Sakata, Appl. Surf. Sci. **169–170**, 658 (2001).
23. E. Herrero, M. J. Llorca, J. M. Feliu, A. Aldaz, J. Electroanal. Chem. **394**, 161 (1995).
24. P. R. Feibelman, D. J. Hamann, Phys. Rev. Lett. **52**, 61 (1984).

ЖУРНАЛ ФИЗИЧЕСКОЙ ХИМИИ, 2009, том 83, № 9, с. 1713–1717

STRUCTURE OF MATTER AND QUANTUM CHEMISTRY

УДК 539.192

SOLVENT–REAGENT EFFECT IN CHEMICAL DETECTION OF ENERGETIC MATERIALS TYPE CONTAMINANTS

© 2009 E. Dimitriu*, S. C. Moldoveanu**, E. E. Iorgulescu***

*REGO COM, Calea 13 Septembrie 115, Bl. 111, Bucharest – 5, Romania

**R.J. Reynolds. Co., 950 Reynolds Blvd,. Winston-Salem NC, USA

***University of Bucharest, Faculty of Chemistry, Department of Analytical Chemistry, Sos. Panduri, no. 90, Bucharest-5, Romania

E-mail: edimit945@yahoo.com; smoldov@aol.com

Abstract – Present study extended the list of solvent and reagents appropriate to use for the colorimetric detection and semi quantitative analysis of various energetic compounds. The new reagents used in this study include DMSO as solvent/reagent, and tetramethylammonium hydroxide and tetrabutylammonium hydroxide for the generation of a basic medium. The advantages of these reagents vs. older procedures are discussed in this paper. Also, a standardized procedure for the analysis of several classes of energetic compounds has been developed, allowing an excellent practical application of the recommended method. The influence of different solvents on the changes in the UV-VIS spectra were evaluated and an attempt to interpret the resulting absorption UV spectra based on quantum chemical calculations has been done.

INTRODUCTION

Detection and identification of energetic compounds is a vital problem, due to the direct risks posed of these substances towards the people life and material damages during explosion (detonation). The environmental contamination with post-blasting reaction products, and with wastes resulted from the reaction products of explosive compounds and munitions or from unexploded ordnance, represents another potential risk [1]. Energetic materials, such as military explosives, propellants and pyrotechnics are classified according to their explosive properties (primary and secondary explosives) and chemical composition (nitroderivates, nitramines, esters nitrates, inorganic salts, peroxide – based explosives). A huge number of studies are dedicated to the synthesis, characterization, detection and identification, degradation and removal of energetic compounds, and identification of their environmental transformation products [2–10]. Experimental results were correlated with theoretical studies for monitoring the environmental contamination risk [11]. An energetic compound is rendered soluble with a suitable solvent. Protic solvents (as ethanol, isopropanol), amphiprotic solvents (as water, methanol) and dipolar aprotic solvents (as acetone, dimethyl sulfoxide (DMSO), dimethyl formamide, acetonitrile) are used for the solvation or extraction of energetic compounds.

Usually, the hydrogen atoms in dipolar aprotic solvents are not ionisable and do not form hydrogen bridges. If the hydrogen atoms are bonded to oxygen, or other more electronegative atom than carbon, hydrogen bridges could occur in the presence of proton-acceptors compounds. The dipolar aprotic solvents are polarized and interact with polarizable ions. These properties, together with values of dielectric constant ($\varepsilon > 15$) higher than in non-polar aprotic solvents, recommend the dipolar aprotic solvents as the best medium for reactions with a nucleophile substitution mechanism and for increase the ratio of energetic materials solvation. For instance, the exhaustive extraction time of secondary explosives from soil, with acetone is 1 min, while with methanol (a protic solvent) is 3 min [10]. The resulted extract is subjected to chemical identifications.

Two types of tests are used for chemical identification of functional groups: a) direct tests, in which they form coloured reaction products, in the presence of certain reagents, and b) indirect tests, in which an intermediary reaction product is formed, and this one is identified with a specific reagent [1, 3, 8]. The nitroaromatic compounds are detected by direct tests from the absorbance of the coloured Meisenhaimer or Janowsky anions [10]. The detection of nitramines and nitrates esters is achieved in three steps. First, the hydrolysis reaction in alkaline medium forms nitrite ions, which allow the diazonium ion formation with sulphanilamide (or other aromatic amine) in acid medium and finally the formation of pigments during a Griess-Ilsovay reaction, with coupling reagents (naphtylamine reagents or any other N-substituted aromatic amine, phenols or naphtols) [12–14].

This study is focused on colorimetric identification of post-explosion debris with simple operations, good selectivity, and sensitivity of the order from nanograms to milligrams. The method is extended to prevent or to manage the environmental pollution with energetic compounds. Mixtures of solvents and reagents are

Table 1. Solvents and reagents used for polynitroaromatics identification

no	Solvent + reagent (proportion by volume)	Explosive compound tested/colour	Colour test with reagents stocked during 10 months
1	Acetone + DMSO + KOH 9 wt % soln. (1 : 1 : 1.3)	TNT/Red-brown	TNT/red-brown
2	Acetone + methanol + DMSO + + KOH 9 wt % soln. (4 : 1 : 1.3 : 3)	TNT/Red-brown	TNT/red-brown Astralita/red-violet
3	Acetone + metanol + DMSO + + TMAH (2 : 1 : 1.5 : 0.5)	TNT/Red-brown Dynamite/yellow-green with violet on the boundary of the spot Astralite/Red-brown -violet	TNT/violet Dynamite/green-brown Astralite/red-violet
4	Methanol + DMSO + TMAH (1.5 : 8 : 5)	TNT/Red- violet	TNT/red-brown Dynamite/green-brown Astralita/red-brown
5	Methanol + DMSO + NaOH soln.	TNT/violet	–
6	DMSO + TBAH	TNT/red-violet	–

tested for colorimetric identification of energetic compounds. Solute–solvent interactions are evidenced by changes in the UV-VIS spectra. Theoretical aspects using a computational method to obtain Highest Occupied Molecular Orbitals (HOMO) and Lowest Unoccupied Molecular Orbitals (LUMO), are presented in an attempt to calculate the expected wavelength of absorption spectra. For this purpose, the energy levels of HOMO and LUMO orbitals were calculated for some explosives and their coloured anions. The stability in time of reagents is discussed, and finally, a procedure for on-site identification of organic energetic compounds is proposed.

EXPERIMENTAL

In this study, an in situ colorimetric method for identification of organic energetic materials was evaluated. The following energetic materials were investigated: polynitroaromatics [2, 4, 6- trinitrotoluene (TNT), trinitrobenzene (TNB), tetranitroaniline (TNA), 2,4,6-trinitro-1,3,5-triazine (TNTA)], nitrates esters [explosive blends with nitroglycerine content (dynamite, astralite, AGP explosive), pentraeritrol tetranitrate (PETN or pentrite)], nitramines [2,4,6-trinitrophenyl-N-methylnitramine (Tetryl), RDX (cyclotrimetilen trinitramine, or Hexogene or Cyclonite)]. Mixtures of amphiprotic solvent (methanol) and dipolar aprotic solvents (acetone, DMSO) have been used.

Three types of reagents were prepared.

Reagent 1: any of the alkaline reagents for polynitroaromatics identification were aqueous solutions of sodium hydroxide and potassium hydroxide, and solutions of tetramethylammonium hydroxide (TMAH) and tetrabutylammonium hydroxide (TBAH) in methanol.

Reagent 2: a) solution containing sulphanilamide 1 wt %, and hydrazine sulphate 1 wt % (10/1, V/V); b) solution containing sulphanilamide 2.5 wt %, and hydrazine sulphate 1 wt % (10/1, V/V)

Reagent 3: a) N-(1-Naphtyl) ethylenediamine dichloride 1 wt %, and b) N-(1-naphtyl) ethylenediamine dichloride 1 wt % + H_3PO_4.

Procedure for energetic materials identification. Amount of energetic materials less than 10^{-3} g were collected on filter paper [1], and solvated with several groups of solvents, presented in Table 1. On the same filter paper reagent 1 is dropped. The presence of TNT or explosives with TNT content is shown by the formation of a pink, or red or red-brown colour, function of the increasing TNT concentration.

If no colour appears, on the same filter paper, one drops, successively, the reagents 2 and 3 for the identification of nitrates esters, nitramines and nitrites. A pink or violet colour formed in less than 30 minutes indicates the presence of the above compounds, for any of the solvents mixtures have been used. The tested compounds and the colour formed were: nitrocellulose/pink, Rovex, pentrite, and EPH88/pinkish violet, AGP/violet.

The differences observed in the coloured anions used for energetic compounds identification were further investigated by computational methods. The calculated maximum wavelength obtained from the differences between the energy levels of HOMO and LUMO orbitals are compared with those resulted from experimental UV-VIS records data, indicated in other studies. The calculations were performed with MOPAC-7, and AM1 parameters [15–17]. The geometries were initially obtained using structures in Alchemy 2000 (Tripos Assoc.) and an original program [17] and further optimized in MOPAC-7 program.

UV-VIS absorption spectra of Janowsky-type anion of TNT in protic and dipolar aprotic solvents were measured on a Jasco (V-530) double beam spectrophotometer. The measurements were done using 1 cm path quartz cells, on the spectral domain 300–600 nm.

The scanning speed for spectra recording was 100 nm/min.

Kits for energetic materials detection: Based on the results of the present study two kits for organic energetic materials detection were proposed. These kits are described below.

Kit 1 contains the following type of materials:

Materials for sample collection: porous paper (for solid samples), pipetes (for liquid samples).

Drop bottles with reagents:

Reagent 1 is a mixture of solvents and organic hidroxide, namely DMSO/methanol/TBAH solution 25 wt % = 3.2/2.8/1; reagent 2 contains sulphanilamide 2.5 wt %, and hydrazine sulphate 1 wt %, acidulated with HCl (10/1 V/V); reagent 3: N-(1-naphtyl) ethylenediamine dichloride 1wt%.

Kit 2 contains reagent 1 and reagent 2 and a limited number of pieces of paper filter impregnated with reagent 3.

The procedure for energetic materials identification has been described previously.

RESULTS AND DISCUSSIONS

The new reagents/solvents utilized in the present study are in the line of previous work that uses acetone and a strong inorganic base (KOH, NaOH) to generate a colour reaction from nitroaromatic compounds. Similarly to acetone, which in the presence of a base forms a Janowsky anion with nitroaromatic compounds, DMSO also forms a coloured compound. The strong base is likely to form with DMSO an anion of the form $CH_3(SO)CH_2^-$. This anion reacts with nitroaromatic compounds forming a Janowsky-type anion [10], as shown in the following reaction for TNT:

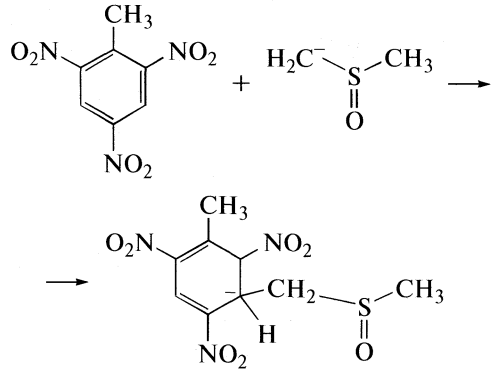

Since DMSO can be a better solvent than acetone, this reagent is preferred. Also, the base KOH or NaOH previously used to form either Meisenheimer ions or (in the presence of acetone) a Janowsky ion, can be replaced with an organic base such as TMAH or TBAH. The advantages of these bases are their solubility in organic solvents and lower propensity to deteriorate the matrix and form interfering colours.

The use of various mixtures of solvents and/or of TMAH and TBAH showed that the addition or absence of a specific solvent or base may induce considerable variation in the UV-VIS spectra of the Janowsky type anion generated from nitroaromatic compounds. This is exemplified in figure, where are given the absorption spectra for TNT/DMSO Janowsky anion in different solvent mixtures.

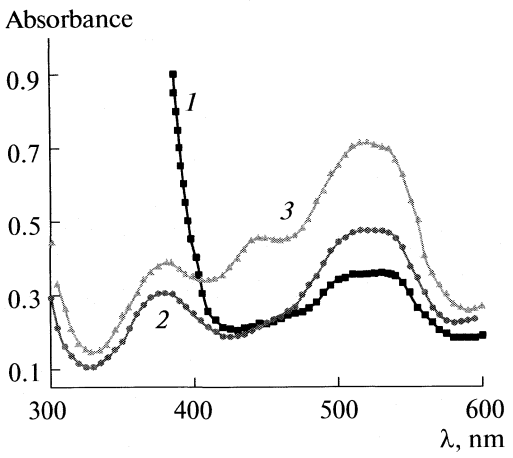

Absorption spectra of (*1*) Janowsky TNT anion in methanol and DMSO with NaOH, (*2*) a mixture of methanol and DMSO with NaOH and TBAH, (*3*) a mixture of DMSO with TBAH

The variability in the maximum intensity and shift in the wavelength with the addition of various solvents/reagents can be caused by both solvent interaction effects, and also by the formation of different molecular coloured species. In an attempt to determine the "theoretical" value for the wavelength of the absorption spectra, a quantum chemical calculation was performed with the determination of the energy levels of HOMO and LUMO orbitals, following the calculation of the maximum absorption wavelength, λ for the molecule in ideal gas form. The calculation was done using the expression:

$$\lambda, \text{nm} = 1240.27/\Delta E(\text{eV}).$$

The results of the calculations for the theoretical expected absorption wavelength are given in Table 2. The calculations were performed for the free compound, expected Meisenheimer ion, Janowsky ion, and DMSO adduct. In addition, for TNA and TNDA it was attempted to calculate the energy levels for a Schiff base formed with acetone by these amines. (Heats of formation and dipole moments are also shown). As seen from Table 2, good agreement of experimental results with the theoretical values for the absorption spectra is observed for many compounds, such as TNB-Meisenheimer anion, TNB-Janowsky anion, TNT-Meisenheimer anion, TNT-Janowsky anion, Tetryl-Meisenheimer anion, and Tetryl-Janowsky anion. However, for the compounds involving DMSO, the results are not in agreement with the experiment, and much longer absorption wavelengths were predicted.

Table 2. Theoretical results for the HOMO, and LUMO energy levels, and the calculated absorption wavelength for several compounds, used for the analysis of energetic compounds and heats of formation ($\Delta_f H$, kcal/mol) and dipole moments (μ, D)

Compound	$-E$(HOMO), eV	$-E$(LUMO), eV	λ, nm	$\Delta_f H$, kcal/mol	μ, D
TNB	12.24	2.53	127.60	44.88	0.02
TNB-Meisenheimer anion	7.82	5.51	536.76	−91.94	1.13
TNB-Janowsky anion	7.85	5.55	539.02	−89.43	2.72
TNB DMSO	6.18	5.57	2020.43	−28.05	3.30
TNT	11.70	2.44	133.94	41.29	1.44
TNT-Meisenheimer anion	7.52	5.43	595.54	−92.82	1.53
TNT-Janowsky anion	7.83	5.56	547.75	−89.29	2.73
TNT DMSO	6.21	5.58	1974.40	−27.88	3.43
TNA	12.45	0.16	100.85	34.16	3.46
TNA-Meisenheimer anion	6.41	5.50	1356.56	−96.69	2.04
TNA-Janowsky anion	6.44	5.59	1455.19	−95.59	1.32
TNA DMSO	6.11	5.60	2404.13	−34.48	2.07
TNA Schiff	10.82	2.29	145.42	61.97	4.53
TNDA	10.28	1.81	146.33	25.39	3.24
TNDA-Meisenheimer anion	6.15	5.61	2315.12	−101.21	3.79
TNDA-Janowsky anion	6.22	5.65	2186.52	−101.64	2.46
TNDA DMSO	5.99	5.65	3687.40	−40.55	1.70
TNDA Schiff	10.28	1.94	148.65	51.82	4.87
TNDA two Schiff	10.43	1.89	145.26	70.33	5.40
TNTA	10.19	1.37	140.65	20.65	0.15
Tetryl	11.71	2.96	141.66	90.80	3.35
Tetryl-Meisenheimer anion	8.03	5.82	563.11	−53.29	2.75
Tetryl-Janowsky anion	8.07	5.85	558.59	−48.71	3.59
Tetryl DMSO	6.30	5.86	2827.11	12.70	3.35
Griess	8.26	1.09	173.03	52.85	5.88

Table 3. Theoretical results using UHF calculations and calculated absorption wavelength for several compounds between DMSO and nitroaromatic compounds, (and heats of formation and dipole moment)

Compound	$-E$(HOMO), eV	$-E$(LUMO), eV	λ, nm	$\Delta_f H$, kcal/mol	μ, D
TNB DMSO	7.89	5.56	532.30	−27.95	3.22
TNT DMSO	7.84	5.57	543.94	−27.35	3.35
TNA DMSO	6.46	5.58	1409.40	−34.44	2.02
TNDA DMSO	5.99	5.63	2067.12	−40.51	1.66
Tetryl DMSO	8.06	5.84	558.68	+12.66	3.30

Performing an Unrestricted Hartree–Fock (UHF) calculation and, considering a different transition than HOMO–LUMO, allowed to predict the absorption wavelength values much closer to those found in experimental spectra for TNB–DMSO, TNT–DMSO and Tetryl-DMSO compounds (Table 3). These results are shown in Table 4. The theoretical results from Tables 2 and 3, and the disagreement with the experimental wavelength of absorption would indicate that TNA, and TNDA do not form either Meisenheimer or Janowsky products.

Their colour may be generated by the formation of other reaction products. The results also show that more than one transition can possibly explain the spectra of the compounds generated in the analytical identification of nitroaromatic compounds in reactions of Meisenheimer–Janowsky type.

Table 4. Visible absorption maxima, (λ_{max}), of some polynitroaromatics explosives [1] (EDA-ethylenediamine)

Compound	Solvent/reagent	λ_{max}, nm
1,3,5-TNB	1% EDA in DMSO	455 540
2,4,6-TNT	50% EDA in DMSO	465 540
2,4,6-TNA	Ethanol + NaOH	488–491 411–412
	2% EDA in DMSO	418
1,3-Diamino-2,4,6-TNB (DATB)	DMSO	417
	2% EDA in DMSO	412
1,3,5-Triamino-2, 4, 6-TNB (TATB)	2% EDA in DMSO	418
2,4,6-TNT [10]	Methanol/NaOH	516
	Acetone/KOH	540

These theoretical values are not identical but close (for most compounds) with those measured in solutions, which are influenced by various additives used for practical purposes during the analytical determination (see figure and Table 4).

Among the solvent/reagents pairs, a special role is played by DMSO. If in the identification of TNT and some of polynitroaromatics, the DMSO is reagent, for all other compounds, DMSO is a very good solvent, with high stability in time, and no effect on the operator health. The solutions of tetramethylammonium hydroxide and tetrabutylammonium hydroxide in methanol presented a higher stability in time compared to NaOH or KOH. The highest stability in time is observed for the reagents 4 and 6 from Table 1, with the content of DMSO and TMAH.

CONCLUSIONS

Solvent/reagent mixtures were used for colorimetric identification of energetic compounds. In the proposed colorimetric procedure, the mixture of methanol with DMSO and TMAH or TBAH is the most suitable for solvation and identification of the polynitroaromatics and for dissolvation of nitrates esters and nitramines. The measured absorption wavelenghts in UV-VIS of coloured products developed during reactions for TNT, TND and Tetryl in DMSO, are in good agreement with those calculated using a computational method to obtain the energy levels of HOMO and LUMO orbitals.

REFERENCES

1. J. Yinon, S. Zitrin, *The Analysis of Explosives. Pergamon Series in Analytical Chemistry*, Vol. 3, Pergamon Press, New York, 1981.
2. A. Beveridge, J. Energetic Materials **4**, 29–75 (1986).
3. T. Urbanski, *Chemistry and Technology of Explosives*, Vol. 3; Pergamon Press: Oxford, 1965.
4. B. Glattstein, European Patent Application, 1988, **0 264 252 A2**, Int. Cl. G 01 N 31/22.
5. D. S. Moore, Sens. Imaging (2007) 8:9–38 DOI 10.1007/s11220–007–0029–8.
6. A. Hilmi, J. H.T. Luong, An-Lac Nguyen, J. Chromatography A **844** (1–2), 97–110 (1999).
7. A. B. Crockett, H. D. Craig, and F. F. Jenkins. **EPA/600/S–99/002**, May 19, 1999.
8. Fritz Feigl, *Spot Tests, Vol. II. Organic Applications*, Fourth, Completely Revised English Edition, Elsevier Publishing Co, Amsterdam, Houston, London, New York, 1954.
9. D. De Tata , P. Collins, N. Campbell, J. Forensic Sciences **51** (2), 303 (2006) doi:10.1111/j.1556–4029.2006.00075.x.
10. T. F. Jenkins, P.W. Schumacher, J. G. Mason, P. G. Thorne, 1996, **Special report 96–10**. US Army Corps of Engineers. Cold Regions Research & Eng. Lab.
11. M. M. Quasim, B. Moore, L. Taylor, P. Honea, L. Gorb, J. Leszcznsky, Int. J. Mol. Sci. 2007, **8**, 1234–1264.
12. Jay B. Fox, Jr. Analytical Chemistry, **51** (9) 1493 (1979).
13. T. F. Jenkins, D. C. Leggett, C. L. Grant, C. F. Bauer, Anal. Chem. **58**, 171 (1986).
14. J. Fries, H. Getrost, *Organic Reagents for Trace Analysis*, E. Merck, Darmstadt, 1977.
15. J. J. P. Stewart, J. Comp.-Aided Mol. Design **4**, 1–105 (1990), Special Issue.
16. J. J. P. Stewart, MOPAC-7, QCPE 113, Indiana Univ. Bloomington, 1994.
17. S. C. Moldoveanu. Unpublished Results.

ЖУРНАЛ ФИЗИЧЕСКОЙ ХИМИИ, 2009, том 83, № 9, с. 1718–1722

STRUCTURE OF MATTER AND QUANTUM CHEMISTRY

УДК 543.42:541.64

COPPER, IRON AND ZINC INTERACTIONS WITH CHLOROPHYLL IN EXTRACTS OF PHOTOSYNTHETIC PIGMENTS STUDIED BY VIS SPECTROSCOPY

© 2009 J. Zvezdanović*** and D. Marković*

*University of Niš, Faculty of Technology, 16000 Leskovac

**Scholar of Ministry of Science and Technological Development of the Republic of Serbia, Belgrade

E-mail: jelite74@yahoo.com, dejan_markovic57@yahoo.com.

Abstract – Interactions of copper, iron and zinc with chlorophyll, the major photosynthesis pigment, were studied by VIS spectrophotometry in extracts of photosynthetic pigments (in vitro). Copper predominantly forms Cu–Chl complexes in all studied systems (Cu-, Cu/Fe-, Cu/Zn-, and Cu/Fe/Zn-incubated pigment solutions). It is not clear whether iron forms Fe–Chl complexes or produces pheophytin. It's effect is dominant over zinc (Fe/Zn-system) but highly minor compared to Cu-effect when all three metals are present (Cu/Fe/Zn–Chl system) in the same concentrations.

INTRODUCTION

Chlorophyll (Chl), a major photosynthesis pigment, in chemical terms is a porphyrin derivative (a cyclic tetrapyrrole with an isocyclic cyclopentanone ring fused to a C-pyrrole ring between the C13 and C15 positions), where the central magnesium (Mg) atom coordinates four symmetric pyrrole rings (Fig.1). Heavy metals can replace the labile bonded central Mg-atom of chlorophyll to form substitutional or "central" Chl-HMS complex (heavy metal complex), or they can play a coordinating role between two O-atoms ($C13^1$ and $C13^3$, Fig. 1) at periphery of Chl-molecule to form a cyclic 6-membered peripheral "chelate" complex [1, 2].

Plants easily absorb many toxic heavy metals. Once absorbed, they penetrate the plant tissues (including the leaves) and, in higher concentrations, they may inhibit photosynthesis [3–6]. In lower concentrations copper, iron and zinc themselves are essential micronutrients for higher plants and algae, and "constituents" of photosynthetic apparatus – photosystems I and II (Cu-protein – plastocyanin, Fe-containing electron-carriers in cytochrom complexes) [7]. Zinc-porphyrins are formed during chlorophyll biosynthesis, but they are also found in Chl-degradation products [8]. However, high external metal-concentrations (copper, iron, zinc) – like the ones used in this work – may produce a lot of damaging effects. Zinc may be included in degradation of chloroplasts stromal proteins [9]. Copper itself may affect all kind of photosynthetic activities, like electron-transport and ATP production [10, 11], or oxygen evolution [12]. In vivo experiments showed that the substitution of central magnesium atom in chlorophyll by heavy metals (observed in vitro) also takes place in living plants leading to permanent damaging effects on photosynthesis function [8]. The formation of Chl–HMS, even in minor proportions relative to the total Chl content, may inhibit photosynthesis completely [8]. The detailed consequences of Chl–HMS for higher plants and green algae have been discussed by Kupper [8, 13, 14]. The general reactions of Chl with heavy metals in vitro [15] and in vivo [16, 17] have been already reported.

Chl–HMS complexes show different spectroscopic behavior from Chl itself [1, 2, 8], qualitatively (shifts of the characteristic bands maximums, A_{Qymax}), as well as quantitavely (different intensities of the corresponding bands). This work deals with interaction and possible formation of Chl–HMS complexes between

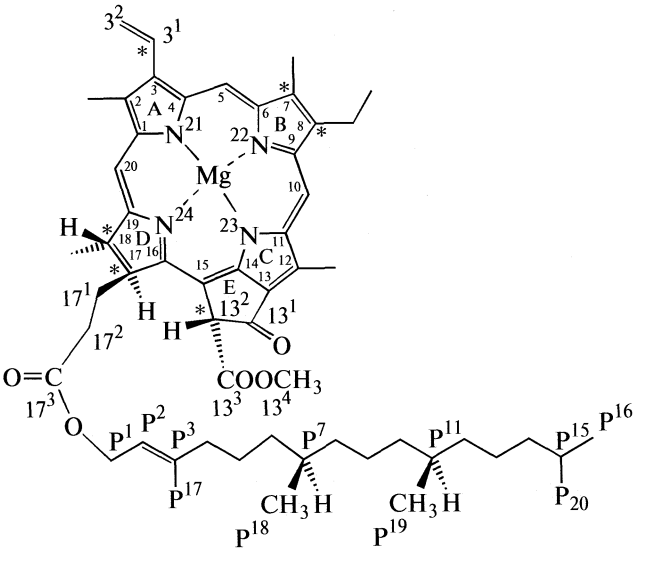

Fig. 1. Structure of chlorophyll a, with numerated C-positions.

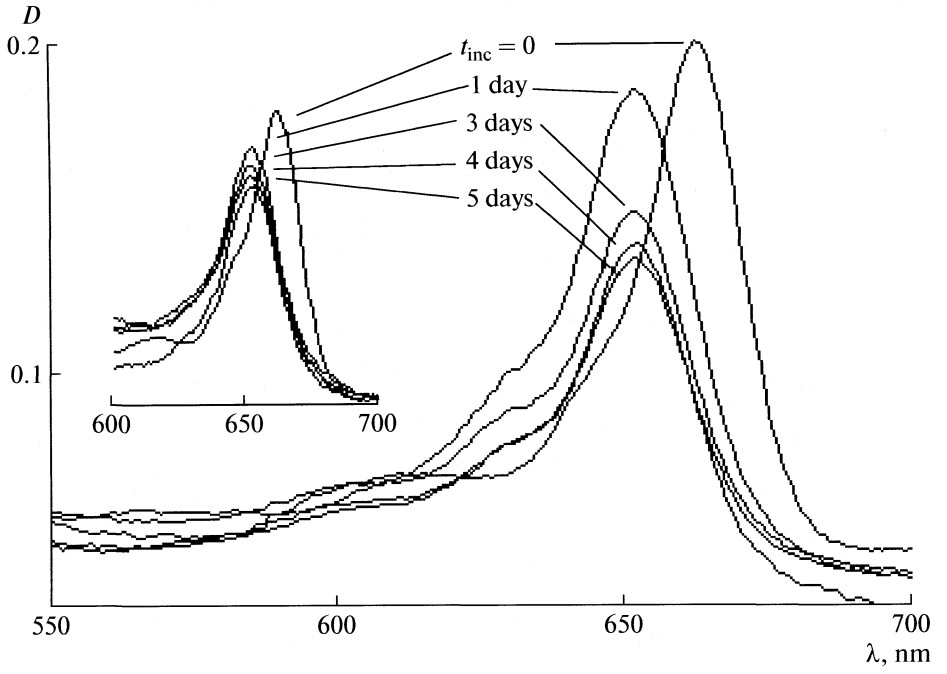

Fig. 2. Absorbance spectra of Cu/Fe- and Cu (left inserted spectra)-incubated pigment solutions for different time periods (t_{inc}), following beginning of the incubation ($t_{inc} = 0$) in 550–700 nm spectral range (Q_y-band).

chlorophyll and three chosen heavy metals in extracts of photosynthetic pigments (i.e. pigment solutions) incubated with different combinations of the three metals - copper (Cu) & iron (Fe), Cu & zinc (Zn), Fe & Zn and, Cu & Fe & Zn (*in vitro*). The interactions were then examined by VIS spectroscopy.

EXPERIMENTAL

Photosynthetic pigments were extracted from spinach leaves (Spinacia oleracea L) by using Swec method [18]. Chlorophylls content has been determined by using spectrophotometric equations for chlorophylls in acetone as reported [19]. The pigment extracts (containing two major Chl-forms, Chla and Chlb, and the accessory pigments, carotenoids) were evaporated and diluted in ethanol [8, 20]. Then, aqueous solutions of $CuSO_4$, $ZnSO_4$, $FeSO_4$ (combinations of metals in ratio 1:1) were added. The Chl concentration in the reaction mixtures (c_{Chl}) has been adjusted to 8.0 μmol/dm^3 and the ratio of total metal ion concentration to chlorophyll concentration ($c_{tot.,M^{2+}}/c_{Chl}$) was in the range of 1000:1. The time periods following the beginning of the Chl incubation (t_{inc}) ranged from 1 to 5 days. The interaction was stopped by dissolving the reaction mixture in cyclohexane and the visible spectra were recorded after different incubation times t_{inc} (on Varian Cary-100 Spectrophotometer). The same experiments were done simultaneously with individual metals to observe the combination effects (in the presence of all three metals) on chlorophylls. All experiments were performed in dark conditions to prevent chlorophyll photodegradation.

RESULTS AND DISCUSSION

Chlorophyll has two major absorption regions in visible range (400–800 nm), producing "red" (Q_y) band and "blue" (Soret or B) band [21]. Although the changes were detected in incubated systems both with B and Q_y-bands, the interaction of heavy metals with chlorophyll was followed in the pigments mixtures (in vitro) by using Q_y-band as sensible indicator, since it belongs to chlorophyll only, and not to accessory pigments, carotenoids [22]. Before any metal ions addition to pigment solutions, a control experiment has been done in order to assign all possible absorption changes to any possible other factors except the Me–Chl interaction. The control was done in a period of 5 days with pigments solution only, by controlling it's absorption spectra in the indicated period. A detectable changes have not been detected (not shown), meaning that changes in VIS spectra of chlorophyll in vitro in an incubation period of 5 days (with Cu, Zn, Fe and their combinations) – and shown in Figs. 2–5 – should primarily be assigned to the Me–Chl interactions.

A hypochromic effect related to absorption maximum of Chl Q_y-band (A_{Qymax}) is observed in all cases, proportional to the length of the incubation period (Figs. 2–5). The changes in VIS spectra of Cu/Fe-, Cu/Zn-, Fe/Zn-, and Cu/Fe/Zn-incubated pigment solutions (with the same metals concentrations) were clearly observed in the period of 5 days (Figs. 2–5).

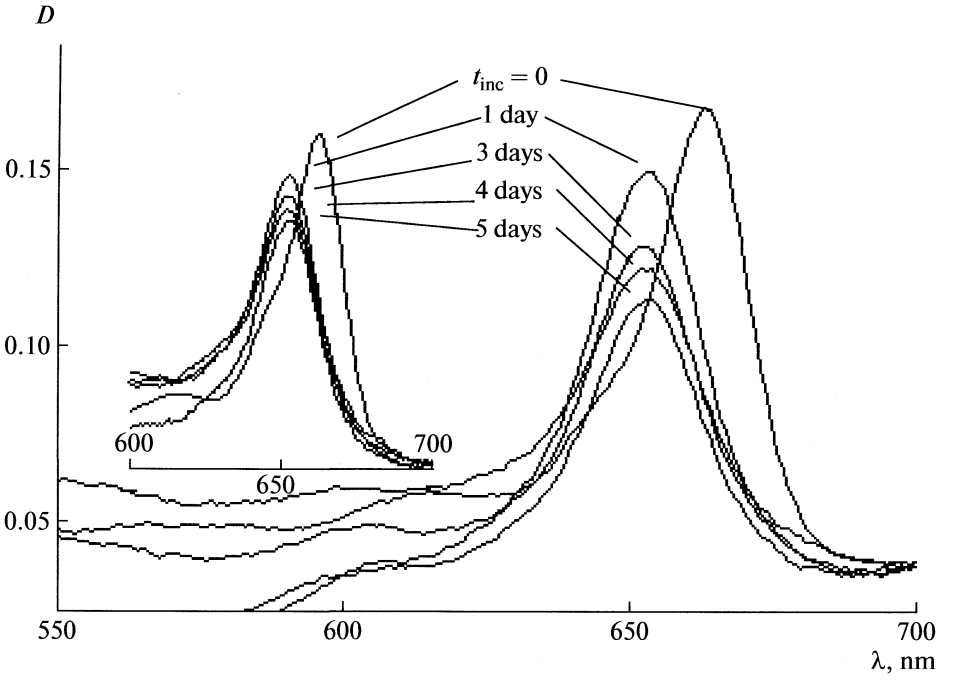

Fig. 3. Absorbance spectra of Cu/Zn-compared to Cu (left inserted plots)-incubated pigment solutions for different t_{inc}, following beginning of the incubation in 550–700 nm spectral range (Q_y-band).

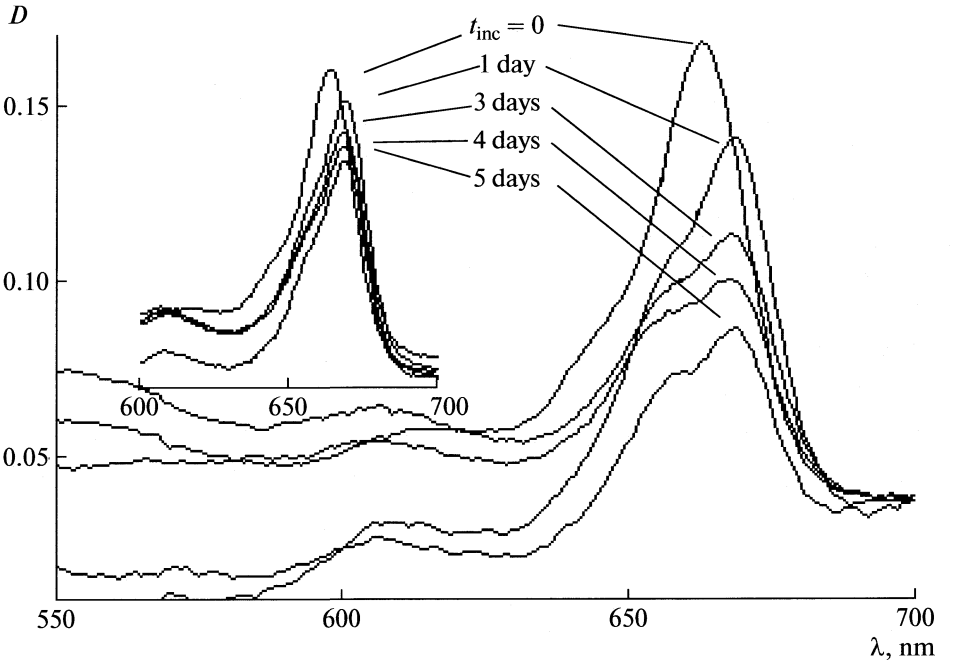

Fig. 4. Absorbance spectra of Fe/Zn- and Fe (left inserted plots)-incubated pigment solutions, for different t_{inc}, following beginning of the incubation in 550–700 nm spectral range.

Clear hypsochromic shifts have been observed for Q_y-band of Cu/Fe-, Cu/Zn-, and Cu/Fe/Zn-incubated pigment solutions (Figs. 2, 3, 5), while batochromic shift was detected for Fe/Zn-incubated pigment solutions only (Fig. 4) relative to t_{inc}. Table shows the shifts values for the Q_y-band ($\Delta\lambda_{Qymax}$) in VIS spectra of heavy metals-incubated pigment solutions after 5 days of incubation.

Comparison of Cu-effect only [23] with those observed in Cu/Fe-, Cu/Zn-, and Cu/Fe/Zn-incubated

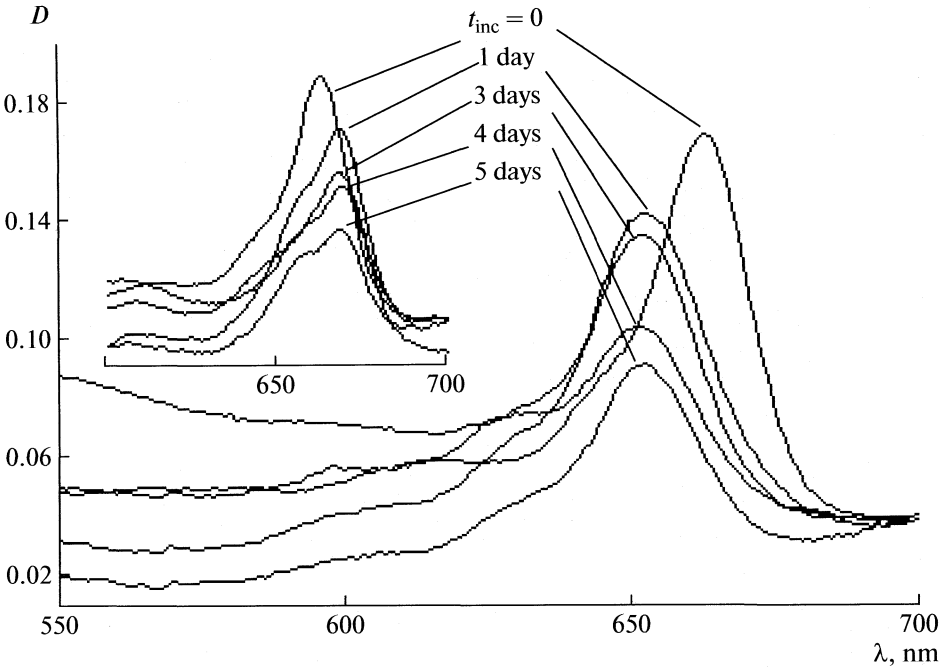

Fig. 5. Absorbance spectra of Cu/Fe/Zn- and Fe/Zn (left inserted picture)-incubated pigment solutions for different t_{inc}, following beginning of the incubation in 550–700 nm spectral range.

pigment solutions led to two major conclusions, (a) in all cases the interaction was finished after 1 day of incubation, and (b) in the same time a strong hypsochromic effect of Q_y-band is observed in the corresponding VIS spectra (Figs. 2, 3, 5, table). The hypsochromic effect for "central" Cu–Chl complex (related to Q_y band) was already confirmed in cyclohexane (A_{Qymax} at 649 and 654 nm for Cu–Chl and Cu-methylpheophorbide, respectively) [1, 8]. In our earlier experiments with Cu-incubated chlorophylls in chlorophyll fractions (a separated fraction of the pigment extract, containing mainly Chla with small contribution of Chlb) the same type of changes was detected, and the formation of "central" Cu–Chl complex was clearly confirmed in vitro by using additional experiments with FTIR and fluorescence spectrophotometry [20, 23]. Our results strongly confirm that Cu–Chl complex formation is not disturbed when one or the two metals are present; the effect of Cu only is shown in the form of the inserted plots (the left plots at Figs. 2, 3, concerning the Cu/Fe and Cu/Zn systems). The spectral behavior shown at Fig. 5 is obviously very similar to the one produced by copper only: the inserted plot related to Fe/Zn system shows the opposite shift direction.

With the Fe/Zn -incubated pigment solutions the observed interaction finished in 1 day only after incubation (Fig. 4). The same, batochromic effect, due to a supposed Fe–Chl interaction, has been seen for the Fe-incubated pigment solution only (Fig. 4 – the left inserted plot). However, this batochromic or "red" shifted absorption (in a range of few nanometers, like these presented in this work) was already seen in pheophytins (Phe), a central Mg-depleted derivatives of chlorophyll [24]. The possibility of pheophytins formation can not be neglected in this case.

In Zn-incubated pigment solutions 5 days after incubation, just a very small hypsochromic effect of Q_y-band in VIS spectra was observed (of 1 nm, table). Zinc interaction with chlorophyll in similar experimental conditions were examined earlier, suggesting that Zn rather forms "chelate" complexes with chlorophyll (proved by FTIR spectra, [23]), than "central" complexes (hardly detectable changes of Q_y-band A_{max} in VIS spectra), providing a shifted equilibrium between "central" and "chelate" Zn–Chl complexes toward the latter ones [20, 23, 25].

Finally, when all three metals are present in the same concentrations the overall effect is clearly very similar to Cu-effect itself (Fig. 5). Metal interaction with chlorophyll in solution can be explained by theoretical analysis of Falk's "stability factor" (includes

The observed shifts of Q_y-band absorbance maximums ($\Delta\lambda$) in VIS spectra of heavy metal incubated chlorophylls in pigment solutions

M–Chl	Δλ, nm	M–Chl	Δλ, nm
Cu–Chl	−10.5	Cu/Fe–Chl	−10.5
Fe–Chl	+6	Cu/Zn–Chl	−10.5
Zn–Chl	−1	Fe/Zn–Chl	+6
		Cu/Fe/Zn–Chl	−10.5

charge number of the metal ion, effective radius of the metal ion in Å and Pauling's electronegativity) [26]. According to Falk's equation, the stability of "central" Chl–HMS complexes is ordered as: Mg–Chl ~ Zn-Chl < Fe–Chl < Cu–Chl. Similar order for tendency of metal ions to be bound in the centre of the chlorophyll molecule was found [8]. Studies of interactions of metal combinations (Cu/Zn, Cu/Fe, Fe/Zn, Cu/Fe/Zn) used in this work in the same concentrations with chlorophyll in pigment solutions confirm the established order.

CONCLUSIONS

From all three chosen heavy metals only copper shows direct and dominant interaction with chlorophyll (in vitro), independently of the other metals presence. The Fe-effect dominates in combination with zinc, though it is not clear whether Fe–Chl complex, or pheophytin is formed. Zinc has the smallest affinity to build "central" Zn–Chl complex, and the effect is completely negligible in the presence of either iron or copper, or in combination with both of them.

ACKNOWLEDGMENTS

This work was supported under the project number TR-19048, by the Ministry of Science and Technological Development of the Republic of Serbia.

REFERENCES

1. L. J. Boucher and J. J. Katz, J. Am. Chem. Soc. **89**, 4703 (1967).
2. H. Scheer, J. J. Katz, J. Am. Chem. Soc. **97**, 3273 (1975).
3. H. Küpper, E. Lombi, F. J. Zhao, G. Wieshammer and S. P. McGrath, J. Exp. Bot. **52**, 2291 (2001).
4. H. Küpper, E. Lombi, F. J. Zhao, S. P. McGrath, Planta **212**, 75 (2000).
5. C. Jegerchöld, J. B. Arellano, W. P. Schröder, P. J. M. Kan, M. Baron and S. Styring, Biochem. **34**, 12747 (1995).
6. B. D. Hsu and J.Y. Lee, Plant Phys. **87**, 116 (1988).
7. M. Baron, J. B. Arellano and J. L. Gorge, Phys. Planta. **94**, 174 (1995).
8. Küpper H., Küpper F. and M. Spiller, J Exp. Bot. **47**, 259 (1996).
9. S. Roulin and U. Feller, Planta **205**, 297 (1998).
10. I. Yruela, G. Montoya and R. Picorel, Photosynth. Res. **33**, 227 (1992).
11. J. L. Stauber and T. M. Florence, Mar. Biol. **94**, 511 (1987).
12. M. Uchimura, A. Rival, A. Nato, R. Sandeaux, J. Sandeaux and J. C. Baccou, J. Appl. Phycol. **12**, 15 (2000).
13. H. Küpper, F. Küpper and M. Spiller, Photosynt. Res. **58**, 123 (1998).
14. H. Küpper, F. Küpper and M. Spiller, in *Chlorophyllsand Bacteriochlorophylls*, Ed. by B. Grimm, R. Porra, W. Rudigger and H. Scheer, Series: *Advances in Photosynthesis* (Springer, The Netherlands, 2006), p. 67.
15. H. Küpper, I. Šétlik, M. Spiller, F. C. Küpper and O. Prášil, J. Physiol. **38**, 429 (2002).
16. H. Clijsters and F. Van Assche, Photosynt. Res. **7**, 31 (1985).
17. C. M. Luna, C. A. González and V. S. Trippi, Plant Cell Physiol. **35**, 5 (1994).
18. W. A. Svec, in *Chlorophylls*, Ed. by H. Scheer (CRC-Press, 1991), p. 89.
19. H. K. Lichtenthaler, Meth. Enz. **148**, 350 (1987).
20. J. Zvezdanović, G. Nikolić and D. Marković, J. Serb. Chem. Soc. **72**(11), 1053 (2007).
21. H. Scheer, in *CRC Handbook of Organic Photochemistry and Photobiology*, Eds. W. Horspool and F. Lenci (CRC Press, 2003), p. 117(1).
22. H. Scheer, in *Advances in Photosynthesis*, Ed. by B. R. Green and W. W. Parson (Kluwer Academic Publishers, 2003), p. 29.
23. J. Petrović, G. Nikolić, D. Marković, J. Serb. Chem. Soc. **71**(5), 501(2006).
24. "*Phytoplankton Pigments in Oceanography: Guidelines to Modern Method*", Ed. by S. W. Jeffrey, R. F. C. Mantoura and S. W. Wright, UNESCO Publishing (1996).
25. Y. Nonomura, S. Igarashi, N. Yoshioka and H. Inoue, Chem. Phys. **220**, 155 (1997).
26. P. H. Hynninen, in *Chlorophylls*, Ed. by H. Scheer (CRC-Press, 1991) p. 145.

ЖУРНАЛ ФИЗИЧЕСКОЙ ХИМИИ, 2009, том 83, № 9, с. 1723–1725

PHYSICAL CHEMISTRY OF SURFACE PHENOMENA

УДК 541.183

^{137}Cs DESORPTION FROM LICHEN USING ACID SOLUTIONS

© 2009 A. Čučulović*, D. Veselinović**, S.S. Miljanić**

*INEP-Institute for the Application of Nuclear Energy, Banatska 31b, Zemun, Serbia

**Faculty of Physical Chemistry, University of Belgrade, P.O. Box 137, Belgrade, Serbia

E-mail: anas@inep.co.rs

Abstract – Desoprtion of ^{137}Cs from samples of *Cetraria islandica* lichen using HCl (**A**) and HNO_3 (**B**) acid solutions with pH values from 2.00 to 3.75 was investigated. After five consecutive desorptions lasting 24 hours it was shown that between 52.2% (solution **B**, pH 3.28) and 72.2% (solution **A**, pH 2.00) of ^{137}Cs was desorbed from the lichen and the initial desorptions were the most successful. Lichen desorbed with the stated solutions did not undergo structural changes. The amount of absorbed water from solutions **A** and **B**, used for desorption from lichen, in relation to the starting volume (expressed in %) showed that solution concentration did not take place. Lichen act as neutralizing agents because the pH of the lichen thallus is higher than the pH value of the solution used.

INTRODUCTION

Lichen can adopt and accumulate polluting substances (radionuclides, heavy metals, pesticides) in tissue or on the thallus surface [1]. After the Chernobyl accident (1986) it was shown that lichen sorption of radionuclides from air was dominant, tolerance to radionuclides was passive and hyper-accumulation of radionuclides in lichen was the consequence of the properties of the genetically independent organism and that lichen tissue reflected the environment composition [2]. Radionuclides entering the lichen body become sources of internal radiation and also radiation sources for other related organisms. Lichen are natural reservoirs of matter that can be periodically released [3–5]. Thus, the investigation of desorption of accumulated metals such as ^{137}Cs with solutions similar to acid rain with a desorption dynamics of successive solution application is important.

EXPERIMENTAL

200 ml of solutions (**A**) HCl and (**B**) HNO_3 was poured over 10 g of dry *C. islandica* lichen, collected from the Sinjajevina Mountain, Montenegro, for commercial purposes in 1994. Solutions **A**, i.e. **B** were made by adding concentrated HCl or HNO_3 to 200 mL of water until a desired pH value of 2.00; 2.58; 2.87; 3.28 and 3.75 was reached. Samples were consecutively desorbed with solutions five times and desorption series were repeated twice. Desorptions were performed at room temperature lasting 24 hours. After each desorption, following filtration, lichen samples were dried at room temperature until they became a constant mass. Activity levels of ^{137}Cs were measured in samples before and after each desorption on an ORTEC-AMETEK gamma spectrometer with 8192 channels, resolution of 1.65 keV and efficiency of 34% at 1.33 MeV ^{60}Co with a measurement error below 5%. The specific activities (Bq/kg) were calculated. All desorptions were repeated twice and the mean values are given in the Tables 1, 2. The sorbent absorbed

Table 1. Total desorbed ^{137}Cs from lichen *C. islandica* (y, %) and percentage of remaining ^{137}Cs in lichen after each desorption using solutions HCl (**A**) and HNO_3 (**B**) (in relation to the starting content in lichen, 100%). Room temperature (~22°C). Desorption time 24 hours for each desorption. Mean measurement error 2.4%

pH	y(A)	y(B)	Solution **A**					Solution **B**				
			I	II	III	IV	V	I	II	III	IV	V
2.00	72.2	58.1	46.4	42.7	39.0	37.3	27.8	60.3	49.9	45.8	44.4	41.9
2.58	64.8	56.6	54.1	43.8	43.6	42.3	35.2	61.7	50.0	47.9	47.2	43.4
2.87	60.6	53.1	56.2	44.8	43.7	41.0	39.4	65.0	57.6	51.5	47.4	46.9
3.28	58.0	52.2	65.6	47.6	46.2	46.1	42.0	61.7	56.3	50.1	49.5	47.8
3.75	56.4	53.7	59.1	52.1	48.4	47.8	43.6	65.3	59.0	51.3	50.0	46.3

Table 2. Mean values of the starting activity of ^{137}Cs (c_0'), determined by extrapolation of the curves in Fig. 2, given as a percentage in relation to the experimentally determined values of c_0 (100%)

Desorption solution	pH	c_0', %
A	3.75	61.6
B	2.87	68.4
B	3.28	63.4
B	3.75	69.8

Note. Solution compositions are given in the Experimental.

a certain volume of water from the added desorption solution after each of the five desorptions. The remaining desorption solution was strained through filter paper and its volume was measured. Knowing the starting and measured solution volumes obtained after each desorption, the absorption percentage of desorption liquid by the lichen was calculated. The pH of the lichen thallus was determined by destructing 100 g of lichen thallus with liquid nitrogen and mixing it with 4 ml of de-ionized water (pH 5.77) followed by treatment in a centrifuge at 100g 10 min. The solution pH value was measured on a pH meter Iskra MA 5730 [6, 7].

RESULTS AND DISCUSSION

Activity levels of ^{137}Cs in samples of *C. islandica* lichen before desorption were from 1786 to 2994 Bq/kg.

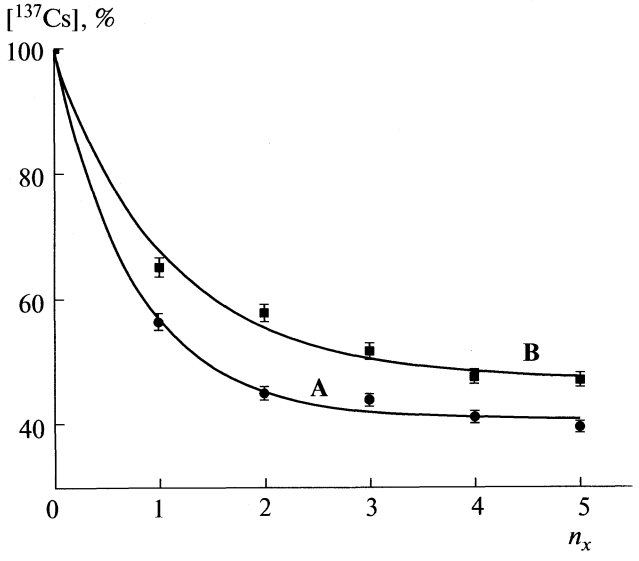

Fig. 1. ^{137}Cs content in lichen (%) in relation to the starting content (100%), in dependence on the successive desorption number (n_x) using solutions **A** and **B**, pH 2.87, for an equilibrium time of 24 h.

After five consecutive desorptions, each lasting 24 hours, at room temperature, the most of 58.1% solution **B** (pH 2.00) and of 72.2% solution **A** (pH 2.00) of the starting value of ^{137}Cs was desorbed (Table 1). The first desorption in relation to the total amount of desorbed ^{137}Cs is smaller than 50.0% in all cases, except case pH 2.00 solution **A**. The pH value has an influence on ^{137}Cs desorption from lichen.

Application of the Origin 7.0 software [8] gave curves showing an exponential dependence of the remaining amount of ^{137}Cs, on the number of successive desorptions, regardless of the solution pH. This is shown in Fig. 1.

The change of the sorbed substance amount, c_x, in the sorbent with the desorption number, n_x, for successive desorptions with the same volume of desorption agent is given by the equation formulated for desorption of ^{137}Cs with water [5]:

$$\ln c_x = \ln c_0 - an_x, \quad (1)$$

where c_0 is the content of the sorbed substance (^{137}Cs) before desorption and a is a constant.

Application of Eq. (1) on the values given in Table 1 resulted in two types of curves. From Eq. (1), it follows that the dependence of the logarithm of the amount of sorbed substance in the solid state is a linear function of the number of successive volumes employed during extraction. For real systems, this is valid when only one type of sorption exists, or if one type is dominant, so that the others can be disregarded. In other cases, deviations from a straight line occur, indicating that the sorbent can bind the sorbed substance by different types of sorption, i.e. different sorbent points. A linear dependence was obtained using solutions **A** for pH 3.75 and **B** for pH 2.87; 3.28 and 3.75. This indicated that one sorption type is dominant in these cases. Ex-

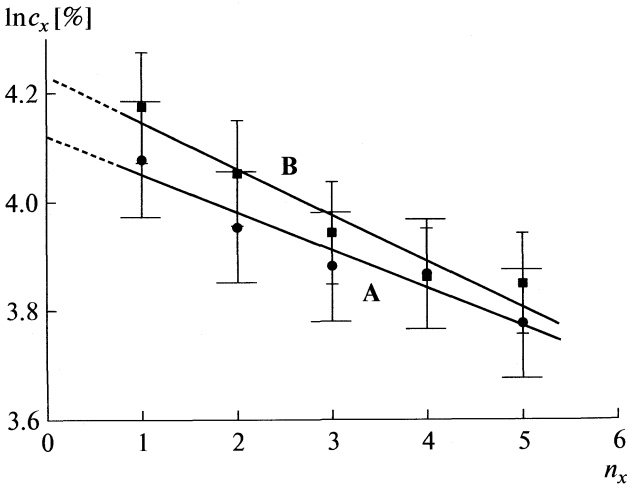

Fig. 2. ^{137}Cs content (%) in the sorbent (*C. islandica*) as a function of the number of successive desorptions (n_x), with solutions **A** at pH 2.87 and **B** at pH 3.75, according to Eq. (1).

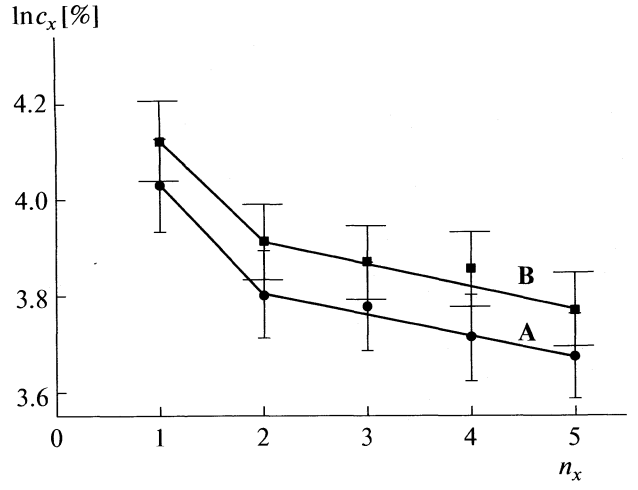

Fig. 3. ^{137}Cs content (%) in the sorbent (*C. islandica*) as a function of the number of successive desorptions (n_x), with solutions **A** at pH 2.87 and **B** at pH 2.58, according to Eq. (1).

trapolation of the obtained linear dependencies (Fig. 2) gave values denoted as c_0' in Table 2. They are lower than the corresponding starting values (100%) indicating the existence of a type of ^{137}Cs sorption that greatly differs in bonding intensity i.e. bonding energy. In all the other cases, curves given in Fig. 3 for selected examples were obtained. They indicate the existence of at least two types of sorption, but when corresponding desorbants are used, desorption of ^{137}Cs is not separated enough to be dominant. Also, a type of ^{137}Cs sorption with high bonding energy cannot be excluded. Desorptions performed with solution **A** for pH 2.00; 2.58; 2.87 and 3.28, **B** for pH 2.00 and 2.58 give this curve type.

The amount of absorbed water from solutions **A** and **B** used for desorption of *C. islandica* lichen in relation to the starting volume (20 ± 1.5 %) shows that the solution concentration effect is not present, and all noted changes are within the margin of error. Table 3 gives measured pH values of the thallus after treatment with desorption solutions **A** and **B**. The pH value of non- treated lichen thallus is 4.83. These results show that lichen act as neutralizing agents since in all cases the thallus pH is higher than the pH value of the solution used. Processes leading to this could be neutralization with inorganic or organic bases, but also possible utilization of acid from desorption solutions in decomposition processes of organic compounds in the lichen tissue.

Table 3. Changes in pH of lichen thallus after treatment with desorption HCl (**A**) and HNO_3 (**B**) solutions

pH	A	B
2.00	2.54	2.66
2.57	3.17	3.28
2.87	3.59	3.75
3.28	4.18	4.26
3.75	4.74	4.72

CONCLUSION

The obtained results indicate that lichen can be considered sorbents which, due to their complex structure in relation to inorganic or synthetic organic sorbents, can have two or more sorption centers of different affinities towards the $^{137}Cs^+$ cation.

Desorption of ^{137}Cs using acid solutions indicates that lichen with previously accumulated ^{137}Cs become secondary sources of pollution with acid rain, all the more as the rain is more acid. This desorption process does not damage lichen to a degree that could be established, as the amount of sorbed water does not change significantly with changes of the solution pH and the number of desorptions.

Since ^{137}Cs is one of the alkaline elements and they behave similarly, the conclusions reached in this work from experiments using ^{137}Cs can be applied to other alkaline element cations.

REFERENCES

1. J. E. Sloof, B. Walterbeek, J. Environ. Radioact. **16**, 229 (1992).
2. M. E. Conti, G. Cecchetti, Environ. Pollut **114**, 309 (2001).
3. A. Čučulović, D. Veselinović, Š. S. Miljanić, J. Serb. Chem. Soc. **72**(7), 673 (2007).
4. A. Čučulović, M. S. Pavlović, D. Veselinović, S. S. Miljanić, J. Serb. Chem. Soc. **73**(4), 405 (2008).
5. A. Čučulović, D. Veselinović, Š. S. Miljanić, J. Serb. Chem. Soc. **71**(5), 565 (2006).
6. Y. Gauslaa, Lichenologist **17**, 117 (1985).
7. O. L. Gilbert, Environ. Pollut. (Ser A) **40**, 227 (1986).
8. http://www.OriginiLab.com.

ЖУРНАЛ ФИЗИЧЕСКОЙ ХИМИИ, 2009, том 83, № 9, с. 1726–1729

PHYSICAL CHEMISTRY OF SEPARATION PROCESSES. CHROMATOGRAPHY

УДК 541.183

MASS TRANSFER AND FLUID FLOW VISUALIZATION IN PACKED AND FLUIDIZED BEDS BY THE ADSORPTION METHOD

© 2009 N. Bošković-Vragolović*, R. Garić-Grulović**, Ž. Grbavčić*, R. Pjanović*

*Faculty of Technology and Metallurgy, University of Belgrade, Belgrade, Serbia

**Institute for Chemistry, Technology and Metallurgy, University of Belgrade, Belgrade, Serbia

E-mail: garic@tmf.bg.ac.rs; nevenka@tmf.bg.ac.rs

Abstract – Mass transfer coefficient (j_D) between fluid and column wall in liquid packed and fluidized beds of spherical inert particle has been studied experimentally using adsorption method. Experiments were conducted in column 40 mm in diameter for packed and fluidized beds. In all runs mass transfer rates were determined in presence of spherical glass particles 2.06 mm in diameter. This paper introduced adsorption method as very suitable method for studies of mass transfer and for fluid flow visualization. The adsorption method is based on the dynamic adsorption of an organic dye onto a surface covered with a thin layer of a porous adsorbent. Local and average mass transfer coefficients were determinated from the surface color intensity of the foils of silica gel. Correlation $j_D = f(\mathrm{Re})$ was derived using mass transfer coefficients data.

INTRODUCTION

Research of transport phenomena in liquid – particles systems, in past years, had more theoretical then practical importance [1–3].For industrial use, especially with fast development of bio and water cleaning processes, better knowing of these systems become more important. Industrial application of these systems requires determination of transfer characteristics, especially mass transfer. Mass transfer in fluidized beds has been widely investigated in terms of particle-fluid mass transfer by dissolution, by electrochemical and by ion-exchange methods [1, 2, 4–8]. Some of the results of the mass transfer in fluidized beds have been obtained as transfer between immersed surface and liquid [9, 10].

The adsorption method was introduced as a relatively simple mass transfer measurement technique, applicable for liquid flow investigations [11]. The method is based on the dynamic adsorption of an organic dye onto a surface covered with a thin layer of a porous adsorbent. The rates of the dye adsorption are supposed to be diffusion controlled. The quantity of the dye transferred during a fixed time period is a function of diffusion boundary layer conditions.

The rate of adsorption decreases from high values at the beginning to a constant value for each dye concentration. This constant value is the actual mass transfer rate through the completely formed boundary layer. For high concentration of the dye the concentration at the film's surface is $c_p \neq 0$ and the adsorption process is controlled by mixed kinetics. Also, for high mass transfer rates mixed kinetics occur at lower concentration.

The adsorption method is based on the experimentally determined fact that under certain conditions mass transfer with adsorption can be treated as a stationary process governed by mass transfer only. Adsorption from a much diluted solution and far from equilibrium conditions is a very fast process. If the exposure time is short (less than 10 min) the mass transfer rate depends only on the diffusion through the boundary layer. The concentration of adsorbate just above the adsorbent's surface is $c_i = 0$.

Mass flux is:

$$N_A = k(c_0 - c_i) = kc_0 \quad (1)$$

and for exposure time t:

$$N_A = c_p/t, \quad (2)$$

where c_p is the surface concentration of organic dye on adsorbent layer, c_0 is the bulk concentration.

If the induction period can be short (in the case of thin boundary layers) a simplified expression to calculate mass transfer coefficient is obtained [12]:

$$k = c_p/tc_0. \quad (3)$$

For this method, value of the surface concentration c_p, is necessary for data quantification. This method is used since 1953, but determination of this parameter, c_p which now can be done easily, using suitable software (Sigma Scan Pro), gives absorption method new actuality.

This paper presents an experimental study of the measurement of the local and average mass transfer coefficient in heterogeneous systems – packed and fluidized beds. This paper, also introduced adsorption method as very suitable method for determination of mass transfer and for fluid flow visualization.

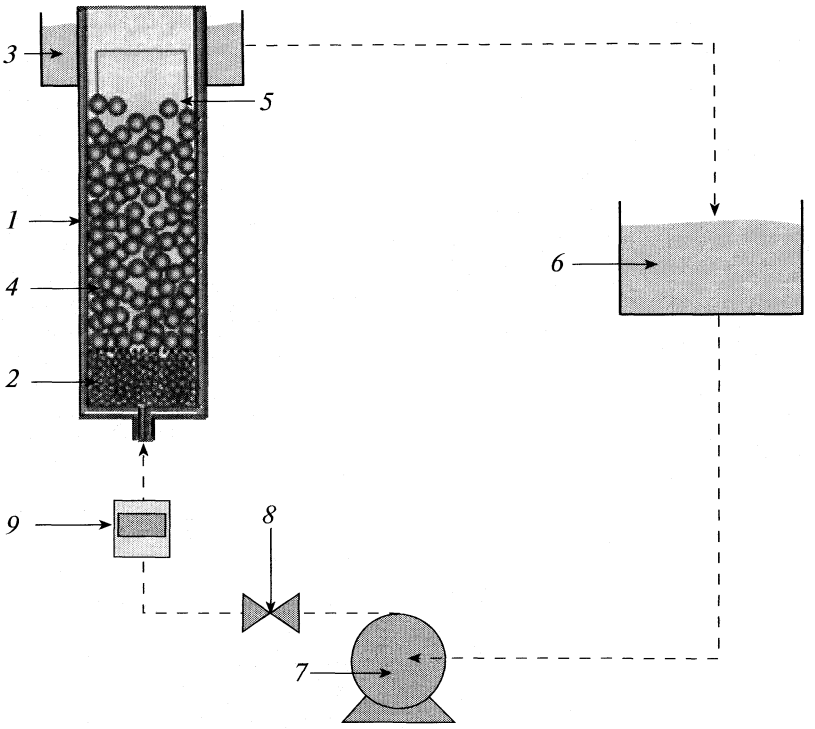

Fig. 1. Experimental system: (*1*) column 40 mm in diameter, (*2*) liquid distributor, (*3*) water overflow, (*4*) glass particles, (*5*) foils of silica gel, (*6*) tank, (*7*) pump, (*8*) valve (*9*) flowmetar.

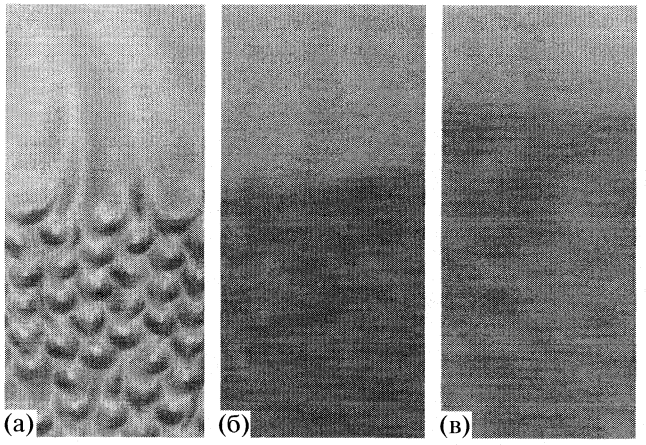

Fig. 2. Chromatograms for flow in packed bed (a), in fluidized bed at minimum velocity (b) and in fluidized bed (c).

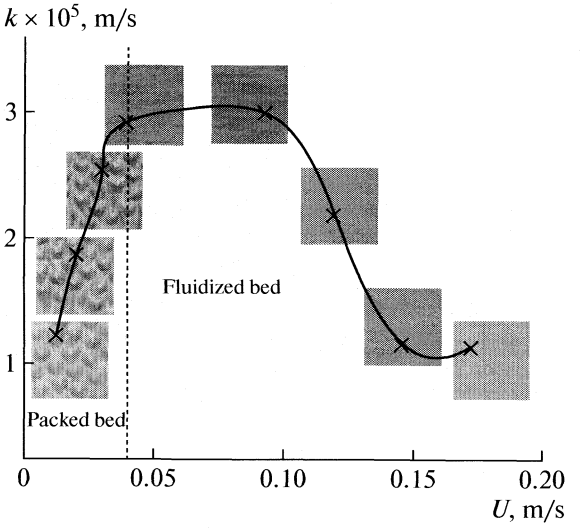

Fig. 3. Relationship between mass transfer coefficient and superficial liquid velocity (U), the particle diameter d_p = = 2.06 mm.

EXPERIMENTAL

Experiments were conducted in columns 40 mm in diameter (Fig. 1, *1*), for packed and fluidized beds.

Very diluted solution of methylene blue ($c_0 = 2.5 \times \times 10^{-3}$ g/dm^3) was used as a fluid in the presence of inert glass particles 2.06 mm in diameter (Fig. 1, *4*). The foils of silica gel (Fig. 1, *5*) was used as adsorbent ("Merck", DC-Alufolien Kieselgel). Concentration profiles of methylene blue were measured in the flow of water through packed and fluidized beds. Colour intensity of the surface was determinated by "Sigma Scan Pro 5" software. The fluid flow was changed with valve (Fig. 1, *8*) and measured by flowmetar (Fig. 1, *9*).

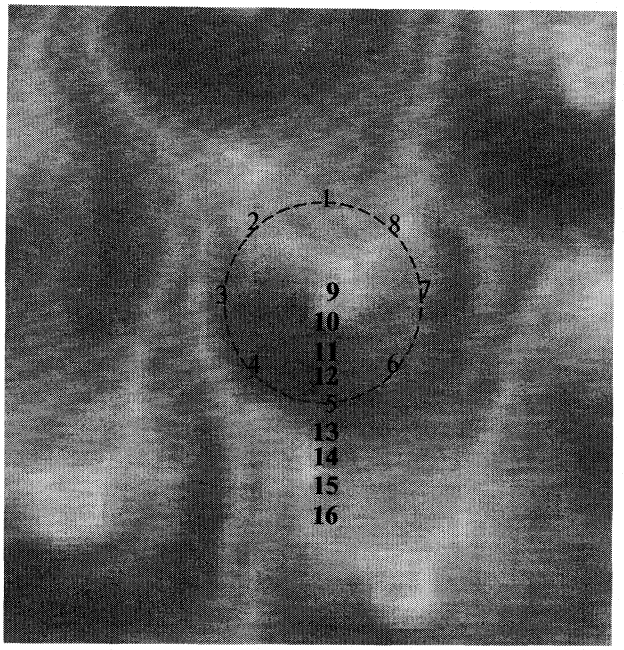

Fig. 4. Fluid flow visualization around spherical particle in packed bed.

RESULTS AND DISCUSSION

Average color intensity of silica gel surface for flow in packed bed (a), in fluidized bed at minimum velocity (b) and in fluidized bed (c) were shown on Fig. 2.

Chromatogram (a) gives clear visualization of fluid flow around particles in the packed bed. Color intensity is proportional to local mass transfer rates. Chromatograms (b) and (c) visualize fluidized beds for minimal velocity and for highly expanded fluidized bed. Uniform color intensity could be observed in both cases, with higher intensity for minimal fluidized bed velocity. This color uniformity indicates uniform mass transfer rates for fluidized beds. Lighter top parts of chromatograms (b) and (c) represents mass transfer in the single phase flow.

The color intensity of silica gel surface varies with fluid flows. Higher color intensity means higher mass transfer coefficient as can be seen on Fig. 3. With increasing liquid velocity in packed beds mass transfer coefficient increases while in fluidized beds mass transfer coefficient decrease. The highest mass transfer coefficient was at minimum fluidization velocity because of high concentration of moving particles.

Adsorption method is also very useful for determination of local mass transfer coefficient and fluid flow visualization as can be seen on Fig. 4. Values of local mass transfer coefficients at a different points are shown in table.

Experiments in packed and fluidized beds were conducted as liquid-to-wall mass transfer. Figure 5 present relationship between mass transfer factor and particle Reynolds number in packed and fluidized bed. Also this picture gives the comparison of our experimental data with tree correlation for mass transfer of liquid in packed and fluidized beds.

Dwivedy and Upadhyay [1]:

$$j_D\varepsilon = 0.765/\mathrm{Re}_p^{0.82} + 0.365/\mathrm{Re}_p^{0.386}, \qquad (4)$$

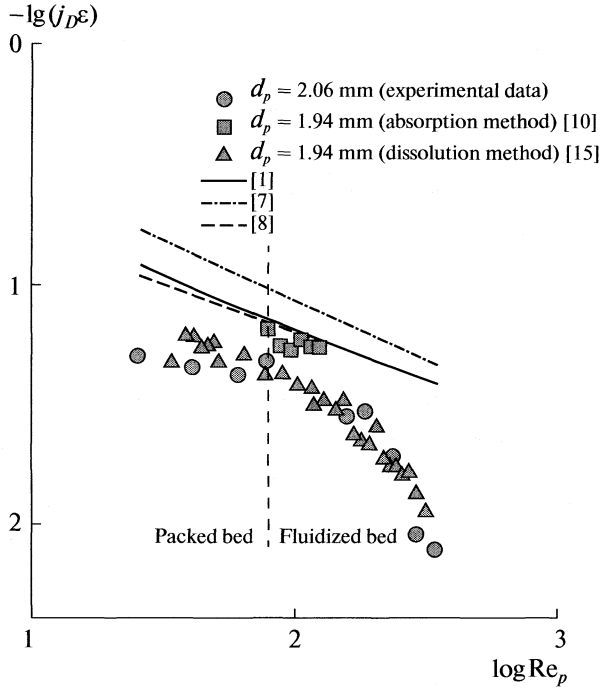

Fig. 5. Mass transfer factor vs. particle Reynolds number

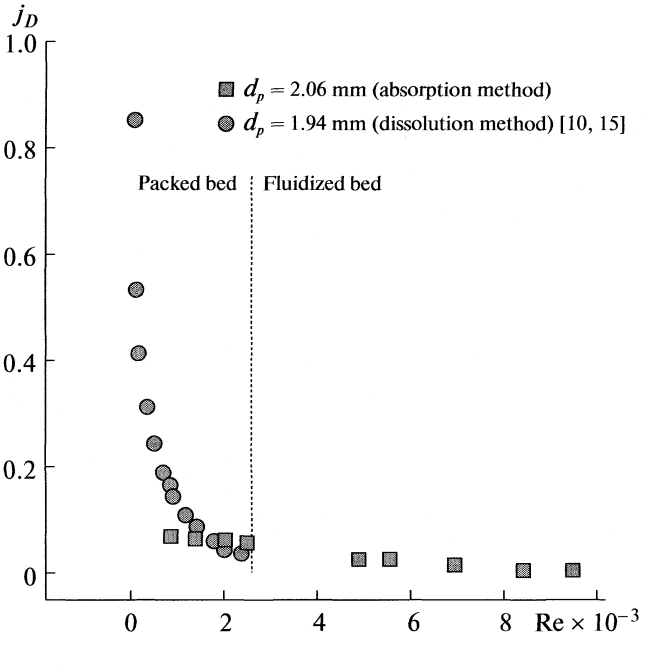

Fig. 6. The relationship between mass transfer factor and Reynolds number.

The local mass transfer coefficients (k) at different points on Fig. 4 (I is average color intensity)

Point	I	$k \times 10^6$, m/s
1	11.36	5.57
2	9.11	3.85
3	14.01	7.82
4	26.53	20.2
5	29.93	24.2
6	25.143	18.7
7	16.43	10
8	6.26	2.02
9	3.74	0.825
10	21.77	15.2
11	26.32	19.9
12	28.57	22.5
13	26.122	19.7
14	24.08	17.6
15	20.95	14.4
16	19.1	12.6

where Re_p is the Reynolds number for particle, (4) $Re_p = Ud_p\rho_f/\mu$; j_D is the mass transfer factor $j_D = (k/U)Sc^{2/3}$, Rahman and Streat (1981) [13]:

$$j_D\varepsilon = 0.86\,Re_p^{-0.5},\ Re_p = 2\text{–}25, \quad (5)$$

Yutani et al. (1987) [14]:

$$j_D\varepsilon = 0.4\,Re_p^{-0.4},\ Re_p = 0.5\text{–}1000. \quad (6)$$

As can be seen, our experimental data are lower than data predicted by all three correlations. Our previous experimental data [10]. Show satisfactory agreement with Dwivedy and Upadhyay and Yutani et al. correlations.

Experimental research showed that adsorption method is very suitable for visualization of fluid flow and for determination of local and average mass transfer coefficients. Adsorption method could be easily employed using novel software solutions.

Figure 6 presents the mass transfer factor as a function of Reynolds number in packed and fluidized beds for different experimental techniques. It could be seen that there is no significant difference between mass transfer factors obtained by this two methods. [10, 15]. Often used dissolution method is very reliable, and agreement of data shows that the adsorption method gives good results also. Advantage of this method is possibility to obtain local mass transfer coefficients.

CONCLUSION

The wall-to-liquid mass transfer in packed and fluidized beds, with the adsorption method of methylene blue was investigated. This method is suitable for fluid flow visualization. The wall-to-liquid mass transfer factor in packed beds is higher then in fluidized beds for Reynolds number of column. Result of adsorption method gives permanent picture of fluid flow and local and average mass transfer coefficients in packed and fluidized beds.

ACKNOWLEDGMENTS

Financial support of the Ministry of Science and Technological Development, Republic of Serbia is gratefully acknowledged.

REFERENCES

1. Dwivedi P. N., Upadhyay S. N., Ind. Eng. Chem. Proc. Des. Dev. **16**, 157 (1977).
2. Chun T., Couderc J. P., Chem. Eng. Sci. **35**(8), 1707 (1980).
3. Coudrec J. P., *Fluidization*, 2nd Edition, Editors Academic Press, London, 1–46, 1985.
4. S. Damronglerd, J. P. Couderc, H. Angelino, Trans. Inst. Chem. Engrs **53**, 175 (1975).
5. S. Kumar, S. N. Upadhyay, Ind. Eng. Chem. Fundam. **20**, 186 (1981).
6. T. Koloini, M. Sopčič, M. Žumer, Chem. Eng. Sci. **32**, 637 (1976).
7. K. Rahman, M. Streat, Chem. Eng. Sci. **36**, 293 (1981).
8. N. Yutani, N. Ototake, L. T. Fan, Ind. Eng. Chem. Res. **26**, 343 (1987).
9. J. P. Riba, R. Routie, J. P. Couderc, *Fluidization*, J. F. Davidson & D. L. Keairns, Eds. Cambridge, U. Press, Cambridge, England, 157,1979.
10. N. Bošković, Ž. B. Grbavčić, D.V. Vuković, M. Marković-Grbavčić, Powder Techn. **79**, 217 (1994).
11. Mitrović M., Končar-Đurđević S., Cvijović S., Voronjec D., Dudukovic A., Fluid flow visualisation and analysis by the adsorption method, J. Serb. Chem. Soc. **54**(8), 383 (1989).
12. Končar-Đurđević S., Nature **172**, 878 (1953).
13. Rahman K., Streat M., Mass Transfer in Liquid Fluidized Beds of Jon Exchange Particles, Chem. Eng. Sci. **36**(2), 293 (1981).
14. Yutani N., Ototake N., Fan L. T., Ind. Eng. Chem. Res. **26**, 343 (1987).
15. N. Boškovic-Vragolović, R. Garić-Grulović, Ž. Grbavcić, J. Serb. Chem. Soc. **72**(11), 1103 (2007).

ЖУРНАЛ ФИЗИЧЕСКОЙ ХИМИИ, 2009, том 83, № 9, с. 1730–1733

PHYSICAL CHEMISTRY OF SEPARATION PROCESSES. CHROMATOGRAPHY

УДК 543.544

HIGH-PERFORMANCE LIQUID CHROMATOGRAPHIC ANALYSIS OF ANTHRAQUINONE COMPOUNDS IN THE LICHEN *LAURERA BENGUELENSIS*

© 2009 N. Manojlović*, Z. Marković**, W. Gritsanapan*** and K. Boonpragob****

*Department of Pharmacy, Medical Faculty, University of Kragujevac, S. Markovića 69, 34000 Kragujevac, Serbia

**Department of Biochemical and Medical Sciences, State University of Novi Pazar, Vuka Karadžića bb, Novi Pazar 36300, Serbia

***Faculty of Pharmacy, Mahidol University, 10040, Bangkok, Thailand

****Faculty of Science, Ramkhamhaeng University, Bangkok, Thailand

E-mail: ntm@kg.ac.yu

Abstract – A High-performance liquid chromatographic (HPLC) method has been developed for the characterization of anthraquinone metabolites in extracts of the lichen *Laurera benguelensis*. With this method four anthraquinone derivatives 1,8-dihydroxy-3-methoxy-6-methylanthraquinone, 1,8-dihydroxy-3-formyl-6-methoxyanthraquinone, 1.8-dihydroxy-3-hydroxymethyl-6-methoxy-anthraquinone and 1,3,8-trihyroxy-6-methylanthraquinone can be analyzed. Components of lichen were detected by characteristic ultraviolet spectra and relative retention times. This is first report of phytochemical analysis of *L. benguelensis*. Importance of this research is in recognizing some new source (lichen and its extracts) as a natural emplacement of antioxidants because oxidation with free radicals or autooxidation is big problem for preservation of food products.

INTRODUCTION

Oxidation with free radicals or auto oxidation is a significant problem for preservation of food products. The presence of natural antioxidants in food products is very important for their stable duration, because they are natural additives. The secondary lichen metabolites show a wide range of potentially useful biological activities including antioxidant activity [1, 2]. Anthraquinones are ingredient in many medications of plant origin, since they possess antibacterial, anti-inflammatory, antitumor, purgative, astringent, antiviral and antifungal properties [3–6]. 1,8-Dihydroxyanthraquinones are the active compounds of many plant-derived drugs that are used as laxatives, and some of them possess antioxidant activity [1]. Lichens produce some characteristic anthraquinone derivatives, which have yet to be found in higher plants [7–11]. Anthraquinones are widely distributed in lichens of the genera *Xanthoria*, *Teloschistes* and *Caloplaca* of the family *Teloschistaceae* [11–13]. In literature the informations about isolation of anthraquinones from the genus *Trupetheliaceae* are very poor. Until now, only 1,5,8-trihydroxy-6-methoxy-3-methyl-anthraquinone has been found in the other species of the genus *Laurera* [14]. Emodin and parietin have also been reported from some other lichens (*Teloschistaceae*) and high plant families [15, 16].

EXPERIMENTAL

Lichen Species Studied

Laurera benguelensis (Mull. Arg.) Zahlbr. belongs to the family *Trypetheliaceae* which is distributed in tropical region [17]. Lichen material was collected from Phi Phi Island, Thailand, during July 2006, and identified by Prof. Dr. Boonpragob, Faculty of Science, Ramkhamhaeng University, Bangkok, Thailand. A voucher specimen (RU–22162) has been maintained at the Lichen herbarium of the Ramkhamhaeng University, Thailand.

Identification of Anthraquinones by High-Performance Liquid Chromatography (HPLC)

Methanol was of HPLC grade, and was purchased from Merck (Darmstadt, Germany). Phosphoric acid was analytical grade reagent. Deionized water used throughout the experiments was generated by a Milli-Q academic water purification system (Milford, MA, USA).

Teloschistin, physcion, emodin, fallacinal, and citreorosein are not commercially available in pure form, and were isolated from lichens *Xanthoria* and *Caloplaca* [6, 12, 13]. These anthraquinones were separated and purified by column chromatography using benzene and benzene acetone mixtures (20:1, 10:1, 5:1 and 1:1), as eluents. These compounds were identified by elemental analysis and spectroscopic studies

(UV, IR and 1H NMR) and compared with literature data [6, 12, 13].

The lichen material was air dried at room temperature (26°C) for one week, after which it was grinded to a uniform powder. The benzene extract was prepared by soaking 10 g of the dry powdered lichen material in 100 ml of benzene at room temperature for 48 h. After that the extract was filtered through a Whatmann filter paper No. 42 (125 mm). The extract was concentrated using a rotary evaporator with the water bath set at 40°C. The percentage yield of the extract was 1.12%, w/w.

HPLC analysis was carried out on Waters HPLC instrument with Waters 717 plus auto sampler, C18 column, 1525 Binary HPLC Pump, and 2478 Dual λ Absorbance UV spectophotometric detector. For the gradient elution two solvent systems were employed: A – methanol and B – methanol–water–phosphoric acid 80:20:0.9 (v/v/v). The gradient was set up as shown in Table 1. Flow was set to 1.0 ml/min and the resulting chromatogram was recorded for 60 min. Peaks were detected over the 200–600 nm range of the absorption spectrum and all chromatograms were plotted at 250 nm. The standards, citreorosein (**1**), teloschistin (**2**), fallacinal (**3**), emodin (**4**) and physcion (**5**), were dissolved in methanol and diluted to different concentrations (1, 0.5, 0.25, 0.125, and 0.0625 mg/ml). 10 μl portion of the samples were subjected to HPLC three times. Calibration plots were obtained by measuring the peak area. The constituents of the benzene extract were identified by comparison of their retention times and UV absorption spectra with those of pure authentic sample from Sigma Company (for emodin) and previously isolated from lichens [6, 12, 13].

RESULTS AND DISCUSSION

In our present study, phytochemical analysis of the lichen *Laurera benguelensis* was performed for the first time. For this purpose, a HPLC method was developed for the characterization of anthraquinones in *L. benguelensis*. The highest sensitivity was obtained at the wavelength of 250 nm, where anthraquinones show their maximum absorbance. Linear calibration graphs, based on the peak area with good correlation (Table 2) were obtained for anthraquinones investigated. The detection limits are also reported in Table 2. Two solvent systems were used: A and B in a linear gradient programme (Table 1). The following compounds were identified in *Laurera benguelensis*: 1.8-dihydroxy-3-methoxy-6-methylanthraquinone (physcion, **5**), 1,8-dihydroxy-3-hydroxymethyl-6-methoxyanthraquinone (teloschistin, **2**), 1,8-dihydroxy-3-formyl-6-methoxyanthraquinone (fallacinal, **3**) and 1,3,8-trihyroxy-6-methylanthraquinone (emodin, **4**).

Table 1. HPLC gradient used for separation of anthraquinones

Step	*t*, min	A, %	B, %
0	0.1	50	50
1	35	95	5
2	15	95	5
3	2	98	2
4	2	98	2
5	2	50	50
6	4	50	50

Note. Solvents A and B are described in the text.

Table 2. Correlation coefficients (*R*) and detection limits (*m*) of anthraquinones **1**–**5**

No.	Name	*R*	*m*, mg
1	Citreorosein	0.9998	3.0
2	Teloschistin	0.9997	2.4
3	Fallacinal	1.0000	1.5
4	Emodin	0.9999	3.4
5	Physcion	0.9999	1.7

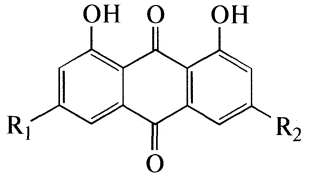

$R_1 = OCH_3$ (**2**, **3**, **5**) and OH (**4**),
$R_2 = CH_3$ (**4**, **5**), CH_2O (**2**), and CHO (**3**).

Figure is shown the HPLC chromatograms of the standard solution and benzene extract of *L. benguelensis*. The t_R values for teloschistin, fallacinal, emodin and physcion amount to 20.3; 29.2; 41.2 and 43.9 min, respectively (figure). The structures of these compounds were determined by comparison of their t_R values with the chromatogram of the standard solution. In addition, the comparison of their UV absorption spectra with those of pure authentic sample, previously isolated from lichens, was also performed [6, 12, 13].

Physcion (t_R = 43.9 min) was dominant anthraquinone in the lichen examined. The content of the physcion in *Laurera benguelensis* was 6.2 mg/g of extract. Other anthraquinones were present in smaller amounts (from 0.7 to 0.9 mg/g of extract).

Physcion (**5**) possesses some biological activities, including purgartive, antibacterial and antifungal properties [1, 13]. In nature it can be also found in plants belonging to *Rhamnus* and *Rheum*, and some lichen belonging to the family *Teloschistaceae*. Emodin

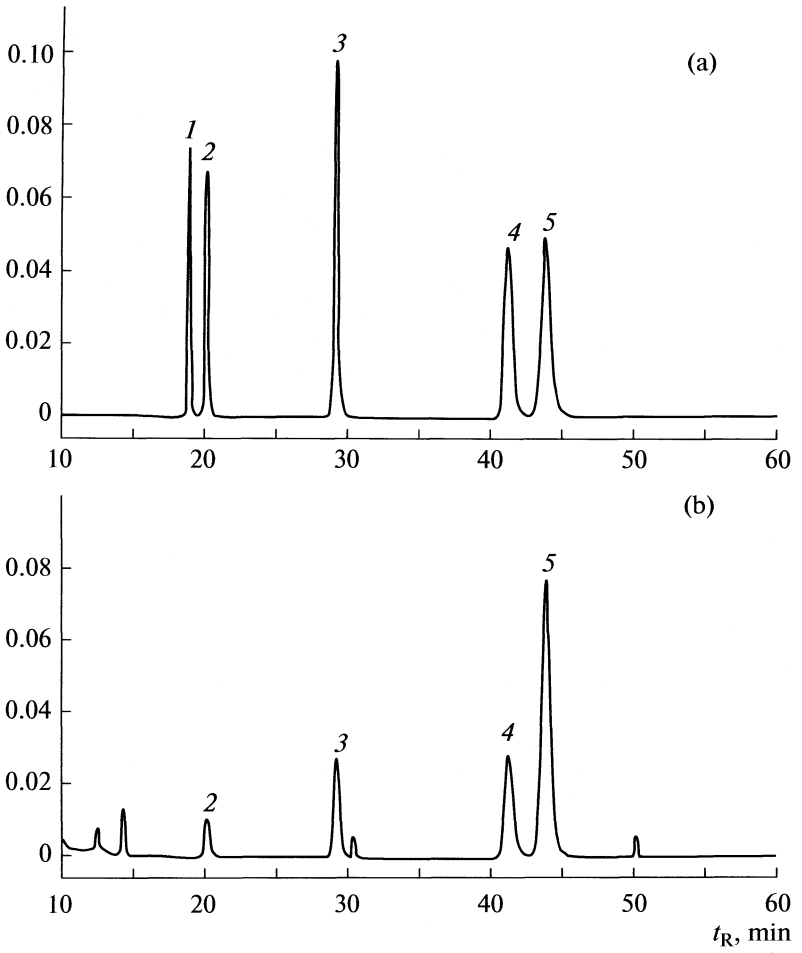

HPLC trace of anthraquinone standards (a) and the extract of L. benguelensis (b). The peaks marked with *1–5* are citreorosein (not found in the extract), teloschistin, fallacinal, emodin and physcion, respectively.

(**4**), well-known light-orange biological active substance is ingredient of some pharmaceutical drugs. Emodin can be found in nature in plants: *Rheum*, *Rhamnus*, some fungi and some lichens belonging to the family *Teloschistaceae*. Fallacinal (**3**) and teloschistin (fallacinol) (**2**) are compounds which have been found mainly in some lichens which belong to the family *Teloschistaceae* (*Caloplaca*, *Xanthoria* and *Teloschistes*).

CONCLUSION

In this paper an HPLC method was developed for the characterization of anthraquinones in the lichen *L. benguelensis*. It was found that good separation was achieved when methanol-water-phosphoric acid was used as the mobile phase in gradient mode (Table 1). We conclude that the above technique is useful for detection and identification of minor anthraquinone metabolites in lichens. These results suggest that the extracts of the lichen *L. benguelensis* can be of use as an accessible source of natural anthraquinones for possible food supplements, and in the pharmaceutical industry. Importance of this research is in recognizing some new source (lichen and its extract) as a natural emplacement of antioxidants, because oxidation with free radicals or autooxidation is an important problem for preservation of food products.

ACKNOWLEDGMENTS

The authors acknowledge financial support by the Ministry of Science and Environmental of Republic of Serbia (Grant No. 142025) and Medical Faculty University of Kragujevac, Serbia (Grant No. 01-1362).

REFERENCES

1. R. A. Muzychkina, *Natural anthraquinones, Biological and Physicochemical Properties*. House Phasis, Moscow, 1998.
2. S. K. Shahi, A. C. Shukla, A. Dikshit, D.K. Uperti, Lichenologist **33**, 177 (2001).
3. M. E. Hale, *The Biology of Lichens*, 4th ed. Edward Arnold, London 1983.

4. Y. Yamamoto, Y. Kinoshita, H. Matsubara, K. Kinoshita, K. Koyama, K. Takahashi, T. Kurokawa, I. Yoshimura, Rec. Res. Phytochem. **2**, 23 (1998).
5. K. S. Agarwal, S. Sudhik, S. Singh, Verma, S. Kumar, J. Ethnopharmacol. **72**, 43 (2000).
6. T.N. Manojlović, S. Solujic, S. Sukdolak, Lichenologist **34**, 83 (2002).
7. N. Manojlović, Z. Markovic, M., Djuric, J. Chil. Chem. Soc. **52**, 1330 (2007).
8. J. Santesson, Phytochem. **9**, 2149 (1970).
9. H. Nakano, T. Komiya, S. Shibata, Phytochem. **11**, 3505 (1972).
10. T. N. Manojlović, W. Gritsanapan, M. Milosev and I. Manojlovic Planta Med. **73**, 801 (2007).
11. U. Søchting, Bibl. Lichen. **78**, 395 (2001).
12. N. T. Manojlović, S. Solujic, S. Sukdolak, L. J. Krstic, J. Serb. Chem. Soc. **7**, 63 (1998).
13. T. N. Manojlović, S. Solujic, S. Sukdolak, M. Milosev, Fitoterapia **76**, 244 (2005).
14. K. E. Stensio, C. A. Wachtmeister, Acta. Chem. Scand. **23**, 144 (1968).
15. J. A. Elix, 1996. Biochemistry and Secondary Metabolites. In: Nash III, T.H. (Ed.)
16. G. F. Barbosa, Maria da Conceição F. de Oliveira, Braz-Filho, R., S. R. Edilberto, 2004França C.V., M. de Fátima Agra, M. J. Barbosa-Filho, E. V. L. da-Cunha, S. M. da-Silva, Biochem. Sys. Ecol. **31**, 1341 (2003).
17. K. Vongkolsuk, P. M. McCarthy, P. Mongkolsuk, K. Boonpragob, Mycotaxon **70**, 227 (1999).

ЖУРНАЛ ФИЗИЧЕСКОЙ ХИМИИ, 2009, том 83, № 9, с. 1734–1738

COLLOID CHEMISTRY AND ELECROCHEMISTRY

УДК 541.18

EFFECT OF SYNTHESIS PARAMETERS ON POLYMETHACRYLIC ACID XEROGEL STRUCTURES AND EQUILIBRIUM SWELLING

© 2009 V. Panić*, J. Jovanović**, B. Adnadjević**, S. Velicković*

*Faculty of Technology and Metallurgy, Karnegijeva 4, 11000 Belgrade

**Faculty of Physical Chemistry, Studentski Trg 12–16. 11000 Belgrade

E-mail: bora@ffh.bg.ac.rs

Abstract – Hydrogels based on crosslinked polymethacrylic acid were synthesized via free-radical polymerization in aqueous solution, using N,N'-methylene bisacrylamide as a crosslinking agent and 2,2'-azobis-[2-(2-imidazolin-2-yl)propane] dihydrochloride as an initiator. The influence of the reaction parameters (the neutralization degree of methacrylic acid and the initial monomer concentration) on the equilibrium swelling degree, the swelling kinetic parameters and the basic structural properties of xerogels, was investigated. The change of synthesis parameters leads to the change of the basic structural parameters of xerogel, as well as the equilibrium swelling degree and the initial swelling rate of the hydrogels. It is found that there are power form relationships between the equilibrium swelling degree, the initial swelling rate and the structural xerogel's properties and the change of the neutralization degree of monomer, i.e. the monomer concentration. The examined correlations proved that the crosslinking density is the crucial parameter which determines all the other investigated structural and swelling parameters.

INTRODUCTION

Applications of hydrogels mainly depend upon their swelling behaviour, which is dependant on their structural properties, especially on the crosslinking density. Due to the enormous both fundamental and practical importance, the consideration of the structural properties of the synthesized xerogels and the correlation between them and their swelling properties are objective of many investigation.

S.K. Bajpai and S. Singh investigated network and swelling parameters of polymethacrylamide-co-methacrylic acid hydrogels and fortified that there were considerable effects of synthesis conditions, such as reaction temperature, initiator content etc. on water absorbency. The obtained results of dynamic water uptake clearly indicate that with increase in crosslinking ratio, the water uptake at different time-intervals decreases [1].

A. Purjavadi et al. synthesized a novel superabsorbent composite hydrogel based on sodium alginate and the inorganic clay kaolin through the graft polymerization of acrylic acid (AA) with N,N'-methylene bisacrylamide (MBA) as a crosslinking agent and ammonium-persulfate (APS) as an initiator. The effects of the reaction variables, such as the MBA, AA and APS concentration as well as the alginate/kaolin weight ratio, on the water absorption of the composite hydrogel were systematically optimized. In that study, a novel alginate-g-PAA Sap-Hg with water absorption about 400 times its weight was synthesized. A reverse relationship between the swelling capacity and the concentration of a crosslinker was found. The influence of the total monomer concentration was studied in series of experiments through the variation of the Na-alginate concentration. The dependence between the initiator concentration and the water absorbency was complex and showed maximum [2].

According to the best of our knowledge there is no sufficient data concerning the investigation of the correlations between the reaction parameters, structural properties of the prepared xerogels and their swelling and other properties concerning the polymethacrylic acid (PMMA) hydrogel. In this investigation, series of PMAA hydrogels with different neutralization degree of methacrylic acid and the monomer concentration were synthesized in order to investigate influence of these reaction variables on the equilibrium swelling degree, the initial swelling rate and the basic structural properties of xerogels (xerogel density, the number average molar mass between the network crosslinks, the crosslink density, the number of elastically effective chains totally induced in a perfect network per unit volume and the distance between the macromolecular chains).

EXPERIMENTAL

Materials

Methacrylic acid (MAA)(99.5%) was purchased from Merck KGaA, Darmstadt Germany, stored in a refrigerator and melted at room temperature before use. N,N'-Methylene bisacrylamide (MBA)(p.a) was supplied from Aldrich Chemical Co., Milwaukee, USA. The initiator, 2,2'-azobis-[2-(2-imidazolin-2-yl)propane] Dihydrochloride (VA-044) (99.8%) was supplied from Wako Pure Chemical Industries, Ltd.

Sodium hydroxide (p.a) was obtained by Aldrich Chemical Co., Milwaukee, USA. All chemicals were used as received. Distilled water was used in all experiments.

PMAA Hydrogels Synthesis

Series of polymethacrylic acid hydrogels with different neutralization degrees of methacrylic acid and monomer concentrations were prepared via free-radical polymerization in aqueous media, using the following general procedure.

Firstly, 15 ml of MAA was dissolved in adequate amount of distilled water and then neutralised with 25 wt% sodium hydroxide solution under the nitrogen atmosphere and with constant stirring. After neutralization of MAA to the required neutralization degree was completed, the crosslinker MBA solved in distilled water, was added. The mixed solution was stirred for approximately 30 min at room temperature and then the initiator (VA-044), dissolved in water , was added to the reaction mixture. In the next 10 min solution was stirred and bubbled with nitrogen, and then poured into the glass moulds (12 × 12 mm, plates) separated by a rubber gasket, 2 mm thick, and placed into the oven at 80°C, for 3 h to complete the polymerization. The resulting products were taken out the moulds and hydrogel disks (10 mm in diameter, and ca. 2 mm thick) were punched from sheets and immersed in distilled water. The water was changed in the next 5 days in order to remove sol fraction of polymer and unreacted monomer. The washed-out hydrogels were dried in an air oven at 50°C until they reached constant mass. The obtained products were stored in a vacuum exicator before use.

PMAA hydrogel samples with different neutralization degree (ND) of MAA were prepared keeping constant concentration of monomer (c_{MAA} (20 wt %) as well as initiator and crosslinker (c_{in} (0.06 mol %) and c_{MBA} (0.4 mol %) (both respective to monomer)). PMAA hydrogel samples with different monomer concentrations and were synthesized keeping constant neutralization degree of monomer (40 %ND) and concentrations of crosslinker (0.4 mol %) and initiator (0.06 mol %).

Characterization of the Xerogels

The following structural properties of the PMAA hydrogel were determined and calculated: xerogel density (ρ_{xg}), average molar mass between the network crosslinks (M_c), crosslinking density (ρ_c), the number of elastically effective chains, totally induced in a perfect network per unit volume (V_e) and distance between the macromolecular chains (pore size)(ξ).

Xerogel densities of synthesized samples were determined by measurements with picnometer method, using the equation:

$$\rho_{xg} = m_{xg}\rho_t/(m_1 + m_{xg} - m_2),$$

where, m_{xg} is the weight of the xerogel sample, m_1 is the weight of picnometer filled with toluene, used as the non-solvent, m_2 is the weight of picnometer filled with toluene and with xerogel sample in it, and ρ_t is the density of the toluene ($\rho_t = 0.87$ g/cm^3).

Values of the other above-mentioned structural properties were determined by using following equations, proposed by Flory and Rehner [3]:

$$M_c = \frac{-\rho_{xg} V_{H_2O} v_{2,s}^{1/3}}{\ln(1 - v_{2,s}) + v_{2,s} + \chi v_{2,s}^2},$$

$$\rho_c = \frac{M_0}{M_c},$$

$$v_{2,s} = \frac{1}{(1 + \rho_{xg} SD_{eq})},$$

where V_{H_2O} is the molar volume of H_2O, χ is the Flory–Huggins interaction parameter between solvent (H_2O) and polymer (PMAA), calculated by following equation :

$$\chi = [\ln(1 - v_{2,s}) + v_{2,s}]/v_{2,s}^2$$

and M_0 is the molar mass of repeat unit, given as:

$$M_0 = [M_{MAA-Na} ND + (100\% - ND) M_{MAA}]/100\%.$$

In this equation ND is neutralization degree of MAA, and M_{MAA} and M_{MAA-Na} are molar masses of methacrylic acid and sodium-methacrylate, respectively.

Another way to formulate crosslinking density is through the number of elastically effective chains totally induced in a perfect network per unit volume (V_e):

$$V_e = d_{xg} N_A / M_c,$$

where N_A is Avogadro number [1].

The mesh size was calculated as:

$$\xi = l v_{2,s}^{-1/3} (2C_n M_c / M_0)^{1/2},$$

where C_n is the Flory characteristic ratio (C_n(MAA) = = 14.6) and l is the carbon–carbon bond length (1.54 Å).

Swelling Experiments

The swelling parameters were determined by leaving dried xerogel disks with an average weight of 0.050g ± 10% to swell in distilled water at 25 ± 0.2°C. At the beginning, hydrogel disks were weighted (m_0) and immersed entirely in excess distilled water. At predetermined time intervals, samples were taken out from the water, dried with gauze and weighted (m_t). The measurements were continued until the hydrogels reached equilibrium and attained constant mass. Since the swollen gel appeared to be fragile the technique with a grid boat was used [4].

The isothermal swelling degree, SD, is defined as the difference between the weights of the swollen hy-

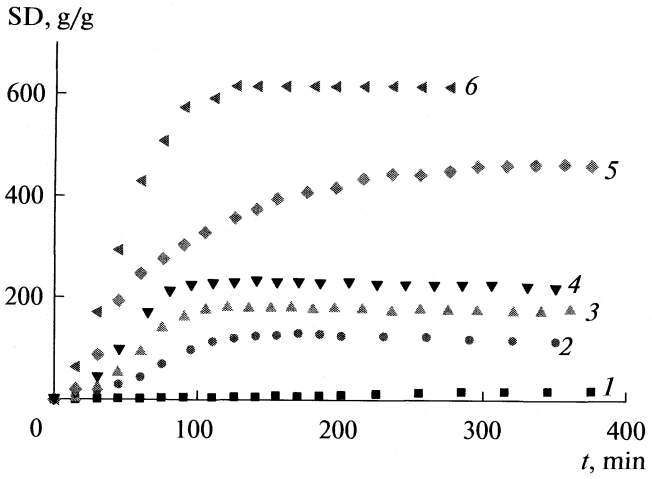

Fig. 1. The isothermal kinetic curves of swelling of PMMA hydrogels obtained at different neutralization degrees of monomer (*1*) 0, (*2*) 20, (*3*) 40, (*4*) 60, (*5*) 80, and (*6*)100.

drogel sample at the time t (m_t) and in the dry state (xerogel) (m_0), divided by the weight of the xerogel sample, and calculated as a function of time, using the following equation:

$$SD = (m_t - m_0)/m_0.$$

When the hydrogel sample reach the constant mass (m_{eq}), the equilibrium swelling degree (SD_{eq}), was determined as follows:

$$SD_{eq} = (m_{eq} - m_0)/m_0.$$

For each sample, at least three measurements were performed and the obtained mean values were reported.

RESULTS AND DISCUSSION

The Influence of the Degree of Neutralization

Figure 1 shows the isothermal swelling kinetics curves of the synthesized poly(methacrylic acid) hydrogels with different neutralization degrees of MMA, in distilled water at 25°C. As can be seen from the results presented in Fig. 1, all of the swelling isotherms of PMMA hydrogels are of a similar shape. Three particular shapes of the change of the swelling degree with time: a linear, non-linear and the saturation part can be noticed in all of the presented swelling curves. In order to determine the influence of the neutralization degree on the shape of the swelling kinetics curves the following parameters were defined: the time of the range of linearity (t_l), the corresponding swelling degree (SD_l) and the initial swelling rate (v_{in}). The time of the range of linearity (t_l) is defined as the time interval within which the dependence between SD and time gives the straight line. Swelling degree reached at time t_l is denoted as SD_l.

Table 1. The effect of the neutralization degree of monomer on the equilibrium swelling degree and the initial swelling rate of PMAA hydrogels

ND, %	SD_{eq}, g/g	SD_l, g/g	t_l, min	v_{in}, min^{-1}
0	27.27	19.1	345	0.06
20	101.29	66.0	94.2	0.81
40	176.42	160	83.4	1.70
60	224.94	210	80.6	2.50
80	419.37	247	79.8	3.94
100	601.67	578	79.0	6.60

The initial swelling rate (v_{in}) is the swelling rate during this range of linearity, and is calculated by the equation:

$$v_{in} = SD_l/t_l.$$

The influence of the neutralization degree of MAA on the equilibrium swelling degree and the initial swelling rate of PMAA hydrogels is presented in Table 1. Based on the results presented in Table 1 it is easy to observe that the equilibrium swelling degree, as well as the initial swelling rate increase with the increase in the neutralization degree of MAA. In contrast to that the time of the range of linearity (t_l) decrease with ND change, significantly from 0 to 20% and further on slightly.

The change of the equilibrium swelling degree values and the initial swelling rate with the change of neutralization degree can be described by the following equations ($R^2 = 0.96$, where R is the linear correlation coefficient):

$$SD_{eq} = 0.66ND^{1.47}, \quad v_{in} = 0.0029ND^{1.67}.$$

The data was analysed by using the commercial program Orgin microcal 7.0 and the relation with the best correlation coefficient are presented.

The structural characteristics of PMAA xerogels with different neutralization degree of monomer are presented in Table 2.

The increase in the neutralization degree of MMA leads to the increase in the values of the xerogel density, the average molar mass between the network crosslinks, the distance between the macromolecular chains, while decreases the values of the crosslinking density and the number of elastically effective chains totally induced in a perfect network per unit volume.

The change of structure characteristics of xerogel that follow the change of the neutralization degree of MAA can be described by the following equations: ($R^2 = 0.99$):

$$\rho_{xg} = 1.03ND^{0.07}, \quad \rho_c = 0.104ND^{-1.50},$$

$$M_c = 1.56ND^{3.06}, \quad \xi = 0.18ND^{1.89},$$

$$V_e = 9.34ND^{-1.51}.$$

Because the crosslinking density is the crucial parameter that influences structural properties of the hydrogels, the influence of ρ_c of hydrogel on the structural characteristics of PMAA xerogels was examined. By analysing the obtained results we found that the relationship be-

tween the structural characteristics of xerogels with different neutralization degrees of monomer and ρ_c can be descried by the following equations:($R^2 = 0.99$):

$$M_c = 60.07\rho_c^{-1.06}, \quad \xi = 1.06\rho_c^{-0.70},$$

$$V_e = 1.10 \times 10^{22}\rho_c^{-1.03}.$$

The changes of the SD_{eq} and v_{in} are also found to be in correlation with ρ_c, as presented: ($R^2 = 0.99$):

$$SD_{eq} = 1.92\rho_c^{-0.58}, \quad v_{in} = 0.011\rho_c^{-0.65}.$$

The observed changes of the SD_{eq}, the initial swelling rate and the structural parameters of xerogel as a function of the neutralization degree of monomer can be explained by interactions between ionized and non-ionized reaction species present in the system.

The monomer can exist in two forms – as methacrylic acid or as a methacrylate anion.

The increase in the neutralization degree increases the concentration of the methacrylate anion. That is the form that does not favourites electron delocalization as much as the acid form. So, the increase in the concentration of methacrylate anion reduces the polymerization rate and reaction yields while the ρ_c value of the network that is formed decreases. The change in the crosslinking density has an effect on all the other hydrogel properties in the way previously described.

The influence of monomer concentration

Figure 2 presents the swelling isotherms of polymethacrylic acid hydrogels synthesized using different concentrations of monomer in the reaction mixtures.

It can be clearly seen from the Fig. 2 that all the curves have a similar shape, as it is described for Fig. 1. The results presented in Fig. 2 are analysed as in the previous part of this work, and the results for the equilibrium swelling degree and the initial swelling rate are obtained and presented in Table 3.

As can be clearly seen from the data presented in Table 3, the values for the equilibrium swelling degree and the initial swelling rate decrease with the increase in the monomer concentration. Opposite to that the increase in monomer concentration leads to the increase in the time of the range of linearity. Dependences between the SD_{eq} and v_{in} and the monomer concentration in the reaction mixture, given in Table 3, can be described with the following equations:

$$SD_{eq} = 506797c_{MAA}^{-2.65} \quad (R^2 = 0.99),$$

$$v_{in} = 35895c_{MAA}^{-3.32} \quad (R^2 = 1).$$

The influence of the monomer concentration in the reaction mixture on the characteristic structural parameters of PMAA xerogels is presented in Table 4. It can be clearly seen from the data presented in Table 4 that the increase in monomer concentration leads to increase in values of the xerogel density, crosslinking density and the number of elastically effective chains totally induced in a perfect network per unit volume, and to the decrease in the values of the average molar mass between the network crosslinks and the distance between the macromolecular chains.

Table 2. The effect of the neutralization degree of monomer on the structural characteristics of PMAA xerogels

ND, %	ρ_{xg}, g/cm^3	M_c, g/mol	$\rho_c \times 10^4$	ξ, nm	$V_e \times 10^{-19}$, cm^{-3}
0	1.33	9725	88.4	29.5	8.22
20	1.29	78211	11.6	124.4	0.99
40	1.35	222820	4.25	250.4	0.36
60	1.38	354536	2.80	337.0	0.23
80	1.42	1.072×10^6	0.97	712.0	0.08
100	1.45	2.079×10^6	0.52	1103.5	0.04

Table 3. The effect of the concentration of monomer on the equilibrium swelling degree and the initial swelling rate of PMAA hydrogels at 25°C

c_{MAA}, wt %	SD_{eq}, g/g	SD_I, g/g	t_I, min	v_{in}, min^{-1}
20	176.4	160.0	94.2	1.70
30	68.1	50.0	105	0.47
40	18.6	13.7	110	0.12

The results presented in Table 4 were analysed and the correlations obtained between c_{MAA} and the characteristic structural parameters of PMAA xerogels are found to be the best fitted with the following equations:

$$\rho_{xg} = 1.03c_{MAA}^{0.09} \quad (R^2 = 1),$$

$$\rho_c = 5.66 \times 10^{-14}c_{MAA}^{7.13} \quad (R^2 = 1),$$

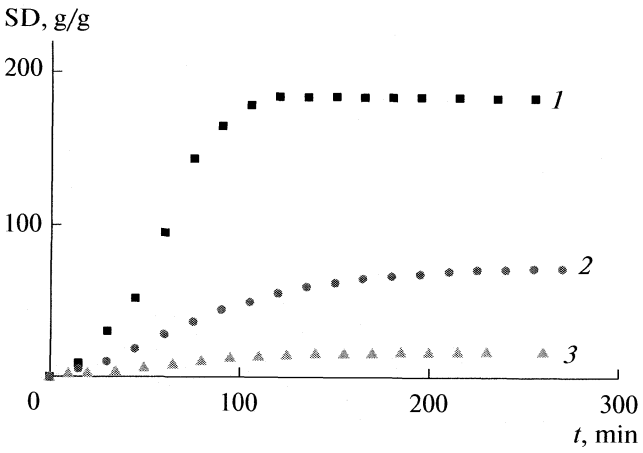

Fig. 2. The isothermal kinetic curves of swelling of PMMA hydrogels, at 25°C, with different concentrations of monomer (*1*) 20, (*2*) 30 and (*3*) 40 wt %.

Table 4. The characteristic structural parameters of PMAA xerogels with different concentrations of monomer

c_{MAA}, wt %	ρ_{xg}, g/cm^3	M_c, g/mol	$\rho_c \times 10^4$	ξ, nm	$V_e \times 10^{-19}$, cm^{-3}
20	1.35	222820	4.25	250.36	0.365
30	1.40	50736	18.7	88.27	1.66
40	1.44	6381	148.6	20.64	13.55

$$M_c = 2.63 \times 10^{10} c_{MAA}^{-3.90} \quad (R^2 = 0.99),$$

$$\xi = 1.415 \times 10^{6} c_{MAA}^{-2.88} \quad (R^2 = 0.99),$$

$$V_e = 3.66 \times 10^{8} c_{MAA}^{7.22} \quad (R^2 = 0.99).$$

The structural xerogel's parameters can also be described as a function of the xerogel crosslinkig density (ρ_c), which appears to be the most important parameter that influences structural properties of the synthesized hydrogels, by using the following expressions: ($R^2 = 1$):

$$M_c = 94.8\rho_c^{-1}, \quad \xi = 1.06\rho_c^{-0.70},$$

$$V_e = 9.63 \times 10^{21}\rho_c^{1.01}, \quad SD_{eq} = 1.22\rho_c^{-0.64},$$

$$v_{in} = 0.0025\rho_c^{-0.84}.$$

The increase in the monomer concentration in the reaction mixture increases the polymerization rate, and that leads to the decrease in the molar mass between crosslinks (M_c) and the increase in xerogel crosslinkig density (ρ_c). Further, as mentioned before, the change in the ρ_c values effects all the other hydrogel properties.

CONCLUSIONS

Poly(methacrylic acid) hydrogels are synthesized with different neutralization degree of monomer and with different monomer concentration in the reaction mixture. The change in the synthesis parameters leads to the change of the equilibrium swelling degree in the range from 18.6 to 601.7 g/g and the initial swelling rate, in the range from 0.06 to 6.60 min^{-1}.

The power form relationships between the equilibrium swelling degree, the initial swelling rate and the structural xerogel's properties and the change of the neutralization degree of monomer, i.e. the monomer concentration are found to exist. The values of the equilibrium swelling degree, the initial swelling rate and the structural parameters of xerogel (ρ_{xg}, V_e, M_c, ξ) are defined by the value of the crosslinkig density (ρ_c), and that those dependences also have power shape.

ACKNOWLEDGMENTS

This investigation was supported by the Ministry of Science of Serbia, through projects 142025G and 142023.

REFERENCES

1. S. K. Bajpai, S. Singh, Reactive & Functional Polymers **66**, 431 (2006).
2. A. Pourjavadi, H. Ghasemzadeh, R. Soleyman, J. Appl. Polym. Sci. **105**, 2631 (2007).
3. P. J. Flory, J. Rehner Jr., J. Chem. Phys. **11**, 521 (1943).
4. B. Adnadjevic, J. Jovanovic, J. Appl. Polym. Sci. **107**, 3579 (2008).

ЖУРНАЛ ФИЗИЧЕСКОЙ ХИМИИ, 2009, том 83, № 9, с. 1739–1746

COLLOID CHEMISTRY
AND ELECTROCHEMISTRY

УДК 541. 13

ELECTROHYDRODYNAMICS OF DEVELOPED LIQUID/LIQUID INTERFACES: FRACTIONAL ORDER TIME DELAY SYSTEMS

© 2009 A. M. Spasic

Institute for Technology of Nuclear and Other Mineral Raw Materials, Dept. of Chem. Engng., 86 F. d'Esperey St., P.O. Box 390, 11000 Belgrade, Serbia

E-mail: a.spasic@itnms.ac.yu

Abstract – This brief comprehensive review presents the recent development in basic and applied science and engineering of finely dispersed particles and related systems in general, but more profound and in-depth treatise are related to the liquid-liquid finely dispersed systems i.e. emulsions and double emulsions. The electroviscoelastic behavior of e.g., liquid/liquid interfaces (emulsions and double emulsions) is based on three forms of "instabilities"; these are rigid, elastic, and plastic. The events are understood as interactions between the internal (immanent) and external (incident) periodical physical fields. Since the events at the interfaces of finely dispersed systems have to be considered at the molecular, atomic, and/or entities level it is inevitable to introduce the electron transfer phenomenon beside the classical heat, mass, and momentum transfer phenomena commonly used in chemical engineering. Three possible mathematical formalisms have been derived and discussed related to this physical formalism, i.e. to the developed theory of electroviscoelasticity. The first is stretching tensor model, where the normal and tangential forces are considered, only in mathematical formalism, regardless to their origin (mechanical and/or electrical). The second is classical integer order van der Pol derivative model. Finally, the third model comprise an effort to generalize the previous van der Pol differential equations, both, linear and nonlinear; where the ordinary time derivatives and integrals are replaced by corresponding fractional-order time derivatives and integrals of order $p < 2$ ($p = n - \delta$, $n = 1$, 2, $\delta \ll 1$). In order to justify and corroborate more general approach the obtained calculated results were compared to those experimentally measured using the representative liquid–liquid system. Also, a new idea related to the probable discussion and/or elucidation of the problems in the theoretical and experimental status of decoherence is mentioned.

INTRODUCTION

Over the last decade the biggest advances in physics, physical chemistry, and biochemistry have come from thinking smaller. This research takes an interdisciplinary approach to the elucidation of the momentum transfer phenomenon as well as the electron transfer phenomenon, at well-characterized developed, both, rigid and deformable liquid-liquid interfaces. The considered scales are micro, nano and atto, using various theoretical approaches. Micro scales may cover more or less classical chemical engineering insight, while nano and atto scales focus on modern molecular and atomic engineering.

A new idea, using deterministic approach, has been applied for the elucidation of the electron and momentum transfer phenomena at, both, rigid and deformable interfaces in finely (micro, nano, atto) dispersed systems. Since the events at the interfaces of finely dispersed systems have to be considered at the molecular, atomic, and/or entities level it is inevitable to introduce the electron transfer phenomenon beside the classical heat, mass, and momentum transfer phenomena commonly used in chemical engineering [1]. Therefore, an entity can be defined as the smallest indivisible element of matter that is related to the particular transfer phenomena. Hence, the entity can be either differential element of mass/demon, or an ion, or a phonon as quanta of acoustic energy, or an infon as quanta of information, or a photon, or an electron [1].

A possible approach is proposed to the general formulation of the links between the basic characteristics, levels of approximation and levels of abstraction related to the existence of finely dispersed systems (DS) [1]. At first for the reason of simpler and easier physical and mathematical modeling, it is convenient to introduce the terms: homo-aggregate (phases in the same state of aggregation, HOA) and hetero-aggregate (phases in a more than one state of aggregation, HEA). Now the matrix presentation of all finely dispersed systems is given by

$$[(\mathrm{DS})^{ij} = (\mathrm{HOA})\delta^{ij} + (\mathrm{HEA})\tau^{ij}], \qquad (1)$$

where i and j refer to the particular finely dispersed system position, i.e. when $i = j$ than diagonal positions correspond to the homo-aggregate finely dispersed systems (plasmas, emulsions and dispersoids, respectively), and when $i \neq j$ than tangential positions correspond to the hetero-aggregate systems (fluosols/fog, fluosols/smoke, foam, suspension, metal, and vesicle, respectively). Furthermore, the interfaces may be deformable (D) and rigid (R) that is presented in table.

Now, related to the levels of abstraction and approximation it is possible to distinguish continuum

A new classification of finely dispersed systems ([3], P. 985)

DP	DM = Gas	DM = Liquid	DM = Solid
Gas	PLASMA D	ROAM D	METAL R
Liquid	FLUOSOL/fog D	EMULSION D	VESICLE D
Solid	FLUOLSOL/smoke R	SUSPENSION R	DISPERSOIDE R

Note: DP – Dispersed Phase; DM – Dispersion Medium.

models (the phases considered as a continuum i.e. without discontinuities inside entire phase, homogeneous, and isotropic) and discrete models (the phases considered according to the Born–Oppenheimer approximation: entities and nucleus/CTE motions are considered separately). Continuum models are convenient for micro-scale description (entire object models), e.g. conventional products, precision products, chemistry/solutions, biochemistry while discrete models are convenient for either nano-scale description (molecular mechanics, molecular orbits), e.g. chemistry/solutions, biochemistry, molecular engineering, and or atto-scale description (quantum electrodynamics), e.g. molecular engineering, atto engineering. Since the interfaces in finely dispersed systems are very developed it is sensible to consider the discrete models approach for description of a related events.

PREVIOUS WORK

Physical Formalisms–Classical Approach and a New Approach

Following a classical deterministic approach, the phases that constitute a multiphase dispersed system are assumed to be a continuum, i.e., without discontinuities inside the entire phase, that is considered homogenous and isotropic [1–7]. Therefore, the basic laws, e.g., conservation of mass, first and second Cauchy's laws of motion, first and second laws of thermodynamics, are applicable.

According to the classical approach, the behavior of liquid–liquid interfaces in fine dispersed systems is based on an interrelation between three forms of "instabilities". These are sedimentation, flocculation/coagulation, and coalescence. These events can be understood as a kind of interaction between the liquid phases involved [1, 7]. Furthermore, the forces responsible for sedimentation and flocculation are gravity and van der Waals forces of attraction, respectively, and the forces responsible for coalescence are not well known [5, 6], although some suggestions have been made recently [1, 3].

A new, deterministic approach discusses the behavior of liquid–liquid interfaces in fine dispersed systems as an intorelation between three other forms of "instabilities". These are rigid, elastic, and plastic [1–7]. Figure 1 shows the events that are understood as interactions between the internal/immanent and the external/incident periodical physical fields. Since both electric/electromagnetic and mechanical physical fields are present in a droplet, they are considered as immanent or internal, whereas ultrasonic, temperature, or any other applied periodical physical fields are considered as incident or external. Hereafter, the rigid form of instability comprises the possibility of two-way disturbance spreading, or dynamic equilibrium. This

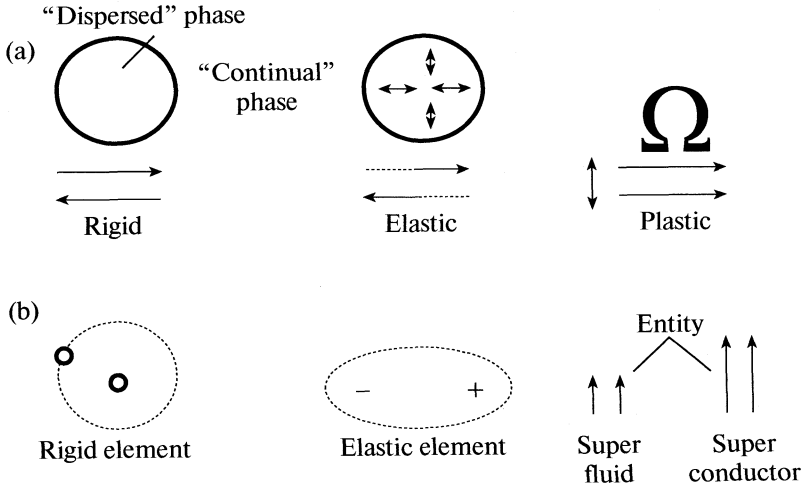

Fig. 1. A new approach, (a) "instabilities", rigid, elastic, plastic; (b) the constructive elements of phases ([4], P. 435).

form of instability, when all forces involved are in equilibrium, permits a two-way disturbance spreading (propagation or transfer) of entities either by tunneling (low energy dissipation and occurrence probability) or by induction (medium or high energy dissipation and occurrence probability).

A classical particle or system could not penetrate region in which its energy would be negative, that is, barrier regions in which the potential energy is greater than the system energy. In the real world, however, a wave function of significant amplitude may extend into and beyond such region. If the wave function extends into another region of positive energy, then the barrier is crossed with some probability; this process is termed tunneling (since the barrier is penetrated rather than climbed). The elastic form of instability comprises the possibility of reversible disturbance spreading, with or without hysteresis. Finally, the plastic form of instability comprises the possibility of irreversible disturbance spreading with a low or high intensity of influence between two entities. Entity is the smallest indivisible element of matter that is related to the particular transfer phenomena. The entity can be either differential element of mass/demon, or phonon as quanta of acoustic energy, or infon as quanta of information, or photon, or electron.

Now, a disperse system consists of two phases, "continuous" and "dispersed". The continuous phase is modeled as an infinitely large number of harmonic electromechanical oscillators with low strength interactions among them. Furthermore, the dispersed phase is a macrocollective consisting of a finite number of microcollectives/harmonic electromechanical oscillators (clusters) with strong interactions between them. The cluster can be defined as the smallest repetitive unit that has a character of integrity. Clusters appear in a micro and nano dispersed systems. The microcollective consists of the following elements: rigid elements (atoms or molecules), the elastic elements (dipoles or ions that may be recombined), and entities (as the smallest elements) [1–4].

Structure, Mechanism, Dynamics

If the liquid–liquid interface, e.g. emulsion or double emulsion, Eq.l. and table, is taken as a central and representative ($i = j = 2$) finely dispersed system it is possible to propose a theory of electroviscoelasticity [1, 2, 5–7] based on a new constitutive model of liquids. The principles of conservation of mass, momentum, energy, and charge are used to define the state of a real fluid system quantitatively. In addition to the conservation equations, which are insufficient to define the system uniquely, statements on the material behavior are also required; these statements are termed constitutive relations, e.g. Fourier's law, Fick's law, and Ohm's law.

Now, the droplet or droplet-film structure is considered as a macroscopic system with internal structure determined by the way the molecules (ions) are tuned (structured) into the primary components of a cluster configuration. At first, during the droplet formation and/or destruction periods, it may be assumed that the electrical analogue consists of a number of serial equivalent circuits; after rearrangement or coupling at resonant/characteristic frequency a probable equivalent circuit is shown in Figs. 2a, and 2b.

Electrical analogue Fig. 2a, consists of passive elements (R, L, and C), and an active element (emitter-coupled oscillator W). Further on the emitter-coupled oscillator is represented by the equvalent circuit as shown in Figs. 2b and 2c shows the electrical (oscillators) and/or mechanical (structural volumes V_j) analogues when they are coupled to each other, e.g. in the droplet. Hence, the droplet consists of a finite number of structural volumes or spaces/electro-mechanical oscillators (clusters) V_j, a finite number of excluded surface volumes or interspaces V_s, and of a finite numbefof excluded bulk volumes or interspaces V_b. Furthermore, the interoscillator/cluster distance or internal separation S_i represents the equilibrium of all forces involved (electrostatic, solvation, van der Waals, and steric) [1, 2, 5, 6]. The external separation S_e is introduced as a permitted distance when the droplet is in interaction with any external periodical physical field. The rigid droplet boundary R presents a form of droplet instability when all forces involved are in equilibrium. Nevertheless, two-way disturbance spreading (propagation or transfer) of entities occur, either by tunneling mechanism (low energy dissipation and occurrence probability) or by induction mechanism (medium or high energy dissipation and occurrence probability).

The elastic droplet boundary $\mathscr{E}$ represents a form of droplet instability when equilibrium of all forces involved is disturbed by the action of any external periodical physical field, but the droplet still exists as a dispersed phase. In the region between the rigid and elastic droplet boundaries, a reversible disturbance spreading occurs with or without hysteresis. After the elastic droplet boundary, the plastic form of droplet instability takes place, then electromechanical oscillators/clusters do not exist any more and the beams of entities or atto-clusters appear. Atto-clusters are the entities that appear in the atto-dispersed systems. In this region one-way propagation of entities occurs.

Mathematical Formalisms–Stretching Tensor Model

Now, using the presented propositions and electromechanical analogies, an approach to non-Newtonian behaviors and to electroviscoelasticity is to be introduced. When the droplet is stopped, e.g., at an inclined plate in the lamellar coallescer, and when the droplet is in the state of "forced" levitation than the volume forces balance each other, and the surface forces alone will be considered [1, 2, 6]. It is assumed that the surface forces are, for the general case that in-

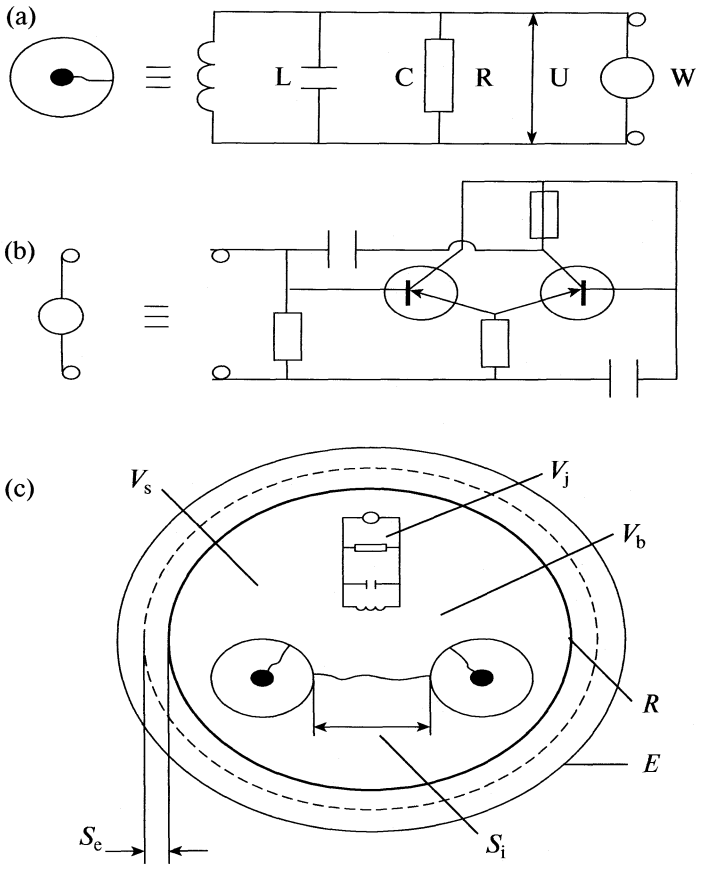

Fig. 2. Graphical interpretation of the structural model: (a) electrical and mechanical analog of the micro collective/cluster; (b) equivalent circuit for the emitter coupled oscillator; (c) the macrocollective: a schematic cross-section of the droplet and its characteristics (V_j – structural volumes/clusters; V_s – excluded surface volumes/interspaces; V_b – excludedmflk volumes/interspaces; S_i – internal separation; S_e – external separation; R – rigidity droplet boundary; E – elasticity droplet boundary) ([1], P. 374).

cludes the electroviscoelastic fluids, composed of interaction terms expressed by

$$dF_s^i = T^{ij}dA_j, \tag{2}$$

where the tensor T^{ij} is given by

$$T^{ij} = -\alpha_0\delta^{ij} + \alpha_1\delta^{ij} + \alpha_2\zeta^{ij} + \alpha_3\zeta_k^i\zeta^{kj} \tag{3}$$

and T^{ij} is composed of two tensors, δ^{ij} is Kronecker symbol, and ζ^{ij} is the stretching tensor. In the first and second isotropic tensors the $\alpha_0 = \alpha_0(\rho, U)$ and $\alpha_1(\rho, U)$ are the potentiostatic pressures, where U represents hydrostatic or electrostatic potential. Now, the general equilibrium condition may be derived from Eq. (3), and may be expressed by

$$\tau = \frac{-\alpha_0 + \alpha_1 + \alpha_2(\sigma/d) + \alpha_3(\sigma/d)}{2(\alpha_2 + \alpha_3)}, \tag{4}$$

where τ is the tangential stress [2, 3]. Note that for dispersed systems consisting of, or behaving as Newtonian fluids, $\alpha_3 = \alpha_3(\rho, U)$ is equal to zero.

The processes of formation/destruction of the droplet or droplet-film structure are nonlinear. Furthermore, the viscosity coefficients μ_i (i = 0, 1, 2), where each consists of bulk, shear, and tensile components, when correlated to the tangential tensions of mechanical origin τ_v can be written as

$$\tau_v = \mu_0\frac{du}{dx} + \mu_1\frac{d^2u}{dx^2} + \mu_2\left(\frac{du}{dx}\right)^2, \tag{5}$$

where u is the velocity and x is one of the space coordinates.

Using the electrical analog, the impedance coefficients Z_i (i = 0, 1, 2), where each consists of ohm, capacitive, and inductive components, will be correlated with the tangential tensions of electrical origin τ_e, as follows:

$$\tau_e = Z_0\frac{d\phi_e}{dt} + Z_1\frac{d^2\phi_e}{dt^2} + Z_2\left(\frac{d\phi_e}{dt}\right)^2, \tag{6}$$

where ϕ_e is the electron flux density, and t is the time coordinate.

Van der Pol Integer Order Derivative Model

Here, postulated assumptions for an Electrical Analogue [1, 2]. are:

1. The droplet is a macro system (collective of particles) consisting of structural elements that may be considered as electro-mechanical oscillators.

2. Droplets as micro collectives undergo tuning or coupling processes, and so build the droplet as a macro collective.

3. The external physical fields (temperature, ultrasonic, electromagnetic, or any other periodic) cause the excitation of a macro system through the excitation of micro-systems at the resonant/characteristic frequency, where elastic and/or plastic deformations may occur.

Hence, the study of the electro-mechanical oscillators is based on electromechanical and electrodynamic principles. At first, during the droplet formation it is possible that the serial analog circuits are more probable, but later, as a consequence of tuning and coupling processes the parallel circuitry become dominant. Also, since the transfer of entities by tunneling (although with low energy dissipation) is much less probable it is sensible to consider the transfer of entities by induction (medium or high energy dissipation). Figure 2b presents the resultant equivalent electrical circuit, rearranged under the influence of an applied physical field, e.g. electromagnetic, such as an antenna output circuit [1, 2].

A nonlinear integral-differential equation of the van der Pol type represents the initial electromagnetic oscillation

$$C\frac{dU}{dt} + \left(\frac{U}{R} - \alpha U\right) + \gamma U^3 + \frac{1}{L}\int U dt = 0, \qquad (7)$$

where U is the overall potential difference at the junction point of the spherical capacitor C and the plate, L is the inductance caused by potential difference, and R is the ohm resistance (resistance of the energy transformation, electromagnetic into the mechanical or damping resistance), t is the time; α and γ are constants determining the linear and nonlinear parts of the characteristic current and potential curves.

The noise in this system, due to linear amplification of the source noise (the electromagnetic force assumed to be the incident external force, which initiates the mechanical disturbance), causes the oscillations of the "continuum" particle (molecule surrounding the droplet or droplet-film structure), which can be represented by the particular integral

$$C\frac{dU}{dt} + \left(\frac{1}{R} - \alpha\right)U + \gamma U^3 + \frac{1}{L}\int U dt = -2A_n \cos\omega t, \quad (8)$$

where ω is the frequency of the incident oscillations.

Finally, considering the droplet or droplet-film structure formation, "breathing", and/or destruction processes, and taking into account all the noise frequency components, which are included in the driving force, the corresponding equation is given by

$$C\frac{dU}{dt} + \left(\frac{1}{R} - \alpha\right)U + \frac{1}{L}\int U dt + \gamma U^3 = \\ = i(t) = \frac{1}{2\pi}\int_{-\infty}^{\infty} \exp(j\omega t) A_n(\omega) d\omega, \qquad (9)$$

where $i(t)$ is the noise current and $A_n(\omega)$ is the spectral distribution of the noise current as a function of frequency [1, 2].

In the case of nonlinear oscillators, however, the problem of determining of the noise output is complicated by the fact that the output is fed back into the system thus modifying in a complicated manner the effective noise input [1, 2]. The noise output appears as an induced anisotropic effect.

RECENT DEVELOPMENT

Van der Pol Fractional Order Derivative Model – Linearized

In an effort to generalize equations (7) and (8) the ordinary time derivatives and integrals are now replaced with corresponding fractional-order time derivatives and integrals [1, 3]. Here, the capacitive and inductive elements, using fractional-order $p < 2$ ($p = n - \delta$, $n = 0$, 1, 2, $\delta \ll 1$) enable formation of the fractional differential equation, i.e. more flexible or general model of liquid–liquid interfaces behaviour. Now, a differ-integral form using Riemann–Liouville definition is given by

$$ {}_0D_t^p[U(t)] = \frac{d^p U}{dt^p} = \frac{1}{\Gamma(1-p)}\frac{d}{dt}\int_0^t \frac{U(\tau)}{(t-\tau)^p} d\tau, \quad 0 < p < 1 \\ {}_0D_t^{-p}[U(t)] = \frac{1}{\Gamma(p)}\int_0^t \frac{U(\tau)}{(t-\tau)^{1-p}} d\tau, \quad p > 0 \qquad (10)$$

Further on, a linear fractional differential equation with zeros initial conditions is obtained

$$C\,{}_0D_t^p[U(t)] + \left(\frac{1}{R} - \alpha\right)U + \frac{1}{L} \times \\ \times\, {}_0D_t^p[U(t)] = i(t). \qquad (11)$$

Further evaluation and calculation related to the solutions of the linearised, both homogeneous and nonhomogeneous, fractional integro-differential equations is presented in references [1, 3].

In the case of nonhomogeneous solution obtained result appears as a band because the input (cos) is of the fractional order too; and output is in a damped oscillatory mode, of high frequencies!

Van der Pol Fractional Order Derivative Model – Nonlinear Case

Nonlinear fractional differential equations have received rather less attention in the literature, partly because many of the model equations proposed have been linear. Here, both cases a nonlinear homogenous ($i(t) = 0$) and nonhomogeneous ($i(t) \neq 0$) are considered. Equivalent nonlinear problem applying differentiation of Eq. (7) is presented by

$$C\frac{d^2U}{dt^2} + \left(\frac{1}{R} - \alpha + 3\gamma U^2\right)\frac{dU}{dt} + \frac{1}{L}U = 0. \qquad (12)$$

In an effort to generalize the previous equation fractional order van der Pol equation become

$$\begin{aligned} {}_0^cD_t^{2p}U(t) = -\frac{1}{C}\left(\frac{1}{R} - \alpha\right){}_0^cD_t^pU(t) - \\ - \frac{3\gamma}{C}U(t)^2{}_0^cD_t^pU(t) - \frac{1}{CL}U(t). \end{aligned} \qquad (13)$$

Further evaluation and calculation related to the solutions of the nonlinear, both homogeneous and nonhomogeneous, fractional integro-differential equations is presented in references [1–3].

Experimental Confirmation

Presented theoretical predictions including both physical and mathematical formalisms have been experimentally corroborated by means of the electrical interfacial potential (EIP) measurements, and by means of the nuclear magnetic resonance spectroscopy (NMR) [1–7]. The obtained experimental results were in good agreement with postulated theory [1, 2].

A NEW PROBABLY POSSIBLE IDEA

This part will treat one important question of the classical limit of quantum mechanics, i.e. is a quantum mechanics applicable at macroscopic level? This question resulted during the research of complex systems by the end of the last century. According to the developed strategy the proposition appeared is: if the macroscopic physical systems are only the special case of a quantum-mechanical systems (e.g. like in von Neumann's theory of the measurement problem) than it is possible to observe, under specified conditions, their quantum mechanical behavior [34].

The behavior of a droplet-film structure submerged into the droplet homophase or double emulsion, including its formation-existence-destruction states, described in this paper [1–36], will be considered as a close to the representative open macroscopic quantum system (OMQS) under the specified conditions. Hence, OMQS are quantum subsystems, i.e. open quantum systems that are in inevitable permanent interaction with other physical systems, which may be named environment [34]. Does the theory of electroviscoelasticity, here presented, may be useful in discussion and/or further elucidation related to the problems of the experimental and theoretical status of decoherence?

Some needed definitions [34]:

1. The choice of an OMQS has to be in accordance to the criteria that confirm its description by the motion equation in a "classical domain".

2. It is convenient that the classical motion equation of the OMQS contain dissipative term.

3. The motion equation of the OMQS must be related, clearly and unequally, to the physical units whose values define distinguishable macroscopic states of the system.

4. The choice of a needed conditions for the following of the behavior of one OMQS have to be limited by the condition that some of the parameters values may correspond to the limit of the correspondence principle, i.e. the condition $n \longrightarrow \infty$ is invalid.

5. It is convenient to consider, theoretically, the behavior of the choused OMQS, and therefore to prepare possible predictions comparable with experimentally attainable situations.

The Leggett's Program: These five points present a Leggett's task and basis for exploration of the macroscopic quantum phenomena of the second kind, i.e. the confirmed quantum mechanical nature of the OMQS is related to these physical situations where the quantum effects are unequally linked to the macroscopically distinguishable states [34].

SUGGESTED PROBLEM – THE MODEL

Finely dispersed system, emulsion/double emulsion, discussed in the paper, now will be considered as the composite system "droplet-film structure + droplet homophase (S + E)". Equivalent electrical circuit of the composite system is presented in Fig. 2 a and b; the history of this system consists of the initial/formation, intermediate/transition, and final/rigid states.

Keeping in mind all the requirements, the needed definitions and Leggett's program the model assumptions are [34–36]:

1. Every stationary state (initial, intermediate, and final) is characterized by interaction in the composite system that is of the same kind – being able to give rise to the occurrence of decoherence with the cluster arrangements as the "pointer basis states".

2. Nonstationary state is characterized by the change in the character of interaction in the composite system. The net effect takes the following "phases" each having its own characteristic time:

a) action of the external/incident physical field/formation of the droplet-film , structure (producing the nonstationary state), taking time, measured using developed liquid/liquid contact cell (LLCC), t_{ext} = 125 ms (Fig. 17 in ref. [7]. or Fig. 8 in ref. [3]);

b) transition/relaxation of the electroviscoelastic droplet-film structure the rigid one (establishing the new, final stationary state), taking time, measured by LLCC, t_{relax} = 8 min (Fig. 18 in ref. [7]. or Fig. 9 in ref. [3]);

c) decoherence process (in the final stationary state), taking time of the "Decoherence time" t_D.

Therefore, the complete generation of the dispersed system/double emulsion takes overall time:

$$t_0 \sim t_{ext} + t_{relax} + t_D, \quad (14)$$

Overall Hamiltonian of the composite system is:

$$H_{overall} = H_{SO} + H_{EO} + H_{int}, \quad (15)$$

where

$$H_{int} = H_{S+E}. \quad (16)$$

SUGGESTED EXPERIMENTAL CONFIRMATION

Since the equivalent electrical circuit, Fig. 2 a may be considered as a kind of Superconducting Quantum Interference Device (SQUID), probably, it may be possible to couple, (at resonant frequency, where all events occur) one adjusted, sensitive tunnel diode oscillator as one detector of Macroscopic Quantum Tunneling Effect (MQTE).

CONCLUSIONS

Recently a number of authors have demonstrated applications of fractional calculus in various fields, such as physics, chemistry, and engineering [2, 3]; also a few works dealing with the application of this mathematical tool in signal processing, anomalous diffusion and control theory were published. Concerning a continuous-time modeling the fractional calculus may be of great interest, e.g. in a problems related to the viscoelasticity [1–3], electrochemical processes, polymer chemistry, heat, mass, momentum and electron transfer phenomena [1, 4]. The main reason for the success of the theory in these cases is that these new fractional-order models are more accurate than integer-order models, i.e. there are more degrees of freedom in the fractional order model. Furthermore, fractional derivatives provide an excellent instrument for the description of a memory and hereditary properties of various materials and processes due to the existence of a "memory" term in a model. This memory term insure the history and its impact to the present and future. Fractional order models have an unlimited memory compared to the integer-order models that have a limited memory. Based on these arguments it was necessary to apply fractional order calculus approach to the recently developed theory of electroviscoelasticity [1]. The obtained results were in much better agreement with experiment than the results obtained using previously developed models, where classical approach was applied. Hence, both the physical and mathematical formalisms were generalized, and a consequence was more accurate and deeper elucidation of the phenomena at the interfaces of finely dispersed systems. Finally, a new, probably possible, idea related to the use of described system (postulated constitutive model of liquids, and developed theory of electroviscoelasticity) [1–9, 11–19], as an OMQS is mentioned [10, 26, 34–36].

ACKNOWLEDGMENTS

This work was supported by Ministry of Science and Technology of Republic of Serbia as fundamental research project "Finely Dispersed Systems: Micro-, Nano-, and Atto-Engineering" 142034. Fruitful consultations, comments, discussions, suggestions, have been held and received from professors J. Jaric, M. Plavsic, M. V. Mitrovic, M. Vojnovic and D.N. Krstic. Substantial encouragements, help and support, during the last two decades, have been received from the late professor Jaroslav Prochazka. Further on, important reviews came out from professors H-J. Bart, A.V. Delgado, H. Oshima, and A.T. Hubbard. At last but not least, invited courses, lectures, and deeper collaboration arrived from professors J.P. Hsu, S. Tseng, S. Alexandrova and A. Saboni.

REFERENCES

1. A. M. Spasic, M. P. Lazarevic, M.V. Mitrovic and D. N. Krstic In A. M. Spasic and J. P. Hsu (Eds.) *Finely Dispersed Particles: Micro-, Nano-, and Atto-Engineering*, CRC Press/Taylor and Francis, Boca Raton London New York, 2005/2006, 3–23 & 371–394.
2. A. M. Spasic, M. P. Lazarevic, J. Coll. Interf. Sci., **282**, 223 (2005).
3. A. M. Spasic, M. P. Lazarevic, J. Coll. Interf. Sci., **316**, 984 (2007).
4. A. M. Spasic, V. Jokanovic and D. N. Krstic, J. Coll. Interf. Sci. **186**, 434 (1997).
5. A. M. Spasic, N. N. Djokovic, M. D. Babic, M. M. Marinko and G. N. Jovanovic, Chem. Eng. Sci. **52**, 657 (1997).
6. A. M. Spasic, Chem. Eng. Sci. **47**, 3949 (1992).
7. A. M. Spasic In A. V. Delgado (Ed.) *Interfacial Electrokinetics & Electrophoresis*, Marcel Dekker, New York. 2001/2002, 837–868.
8. A. M. Spasic, V. Jokanovic, J. Coll. Interf. Sci., **170**, 229 (1995).
9. A. M. Spasic, N. N. Djokovic, M. D. Babic, G. N. Jovanovic, Chem. Biochem. Eng. Q. **5**, 35 (1991).
10. P. A. M., Dirac, *The Principles of Quantum Mechanics,* forth ed. Clarendon, Oxford, 2003, Chaps. XI and XII.
11. A. M. Spasic, D. N. Krstic, in *Chemical and Biological Sensors and Analytical Electrochemical Methods*, (Eds.) A. J. Rico, M. A. Butler, P. Vanisek, G. Horval, A. E. Silva, ECS Penigton, N. J. 415 (1997).
12. A. M. Spasic, M. D. Babic, M. M. Marinko, N. N. Djokovic, M. V. Mitrovic, D. N. Krstic, In 4th

European Congress of Chemical Engineering, Granada, Spain, Sept. 21–25, 2003, CD.
13. A. M. Spasic, M. P. Lazarevic, In 16th International Congress of Chemical and Process Engineering, Prague, Czech Republic, Aug 22–26, 2004, D5. 4.
14. A. M. Spasic, M. D. Babic, M. M. Marinko, N. N. Djokovic, M. V. Mitrovic, D. N. Krstic, In 16th International Congress of Chemical and Process Engineering, Prague, Czech Republic, Aug. 22–26, 2004, D5. 1.
15. A. M. Spasic, M. P. Lazarevic, In 16th CHISA, Prague, 2004, D.5.4.
16. M. P. Lazarevic, A. M. Spasic, In 4th European Congress of Chemical Engineering, Granada, Spain, Sept. 21–25, 2003, 5.2. 33.
17. A. M. Spasic, M. P. Lazarevic, In 7th World Congress of Chemical Engineering, Glasgow, Scotland, July 10–14, 2005, 506.
18. M. P. Lazarevic, A. M. Spasic, In 7th World Congress of Chemical Engineering, Glasgow, Scotland, July 10–14, 2005, p. 288.
19. A. M. Spasic, M. P. Lazarevic, M. V. Mitrovic, D. N. Krstic, In: 1st South East-European Congress of Chemical Engineering, Belgrade, Serbia & Montenegro, September 25–28, 2005, 125.
20. R. F. Probstein, *Physicochemical Hydrodynamics*, John Wiley & Sons, INC.: New York, 1994, 352–369.
21. H. R. Kruyt, *Colloid Science*, Vol. I; Elsevier Publishing Company: Amsterdam, Houston, New York, London, 1952, 302–341.
22. C. R. Reid, J. M. Prausnitz, B. E. Pauling, T*he Properties of Gasses and Liquids*, Mc-Graw-Hill, New York, 1989, 632–655.
23. E. U. Condon, H. Odishaw, Eds. *Handbook of Physics*; McGraw Hill: New York, 1958, 4/p. 13.
24. M. J. Pilling, *Reaction Kinetics*, Clarendon Press: Oxford, 1975, 37–48.
25. E. N. Yeremin, *The Foundation of Chemical Kinetics*, Mir Publishers: Moscow, 1979, 103–149.
26. I. S. Leonard, *Quantum Mechanics*, Mc Graw-Hill Inc.: New York, 1955, 7–90, 402–459.
27. A. N. Krall, W. A. Trivelpiece, *Principles of Plasma Physics*, Mc Graw-Hill: New York, 1973, 98–128.
28. R. P. H. Gasser, W. G. Richards, *Entropy and Energy Levels*; Clarendon Press: Oxford, 1974, 27–38.
29. J. O. Hirchfelder, Ch. F. Curtiss, R. B. Bird, *Molecular Theory of Gases and Liquids*, Wiley: New York, 1954, 139 pp.
30. E. K. Drexler, *Nanosystems: Molecular Machinery, Manufacturing and Computation*; Wiley: New York, 1992, 161–189.
31. I. Podlubny, *Fractional Differential Equations*, Academic Press, San Diego, 1999.
32. E. Tarasov, G. Zaslavsky, Physica A 368 (2006) 399.
33. R. Hilfer, *Applications of Fractional Calculus in Physics*, World Scientific, Singapore, 2000.
34. M. Dugic, *Decoherence in a classical limit of quantum mechanics*, Notebooks of Physical Sciences, SFIN XVII (2) (1–189), Institute of Physics, Belgrade, 2004.
35. H.-T. Elze (Ed.), *Decoherence and Entropy in Complex Systems,* Selected lectures from DICE 2002, Springer, Lecture Notes in Physics, Berlin Heidelberg New York, 2003, 403.
36. M. Dugic, D. Rakovic, M. Plavsic, *The Polymer Conformational Stability and Transitions: A Quantum Decoherence Theory Approach* In A.M. Spasic and J.P. Hsu (Eds.) *Finely Dispersed Particles: Micro-, Nano-, and Atto-Engineering,* CRC Press-Taylor & Francis, Boca Raton London New York, 2006, 217–231.

ЖУРНАЛ ФИЗИЧЕСКОЙ ХИМИИ, 2009, том 83, № 9, с. 1747–1752

COLLOID CHEMISTRY AND ELECTROCHEMISTRY

УДК 541.13

CYCLIC VOLTAMMETRY STUDY OF (5-ETHOXYCARBONYLMETHYLIDENE-4-OXOTHIAZOLIDIN-2-YLIDENE)-N-PHENYLETHANAMIDE

© 2009 I. Cekić-Laskovićˢ·ᵃᵇ, D. M. Minićˢ·ᵃᵇ, M. Baranac-Stojanovićᵃᵇ·ᶜ, R. Markovićᵃᵇ·ᶜ, E. Volanschiᵈ

ˢ Faculty of Physical Chemistry, University of Belgrade, Studentski trg 12, Belgrade, Serbia
ᵃᵇ Center for Chemistry ICTM, P.O. Box 473, 11001 Belgrade, Serbia
ᶜ Faculty of Chemistry, University of Belgrade, Studentski trg 16, 11001 Belgrade, Serbia
ᵈ Department of Physical Chemistry, University of Bucharest, Blvd Elisabeta 4-12, RO-030018, Bucharest, Romania

Abstract – As a continuation of our ongoing project on electrochemical properties of *push-pull* 5-substituted 2-alkylidene-4-oxodiiazolidines (**1a**), differing in substituent R at C5-position and electron withdrawing group (EWG), we have investigated the electrochemical behaviour of (5-etoxycarbonylmethylidene-4-oxothiazolidin-2-ylidene)-N-phenylethanamide **1a** (R: =$CHCO_2Et$; EWG: CONHPh), consisting as a (2*E*, 5*Z*)/(2*Z*, 5*Z*) mixture, by cyclic voltammetry in polar as well as non-polar solvent (0.1 M TBAHFP in DMSO and $CHCl_3$, respectively). Cyclic voltammetry at stationary electrode was employed to characterize the elecIron transfer steps. Based on electrochemical criteria and correlation with the DigiSim simulations, an ECE mechanism, involving two electrochemical steps and one isomerisation step, was suggested.

INTRODUCTION

Push-pull alkenes are defined as substituted olefins containing one or two electron-donating substituents (D) on one end of a C=C double bond and one or two electron-accepting substituents (A) at the other end. Electronic D–A interactions *via* the C=C bond result in a polarization of the "*push-pull*" system [1]. Consequently, an increase of the *push-pull* character is associated with a decrease of the π-bond character of the polarized C=C bond. In turn, the corresponding π-bond orders of the C–D and C–A bonds are increased. The *push-pull* effect has major impact on both, the dynamic behavior and the chemical reactivity of these compounds:

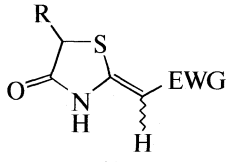

(1)

EWG = COPh, CONHPh, CN
R = Me, CH_2CO_2Et, H,
=$CHCO_2Et$

Stereodefined 2-alkylidene-4-oxothiazolidines (**1**), which have been previously characterized by ^1H NMR, ^{13}C NMR, IR, UV, MS spectroscopy and X-ray structural analysis [2], exemplify typical *push-pull* compounds. They exist in different configurational and conformational forms. One of the characteristic processes of *push-pull* alkenes **1**, based on a lowering of the rotational barrier of the C=C bond at the C2 position, is configurational isomerization which can be followed, under proper experimental conditions, by dynamic ^1H NMR spectroscopy [3].

Herein, we report an extension of our study on electrochemical behavior of *push-pull* alkenes, that is the functionalized 4-oxothiazolidine **1a** (R: =$CHCO_2Et$; EWG: CONHPh), having two exocyclic C=C bonds at C2 and C5 positions. In addition, the configurational isomerization at the C2 double bond, occurring during the electrochemical reduction in wet DMSO, has been examined.

EXPERIMENTAL

Cyclic voltammetry (CV) experiments were performed on a VOLTALAB-40 electrochemical device using thermostated one-compartment electrolytic cell with stationary Pt-EDI 101 of 2 mm diameter as working electrode, Pt counter electrode and Ag-quasi reference electrode. Tetra-*n*-butylammonium hexafluorophosphate (TBAHFP) 0.1M was employed as supporting electrolyte. The solution in the electrochemical cell was deaerated with high-purity Ar before starting the CV experiments and an atmosphere of Ar was maintained over the solution in the cell during measure-

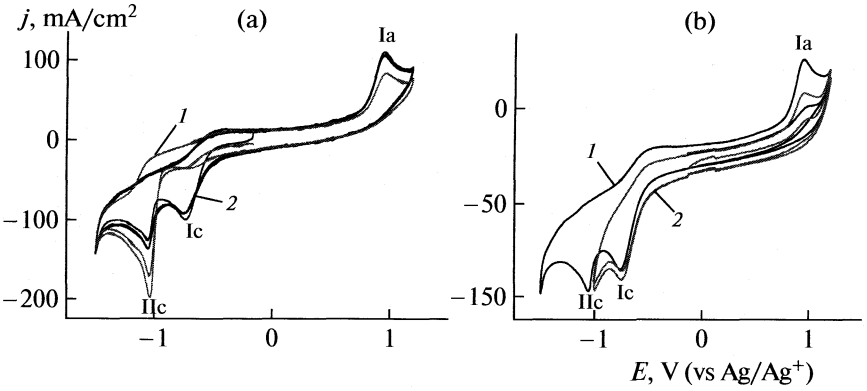

Fig. 1. Cyclic voltammograms of mixture of the 2*E*, 5*Z*-**1a** and 2*Z*, 5*Z*-**1a** isomers in 0.1M TBAHPF/DMSO; c = 4mM; v = = 0.1 V/s, room temperature; (a) starting with reduction (potential range −1.5 V to 1.2 V); (b) starting with oxidation (potential range 1.2 V to −0.95 V); (*1*) freshly dissolved isomer mixture, (*2*) after a few polarization cycles; (Ic) is first cathodic peak, (IIc) is second cathodic peak, Ia is first anodic peak.

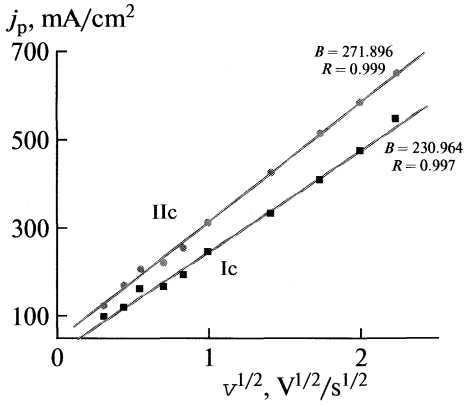

Fig. 2. Cathodic peak current density (j_p)-square root of the scan rate ($v^{1/2}$) relationship of the 2*E*, 5*Z*-**1a**/2*Z*, 5*Z*-**1a** mixture in 0.1M TBAHPF/DMSO.

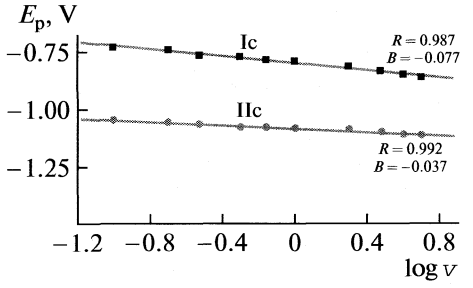

Fig. 3. E_p – log$v$ relationship of (2*E*, 5*Z*)-**1a**/(2*Z*, 5*Z*)-**1a** (mixture of isomers) in 0.1 M TBAHPF/DMSO.

ments. Experimental results were correlated with results obtained by simulation, accomplished by the software DIGISIM 3.03. Bioanalytical Systems Inc.

RESULTS AND DISSCUSION

CV Measurements were performed in solution of the mixture of configurational isomers (2*E*, 5*Z*)-**1a** and (2*Z*, 5*Z*)-**1a**, in molar ratio 63 : 37 (total concentrations 2. 4, 6 and 8 mM) in 0.1 M TBAHFP/DMSO and 0.1 M TBAHFP/$CHCl_3$, used without further purification, by variation of temperature and scan rate.

The voltammetric reduction of freshly dissolved mixture of the 2*E*, 5*Z*-**1a** and 2*Z*, 5Z-**1a** isomers, in the potential range −1.5 to +1.2V starting from the open circuit potential (−0.16V), is characterised by an appearance of two irreversible cathodic peaks located at −0.73V (Ic) and −1.04V (IIc), and one anodic peak at +0.95V respectively (Fig. 1a).

Starting with oxidation, 4mM compound **1a**, in the potential range 1.2V to −1.5V, at the first scan, practically no peak is observed on the first cycle, showing that this substance is not electrochemically active in the investigated oxidation range up to 1.2 V. An appearance of one oxidation peak after sweeping the potential in reduction till −1V, suggests that the oxidation peak is the result of the prior reduction, after the first, as well as after the second peak. On subsequent scans, the peak Ia increases (Fig. 1b).

Analysis of the cathodic peaks according to usual electrochemical criteria allows characterization of the electron transfer steps involved [4]. The peak current density increases with square root of the scan rate for both reduction peaks of the isomer mixture **1a**.

The plot of the peak current density versus the square root of the scan rate ($j_{pc} = f(v^{1/2})$, Fig. 2) is fairly linear, which is characteristic for diffusion controlled processes, R = 0.997 for the first peak and R = = 0.999 for the second peak [5].

The $E_p = f(\log v)$ dependence (Fig. 3) for both reduction peaks has linear character with the slope values corresponding to B = 77 and 37 mV, respectively, indicating either, a slow electron transfer, or an ET followed by a chemical step (EC sequence).

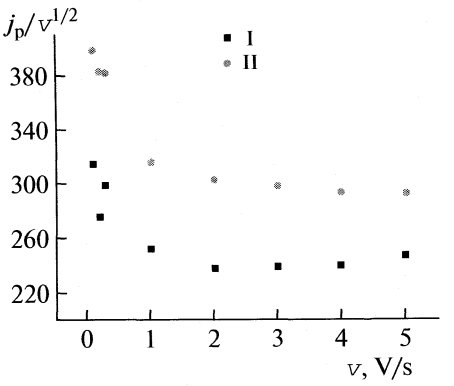

Fig. 4. Current density function ($j_p v^{-1/2}$)–v relationship.

The current function ($j_p/v^{1/2}$ vs v) dependence on the scan rate for both electron transfer steps Ic and IIc, presented in Fig. 4, corroborated with all electrochemical criteria discussed above, is an indication that both reduction peaks steps can be assigned to quasireversible ET steps, followed by a chemical reaction, (i.e. ECE sequence), as demonstrated for numerous organic compounds [4, 6, 7].

Influence of concentration

The effect of the concentration was followed at T = = 20°C, in the range from 2 mM to 4, 6 and 8 mM by considering the dependences of E_p vs. log c and j_p vs. c for both reduction peaks. These dependences show only the decrease of the current density for second reduction peak with dilution starting from 8 mM solution. The current density for the first reduction potential, as well as the potential values for both peaks, stay unchanged, thus, indicating a pseudo-first order chemical step in the electrode process. This chemical step can be assigned to the (2E, 5Z)/(2Z, 5Z)-isomerization process already mentioned above. The fact that the height of the first peak remains unchanged in spite of the dilution is a consequence of the isomerization in polar solvent, such as DMSO.

In order to assign these processes and to elucidate the nature of the chemical steps involved, the influence of the solvent polarity and temperature on the electrochemical behavior was also investigated.

Influence of solvent

The influence of solvent polarity on reduction processes was studied in the polar DMSO and non-polar $CHCl_3$ solvent for scan rate 0.1 V/s at 20°C, in potential range from –1.6V to 0.1V (Fig. 5). The appearance of only one reduction peak on the CV of compound **1a** in non-polar solvent ($CHCl_3$) is in accordance with our previous results which indicated the presence of only (2*E*, 5*Z*)-isomer, being the dominant one in non-polar solvents[3, 8, 9]. On the contrary, the appearance of two reduction peaks on the CV of compound **1a** (involving a mixture of both isomers) in a polar solvent may be assigned to the reduction of both isomers at different potential values.

This is in agreement with the ratio of the peak currents Ic/IIc of about 0.6 in the fresh solution after a few reduction cycles, corresponding to the 2*Z*, 5*Z*/2*E*, 5*Z*-molar ratio of 37 : 63 in the starting compound. Variation of the intensity ratio in time and/or by increasing temperature is the result of the isomerization occurring in the polar solvent [3, 10] attenuated by the electrochemical reduction. According to this, the first reduction peak (Ic) at potential –0.73 V can be assigned to (2*Z*, 5*Z*)-isomer, whereas the second reduction peak (IIc) at potential –1.04 V can be assigned to (2*E*, 5*Z*)-isomer. This assignment is justified because the (2*E*, 5*Z*)-isomer is expected to be less prone to reduction and consequently appears at the more negative potential, due to the intramolecular H-bond stabilization. The appearance of the oxidation peak after sweeping the potential in reduction, suggests that the

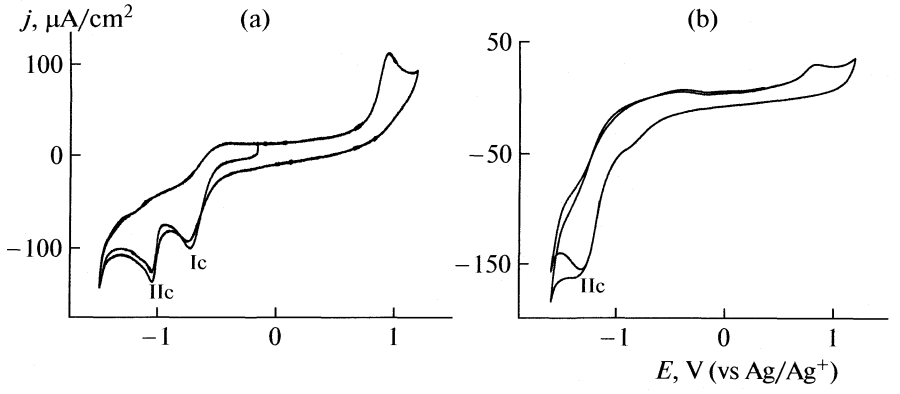

Fig. 5. Cyclovoltamogramms of 2 mM compound **1a** in(a) DMSO and (b) $CHCl_3$, at 20°C, potential range from –1.6 V to 1.2 V, v = 0.1 V/s.

oxidation peak is the result of the prior reduction of both isomers.

Influence of temperature

The influence of temperature on reduction processes was investigated at scan rate 0.1 V/s, in DMSO in temperature range 20–65°C (Fig. 6).

The increase of the temperature in the polar solvent (DMSO) causes a change of intensities of both cathodic peaks, leading to a reverse ratio of the current density of the first reduction peak (Ic) (assigned to the 2*Z*, 5*Z*-isomer) as against that of the second reduction process (IIc) (assigned to the reduction of the 2*E*, 5*Z*-isomer). This is most likely the consequence of the 2*E*, 5*Z*/2*Z*, 5*Z*-isomerization process, induced by the electrochemical reduction in the presence of a polar solvent. The *cis–trans* isomerization under cathodic electron transfer is a frequent reaction for the organic compounds containing sulphur and nitrogen [11, 12].

This process is well accounted for by Digisim simulations with an ECE-Disp sequence (Fig. 6), together with the experimental curves in the potential range –1.5–0 V, and parameters given below.

Proposed mechanism of the reduction

Taking into account electrochemical criteria, the following reduction mechanism of compound **1a**, based on an ECE-Disp sequence and experimental results regarding the influence of solvent, concentration and temperature on CV curves, can be suggested:

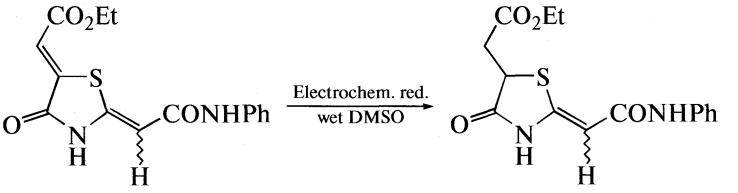

The thermodynamic and kinetic data used to perform the simulation of the experimental voltammograms are presented below:

$$(2E, 5Z)\text{-}\mathbf{1a} + e^- \longrightarrow (2E, 5Z)^{-\bullet}\text{-}\mathbf{1a} \qquad E_0 = -0.8\ \text{V},\quad k_s = 0.0005\ \text{cm/s},$$

$$(2E, 5Z)\text{-}\mathbf{1a} \rightleftharpoons (2Z, 5Z)\text{-}\mathbf{1a} \qquad K_{eq} = 2000,\quad k_f = 10\ \text{s}^{-1},$$

$$(2Z, 5Z)\text{-}\mathbf{1a} + e^- \longrightarrow (2Z, 5Z)^{-\bullet}\text{-}\mathbf{1a} \qquad E_0 = -0.6\ \text{V},\quad k_s = 0.000625\ \text{cm/s},$$

$$\Downarrow\Uparrow$$

$$(2E, 5Z)^{-\bullet}\text{-}\mathbf{1a} + (2E, 5Z)^{-\bullet}\text{-}\mathbf{1a} \rightleftharpoons (2E, 5Z)\text{-}\mathbf{1a} + (2Z, 5Z)^{2-}\text{-}\mathbf{2a}$$

$$\underline{(2Z, 5Z)^{2-}\text{-}\mathbf{2a} + (2E, 5Z)\text{-}\mathbf{1a}} \rightleftharpoons \underline{(2Z, 5Z)^{-}\text{-}\mathbf{1a} + (2E, 5Z)^{-}\text{-}\mathbf{1a}}$$

$$(2E, 5Z)^{-\bullet} + (2E, 5Z)^{-\bullet} \rightleftharpoons (2Z, 5Z)^{-} + (2E, 5Z)^{-} \qquad K_{eq} = 10,\ k_f = 10\ \text{s}^{-1},$$

$$(2Z, 5Z)^{-}\text{-}\mathbf{1a}, (2E, 5Z)^{-}\text{-}\mathbf{1a} \longrightarrow P_{ox} + e^- \qquad E_0 = 1\ \text{V},\quad k_s = 0.001\ \text{cm/s}.$$

On the first scan the major 2*E*, 5*Z*-isomer is reduced in a monoelectronic step to its anion radical at the potential corresponding to the IIc couple. As electrochemical reduction implies diminished double bond character of the C(2) double bond, the isomerization is possible and is favored thermodinamically, the 2*Z*, 5*Z*-**1a**-isomer being reduced at a less negative potential of peak Ic [10, 13]. The second electron transfer step corresponds to the monoelectronic reduction of the 2*Z*, 5*E*-**1a**-isomer. This is followed by a chemical step, that is, an intermolecular disproportionation consisting of successive electron and proton transfers leading to the anions of both isomers [14], which can be subsequently oxidized (P_{ox}) in the reverse anodic scan.

The simulated CV as well as the experimental CV are presented in Fig. 6. The temperature dependence was simulated by varying the equilibrium constant in a range from 2000 at 20°C to 4000 at 40°C and 5800 at 65°C.

Reasonably good agreement between the experimental and simulated CV was obtained at all three selected temperatures, indicating that the proposed mechanism accounts correctly for the main features of the investigated process. However, we found that there is no exact correlation between the experimental and simulated behavior because of the great number of variables involved in the simulation, and due to the limitations of the program, allowing only three electron transfer steps [15].

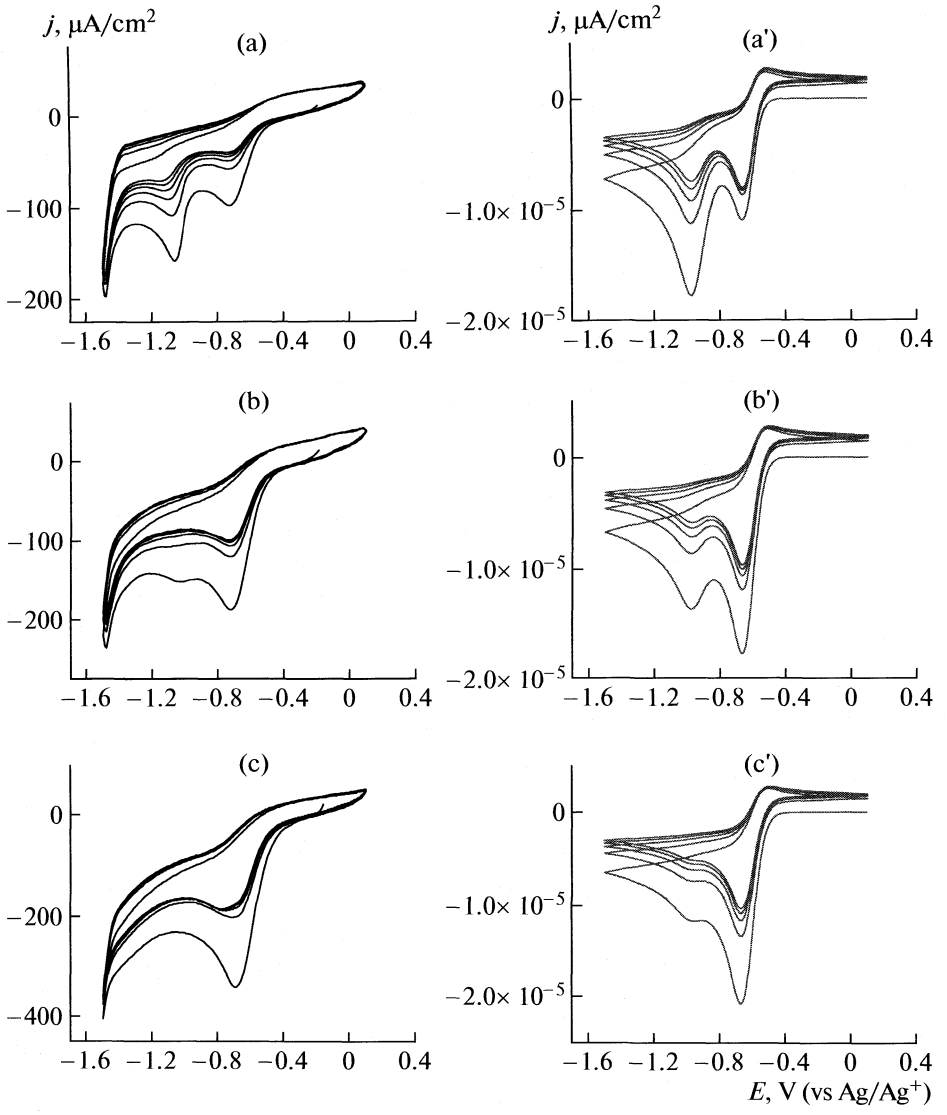

Fig. 6. (a–c) Experimental and (a'–c') simulated cyclic voltammetry curves of compound **1a** at (a, a') 20, (b, b') 40 and (c, c') 65°C; $c = 2$ mM (mechanism and parameters in the text).

CONCLUSION

Electrochemical properties of (5-ethoxycarbonylmethylidene-4-oxothiazolidin-2-ylidene)-N-phenylethanamide (**1a**) as the 2*E*, 5*Z*/2*Z*, 5*Z*-isomer mixture, were studied by cyclic voltammetry in polar solvent (DMSO), as well as in non-polar solvent ($CHCl_3$), at various temperatures and for different concentrations. By correlation of the experimental results and simulation of experimental CV, using the electrochemical package (DigiSim 3.03 Bioanalytical Systems Inc.) the most probable mechanism of the reduction of compound **1a** in DMSO, involving electrochemical reduction and that of the 2*E*, 5*Z*/2*Z*, 5*Z*-**1a**-isomerization, was proposed.

ACKNOWLEDGMENTS

We wish to acknowledge financial support by the Ministry of Science of the Republic of Serbia, Grant No. 142007 (to R.M.).

REFERENCES

1. R. G. Giles, N. J. Lewis, J. K. Quick, M. J. Sasse, M. W. J. Urquhart, Tetrahedron **56**, 4531 (2000).
2. R. Marković, M. Baranac, Z. Džambaski, M. Stojanović, P. J. Steel, Tetrahedron **59**, 7803 (2003).
3. R. Marković, M. Baranac, N. Juranić, S. Macura, I. Cekić, D. Minić, J. Mol. Structure **800**, 85 (2006).
4. D. M. Minić, I. Cekić, F. T. Pastor, V. Jovanović, R. Marković, Rus. J. Phys. Chem. A **81**(9), 1458 (2007).

5. Southampton Electrochemistry Group, *Instrumental Methods in Electrochemistry*, 1st ed., Ellis Horwood, London, 1985.

6. M. Enache, C. Bendic, E. Volanschi, Bioelectrochemistry **72**, 10 (2008).

7. L. Preda, V. Lazarescu, M. Hillebrand, E. Volanschi, Electrochimica Acta **51**, 5587 (2006).

8. R. Marković, A. Shirazi, Z. Džambaski, M. Baranac, D. Minić, J. Phys. Org. Chem. **17**, 118 (2004).

9. R. Marković, Z. Džambaski, M. Baranac, Tetrahedron **57**, 5833 (2001).

10. R. Marković, Ž. Vitnik, M. Baranac, I. Juranić, J. Chem. Research (S) 485 (2002).

11. A. J. Bard, L. R. Faulkner, *Electrochemical Methods, Fundamentals and Applications*, J. Wiley & Sons, Inc., New York, 2001, 476–512.

12. J. Simonet and N. Gueguen-Simonet, *Cathodic and anodic behaviour of organic compounds possessing –N=N– or >N–N< linkages*. In: S. Patai, Editor, *The chemistry of the hydrazo, azo and azoxy groups*, Wiley, New York, 1997.

13. C. P. Andrieux, J. M. Saveant, *Investigation of rates and mechanism of reactions*, Vol. 6, Ed. Claude Bernasconi, John Wiley & Sons, Inc. 1986, 335–368.

14. J. Simonet. In: S. Patai and Z. Rappaport, Editors, *The Chemistry of Sulphur-containing Functional Groups*, John Wiley& Sons Ltd., 1993.

15. M. W. Lehmann, D. H. Evans, J. Phys. Chem. B **105**, 8877 (2001).

ЖУРНАЛ ФИЗИЧЕСКОЙ ХИМИИ, 2009, том 83, № 9, с. 1753–1757

PHOTOCHEMISTRY AND MAGNETOCHEMISTRY

УДК 541.14

MICRO- AND NANOSECOND LASER TiN COATING/STEEL MODIFICATION: MORPHOLOGY STUDIES

© 2009 M. Trtica*, V. F. Tarasenko**, B. Gaković*, A. N. Panchenko**, B. Radak* and J. Stasić*

*Institute of Nuclear Sciences Vinča, P.O. BOX 522, 11001 Belgrade, Serbia

**High Current Electronics Institute SB of RAS, 634055 Tomsk, Russia

E-mail:@ etrtica@vin.bg.ac.yu

Abstract – Morphology effects induced during interaction of μs- (Transversely Excited Atmospheric (TEA) CO_2 laser) or ns- (HF laser) pulses with titanium nitride (TiN) coating, deposited on austenitic stainless steel AISI 316, were studied. Experiments were carried out in regime of focused laser beam in air at atmospheric pressure. The used laser fluences were found to be sufficient for inducing intensive surface modifications of the target. The energy absorbed from the CO_2 as well as HF laser beam is mainly converted into thermal energy, causing different effects like ablation, appearance of hydrodynamic features, etc. Morphology characteristics obtained during ns-pulses irradiation (HF laser) were different to those initiated by μs-pulses (TEA CO_2 laser). The changes on the target surface in form of massive resolidifed droplets and crown-like structures were observed only for ns- (HF laser) pulses. It was found that these effects are a consequence of higher temperature and better coupling of the HF laser radiation with the target. Recent investigations of ps-Nd:YAG laser interaction with the same TiN coating showed that morphology picture is quite different including the reduction of thermal effect.

INTRODUCTION

The phenomena and processes generating in a target material by pulsed laser radiation are generally characterized by a combination of optical, mechanical, thermodynamic features of the material, as well as the laser parameters such as pulse length, fluence, etc. In the main, the pulsed laser-induced processes on a target are very complex. In this context, the study of morphology effects provoked on titanium-based ceramic/coating, especially titanium nitride deposited on a steel substrate, has fundamental and applicative significance.

The last decade saw most of the studies of laser beam interaction with titanium-based ceramic coatings, including titanium nitride, deposited on high quality steel substrates. Beams of Nd:YAG- [1], Ti:Sapphire- [2], excimer, KrCl- [3], and CO_2- [4, 5]. lasers have so far been employed. Studies of pulsed TEA CO_2 and especially HF laser beams interaction with titanium nitride are scarce in literature. Due to extraordinary physical and chemical properties, TiN is attractive for various applications, e.g. nuclear technology; industry; microelectronics; sensor technologies; bio-medicine, etc. In nuclear technology, especially thermonuclear fusion devices, TiN was considered as one of the potential materials for protective coating of vessel walls (i.e. plasma facing materials) [6].

The present paper is focused on the study of energetic laser beam effects on polycrystalline titanium nitride, deposited on austenitic stainless steel (AISI 316). Beams from pulsed infrared lasers, emitting at ~10 μm (TEA CO_2 laser; μs- time domain) or ~2.8 μm (HF laser; ns- time domain) were used for irradiation. An attention was paid to observation of morphological effects on the target surface induced under the high laser fluence regime used.

EXPERIMENTAL

The irradiation experiments were conducted with two different infrared laser systems operating in μs- or ns- time domain. The material/target used is complex, consisted of polycrystalline TiN coating/layer (thickness 1 μm) deposited on bulk substrate. Substrate, AISI 316 steel, was rectangular with dimensions 20 mm × 12 mm × 2 mm. The coating deposition was performed by reactive d.c. magnetron sputtering [7]. The deposition method provided good quality of coatings.

Irradiations in regime of high laser fluence were performed with laser beams focused using a KBr/NaCl lens of focal length of 6.0/13.0 cm. The angle of incidence of the laser beam with respect to the surface plane was 90°. Experiment was carried out in air atmosphere, at a pressure of 1013 mbar. During the target irradiation, TEA CO_2 as well as HF laser system operated in TEM_{00} or in the lower order mode (TEM_{10}). The μs-experiments were carried out with TEA CO_2 laser [8]. The laser used conventional (1 atm) $CO_2/N_2/He$ gas mixtures, yielding pulses with a gain switched peak (GSP) followed by a slowly decaying tail. Full width at half maximum (FWHM) of a GSP was approximately 100 ns, whereas the duration of a tail was about 2 μs. The ns- irradiations were per-

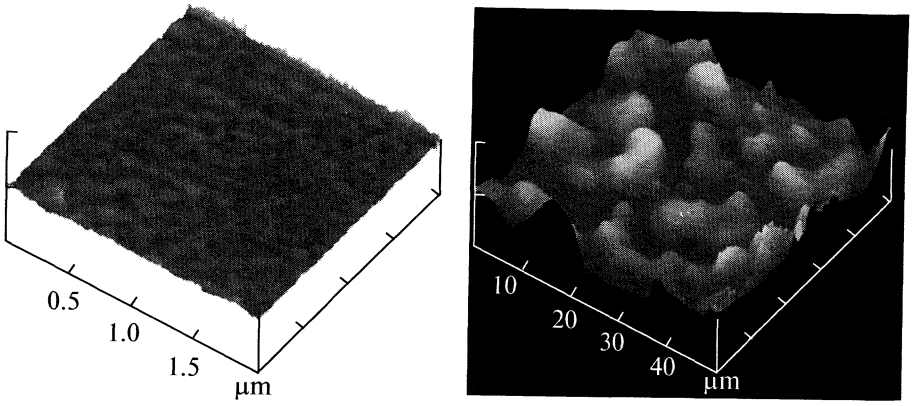

Fig. 1. AFM images of a TiN/steel target before (left) and after (right) TEA CO_2 laser irradiation by 500 pulses ($\Phi \sim 43$ J/cm^2); TiN coating 1 μm; AISI 316 steel substrate.; z : 20 nm/div (left) and 3 μm/div (right).

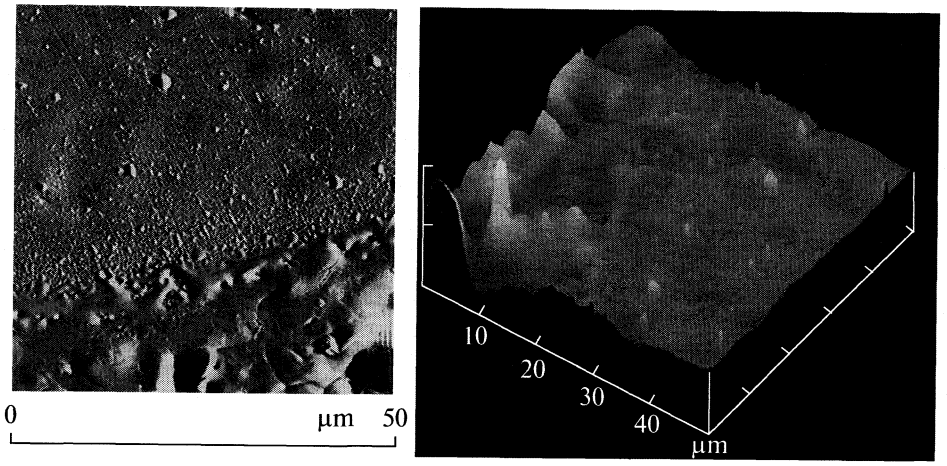

Fig. 2. SEM images of periphery of irradiated area of TiN/steel target. Experimental conditions are the same as in Fig. 1; z : 1 μm/div.

formed by HF laser, operating with typical H_2/SF_6 gas mixtures [9] at a pressure of 0.1 atm FWHM of laser pulse was about 230 ns.

Various analytical techniques were used for characterization of the TiN/steel samples before and after laser irradiation. The phase composition and crystallite structure of TiN coating and substrate were determined by X-ray diffractometer (CuK_α radiation was utilized). Surface morphology was monitored by optical (OM), scanning electron (SEM) and, atomic force microscopy (AFM). The SEM was coupled to an energy dispersive analyzer (EDX) for determining surface composition of the targets. Profilometer was used to characterize topographic changes of the irradiated area.

RESULTS AND DISCUSSION

X-ray analysis of austenitic stainless steel AISI 316 substrate as well as titanium nitride coating, prior to irradiation, showed that: (i) steel substrate consists of γ-Fe phase with face centered cubic structure. Grain size was on the order of tenths of microns; and, (ii) titanium nitride coating/layer has a cubic B1 structure of the NaCl-type with preferred (111) orientation. Polycrystalline structure is similar to that reported in reference [5]. The surface roughness, less than 50 nm, was evaluated by AFM.

Generally, the morphological features induced by laser on TiN/AISI 316 steel target showed their dependence on beam characteristics, primarily on the laser pulse energy, laser beam intensity, pulse duration, number of accumulated pulses, wavelength, etc. Morphological changes of TiN/AISI 316 steel target after 500 (TEA CO_2 laser) and 20, 100 accumulated pulses (HF laser) are presented in Figs. 1, 2 and 3, 4, respectively. The high laser fluences (Φ, energy densities) were: 43 (for 10.6 μm), and 40 and 48 J/cm^2 (for 2.8 μm). These fluences induced significant surface modifications of the target. The results of the induced modifications are presented below.

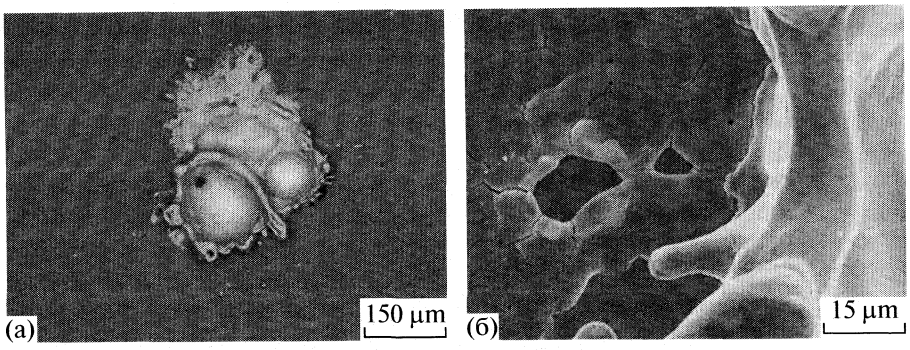

Fig. 3. Morphology changes of a TiN/steel target induced after 20 pulses of HF laser ($\Phi \sim 48$ J/cm^2). SEM analysis of the entire spot (left) and the periphery (right); TiN coating 1 μm; AISI 316 steel substrate.

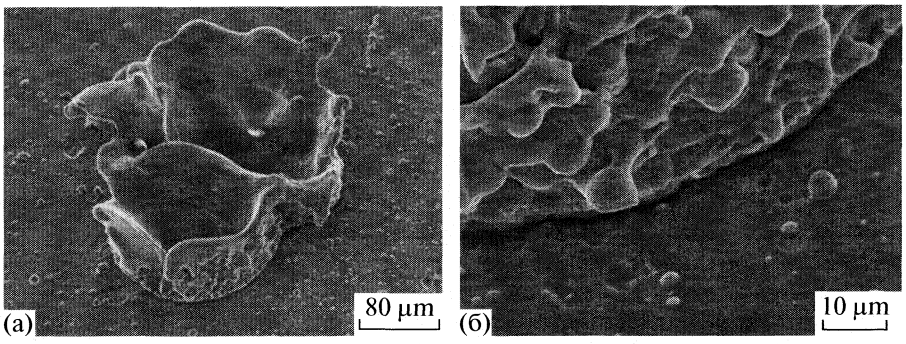

Fig. 4. Morphology changes of a TiN/steel target induced after 100 pulses of HF laser ($\Phi \sim 40$ J/cm^2). SEM analysis of the entire spot (left) and the periphery (right). Experimental conditions are the same as in Fig. 3.

TEA CO_2 Laser

The changes/effects on TiN/AISI 316 steel target upon laser irradiation with 500 pulses are presented in Figs. 1 (right) and 2. They can be summarized as: (i) ablation of TiN coating in the central part of the interaction area (Fig. 1, right), with the appearance of lens-shaped structures; (ii) presence of hydrodynamic effects (like resolidified droplets) at the periphery (Fig. 2) and, (iii) initiation of spark-like plasma, in front of the target. The plasma appeared after 35 accumulated laser pulses. At the Φ of 43 J/cm^2, the TiN coating was ablated after first laser pulse [4], thus the subsequent pulses induced damage of the steel substrate. Profilometric analysis of the central damage zone showed that the material has a tendency of lifting. The average level of lifted material was about 1.5 μm.

Physico-chemical picture during interaction of both lasers with TiN/AISI 316 steel target can be considered, in one approximation, as an interaction of surface thermal source [10]. Therefore, the laser beam-target interaction can be satisfactorily explained by the linear heat conduction theory [11]. After irradiation with the first laser pulse, the absorptivity of the target is changed (its higher), thus the large fraction of the absorbed laser energy reaching the target is transformed into heat and the surface modifications can be very efficient. Generally, a series of effects such as melting, vaporization of the molten materials, dissociation and ionization of the vaporized material, etc., occur in the target. The evaluation of the target surface temperature as a function of time was carried out by using the Equation (1) from [5, 12]. In the main, the equation comprises target absorptivity, specific heat, thermal diffusivity, target density and the laser beam intensity. For a given TEA CO_2 laser pulse shape, laser intensity of ~110 MW/cm^2 and target absorptivity ~0.09, the calculation showed that the maximum surface temperature of 3300 K was reached, approximately after 1.2 μs. High surface temperature resulted in decomposition/ablation of the TiN coating during the first laser pulse, so that each subsequent pulse practically interacted with the AISI 316 steel substrate.

HF Laser

After the exposure of TiN/AISI 316 steel target to Φ of 40 and 48 J/cm^2, the surface was modified (Figs. 3 and 4). Irradiation of the target with a greater number of accumulated laser pulses, e.g. 100 (Fig. 4) in respect to 20 pulses (Fig. 3), resulted in a more pronounced surface modification. Surface features/phenomena can be summarized as follows: (i) ablation of the TiN coating in the central zone (Figs. 3, 4); (ii) de-

A comparative sum-up effects produced by μs- and ns-laser pulses

μs- pulse (TEA CO_2 laser)	*ns-pulse (HF laser)*
Material lifting in the central irradiated zone	Intensive material lifting expressed after 20 laser pulses
Hydrodynamic features (HDF), appearance of droplets at the periphery	Presence of HDF at the periphery. Creation of a specific form of crown like structure
Maximum surface temperature (calculated), 3300 K	Maximum surface temperature (calculated), 4500 K

velopment of hydrodynamic structures resembling resolidified material and droplets at the periphery. The specific crown-like structure (Fig. 4) was created, too; and, (iii) appearance of plasma in front of the target (after the first HF laser pulse).

EDX elemental analysis of the center of irradiated area confirmed that only austenitic stainless AISI 316 steel is present in this zone. The main constituents were Fe, Cr and Ni implying that TiN coating was removed. Evaluation of the target surface temperature versus time, induced by HF laser, was carried out using the same equation as for the case of TEA CO_2 laser. For a given HF laser pulse shape, laser intensity of ~225 MW/cm^2, and estimated target absorptivity [13, 14], the calculation showed that the maximum target surface temperature was above 4500 K and it was achieved after 230 ns. The value of 230 ns corresponded to the half of the HF laser pulse duration. Generally, the interaction of HF laser with TiN/steel target is a complex phenomenon. The main part of the absorbed HF laser energy was rapidly transformed into heat and thus the intensive modifications on the target surface can occur. Formation of a crown-like structure (CLS), Fig. 4 (left), is surprising. CLS can be created at different materials under high laser beam intensity, i.e. for intensities $>1 \times 10^8$ W/cm^2, [14–17]. Generation of the CLS is a consequence of several physical mechanisms. It is almost certain that a radial liquid flow of the materials induced by plasma recoil pressure affects the appearance of the CLS [14, 16]. The recoil pressure can reach value of several tens of atmospheres [14, 16].

Generally, a comparative sum-up effects on the target produced by μs- (TEA CO_2 laser) and ns- (HF laser) pulses are presented in table.

There is a difference in morphology between the used laser systems. The differences can be attributed to the: (i) laser wavelength; (ii) achievement of the higher temperature in shorter time on the target surface (case of HF laser); (iii) higher laser peak power for HF in respect to the TEA CO_2 laser and, (iv) better coupling of the HF laser radiation with the target. Recent investigations of ps- Nd:YAG laser interaction with TiN coating [1] showed that morphology picture is quite different including the surface changes at periphery which are spatially sharper/better defined.

CONCLUSION

The experimental studies of morphological features at the interaction of μs- (TEA CO_2 laser) or ns- (HF laser) pulses with titanium nitride coating deposited on high quality steel AISI 316 were presented. The laser fluences used were found to be sufficient for inducing intensive surface modifications of the target. The energy absorbed from the CO_2 as well as HF laser beam is mainly converted into thermal energy causing different effects like ablation, appearance of hydrodynamic features including the creation of specific form, i.e. crown-like structure. The latter structure is recorded only upon action of HF laser.

Generally, irradiation of TiN coating/AISI 316 steel target with μs-, or ns-, laser pulses showed that thermal effects were dominant on the surface. Irradiation of the same target with ps- pulses (investigation was conducted recently) showed that thermal impact was significantly reduced.

ACKNOWLEDGMENTS

This research was sponsored by the Ministry of Science and Technological Development of the Republic of Serbia, Contract No. 142065. The authors would like to thank Dr. Peter Panjan, Jozef Stefan Institute, Ljubljana, for valuable help and support.

REFERENCES

1. B. Gakovic, M. Trtica, D. Batani, T. Desai, P. Panjan, and D. Vasiljevic-Radovic, J. Opt. A: Pure Appl. Opt. **9** S76 (2007).
2. J. Bonse, H. Sturm, D. Schmidt, and W. Kautek, Appl. Phys. A **71**, 657 (2000).
3. M. S. Trtica, B.M. Gakovic, Lj.T. Petkovska, V.F. Tarasenko, A.V. Fedenev, E.I. Lipatov, and M.A. Shulepov, Appl. Surf. Sci. **225**, 362 (2004).
4. B. M. Gakovic, M.S. Trtica, T.M. Nenadovic, and B. J. Obradovic, Thin Solid Films **343–344**, 269 (1999).
5. M. S. Trtica, B.M. Gakovic, and B.B. Radak, Russ. J. Phys. Chem. A, **81**, 1429 (2007).
6. T. M. Nenadović, Sputter-induced erosion of hard coatings for fusion reactor first-wall (inAtomic Collision Processes and Laser Beam Interactions with Solids), pp. 153–174. Nova Science Inc. New York (1996).
7. B. M. Gaković, Z. Rakočević, T. M. Nenadović, D. Peruško, M. S. Trtica, and S. Zec, Solid State Phenomena **61**, 357 (1998).
8. M. S. Trtica, B. M. Gakovic, B. B. Radak, and S. S. Miljanic, Proceedings of SPIE **4747**, 44 (2002).

9. A. V. Fedenev, I. M. Goncharenko, N. N. Koval, V. M. Orlovski, V. F. Tarasenko, A.N. Panchenko, and E. I. Lipatov, Appl. Surf. Sci. **197–198**, 45 (2002).

10. A. L. Thomann, C. Boulmer-Leborgne, C. Andreazza-Vignolle, P. Andreazza, J. Hermann, and G. Blondiaux, J. Appl. Phys. **80**, 4673 (1996).

11. Von M. Allmen, Laser-Beam Interaction with Materials (Moorradian, A., Ed.), Springer, Berlin, (1987).

12. J. Hermann, C. Boulmer-Leborgne, I. N. Mihailescu, and B. Dubreuil, J. Appl. Phys. **73**, 1091 (1993).

13. J. Bonse, S. Baudach, J. Kruger, and W. Kautek, Proceedings of SPIE, **4065**, 161 (2000).

14. D. Baurle, Laser Processing and Chemistry, Springer, Berlin (1996).

15. M. Bereznai, I. Pelsoczi, Z. Toth, K. Turzo, M. Radnai, Z. Bor, and A. Fazekas, Biomaterials, **24**, 4197 (2003).

16. E. Gyorgy, I. N. Mihailescu, P. Serra, Del Pino A. Perez, and J. L. Morenza, Appl. Phys. A **74**, 755 (2002).

17. E. Gyorgy, I. N. Mihailescu, P. Serra, Del Pino A. Perez, and J. L. Morenza, Surf. Coat. Tech. **154**, 63 (2002).

ЖУРНАЛ ФИЗИЧЕСКОЙ ХИМИИ, 2009, том 83, № 9, с. 1758–1767

BIOPHYSICAL CHEMISTRY

УДК 541.64

MECHANISMS AND PARAMETERS OF TRANSIENTS AND OSCILLATIONS OF DELAYED CHLOROPHYLL FLUORESCENCE IN THE THYLAKOID MEMBRANE OF THE INTACT MAIZE LEAF

© 2009 Č. N. Radenović*, **, M. G. Jeremić**, G. V. Maximov***, M. V. Beljanski**** and A. R. Radojčić*

*Maize Research Institute, Zemun Polje, Belgrade, Serbia

**Faculty of Physical Chemistry, University of Belgrade, Belgrade, Serbia

***Lomonosov State University, Moscow, Russia

****Institute of General and Physical Chemistry, Belgrade, Serbia

E-mail: radenovic@beotel.yu

Abstract – Standard induction processes of delayed fluorescence (DF) of chlorophyll (induction signals) occur when an intact leaf segment of maize inbreds and hybrids is initially kept in the phosphoroscope darkroom for more than 15 min ($\tau > 15$ min), and then the leaf is illuminated with the intermittent white light and measured. Resolved induction processes of DF chlorophyll into transients: A, B, C, D and E occur when the intact leaf segment of maize inbreds and hybrids is kept in the phosphoroscope darkroom for a significantly shorter period (30 s $\leq \tau \leq$ 240 s), with the time rate τ of 30 s, prior to its illumination with the intermittent white light. Induction transients: A, B, C, D and E are characterised with their temporal parameters: t_A, t_B, t_C, t_D and t_E, dynamics of changes in transients intensities and mechanisms of their generation. The induction processes of chlorophyll DF of the intact leaf of maize inbreds and hybrids resolved into transients: A, B, C, D and E are accompanied by the occurrence and different levels of activation energy (E_a, kJ mol^{-1}) that correspond to different critical temperatures. The generation mechanisms of induction transients: A, B, C, D and E are classified into two groups. Transients A and B are of a physical character, while the transients: C, D and E are of a chemical character. It is shown that the generation of the induction transients: B, C, D and E simultaneously follows establishing of the oscillations of induction processes of the DF chlorophyll. Oscillating of induction processes of DF chlorophyll is explained by the ion (K^+, Na^+, H^+, Cl^-) transport mechanism across the thylakoid membrane of the intact leaf of maize inbreds and hybrids grown under conditions of air drought, increased temperatures and water deficiency in the medium.

INTRODUCTION

In recent times, binding complex processes of fundamental sciences with multidisciplinary ones has become the necessity. Such attempts have been made between breeding, photosynthesis, biophysical chemistry and fluorescence in maize inbreds and hybrids. The present study analyses the development of dominant processes of the stated scientific disciplines and determines the sites of their mutual dependence and application. Maize breeding has been intensively developed during the last 60 years. As a result of such an activity, over 1.100 maize hybrids for grain and silage have been developed. Contemporary technical and technological prerequisites for conducting a modern process of breeding were provided [1–4]. Regardless of such a colossal success in maize breeding, eagerness and enthusiasm of the total research have not been slowing down. The search for new methods and exact approaches in the completion and enrichment of the research within maize breeding and seed production has been continued. Our photosynthetic- fluorescent method is one of such models.

The development of studies on maize photosynthesis was quite different. Namely, although photosynthetic processes are very spread, highly productive in their intensity, very complex in their nature, and vastly studied in their scientific actuality, their application in maize breeding is still insignificant. It is almost impossible to make a distinct, direct interrelationship between photosynthesis and breeding. Such a state is probably a consequence of the existence of several functional interrelations that unify conformational and dynamic changes within chloroplasts and their thylakoid membranes, on the one hand, and effects of numerous environmental stress factors on them, on the other hand.

Biophysical chemistry contributed, to a great extent, to connecting photosynthetic processes in the thylakoid membrane to the processes of fluorescence spectroscopy and chemical kinetics [5, 6]. The delayed chlorophyll fluorescence (DF) phenomenon can be described as an occurrence of luminescence (bioluminescence) within the red range of the visible spectrum produced by plant systems: bacteria, algae and higher plants (maize) immediately upon their intermittent il-

lumination (excitation) (in case of maize upon illumination of the intact leaf) [5, 7–11]. DF was discovered by Strehler and Arnold (1951) [12] in their attempt to reveal a nature of induction illumination in a form of bioluminescence. Numerous studies, especially those of the last 25 years [7–11, 13–19], revealed the direct connection between DF and photosynthetic processes, in which DF was considered an unavoidable indicator – a susceptible "probe" for experimental photosynthetic studies in the intact leaf of maize inbreds and hybrids [7–11, 16, 17, 20]. Today, as well as, in the near future, DF shall be an efficient tool, i.e. a modern methodological approach in studies of certain, often very complex photoprocesses in the light phase of photosynthesis. In relation to this approach, induction processes of chlorophyll DF, their resolution into several mutually dependent transients, generating of oscillations and rhythms and their correlation are considered actual scientific issues. Within the scope of the stated, issues on activation energy and critical temperatures within activities of the total induction processes of chlorophyll DF, arise. Hence, these issues and their mutual relations are an objective of the present study.

EXPERIMENTAL

The studies were done with the intact leaf of the selected hybrids: ZPDC 370, ZPSC 46A, ZPSC 704 and ZPSC 71, and inbred lines: ZPR 70ž and Oh 43, tolerant and resistant to effects of increased and high temperatures, as well as, drought. The test plants were grown in pots in the glass-house under conditions of controlled air drought and a reduced amount of water in the medium. The change in the temperature was controlled and it reached the level of 38°C, although it mostly ranged from 28 to 38°C. Plants were grown under such conditions through all stages of their growth and development. Recordings were done for four years in June, July and August. Maize plants were brought from the glass-house into the laboratory during morning hours (between 7 and 8 a.m.). Plants sampled in the glass-house were transversally cut in the ground internode. In the laboratory, plants were internode lengthwise placed in water. Two hours prior to the bioluminescence experiment, the plants were kept under the black ball glass. A segment of ear intact leaves was taken from such plants and placed into a chamber of the modified Becquerel phosphoroscope. These studies were done with 40 plants each of maize hybrids and maize inbreds.

The non-invasive photosynthetic fluorescence method was used to measure the intensity of the chlorophyll DF induction process. These measures also included the resolution of the induction curve into the transients: A, B, C, D and E, as well as, recording of the generation of oscillations and rhythms.

The improved non-invasive photosynthetic fluorescence method used to measure induction processes of chlorophyll DF is schematically presented in Fig. 1.

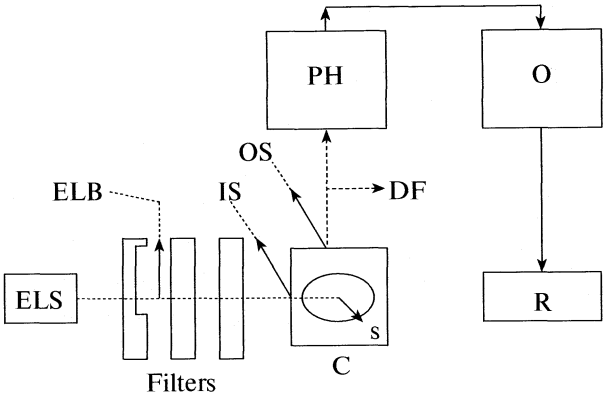

Fig. 1. Experimental setup of the photosynthetic fluorescence method and measuring equipment for delayed chlorophyll fluorescence: ELS – excitation light source; filters; ELB – excitation light beam; IS – input dark chamber slot; C – dark chamber with a sample stand; s – sample (intact leaf segment); OS – output dark chamber slot; DF – luminescent light (delayed fluorescence); PH – photo-multiplier; O – oscilloscope; R – printer.

This block scheme of the photosynthetic fluorescence method was developed at the Maize Research Institute, Zemun Polje. Measurements of changes in the intensity of induction processes of chlorophyll DF were performed after a method that had been both, in principle and details, described in previous papers [5, 7–10, 21].

RESULTS AND DISCUSSION

Standard Induction Processes

Standard induction processes of delayed fluorescence (DF) of chlorophyll (induction signals) occur when an intact leaf segment of maize inbreds and hybrids is kept in the phosphoroscope darkroom for more than 15 min ($\tau > 15$ min), and then it is illuminated with the intermittent white light. Results of induction processes of chlorophyll DF are presented in Fig. 2. Under given conditions the induction curve of chlorophyll DF does not provide the possibilities of oscillations generation or the formation of transients: A, B, C, D and E of induction processes. The registered form of the standard induction curve of chlorophyll DF has four typical parts. The part *a* is formed very quickly, for about 1–2 s, the part *b* designates the maximum level of the induction curve intensity, the part *c* is gradually formed in the exponential trend, and at the end, the part *d* represents the stationary level of the induction curve of chlorophyll DF (Fig. 2).

Induction Processes Resolved into Transients

The resolution of the induction processes of chlorophyll DF into transients: A, B, C, D and E and the appearance of oscillations occur when the intact leaf segment of maize inbreds and hybrids is kept in the

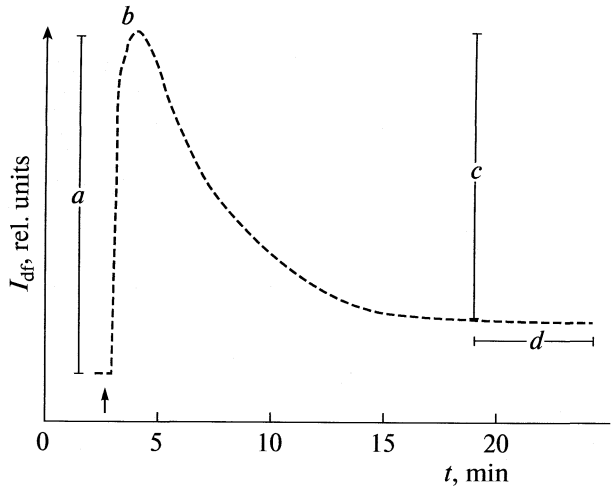

Fig. 2. Schematic illustration of a standard induction curve of chlorophyll DF typical for the intact leaf of maize inbreds and hybrids kept in the phosphoroscope darkroom for more than 15 min ($\tau > 15$ min). The arrow indicates the beginning of the measurement.

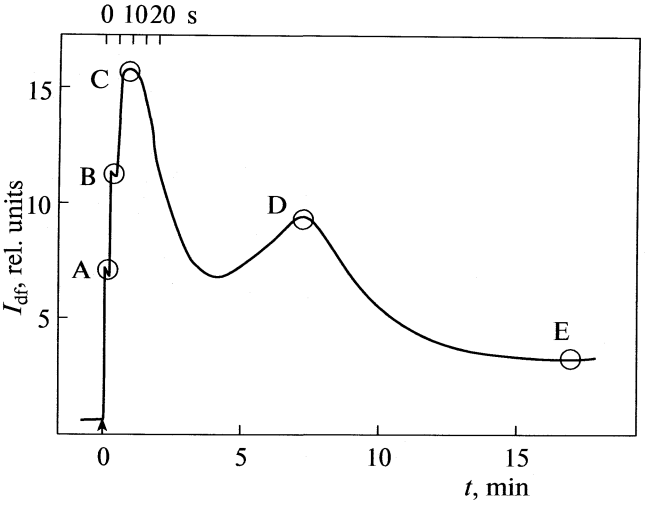

Fig. 3. Schematic illustration of possible sites of the oscillation generation and the formation of transients: A, B, C, D and E of the induction processes of delayed chlorophyll fluorescence in the intact leaf of maize inbreds and hybrids. The arrow indicates the beginning of the measurement.

phosphoroscope darkroom for a significantly shorter period (30 s $\leq \tau \leq$ 240 s) prior to its illumination with the intermittent white light (Fig. 3).

Results of the experimental resolution of induction processes of chlorophyll DF into transients: A, B, C, D and E are presented in Figs. 4–6 and Table 1.

Dynamics of Changes in Intensities of Transients of Delayed Chlorophyll Fluorescence Induction Processes in Dependence on Temperature

Obtained results on changes in the intensity of induction transients: B, C, D and E in maize inbreds and hybrids in dependence on temperature and for τ =30 s are presented in Fig. 7. However, the changes in the intensity of these induction transients for the time of 60 s $\leq$ $\leq \tau \leq$ 240 s are notably more complex 11].

Figure 7 shows that changes in the intensities of transients B and D are similar. In the beginning, the intensity of the transient B (I_B) increases at the temperature range of 24–29°C, then reaches and maintains the maximum value within the temperature range of 29–32°C, and after that, it gradually decreases at the temperature range of 32–38°C. The intensity of the transient D (I_D) shows the similar trend, but its parabola has a somewhat steeper slope. On the other hand, the dynamics of changes in the intensity of the transient C (I_C) is different. It is an inverse sigmoid (in the beginning, the intensity of the transient C increases at the temperature up to 27°C, when it reaches its maximum, then it gradually decreases at the temperature of 35.5°C at which it reaches its minimum and then again it increases up the temperature range of 35.5–38.0°C). Changes in the intensity of the transient E (I_E) are standard and expected.

Critical temperature and activation energy of transients of delayed chlorophyll fluorescence induction processes

Tables 2 and 3 present results obtained on critical temperatures and the activation energy (E_a) of transients B, C, D and E of chlorophyll DF induction processes. All critical temperatures at which even the slightest conformational changes occurred in the thylakoid membranes of studied maize inbreds and hybrids were determined by the application of the Arrhenius plot to the temperature dependency of induction

Table 1. Temporal parameters of transients: A, B, C, D and E of the induction processes of delayed chlorophyll fluorescence in the intact leaf of maize inbreds and hybrids at 25°C

Parameter	t_A, ms	t_B, s	t_C, s	t_D, s	t_E, s
Time of the beginning of transient generation	2–4	0.8–1.0	9–11	110–130	180–240
Longest time of transient duration	75–80	8–9	21–23	480–500	8400
Average time of transient duration	31 ± 6	5 ± 0.5	15 ± 5	360 ± 20	670 ± 35

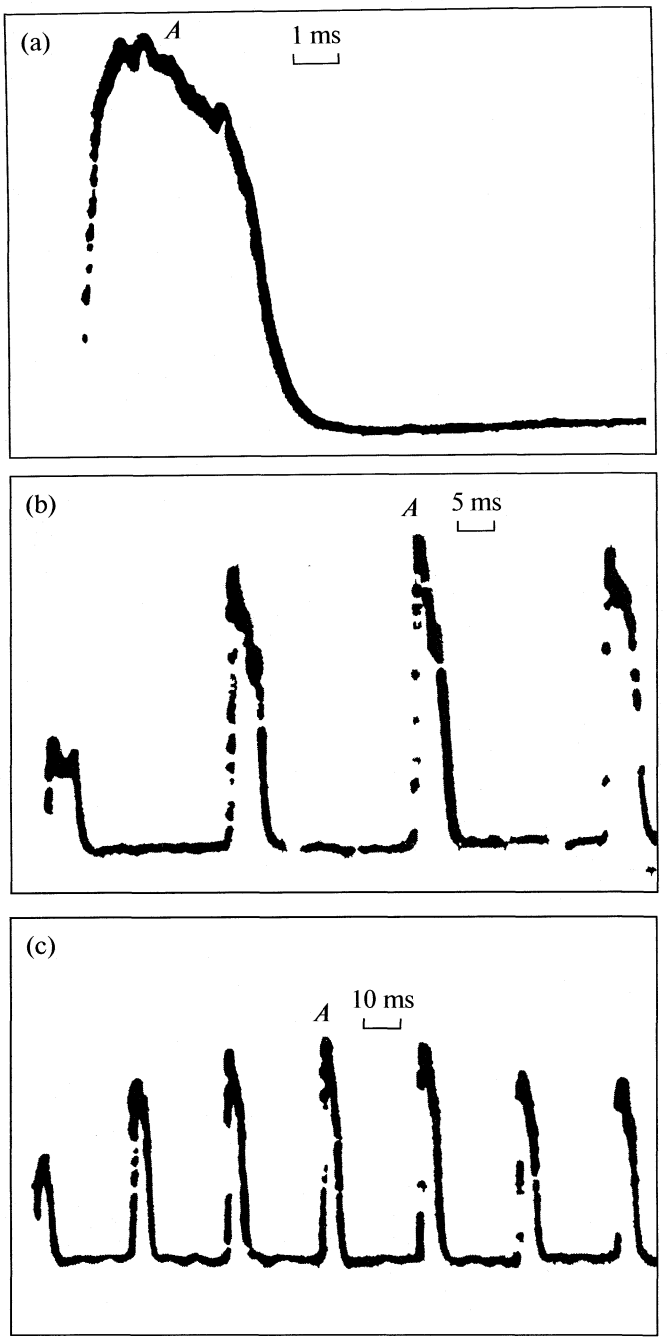

Fig. 4. Experimental detection of the transient A of the induction processes of delayed chlorophyll fluorescence in the intact leaf of maize inbreds and hybrids with the use of the storage oscilloscope and a time scale of 1, 5 and 10 ms.

transients. The values of critical temperatures (in °C) point out to a complexity of photosynthetic-fluorescent processes in the thylakoid membrane, but also to the phenomenon of resistance and adaptability of observed maize inbreds and hybrids to the environmental impacts (Table 2). The Arrhenius plot ($\ln I_{DF} = f(1/T)$) and the possibility of its linearisation, where each line represents its activation energy, are given in Table 3, while the interception of two lines is determined by the critical temperature (Table 2). Values of activation energy obtained at the generation of transients B, C, D and E and oscillations for the chlorophyll DF induction curve point out that the temperature increase results in smaller or greater conformational changes in molecules (mainly chlorophyll molecules) in the thylakoid membrane, due to which, these molecules become more reactive and gain additional energy that is used in recombination chlorophyll DF induction processes.

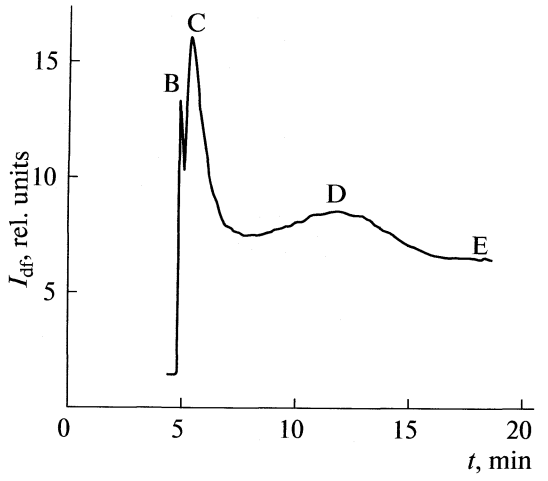

Fig. 5. Typical presentation of the experimental results on the resolution into transients: B, C, D and E of the induction processes of delayed chlorophyll fluorescence in the intact leaf of maize inbreds and hybrids for the time τ (30 s ≤ τ ≤ 240 s). The arrow indicates the beginning of the measurement.

The Correlations of Transients with Oscillations in the Delayed Chlorophyll Fluorescence Induction Processes

Experimental results on dependency of intensities of transients B, C, D and E and oscillations in chlorophyll DF induction processes in maize inbreds and hybrids are presented in Fig. 8–11. If observed objects of studying – maize inbreds and hybrids – are grown under conditions of different intensities of air drought, obtained fluorescence responses of induction processes will be not only with transients but also with oscillations.

According to such studies the intensities of transients: B, C, D and E of chlorophyll DF induction processes are connected to inducing and establishing processes of instability, excited state, fluctuations and oscillations in thylakoid membranes in the intact leaf of maize inbreds and hybrids. Such a response was obtained in observed objects that were tolerant and resistant to drought (Figs. 8–11).

Table 2. Critical temperatures (°C) of transients: B, C, D and E of delayed chlorophyll fluorescence induction processes in the intact leaf of maize inbreds and hybrids

τ, s	B	C	D	E
30	33.3±0.2	28.5±2.5	31.6±0.2	30.8±0.2
60	23.4±0.3	32.7±3.0	25.4±0.3	22.0±0.3
90	19.5±0.2	25.8±0.3	26.5±0.2	20.5±0.4
120	17.9±0.2	25.0±0.5	22.5±0.2	21.0±0.4
150	24.7±0.4	26.3±0.4	22.5±0.2	25.0±0.3
180	24.0±0.3	26.3±0.3	23.1±0.2	23.8±0.5
210	24.3±0.3	31.0±0.4	22.0±0.2	22.2±0.3
240	26.1±0.3	32.0±0.4	23.8±0.2	22.8±0.5

Note: τ is the previous intact leaf dark period.

In the experimental resolution of chlorophyll DF induction processes, transients B, C, D and E were initially revealed by the application of the standard procedures for chlorophyll DF detection [5]. Much later, the transient A was revealed [9]. It was much more difficult to be detected. It was necessary to provide a storage oscilloscope and to connect it to the equipment set up to register chlorophyll DF induction processes (Fig. 1). Recorded induction transients: A, B, C, D and E are characterised by their general and physical and chemical parameters, i.e. temporal parameters of transients (time of the beginning of transient generation and time of transient duration), dynamics of changes in transient intensities and mechanisms of their generation (Table 1 and Fig. 7).

Generation Mechanisms of Transients A, B, C, D and E

The generation mechanism of the transient A is explained by its connection to the primary photochemical act that predominantly affects the formation of the induction dipole within the photosystem II reaction centre. The generation of this transient is a result of the orientation of electric dipoles in the thylakoid membrane under effects of the illumination with the intermittent white light that excites them. The dipole orientation induces an electric field. Such dipoles define the transient A pointing out to its physical nature and its effects on the delayed chlorophyll fluorescence induction processes.

The transient B generation is primarily attributed to the formation of the electrochemical gradient across the thylakoid membrane after the illumination of the intact leaf segment with the intermittent white light. More precisely, this transient strongly depends on the electrical component of the electrochemical gradient (ΔΨ). The transient B is a direct product of the thylakoid membrane excitation under the illumination with the intermittent white light. It is believed that a photodipole interacts with other membranous structures and that this interaction causes the excitation that is in fact expressed as the transient B of the chlorophyll DF induction processes. As this interaction is rapid, more rapid than chemical reactions, its basis is not purely chemical but much more physical.

It is considered that the transient C generation depends on photosensitive reactions centres. These centres depend on τ (previous intact leaf dark period), i.e. their number increases in dependence on τ, and then conformational and functional changes occur in certain protein structures that determine mutual position of acceptors (Chl *a*) in the reaction centre. This transient has kinetic characteristics similar to the transient B as it is susceptible to the presence of valomycin,

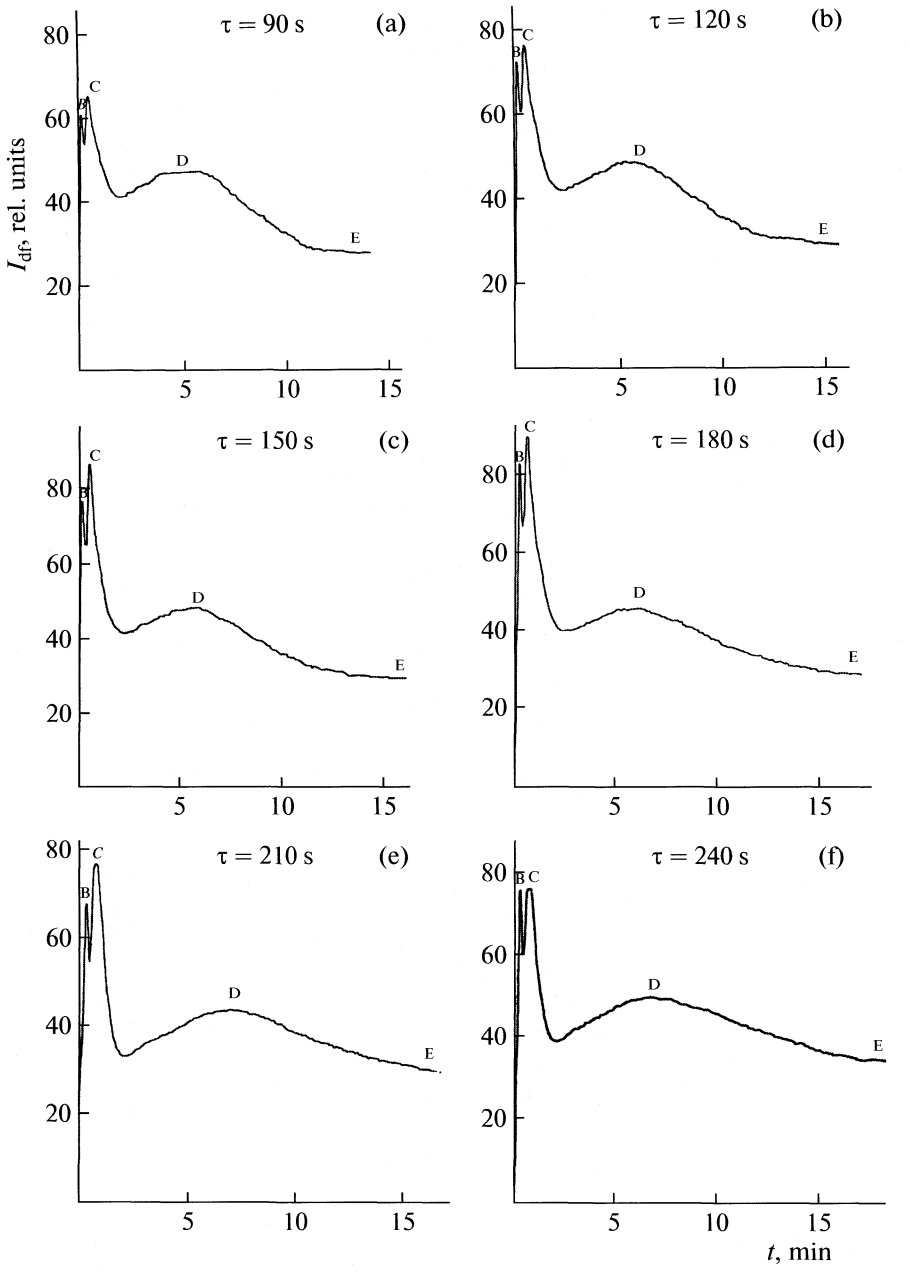

Fig. 6. Experimental results on the resolution of the induction curve of delayed chlorophyll fluorescence into transients: B, C, D and E for the following values of τ: 90, 120, 150, 180, 210 and 240s.

which is capable to eliminate the electrochemical gradient [9, 11, 18, 19, 22]. The transient C depends on the electron transport between two photosystems (PS II and PS I). In particular, the intensity of this transient increases with the increase of the accumulation of X^- (secondary PS I electron acceptor in the reduction form until it reaches its peak that corresponds to the electrochemical gradient maximum). The X^- accumulation corresponds to the accumulation of PS II Ph^- and Q^-. Similarly, the drop in the transient C intensity is caused by the decrease of the electrical component of the electrochemical gradient ($\Delta\Psi$), and cation diffusion from thylakoids, is in fact, the indication of the dissipation of the electrochemical gradient. Kinetic characteristics of this transient depend on the duration of the dark period. The prolongation of the dark period leads to the decrease in the transient C intensity and simultaneously to the increase in the transient D intensity.

The transient D of the chlorophyll DF induction curve appears, and therefore it is easily detected, only when its observation is performed outside of the optimal temperature range (16°C < T < 28°C). Hence, this transient primarily depends on the temperature.

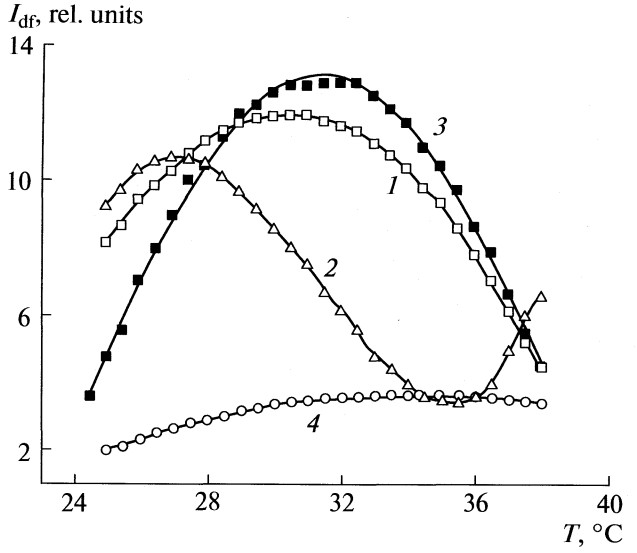

Fig. 7. Dynamics of changes in intensities of transients (*1*) B, (*2*) C, (*3*) D and (*4*) E of delayed chlorophyll fluorescence induction processes in dependence on temperature and for $\tau = 30$ s.

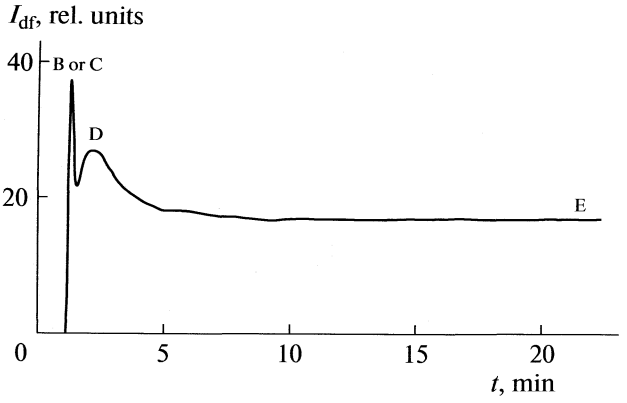

Fig. 8. Generation of the standard induction curve of delayed chlorophyll fluorescence with transients B or C, D and E in the intact leaf of maize and hybrids grown under common physiological conditions.

The transient D also depends on the electrochemical gradient, particularly on its proton component (ΔpH). The formation of the electrochemical gradient relates to "energisation" of thylakoids, which are dynamic entities whose structures and functional properties response to environmental stimuli. So, if the transient D amplitude increases, corresponding changes in the thylakoids structure will occur in the course of prtonation and phosphorylation. In case of the transient D drop, changes in the structure of thylakoids cause mutual nearing of photosystems I and II and alleviate the intersystem electron transmission. It was determined that transients C and D can be kinetically expressed by two consecutive chemical reaction of the first order with different rate constants (Table 4).

The stationary level is regularly established in the course of recording of all induction signals of delayed chlorophyll fluorescence. In case of its dissipation, this level is designated as the transient E. The stationary level of the chlorophyll DF induction curve is established by the drop of the electrochemical gradient across the thylakoid membrane and it maintains the slow changes in the intensity of the chlorophyll DF induction processes. Furthermore, the stationary level of the chlorophyll DF induction curve generally raises with the temperature increase. However, this level depends on the state of photosynthetic structures in observed intact leaves of maize inbreds and hybrids. Under particular conditions including effects of environmental factors, the transient E can take oscillatory properties [5].

Table 3. Activation energy (E_a, kJ mol^{-1}) of transients: B, C, D and E of delayed chlorophyll fluorescence induction processes in the intact leaf of maize inbreds and hybrids

τ, s	B	C	D	E
30	65.37	83.69	266.98	32.08
60	32.90	23.80	39.66	26.28
90	51.81	14.03	27.83	53.68
120	52.96	47.68	63.68	92.53
150	30.07	68.52	93.53	106.62
180	25.97	75.05	116.27	106.32
210	22.35	34.43	132.19	92.74
240	21.60	30.09	131.80	74.49

Note: τ is the previous intact leaf dark period.

Table 4. Rate constants (s^{-1}) of chemical reactions in the thylakoid membrane of the intact leaf of maize inbreds and hybrids for transients C and D of delayed chlorophyll fluorescence induction processes at 25°C

Intact leaf of maize inbreds and hybrids	$k_1 \times 10^3$	$k_2 \times 10^3$	$k_1 \times 10^3$	$k_2 \times 10^3$
	Transient C		Transient D	
ZPDC 370	5.13	2.41	3.98	2.04
ZPSC 46A	5.41	6.13	4.88	2.10
ZPSC 704	2.60	8.30	3.70	3.20
ZPSC 71	2.82	3.16	3.55	4.28
ZPR 70ž	4.80	6.10	3.50	3.20
Oh 43	5.10	6.30	4.60	2.90

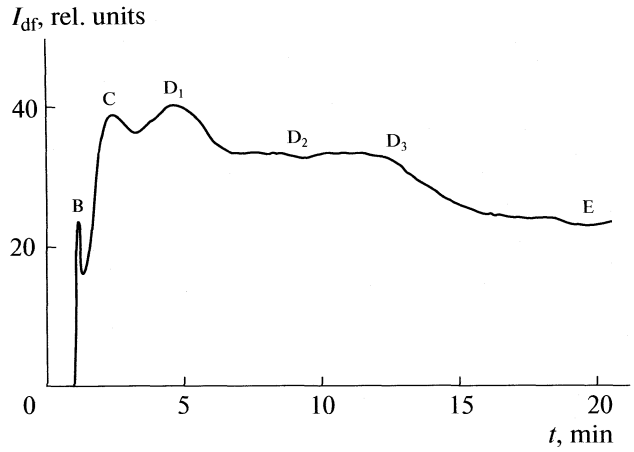

Fig. 9. Generation of the excited state of the induction curve of delayed chlorophyll fluorescence with transients B, C, D_1, D_2, D_3 and E in the intact leaf of maize inbreds and hybrids grown under conditions of weak air drought.

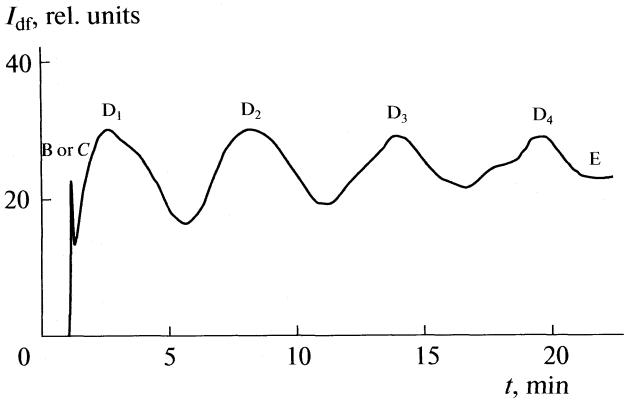

Fig. 10. Generation of the fluctuation of induction curve of delayed chlorophyll fluorescence with transients B or C, D_1, D_2, D_3, D_4 and E in the intact leaf of maize inbreds and hybrids grown under conditions of severe air drought.

The Correlations of Transients with Oscillations in Induction Processes

Studies on oscillatory phenomena in biological systems, and especially in photosynthetic structures, are relatively a novel subject matter. A great number of issues within the filed of oscillatory phenomena has been just set up, initiated or only processed to some extent. Namely, a matter of dispute concerns the correlation of transients of chlorophyll DF induction processes with provoking and establishing instabilities, excited states, fluctuations and oscillations in thylakoid membranes of segments of the maize intact leaf. Such an response was obtained in maize inbreds and hybrids that were tolerant and resistant to drought. The test plants were grown in pots with soil in the glass-house under conditions of controlled air drought and a reduced amount of water in the medium.

Studying chlorophyll DF induction processes in the intact leaf of maize grown under common and physiological conditions the obtained response was in a form of a chlorophyll DF induction curve in which transients were only partially expressed (Fig. 8). Instabilities, excited states, fluctuations and oscillations were not detected in them. However, when observed objects had been grown under conditions of weak air drought then fluorescence responses with rhythmical characteristics were obtained and significantly differed from the common chlorophyll DF induction curve.

One of such responses with the oscillatory characteristics of chlorophyll DF induction processes can have an excited state of the induction curve that remains within the region of its stationary level, which can be affected by transients (Fig. 9). Rhythms can occur in the form of fluctuations of the chlorophyll DF induction curve and can be significantly affected by transients (Fig. 10). At the end, oscillations of the chlorophyll DF induction curve can be expressed in a form of a regular oscillation of the delayed chlorophyll fluorescence stationary level (Fig. 11). It means that when a photosynthetic apparatus of the intact leaf functions under conditions depending on the environmental factors, a periodicity (rhythmicity) of the temporal dependence of structural and functional parameters of the maize leaf occurs.

The correlation of transients of chlorophyll DF induction processes with phenomena of instabilities, fluctuations and oscillations is difficult to explain. However, it is believed that transients B, C and D initiate and provoke the stated phenomena [5]. Two explanations of their correlations will be briefly present-

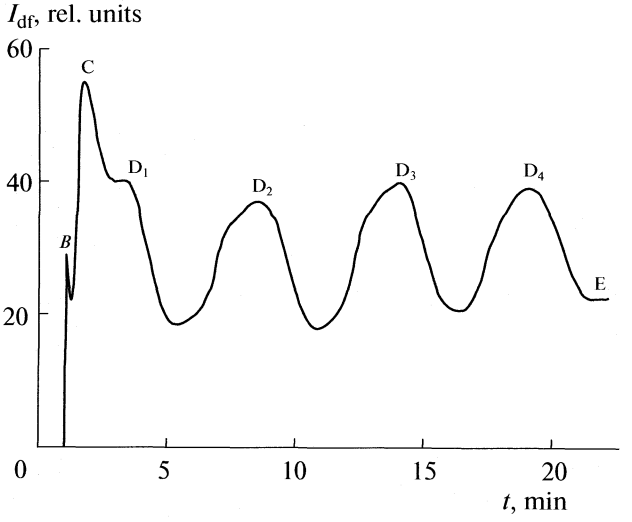

Fig. 11. Generation of the oscillations of the induction curve of delayed chlorophyll fluorescence with transients B, C, D_1, D_2, D_3, D_4 and E in the intact leaf of maize inbreds and hybrids grown under conditions severe air drought and reduced water in the medium.

ed in this paper. The first explanation is based on the existence of structural and functional regulation within the system of chloroplast of the maize intact leaf in the process of its formation. In other words, this explanation is based on the existence of active reversible links in the system functioning in the rhythmic fluctuating regime.

The starting point of the second explanation is that the phenomena of instabilities, fluctuations and oscillations in the assumed liquid mosaic membranous model can be correlated with the excited state of the thylakoid membrane. The excited state of the thylakoid membrane implies complex conformation changes, and by it, significant functional changes. Namely, proteins migrate on the surface of the thylakoid membrane (changes in the surface charge density) and provoke transport process of K^+, Na^+, H^+ and Cl^- [23]. It is quite possible to expect that changes in ions within and across the thylakoid membrane reflect on the stability of the stationary level of the chlorophyll DF induction curve in such a way that it acquires properties of the oscillator. It should also be mentioned that one of the pathways of normalising the structure and function of the excited thylakoid membrane leads via the process of phospholipid oxidation, and then via a process of resynthesis of non-oxidative products. These facts are also favoured by the information that the active transport and passive exit of cations and anions are closely related to the periodicity of the hydrolysis and resynthesis of phospholipids, as well as, that they affect activities of macroenergetic compounds (ATP and ADP) in the thylakoid membrane, which can express instabilities, fluctuations and can assume the property of the oscillator and therefore it can transmit them on the chlorophyll DF induction processes [5, 23].

CONCLUSION

According to gained and presented results it can be concluded that the improved photosynthetic-fluorescence method can be successfully applied in the studies on chlorophyll DF induction processes that are resolved into transients A, B, C, D and E and in which oscillations can be generated.

The interdependence of oscillations and induction transients A, B, C, D and E occurs in the intact leaves of maize inbreds and hybrids grown in the glass-house under different conditions of air drought, temperatures and the water deficiency in the medium.

The following properties of the chlorophyll DF induction processes were determined: conditions under which standard induction processes of chlorophyll DF were established in the intact leaf of maize inbreds and hybrids; conditions under which the induction signal was resolved into transients. The existence of transients A, B, C, D and E was identified. Temporal, physical and chemical parameters for stated transients were shown. Mechanisms of their occurrence were explained.

The following properties of oscillations of the chlorophyll DF induction processes were determined: conditions under which the exited state occurred, fluctuations appeared and oscillations were established in the thylakoid membrane of the intact leaf of maize inbreds and hybrids; the hypothesis on the mechanism of the generation of oscillations; the interdependence of the generation of oscillations and transients of chlorophyll DF induction processes was explained.

ACKNOWLEDGMENTS

These studies were mainly supported by the Maize Research Institute, Zemun Polje, Belgrade and partially by the Ministry of Science of Serbia (projects: 03E22, 12E11 and 142025).

REFERENCES

1. D. N Duvick, Genetic contribution to yield gains of U. S. hybrid maize, 1930–1980. In: W. R. Fehr (Ed.), Genetic contributions to yield gains of five major crop plants. CSSA, Spec. Publ. 7, (1984) 15–47, CSSA and ASA, Medison, WI.
2. V. Trifunović, Fourthy years of modern maize breeding in Yugoslavia. In: Proc. Genetics and breeding of Maize. December 11–12, 1986, Ed. Maize Research Institute, Zemun Polje, Belgrade, Yugoslavia.
3. M. Ivanović, R. Petrović, G. Drinić, et al., Fifty years of ZP hybrids breeding. pp 3–16 In: Proc. Breeding, Production and Maize Utilization. 50 Years of Maize Research Institute "Zemun Polje", September 28–29, 1995, Ed. Maize Research Institute, Zemun Polje, Belgrade.
4. Č. Radenović, M. Somborac, eds., Maize at the threshold of the third millenium- recollections, recountings and predictions, (2000). Published by: Maize Research Institute "Zemun Polje", Belgrade.
5. Č. Radenović, Ž. Vučinić, D. Fidler, M. Penčić, Studia biophisica **86**,143 (1981).
6. A. B. Rubin, A.A Focht, P.S. Venediktov, Transaction of the Moscow Society of Naturalists **28**, 172 (1988).
7. Č. Radenović, Contemp. Agric. **40**(6), 15 (1992).
8. Č. Radenović, J. Serb. Chem. Soc. **59**(9), 595 (1994).
9. Č. Radenović, Proceedings for Natural Sciences of Matica Srpska **93**, 5 (1997).
10. D. Marković, M. Jeremić, Č. Radenović, Savremena biofizika **4**, 1 (1996). Izdavač "Velarta", Beograd.
11. D. Marković, Č. Radenović, L. Rafailović, S. Žeraić, M. Marković, General Physiol. Biophysics. **18**(3), 257 (1999).
12. L. B. Strehler, W. Arnold, Journal of Genetics and Physiology **34**, 809 (1951).
13. P. Jurisnic, M. Govindjee van der Ven, Photosynthesis Research **3**(3), 161 (1982).
14. P. Jursnic Delayed fluorescence, Current Conpects and Status. In: "Light Emission by plants and Bacteria",

Eds: M. Govindjee van der Ven, J. Amesz and C. D. Fork, Academic Press, Orlando, Fl. USA, 291 (1986).

15. V.A. Veselovski, T.V. Veselova, Luminiscent Characteristic of Plants Photosynthetic Apparatus. In: "Luminiscence of Plants". Ed. Nauka, Moscow, 8–78 (1990).
16. Ch. Radenovich, M. Eremich, D. Markovich, Fiziologiya i biohimiya kul'turnih rastenii, **26**(5), 419 (1994a).
17. Č. Radenović, D. Marković, M. Jeremić, Photosynthetica **30**(1) 1 (1994b).
18. A. Kalauzi, D. Marković and Č. Radenović, Russian Journal of Plant Physiology **53**(3), 289 (2006).
19. D. Z. Marković, A. Kalauzi and Č. N. Radenović, Gen. Physiol. Biophys. **20**, 303 (2001).
20. Č. Radenović, M. Jeremić, Arch.biol. Sci. **48**, 1 (1996).
21. Č. Radenović, M. Jeremić, D. Fidler, D. Marković, Ž. Vucinić, Period. biol. **87**(2), 304 (1985).
22. Č. Radenović, A. Kalauzi, K. Konstantinov and G. Drinic, Proc. Nat. Sci. Matica Srpska Novi Sad **112**, 5 (2007).
23. Č. Radenović, Novi Sad **100**, 91 (2001).

ЖУРНАЛ ФИЗИЧЕСКОЙ ХИМИИ, 2009, том 83, № 9, с. 1768–1771

BIOPHYSICAL CHEMISTRY

УДК 541.64

EFFECT OF EDTA ON COPPER-INDUCED INHIBITION OF RAT MYOMETRIAL ecto-ATPase ACTIVITY

© 2009 M. Milošević, S. Petrović, I. Stanojević, D. Drakulić, N. Veličković and A. Horvat

Laboratory for Molecular Biology and Endocrinology,
"Vinča" Institute of Nuclear Sciences, P.O. Box 522, 11001 Belgrade, Serbia
E-mail: mmilosevic@vinca.rs

Abstract – The aim of this study was to examine *in vitro* chelator's ability to prevent copper-induced inhibition of rat myometrial ecto-ATPase activity. The effects of increasing $CuSO_4$ concentrations, in the absence and presence of 1mmol/l EDTA, showed sigmoidal and complete inhibition relative to the control enzyme activity. IC_{50} values, 1.15×10^{-4} and 1.71×10^{-3} mol/l in the absence and presence of EDTA, respectively, were determined by Hill analysis from experimental curves. According to the results presented in this work, 1 mmol/l EDTA increased by one order of magnitude $CuSO_4$ concentration for half-maximal inhibition (IC_{50}), by decreasing Cu^{2+} concentrations, available to form inactive $CuATP^{2-}$ complex.

INTRODUCTION

ATP and other nucleotides/nucleosides in extracellular medium express signaling roles, via nucleotide selective P1 and P2 receptors, controlling the various physiological processes in brain, heart, lungs, gastrointestinal tract, liver, urogenital and immune system [1]. For proper functioning of cells, after signal transduction, extracellular nucleotides should be rapidly inactivated. Ecto-ATPases (EC 3.6.1.3) is a family of cation dependent enzymes that hydrolyzes extracellular nucleoside tri- and/or diphosphates. The members of this family are highly glycosylated cell surface enzymes, ubiquitously expressed on plasma membranes of almost all organisms [2]. By controlling extracellular ATP concentration, ecto-ATPase family enzymes are important modulators of purinergic signaling cascade.

ATP exerts different responses in various cells of the female reproductive system. In uterus, purinergic signaling has role in regulating uterine fluid microenvironment [3], prostaglandin secretion, uterine smooth muscle contraction [4], preparation and remodeling of uterine tissue before implantation and events during early pregnancy [5, 6]. The physiological source of extracellular nucleotides in the uterine tract is autonomic nerves, platelets and semen.

Copper is essential trace element, required for the activation of enzymes associated with iron metabolism, elastin and collagen formation, melanin production, proper immune response and central nervous system integrity. There are also data that indicate importance of copper in embryonic and fetal development [7]. Copper toxicosis is usually due to occupational exposure, accidental agricultural overspray, excessive supplementation, contamination of food and water in contact with copper vessels and external exposure such as copper intrauterine devices and elevated levels of estrogens. Its toxicity is an important contributor to at least a hundred different symptoms and disease conditions. Copper ions catalyze peroxide decomposition, resulting in ROS formation and oxidative damage of lipids, proteins and DNA. Although the copper toxic action is mainly attributed to binding of Cu^{2+} ions to functional sulfhydril (-SH) group, it also may interact with $-NH_2$, $-COOH$, $-OH$ groups of membrane proteins or compete with Mg^{2+} in the $MgATP^{2-}$ complex and in that way decreases Mg^{2+}-dependent enzyme activity.

The literature data classify copper as a reproductive toxicant [8, 9]. Our previous study showed that Cu^{2+} ions induce inhibition of uterine plasma membrane ecto-ATPase activity [10]. Copper is also able to act as an alosteric modulator of ionotropic P2X receptors [11, 12]. These results suggest that alterations in purinergic signaling could be one of mechanisms for copper-induced toxicity on reproductive organs in mammals.

EDTA, one of the strongest metal ion chelators, has been used for years as a drug of choice for metal overload, but also as a model substance for *in vitro* studies of ATPase activity prevention and recovery in the presence of heavy metals [13, 14]. The present study examines *in vitro* $CuSO_4$ effect on ecto-ATPase activity in uterine plasma membranes, in the presence and absence of EDTA. Chelating copper ions, EDTA decreases free ion concentrations, which may interact with the enzyme protein or ATP. Since ATP has a higher affinity for Cu^{2+} than Mg^{2+}, and EDTA may bind both, copper and magnesium ions, concentrations of all free ions and complexes were calculated using computer-base program JONCONC.

EXPERIMENTAL

Animals. Experiments were performed on 3-months-old female Wistar albino rats obtained from the local colony. Animals were held under standard laboratory conditions and "Protocol of the Vinca institute on care and treatment of laboratory animals" were followed.

Isolation of plasma membranes. Myometrial plasma membranes (MPM) were isolated by the modified Krall method [15]. Animals were decapitated and the uteri were trimmed of fat, minced and homogenized in isolation buffer (5mmol/l Tris, pH 7.4, 0.32 mol/l sucrose) using an UltraTurex homogenizer. In second step, the suspension was further homogenized with 20 strokes in Potter homogenizer, with teflon pestile at 900 rpm. Homogenate was filtrated through surgical gauze and centrifuged for 10 min at 1000*g*. The supernatant was saved and pellet was resuspended in 10 ml of the same medium and centrifuged for a second time under the same conditions. The supernatants were pooled and centrifuged at 10.000*g* for 35 minutes at 4°C. Obtained supernatant was recentrifugated for 60 minutes at 50.000*g* and the pellet was resuspended in 5 mmol/l Tris-HCl and refrigerated at −20°C, over night.

Next day, the suspension was homogenized with 10 strokes of a manual homogenizer and placed on the top of discontinuous gradient of sucrose. The gradient was centrifuged for 120 min at 100.000*g*, in ultracentrifuge at 8°C. The interface of 1.2–1.0 mol/l and 1.0–0.8 mol/l sucrose, containing plasma membrane were pooled, diluted by 5 mmol/l Tris-HCl (pH 7.4) and pelleted by centrifugation for 35 minutes at 11.000*g* in order to eliminate sucrose present in sample. The membrane pellets were resuspended in 5 mmol/l Tris-HCl (pH 7.4) and then homogenized with manual homogenizer. The membrane preparations were kept at −70°C until use.

Protein determination. Protein was measured according to the modified Lowry procedure for protein determination in membrane and lipoprotein samples [16].

Enzyme assays. NTPDase activity was determined by the measuring the amount of liberated inorganic phosphate from hydrolyzed ATP. The Pi was assayed according to Penniel method [17]. The incubation mixture contained 1 mmol/l $MgCl_2$, 7 μg membrane protein and 50 mmol/l Tris-HCl, pH 7.4 in a final volume of 200 μl. The reaction medium was preincubated for 30 minutes at 37°C without or with copper sulphate (1×10^{-7} to 5×10^{-2} mol/l). The assay was initiated by adding the substrate, 1 mmol/l ATP. Incubation lasted 10 min at 37°C in water bath and reaction was stopped with 22 μl of 3 mol/l perchloric acid and chilled on ice for 15 min. The inorganic phosphate concentration, liberated from the hydrolysis of ATP, was determined by spectrofotometric method on 700 nm. The effects of increasing concentrations of Cu^{2+} were measured in the absence and presence of 1 mmol/l EDTA.

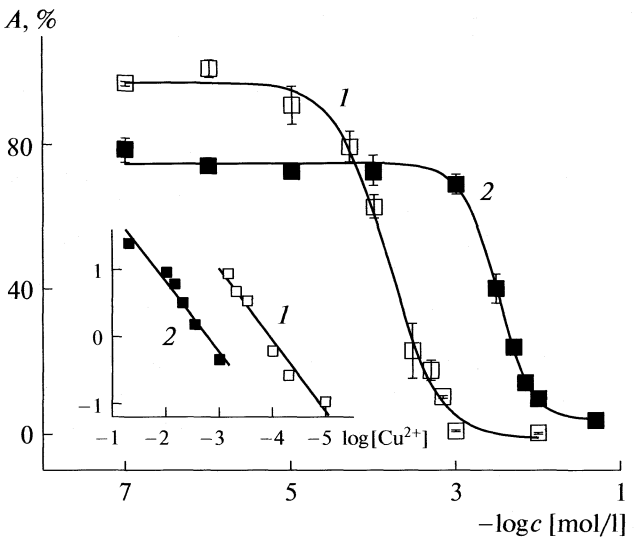

Fig. 1. Ecto-ATPase activity inhibition by $CuSO_4$ (*c* is concentration of added Cu^{2+}) (*1*) in the absence and (*2*) in presence of 1×10^{-3} mol/l EDTA. The values given are the mean percentage in respect to the control enzyme activity (*A*) of at least three experiments ±S.E.M. Inset: Hill plot of experimental data.

Experiments were repeated at least three times in triplicate with different enzyme preparations. The results are expressed as a mean percent enzyme activity compared to corresponding control value.

Statistical analysis. The data were analyzed by means of the Student *t* test; the values of $p < 0.05$ considered as significant.

RESULTS AND DISCUSSION

Prevention of $CuSO_4$ induced inhibition. The effects of increasing concentrations of Cu^{2+} (1×10^{-7} to 5×10^{-2} mol/l) were measured in the absence and presence of 1 mmol/l EDTA. The concentrations of ionic species were calculated, taking into account equilibrium reactions involving Mg^{2+}, ATP, EDTA and Cu^{2+} (table). The stability constants were found in the literature [18].

In the absence of EDTA, ecto-ATPase activity showed complete inhibition, relative to the control samples when 1×10^{-3} mol/l of $CuSO_4$ was added, but the same metal concentration in the presence of EDTA inhibited enzyme activity for about 30% (Fig. 1). The half-maximum inhibitory activities (IC_{50}) in absence of EDTA, determined by Hill analysis of experimental curves (Fig. 1, inset), were 1.15×10^{-4} mol/l of added $CuSO_4$ and 1.43×10^{-5} mol/l for calculated free Cu^{2+} concentration (table). The IC_{50} value in presence of EDTA was 1.71×10^{-3} mol/l of added $CuSO_4$.

Effect of Cu^{2+} on substrate concentration. Calculated values show that competition between Cu^{2+} and Mg^{2+} ions in the $MgATP^{2-}$ complex, starts at 1×10^{-4} mol/l

The values of free Cu^{2+} (c_0), $CuATP^{2-}$ and $CuEDTA^{2-}$(M) calculated in the medium assay containing various Cu^{2+} concentrations (c, M) in the presence and absence EDTA

Without EDTA			With 1mmol/l EDTA			
c	c_0	$CuATP^{2-}$	c	c_0	$CuATP^{2-}$	$CuEDTA^{2-}$
1×10^{-7}	1.1×10^{-9}	9.9×10^{-8}	1×10^{-7}			0.9×10^{-7}
1×10^{-6}	1.1×10^{-8}	9.9×10^{-7}	1×10^{-6}			0.9×10^{-6}
1×10^{-5}	1.1×10^{-7}	9.9×10^{-6}	1×10^{-5}			0.9×10^{-5}
5×10^{-5}	6.4×10^{-7}	4.9×10^{-5}	1×10^{-4}			9.9×10^{-5}
1×10^{-4}	1.5×10^{-6}	9.8×10^{-5}	1×10^{-3}	1.2×10^{-12}	1.1×10^{-10}	9.9×10^{-4}
3×10^{-4}	9.1×10^{-6}	2.9×10^{-4}	3×10^{-3}	1.1×10^{-10}	9.5×10^{-4}	9.9×10^{-4}
5×10^{-4}	2.8×10^{-5}	4.7×10^{-4}	5×10^{-3}	3.1×10^{-3}	9.8×10^{-4}	9.9×10^{-4}
7×10^{-4}	6.8×10^{-5}	6.3×10^{-4}	7×10^{-3}	5.1×10^{-3}	9.9×10^{-4}	9.9×10^{-4}
1×10^{-3}	1.9×10^{-5}	8.0×10^{-4}	1×10^{-2}	8.0×10^{-3}	9.9×10^{-4}	9.9×10^{-4}
1×10^{-2}	9.0×10^{-3}	9.9×10^{-4}	5×10^{-2}	4.8×10^{-3}	9.9×10^{-4}	9.9×10^{-4}

Note. Concentrations below 1×10^{-12} are not presented.

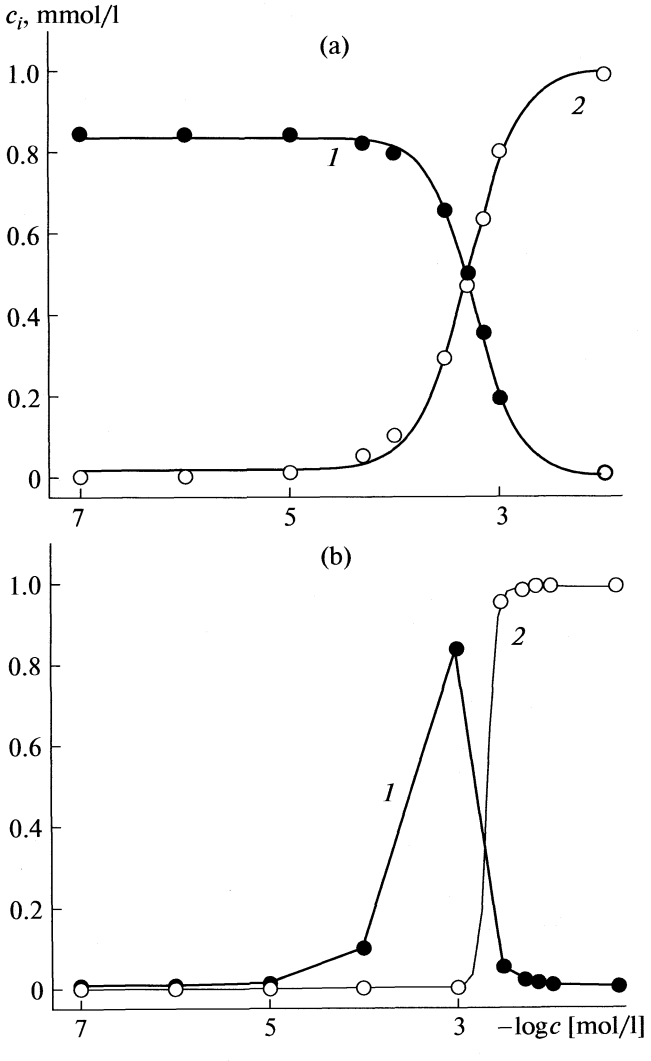

Fig. 2. The dependence of the concentration (c_i) of (*1*) $MgATP^{2-}$ and (*2*) $CuATP^{2-}$ complexes in the reaction mixture containing 1mmol/l ATP and 1mmol/l $MgCl_2$ on the experimental $CuSO_4$ concentration, (a) in the absence and (b) in the presence of 1mmol/l EDTA.

of added $CuSO_4$, since copper ions form inactive and more stable complex with ATP. Experimental curves show that inhibition of enzyme activity starts at $CuSO_4$ concentrations less than 10^{-4} mol/l, indicating that inhibition depend on free Cu^{2+} concentration, rather than a formation of $CuATP^{2-}$. Although, ecto-ATPase has no free SH groups [19], free copper ions may non-specifically bind to other functional enzyme residues and decrease enzyme activity.

Effect of EDTA. In the presence of 1 mmol/l EDTA, inhibition of enzyme activity by $CuSO_4$ is prevented below 1mmol/l. According to calculation, in range of 10^{-7}–10^{-3} mol/l of $CuSO_4$, almost total concentration of added copper ions is trapped in complex with EDTA (table). But initial enzyme activity is maximum 80% of control activity measured in the absence of EDTA. It may be explained by lowering the $MgATP^{2+}$ concentration, due to Mg^{2+} ions chelation. Adding $CuSO_4$ in reaction mixture, Cu^{2+} ions replace Mg^{2+} in complex with EDTA and concentration of $MgATP^{2+}$ increases (Fig. 2). However, enzyme activity remains merely the same until 1mmol/l $CuSO_4$ was added. Inhibition of the activity may be due to interaction of EDTA or CuEDTA complex with the enzyme or other plasma membrane proteins in the vicinity.

In our previous study of copper induced inhibition ecto-ATPase activity [10], reaction medium contained excess of Mg^{2+} and ATP (5 mmol/l $MgCl_2$, 2 mol/l ATP), in order to maintain constant concentration of $MgATP^{2+}$, substrate for ecto-ATPase. Kinetic analysis revealed uncompetive type of inhibition and our results were consistent with previously reported study with ecto-ATPase in rat brain synaptic membranes [14]. But 5 mmol/l Mg^{2+} is not likely to be physiological concentration since normal plasma levels of magnesium are in range from 0.7 to 1.0 mmol/l. Estimated concentrations of ATP that produce physiological response are even smaller, within the range of 10^{-4}–10^{-6} mol/l [20]. In this study, substrate concentrations (1 mmol/l Mg^{2+}, 1 mmol/l ATP) that produce

maximum enzyme activity and yet are more similar to physiological level in extracellular space, have been chosen. By decreasing concentration of added $MgCl_2$ in reaction medium, IC_{50} values and percentage of maximum inhibition (I_{max}) changed approximately proportional [10]. The half-maximum inhibitory activities were 1.15×10^{-4} and 5.56×10^{-4} mol/l in the presence of 1 and 5mmol/l $MgCl_2$, respectively. The composition of reaction mixture and component's concentrations of model system *in vitro* may be important when estimate Cu^{2+} concentration needed to achieve biological response in system *in vivo*.

Some resent data suggest that EDTA cause membrane destabilization, by chelating divalent cations on lipid surface (Mg^{2+}, Ca^{2+}) and by direct insertion in membrane [21]. These findings are important since EDTA has been used for years as a drug and additive to food and cosmetics. Our results suggest that effects of the EDTA on the enzyme activity inhibition could not be excluded, since initial enzyme activity is maximum 80% of control activity, measured in the absence of EDTA.

CONCLUSION

EDTA, having high affinity for Cu^{2+}, may prevent or decrease the toxic effects of this metal ion. According to the results presented in this work, 1 mmol/l EDTA increase by one order of magnitude $CuSO_4$ concentration for half-maximal inhibition (IC_{50}), by decreasing Cu^{2+} concentrations, available to form inactive complex $CuATP^{2-}$.

ACKNOWLEDGMENTS

This study was supported by the Serbian Ministry of Sciences, Project No. 143044.

REFERENCES

1. G. Burnstock, Physiol. Rev. **87**, 659 (2007).
2. H. Zimmermann, Trends Pharmacol Sci. **20**, 231 (1999).
3. X. F. Wang and H. C. Chan, Biol. Reprod. **63**, 1918 (2000).
4. H. Aitken, N. L. Poyser and M. Hollingsworth, Br. J. Pharmac. **132**, 709 (2001).
5. R. Koshi, R. Coutinho-Silva, C. M. Casabulho et al., J. Reprod. Immunol. **66**, 127 (2005).
6. M. Slater, C. R. Murphy and J. A. Barden, Cell Calcium **31**(5), 201 (2002).
7. C. L. Keen, J. Y. Uriu-Hare, S.H. Hawk et al., Am. J. Clin. Nutr. **67**, 1003S (1998).
8. M. K. Chung, S. S. Beak, A. H. Lee et al., Environ. Toxicol. (2008).
9. P. Kovacic and J. D. Jacinto, Current Medicinal Chemistry **8**, 863 (2001).
10. M. Milosevic, M. Demajo, A. Horvat, Environ. Chem. Lett. (2009).
11. C. Virginio, D. Church, R. A. North, Neuropharmacology. **36**(9), 1285 (1997).
12. C. Coddou, R. A. Lorca, C. Acuña-Castillo et al., Toxicol. Appl. Pharmacol. **202**(2), 121 (2005).
13. D. Krstic, K. Krinulovic, V. Vasic, J. Enz. Inh. Med. Chem. **20**(5), 469 (2005).
14. V. Vasic, D. Jovanovic, D. Krstic et al., Toxicol. Lett. **110**, 95 (1999).
15. J. F. Krall and S. G. Korenman, Biochim. Biophys. Acta **556**, 105–111G. (1979).
16. M. A. Markwell, S. H. Haas, L. L. Bieber, et al., Anal. Biochem. **87**, 206 (1978)
17. R. Pennial, Anal. Biochem **14**, 87 (1966).
18. L. G. Silen, A.E Martell, Stability Constants of Metal-Ion Complexes. The chemical Society, London Special Publication № 25, 1971.
19. V. V. Ivanenkov, J. Meller and T. L. Kirley, Biochemistry, **44**(25), 8998 (2005).
20. G. G. Yegutkin, Bioch Biophy Acta **1783**(5), 673 (2008).
21. V. Prachayasittikul, C. Isaramkura-Na-Ayudhya, T. Tantimongcolwat et al., Acta Bioch Bioph Sinica **39**(11), 901 (2007).

ЖУРНАЛ ФИЗИЧЕСКОЙ ХИМИИ, 2009, том 83, № 9, с. 1772–1777

BIOPHYSICAL CHEMISTRY

УДК 541.64

EFFECTS OF ACUTE GAMMA-IRRADIATION ON EXTRACELLULAR ADENINE NUCLEOTIDE HYDROLYSIS IN DEVELOPING RAT BRAIN

© 2009 I. Stanojević, D. Drakulić, N. Veličković, M. Milošević, S. Petrović and A. Horvat

Laboratory for Molecular Biology and Endocrinology, "Vinča" Institute of Nuclear Sciences, P.O.Box 522, 11001 Belgrade, Serbia

E-mail: istanojevic@vinca.rs

Abstract – Cell membrane is highly sensitive to irradiation which, acting directly or indirectly, may disturb functions of constitutive proteins including membrane enzymes. Plasma membrane surface-located enzyme chain of ecto-nucleotide triphospho diphosphohydrolases (NTPDases) and 5'-nucleotidase are involved in termination of cell purinergic signalization by hydrolyzing extracellular, excitatory adenosine triphosphate (ATP), as well as nucleotide di-, and mono-phosphate (ADP and AMP) to neuroprotective adenosine. Extracellular ATP, ADP and AMP hydrolyzes were examined in purified synaptic plasma membranes after whole-body acute irradiation. All measurements were done 24 h after irradiation of developing (15-, 30-day-old) and adult (90-day-old) rats with low (50 cGy) and high (2 Gy) dose of gamma-rays. Both, high and low doses inhibited nucleotide hydrolyses in 15-day-old rats; in 30-day-old rats low dose of radiation inhibited ADP and AMP hydrolyses while high dose inhibited only ATP hydrolyse. In adult rats high dose induced no effects, while low dose stimulated nucleotides hydrolyses. According to obtained results it was concluded that ecto-nucleotidases of young rats are more sensitive to irradiation, since even low dose induces inhibition of ecto-nucleotidases activities. Ionizing radiation, by decreasing brain nucleotide hydrolyses in developing rats, induces accumulation of ATP and decreases production of adenosine in synaptic cleft which could be neuro-cytotoxic. On the contrary, in adult rats low dose of radiation stimulates NTPDase and 5'-nucleotidase activity and protective adenosine production which indicates protective and adaptive mechanisms developed in adult brain neuronal cells.

INTRODUCTION

Ionizing radiation (IR) can cause significant damage to normal brain. In everyday life, brain is frequently exposed to ionizing radiation due to diagnostic, therapeutic, occupational and environmental sources. Irradiation remains one of the major treatments for certain types of cancer and such therapy may require cephalic or whole-body irradiation. The aim of radiation therapy is to kill tumor cells while minimizing damage to normal cells. The ultimate effect of radiation can be apoptotic or necrotic cell death as well as cytogenetic damage resulting in genetic instability and/or cell death. The destructive effects of radiation arise from direct and indirect ionization events leading to peroxidation of macromolecules. Plasma membrane is highly sensitive to IR, especially in early period after irradiation [1]. Reactive oxygen species (ROS) formation and oxidative stress that follow are very important in injuries induced by ionizing radiation. Lipid peroxidative end-products may damage DNA and proteins [2].

Whole-body or whole-brain gamma-radiation causes significant changes in the level of central nervous system (CNS) proteins, and it is able to induce plasma membrane structure alterations, metabolic process inhibition, ion transport changes, protein-lipid and protein-protein interactions [1], enzyme activity inhibition or stimulation in dose-dependent manner [3]. Relatively low doses of gamma irradiation in mammals induce numerous functional disorders and provoke a transient encephalopathy depending on absorbed dose, distribution and dose rate [4]. Juvenile rats' irradiation leads to reduction of neuronal progenitor cells and neuronal apoptosis [5] and disturbance of the electrical activity of neurons [6]. Simultaneously, large localized lesions are seen in brain regions less than 24 h after irradiation [7].

Adenine nucleotides, such as ATP and adenosine are involved in the regulation of a variety of physiological and pathological processes in the CNS, including development and tissue remodelling following trauma, stroke, ischemia or neurodegenerative disorders [8]. The ATP is stored in synaptic vesicles and released into synaptic cleft, activating the P2 purino-receptors [9]. Extracellular ATP may act as a fast excitatory neurotransmitter and neuromodulator [10] or have long lasting trophic effects [11].

The events induced by extracellular adenine nucleotides are controlled by the action of ecto-nucleotidases family members, NTPDase and 5'-nucleotidase [12]. Up to date, three NTPDases (NTPDase 1–3), that are different in their preference for a substrate (ATP and ADP), have been localized in the brain plasma membranes. Hydrolysis of ATP and ADP are followed with hydrolysis of produced AMP by 5'-nucleotidase generating adenosine [12, 13]. Adenosine elic-

its important physiological responses related to neurotransmission modulation, neuroprotection and cell survival/death, activating specific P1 receptor subtypes [14, 15]. Thus, ecto-nucleotidase pathway has a double function of removing one signal (ATP) and generating second one (adenosine), and controlling the levels of adenine nucleotides in the extracellular environment and the duration and extent of their receptor activation.

Cellular damage under pathological conditions results in a massive and dramatic release of ATP into extracellular environment [16]. ATP released from damaged or dying cells has been demonstrated to be crucial in mediating the injury-induced defensive responses. Massive ATP accumulation in synaptic cleft could be neuro-cytotoxic, while prolonged P2 receptor stimulation promotes neuronal injury by increasing intracellular calcium concentration [17] and enhancing cytotoxic glutamate effects [18]. Since, adenine nucleotides perform important roles in brain response to damage, modulation of the enzymes directly involved in their extracellular metabolism could have potential therapeutic importance. Sangsuwan and Haghdoost (2008) suggested that the nucleotide pool is an important target for radiation-induced stress response [19].

Therefore, present study was performed to obtain how low (50 cGy) and high (2 Gy) doses of gamma-ray radiation affect neuronal function by modulating nucleotide hydrolysis induced by NTPDase and 5'-nucleotidase. Also, developmental-dependent effects of radiation were inspected by acute whole-body irradiation of rats in different phases of postnatal development.

EXPERIMENTAL

Materials

All chemicals were purchased from Sigma Chemical Co. (St. Louis, MO) and were analytical graded.

Animals

Female rats of the Wistar Albino strain from the local colony in different phase of development were used throughout this study: infant (15-days-old rats), prepubertal (30-days-old rats) and sexually mature adult (90-days-old rats). All animal treatments were in accordance with the 'Guidelines for scientific experiments on animals' of the Institute Ethical Committee for experimental animals use and all efforts were made to reduce the number of animals used in the experiment.

Gamma-Irradiation Procedure

Female rats 15-, 30-, and 90-days old were divided in two groups: whole-body irradiated with single 50 cGy or 2 Gy dose of gamma (γ)-rays (10.7 cGy/min, ^{60}Co source from Institute of Nuclear Sciences "Vinca") (Ir group) and control group – sham irradiated (C group). During irradiation, the animals were confined in plywood boxes with circle holes for breathing. The control group was treated as the irradiated group but not subjected to irradiation. All groups were sacrificed 24 hour after irradiation.

Synaptosomal Preparation

After decapitation with a small animal guillotine (Harvard Apparatus) brains were rapidly excised for immediate synaptosomal plasma membrane isolation. Brains were quickly removed on ice ($n = 3$ animals of each group) and placed in isotonic medium (0.32 mol/l sucrose, 5 mmol/l Tris-HCl, pH 7.4). Synaptosomes were purified according to a procedure described previously [20] and derived from Cotman and Matthews method [21].

Synaptosomal Plasma Membrane Preparation

Synaptosomal plasma membrane fraction (SPM) was prepared following Towle and Sze procedure (1983), as previously described [22]. Protein content was determined according to Markwell et al. method [23] and samples were kept frozen at –70°C until use.

Enzyme Assays

The reaction medium used to assay nucleotide hydrolysis by NTPDase or 5'-nucleotidase contained (in mmol/l): 50 Tris-HCl buffer, pH 7.8, 5 $MgCl_2$ in the final volume of 200 μl. The SPM (40 μg of proteins for ATP and ADP and 80 μg of proteins for AMP hydrolysis assay) was added to the reaction mixture and pre-incubated for 10 min at 37°C. The reaction was initiated by the adding of ATP, ADP or AMP to a final concentration of 1.0 mmol/l and incubated for additional 15 min in ATP or ADP assay or 30 min in AMP assay. The enzyme reaction was stopped by the addition 22 μl of ice-cold 3 mol/l perchloroacetic acid. The samples were chilled on ice and released inorganic phosphate (P_i) from nucleotides hydrolysis was measured by modified Pennial method [24], based on colorimetric determination of Sn-phosphomolybdate complex, produced by liberated inorganic phosphate (P_i) (as product of enzymatic hydrolysis of adenine nucleotides), ammonium molybdate and $SnCl_2$.

The optical density was measured with spectrophotometer on 700 nm. The KH_2PO_4 was used as referent standard, that enables to calculate liberated P_i in assay and was expressed in μmol P_i (the upper and lower limits of the sensitivity of the procedure is from 0.025 to 1.00 μmol P_i). Breafly, in assay mixture, 3ml benzene:isobutanol (1:1) solution, 0.5 ml 1% ammonium-molybdate and 0.5 ml 0.28 mmol/l H_2SO_4 were added and incubated 45 min at room temperature for P_i extraction. One ml of upper layer, containing inorganic phosphate, was mixed with 4 ml 3.4% H_2SO_4 in

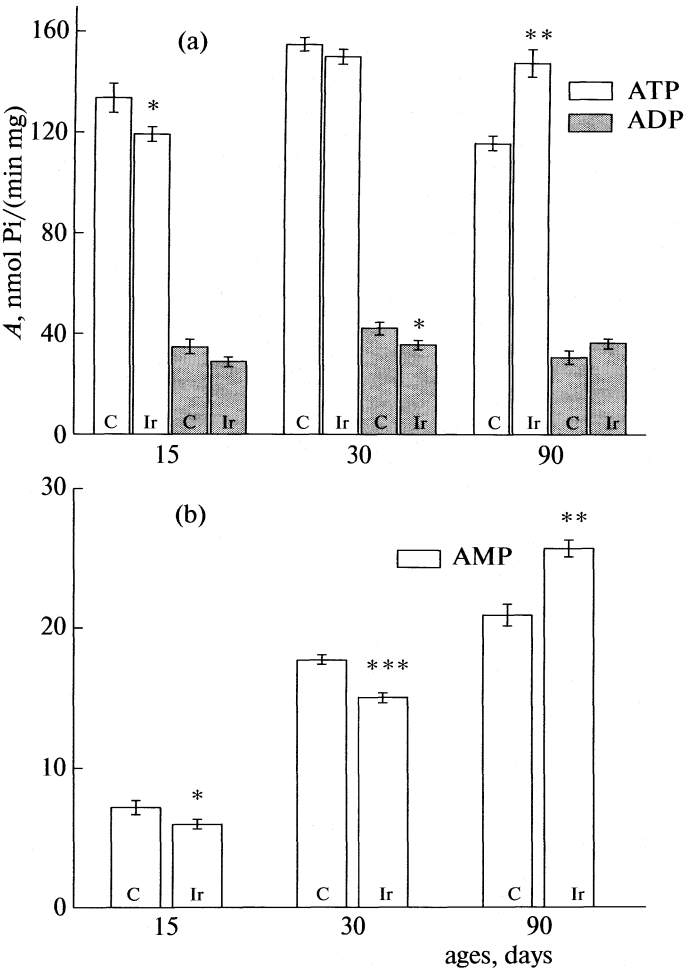

Fig. 1. The NTPDase (a) and 5'-nucleotidase (b) activity (A) in synaptic plasma membranes from 15, 30 and 90-day-old rats, 24 h after irradiation with 50 cGy. Results represent mean ±SEM from three independent experiments done in triplicate. Significance of irradiated group (Ir) in respect to non-irradiated controls (C), $*p < 0.05$, $**p < 0.01$, $***p < 0.001$.

ethanol and 0.5 ml $SnCl_2$ in 1.5 mmol/l H_2SO_4 and again incubated for 45 min at room temperature in order to develop blue colour, which is stable for a few ours. Absorption was measured at 700 nm, and amount of liberated inorganic phosphate was calculated from standard curve.

The purity of SPM was evaluated with the use of several inhibitors (data not shown) and the results obtained indicated no significant cross-contamination with other subcellular fractions (<10%). In all enzyme assays, incubation times and protein concentration were chosen in order to ensure the linearity of the reactions. Other conditions, such as medium reaction, pH and cation concentration were used to assure the optimal enzyme activities. Enzyme specific activity was expressed as nmolP_i/(min mg) of SPM proteins.

Data Analysis

The data obtained for the enzyme activities are presented as mean specific enzyme activity ±SEM, from 3 independent SPM isolations performed in triplicate. Statistical analyses were performed by one-way analysis of variance (ANOVA), followed by a Tukey's test as post-hoc, considering $p < 0.05$ as significant.

RESULTS AND DISCUSSION

The effects of low (50 cGy) dose radiation on the synaptosomal plasma membrane NTPDase and 5'-nucleotidase activity, 24 h after irradiation are presented in Fig. 1a and b, respectively. Irradiation with 50 cGy dose in 15-day-old rats, significantly ($p < 0.05$) decreased rate of ATP hydrolysis by 18% and in 30 day-old animals only ADP hydrolysis was decreased by 20% ($p < 0.05$) compared to non-irradiated control. In the nerve terminals of adult rat brain, 24 h after irradiation, ATP hydrolysis is increased by 30% ($p < < 0.001$) compared to non-irradiated control (Fig. 1a).

It was found out decreased ecto-5'nucleotidase hydrolyzing activity 24 h after 50 cGy dose irradiation in 15- and 30-day-old rats by 15% ($p < 0.05$ and $p <$

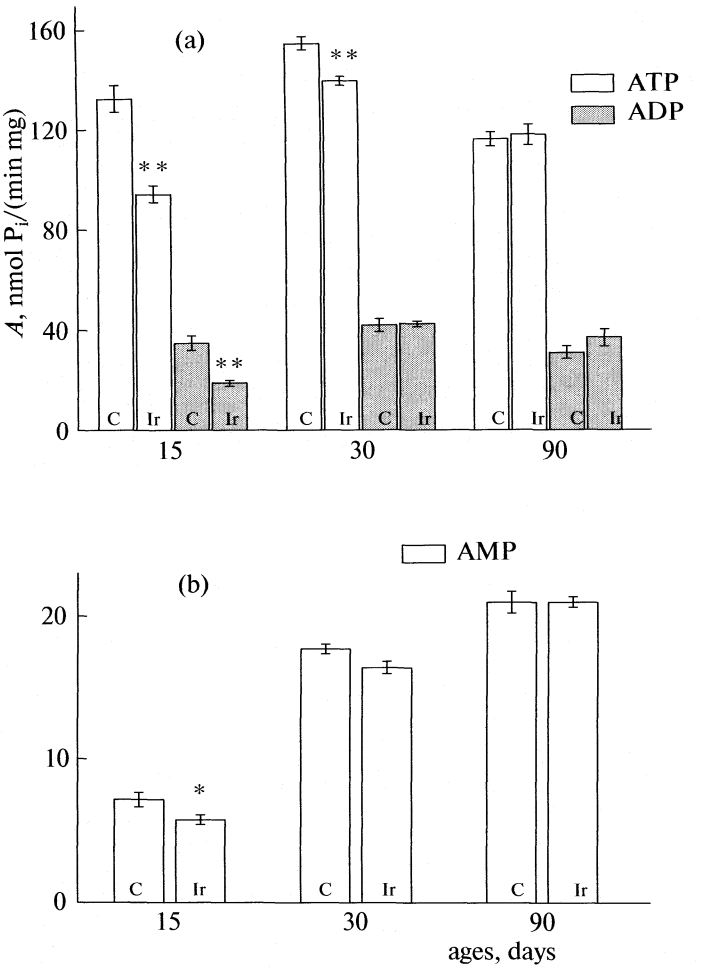

Fig. 2. The NTPDase (a) and 5'-nucleotidase (b) activity (A) in synaptic plasma membranes from 15, 30 and 90-day-old rats, 24 h after irradiation with 2 Gy. Other conditions are the same as in Fig. 1.

< 0.001 respectively) in respect to appropriate controls (Fig.1b). In the nerve terminals of adult rat brain, 24 h after irradiation, AMP hydrolysis was increased by 25% ($p < 0.001$) compared to non-irradiated control (Fig. 1b).

The results indicate that even a low, 50 cGy, dose was enough to induce inhibition of NTPDase as well as 5'-nucleotidase activity 24 h after irradiation of infant and prepubertal rats. Opposite effect has been seen in adult rats, the same dose induced increased NTPDase and 5'-nucleotidase activities.

The initiation of any low-dose effect is not specific for ionizing radiation, it occurs under the action of many other external factors, including non-genotoxic agents [1].

The results of high (2 Gy) dose radiation on the synaptosomal NTPDase and 5'-nucleotidase activity, 24 h after irradiation are presented in Fig. 2. In 15-day-old rats, dose of 2 Gy significant decreased ATP and ADP hydrolysis by 30% ($p < 0.001$) and 46% ($p < < 0.001$) respectively, while in 30-day-old rats only ATP hydrolysis was decreased by 11% ($p < 0.001$), compared to appropriated non-irradiated control. In the nerve terminals of adult rat brain, 24 h after irradiation, ATP and ADP hydrolysis were not affected (Fig. 2a). AMP hydrolysis was significantly decreased only in infant, 15-day-old rats, by 20% ($p < 0.05$) (Fig. 2b).

According to acquired results, both doses of radiation modulated NTPDase and 5'-nucleotidase activity in rat brain neuronal endings. During first postnatal month low- and high-dose radiation, by decreasing ecto-nucleotidase activity, persuade ATP accumulation in synaptic cleft. Since ATP is recognised as an excitatory neurotransmitter in CNS [25], the inhibition in ATP hydrolysis may have critical consequences. Large amount of extracellular ATP may cause cell death *via* activation P2X7 receptors [26] and could be harmful for neurons. Inhibition of ecto-ATPase activity would be expected to potentiate excitatory synaptic transmission by supporting synaptic ATP efficacy and inhibiting the adenosine formation [16], as a neuroprotective agent. Also, decreased 5'-nucleotidase activity by radiation contribute to lesser extracellular ad-

enosine content. Adenosine *via* interaction with the A1 receptors is particularly important during maturation and have numerous and diverse effects on brain development.

During postnatal brain development synaptic contacts, dendrite elongation and myelinization, as well physiological apoptosis are more potent events. Ecto-5'-nucleotidases plays a significant role in neurogenesis and in cellular contact formation within synaptic cleft [27]. It is well known that immature neurons are more sensitive to ionizing irradiation. By decreased NTPDase and 5'-nucleotidases activity in infant and prepubertal rats and consequently decreased adenosine production, neuronal cells in that stage of development were susceptible to apoptosis. Certain cells of the CNS have been reported to undergo p53-dependent apoptosis after 2 Gy irradiation and its inhibition of NTPDase activity may have implication in cell death of immature brain. Whole-brain irradiation with large-scale doses (2–10 Gy) also caused a decrease in number of cells and their progenitor cells in young rodent brain in the dose-dependent fashion a few hours after irradiation [28].

Radiation damages many components of the cell, including the DNA and lipid membranes by free radicals generation, where oxygen consuming chain reactions are started [29]. Several previous studies have reported that rat brain ecto-ATPase activity was decreased under conditions that either promote or were associated with increased lipid peroxidation. It was found that 4-hydroxynonenal, the major product of membrane lipid peroxidation inhibits SPM ecto-ATPase activity [30]. Our results suggest that similar mechanisms may induce inhibition of ecto-nucleotidases in infant and prepubertal rats.

In our experiments, in adult rats low-dose radiation stimulates NTPDase as well as 5'-nucleotidase activity. It may be one of defence mechanism against low-dose radiation developed during brain maturation. Increased ATP hydrolysis indicates augmented adenosine formation, possessing neuroprotective effects. In the mature brain, adenosine A1 receptors are among the most widely distributed receptors, permitting adenosine to broadly influence neural function, modulating the release of neurotransmitters and conferring protection against damages [31]. Abou-Seif and colleges [3] reported significant reduction in ATPase activity in brain of whole-body irradiated rats with 6 Gy. They considered that this observed inhibition in ATPase activity might be attributed to change in the molecular structure of the protein part of the enzyme, which might lower the affinity of enzyme-substrate binding or decrease the rate of dissociation of the enzyme substrate complex [32]. In our experiments no effects on NTPDase or 5'-nucleotidase activity were detected with dose of 2 Gy. It is known that cells own defence mechanisms against homeostasis perturbation such as antioxidative defence against reactive oxygen species formation and oxidative stress and cell death induction. Possible explanation for the absence of effects with 2 Gy is that this dose is not high enough to turn off defends mechanisms while 6 Gy is.

CONCLUSION

Whole-body ionizing irradiation with doses of 50 cGy and 2 Gy affect developing rat brain purinergic signalization by decreasing activity of ecto-nucleotidase and consequently increasing extracellular content of neurotoxic ATP and decreasing neuroprotective adenosine. In adult rat brain dose of 50 cGy increased activity of ecto-nucleotidases supplying neuronal cell's environmental with adenosine providing protection against radiation damages.

ACKNOWLEDGMENTS

This study was supported by the Serbian Ministry of Science, Project No. 143044.

REFERENCES

1. L. Kh. Eidus, Radiat. Environ. Biophys. **39**, 189 (2000).
2. W. M. Przybyszewski, M. widel, A. Szurko, Z. Maniarkowski., Postepy. Hig. Med. Dosw. **62**, 468 (2008).
3. M. A. M. Abou-Seif, M.M. El-Naggar, M. El-Far, M. Ramadan, N. Salah. Clinica Chimica Acta. **337**, 23 (2003).
4. F. Alaoui, J. Pratt, S. Trocherie, L. Court, J. M. Stutymann. Europ Jour. Pharmacol. **276**, 55 (1995).
5. T. Amano, T. Wu. Inamura, S. Kura, A. Nakamizo, S. Inoha, M. Miyazono, K. Ikezaki. Neurol. Res. **24**, 809 (2002).
6. M. H. Bassant, and L. Court. Radiat. Res. **75**, 593 (1978).
7. G. Gueneau, A. Privat, J. Drouet and L. Court. Dev. Neurosci. **5**, 345 (1982)
8. G. Burnstock, Physiol. Rev. **87**, 659 (2007).
9. M. P. Abbracchio, G. Burnstock. Pharmacol. Ther. **64**, 445 (1994)
10. G. Burnstock. Pharmac. Rev. **24**, 509–581 (1972).
11. M. P Rathbone, P. J. Middlemiss, J. W. Gysbers et al. Prog Neurobiol. **59**, 663 (1999).
12. H. Zimmermann. Naunyn-Schmiedeberg's Arch Pharmacol. **362**, 299 (2000).
13. F. Kukulski, M. Komoszynski. Eur. J. Biochem. **270**, 3447 (2003).
14. H. Zimmermann. Trends Neurosci. **17**, 420 (1994).
15. N. Strater. Pur. Signal. **2**, 343 (2006).
16. C. Robson, J. Sevigny and H. Zimmermann, Pur. Signal. **2**, 409 (2006).
17. M. Sorimachi, K. Yamagami, M. Wakomori. Brain Res. **935**, 129 (2002).
18. K. Inoue, S. Koizumi, K. Nakazawa. Neuroreport. **6**, 437 (1995).
19. T. Sangsuwan and S.Haghdoost. Radiation Research. 776 (2008).

20. A. Horvat. G. Nikezic, S. Petrovic, D. T. Kanazir. Cell. Mol. Life Sci. **58**, 636 (2001).
21. C. W. Cotman and D. A. Matthews. Biochem.Biophys. Acta. **249**, 380 (1971).
22. A. Horvat, G. Nikezic, J. V. Martinovic. Experientia. **51**, 11 (1995).
23. M. A. Markwell, S. A. Haas, L.Lieber, N. A. Tolbert. Anal. Biochem. **87**, 206 (1978).
24. R. Pennial. Anal. Biochem. **14**, 87 (1966).
25. H. Zimmermann. Eur. J. Physiol. **452**, 573 (2006).
26. P. Di Lorio, P. Ballerini, F. Caciagli, R. Cacarelli. Pharmacol Res. **37**, 169 (1998).
27. H. Harada,C. M. Chan, A. Loesch, R. Unwin, G. Burnstock. Kidney Int. **57**, 949 (2000).
28. S. M. Reppert. D. R. Weawer, J. H. Stehle, S. A. Rivkees. Mol Endocrinol. **5**, 1037 (1991).
29. D. R Weawer. Dev. Brain Res. **9**, 205 (1996).
30. B. Halliwell and J. M. C. Gutteridge, Arch. Biochem. Biophys. **246**, 501 (1986).
31. T. D. Foley, Neurochem. Res. **24**, 1241 (1999).
32. J. Verheyde, M. A. Benotmane, Brain Res. Rev. **53**, 312 (2007).

ЖУРНАЛ ФИЗИЧЕСКОЙ ХИМИИ, 2009, том 83, № 9, с. 1778–1784

BIOPHYSICAL CHEMISTRY

УДК 541.64

Na^+/K^+-ATPASE – ACTIVITY AND INHIBITION

© 2009 M. Čolović*, D. Krstić**, K. Krinulović*, T. Momić*, J. Savić*, A. Vujačić*, and V. Vasić*

*Department of Physical Chemistry, Institute of Nuclear Sciences Vinča, P.O. Box 522, 11001 Belgrade, Serbia

**Institute of Medicinal Chemistry, University School of Medicine, University of Belgrade, Višegradska 26, Belgrade, Republic of Serbia

*Corresponding author. Tel.: +381-11-2453-967; fax: + 381-11-2447-207

E-mail: evasic@vin.bg.ac.yu

Abstract – The aim of the study was to give an overview of the mechanism of inhibition of Na^+/K^+-ATPase activity induced by some specific and non specific inhibitors. For this purpose, the effects of some ouabain like compounds (digoxin, gitoxin), noble metals complexes ($[PtCl_2DMSO_2]$, $[AuCl_4]^-$, $[PdCl_4]^{2-}$, $[PdCl(dien)]^+$, $[PdCl(Me_4dien)]^+$), transition metal ions (Cu^{2+}, Zn^{2+}, Fe^{2+}, Co^{2+}) and heavy metal ions (Hg^{2+}, Pb^{2+}, Cd^{2+}) on the activity of Na^+/K^+-ATPase from rat synaptic plasma membranes (SPM), porcine cerebral cortex and human erythrocytes were discussed.

INTRODUCTION

Na^+/K^+-ATPase (EC 3.6.1.3) is a cell membrane located enzyme, which plays a key role in the active transport of monovalent cations (Na^+ and K^+) across the cell membrane [1, 2]. The enzyme is composed of a α subunit, which contains the adenosinetriphosphate (ATP) - Na^+, K^+ and ouabain-binding sites, as well as the site for phosphorylation and a β-subunit, which stabilizes the K^+ binding cage. Na^+/K^+-ATPase acts as a dimer (αβ–βα). The most widely accepted view related to such a dimmer to act is a "flip-flop" model, in which both subunits show complementary conformation:

$$E_1E_2 \rightleftharpoons E_2E_1,$$

where E_i is the conformation of each α subunit. The activity of this enzyme is very sensitive to the presence of some metal ions [3, 4] and organic compounds of various structures, especially some drugs and pesticides [5, 6]. Beside its transporter function, Na^+/K^+-ATPase acts as the receptor for cardiac glycosides such as ouabain like compounds [7], which are the specific inhibitors of the enzyme. Ouabain binds to the extracellular part of the protein with very high affinity, leading to the inhibition of enzymatic activity. The non specific inhibitors, e.g. metal ions and complexes, interfere with the enzyme due to the complex formation with sulfhydril groups of cysteine residues. Furthermore, nephrotoxicity, ototoxicity etc. of platinum anticancer drugs, such as cisplatin and chloroplatinic acid, is related to inhibition of Na^+/K^+-ATPase activity. Since Pd(II) complexes have great affinity for binding with –SH containing ligands [8, 9] and react about 10^5 times faster, these complexes represent an excellent model for investigation of the reaction between Na^+/K^+-ATPase and platinum group anticancer drugs. The similar kind of interaction with Na^+/K^+-ATPase was also observed for heavy and transition metal ions [10].

Our study was undertaken with the aim to make an overview concerning the mechanism of interaction between ouabain-like compounds, noble metals complexes, metal ions and Na^+/K^+-ATPase. The extensive kinetic analysis was done in order to determine kinetic parameters and type of Na^+/K^+-ATPase inhibition. In addition, the ability of sulphur-donor ligands (L-cysteine and glutathione) to prevent metal ions and complexes induced inhibition of Na^+/K^+-ATPase and to recover enzymatic activity was investigated. Finally, development of highly sensitive and selective analytical tools using the immobilized enzyme is discussed in this paper.

EXPERIMENTAL

Chemicals. All chemicals were of analytical grade. Na^+/K^+-ATPase from porcine cerebral cortex and ATP were purchased from Sigma Co., as well as some chemicals for medium assay (magnesium chloride and Tris-HCl). The specific Na^+/K^+-ATPase activity was 25.8 μmol P_i/(h mg protein), P_i is the inorganic *ortho*-phosphate). Other medium assay chemicals (sodium chloride, potassium chloride) and chemicals for determination of P_i (stannous chloride and ammonium molybdate) were from Merck (Darmstadt, Germany).

Red cells membranes preparation. Red cells membranes were prepared according to the method of Post et al. [11] with certain modifications. Whole blood, 5 ml, was suspended in 0.5 ml of 0.2 M Na_4EDTA and 30 ml

of 0.15 M NaCl. The cells were packed by centrifugation at 12000 rpm for 10 minutes and were washed three times in 0.15 M NaCl. Cell lyses was performed with 5 mM Tris-HCl (pH 7.4) and freezing on –20°C. The haemoglobin free membranes were sedimented at 3000 rpm for 30 minutes and washed three times in this buffer. All procedures were carried out at 0–2°C. Protein concentration measurements were made according to the method of Bradford using crystalline bovine serum albumin (BSA) as a standard. The specific Na^+/K^+-ATPase activity was 0.288 μmol P_i/(h mg protein).

Synaptic plasma membranes (SPM) preparation. SPM were isolated from the whole brain of 3-month-old male Wistar albino rats from the local colony. Animals were kept under controlled illumination (lights on: 5:00am–5:00pm) and temperature (23 ± 2°C), and had free access to food and water. The "Guiding Principles for the Care and Use of Animals" based upon Helsinki Declaration (1964) and "Protocol of the "Vinča" Institute on care and treatment of laboratory animals" were strictly followed. After decapitation with a guillotine (Harvard Apparatus), brains were rapidly excised and pooled (six per pool) for immediate preparation of synaptic plasma membranes. The SPM were isolated according to the method of Cohen [12] and were stored at –70°C until used.

ATPase assay. The enzyme activity was determined in a standard incubation medium (200 μl), containing 50 mM Tris-HCl (pH 7.4), 100 mM NaCl, 20 mM KCl, 5 mM $MgCl_2$, 2 mM adenosinetriphosphate (ATP) and erythrocyte membrane fragments (100 μg protein) or 25 μg SPM proteins (i.e.58 μg commercial porcine cerebral cortex proteins in the presence or absence (control) of the desired concentration of inhibitor. Incubation mixtures were preincubated at 37°C in the presence of inhibitor or distilled water (control). The reaction was started by the addition of ATP, and allowed to proceed until stopped by ice cold $HClO_4$. The activity obtained in the presence of 2 mM ouabain (without the NaCl and KCl) was attributed to Mg^{2+}-ATPase. Na^+/K^+-ATPase activity was calculated as a difference between the total ATPase and Mg^{2+}-ATPase activity. The inorganic *ortho*-phosphate (P_i) liberated due to the hydrolysis of ATP was measured using modified spectrophotometric procedure based on the stannous chloride method [3, 4], by reading the absorbance at 690 nm. In addition, the concentration of liberated P_i was compared to the concentration of adenosinediphosphate (ADP) measured by slightly modified ultra performance liquid chromatography (UPLC) method [13]. Excellent agreement was obtained, confirming that only orthophosphates liberated from enzyme catalyzed ATP hydrolysis were detected.

Kinetic experiments were carried out according to the slightly modified method of Philips [14] using the commercial porcine cerebral cortex Na^+/K^+-ATPase. The initial velocities were measured in the same incubation medium as a function of rising concentrations of $MgATP^{2-}$(0.1–5.0 mmol / l). The measurements were performed in the absence and presence of inhibitor, while maintaining the concentrations of other ions (Na^+, K^+ and Mg^{2+}) constant. The experimental data were fitted to the Michaelis–Menten equation by nonlinear regression analysis using EZ FIT [15]. V_{max} and K_m values were derived from a Lineweaver–Burk plot and expressed in μmol Pi/(h mg protein) and mmol l^{-1} of ATP. Results are given as means ±S.E.M.

Apparatus. The spectrophotometric measurements were performed on Beckman 5260 UV VIS spectrophotometer. The chromatographic experiments were performed on Waters ACQUITY Ultra Performance Liquid Chromatography (UPLC) system, using an ACQUITY UPLC™ BEH C_{18}, 1.7 μm, 50 mm × × 2.1 mm column as a stationary phase. The mobile phase was composed of 4 mM tetrabutylammonium hydroxide (TBAH) in 4 mM phosphate buffer (phase A) and methanol (phase B) in the ratio 75:25. Flow rate was 0.25 ml/min, injection volume 10 μl and the column temperature 40°C. The separation was monitored in a single wavelength mode at 254 nm.

RESULTS AND DISCUSSION

Inhibition of Na^+/K^+-ATPase activity by digitalis

Some widely used digitalis glycosides (synthetic drugs and medical plants isolates) strongly modulate enzyme activity in a concentration dependent manner. The basic cardenolide structure of specific Na^+/K^+-ATPase inhibitors is schematically presented in Fig. 1.

Recently, it was confirmed that basicity, i.e. a strong ionic interaction between one of carboxylate residues present in the α subunit of the Na^+/K^+-ATPase and the cationic form of some digitalis like derivatives is relevant for interference with enzyme activity [16]. In naturally occurring digitalis glycosides the unsaturated γ- and δ-lactones present in 17β-position of the steroidal skeleton are associated with high affinity for the Na^+/K^+-ATPase receptor. The presence of -OH groups at different positions of the steroidal skeleton reduces, in general, the interaction energy, though it depends on

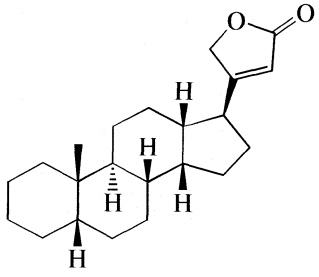

Fig. 1. Basic cardenolide structure of specific Na^+/K^+-ATPase inhibitors.

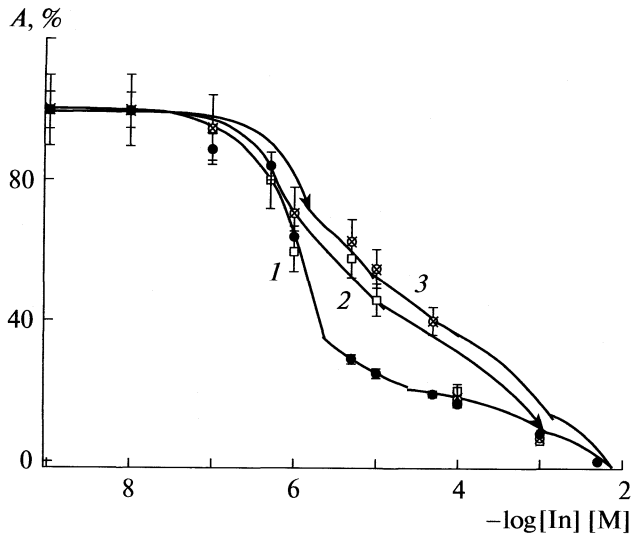

Fig. 2. Inhibition of Na^+,K^+-ATPase activity (A) by digoxin in cerebral cortex of (*1*) pig, (*2*) human erythrocyte membranes and (*3*) rat brain.

the location and spatial disposition of such –OH groups.

Digitoxin, one of the most frequently used drugs to improve cardiac contractility, undergoes a complex metabolic degradation generating digitoxigenin, digitoxigenin mono-digitoxoside and gitoxin [16]. The structural difference between digoxin and its isomer gitoxin, that usually appears as a result of metabolic degradation of digitoxin, is just the hydroxyl (–OH) group close to the C–17β position, which changes the pharmacokinetics and pharmacodynamics of these substances considerably. It has been recognized that digoxin induced inhibition is not only reversible, but also that the enzyme could be reactivated by the specific antidigoxin antibody. The inhibitory effect depends on type of tissue, as well as isolate purity [6].

The inhibition of Na^+/K^+-ATPase induced by digoxin, gitoxin and methyldigoxin was investigated in the concentration range from 10^{-9}–10^{-3} M, using three model systems. The inhibition curves obtained for digoxin using all three models are presented in Fig. 2. It is obvious that biphasic inhibitory curves were obtained in all enzyme preparations, indicating the interference of two distinct inhibitor binding sites. The measured activity was ascribed to the overall activity of the high and low affinity isoenzymes. In the mathematical analysis of the results (Fig. 2) it was assumed that the mass action principles were fully satisfied [3, 6] and that the plot of the total activity represents the line for "two enzymes acting on one substrate". The computer program was set up for the analysis of the data, assuming a two-site model fit. In the first approximation the half maximum inhibition concentrations (IC_{50} values) for the high and low inhibitor affinity isoenzymes, respectively, were calculated by fitting the experimental results to the sum of two sigmoid curves (Table 1).

The heterogeneity of digoxin sites has been reported in rat brain and beef heart Na^+/K^+-ATPase and has been related to 2 distinct isoforms of the α subunit. It is well known that the α_1 isoform is ubiquitous while α_3 isoform is especially abundant in the brain and some other vertebrate tissues [17]. Western blot analysis of the Na^+/K^+-ATPase from mature human erythrocytes, purified by ouabain column chromatography, has shown that erythrocytes contain the α_1 and α_3 isoforms of the α subunit. Our results indicated that the low sensitive α_1 isoform was also present. The results of inhibition experiments and kinetic analysis are presented in Table 1. IC_{50} values, i.e. inhibitor concentration that induced 50% of enzyme activity inhibition, were obtained by Hill analysis of inhibition curves [6]. However, human blood erythrocytes Na^+/K^+-ATPase was more sensitive to exposure to gitoxin, compared to that from porcine cerebral cortex.

Table 1. IC_{50} values and kinetic parameters for some ouabain like Na^+/K^+-ATPase inhibitors

Inhibitor	IC_{50}, M	*n*	V_{max}, μmol P_i/(h mg)	K_m, mM
Control	–	–	**1.43 ± 0.06	**0.81 ± 0.05
Digoxin	*(4.64 ± 0.07) × 10^{-6}	*1.24 ± 0.15		
	**(2.18 ± 0.20) × 10^{-6}	**1.43 ± 35	**1.06 ± 0.08	**0.60 ± 0.07
	(*(1.04 ± 0.05) × 10^{-3})	*1.92 ± 0.13		
	(**(8.67 ± 1.08) × 10^{-5})	**1.29 ± 0.09		
Gitoxin	*(2.98 ± 0.10) × 10^{-7}	*2.01 ± 0.19	**1.01 ± 0.09	**0.58 ± 0.08
	**(1.18 ± 0.10) × 10^{-6}	**1.52 ± 0.09		
	(*(4.10 ± 0.90) × 10^{-4})	*1.08 ± 0.22		
	(**(2.85 ± 0.08) × 10^{-5})	**2.59 ± 0.66		

Note. The IC_{50} value for β-methyldigoxin is equal (6 ± 0.90) × 10^{-6} (for rat brain Na^+/K^+-ATPase). Values in paranthesis present results obtained for low affinity isoform; * for human erythrocytes Na^+/K^+-ATPase, ** for porcine cerebral cortex Na^+/K^+-ATPase.

In our study the IC_{50} values for the high activity isoenzyme in both enzyme preparations were more than two orders of magnitude higher compared to the low affinity isoenzyme. Moreover, the concentration of digoxin that produced 30% inhibition reached the toxic level for gitoxin, displaying the complete inhibition of the high affinity isoenzyme. The high affinity to digoxin and gitoxin can be attributed to the binding to α_3 isoform, which is known to be the most sensitive towards the cardiac glycosides [16]. Kinetic analysis of the results showed that digoxin and gitoxin behave as uncompetitive inhibitors (Table 1) of Na^+/K^+-ATPase activity. The inhibitors interfered with the enzyme by binding to the enzyme – substrate complex causing the structural distortion of the active sites. The results showed that the both inhibitors decreased K_m and V_{max} values of the enzyme to the same extent. However, parallel straight lines were obtained from Lineweaver–Burck analysis of kinetic data (data not presented) in the absence and presence of both inhibitors, i.e. the constant ratio $K_m/V_{max} = 0.57$ confirmed the uncompetitive mode of interaction.

Further experiments demonstrated that elevated potassium concentrations were also able to reactivate the enzyme inhibited by digitalis glycosides to a certain extent, and that the reactivation was proportional to the time of exposure to increased K^+ concentration [9]. It was postulated that higher potassium concentrations shift the balance between E_1 and E_2 Na^+/K^+-ATPase conformations in favor of E_1 and, consequently, enable the continuation of the digoxin impeded enzymatic cycle [9]. Therapeutic effect is achieved with a digoxin concentration that produces a moderate enzyme inhibition (about 30%), whereas the toxic concentrations inhibit over 60% of the enzyme activity [16].

Inhibition by noble metals complexes

The modification of cysteine residues in proteins due to its ability to strongly coordinate complex metal ions is one of the arguments of critical importance for the design of novel types of pharmacological agents, based on the Pt(II), Au(III) and Pd(II) complexes. Our study was undertaken with the aim to examine the mechanism of their interaction with Na^+/K^+-ATPase [8, 9, 18]. All investigated species induced the concentration-dependent inhibition of Na^+/K^+-ATPase activity in the concentration range from 10^{-9}–10^{-3} M, and their potency to inhibit Na^+/K^+-ATPase depended on the rate of ligand exchange in the coordinative sphere of the metal ion. As an example, Fig. 3 represents the inhibition curves for $[PtCl_2(DMSO)_2]$ and $[AuCl_4]^-$ induced inhibition of Na^+/K^+-ATPase activity. It is worthy to notice (data not shown) that L-cysteine partially prevented the inhibition induced by $[PtCl_2(DMSO)_2]$. The Hill plots for the investigated complexes were used to calculate IC_{50} values. IC_{50} values and kinetic parameters are given in Table 2.

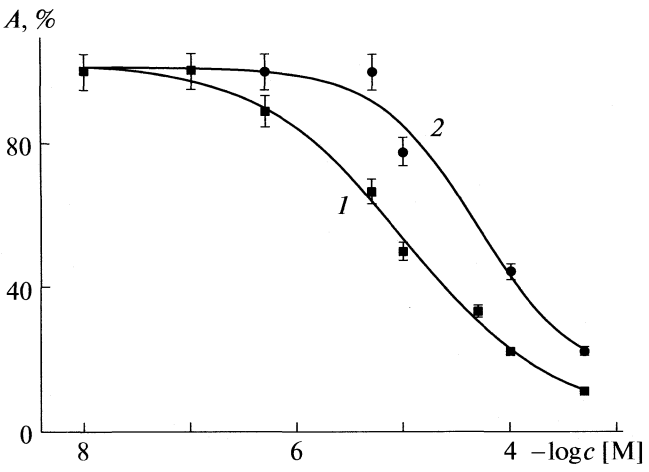

Fig. 3. Dependence of the Na^+/K^+-ATPase activity on (*1*) $[PtCl_2DMSO_2]$ and (*2*) $[AuCl_4]^-$, *A* is the activity of the enzyme.

However, the stability constants of complexes between the enzyme and platinum group compounds were close to the value of the overall binding constant that was reported for the interaction of Na^+/K^+-ATPase with cisplatin [19], but were also two orders of magnitude lower compared to the aqua complexes of heavy and transition metals. Kinetic analysis indicated a noncompetitive type of inhibition and suggested that the complexes did not affect the binding of the substrate. As an example, the Michaelis–Menten dependence of initial reaction rate against substrate ($MgATP^{2-}$) concentration in absence and presence of

Table 2. IC_{50} values and kinetic parameters for Na^+/K^+-ATPase inhibition by Au(III), Pt(II) and Pd(II) complexes obtained for human erythrocytes

Complex	$IC_{50} \times 10^5$, M	$K_i \times 10^{-4}$, M	V_{max}, μmol P_i/(h mg)	K_m, M
Control	–	–	2.71 ± 0.03	0.29 ± 0.01
$[PtCl_2DMSO_2]$	1.20 ± 0.14	23.3	–	–
$[AuCl_4]^-$	7.15 ± 0.19	1.9	–	–
$[PdCl_4]^{2-}$	2.25 ± 0.21	39.7	1.17 ± 0.03	0.29 ± 0.02
$[PdCl(dien)]^+$	12.1 ± 1.3	1.04	1.39 ± 0.02	0.29 ± 0.01
$[PdCl(Me_4dien)]^+$	23.6 ± 3.0	4.20	1.94 ± 0.03	0.29 ± 0.01

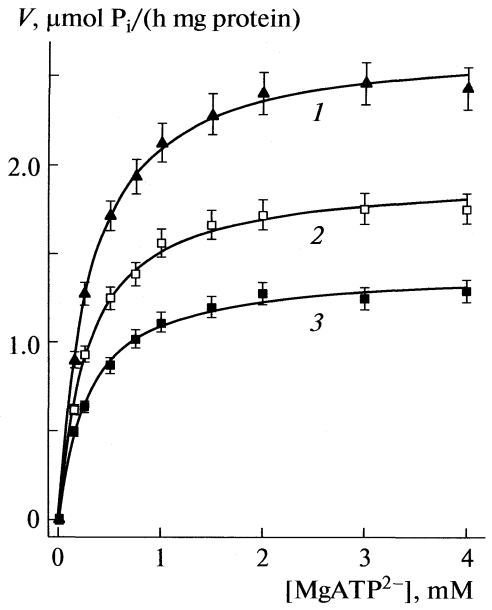

Fig. 4. Michaelis–Menten dependence of initial reaction rate against substrate ($MgATP^{2-}$) concentration in (*1*) absence and presence of (*2*) 5×10^{-5} and (*3*) 1×10^{-4} M $[PdCl(dien)]^+$. The experimental points are the mean of at least three experiments ±SEM, done in duplicate.

$[PdCl(dien)]^+$ is presented in Fig. 4. Furthermore, kinetic analysis showed that $[PdCl(dien)]^+$ inhibited Na^+/K^+-ATPase by reducing enzyme's ability to convert substrate to product (V_{max}) rather than apparent affinity for substrate (K_m) implying the noncompetitive nature of enzyme inhibition. The obtained results suggested that the inhibitor interfered with an inhibitory site on the enzyme that was remote from the active site for the substrate ($MgATP^{2-}$). The similar behavior was noticed by other complexes.

Considering the fact that Pd(II) complexes are model compounds for their Pt(II) analogs, which showed similar inhibitory effects on Na^+/K^+-ATPase, the conclusion can be drawn that the same kind of enzyme-inhibitor interaction can be expected for the widely-used platinum anticancer drugs. Our earlier studies showed that these complexes strongly interact with sulphur containing ligands, such as L-cysteine, glutathione and methionine [20–22] and are able to act as potent reactivators of enzyme activity. The reactivation is usually due to the formation of complex be-

Table 3. IC_{50} values (μM) for investigated metal ions

Ion	IC_{50}	Ion	IC_{50}
Fe^{2+}	34	Hg^{2+}	0.7
Co^{2+}	168	Cd^{2+}	1
Cu^{2+}	7.1	Pb^{2+}	15
Zn^{2+}	22	–	–

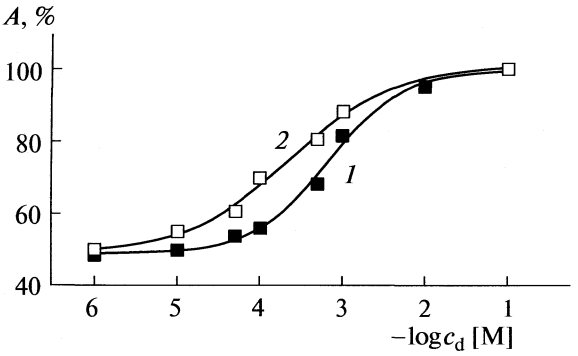

Fig. 5. Recovery effect of (*1*) L-cysteine and (*2*) GSH on the Na^+/K^+-ATPase activity inhibited in the presence of 1×10^{-4} M $[Pd(dien)Cl]^+$; c_d is the SH-donor ligand concentration.

tween thiols and the metal ion bonded to the –SH groups of the enzyme. More likely, the mechanism of interaction of enzyme, L-cysteine and GSH with Pd(II) complexes was similar, since it involved substitution of the Cl^- ligand by SH-donor ligands [8, 9]. However, the affinity of L-cysteine or GSH for this reaction was much higher compared to the Na^+/K^+-ATPase affinity.

The inhibitory effects of Pd(II) complexes were prevented and recovered by the addition of L-cysteine or GSH, which showed high potency to extrude and substitute the enzyme from the Pd(II) complex (Fig. 5). Is seems that prevention and recovery of Pd(II) complexes-induced Na^+/K^+-ATPase inhibition were realized due to the competition between the SH functional groups of protein and thiols (L-cysteine or GSH) for substitution of the Cl^- ligand in the coordination sphere. These results are consistent with the kinetic analysis, suggesting that these complexes are reversible noncompetitive inhibitors of this enzyme. Since platinum anticancer drugs react in the same manner as their palladium analogs, it was also suggested that L-cysteine or GSH might have the ability for detoxification after chemotherapy.

Inhibition by inorganic salts

The highly toxic heavy metals induced inhibition of Na^+/K^+-ATPase activity in concentration dependent manner. The influence of Pb^{2+}, Cd^{2+}, Hg^{2+}, Cu^{2+}, Fe^{2+}, Co^{2+} and Zn^{2+} on Na^+/K^+-ATPase activity was investigated by single exposure to inhibitors in the concentration range from 1×10^{-9} to 1×10^{-3} M [3, 4]. Results of our study showed that considered metal ions inhibited Na^+/K^+-ATPase activity by various potencies. The obtained IC_{50} values were ranging from 10^{-7}–10^{-4} M and are given in Table 3. It is reasonable to assume that this potency depends on the nature of the metal ion as well as the enzyme. For instance, Na^+/K^+-ATPase from the kidney contains 36 sulfhydril groups with 34 of them found in the catalytically

active α subunit. Since the considered metals belong to the first transition series (Zn^{2+}, Fe^{2+}, Co^{2+} and Cu^{2+}) and heavy metals group (Cd^{2+}, Pb^{2+}, Hg^{2+}), they are expected to affect ATPases binding to the same reactive place of enzymes. It can be assumed that induced inhibition depends sensitively on their affinity to form complexes with the ligands containing –SH, $-NH_2$ or –COOH groups, but it is now generally accepted that the most toxic effect of heavy metals is due to their binding to sulfhydril groups of enzymes.

It seems reasonable to correlate the induced inhibition of Na^+/K^+-ATPase, expressed as IC_{50} values, with the stability constants of the corresponding metal ion complex with –SH containing ligands [10, 23]. Therefore, L-cysteine was chosen as a model compound. The log IC_{50} vs. $\log K_s$ (K_s is the stability constant of the corresponding metal ion – L-cysteine complex) plot, shown in Fig. 6, compares all the inhibition data in a single graph. The obtained linear dependence of the toxicity vs. stability constants suggests that enzyme inhibition is a consequence of non-specific binding of metal ions to the –SH groups of the enzymes.

As is obvious from the plots in Fig. 6, the IC_{50} values of the heavy metal ions fit well in the curve obtained for the K_s values of the first transition series metal ions. However, Hg^{2+} which was found to be the most toxic one, does not show the highest affinity to the sulfhydryl group [23]. This result suggests that Hg^{2+} induced inhibition may involve some other mechanism besides the non-specific binding of Hg^{2+} to the sulfhydryl groups of the proteins.

Heavy metal ions, such as Cd^{2+} and Hg^{2+}, exerted a potent inhibitory effect on Na^+/K^+-ATPase isolated from different tissues, like rat brain and rat liver, by binding avidly to sulfhydryl groups with similar affinities. Sensitivity of enzyme toward Cd^{2+} and Hg^{2+} increased due to its immobilization by adsorption on a nitrocellulose membrane [4, 24]. Inhibitory effects of Cu^{2+}, Zn^{2+} and Fe^{2+} on bovine cerebral cortex Na^+/K^+-ATPase activity were obtained and the extent of inhibition seems to depend on the presence of chelators. Kinetics analysis showed that the nature of enzyme inhibition by metals was non competitive. The inhibitory effects of Fe^{2+}, Co^{2+}, Zn^{2+} and Cu^{2+} could be prevented by addition of 1mM strong metal-ion chelator EDTA, 10 mM L-cystein or 10 mM GSH and the effect was dose dependent [3, 10]. Recovery of the Hg^{2+}-induced inhibition was not achieved, even when the chelators were present at concentration above 0.01 M.

The synergistic effects with binary combinations of heavy metals on the activity of Na^+/K^+-ATPase using the mixtures of Cu^{2+}/Zn^{2+}, Cu^{2+}/Fe^{2+}, Zn^{2+}/Fe^{2+}, Pb^{2+}/Cd^{2+}, and $Cu^{2+}/Pb^{2+}/Zn^{2+}/Cd^{2+}$ u ions were obtained in all cases [25]. Moreover, all metal ions in the mixture at concentration levels near IC_{50} values inhibited the enzyme activity completely. The inhibition induced by combination of Pb^{2+} with Cd^{2+} was time dependent [26]. Addition of 1mM EDTA in the medium assay recovered 100% of the inhibited enzyme activity.

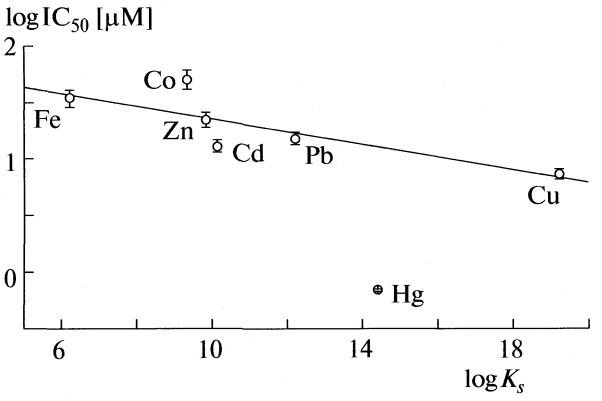

Fig. 6. Dependence of IC_{50} values of metal induced inhibition of Na^+/K^+-ATPase on metal-ion – L-cysteine stability constants.

Na^+/K^+-ATPase as an analytical tool

In summary, the study of the mechanism of enzyme inhibition by various compounds is of great importance for elucidation of their potential toxicity. Moreover, development of highly sensitive and selective analytical tools using the immobilized enzyme is currently among the topic interest in the bioanalytics.

The effect of certain metal ions (Pb^{2+}, Cd^{2+}, Hg^{2+}, Cu^{2+}, Fe^{2+}, Zn^{2+}) and various organic compounds (cardiotonic drugs, organic solvents, pesticides) on Na^+/K^+-ATPase activity, as described in the previous part, offers the possibility to develop a simple qualitative and semi-quantitative test method for selective detection of these analytes in aqueous solutions [24–27]. The method is based on the spectrophotometric determination of inorganic ortho-phosphate (P_i), liberated from ATP in the Na^+/K^+-ATPase-catalysed reaction, that serves as a measure of the enzymatic activity [3, 25]. The concentration of P_i liberated in the reaction medium from ATP after exposure of the enzyme to analytes was dose dependent on the analyte concentration. Heavy metals (Pb^{2+}, Cd^{2+}, Hg^{2+}, Cu^{2+}, Fe^{2+}, Zn^{2+}), toxic organic compounds (pyridine, urea) and some pesticides (malathion and the products of its chemical and photochemical transformations, chlorpyrifos, permethrin) showed diverse effects, either the inhibition or stimulation of the enzyme activity. The potency of using ATPase system as a biological component for semi-quantitative and qualitative multi - response sensing system for detection of different compounds is based on the level of change of enzyme activity in the presence of analytes. By varying the medium assay composition, some organic compounds and heavy metal salts can be simultaneously detected using the reaction of ATPases catalysed ATP hydrolysis. Moroever, the test based on the Na^+/K^+-ATPase

for detection of analytes is simple and useful for quick measurements.

This proposed method was already applied to the quality control of photodegradation of digoxin, and its concentration in Lanoxin injection [5, 25]. The tested sample of Lanoxin injection was added to the standard medium assay (0.2 ml final value), containing 1 mM EDTA. The activity was measured as described, and compared to the control value. The same result, $(0.31 \pm 0.02) \times 10^{-3}$ M, was obtained using standard method (HPLC) with the mean standard deviation of 6.45%. This finally confirms applicability of sensing system based on the Na^+/K^+-ATPase in the product quality control.

ACKNOWLEDGMENTS

Authors would like to thank to the Ministry of Science and Technological Development of the Republic of Serbia for their financial support (Project No. 142051).

REFERENCES

1. L. A.Vasilets and W. Schwarz, Biochem. Biophys. Acta **1154**, 201 (1993).
2. P. L. Jorgensen, K. O. Hakansson and S. J. D. Karlish, Annu. Rev. Physiol. **65**, 817 (2003).
3. V. Vasić, D. Jovanović, D. Krstić, G. Nikezić, A. Horvat, Lj. Vujisić and N. Nedeljković, Toxicol. Let. **110**, 95 (1999).
4. V. Vasić D. Jovanović, A. Horvat, T. Momić and G. Nikezić, Analyt. Biochem. **300**, 113 (2002).
5. V. Vasić U. Černigoj, K. Krinulović, G. Joksić and M. Franko J. Pharm. Biomed. Anal. **40**(2), 404 (2006).
6. D. Krstić, K. Krinulović, V. Spasojević-Tišma, G. Joksić, T. Momić and V. Vasić, J. Enz. Inh. Med. Chem. **19**(5), 409 (2004).
7. P. A. Luchessi, J. Biol. Chem. **226**, 9327 (1991).
8. K. Krinulović, Ž. Bugarčić, M. Vrvić, D. Krstić and V. Vasić, Toxicol. In Vitro **20**, 1292 (2006).
9. D. Krstić, N. Tomić, K. Krinulović and V. Vasić, J. Enz. Inh. Med. Chem. **21**, 471 (2006).
10. Lj. Vujisić, D. Krstić, K. Krinulović and V. Vasić, J. Serb. Chem. Soc. **69**(7), 541 (2004).
11. R. I. Post, C. R. Merit, C. R. Kosolving and C. D. Albbright, J. Biol. Chem. **235**, 1796 (1960).
12. R. S. Cohen, F. Blomberg, K. Berzins and P. Siekevitz, J. Cell Biol. **74**, 181 (1977).
13. J. Sudo, J. Terui, H. Iwase and K. Kakuno, J. Chromatogr. B, **744**, 19 (2000).
14. T. D. Philips, A. W. Hayes, I. K. Ho and D. Desiah, J. Biol. Chem. **253**, 3487 (1978).
15. F. W. Perrella, Anal. Biochem. **174**(2), 437 (1988).
16. C. P. Melero, M. Maderade and A. S. Feliciano, Molecules **5**, 51 (2000).
17. P. L. Jorgensen, K.O. Hakansson and J.D. Karlish, Annu. Rev. Physiol. **65**, 817 (2003).
18. D. Vasić, J. Savić, Ž. Bugarčić, D. Krstić, N. Tomić, M. Čolović, M. Petković and V. Vasić, Z. Naturforsh. **64c**, 103 (2009).
19. J. F. Neault, A. Benkirane, H. Malonga and H. A. Tajmir-Riahi, J. Inorg. Biochem. **86**, 603 (2001)
20. V. Vasić, M. Čakar, J. Savić, B. Petrović, J. Nedeljković and Ž. Bugarčić, Polyhedron **22**, 279 (2003).
21. V. M. Vasić, M. A. Živanović, M. M. Čakar, J. Z. Savić, J. M. Nedeljković and Ž. D. Bugarčić, J. Phys. Org. Chem. **18**, 441 (2005).
22. A. Vujačić, J. Savić, S. Sovilj, K. Mészáros Szécsényi, N. Todorović, M. Petković and V. Vasic, Polyhedron, **28**, 593 (2009).
23. Högfeldt, Stability constants of metal-ion complexes, Part A: Inorganic ligands, Pergamom Press, Oxford, 1983
24. T. Momić, Z. Vujčić, V. Vasić and A. Horvat, J. Serb. Chem. Soc. **67**(12), 809 (2002).
25. V. Vasić, K. Krinulović, D. Krstić, T. Momić and A. Horvat, Monatshefte fur Chemie, **135**, 605 (2004).
26. V. Vasić, D. Kojić, K. Krinulović, M. Čolović, A. Vujačić and D. Stojić, Russ. J. Phys. Chem. **81**(9), 1402 (2007).
27. V. Vasić, K. Krinulović, T. Momić, M. Čolović and A. Vujačić, Journal of Environmental Protection and Ecology, **9**(3), 583 (2008).

ЖУРНАЛ ФИЗИЧЕСКОЙ ХИМИИ, 2009, том 83, № 9, с. 1785–1787

BIOPHYSICAL CHEMISTRY

УДК 541.64

DEVELOPMENT AND VALIDATION OF A NEW HIGH-PERFORMANCE LIQUID CHROMATOGRAPHIC METHOD FOR THE LOPERAMID HYDROCHLORIDE DETERMINATION IN DRUGS

© 2009 G. S. Nikolić*, I. Savić*, and V. Marinković**

*Faculty of Technology, Bulevar Oslobođenja 124, RS-16000 Leskovac, Serbia

**Pharmaceutical and chemical industry Zdravlje-Actavis, Vlajkova 199, RS-16000 Leskovac, Serbia

E-mail: goranchem_yu@yahoo.com

Abstract – A selective, precise and new high-performance liquid chromatographic method for the analysis of loperamid hydrochloride in pharmaceutical formulations was developed and validated. The mobile phase consisting buffer (sodium-octansulphonate, triethylamine and ammonium hydroxide) in water : acetonitrile (45:55, v/v) (pH 3.2). The absorbance was monitored with a DAD detector at 226 nm. The flow rate was 1.5 cm^3 min^{-1}. The linearity ($r = 0.9947$) and the recovery (98.58–100.42%) were found to be satisfactory. The detection and quantitation limits were found to be 0.95 and 3.12 μg cm^{-3}. The results demonstrated that the procedure was accurate, precise and reproducible. It can be suitably applied for the estimation of loperamid hydrochloride in pharmaceutical formulations.

INTRODUCTION

Loperamid (4-(*p*-chlorophenyl)-4-hydroxy-N,N,-dimethyl-diphenyl-l-piperidine butyramide hydrochloride) is an opiate agonist widely used as an effective drug for the control and symptomatic relief of the acute non-specific diarrhea [1]. More recently, it has also been reported that loperamide could have some interest as an antihyperalgesic agent reducing pain without any central nervous system side effects [2]. Loperamid is orally administered and is moderately absorbed (~40%) from the gastrointestinal tract to undergo the first-pass metabolism in the liver and the excretion in the faces via the bile as inactive conjugates (sulfo- and glucurono combination). For the routine analysis, a simple and rapid analytical high-performance liquid chromatographic (HPLC) method is suggested in the paper. The objective of the present study was to develop simple, precise, accurate and validated, economic analytical methods for estimating loperamid hydrochloride in a pure form and in pharmaceutical formulations. The developed analytical method was validated as per ICH guidelines [3] and Serbian requirements [4]. Statistical tests were performed on validation data [5].

EXPERIMENTAL

Chromatographic conditions

The method development was performed with an Agilent 1100-Series HPLC system. The repeatability was performed with another LC system consisting of an Agilent 1200-Series binary pump and the UV detector. The separation was carried out at ambient temperature using a ZORBAX Eclipse XDB-C18 column, (4.6 × 250 mm, 5 μm). RP-HPLC analysis was performed by isocratic elution with a flow rate of 1.5 cm^3 min^{-1}. The mobile phase cosisted of 0.1% sodium-octansulphonate, 0.05% triethylamine, 0.1% ammonium hydroxide in water : acetonitrile (45:55, v/v). pH value at 3.2 adjusted with phosphoric acid. All solvents were filtered through a 0.45 μm millipore filter. The volumes of 50 μl of the solutions and samples were injected into the column. The quantification was effected by measuring at 226 nm as established from the two-dimensional chromatogram. Throughout the study, the suitability of the chromatographic system was monitored the efficiency column and peak asymmetry.

Chemicals

The standard of loperamid hydrochloride (99.96%) and commercial pharmaceutical preparations Loperamid were kindly donated by the Pharmaceutical and Chemical Industry Zdravlje-Actavis (Leskovac, Serbia) and used without further purification. Loperamid was labelled to contain 2 mg of loperamid hydrochloride.

Procedure for calibration curve

For preparing different concentrations, aliquots of the stock solution were transferred into a series of 10 cm^3 standard volumetric flasks and the volumes were made with the respective media. Ten different concentrations were prepared in the range of 10–100 μg cm^{-3} of loperamid hydrochloride in mobile phase for a standard curve. Triplicate 50 μl injections were made for each solution. The final concentrations of loperamid hydrochloride in the samples were calcu-

Table 1. Accuracy and the precision data method for the developed method ($n = 10$)

Level	c, μg cm^{-3}	Predicted concentration, μg cm^{-3}			Mean recovery, % (±SD)	Accurace, %
		Range	Mean (±SD)	R.S.D., %		
LC	20	18.9–20.8	19.85 ± 0.137	0.683	99.25 ± 0.137	−0.75
IC	40	38.1–42.3	40.21 ± 0.337	0.672	100.42 ± 0.337	0.42
HC	60	58.9–59.4	59.15 ± 0.179	0.303	98.58 ± 0.179	−1.42

lated by comparing the sample and standard peak obtained with the average of three injections of standard solutions.

Sample Preparation

Aliquot (1 cm^3) of preparation (loperamid) equivalent to 2 mg of loperamid hydrochloride was taken and suitably diluted with the mobile phase in order to get a 20 μg cm^{-3} concentration and the samples were injected into the chromatograph.

RESULTS AND DISCUSSION

The mobile phase consisting buffer in water : acetonitrile (45:55, v/v) was selected to achieve the maximum separation and sensitivity. A flow rate of 1.5 cm^3 min^{-1} gave an optimal signal to the noise ratio with a reasonable separation time. The maximum absorption of loperamid hydrochloride was detected at 226 nm and this wavelength was chosen for the analysis. Using a reversed-phase C18 column, the retention times for the standard solution of loperamid hydrochloride (c = = 0.1 mg cm^{-3}) and loperamid hydrochloride in preparation were observed to be 5.54 min and 5.58 min, respectively. The chromatographic parameters such as the efficiency column and the peak asymmetry were reconsidered for the loperamid hydrochloride standard. According to the Number of Theoretical Plato (N = 9133), the conclusion was that the efficiency column was satisfactory (HETP = 0.027).

The excellent linearity was obtained between the peak areas and the concentrations. The linear regression equation obtained with a regression coefficient (r) of 0.9947 and standard deviation (SD) of 56.0222 was:

$$A_{226} = 20523.028c(\text{mg cm}^{-3}) + 117.65. \quad (1)$$

Beer's law was obeyed in the range of 10–100 μg cm^{-3}.

Table 2. Standard addition of loperamid hydrocloride for accuracy ($n = 10$)

c_1	c_2 ± SD	Mean recovery, % (±R.S.D)
0	19.85 ± 0.137	99.25 ± 0.683
10	29.92 ± 0.32	99.73 ± 0.58
20	40.35 ± 0.45	100.87 ± 0.64
30	49.87 ± 0.42	99.74 ± 0.53

Note. Drug in formulation is equal 20 μg cm^{-3}; c_1 and c_2 are pure drug added and total drug found, respectively, μg cm^{-3}.

Validation

The chromatogram of loperamid hydrochloride was not changed in the presence of common excipients used in the pharmaceutical preparations. The chromatogram of the pure drug sample was matched with the formulation samples in the mobile phase. The calculated t-values of 1.96 were found to be less than that of the tabulated t-values (2.225). Therefore, the proposed analytical method is specific and selective for the drug.

The linearity range for loperamid hydrochloride estimation was found to be 10–100 μg cm^{-3} (r = = 0.9947). The goodness of the fit of the regression equations was supported by high regression coefficient values. The accuracy ranged from 20 to 60 μg cm^{-3}. The excellent mean percentage recovery values, close to 100 %, and their low standard deviation values (SD < 1.0) represent high accuracy of the analytical methods. The validity and reliability of the proposed methods were assessed by the recovery studies. The mean percentage recoveries (% RSD) for lower, intermediate and higher concentrations were found to be 99.25 (20 μg cm^{-3}), 100.42 (40 μg cm^{-3}) and 98.58 (60 μg cm^{-3}), respectively (Table 1).

The validity and reliability of the proposed methods were further assessed by the recovery studies via a standard addition method. The mean percentage recoveries (% RSD) for the concentration from 20 μg cm^{-3} were found to be 99.73 (0.58), 100.87 (0.64) and 99.74 (0.53), respectively (Table 2). These results revealed that any small change in the drug concentration in the solutions could be accurately determined by the proposed analytical methods.

The precision was determined by studying the repeatability and the intermediate precision. The repeatability (% RSD) ranged from 20 to 60 μg cm^{-3}. The repeatability results indicated the precision under the same operating conditions over a short interval of time and the inter-assay precision. The intermediate precision expresses within-laboratory variations in different days and in different instruments. In the intermediate precision study, RSD values were not higher

Table 3. System precision study ($n = 10$)

c, μg cm^{-3}	Intra-day repeatability R.S.D., %			Intra-instrument repeatability R.S.D., %
	Day 1	Day 2	Day 3	
20	19.85 (0.683)	19.94 (0.672)	20.48 (0.512)	18.96 (0.889)
40	39.85 (0.05)	40.32 (0.212)	39.88 (0.08)	40.35 (1.408)
60	60.55 (0.183)	60.51 (0.842)	60.15 (0.083)	60.34 (1.547)

than 2.0% in all the cases. RSD values found for the proposed analytical method were well within the acceptable range indicating that the method has excellent repeatability and the intermediate precision. RSD values for the precision studies with real samples of tablets were found to be less than 2% (Table 3).

LOD and LOQ for loperamid hydrochloride were found to be 0.95 and 3.12 μg cm^{-3}. The assay value of loperamid hydrochloride in preparations 1.964 mg cm^{-3} was found to be 98.20% with the standard deviation not more than 0.0091%. The assay values of formulations were the same as mentioned in the label claim indicating that the interference of the excipient matrix is insignificant in estimation of loperamid hydrochloride by the proposed analytical methods. The estimated drug content with low values of the standard deviation established the precision of the proposed method. The calculated Student's t-values (1.98) did not exceed the tabulated values (2.225).

CONCLUSION

The proposed RP-HPLC method was developed for loperamid hydrochloride. The analytical method is simple, sensitive, rapid and specific and it can be conveniently employed for the routine analysis and the quality control of loperamid hydrochloride in pharmaceutical dosage forms. The method was suitable to determine concentrations in the range 0.01 to 0.1 mg cm^{-3}, precisely and accurately. The limits of detection and quantitation for loperamid hydrochloride with a lower concentration were 0.95 and 3.12 μg cm^{-3}, respectively, the values which are under the lowest expected concentrations in the sample. The sample recovery from the formulation was in good agreement with its respective label claim, which suggested noninterference of formulation excipients in the estimation.

REFERENCES

1. K. Lavrijsen, D. Van Dyck, J. Van Houdt, J. Hendrickx, J. Monbaliu, R. Woestenborghs, W. Meuldermans, J. Heykants, J. Pharmacol. Exp. Ther. **23**, 354 (1995).
2. D. L. DeHaven-Hudkins, L. Cortes Burgos, J. A. Cassel, J. D. Daubert, R. N. DeHaven, E. Mansson, H. Nagasaka, G. Yu, T. Yaksh, J. Pharmacol. Exp. Ther. **289**, 494 (1999).
3. The European Agency for the Evaluation of Medicinal Products. ICH Topic Q2B Note for Guideline on Validation of Analytical Procedures: Methodology GP-MP/ICH/281/95, (1996).
4. Jugoslovenska Pharmacopoeia, V ed., Savremena administracija, Beograd, (2000).
5. S. Bolton, Pharmaceutical Statistics: practical and clinical application, III ed., Marcel Dekker, New York, 216 (1997).

ЖУРНАЛ ФИЗИЧЕСКОЙ ХИМИИ, 2009, том 83, № 9, с. 1788–1792

BIOPHYSICAL CHEMISTRY

УДК 541.64

IDENTIFICATION AND COMPATIBILITY OF THE MAJOR ACTIVE PRINCIPLES IN SOME NEW NATURAL ORIGIN ANTISEPTICS

© 2009 G. S. Nikolić*, S. Zlatković** and N. Nikolić*

*Faculty of Technology, Bulevar Oslobođenja 124, RS-16000 Leskovac, Serbia,
**Actavis Trading Ltd., Djordja Stanojevica 12, RS-11070 Beograd, Serbia
E-mail: goranchem_yu@yahoo.com

Abstract – The newly established instrumentation of HPLC/DAD, FTIR, and NMR techniques have been applied for simultaneous identification and physicochemical compatibility determination of the potential major antiseptic constituents (*Hypericum perforatum* L. and *Usnea barbata* extracts) which can be present in some new origin pharmaceutical preparation. Based on the obtained results the conclusion is that a simultaneous use of the analyzed constituents in production of some new preparations with antiseptic properties is possible. The chromatographic separation of antiseptic mixture was performed on a RP-HPLC C18 column. For the NMR detection, the analytes eluted from LC column were trapped and hereafter transported into the NMR flow-cell. The NMR and FTIR techniques allowed the characterization of the major constituent of *Hypericum perforatum* L., mainly hypericin, as well as of *Usnea barbata*, mainly usnic acid.

INTRODUCTION

A number of effective oral antiseptic compounds administered either topically or systemically is available for the treatment of throat diseases (pharyngitis, laryngitis and tonsillitis) [1, 2]. This work is an attempt to provide a simultaneously application of some bioactive natural origin components in new oral antiseptic preparations [3]. A specific mechanism of the influence and new technological solution of manufacturing gives bigger stability and efficiency of natural origin oral antiseptic at an oral tissue [4, 5]. Usnic acid, a yellow crystal substance of natural origin [6], is one of the most important components from the standpoint of pharmacological activity of domestic oral antiseptic (Fig. 1A). Usnic acid, isolated from the lichen *Usnea barbata*, having significant antibacterial activity [7–12]. It is the fact that ifnot complied to directions of oral antiseptic consumption they may cause a serious damage lip cavity mucous membrane by usnic acid. Conversely, *Hypericum perforatum* L. extract, besides antiseptic, shows regenerative abilities to the mucous membrane [13–15]. The advantage of the new oral antiseptic, including *Hypericum perforatum* L. extract, is the inhibition of the negative influence from other present ingredients of oral antiseptics to the lip cavity mucous membrane. Hypericin (Fig. 1B) is one of the most important components from the standpoint of pharmacological activity si *Hypericum perforatum* L. [16].

Extended number of patented and described procedures for isolation and characterization of usnic acid [6–12, 17–21] and hypericin [22–24] are described in detail in literature. Usnic acid can be produced synthetically and a broad spectrum of derivatives and condensation products based on usnic acid are also known [25, 26]. The study of usnic acid and hypericin is of particular importance due to its practical application in the production of the antiseptic pharmaceutical preparations. Therefore, the compatibility of hypericin and usnic acid in pharmaceutical antiseptics mixture, directly or combined with other excipients, were analyzed by certain instrumentation.

EXPERIMENTAL

The liquid extract of St. John's wort was obtained by maceration with 70% methanol, ratio 1:10, during 48 h. The dry extract of St. John's wort was separated by drying the liquid extract in hot air stream. Usnic acid, freshly isolated from *Usnea barbata*, and its sodium salt was obtained according literature data [17]. The content of total hypericin in the extracts was determinated spectrophotometrically as the sum of the content of hypericin and pseudohypericin [23]. The absorbtion of sample of the final solution was measured at 590 nm, using a Cary-100 Cone. UV-VIS Spectrophotometer (Varian).

The quality of hypericin contained in liquid and dry extracts from the locality of southeast Serbia was determined by HPLC method under the following conditions: Hewlett Packard 1100 Agilent, Lichrosorb RP-C18 column (5 μm, 250 × 4 mm), methanol–ethyl acetate–NaH_2PO_4 mobile phase (pH 2.1), 0.8 cm^3 min^{-1} flow rate, 590 nm detection DAD, 20 μl injection volume. The identification of hypericin were determined using the standard substances.

The identification of usnic acid was performed by ^1H NMR (400 MHz) spectrum was run in $CDCl_3$ on a Bruker-Spectrospin Avance DPX 400 with TMS as internal standard. The compatibility of hypericin and usnic acid was analyzed by spectrophotometric FTIR and NMR methods.

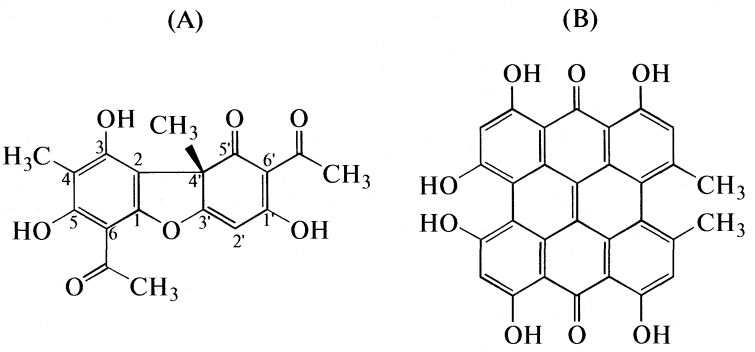

Fig. 1. Structure of usnic acid (A) and hypericin (B).

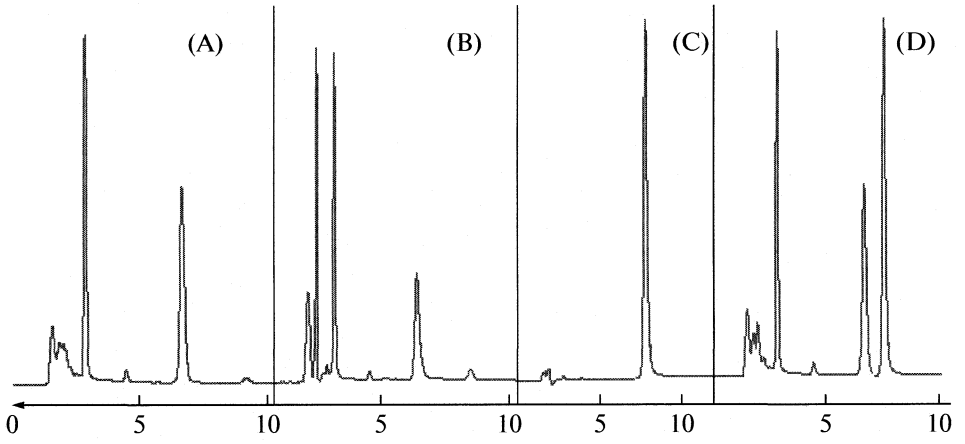

Fig. 2. Typical HPLC chromatograms of: (A) *Hypericum perforatum* L. liquid extract (identified as hyperoside t_R = 1.8 min, isoquercitrin and pseudohypericin t_R = 2.1 min, hyperforin t_R = 2.9 min, quercitrin t_R = 4.7 min, hypericin t_R = 6.8 min, quercetin and catehin t_R = 9.2 min); (B) *Hypericum perforatum* L. dry extract, (C) usnic acid, and (D) pharmaceutical product (mixture of *Hypericum perforatum* L. dry extract and usnic acid).

The quality of pharmaceutical product (mixture of *Hypericum perforatum* L. extract and usnic acid) was determined by FTIR method (Bomem MB-100 FTIR spectroscop equipped with a standard DTGS/KBr detector, Hartmann&Braun, Canada). The FTIR spectra as an average of 40 scans in the range 4000–400 cm^{-1}, with resolution of 2 cm^{-1}, were recorded at room (298 K) temperature. In the region all spectra were baseline-corrected and area-normalized. A Fourier self-deconvolution based on the Griffths/Pariente method was applied to enhance the resolution in a spectral region of 4000–400 cm^{-1}. A gamma factor of 12 corresponding to a peak width of 24 cm^{-1} was used. Deconvoluted spectra were smoothed by the 30-point Savitzky–Golay filter method. For a sample preparation the KBr pastille method was used. Fine pulverized, water-free samples (1 mg) were mixed with potassium bromide (150 mg, Merck) stored at 80°C for 6 h, and then pressed at 1000 MPa to obtain a transparent pellet. The reference measurement was performed with pure KBr. The dryness of the pastille was controlled using the Win-Bomem Easy software, by the band at cca. 1640 cm^{-1}, which is associated with the deformation vibrations of the O–H bond from water molecules.

RESULTS AND DISCUSSION

The HPLC chromatography method was developed to profile the major constituents of *Hypericum perforatum* L. extract. The objective was to simultaneously separate, identify and quantify hypericin and usnic acid using HPLC (Fig. 2). Quantification was performed using an external standardization method with reference standards. The method consisted of two protocols: one for the analysis of flavonoids and the other for the analysis of the usnic acid. Both protocols used a reverse phase C18 column. The separation of the flavonoids and the usnic acid was achieved within 10 min. The linear response range was established for

Table 1. Spectral ^{1}H NMR data (ppm) for usnic acid ($CDCb_3$, 400 MHz, ppm), assignments based on HMBC data

Position	δ_H	Assign.	HMBC	Position	δ_H	Assign.	HMBC
1	–	–	4-Me	1'	–	–	1'-OH
2	–	–	4'-Me, 4-Me, 3-OH	2'	7.32	Ar-H, H-2', 1H	–
3	–	–	4-Me, 3-OH	3'	–	–	4'-Me, 2'-H
4	–	–	4-Me, 3-OH 5-OH	4'	–	–	4'-Me, 2'-H
5	–	–	4-Me, 5-OH	5'	–	–	4'-Me
6	–	–	6-COMe, 5-OH	6'	–	–	6'-COMe, 2'-H, l'-OH
4-Me	2.08	H-9, 3H	–	6-COMe 6'-COMe	2.71	H-8, s, 3 H H-8', s, 3H	
3-OH 5-OH	5 95	Ar-OH, 1H	–	4'-Me	1.81	3H	–

Table 2. Approximate infrared band wavenumbers (cm^{-1}) and vibrational assignments for usnic acid

ν, cm^{-1}	Assignment	ν, cm^{-1}	Assignment
3100 vw, 3091 w, 3009 w, br	ν(CH) aromatic	1541 s, br, 1483 ms, sh	ν(C=C) aromatic
2983 w, 2930 m	ν(CH_3) asymmetric	1458 s, br, 1440 m, sh, 1376 m, 1358 w	δ(CH_2, CH_3)
2880 w, 2869 w, br	ν(CH_3) symmetric	1317w	Ring stretch
1716 w	ν(C=O) cyclic ketone	1291 vs, br, 1221 w	ν$(COC)_{as}$ aryl alkyl ether
1692 ms	ν(C=O) conjugated cyclic ketone	1191 vs, 1144 ms, 1118 ms	δ(OH) phenyl, in plane
1676 w, sh	ν(C=O) non-aromatic methyl ketone	1071 s, 1040 s, 992 mw, 959 mw, 931 w, 870 vw, 841 s, 733 w,	ν$(COC)_s$ aryl alkyl ether
1630 vs	ν(C=O) aromatic ketone	700 mw	δ(OH) phenyl, out of plane
1611 s,sh	Quadrant ring stretch	601 m	δ(OH) phenyl, out of plane

each compound and all had linear regression coefficient values greater than 0.97. Both protocols proved to be very specific for the constituents analysed.

The method was applied to evaluate the quality of *Hypericum perforatum* L. phyto-pharmaceutical preparation in order to test the method and investigate if they contain at least the main constituents and at what concentrations. The identification and adequate structure of isolated usnic acid (Fig. 1A) was confirmed by ^{1}H NMR and HMBC data (Table 1).

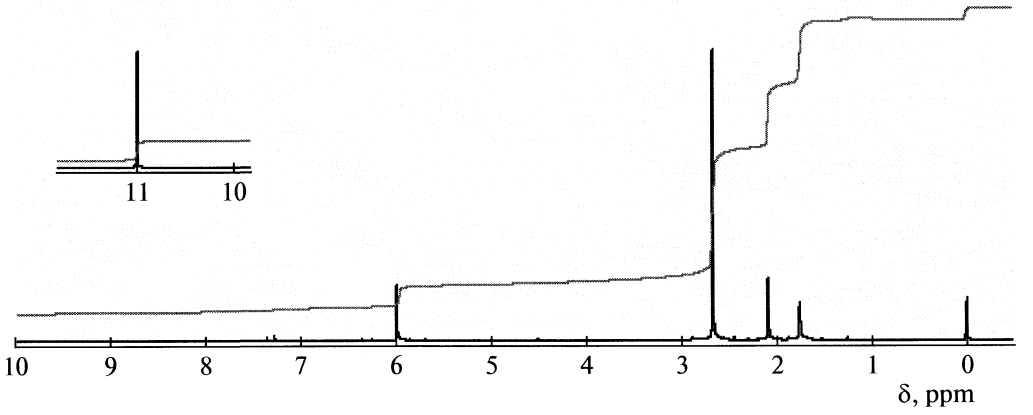

Fig. 3. Typical NMR spectrum of usnic acid isolated from *Usnea barbata*.

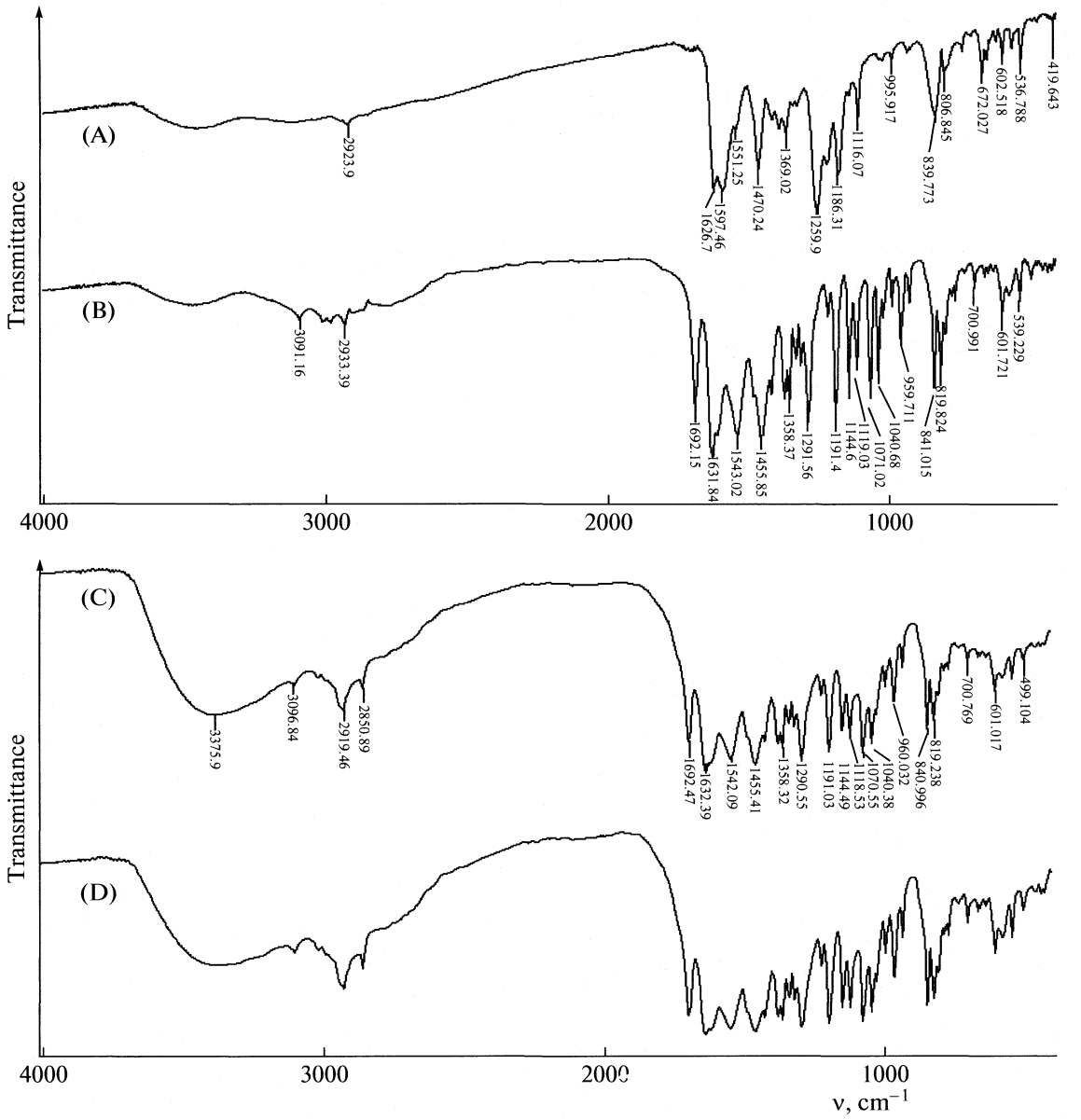

Fig. 4. Typical FTIR spectra of: (A) Hypericin standard, (B) Usnic acid isolated from *Usnea barbata*, and pharmaceutical preparation, i.e. mixture of hypericin and usnic acid in mass ratio of (C) 1:1 and (D) 1:3.

The adequate proton NMR spectrum of usnic acid is shown in Fig. 3. In the proton NMR spectrum, multiplet at 7.32 ppm was assigned to Ar–H proton. Singlet at 5.95 ppm was assigned to Ar–OH protons. The singlet at 2.71 ppm was assigned to two aromatic CO–CH_3 groups. In the NMR spectrum, a singlet at 2.08 ppm belonged to CH_3 protons which are bonded to ring A. The methyl protons were observed at 1.81 ppm as a singlet. In the proton NMR spectrum, the acidic proton signal was observed at 11.06 ppm.

The infrared spectrum of hypericin standard is shown in Fig. 4A. The infrared spectrum of isolated usnic acid is shown in Fig. 4B, with the wavenumber listing and vibrational assignments in Table 2. Here, it is possible to assign the conjugated cyclic ketone group to the 1692 cm^{-1} band. Weak bands at 1716 and 1676 cm^{-1} in the infrared spectrum are assigned to the ν(C=O) non-conjugated cyclic ketone and the non-aromatic methyl ketone, respectively. Conjugation, electron donating ring substituents and possible intramolecular hydrogen-bonding, all contribute to the lower wavenumber position of the aromatic methyl ketone to 1630 cm^{-1}. It is also possible to assign the antisymmetric and symmetric ν(COC) aryl alkyl ether modes to bands at approximately 1291 and 1071 cm^{-1}, respectively, with the aid of the infrared spectrum.

The FTIR analysis of pharmaceutical products (mixture of *Hypericum perforatum* L. extract and usnic

acid) showed no other signals within the analyte peaks (Fig. 4C, D).

CONCLUSION

The analysis and compatibility studies of the major natural origin active principles were performed for the some new antiseptic products based of *Hypericum perforatum* L. and lichen *Usnea barbata*. The identification and compatibility of *Hypericum perforatum* L. extracts with active solid state substance from lichen Usnea barbata, in various quantitative ratios, was confirmed by use of HPLC, FTIR and NMR spectroscopy. By correlation of spectroscopic data of initial reference compounds (usnic acid and hypericin) and their mixture, it was found that tested pharmaceutical product (mixture) retained physicochemical properties qualitatively and quantitatively.

REFERENCES

1. Nada Kovačević, Osnovi farmakognozije, Srpska školska knjiga, Beograd 2004.
2. S. Zlatković, S. Đorđević, G. Nikolić, *in Proceeding of the 7th Symposium Novel technologies and economic development*, (Leskovac Serbia, 2007), SEI-13, p. 208–209.
3. S. Zlatković, G. S. Nikolic, N. Nikolic, *in Proceeding of the 9th International Conference on Fundamental and Applied Aspects of Physical Chemisty,* (Belgrade Serbia, 2008), Vol. II, A-12-P, p. 735–737.
4. S. Zlatković, G. Nikolić, S. Đorđević, A Đorđević, *in Proceeding of the 5th International Conference of the Chemical Societies of the South-East European Countries. Chemical Sciences and European Crossroads, ICOSECS 5,* (Ohrid Macedonia, 2006), ACH-52, pp. 98–99.
5. G. Nikolić, S. Zlatković, S. Đorđević, Correaltion of bioactive components in the preparations for the treatment of throat diseases, *in Proceeding of the 7th Symposium Novel technologies and economic development,* (Leskovac Serbia, 2007), FKI/PCE-1, pp. 99–100.
6. M. Cocchietto, N. Skert, P. Nimis, G. Sava, Naturwissenchaften **89**, 137 (2002).
7. K. Ingolfsdottir, Usnic acid, Phytochemistry **61**, 729 (2002).
8. T. Kristmundsdottir, R. Aradottir, K. Ingolfsdottir, R. Ogmundsdottir, J. Pharm. Pharmacol. **54**(11), 1447 (2002).
9. Martindale, The Complete Drug Reference, Pharmaceutical Press, London 2005, p. 1711.
10. B. Proska, M. Sturdikova, N. Pronayova, T. Liptaj, Pharmazie **51**, 195 (1996).
11. C. Vijayakumar, S. Viswanathan, M. Kannappa-Reddy, S. Parvathavarthini, S. Kundu, E. Sukumar, Fitoterapia **71**, 564 (2000).
12. Y. Yamamoto, Y. Miura, Y. Kinoshita, M. Higuchi, Y. Yamada, A. Murakami, H. Ohigashi, K. Koshimizu, Chem. Pharm. Bull. **43**(8), 1388 (1995).
13. J. Reichling, A. Weseler, R. Sailer, Pharmacopsychiatry **34**, 116 (2001).
14. C. M. Schempo, K. Pelz, A. Wittmer, E. Schopf, J. C. Simon, Lancet **353**, 2129 (1999).
15. O. Kelet, T. Bakyrel, S. Ak, A. Alpmar, Folia Veterinaria, **45**(1), (2001).
16. S. Glišic, S. Popadić, D. Skala, Chem. Ind. (Serb) **60**(3–4), 61 (2006).
17. M. Stanković, S. Stanković, Z. Djordjević, S. Djordjević, Yu Pat 43978 (1989).
18. S. Stanković, I. Djordjević, Z. Kocić, Pat WO 01/95900 and EP 1294373 (2001).
19. S. Stankovic, Z. Djordjevic, M. Stankovic, S. Djordjevic, Yu Pat P-2061/88 (1988).
20. M. Cakic, G. Nikolic, N. Nikolic, M. Stankovic, *in Proceeding of the III Symposium New technologies and economic development*, Faculty of Technology, (Leskovac Serbia, 1998), p. 74.
21. M. Stankovic, M. Randjelovic, Yu Pat 42564 (1981).
22. A. Smelcerovic, M. Spiteller, S. Zuehlke, J. Agric. Food Chem., **54**(7), 2750 (2006).
23. A. Smelcerovic. S. Djordjevic, Z. Lepojevic, D. Velickovic. J. Serb. Chem. Soc. **67**(6), 457 (2002).
24. F. Liu, C. Ang, J. Chromatography, **888**(1–2), 85 (2000).
25. D. Sladic, V. Beljanski, B. Prelesnik, G. Bogdanovic, I. Ivanovic, K. Andjelkovic, J. Serb. Chem. Soc. **63**(3), 171 (1998).
26. O. A. Luzina, M. P. Polovinka, N. F. Salakhutdinov, G. A. Tolstikov, Russ. Chem. Bull., Int. Ed., **56**(6), 1249 (2007).

ЖУРНАЛ ФИЗИЧЕСКОЙ ХИМИИ, 2009, том 83, № 9, с. 1793–1796

BIOPHYSICAL CHEMISTRY

УДК 541.64

ANTIOXIDANT ENZYMES EXPRESSION AND ACTIVITY IN LIVER OF STRESSED WISTAR RAT

© 2009 J. Djordjević, A. Nićiforović, and M.B. Radojčić

Laboratory of Molecular Biology and Endocrinology, VINCA Institute of Nuclear Sciences

P.O. Box 522, 11001 Belgrade, Serbia E-mail: marija@vinca.rs

Abstract – Altered activities of antioxidant defence system enzymes and the levels of free radicals scavengers have been found to correlate with various physiological or pathological conditions, including stress. The aim of this study was to determine the effects of chronic 21 day isolation stress on antioxidant enzymes (AOEs) expression and activity in Wistar rat liver tissue. The serum corticosterone (CORT) and glucose (GLU) levels were also measured, as one of the most important indicators of stress. Our data revealed that in chronic stress conditions, when both CORT and GLU were low, the AOEs expression was markedly induced. This increase in MnSOD, CuZnSOD, and catalase exhibited similar trend implying efficient detoxification of $O_2^{\cdot-}$ and H_2O_2. However, this trend was not followed by the respective enzyme activity. While the total SOD activity was induced by the stress, catalase activity remained unaltered. This discrepancy led us to a conclusion that chronic isolation stress may cause oxidant-antioxidant imbalance in rat liver tissue, favoring H_2O_2 accumulation.

INTRODUCTION

Stress has been recognized to affect the progression and severity of several diseases such as diabetes, hepatitis C, variety of skin diseases etc. The influence of stress on liver tissue is of particular interest from the clinical point of view because stress plays a potential role in aggravating liver diseases and hepatic inflammation in particular, probably through generation of reactive oxygen species [1]. Adaptation to neuroendocrine stress involves action of glucocorticoids (GCs), the hormones of hypothalamo-pituitary-adrenal (HPA) axis, which mediate central and peripheral recovery of organism's homeostasis. The main peripheral GCs target is liver, in which GCs stimulate metabolic processes serving to increase and/or maintain normal concentrations of blood glucose, thus providing other organs with energy necessary for successful adaptation [2]. Glucocorticoids induce anabolic effects in liver while catabolic in all other tissues. Although beneficial, the increased energy requirements are also followed by the enhanced production of potentially toxic reactive oxygen species (ROS) [3]. A physiological rate of ROS production activates cellular signaling pathways necessary for cell growth and proliferation, while an excessive production of ROS, overmatching the antioxidant capacities of the cell, leads to the state of oxidative stress. If the conditions of oxidative stress persist in prolonged time periods, they may lead to metabolic disturbances of cellular homeostasis, damage of cell structures, including lipids and membranes, proteins and DNA, and finally to cell death [4].

The cellular regulatory pathways activated by ROS involve action of antioxidant defence enzymes (AOEs) that may efficiently detoxify cells from transiently elevated ROS. Antioxidants are agents that scavenge ROS, prevent their formation, or repair the damage they cause. Superoxide dismutases catalyse the conversion of two superoxide molecules to hydrogen peroxide and molecular oxygen, while hydrogen peroxide is mainly eliminated by catalase and glutathione peroxidase. However, prolonged stress and constantly high (μM) concentration of ROS may compromise AOEs detoxifying capacity of cells, and thus influence energy/glucose production necessary for successful cell/organism adaptation. For certain liver diseases, defective HPA axis activation, which probably contributes to the exacerbation of the liver disease, has been reported [5]. The aim of the presented study was to characterize AOEs protein expression levels, as well as their enzymatic activity in Wistar rat liver under psychosocial type of prolonged stress by chronic 21 day isolation. Liver enzymes: CuZn-superoxide dismutase (CuZnSOD), Mn-superoxide dismutase (MnSOD), and catalase (CAT), were measured and their expression and activity were correlated with the input signal of serum GCs and the resulting glucose level. In the present study, we investigated the hypothesis that chronic psychosocial stress alters antioxidant enzyme activities in the liver and that these changes may be causally related to serum GC levels (corticosterone in rats).

Stress effect on serum corticosterone (c_1) and glucose (c_2) level

Parameters	Control	Chronic
c_1, ng/ml	137 ± 45	65 ± 28 ($p < 0.01$)
c_2, mmol/l	5.7 ± 0.8	3.4 ± 0.7 ($p < 0.001$)

Note. Results are presented as mean ±SD ($n = 4$).

EXPERIMENTAL

Animal care and treatment: All experiments were carried out on adult male Wistar rats (3 months old), weighing 330–400g. Animals were kept according to the standards of the Ethical Committee for the Use of Laboratory Animals of the VINCA Institute. For the experiment purpose the animals were divided into two groups: (a) unstressed animals-control group, and (b) animals subjected to chronic isolation stress by individual housing for 21 day.

Serum corticosterone and glucose level. After sacrifice, blood was immediately collected and blood serum was prepared by 15 min centrifugation at 3000 rpm. Serum corticosterone was determined by OCTEIA Corticosterone EIA kit, and blood glucose level was determined by Accutrend strips.

Preparation of liver cell extracts. Livers were perfused in situ, homogenized in buffer (containing 10mM TrisHCl pH 7.4, 0.32M sucrose and 5mM $MgCl_2$) using 20 strokes of Potter-Elvehjem homogenizer and lysed by ice-cold 1% Triton X–100 for 2 hours in the same buffer. After that, cell lysate was centrifuged at 12,000rpm for 15 min to obtain supernatant with cell extract. Protein concentration in the cell extract was determined by the method of Lowry et al. [6].

Western blot analysis. Cell extracts were denatured in sodium dodecyl-sulphate (SDS) containing buffer, separated by 7.5% SDS-polyacrylamide gel electrophoresis according to Laemmli [7], transferred to PVDF membranes, and probed with the specific primary antibodies: anti-MnSOD, anti-CuZnSOD, anti-catalase or anti-β-actin, and the secondary goat anti-rabbit IgG-HRP conjugate. Immunoreactive protein bands were detected by X-ray film and their quantification was performed by Image J PC software analysis.

Antioxidant enzymes activity. Total SOD activity was measured according to McCord and Fridovich [8], by following the inhibition of cytochrome c reduction. SOD activity was expressed as U/mg of protein. Catalase activity was determined by the method of Claiborn [9], using H_2O_2 as substrate. The disappearance of H_2O_2 was followed spectrophotometrically at 240 nm. Catalase activity was also expressed as U/mg of protein.

Statistical analysis: The data were presented as mean ±SD. Statistical significance was determined by Students t-test and accepted at the level $p < 0.05$.

RESULTS AND DISCUSSION

Since it is known that neuroendocrine stress may alter the level of corticosterone (CORT) in the blood serum and through it affect gluconeogenesis in the liver as well as glucose (GLU) levels in blood, we first determined both parameters (CORT and GLU) in Wistar rats subjected to chronic 21 day social isolation. The results indicated that serum CORT in the isolated animals was decreased below the level found in the control group (table). The decrese in CORT was also reflected in the decreased concentration of blood GLU (table). At the same time, the quantification of protein expression of the antioxidant enzymes (AOEs): Mn and CuZn-superoxide dismutases (MnSOD and CuZnSOD), and catalase (CAT) indicated that all three enzymes were increased under the chronic isolation stress (Fig. 1). Since the increased expression of AOEs is well known indicator of elevated ROS these data suggested that state of oxidative stress may exist under chronic isolation stress, i.e. under low CORT conditions. The observed increase in MnSOD, CuZn-SOD and CAT in chronic stress exhibited similar degree, which may imply efficient detoxification of $O_2^{\cdot}$ and H_2O_2 under these conditions.

However, the respective enzyme activities did not follow the same pattern. Thus, while the total SOD activity was induced by the stress, catalase activity remained unaltered (Fig. 2), which led us to a conclusion that chronic isolation stress may, even if the CORT was low, cause oxidant-antioxidant imbalance in rat liver tissue, favoring H_2O_2 accumulation. Accumulation of H_2O_2 may further be connected with the observed decreased level of blood glucose under the chronic stress since it is known that suppression of hepatic gluconeogenesis is also ROS-dependent [10]. Our results also suggested possibility that either H_2O_2 itself or OH^- which may be generated in vivo by H_2O_2 decomposition, may both cause direct damage to hepatic cell components, particulary to hepatic proteins since liver is known to be extremely protein-rich tissue. Consequently, the decreased activity of CAT found under chronic stress may result from CAT protein damage. Such inactivation of antioxidant enzymes as the one observed in the case of CAT, may further lead to the increment of lipid peroxidation levels especially in membranes and can play an important role in hepatic tissue injury in general.

HPA dysfunction or stress conditions missing CORT, such as those found in our experiments, are known to be associated with negative health outcomes due to another mechanism which involves immunosuppression [11]. In this case, the apparent discrepancy between the stress intensity defined by CORT level, and oxidative stress, defined by AOEs expression, may

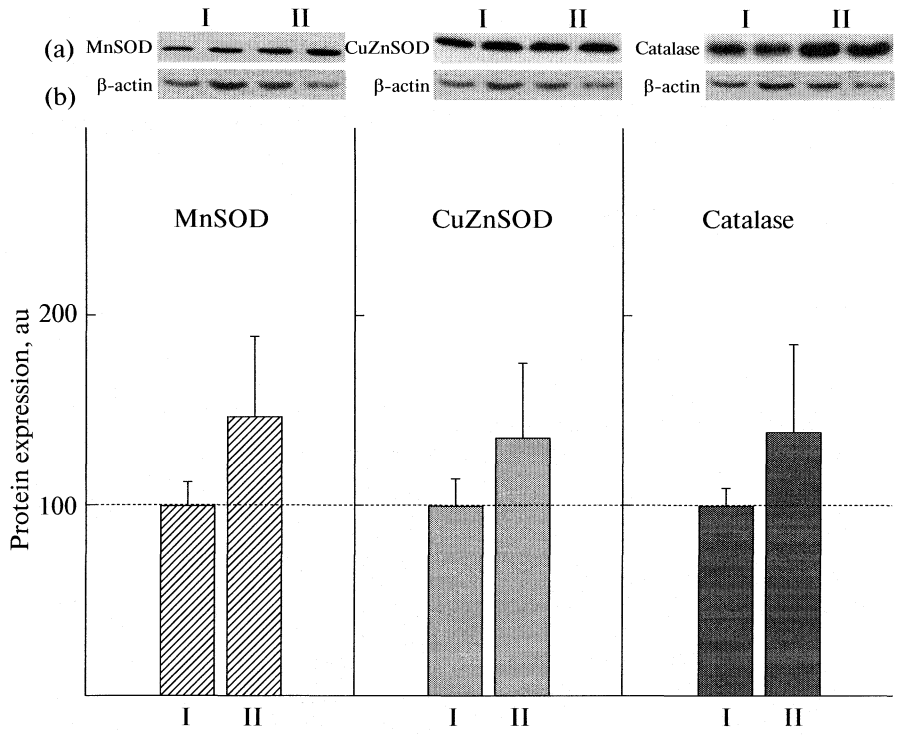

Fig. 1. Stress effect on antioxidant enzymes expression in rat liver: control (I) and chronic stress (II) measured by Western blot (a) and quantified by Image J analysis PC software (b). Results are presented as mean ±SD ($n = 4$), $p < 0.05$ for II.

be due to downregulation of AOEs through glucocorticoid receptor [12] or to altered activity of AOEs due to inhibitors, such as NO or H_2O_2 [13]. Namely, it is well known that low CORT may trigger NO synthesis and that nitric oxide interacts with the haem group of CAT, thus inhibiting its enzymatic activity, while keeping the overall protein or mRNA structure and expression intact [14].

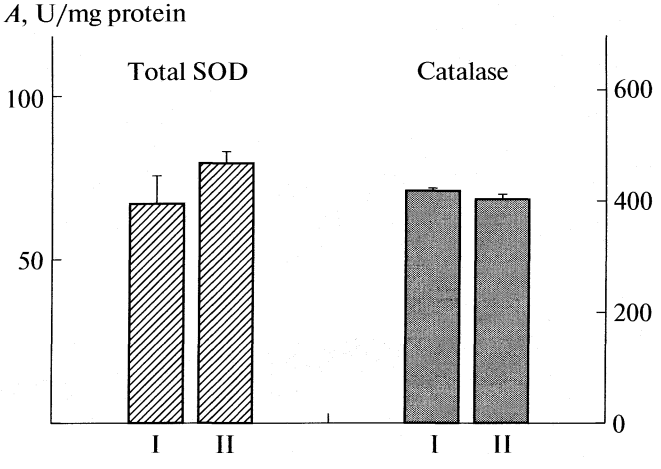

Fig. 2 Stress effect on antioxidant enzymes activity (A) of total SOD ($p < 0.05$) and catalase in rat liver: control (I) and chronic stress (II). Results are presented as mean ±SD ($n = 4$).

The medical significance of oxidative stress has become increasingly recognized to the point that it is now considered to be a component of virtually every disease process. The results of our study may contribute to future investigations related to stress-induced diseases.

CONCLUSION

Chronic psychosocial stress is acompanied by decrease in blood glucose (GLU) due to low CORT (i.e. decreased rate of gluconeogenesis) in rat liver, but is not followed with the respective decrease in antioxidant enzymes (AOEs) expression. These conditions may lead to oxidative stress by displacing the prooxidant-antioxidant balance of this defense system through increasing the prooxidants (enhanced production of H_2O_2 by SOD enzymes) while depleting the antioxidant capacity of catalase.

ACKNOWLEDGMENTS

This work was supported by the Ministry of Science and Technological Development of the Republic of Serbia, Grant No. 143042B.

REFERENCES

1. S.M. Zaidi, T.M. Al-Qirim and N. Banu, Drugs RD **6**(3), 157 (2005).

2. H. DeWulf and H. G. Hers, European J. Biochem. **2**(1), 57 (1967).
3. N. Lane, J. Theor. Biol. **225**(4), 531 (2003).
4. K. Hensley, K. A. Robinson, S. P. Gabbita, S. Salsman and R.A. Floyd, Free Radic. Biol. Med. **28**(10), 1456 (2000).
5. Y. Chida, N. Sudo and C. Kubo, J. Gastroenterol. Hepatol. **21** (1 Pt 2), 202 (2006).
6. O. H. Lowry, N. J. Rosebrough, A. L. Farr and R. J. Randall, J. Biol. Chem. **193**(1), 265 (1951).
7. U. K. Laemmli, Nature **227**(5259), 680 (1970).
8. J. M. Mc Cord and I. Fridovich, J. Biol. Chem. **224**(22), 6049 (1969).
9. A.Claiborne, Handbook of Methods for Oxygene Radical Research. 283 (1985).
10. Q. F. Collins, H.Y. Liu, J. Pi, Z. Liu, M. J. Quon and W. Cao, J. Biol. Chem. **282**(41), 30143 (2007).
11. C.L. Raison and A. H. Miller, Am. J. Psychiatry, **160**(9), 1554 (2003).
12. H. T. Kim, Y.H. Kim, J. W. Nam, H. J. Lee, H. M. Rho and G. Jung, Biochem. Biophys. Res. Commun. **201**(3), 1526 (1994).
13. Y.S. Kim and S. Han, Biol. Chem. **381**(12), 1269 (2000).
14. L. A. Sigfrid, J. M. Cunningham, N. Beeharry, S. Lortz, M. Tiedge, S. Lenzen, C. Carlsson and I. C. Green, J. Mol. Endocrinol. **31**(3), 509 (2003).

ЖУРНАЛ ФИЗИЧЕСКОЙ ХИМИИ, 2009, том 83, № 9, с. 1797–1800

OTHER PROBLEMS OF PHYSICAL CHEMISTRY

УДК 541.183

β-CAROTENE REMOVAL FROM SOYBEAN OIL WITH SMECTITE CLAY USING CENTRAL COMPOSITE DESIGN

© 2009 L. Rožić, S. Petrović, T. Novaković

ICh TM - Department of Catalysis and Chemical Engineering, University of Belgrade, Njegoševa 12, Belgrade, Serbia

e-mail: ljrozic@naosys.intm.bg.ac.rs

Abstract – In this study removal of β-carotene from soybean oil by adsorption on acid activated smectite clay from Serbia was investigated and a factorial 2^3 experimental design was applied. The effects of relevant factors, such as temperature, solid-to-liquid ratio and time, on removal of β-carotene were investigated. In order to check these factors and their effect on the removal of β-carotene, we have established a model of this technique following a methodological strategy using experiments design. The mathematical model is established using a central composite design. The model describes the changes of the measured responses of β-carotene removal efficiency according to the temperature, solid-to-liquid ratio and time. The graphical representation of this model in the space of the variables enabled us to define the optimum conditions of these parameters. The optimum conditions to obtain the maximum removal of β-carotene from soybean oil were a temperature of 80°C, a solid-to-liquid ratio of 1:25 and a time of 1255 s. Under these optimal conditions, the experimental values agreed with the predicted values, using analysis of variance, indicating a high goodness of fit of the model used and the success of response surface methodology for optimizing adsorption β-carotene of acid activated smectite clay from soybean oil.

INTRODUCTION

Clay minerals can be modified in different ways in order to obtain the desired properties. Acid activation of bentonite is an important process for modifying the physical and chemical properties of the clay. The chemical, surface and structural properties of activated clay determine and limit their potential applications [1]. Acid-activated bentonites are mainly used for the purification, decolorization and stabilization of vegetable oils. They remove phospholipids, soaps, trace metals, carotenoides, xanthophylls, chlorophyll, tocopherols, gossypol and their degradation products which impart undesirable colors to the edible oils [2–5]. The mechanism of retention of the pigments, including carotene and carotenoids, at the surface of an activated clay is not clear. The rate of adsorption is controlled by mass transfer, because the adsorption rate of β-carotene is very fast compared to its transfer from the bulk oil to the clay surface. The first fast step of adsorption represents the chemical interaction between the acid centers at smectite surface and β-carotene, while the second slow step may indicate physical adsorption of β-carotene on those molecules adsorbed during the first step. The heterogeneity of active centers explains the gradual increase of adsorption of β-carotene with temperature at different clay/oil ratios, because a proportion of these centers are activated at higher temperatures [6, 7].

A technique known as statistical design of experiments is a powerful technique for process characterization, optimization and modeling. It basically involves the process of planning and designing an experiment so that the appropriate data may be collected which then can be analyzed and interpreted, resulting in valid and objective conclusions.

Experiments in which the effects of more then one factor on response are investigated are known as factorial experiments. Central composite design using response surface methodology is a method suitable for identifying the effects of individual variables and for seeking the optimal conditions for multivariable system efficiency. This approach reduces the number of experiments, improves statistical interpretation possibilities and indicates whether parameters interact [8–10].

In this study removal of β-carotene from soybean oil by acid activated smectite clay was investigated using statistical design of experiments. The effects of temperature, solid-to-liquid ratio and time on removal of β-carotene were investigated. Response surface methodology was used to build a model between the β-carotene removal efficiency and these independent factors, and to optimize the adsorption conditions.

EXPERIMENTAL

Materials and Methods

Smectite clay from Serbia was used as the raw material. Chemical activation of smectite was carried out in glass reactor at 80°C, during 2.8 h with solid-to-liq-

Table 1. Variables and experimental design levels

Variable	Level				
	$-a$	-1	0	$+1$	$+a$
X_1, °C	52	60	72.5	85	94
X_2, s	57	500	1150	1800	2243
X_3	1 : 76	1 : 50	1 : 33	1 : 25	1 : 21

Table 2. Composition of the various runs of the central composite design, actual and predicted responses

Run	X_1	X_2	X_3	Measured RE, %	Predicted RE, %
1	–	–	–	65.10	64.68
2	+	–	–	79.03	77.10
3	–	+	–	79.13	71.27
4	+	+	–	83.70	83.69
5	–	–	+	96.56	92.64
6	+	–	+	94.22	94.62
7	–	+	+	96.67	99.23
8	+	+	+	96.64	101.21
9	$-a$	0	0	77.48	82.41
10	$+a$	0	0	97.12	94.52
11	0	$-a$	0	81.31	87.59
12	0	$+a$	0	95.47	98.68
13	0	0	$-a$	51.96	57.24
14	0	0	$+a$	98.43	95.49
15	0	0	0	94.22	93.14
16	0	0	0	94.55	93.14
17	0	0	0	94.22	93.14
18	0	0	0	94.28	93.14
19	0	0	0	94.32	93.14
20	0	0	0	94.78	93.14

uid ratio 1:4.5, with HCl concentration of 4.8 M [11]. Adsorption efficiency of acid activated smectite clay was evaluated by means of removal of β-carotene from soybean oil. The color changes in the treated oils were determined by using UV-visible spectrophotometer, Thermo Electron Corporation, Evolution 500, at the wavelength corresponding to the maximum absorbance of β-carotene, 455 nm.

Statistical Design of Experiments

The use of statistical design of experiments is advantageous as it allows one to obtain conditions through a relatively small number of systematic experiments. Using a proper design matrix one can obtain a regression equation, which highlights the effect of individual parameters and their relative importance in a given operation process. The interaction effects of two or more variables can also be known, which is not possible in a classical experiment.

The principal steps of statistically designed experiments are: determination of response variables, factors and factor levels, choice of the experiment design and statistical analysis of the data. Today, the most widely used experimental design to estimate main effects, as well as interaction effects, is the 2^n factorial design, where each variable is investigated at two levels. So, tree-factor-two level central composite design was employed in this study, requiring 20 experiments. The fractional factorial design consisted of eight factorial points, six axial points and six center points. The variable and their levels selected for the removal of β-carotene from soybean oil were: temperature (52–94°C), time (57–2243 s) and solid to liquid ratio (1:76, 1:21).

The regression equation developed from different sets of experiments shows the dependence of yield on individual parameters as well as interactions for simultaneous variations of parameters. An analysis of variance was used to determine whether the constructed model was adequate to describe the observed data. The R^2 statistic indicates the percentage of the variability of the optimization parameters that is explained by the model. Three-dimensional surface plot were drawn to illustrate the main and interactive effects of the independent variables on the dependent ones.

RESULTS AND DISCUSSION

In order to examine the main factors and their interaction for β-carotene removal from soybean oil by adsorption 2-level-3-factor central composite design (CCD) was applied. Temperature (X_1), contact time (X_2) and solid to liquid ratio (X_3) were chosen as independent variables to model. Variables and levels for the study are given in Table 1.

The experimental design matrix in coded form for three parameters X_1, X_2, X_3 based on CCD design and measured and predicted corresponding results (β-carotene removal efficiency) are shown in Table 2. The experiments were produced in random order and triplicate measurements of absorbance of β-carotene at 455nm were run on each experiment. β-carotene removal efficiency (*RE*) from soybean oil was determined from the following equation:

$$RE = 100(A_0 - A)/A_0, \quad (1)$$

where A_0 and A are the absorbance of the crude and bleached oil, respectively.

The predicted values were obtained by a model fitting technique using the software Design Expert version 6.0.6 and were seen to be sufficiently correlated with observed values. The best fitting model was determined by regression analysis. Fitting of the data to various model (linear, two factorial, quadratic and cubic) and their subsequent analysis of variance showed that

Table 3. Analysis of variance

Source of variance	Sum of squares	Degree of freedom	Mean of squares	*F*-Test	*P*
X_1	176.96	1	176.96	9.75	0.0081
X_2	148.57	1	148.57	8.19	0.0134
X_3	1765.62	1	1765.62	97.33	<0.0001
X_1^2	39.64	1	39.64	2.18	0.1632
X_3^2	511.82	1	511.82	28.21	<0.0001
X_1X_3	54.44	1	54.44	3.00	0.1068
Model	2675.65	6	445.94	24.58	<0.0001
Residual	235.83	13	18.14		
Lack of fit	235.58	8	29.45	583.47	<0.0001
Pure error	0.25	5	0.050		
Total	2911.48	19			

the β-carotene removal from soybean oil was suitably described with a quadratic polynomial model as follows:

$$Y = 93.14 + 3.60X_1 + 3.30X_2 + 11.37X_3 - \\ - 1.65X_1^2 - 5.93X_3^2 - 2.61X_1X_3, \quad (2)$$

where Y is response (β-carotene removal efficiency), and X_1, X_2 and X_3 are the coded variables for temperature, contact time and solid to liquid ratio, respectively.

Analysis of variance followed by Fisher's statistical test was applied to evaluate the significance of each variable. The F value is the ratio of the mean square due to regression to the mean square due to real error

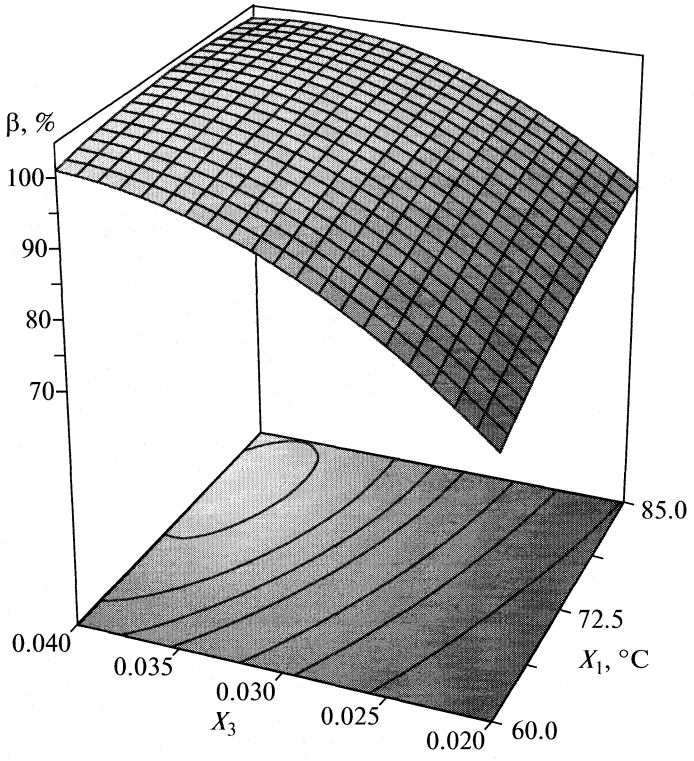

Response surface plot of β-carotene removal efficiency (β).

and indicates the influence (significance) of each controlled factor on the tested model. Values of probability $P > F$ less than 0.05 indicate that model terms are significant. The analysis of variance for the response surface methodology is shown in Table 3.

It was clear that, among the independent variables, X_1 and X_2 are had a significant effect and X_3 had a highly significant effect. They had a positive coefficient, which means that increasing their levels would increase the β-carotene removal efficiency. The coefficient, X_3^2 , for squer effects was highly significant in comparison with interaction effects.

The computed F-value of the model is very high compared with the tabular value, implying that the model is significant. The very small P-value (0.0001) and a suitable coefficient of determination (R^2 = = 0.9190) also show that the quadratic polynomial model is significant and sufficient to represent the actual relationship between the response and significant variable. P-values less than 0.05 indicate model terms are significant.

The 3D response surfaces and 2D contour plot are generally the graphical representation of the regression equation. This representation shows the relative effects of any two variables when the remaining variables are kept constant. Response surfaces plots to estimate β-carotene removal efficiency over independent variables are presented in Figure. Figure shows the effects of the interaction between temperatures and solid to liquid ratio on β-carotene removal efficiency, when the time is constant.

The response surface of mutual interaction between the variables is found to be elliptical. The maximum β-carotene removal efficiency is obtained when a) the temperature and solid to liquid ratio increase simultaneously, b) the temperature increases and the solid to liquid ratio remains unchanged in the interval 0.035–0.04 and c) the solid to liquid ratio increase and temperature remains stable from 72.5 to 85°C. As, a consequence, the best adsorption conditions for β-carotene were obtained at a temperature 80°C, a time of 1255 s and 1:25 of a solid to liquid ratio.

CONCLUSION

The present study has demonstrated the use of central composite design by determining the conditions leading to high β-carotene removal efficiency. The results clearly showed that response surface methodology is one the suitable methods to optimize the best operating conditions to maximize the β-carotene removal. An orthogonal central composite design is successfully employed for experimental design and analysis of the results. The R^2 value of 0.92 indicated a good fit of the model with experimental data.

Graphical response surface and contour plot was used to locate the optimum point. The results of the design showed that the optimal conditions to obtain the highest β-carotene removal efficiency were: a temperature of 80°C, a time of 1255 s and 1:25 of a solid to liquid ratio. These obtained results were important before detailed kinetics, mechanisms and optimization.

ACKNOWLEDGMENTS

This work was supported by the Ministry of Science of the Republic of Serbia (Projects number ON 142019B).

REFERENCES

1. Srasa E., Bergaya F., van Damme H., Arguib N. K., Applied Clay Science **4**, 411 (1989).
2. Boki K., Kubo M., Kawasaki N., Mori H., J. Am. Oil Chem. Soc. **69**, 372 (1992b).
3. Christidis G. E., Scott P. W., Dunham A. C., App. Clay Sci. **12**, 329 (1997).
4. Falaras P., Kovanis I., Lezou F., Seiragakis G., Clay Minerals. **34**, 221 (1999).
5. Zschau W., Euro. J. Lipid Science and Technology **103**, 505 (2001).
6. Kheok S. C., Lim E. E., J. Am. Oil Chem. Soc. **59**, 129 (1982).
7. Christidis, G.E., Kosiari, S., Clays and Clay Minerals, **51**(3), 327 (2003).
8. Lazić, Ž., Design of Experiments in Chemical Engineering, ed. *Wiley-VCH Verlag GmbHCo. KGaA, Weinheim* (2004).
9. Ôayan, E., Bayramolu, M., Hydrometallurgy **57**, 181 (2000).
10. Gülßah Kirali, E., Laçin, O., Journal of Food Engineering, **75**, 137 (2006).
11. Novaković, T., Rozić, Lj., Petrović, S., Rosić, A., Chem. Engin. J. **137**, 436 (2008).